A Combined ν_μ and ν_e Oscillation Search at MiniBooNE

Jocelyn Rebecca Monroe

Submitted in partial fulfillment of the
requirements for the degree
of Doctor of Philosophy
in the Graduate School of Arts and Sciences

COLUMBIA UNIVERSITY

2006

ABSTRACT

A Combined ν_μ and ν_e Oscillation Search at MiniBooNE

Jocelyn Rebecca Monroe

MiniBooNE seeks to corroborate or refute the unconfirmed oscillation result from the LSND experiment. If correct, the result implies that a new kind of massive neutrino, with no weak interactions, participates in neutrino oscillations. MiniBooNE searches for $\nu_\mu \rightarrow \nu_e$ oscillations with the Fermi National Accelerator Laboratory 8 GeV beam line, which produces a ν_μ beam with an average energy of $\sim$0.8 GeV and an intrinsic ν_e content of 0.4%. The neutrino detector is a 6.1 m radius sphere filled with CH_2, viewed by 1540 photo-multiplier tubes, and located 541 m downstream from the source. This work focuses on the estimation of systematic errors associated with the neutrino flux and neutrino interaction cross section predictions, and in particular, on constraining these uncertainties using in-situ MiniBooNE ν_μ charged current quasi-elastic (CCQE) scattering data. A data set with $\sim$100,000 events is identified, with 91% CCQE purity. This data set is used to measure several parameters of the CCQE cross section: the axial mass, the Fermi momentum, the binding energy, and the functional dependence of the axial form factor on four-momentum transfer squared. Constraints on the ν_μ and ν_e fluxes are derived using the ν_μ CCQE data set. A Monte Carlo study of a combined ν_μ disappearance and ν_e appearance oscillation fit is presented, which improves the $\nu_\mu \rightarrow \nu_e$ oscillation sensitivity of MiniBooNE with respect to a ν_e appearance-only fit by 1.2 - 1.5σ, depending on the value of Δm^2.

Contents

List of Tables

List of Figures

Acknowledgments

First, my sincere thanks go to the MiniBooNE collaboration, and especially its spokespeople Janet Conrad, Bill Louis, Steve Brice, and Richard Van de Water, whose dedication and hard work made my thesis possible. I am often impressed by the creativity and focus of my collaborators, and I thank you for four years of excellent questions, useful suggestions, and helpful comments on my analysis.

To my fellow students, especially Jen Raaf, Michel Sorel, Dave Schmitz, Ryan Patterson, Alexis Aguilar-Arevalo, and Kendall Mahn, it has been a privelege and an honor to be your colleague. I could not have done this without your help and encouragement, your sympathy, your expertise, and your code. You are the brightest and hardest-working group I could ever imagine, and a lot of your efforts appear in this thesis. Thank you. You made working on MiniBooNE fun, and I hope we work together again in the future.

I feel very fortunate to have had the opportunity to work with the post-docs in the Columbia neutrino group, Sam Zeller and Jon Link. You have been wonderful mentors, always willing to spend time discussing my problems, and usually key to solving them. You've taught me much of what I know about neutrino physics, data analysis, statistics, the weak interaction, and Italy. You have been a great source of inspiration for me, with your many references, good ideas, and practical jokes. Thank you.

To my Ph.D. advisors, being a member of the Columbia neutrino group has been a wonderful experience because you love what you do, you make every opportunity possible for your students, and you foster an enviroment of intellectual freedom. To my unofficial advisor, Professor Janet Conrad, you have taught me the importance of creativity in thinking about physics, how to communicate clearly, and the value of sheer determination. You inspired me to study physics as an undergraduate, and to pursue physics in graduate school at Columbia. I wouldn't be here if it weren't for you. Thank you. To my official advisor, Professor Mike Shaevitz, you have taught me how to think like a physicist, how to write code with (almost) no bugs, how to fit anything with Minuit, and never to put the fit parameters in the denominator of the χ^2 function. Most importantly, you have taught me that, from the right viewpoint, everything is simple. You always inspire me to do my best. Thank you.

Through my years as a graduate student, my family has been a constant source of support and encouragement, with boundless generosity, and unflagging interest in particles they can't see. To my in-laws, Eileen and Kevin O'Hagan, who sheltered, fed, and cheered me on through the dog-days of dissertation writing, thank you. To my parents, Joanne and Bob Ladenson, I gratefully acknowlege the two precious gifts you gave me, among many, that made this dissertation possible: my education, and the discipline to finish what I start. Thank you. And finally, to my wonderful husband, Morgan Wascko, thank you for the many hours of fruitful discussion about all aspects of the analysis, for proofreading every page of this thesis, for your unfailing empathy and support, and, especially, for putting up with me for the last four months. I feel that this is almost as much your achievement as it is mine.

Chapter 1

Introduction

In the Standard Model of particle physics neutrinos are massless particles, however, neutrino flavor oscillation data conclusively demonstrates the existence of neutrino mass. As such, massive neutrinos are the only experimentally verified occurrence of physics beyond the Standard Model at the present time.

Neutrinos are unique in the Standard Model for two reasons. First, they are the only nearly-massless fermions, lighter than the next-lightest particle, the electron, by at least 5 orders of magnitude. Second, only left-handed neutrinos have ever been observed, via their participation in weak interactions, and since neutrinos are now known to be massive, there must be right-handed neutrinos as well, if neutrinos are Dirac particles like all other constituents of the Standard Model. These strange properties of the neutrino sector raise a number of questions. Given that neutrinos do have mass, how is that mass generated, and why is it so small? Are there right-handed neutrinos, and if so, where are they?

The neutrino oscillation data pose these questions, and more, since all of the positive signals cannot be accomodated with only three neutrinos. The MiniBooNE experiment seeks to corroborate or refute the unconfirmed evidence that a new kind

of massive neutrino, which is "sterile", participates in neutrino oscillations.

1.1 Field Theory of Neutrino Mass

The Dirac Lagrangian for a spinor field Ψ is of the form

$$\mathcal{L} \;=\; i(\hbar c)\overline{\Psi}\gamma^{\mu}\partial_{\mu}\Psi \;-\; (mc^2)\Psi\overline{\Psi}. \tag{1.1}$$

The Euler-Langrange equation, applied to Ψ gives

$$\frac{\partial\mathcal{L}}{\partial(\partial_{\mu}\overline{\Psi})} \;=\; 0, \quad \frac{\partial\mathcal{L}}{\partial\overline{\Psi}} \;=\; i\hbar c\gamma^{\mu}\partial_{\mu}\Psi \;-\; mc^2\Psi$$

which is the Dirac equation for a massive spinor

$$i\gamma^{\mu}\partial_{\mu}\Psi \;-\; (mc/\hbar)\Psi \;=\; 0, \qquad \Psi = \begin{bmatrix} \Psi_R \\ \Psi_L \\ (\Psi^c)_R \\ (\Psi^c)_L \end{bmatrix} \tag{1.2}$$

The mass term for leptons in the Lagrangian density for the Standard Model, written in terms of the left and right-handed projections, is of the form

$$\mathcal{L} \;=\; m\Psi\overline{\Psi} \;=\; m(\overline{\Psi_R}\Psi_L + \overline{\Psi_L}\Psi_R) \tag{1.3}$$

following the notation of reference [1]. However, this is not the only Lorentz invariant quantity that is quadratic in the fields, and therefore there can be other mass terms. From the fermion fields $\Psi_L, \Psi_R, (\Psi^c)_L, (\Psi^c)_R$ and the adjoint fields, the unique and non-vanishing combinations are

$$(\overline{\Psi_L}\Psi_R + h.c.),\ ((\overline{\Psi^c})_R\Psi_L + h.c.),\ ((\overline{\Psi^c})_L\Psi_R + h.c.)$$

where $h.c.$ is the hermitian conjugate, and Ψ^c is the charge conjugate field. The most general free-field Lagrangian density for the field Ψ is

$$\mathcal{L} \;= \overline{\Psi}\gamma_{\mu}\partial^{\mu}\Psi + \; M_D[\overline{\Psi_L}\Psi_R + h.c.] + \frac{M_L}{2}[(\overline{\Psi^c})_R\Psi_L + h.c.] + \frac{M_R}{2}[(\overline{\Psi^c})_L\Psi_R + h.c.] \tag{1.4}$$

where the new constants M_D, M_L, and M_R have dimensions of mass, and correspond to the Dirac mass term, and the Majorana mass terms respectively.

In terms of the chiral fields f and F,

$$f \;=\; \frac{\Psi_L + (\Psi_L)^c}{\sqrt{2}} \qquad F \;=\; \frac{\Psi_R + (\Psi_R)^c}{\sqrt{2}}, \tag{1.5}$$

the Lagrangian density becomes

$$\begin{aligned} \mathcal{L} \;&=\; \overline{f}\gamma_\mu\partial_\mu f + \overline{F}\gamma_\mu\partial_\mu F + M_D(\overline{f}F + \overline{F}f) + M_L\overline{f}f + M_R\overline{F}F \qquad (1.6)\\ &= \overline{f}\gamma_\mu\partial_\mu f + \overline{F}\gamma_\mu\partial_\mu F + \left[\overline{f}, \overline{F}\right] \begin{bmatrix} M_L & M_D \\ M_D & M_R \end{bmatrix} \begin{bmatrix} f \\ F \end{bmatrix}. \end{aligned}$$

The neutrino mass matrix M is real and symmetric in this basis,

$$M \;=\; \begin{bmatrix} M_L & M_D \\ M_D & M_R \end{bmatrix} \tag{1.7}$$

and has eigenvectors ν' and N. In terms of the eigenvector fields, the Lagrangian density is

$$\mathcal{L} \;=\; \overline{\nu}'\gamma_\mu\partial_\mu\nu' + \;\overline{N}\gamma_\mu\partial_\mu N + M_{\nu'}\overline{\nu}'\nu' + M_N\overline{N}N, \tag{1.8}$$

which is the free-field Lagrangian for not one, but *two* particles, ν' and N, which are the mass eigenstates of the neutrino mass matrix.

The initial Dirac fermion field Ψ had four states: two spin states of a particle, Ψ_R and Ψ_L, and two anti-particle spin states $(\Psi^c)_R$ and $(\Psi^c)_L$. The defining characteristic of a Majorana particle is that it is CPT self-conjugate, i.e. $\Psi_L \;=\; (\Psi_L)^c$ and $\Psi_R \;=\; (\Psi_R)^c$ [2]. To respect the number of degrees of freedom of the initial Lagrangian, the mass eigenstates, ν' and N must each have only 2 spin states, and are therefore Majorana fermions. Hence, the additional Majorana mass terms in the Dirac Lagrangian split the four mass-degenerate states of the Dirac field Ψ into two non-degenerate Majorana fermions ν' and N.

Standard Model: Massless Dirac Neutrinos

In the Standard Model, with massless Dirac neutrinos, the left-handed neutrino field and lepton of the same family form an SU(2) doublet, while the right-handed lepton is an isosinglet. The first generation fields are:

$$\begin{bmatrix} \\ e_R \end{bmatrix}, \begin{bmatrix} \Psi_L \\ e_L \end{bmatrix}.$$

In this case, the neutrino mass eigenstates are degenerate, and there is no difference between the mass and flavor eigenstates, which are both are described by f in equation 1.5. Generalizing to three generations, an important consequence is that there can be no mixing whatsoever between the lepton families. For a Lagrangian density of the form $\mathcal{L} = \overline{\Psi}\gamma_\mu\partial^\mu\Psi$, there is no mixing between left and right handed states either, and so in addition to the mass and flavor eigenstates being identical, chirality is preserved as well. Therefore, electron number, muon number, tau number, and chirality are strictly conserved, separately, in weak interactions [3], and there can be no neutrino oscillations.

From the experimental point of view, the Standard Model contains no right-handed neutrino fields because neutrino mass had not been observed when the theory was constructed. From the gauge theory point of view, the Standard Model neutrino is massless because in the SU(2)×U(1) theory, there are no Lorentz invariant mass terms to which the Higgs can couple. From either vantage point, neutrino mass has now been observed, and must be accomodated in the theory. This can be done with extensions of the Standard Model in either the lepton or the Higgs sectors.

Beyond the Standard Model: Massive Neutrinos

If the Standard Model lepton sector is extended by adding Ψ_R, the fields of the first generation SU(2) doublets are

$$\begin{bmatrix} \Psi_R \\ e_R \end{bmatrix}, \begin{bmatrix} \Psi_L \\ e_L \end{bmatrix},$$

For massive Dirac neutrinos, M_L and M_R are zero in the neutrino mass matrix of equation 1.6, and the Lagrangian density is

$$\mathcal{L} \;=\; \overline{f}\gamma_\mu\partial_\mu f + \overline{F}\gamma_\mu\partial_\mu F + [\overline{f},\overline{F}] \begin{bmatrix} 0 & M_D \\ M_D & 0 \end{bmatrix} \begin{bmatrix} f \\ F \end{bmatrix}. \tag{1.9}$$

This Lagrangian density connects left and right handed components of the same fields since $f \sim (\Psi_L + (\Psi^c)_L)$ and $F \sim (\Psi_R + (\Psi^c)_R)$, and therefore the massive field terms are $\sim M_D(\overline{\Psi_L}\Psi_R + h.c.)$. The Lagrangian density, in terms of the flavor states, can be diagonalized with a change of basis to have mass eigenstates which are combinations of left and right handed fields as in equation 1.5. In terms of the flavor eigenstates, considering only the first two generations for simplicity, the mass term is [4]

$$\mathcal{L} \;=\; m_{\nu_e\nu_e}\nu_e\overline{\nu_e} + m_{\nu_\mu\nu_\mu}\nu_\mu\overline{\nu_\mu} + m_{\nu_e\nu_\mu}(\overline{\nu_e}\nu_\mu + \overline{\nu_\mu}\nu_e) \tag{1.10}$$

which can be diagonalized by the choice of bases

$$\nu_e \;=\; cos\theta\nu_1 + sin\theta\nu_2; \qquad \nu_\mu \;=\; -sin\theta\nu_1 + cos\theta\nu_2. \tag{1.11}$$

For $\theta \neq 0$, the mass eigenstates are not equal to the flavor eigenstates. Under this change of basis, $\mathcal{L}$ becomes the Lagrangian density for two particles, ν_1 and ν_2. These states evolve in time as

$$|\nu_e(t)> = \; cos\theta\; e^{-iE_1t}|\nu_1> + sin\theta\; e^{-iE_2t}|\nu_2> \tag{1.12}$$

$$|\nu_\mu(t)> = \; -sin\theta\; e^{-iE_1t}|\nu_1> + cos\theta\; e^{iE_2t}|\nu_e>;$$

where $E_1 = \sqrt{m_1^2c^2 + p^2c^2}$, $E_2 = \sqrt{m_2^2c^2 + p^2c^2}$, and p is the neutrino momentum. The ansatz is made that the momentum p of the mass eigenstates is the same, but the energies are different; an identical result is arrived at for the converse assumption. The original number of degrees of freedom in the Lagrangian have been preserved in this transformation since there were initially two flavor states, and here there are two mass eigenstates. Therefore, these are Dirac, not Majorana, neutrinos.

If $m_1 \neq m_2$, then the electron neutrino and muon neutrino flavor eigenstates propagate with different frequencies, which gives rise to the quantum mechanical phenomenon of neutrino oscillations [4]. The probability of oscillation between flavor states for a pure electron neutrino flavor state at time $t = 0$ is

$$P(\nu_e \rightarrow \nu_\mu) = |<\nu_\mu|\nu_e(t)>|^2 = sin^2 2\theta sin^2\Big(\frac{(E_2 - E_1)t}{2}\Big) \tag{1.13}$$

$$= sin^2 2\theta sin^2\Big(\frac{1}{4}\Delta m^2 \frac{L_\nu}{E_\nu}\Big),$$

with $\hbar = c = 1$, and the approximation that the energies of the propagating mass eigenstates i are $E_i = \sqrt{p^2 + m_i^2} \simeq p + \frac{m_i^2}{2p}$. The factor Δm^2 is $|m_2^2 - m_1^2|$, L_ν is the distance travelled by the neutrino between production and detection, and E_ν is the neutrino energy.

As a result, if the mass eigenstates are not equal to the flavor eigenstates, and the mass eigenstates are not degenerate, then even with purely Dirac mass terms, lepton flavor number is not individually conserved. The sum of the lepton numbers $L_{total} = L_e + L_\mu + L_\tau$ is conserved, since no leptons are disappearing into thin air, however, because neutrinos can oscillate between flavors, individual lepton number, e.g. L_e, is no longer conserved. While this is a departure from the Standard Model, is it not entirely unexpected, since there is no analogue of individual lepton number conservation in the quark sector. Instead, there is the larger symmetry of baryon number conservation.

Generalizing to three generations and assuming CP and CPT invariance, the probability for neutrino oscillations is [5]:

$$P(\nu_\alpha \rightarrow \nu_\beta) \;=\; \delta_{\alpha\beta} - 4\sum_{i>j}^{n} U_{\alpha,j}U_{\beta,j}U_{\alpha,i}U_{\beta,i}sin^2x_{j,i} \tag{1.14}$$

where α and β index the weak eigenstates (e, μ, τ), i and j index the mass eigenstates (1, 2, 3), n is the number of generations, U is the neutrino mixing matrix, and $x_{j,i}$ is the oscillation frequency given in terms of experimental quantities ($1.27\Delta m^2_{j,i}L_\nu/E_\nu$), where Δm^2 is the difference of the squares of the masses for eigenstates j and i, L_ν is the distance travelled by the neutrino between production and detection, E_ν is the neutrino energy, and the 1.27 comes from including factors of $\hbar$ and c. The unitary matrix U describes the mixing betwen the weak and mass eigenstates, which for three generations is given by:

$$U \;=\; \begin{bmatrix} U_{e1} & U_{e2} & U_{e3} \\ U_{\mu1} & U_{\mu2} & U_{\mu3} \\ U_{\tau1} & U_{\tau2} & U_{\tau3} \end{bmatrix}. \tag{1.15}$$

This matrix has six independent elements, which can be written in terms of mixing angles and complex phases [5]

$$U \;=\; \begin{bmatrix} 1 & 0 & 0 \\ 0 & c_{2,3} & s_{2,3} \\ 0 & -s_{2,3} & c_{2,3} \end{bmatrix} \begin{bmatrix} c_{1,3} & 0 & s_{1,2}e^{-i\delta} \\ 0 & 1 & 0 \\ -s_{1,2}e^{i\delta} & 0 & c_{1,3} \end{bmatrix} \begin{bmatrix} c_{1,2} & s_{1,2} & 0 \\ -s_{1,2} & c_{1,2} & 0 \\ 0 & 0 & 1 \end{bmatrix} \times \tag{1.16}$$

$$\begin{bmatrix} e^{i\frac{\alpha_1}{2}} & 0 & 0 \\ 0 & e^{i\frac{\alpha_2}{2}} & 0 \\ 0 & 0 & 1 \end{bmatrix}$$

where $c_{i,j}$ and $s_{i,j}$ are abbreviations for $sin\theta_{i,j}$ and $cos\theta_{i,j}$, θ are the mixing angles between mass eigenstates i and j, and δ, α_1, and α_2 are the matrix phases. If neutrinos are Dirac particles, then the matrix can be written in terms of only one phase, δ.

The question of why the neutrino masses are so much smaller than other fermion masses has not yet been addressed here, and purely Dirac mass terms in the Lagrangian density cannot solve this problem easily for the following reason. In a minimal extension of the Standard Model, which includes a Ψ_R field, the spontaneous symmetry breaking that leads to Dirac neutrino mass also leads to the fermion masses. The Yukawa coupling for a Higgs field Φ to the Dirac neutrino field Ψ is of the form $\overline{\Psi_R}\Phi\Psi_L$. One would expect that the Dirac mass M_D would be of the order of the symmetry breaking scale, that is, the non-zero vacuum expectation value of the Higgs field $\langle\Phi\rangle$. When SU(2) is spontaneously broken in this way, the fermions and weak gauge bosons acquire mass at this scale. If there are no non-zero Majorana terms in the neutrino mass matrix, then neutrinos also acquire a mass at the scale of the Dirac mass, which must be of the order of MeV. Since no MeV-mass neutrinos have been observed, there must be a mechanism for the suppression of fermion scale neutrino mass by many orders of magnitude [6].

The canonical mechanism for the suppression of neutrino mass involves an extension of the Standard Model in both the lepton and Higgs sectors, which requires the right-handed state Ψ_R and non-zero Majorana mass terms. If two new Higgs fields are introduced, Δ_R and Δ_L, in addition to the original field Φ, then the mass terms allowed by isospin invariance in the Dirac Lagrangian density are

$$\overline{\Psi_R}\ \Phi\ \Psi_L, \qquad (\overline{\Psi_L})^c\Delta_L\Psi_L, \qquad (\overline{\Psi_R})^c\Delta_R\Psi_R.$$

For the general free-field Lagrangian density of equation 1.4, when the SU(2) symmetry is spontaneously broken by non-zero vacuum expectation values of the Higgs fields, the terms quadratic in the neutrino field have $M_D \sim \langle\Phi\rangle, M_L \sim \langle\Delta_L\rangle$, and $M_R \sim \langle\Delta_R\rangle$. Constraints on the values of the additional Higgs fields' expectation values come from the ratio of the W boson mass to the Z mass, which effectively restrict $\langle\Delta_L\rangle$ and therefore M_L to be zero [7]. A second consideration comes from

the coupling of the right-handed Higgs field Δ_R to the gauge bosons: since no W_R is observed, the mass scale for the breaking of chiral symmetry must be much greater than that of the electroweak symmetry breaking, and so there is a hierarchy of the vacuum expectation values of the Higgs fields: $\langle\Delta_R\rangle \gg \langle\Phi\rangle$. It is conventional to take $M_R \gg M_D$. In this case, the neutrino mass matrix is of the form

$$M \;=\; \begin{bmatrix} 0 & M_D \\ M_D & M_R \end{bmatrix} \tag{1.17}$$

with eigenvalues

$$M_N \;\approx\; M_R, \quad M_{\nu'} \;\approx\; -\frac{M_D^2}{M_R} \tag{1.18}$$

and eigenvectors

$$N \simeq F + \frac{M_D}{M_R} f, \quad \nu' \simeq f - \frac{M_D}{M_R} F. \tag{1.19}$$

This result leads to the see-saw relation [8], which connects the neutrino mass scale to the Dirac mass scale of the quarks ($M_{quark} = M_D$):

$$M_\nu M_N \;=\; {M^2}_{quark}. \tag{1.20}$$

Therefore, with the addition of Higgs fields to generate the Majorana mass terms, the very tiny size of the neutrino mass can be motivated by having a right-handed neutral heavy lepton isosinglet. For example, if $M_\nu = 1\ eV$, and $M_{quark} = 200\ MeV$, then M_N must be $4 \times 10^{16}\ eV$.

With this potential solution to the problem of small neutrino mass, one might ask whether the addition of Majorana mass terms to the Standard Model Lagrangian density has any effect on the masses of other fermions. Fortunately, the answer is no, because Majorana particles are self-conjugate under CPT transformations, and therefore cannot carry electric charge. The quarks are charged, and so the addition of Majorana mass terms to the Standard Model Lagrangian affects only the neutrino sector.

If neutrinos are Majorana particles, then there are additional consequences beyond flavor oscillations in the neutrino sector. Rewriting the chiral states that can participate in the weak interaction in terms of the Majorana mass eigenstates gives, for example,

$$f \;=\; \nu' + VN; \quad V \;=\; \frac{M_D}{M_R}, \tag{1.21}$$

which contains both the left- and right-handed mass eigenstates ν and N of *one* generation, where $\nu_L \sim \nu'$ and $\nu_R \sim N$, with V setting the degree of mixing. There is, therefore, a small probability for the weakly interacting left-handed neutrino to oscillate into a right-handed neutral heavy lepton of the same flavor, given by [1]

$$P(\nu_L \rightarrow N_L) \;\approx\; V^2 \;=\; \frac{{M_D}^2}{{M_R}^2} \;=\; \frac{M_\nu}{M_N}, \tag{1.22}$$

which for the previous numerical estimate gives $V \;=\; 2.5 \times 10^{-8}$. Oscillation from $\nu_L \rightarrow \nu_R$ is equivalent to a matter - anti-matter oscillation, since for Majorana particles $\nu_R \;=\; -\,(\nu_L)^c$. This process violates lepton flavor number by 2 units, and so with the addition of Majorana mass eigenstates, lepton number conservation is completely violated, and not even the sum of the individual lepton numbers can be conserved.

In summary, the extension of the Standard Model to accommodate non-zero neutrino mass has a number of interesting implications that may be elucidated by testing individual and total lepton number conservation laws. Neutrino flavor oscillations are possible only if neutrinos have mass, the mass eigenstates have different masses, the mixing between mass and flavor eigenstates is non-zero, and right-handed neutrinos exist. Further, depending on whether the mass is Dirac or Majorana in nature, even more exotic transformations are possible. If neutrinos are Majorana particles, they may also oscillate between left-handed and right-handed, or matter and anti-matter states.

1.2 Experimental Evidence for Neutrino Mass

Conclusive evidence for neutrino mass was discovered in 1998 by the Super-Kamiokande experiment's observation of neutrino oscillations [9]. This phenomenon can only occur if neutrinos have mass, and their masses are different, as in equation 1.13. This was the result that convinced the particle physics community at large that neutrinos oscillate, and it inspired a generation of new experiments.

Neutrino oscillation experiments can use several different kinds of neutrino beams: those produced in collisions of cosmic rays with the earth's atmosphere, those produced in solar fusion processes, those produced in nuclear reactors, and those produced at accelerator facilities. The phenomenon of neutrino oscillations has been observed in all of these types of experiments, however, the specific observations differ sigificantly. Combining oscillation measurements can map out the neutrino mixing matrix of equation 1.14, determine the neutrino mass hierarchy, and possibly even discover new physics in the neutrino sector. However, neutrino oscillation searches measure the mass difference Δm^2, rather than the neutrino mass itself, and so while oscillation experiments provide evidence of mass they cannot measure the absolute scale. Therefore, this type of experiment is an indirect search for neutrino mass.

Direct neutrino mass measurements are experimentally very difficult because neutrino masses are so small, of the order of eV or less. Direct searches have historically tried to measure neutrino mass using conservation of energy and precision measurements of the final state kinematics in weak decays. So far they have only set upper limits on the values of the neutrino masses. Another class of direct mass searches seeks to measure the Majorana mass term using the rate of neutrino-less double beta decay ($0\nu\beta\beta$). These measurements have also mostly resulted in upper limits, however, there is one controversial signal which indicates a non-zero Majorana mass.

Table 1.1: *Direct neutrino mass measurement results in units of eV. Table from reference [11]. References for each result are given in the text.*

ν_e	ν_e *Majorana*	ν_μ	ν_τ	$\sum_i m_i$
< 2.2	< 0.24	$< 0.17\times10^6$	$< 18.2\times10^6$	$<$ 0.7-1.0

Recently, precision astrophysical data have also been used to set limits on the sum of the neutrino masses. These measurements are in a sense both direct and indirect because while they have sensitivity to the absolute scale of neutrino mass, many theoretical assumptions about the evolution of the universe are necessary to extract a limit.

One additional constraint on the neutrino sector that is very important for neutrino mass searches is the limit on the number of weakly-interacting, or "active", neutrinos. The LEP experiments in combination measure this from the lineshape of the decay width of the Z-boson to be 2.92 ± 0.07. [10]. This constraint plays a role in combining measurements from oscillation experiments, and in model-building needed to interpret astrophysical data.

Direct Searches

The best current direct neutrino mass measurement results are summarized in table 1.1. These include limits on the ν_e mass from β-decay, limits on the ν_μ mass from π decay, limits on the ν_τ mass from τ decay, as well as searches for Majorana mass, and astrophysical limits on the sum of the neutrino masses.

Direct searches for the mass of the ν_e use the β decay of tritium via ${}^3H \rightarrow {}^3He\ e^-$, where the underlying process is $n \rightarrow p\ e^-\ \overline{\nu}_e$. The electron kinetic energy spectrum

can be predicted analytically,

$$\frac{d\Gamma}{dE} = N\frac{G_F^2}{2\pi^3\hbar^7c^5}cos^2(\Theta_c)|\mathcal{M}|^2F(E,Z+1)\cdot p(E+m_Ec^2)\cdot \sum_{i,j}P_i(E_0-V_i-E)\cdot|U_{e,j}|^2\sqrt{(E_0-V_i-E)^2-m^2(\nu_j)c^4} \quad (1.23)$$

where N is the number of parent nuclei, G_F is the Fermi constant, Θ_c is the Cabibbo angle, $\mathcal{M}$ is the nuclear decay matrix element, $F(E,Z+1)$ is the Fermi function, p is the electron momentum, m_e is the electron mass. P_i is the probability to find a final state with a daughter nucleus with excitation energy V_i, and $|U_{e,j}|^2$ is the probability to find a neutrino in mass eigenstate $m(\nu_j)$. E_0 is the endpoint of the electron spectrum in the case of $m_\nu = 0.0$, which is the Q value of the decay minus the energy of the daughter nucleus. By comparing the measured endpoint of the electron kinetic energy spectrum with E_0, experiments extract an upper limit on the $\overline{\nu}_e$ mass. The best limit comes from the Mainz experiment, which measures $m^2_{\overline{\nu}_e}$ = -1.6 $\pm$ $2.5_{stat.}$ $\pm$ $2.1_{sys.}$ eV^2/c^4, which is usually expressed as a limit $m_{\overline{\nu}_e} < 2.2\ eV$ at 95% confidence level [12]. The planned KATRIN experiment is projected to have sensitivity down to $m_{\overline{\nu}_e} = 0.3\ eV$ [18].

Direct mass searches for the ν_μ and ν_τ mass are based on a similar concept of precisely measuring the final state kinematics of weak decays and comparing with the predicted spectrum. The best ν_μ mass limit comes from high precision measurements of the μ^+ momentum in $\pi^+ \rightarrow \mu^+\nu_\mu$ decays from a stopped pion beam at the PSI. The experimental result is $m^2_{\nu_\mu} = -0.016 \pm 0.023\ MeV^2$, which is converted into an upper limit of 0.17 MeV at 90% confidence level [14] [1]. The experimental precision is limited by the muon momentum measurement accuracy. The ν_τ mass searches use the decays $\tau^- \rightarrow 2\pi^-\pi^+\nu_\tau$ and $\tau^- \rightarrow 3\pi^-2\pi^+(\pi^0)\nu_\tau$ at the ALEPH experiment. The

[1] This analysis assumed that the ν_μ is created in a mass eigenstate, which is not strictly correct now that neutrino oscillations have been conclusively established.

experimental result is derived from fitting the visible energy distribution as a function of invariant mass, with m_{ν_τ} as a free parameter. The final state identification and energy resolution of the detector are the limiting factors in the experimental precision. The resulting limit is $m_{\nu_\tau} < 18.2\ MeV$ at 95% confidence level [15].

The Majorana or Dirac nature of the neutrino is probed by neutrino-less double beta decay ($0\nu\beta\beta$) experiments, which seek to directly measure the Majorana mass component of the ν_e. Double beta decay is a rare process predicted by the Standard Model weak interaction in which a nucleus that is stable against single beta decay can decay by a double weak interaction via $A(Z,N) \rightarrow A(Z+2,N-2)+2e^- + 2\overline{\nu_e}$. Typical nuclei that posess this property are ^{76}Ge, ^{100}Mo, and ^{82}Se. This process changes the charge of nucleus by 2 units, and two neutrinos are emitted. Neutrino-less double beta decay measurements search for interactions where no neutrinos emerge. If neutrinos have non-zero Majorana mass, the emitted $\overline{\nu}_e$ from the first beta decay can interact as a ν_e within the nucleus and instigate the second beta decay signature via $\nu_e n \rightarrow e^- p$. This requires Majorana mass because for the neutrino to interact as both $\overline{\nu}_e$ and ν_e it must be its own anti-particle. The Majorana mass experiments measure the half-life for ($0\nu\beta\beta$) $[T^{0\nu}_{1/2}]^{-1}$, which depends on the "effective" Majorana mass $\langle m_\nu \rangle$ via

$$[T^{0\nu}_{1/2}]^{-1} \ = \ G^{0\nu}(E_0,Z)|\langle m_\nu \rangle|^2 |M^{0\nu}_f - \left(\frac{g_A}{g_V}\right)^2 M^{0\nu}_{GT}|^2 \tag{1.24}$$

where $G^{0\nu}(E_0,Z)$ is related to the kinematic phase space for the decay, $\left(\frac{g_A}{g_V}\right)$ are the familar weak interaction axial and vector charges, and $M^{0\nu}_f$ and $M^{0\nu}_{GT}$ are nuclear decay matrix elements. The "effective" Majorana mass is really a sum over mass eigenstates [5]:

$$\langle m \rangle \ = \ \sum_i |U_{e,i}|^2 m_i \tag{1.25}$$

where i indexes the (Majorana) mass eigenstates m, and $U_{e,i}$ are the neutrino mixing matrix elements. These searches are quite difficult because very low noise conditions

are necessary, a large amount of data is required, and the matrix elements have large uncertainties of order 50%. The best limit is set by the Heidelberg-Moscow experiment, $\langle m \rangle < 0.2\ eV$ at 90% confidence level [19], however, a sub-set of this experiment also reports a positive signal, $0.11\ eV < \langle m \rangle < 0.56\ eV$ [20], which is very controversial [21]. The sensitivity of future $(0\nu\beta\beta)$ experiments is projected to be $\langle m \rangle \sim 0.01\ eV$ [22].

An interesting corollary is that Majorana mass terms in the neutrino mass matrix also cause the appearance of a right-handed isosinglet partner of the left-handed neutrino. Experimental searches for the neutral heavy lepton set an upper limit on the mixing probability V between ν and N, of $\sim 10^{-6}$ at $m_N = 5$ GeV, however, three anomalous events were observed in a 2 GeV - 10 GeV mass neutral heavy lepton search at the NuTeV experiment [23].

The sum of the neutrino masses can be inferred from astrophysical data combined with models for the evolution of cosmic matter density fluctuations. There are $\sim$100 ν/cm^3 in free space, and therefore even a small neutrino mass would have a significant impact on the matter distribution in the universe. Precision measurements of the matter density fluctuations are sensitive to the total mass of neutrinos because neutrinos tend to suppress small-scale fluctuations [24]. The degree of suppression depends on the mass of neutrinos as [25]

$$\frac{\Delta P_M}{P_M} \simeq -8\frac{\Omega_\nu}{\Omega_M} \tag{1.26}$$

where P_M is the power spectrum of matter density fluctuations, Ω_ν is the fraction of the universe's mass carried by neutrinos, and Ω_M is the total matter mass fraction. The absence of small-scale fluctuation suppression is interpreted as an upper limit on the sum of the neutrino masses. The current limit which is most model-independent is $\sum_i m_i < 2.1\ eV$ at 95% confidence level [16]. A more agressive limit can be

derived by using data other than the small-scale power spectrum to constrain model uncertainties, in this case the limit is $\sum_i m_i < 0.7\ eV$ at 90% confidence level [17].

With the exception of $0\nu\beta\beta$ searches, all of the direct neutrino mass measurements are sensitive only to Dirac neutrinos that interact via the weak interaction, that is, left-handed neutrinos that couple to the W and Z bosons. Neutrino oscillations and Majorana mass raise the possibility of right-handed neutrinos that mix only with the light, weakly interacting neutrinos. These hypothetical particles would be "sterile" in the sense that they would not participate in the weak interaction. In contrast to the direct neutrino mass measurements, oscillation searches are sensitive to "sterile" neutrinos, and in fact, require them to accomodate all of the current oscillation results.

Indirect Searches

Neutrino oscillation experiments typically cast their results in terms of the neutrino mass eigenstate difference Δm^2 and the degree of mixing between a particular mass and weak eigenstate, given by a mixing angle $\sin^2 2\theta$. These quantities are directly related to the mass eigenstates if only two are involved, however, they may be "effective" parameters, that is, useful for describing an experiment's observation but not the physical quantities involved in oscillations, in cases where more than two mass eigenstates participate. Different neutrino experiments are sensitive to different parameter combinations, due to the energy and composition of their neutrino beam, and the distance of the detector from the neutrino source.

Oscillation searches can be categorized experimentally as "appearance" or "disappearance:" in an "appearance" analysis one searches for the oscillation of one flavor into another, e.g. $\nu_\mu \rightarrow \nu_e$, while in a "disappearance" analysis the experimental observation is that the rate and/or energy spectrum of interactions of a particular flavor is reduced with respect to the expectation, e.g. fewer ν_μ are measured than expected.

In contrast to direct mass searches, neutrino oscillations can produce very large experimental signals, of the order of 50% effects, depending on the underlying oscillation parameters. The experimental constraints on the neutrino oscillation parameter space are summarized in figure 1.1, which includes the results from atmospheric neutrinos, solar neutrinos, reactor neutrinos, and accelerator neutrino experiments.

Atmospheric neutrinos typically travel a distance between production and detection of a few hundred km if coming from straight overhead (zenith angle of 0^o) or $\sim$10,000 km if travelling upwards through the earth (zenith angle of 180^o), and have energies ranging from sub-GeV to multi-GeV. Therefore, in the oscillatory term in the oscillation probablity, $sin^2\left(\frac{1.27\Delta m^2 L_\nu(km)}{E_\nu(GeV)}\right)$, Δm^2 must be of order 10^{-2}-10^{-3} for the term to be near a maximum. This roughly determines the oscillation parameter sensitivity of atmospheric neutrino experiments. Neutrinos produced in the atmosphere possess a very useful property for oscillation measurements, which is that the predicted ratio of of ν_μ to ν_e is well understood. When cosmic rays, which are mostly protons, interact with the atmosphere, they produce the following chain of reactions: (i) $pN \rightarrow \pi^\pm X$, (ii) $\pi^\pm \rightarrow \mu^\pm \overset{(-)}{\nu}_\mu$, (iii) $\mu^\pm \rightarrow e^\pm \overset{(-)}{\nu}_e \overset{(-)}{\nu}_\mu$. This chain of interactions produces 2 ν_μ flavor particles for each ν_e flavor. Therefore the accessible oscillation channels are $\overset{(-)}{\nu}_\mu$ disappearance, $\overset{(-)}{\nu}_e$ disappearance, and $\overset{(-)}{\nu}_\mu \rightarrow \overset{(-)}{\nu}_e$ oscillations, however, atmospheric neutrino detectors typically cannot distinguish ν from $\overline{\nu}$. To reduce the systematics associated with predicting the absolute rate of atmospheric neutrino production, experiments typically measure the ratio of the observed to predicted ν_μ:ν_e ratio, or the ratio of ratios. In the absence of oscillations this should 1.0, however, the Super-Kamiokande observation is that the ratio is 0.65-0.7. The conclusive piece of evidence for atmospheric neutrino oscillations was the observation of zenith angle dependence of the ratio of ratios consistent with the prediction of the oscillation hypothesis [9]. The current best measurement of the atmospheric neutrino oscillation

parameters is $1.5 \times 10^{-3} < \Delta m^2_{2,3} < 3.4 \times 10^{-3} eV^2$ and $sin^2 2\theta_{2,3} > 0.92$ at 90% confidence level, from the Super-Kamiokande experiment [26]. The subscript $(2,3)$ indicates that the oscillations observed by atmospheric neutrino experiments are primarily due to the participation of neutrino mass eigenstates 2 and 3 and $\nu_\mu \rightarrow \nu_\tau$ transitions.

Solar neutrinos travel much longer distances between production and detection, L$\sim 10^8$ km, and have very low energies $\sim$10 MeV, consistent with fusion products. The composition of solar neutrinos should be pure ν_e given the processes associated with solar fusion, and the predicted rate of solar neutrino production has very small errors because the visible luminosity, which is is strongly correlated with the fusion rate, is well measured. A deficit of solar neutrinos with respect to the predicted rate was first observed in the 1950s, and was termed the "solar anomaly" [27]. It was not until recently when experiments observed an energy spectrum deformation characteristic of oscillations that the "solar anomaly" was resolved. Historically, solar neutrino oscillation experiments could only detect ν_e and search for oscillations via ν_e disappearance, therefore they did not take advantage of the beam composition information. However, the recent SNO experiment was designed to measure not only the ν_e from the sun, but also search for solar ν_μ and ν_τ, which could only be produced by $\nu_e \rightarrow \nu_{\mu,\tau}$ oscillations. SNO observes a $\sim$50% deficit of ν_e with an energy spectrum consistent with the oscillation prediction, and a relative excess of ν_μ and ν_τ events combined [28]. In combination with previous solar neutrino experiments, this gives the best current measurement of the solar oscillation parameters, $\Delta m^2_{1,2} = 6.5^{+4.4}_{-2.3} eV^2$ and $tan^2 2\theta_{1,2} = 0.45^{+0.09}_{-0.08}$ at 1σ [29]. The subscript $(1,2)$ indicates that the oscillations observed by solar neutrino experiments are primarily due to the participation of neutrino mass eigenstates 1 and 2 and $\nu_e \rightarrow \nu_\mu$ transitions.

Reactor neutrino beams are very similar in energy spectrum to solar neutrinos,

because they are side-products of fission, with typical energies of a few MeV. Unlike solar neutrinos, reactor beams are composed exclusively of $\overline{\nu}_e$. An attractive feature of reactor neutrino beams is that the predicted energy spectrum has very small uncertainties. Reactor neutrinos are radiated isotropically, therefore detectors are usually sited within 1 km of the source, which determines the sensitivity to oscillation parameters. The experimental channel for oscillation searches is $\overline{\nu}_e$ disappearance, and until recently, reactor neutrino oscillation experiments had only set limits because they didn't see any signals. However, the KamLAND experiment, which was specifically designed to have sensitivity to the allowed solar oscillation parameter space and has a baseline of $\sim$180 km, observes a deficit with an energy spectrum consistent with oscillations in agreement with the solar oscillation results [30]. The current best oscillation parameter measurement from KamLAND in combination with the solar neutrino data is $\Delta m^2_{1,2} = 8.0^{+0.6}_{-0.4} eV^2$ and $tan^2 2\theta_{1,2} = 0.45^{+0.09}_{-0.07}$ at 1σ [29]

Accelerator neutrino experiments are unique in that they can control both the energy of the neutrino beam and the distance of the detector from the source. In principle this allows for more controlled experimental conditions. Accelerator neutrino beams are composed of either ν_μ or $\overline{\nu}_\mu$ from $\pi^\pm$ decays, with small backgrounds from $\overset{(-)}{\nu}_e$. The accessible experimental channels are $\overset{(-)}{\nu}_\mu$ disappearance, $\overset{(-)}{\nu}_e$ appearance, and possibly even ν_τ appearance. Only one short-baseline accelerator neutrino oscillation experiment has observed a signal: the LSND experiment, which searched for $\overline{\nu}_\mu \rightarrow \overline{\nu}_e$ in a $\overline{\nu}_\mu$ beam with $20 < E_\nu < 60$ MeV and an L_ν of 30 m, observes an excess consistent with $0.2 < \Delta m^2 < 10$ eV^2 over a range of $0.003 < sin^2 2\theta$ values < 0.03. The best-fit point is (Δm^2, $sin^2 2\theta$) = (1.2 eV^2, 0.003) [31], corresponding to an oscillation probability of $\sim$0.3%. Precisely which mass eigenstates are involved in the oscillations observed by LSND is unknown. Other short-baseline accelerator neutrino experiments did not observe signals and therefore set limits, none of which quite cover

the same region of parameter space as the LSND result. Two long-baseline accelerator neutrino experiments, both of which were designed specifically to have sensitivity to the allowed atmospheric oscillation parameter space, have observed oscillation signals. The MINOS experiment has an average E_ν of 7-10 GeV depending on the beamline configuration and a baseline L_ν of 735 km. Their observation is $\Delta m^2_{2,3} = 3.05^{+0.60}_{-0.55}$ $\times 10^{-3} eV^2$ and $sin^2 2\theta_{2,3} = 0.88^{+0.12}_{-0.15}$ at 1σ [32], which agrees within the experimental uncertainties with the atmospheric neutrino oscillation results. The K2K experiment has an average E_ν of $\sim$1.3 GeV and L_ν of 250 km, and observes an energy spectrum distortion consistent with $1.9 \times 10^{-3} < \Delta m^2_{2,3} < 3.5 \times 10^{-3} eV^2$ at $sin^2 2\theta_{2,3} = 1.0$ at 90% confidence level [33].

The results of all of the oscillation experiments are shown in figure 1.1. The regions of parameter space allowed by the positive signals are indicated by the enclosed shaded regions, and the experiments which set limits rule out the parameter space above and within the lines. With three neutrinos, there can only be 2 independent values of the oscillation parameter Δm^2, since $\Delta m^2_{1,2} + \Delta m^2_{2,3} \equiv \Delta m^2_{1,3}$. At present, there are three irreconcileable values of Δm^2 at $\sim 10^{-5}$, $\sim 10^{-3}$ and $\sim 1\ eV^2$, as figure 1.1 shows. One solution to this problem is that one of the experimental signals in incorrect. Both the solar and atmospheric signals have been confirmed by multiple experiments, however, the LSND signal has not. The purpose of the MiniBooNE experiment is to confirm or refute the LSND results. If MiniBooNE refutes LSND, then the neutrino oscillation picture is fairly well understood, with ($\Delta m^2_{1,2}$, $sin^2 2\theta_{1,2}$) and ($\Delta m^2_{2,3}$, $sin^2 2\theta_{2,3}$) measured by the solar/reactor and atmospheric/long-baseline accelerator experiments respectively. The remaining unknowns are the value of $sin^2 2\theta_{1,3}$, which is limited to be $\leq$0.032 [35], the neutrino mass hierarchy, and whether the phase of the neutrino mixing matrix is non-zero.

On the other hand, if MiniBooNE confirms LSND, the most straightforward

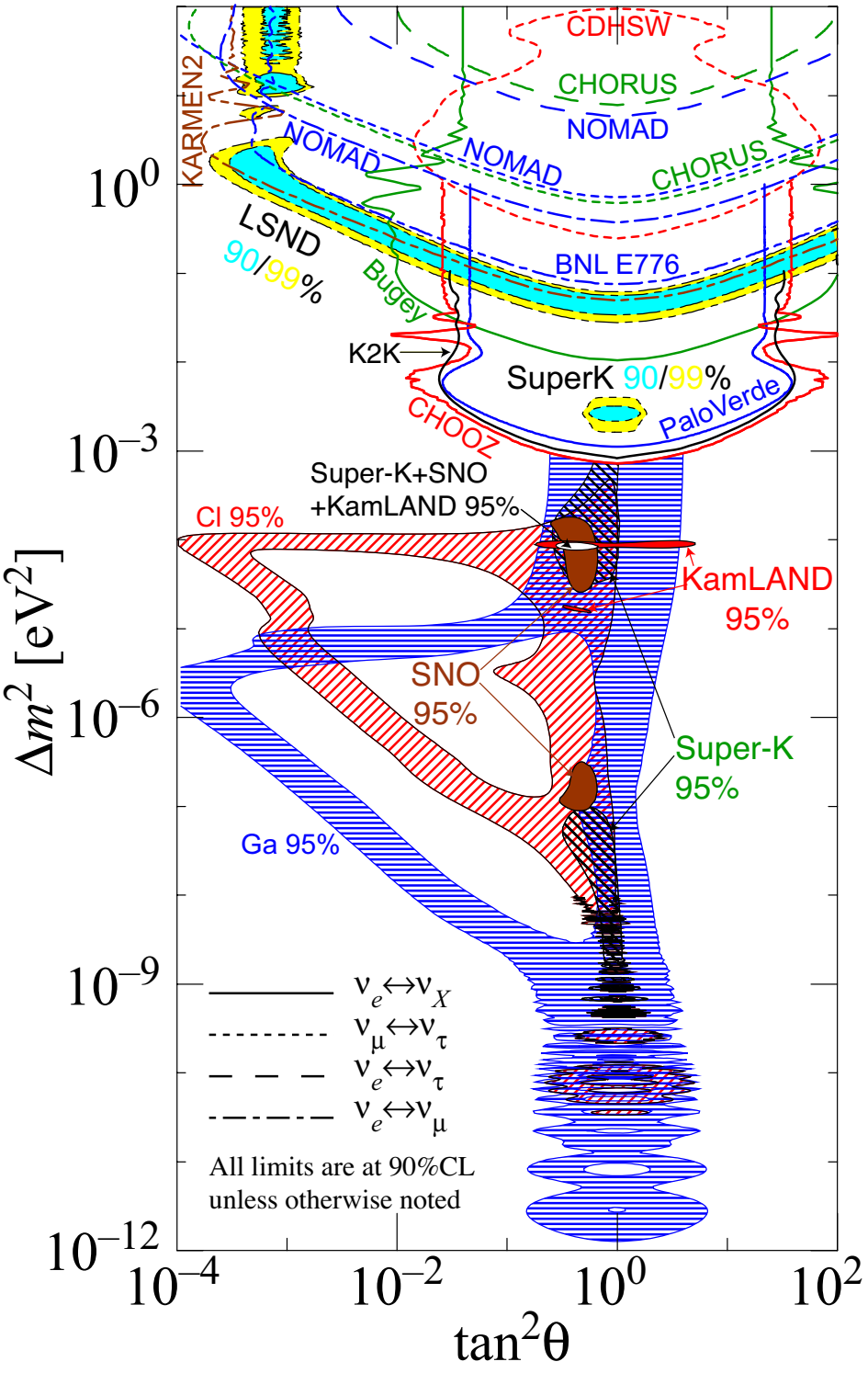

Figure 1.1: *Summary of neutrino oscillation results. Figure from reference [34].*

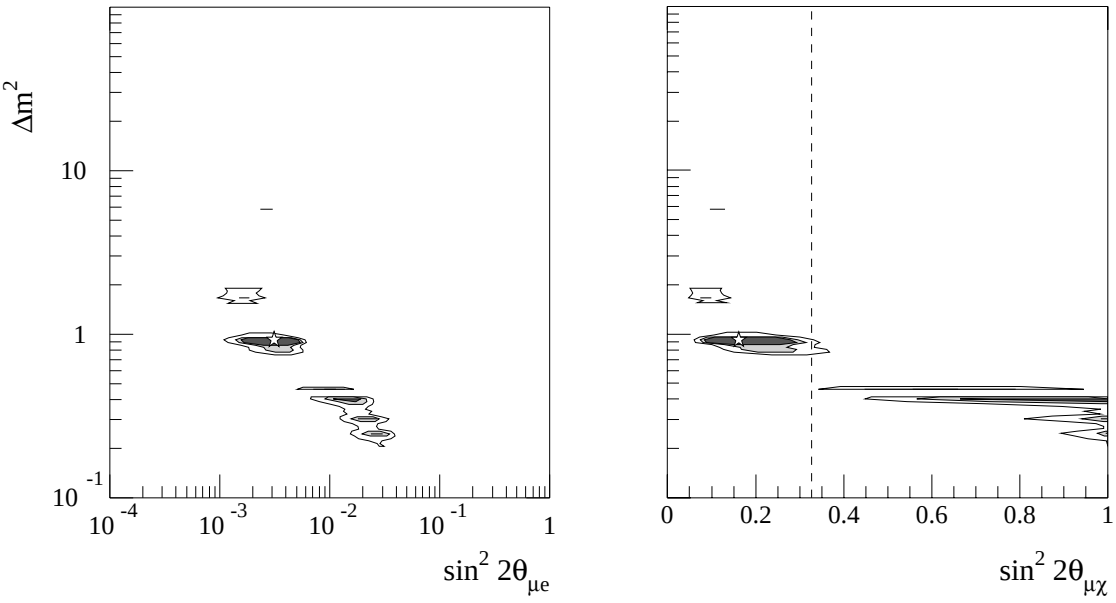

Figure 1.2: *Allowed parameter space in 3+1 sterile neutrino models from a joint fit to the null short-baseline and LSND data at 90, 95, and 99% confidence level, assuming statistical compatibility. Left: ν_e appearance via $\nu_\mu \rightarrow \nu_e$ Δm^2 (eV^2) vs. $sin^2 2\theta$. Right: ν_μ disappearance via $\nu_\mu \rightarrow \nu_4$ Δm^2 (eV^2) vs. $sin^2 2\theta$. Figures from reference [36].*

solution to the Δm^2 sum rule problem is to introduce a fourth or more neutrino participants in oscillations, which would allow at least three independent values of Δm^2. However, this neutrino would have to be "sterile" since the number of neutrinos that participate in the weak interaction is strongly constrained to be three by the precision electro-weak data from LEP [10]. These "sterile" neutrinos do not exist in the Standard Model of particle physics, and therefore a MiniBooNE confirmation of the LSND result would have profound implications.

In models with sterile neutrinos, the LSND observation is a product of two or more transitions. For example, for models with 1 sterile neutrino ν_s,

$$P_{LSND}(\nu_\mu \rightarrow \nu_e) \propto P(\nu_\mu \rightarrow \nu_s) \times P(\nu_s \rightarrow \nu_e). \tag{1.27}$$

In this case, the measured $sin^2 2\theta_{LSND}$ and Δm^2_{LSND} are really effective parameters describing the experimental observation, and do not correspond directly to two participating mass eigenstates. The neutrino oscillation probability in equation 1.14 is modified by changing n from 3 generations to 4, and the dimension of the mixing matrix U changes from [3×3] to [4×4]:

$$U = \begin{bmatrix} U_{e1} & U_{e2} & U_{e3} & U_{e4} \\ U_{\mu 1} & U_{\mu 2} & U_{\mu 3} & U_{\mu 4} \\ U_{\tau 1} & U_{\tau 2} & U_{\tau 3} & U_{\tau 4} \\ U_{s1} & U_{s2} & U_{s3} & U_{s4} \end{bmatrix}. \tag{1.28}$$

Models that add one sterile neutrino are highly constrained by the short-baseline accelerator experiment null results; the allowed regions for ν_e appearance and ν_μ disappearance are shown in figure 1.2. Models with more than one sterile neutrino are much less constrained [36].

1.3 The Search for Oscillations at MiniBooNE

MiniBooNE was designed to confirm or refute the LSND oscillation signal, with higher statistics and different systematics. MiniBooNE is located at the Fermi National Accelerator Laboratory, on the 8 GeV proton beam line, which produces a ν_μ beam with an average energy of $\sim$0.8 GeV. The neutrinos in the MiniBooNE beam come from the decays of mesons produced in collisions between the 8 GeV primary proton beam and a neutrino production target. The neutrino detector is located 541 m downstream from the neutrino source. The detector is an open volume tank of mineral oil, CH_2, viewed by photo-multiplier tubes, surrounded by an instrumented veto region. Neutrino interactions are detected primarily via the Cherenkov radiation and scintillation light creation by final-state particles. An overview of the experimental apparatus, the neutrino interaction reconstruction, and the detector calibration is given in chapter 2.

Two kinds of oscillation searches are possible at MiniBooNE: ν_e appearance, and ν_μ disappearance. These two analyses each have unique signals and backgrounds, and therefore have different systematic errors. Depending on the underlying oscillation physics, they may also be sensitive to different oscillation parameters. For example, in models with one sterile neutrino, ν_μ disappearance probes $\nu_\mu \rightarrow \nu_s$, while ν_e appearance depends on the product of $\nu_\mu \rightarrow \nu_s$ and $\nu_s \rightarrow \nu_e$.

The appearance analysis is the flagship measurement of MiniBooNE because, assuming CP conservation, $\nu_\mu \rightarrow \nu_e$ is the LSND signal channel. The analysis requires predicting both the ν_μ and ν_e components of the neutrino beam, then measuring the ν_e interactions in the detector and searching for an excess of ν_e due to $\nu_\mu \rightarrow \nu_e$ oscillations above background. The oscillated ν_e spectrum would have the energy distribution of the un-oscillated ν_μ events, and the number of oscillation ν_e events

would be determined by the size of the mixing angle $sin^2 2\theta$. In a two neutrino model where the participating states are ν_μ and ν_e, the observed number of ν_e from oscillations would be

$$N^{obs}_{\nu_e}(E_\nu) \;=\; N_{\nu_\mu}(E_\nu) \times P(\nu_\mu \rightarrow \nu_e) \tag{1.29}$$

$$=\; N_{\nu_\mu}(E_\nu) \times sin^2 2\theta \; sin^2\Big(\frac{1.27\Delta m^2 L_\nu}{E_\nu}\Big)$$

At MiniBooNE, where $< E_\nu > = \; 0.8 \; GeV$ and $L_\nu \; \simeq \; 0.541 \; km$, the first oscillation maximum occurs at $\Delta m^2 \; = \; 1.83 \; eV^2$. An oscillation signal near this Δm^2 would have a characteristic neutrino energy dependence, and therefore good neutrino energy resolution is important to the experimental oscillation sensitivity. For this reason, ν_e charged current quasi-elastic (CCQE) interactions are selected for the analysis, and good particle identification is important. For Δm^2 values above $\sim$10 eV^2, the oscillation frequency is too rapid for MiniBooNE to resolve the energy spectrum distortions. In this case, the oscillation sensitivity depends on the observed rate only. Overall, the appearance sensitivity at MiniBooNE depends approximately equally on the ν_e rate and energy distribution measurements.

The background comes from both intrinsic ν_e in the neutrino beam, and mis-identified ν_μ interactions. The intrinsic ν_e content of the MiniBooNE beam is $\sim$0.5%, which comes from the meson decays $K^+ \rightarrow e^+ \nu_e \pi^0$, $K^0_L \rightarrow e^\pm \pi^\mp \overset{(-)}{\nu}_e$, and $\mu^+ \rightarrow e^+ \nu_e \overline{\nu_\mu}$ in the neutrino beam line. The energy distribution of ν_e from kaon decays peaks at $\sim$1.5 GeV and falls off to the kinematic limit, $\sim$7 GeV. The energy distribution of ν_e from muon decays is peaked at $\sim$0.6 GeV, and, this source is the largest intrinsic beam background to oscillation signal events. The neutrino interaction processes that fake ν_e events in the detector mostly come from mis-identified neutral current π^0 production via $\nu_\mu n \rightarrow \nu_\mu n \pi^0$ and $\nu_\mu p \rightarrow \nu_\mu p \pi^0$, where the electromagnetic π^0 decay, $\pi^0 \rightarrow \gamma\gamma$, fakes the signature of a single electron in the detector. Another important

source of neutrino interaction background is from radiative delta decays, $\Delta \rightarrow N\gamma$, where the final state photon gets mistaken for an electron. The event selection cuts for the ν_e appearance analysis must both select ν_e CCQE events and get rid of mis-identified backgrounds at a very high level since the size of an LSND-like signal would comprise $< 1\%$ of the total neutrino interactions in MiniBooNE. Consequently the event selection cuts for the appearance analysis are very harsh: the efficiencies are $\sim$50% for the signal ν_e CCQE events, and $\sim$1% for the background, in the fiducial volume.

The most important sources of systematic error for the appearance analysis are related to the ν_e background predictions. The errors associated with predicting the intrisic beam ν_e rates and energy distributions come primarily from the uncertainties on the meson production cross sections. Particle production at 8 GeV proton kinetic energy historically is not well measured, and therefore the π^+, K^+, and K^0_L production have 10-30% uncertainties. The π^+ uncertainty determines the μ^+ error because the μ^+ are produced via $\pi^+ \rightarrow \mu^+\nu_\mu$. However, as shown in chapter 5, the π^+ rate can be constrained to high precision by the observed ν_μ events. The π^0 and radiative Δ decay background prediction errors come from the neutrino interaction cross section uncertainties. Before MiniBooNE, there were no measurements of neutral current π^0 production on carbon below $E_\nu = 2\ GeV$, and the radiative Δ decay had never been observed in neutrino-induced Δ production. Uncertainties on these processes derived from extrapolating measurements from past experiments are at the 50-100% level. Modelling the detector response is also an important component of the background uncertainties due to its effect on particle identification. MiniBooNE employs a number of in-situ calibration analyses to constrain the detector response prediction, which result in uncertainties of 5-10%.

If LSND-type oscillations occur, the disappearance signal in MiniBooNE can be as

large as ∼10%, compared with ∼1% effect in the appearance channel. This is because much larger mixing angles are allowed for ν_μ disappearance than ν_e appearance in models with sterile neutrinos, as figure 1.2 shows. The disappearance analysis depends on predicting the number of ν_μ produced in the neutrino beam, and measuring the number of ν_μ interactions in the MiniBooNE detector. If oscillations are occuring, then the number of observed ν_μ interactions would be less than the number predicted, and the energy spectrum may be modified. In a model with only two neutrinos, ν_μ and ν_s, the probability for ν_μ disappearance is $P(\nu_\mu \rightarrow \nu_s)$, and the observed ν_μ spectrum in the detector depends on the survival probability as

$$N^{obs}_{\nu_\mu}(E_\nu) = N_{\nu_\mu}(E_\nu) \times P(\nu_\mu \rightarrow \nu_\mu) = N_{\nu_\mu}(E_\nu) \times \Big[1 - P(\nu_\mu \rightarrow \nu_s)\Big] \quad (1.30)$$

$$= N_{\nu_\mu}(E_\nu) \times \Big[1 - sin^2 2\theta \; sin^2\Big(\frac{1.27\Delta m^2 L_\nu}{E_\nu}\Big)\Big]$$

As for ν_e appearance, the first oscillation maximum occurs at $\Delta m^2 = 1.83\ eV^2$. For values near to this Δm^2, oscillations would modify both the number and the energy distribution of detected muon-flavor neutrinos, and therefore ν_μ CCQE interactions are selected for the analysis. However, at high Δm^2, the survival probability reduces to $P(\nu_\mu \rightarrow \nu_\mu) = 1 - sin^2 2\theta \times \frac{1}{2}$, and so the oscillation sensitivity in this region comes entirely from the measured rate, since there would be no information contained in the detected E_ν spectrum.

The MiniBooNE neutrino beam is composed almost entirely of ν_μ type neutrinos, and ν_μ charged current interactions produce a clear signature: a muon in the MiniBooNE detector. Therefore, to first order, there are no backgrounds to the ν_μ disappearance analysis. However, the neutrino energy resolution affects the sensitivity to oscillations at low Δm^2, and therefore it is desireable to use only events where the E_ν reconstruction resolution is good. For this reason, the disappearance analysis uses charged-current quasi-elastic (CCQE) ν_μ interactions to search for oscillations.

Unfortunately, there is some background left after the ν_μ CCQE selection cuts due to charged current single pion (CC1π) production, where the π is absorbed inside the nucleus, or in the detector oil. These events fake the quasi-elastic final state, and therefore pass the selection cuts, but degrade the E_ν resolution. A set of selection criteria for ν_μ CCQE events is developed in chapter 4 of this thesis.

The most important systematic errors for the disappearance analysis are those related to predicting the ν_μ CCQE spectrum. These include the π^+ production cross section prediction, which has $\sim$10% uncertainty, the ν_μ CCQE and ν_μ CC1π cross sections, which have 10-20% uncertainties, and the detector response model, which has $\sim$5% effect on the muon energy scale and therefore on the reconstructed E_ν distribution. The relevant neutrino cross sections have been measured by several past experiments, but only for $E_\nu > 1\ GeV$. The uncertainty estimate is derived from extrapolating these higher-energy past measurements.

It is useful to categorize the disappearance systematics as normalization or shape contributions, since, unlike the appearance analysis, the disappearance sensitivity comes primarily from the distortion of the shape of the E_ν spectrum due to oscillations. The prediction for the overall rate of ν_μ CCQE events has a much larger uncertainty than the prediction for the shape of the E_ν distribution. In general this is because it is more difficult experimentally to measure absolute production rates than a bin-to-bin rate variation, and the ν_μ spectrum prediction uncertainties are mostly based on past cross section measurements.

In general, since MiniBooNE is an experiment with one detector, it relies on predicting the absolute flux, neutrino interaction cross sections, and detector response using data external to the experiment combined with Monte Carlo methods. The assumptions in the simulation of the experiment contribute most of the sources of systematic error for MiniBooNE. For the flux prediction, MiniBooNE relies on global

fits to data from past experiments to predict the π^+, π^-, K^+, and K^0_L meson production cross sections and to determine their uncertainties. A survey of the available data and the global fitting analysis are described in chapter 3 of this thesis. For the neutrino interaction cross section predictions, MiniBooNE uses a combination of previous measurements and theoretical calculations. For the detector response, a complete optical model for light propagation in the detector oil is employed, with free parameters measured in external specialty tests and where possible with MiniBooNE calibration data. These aspects of the simulation of the experiment are summarized in chapter 3.

Given the dearth of measurements from previous experiments of the important sources of systematic error for MiniBooNE, it is important to constrain the Monte Carlo predictions and associated uncertainties with in-situ data wherever possible. This project is the bulk of the work in this thesis. The overall strategy is to use the copious ν_μ data in MiniBooNE to check or tune the Monte Carlo predictions and constrain the uncertainties. Care must be taken to determine the sensitivity of each analysis to ν_μ disappearance, which, if LSND is correct, may occur at a non-negligble rate. The other major obstacle is the MiniBooNE blind analysis. In an effort to minimize bias in simulation tuning for the appearance analysis, ν_e data is sequestered, and therefore not available for constraining Monte Carlo predictions. Without reference to ν_e data, in-situ constraints on the flux predictions can be measured for all contributions to the neutrino flux with the exception of the K^0_L production. Similarly, the cross section predictions for the most important channels for the oscillation analyses can all be constrained without ν_e data, with the exception of the radiative delta decay branching ratio. Once the ν_e "box" is opened, the K^0_L and $\Delta \rightarrow N\gamma$ rates can be measured.

The ν_e from muon decay rate and uncertainty can be extracted with high precision

from the ν_μ data set, since the ν_e are produced via $\pi^+ \rightarrow \nu_\mu \mu^+$ followed by $\mu^+ \rightarrow e^+ \nu_e \overline{\nu_\mu}$, and the π^+-decay ν_μ comprise the vast majority of the MiniBooNE neutrino beam. This analysis uses the ν_μ CCQE selection described in chapter 4, which results in ∼100,000 events after cuts, with 90% ν_μ CCQE purity and 10% E_ν resolution at 1 GeV. The ν_e from μ decay constraint analysis comprises chapter 5 of this thesis. This analysis method is also used to extract a constraint on the ν_μ flux uncertainty for the appearance analysis.

The ν_e from K^+ decay can be constrained using the high energy ν_μ data, since 2-body K^+ decays can produce neutrino energies much higher than those of π^+-decay ν_μ at MiniBooNE; K^+ decay ν_μ dominate over π^+-decay ν_μ for energies above $E_\nu \simeq 2.25\ GeV$. MiniBooNE also has a beam line monitoring device that measures high angle muons, which are much more likely to come from kaon decays than pion decays. Both of these are primarily sensitive to the rate of kaon production, and therefore external input to constrain the shape of the K^+ spectrum at production is needed as well. A global fit to combine these two in-situ measurements with the external production data is described in appendix D.

The neutrino CCQE interaction cross section prediction comes from a theoretical model for neutrino scattering from a bound nucleon, with a few free parameters and form factors measured in electron-Carbon scattering data and/or light-target neutrino scattering data. The parameter uncertainties are derived from the spread in external measurements of the ν_μ CCQE cross section. The resulting CCQE cross section uncertainty is ∼10%. Constraining the cross section prediction and associated uncertainties using in-situ data is particularly important because CCQE interactions are the signal channel for both the ν_e appearance and the ν_μ disappearance oscillation searches. The high-statistics MiniBooNE ν_μ CCQE data set is used to measure the bound-nucleon CCQE cross section parameters and their uncertainties, as well as the

functional form of the axial form factor. This analysis is described in chapter 6. The measured values are rather different from the world light-target averages, but, these results are in good agreement with a recent Carbon-target measurement at $E_\nu = 1.2$ GeV from the K2K experiment [37].

A number of other cross section measurements have been made at MiniBooNE to constrain the predictions of the Monte Carlo. For the ν_μ disappearance analysis, the ratio of the inclusive cross section for the main background channel, resonant single π^+ production, to CCQE has been measured as a function of neutrino energy [38]. For the ν_e appearance analysis, the ν_μ neutral current π^0 cross section has been measured, as well as the ratio of resonant to coherent production channels [40]. Other measurements in progress include deep inelastic scattering, $\nu - e^-$ elastic scattering, and ν_μ neutral current elastic scattering cross sections.

Constraints derived from the ν_μ data can be incorporated in oscillation analyses in several ways. First, the MiniBooNE ν_μ data can provide in-situ constraints on the systematic errors associated with predicting the neutrino flux and interaction cross sections. In most cases, these systematic errors are smaller than uncertainties based on external data only. Second, fitting the ν_μ and ν_e data sets together in a simultaneous fit for ν_e appearance and ν_μ disappearance adds a strong constraint on the predicted systematic errors that are joint to the two analyses. These include the uncertainties associated with predicting the π^+ and K^+ fluxes and the neutrino CCQE interaction cross section. The impact of both of these approaches on MiniBooNE's ν_e appearance and ν_μ disappearance oscillation sensitivity is described in chapter 7.

Chapter 2

Overview of the Experiment

MiniBooNE is located at the Fermi National Accelerator Laboratory (FNAL) on the 8 GeV beam line, which transports protons from the Booster accelerator to a neutrino production target. From August 2001 through December 2005 MiniBooNE amassed 6×10^{20} protons on target in neutrino beam configuration, corresponding to ∼500,000 neutrino interaction candidate events contained in the MiniBooNE detector. From January 2006 through the present, MiniBooNE has collected 3.7×10^{19} protons on target in anti-neutrino beam configuration, corresponding to ∼8500 contained anti-neutrino interaction candidates. The experiment will continue to run in this mode for some time. The primary goal of MiniBooNE is to confirm or refute the LSND oscillation result with different systematic errors and higher statistics. To change the systematics, the MiniBooNE neutrino beam energy and baseline are an order of magnitude larger than those of LSND. To achieve higher statistics, MiniBooNE has amassed the world's largest data set of neutrino interactions in the 1 GeV energy range [41].

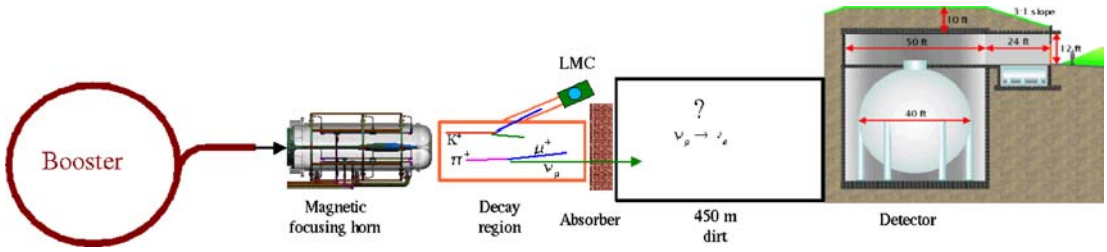

Figure 2.1: *Schematic of the MiniBooNE beam line, not to scale.*

2.1 Neutrino Beam

The MiniBooNE neutrino beam is produced from 8.89 GeV/c protons incident on a beryllium target located inside a magnetic focusing horn. A collimator and 50 m air-filled decay region follow, which is terminated by an iron and concrete absorber. The absorber and the neutrino detector are separated by a 450 m dirt berm. The center of the detector is located 541 m from the target face. A schematic of the beam line is shown in figure 2.1.

Typical proton beam operating conditions, determined by the FNAL Booster accelerator performance, are 4×10^{12} protons per pulse, at 3-5 Hz, with a beam uptime of $\sim$ 88%. The beam spill duration is 1.6 μs. The intensity of the proton pulse is measured by two toroids in the MiniBooNE proton beam line. This measurement is used to absolutely normalize neutrino events per proton, and is described in detail in appendix A. Figure 2.2 shows the accumulation of protons incident on the MiniBooNE target as a function of time. The drop in the neutrino interaction rate by a factor of $\sim$6 after January 2006 is due to MiniBooNE's change to $\overline{\nu}$ running mode.

The targeting efficiency, which describes the fraction of the proton beam that transits the entire length of the target, is determined by the proton beam location and angle of incidence at the face of the MiniBooNE target. The average position and angle of the beam at the target face depend on the proton beam line dipole mag-

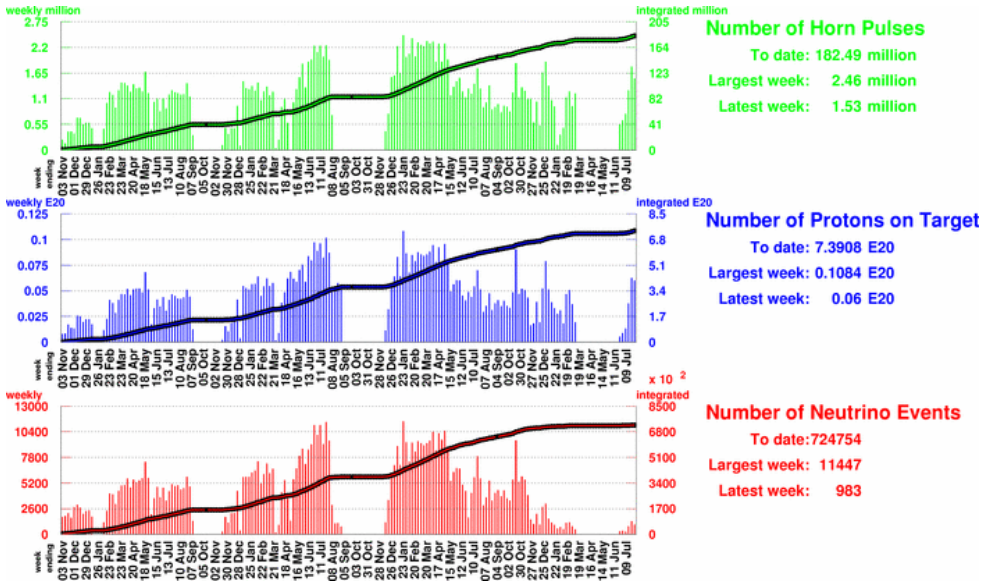

Figure 2.2: *Accumulation of protons on target (top), horn pulses (middle), and neutrino event candidates (bottom) since the start of the MiniBooNE neutrino run.*

net currents, which are changed continuously by an automatic tuning program [42]. Therefore, these quantities are measured on a pulse-by-pulse basis using beam position monitors. The beam widths in the plane perpendicular to the direction of motion depend on the quadrupole magnet currents, which are only changed during manual tuning. The widths are measured in a special beam line configuration in which multi-wire proportional chambers are inserted into the proton beam, which occurs approximately once every few months. The commissioning of the MiniBooNE proton beam line is described in detail in reference [43]. Typical beam parameters at the target face are summarized in table 2.1.

The beryllium target is 71 cm long and 1 cm in radius. The MiniBooNE proton beam line was designed such that all of the proton beam transits all of the target. In practice, a data quality cut is applied such that the measured targeting efficiency is $\geq$95%. The interaction length λ_I for protons in beryllium is 41.8 cm, therefore the fraction of the beam that interacts is $\sim$0.82, given by $(1 - exp[-71/\lambda_I])$. When

Table 2.1: *Typical proton beam parameters.*

quantity	x	y
beam center position	0.0 mm	0.0 mm
beam r.m.s. width	1.51 mm	0.75 mm
beam center angle	0.0 mr	0.0 mr
beam r.m.s. angle	0.66 mr	0.40 mr

protons interact in the target, the dominant processes are inelastic π^+ and K^+ production. From Monte Carlo simulations, the average multiplicity of π^+ (K^+) produced per event is $\sim$0.7 (0.05). The small radius of the target is designed to minimize absorption of these secondary pions. The inelastic interaction length for 2 GeV pions in beryllium is similar to that of protons, therefore a pion that transits the target radially has a $\sim$5% probabliity of being absorbed before escaping.

The target is situated inside an aluminum focusing horn, which produces a toroidal magnetic field in the plane perpendicular to the proton beam direction, which focuses secondary particles towards the beam axis. The inner conductor inner radius is 2.54 cm in the region surrounding the target, and the inner radius of the outer conductor is 30 cm. The horn is triggered to pulse with 170,000 A of current for each proton spill, producing a magnetic field of $\sim$1 T. The magnetic field was measured before installation, and found to follow the ideal radial field for a line current, $B(r) = \mu_0 I/2\pi r$ where r is the radial distance from the longitudinal axis of the horn, within the measurement precision of 10% [44].

The power supply for the horn can be set to either positive or negative polarity. For neutrino running, the polarity is set such that the horn focuses positive sign mesons, e.g. π^+, and defocuses the negative sign. For anti-neutrino running the

polarity is reversed. From systematic runs with the horn off, MiniBooNE determines that the horn (when on) increases the neutrino flux at the detector by a factor of ∼5. From Monte Carlo simulations of neutrino running, the horn acceptance includes ranges of meson production momenta and angles from $1 < p_\pi < 4\ GeV/c$ and $0 < \theta_\pi < 0.2\ radians$ respectively.

Mesons produced in the target and focused by the horn pass through a collimator with a 30 cm radius aperture, which is located ∼2 m downstream of the end of the horn, and decay in a 50 m long decay pipe with a radius of 90 cm. The collimator is used to localize the radiation produced by secondary particles which are destined to stop in the decay pipe walls. The limiting aperature for flux acceptance is the detector cross sectional area, which, when viewed from the target, subtends 0.011 $radians$. For small angles, $tan(\theta) \simeq \theta = (6.10\ m)/(541.00\ m) = 0.011$, where 6.10 m is the MiniBooNE detector radius, and 541.00 m is the distance from the upstream target face to the detector center. Therefore, only the most forward meson decays produce neutrinos that hit the MiniBooNE detector. The coordinates of a neutrino when it arrives at the detector with respect to its origin are

$$x = x^0 + (Z_{det} - z^0) \times \left(\frac{p_x^0}{p_z^0}\right), \qquad y = y^0 + (Z_{det} - z^0) \times \left(\frac{p_y^0}{p_z^0}\right) \tag{2.1}$$

$$r = \sqrt{x^2 + y^2}$$

where $(x^0,\ y^0,\ z^0)$ are the coordinates of the neutrino at production in cm with respect to the target face, $Z_{det} = 541.00\ m$ is the distance from the target face to the detector center, and $(p_x^0,\ p_y^0,\ p_z^0)$ are the components of the neutrino's three momentum at production. The Monte Carlo detector acceptance cut requires

$$r < R_{det}, \tag{2.2}$$

where $R_{det} = 6.10\ m$ is the radius of the cross sectional area of the detector, viewed from the target.

For two-body decays, there is a simple relationship between the energy of the neutrino and the energy of the parent meson, if one assumes that the meson is on-axis and that the decay angle with respect to the beam direction is zero:

$$E_\nu^{LAB} \;=\; \gamma_{meson} E_\nu^{CM} (1 + \beta_{meson}) \tag{2.3}$$

where E_ν^{LAB} is the ν energy in the lab frame, E_ν^{CM} is the ν energy in the meson center of mass frame, and γ and β are the usual relativistic factors for the parent meson. For π^+ (K^+), this relation gives a maximum ν_μ energy of $0.43 \times E_\pi$ ($0.9 \times E_K$). Thus, for a given meson energy, two-body K^+! decays can produce higher energy neutrinos than π^+ decays.

The π^+ and K^+ lifetimes are 26.03 and 12.37 ns respectively [45], and the fraction of mesons that decay over a distance of 50 m is $(1 - exp[-50.0/\gamma\beta c\tau])$ where τ is the meson lifetime. In the MiniBooNE beam line, the average energy of π^+ (K^+) that decay to neutrinos in the MiniBooNE detector acceptance is 1.89 (2.66) GeV. Therefore 41.6% (92.1%) decay before the end of the 50 m long decay region. The most relevant decay modes for MiniBooNE are $\pi^+ \rightarrow \mu^+\nu_\mu$, $K^+ \rightarrow \mu^+\nu_\mu$, which produce 99.4% of the neutrino beam, and $K^+ \rightarrow \pi^0 e^+ \nu_e$, $\mu^+ \rightarrow e^+ \overline{\nu}_\mu \nu_e$, $K_L^0 \rightarrow \pi^- e^+ \nu_e$, and $K_L^0 \rightarrow \pi^+ e^- \overline{\nu}_e$, which produce the remaining 0.4%. The resulting neutrino flux is shown in figure 2.3, which has an average neutrino energy of 0.8 GeV. The Monte Carlo simulation of the neutrino beam production is discussed in depth in chapter 3.

For the $\nu_\mu \rightarrow \nu_e$ oscillation analysis, the ν_e in the neutrino beam are usually termed "intrinsic" backgrounds. The ν_e background from μ decay can be constrained by measuring the ν_μ from π decay in the MiniBooNE detector. The ν_e from kaon decays are more problematic, and are addressed in several ways: ν_μ from two-body K decays are measured in the detector, and, μ from two-body K decays are measured in a dedicated neutrino beam line detector, the "Little Muon Counter" (LMC). By combining these measurements, MiniBooNE can constrain the overall rate of kaon

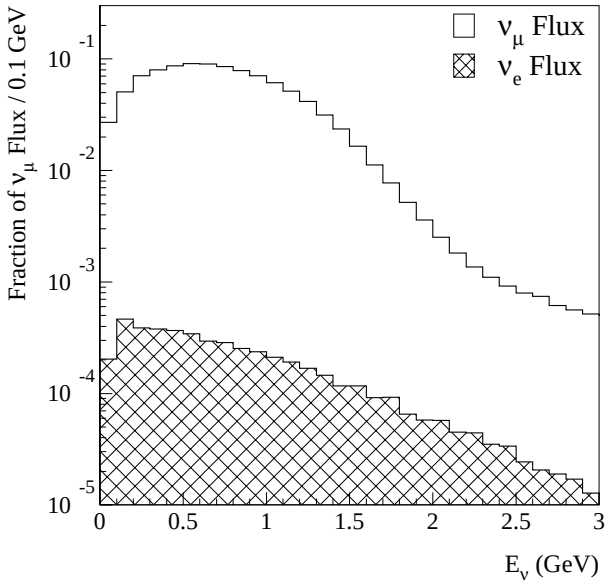

Figure 2.3: *Predicted ν_μ and ν_e flux distributions as a function of neutrino energy in MiniBooNE.*

production, and use a Monte Carlo simulation of the neutrino beam line to predict the ν_e background from K decays. Constraints on the intrinsic ν_e backgrounds based on MiniBooNE data are described in detail in Chapter 5.

2.2 Neutrino Detector

The MiniBooNE neutrino detector is a steel sphere of radius 610 cm, located beneath 3 m of soil shielding. The detector is filled with mineral oil (CH_2) which is both the neutrino target and the detector medium. The detector is divided into an inner sphere of radius 5.5 m, and an outer shell with outer radius 6.1 m. The two regions are separated by an optical barrier, but share oil circulation. The inside of the optical barrier is instrumented with 1280 inward-facing photo-multiplier tubes (PMTs) which view the detector fiducial volume. The outside of the optical barrier supports 240 pair-mounted PMTs, which view the outer shell of oil. This outer shell region is

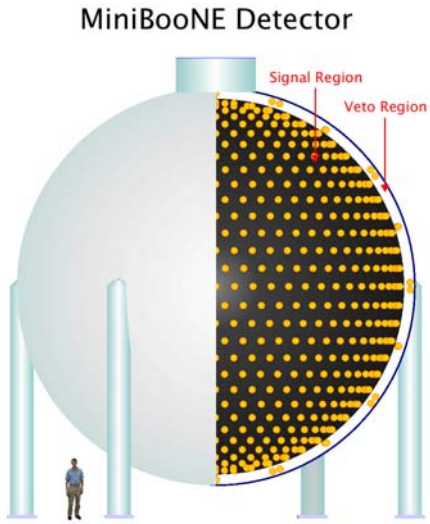

Figure 2.4: *Schematic of the MiniBooNE detector, not to scale.*

used to veto incoming particles, typically cosmic rays. A schematic of the detector is shown in figure 2.4.

When neutrinos interact in the detector, they may scatter off of 6 bound neutrons, 6 bound protons, or 2 free protons in the CH_2 molecule, or they may scatter coherently off the whole Carbon nucleus, or they may scatter off of the 6 electrons. At MiniBooNE neutrino energies, roughly 60% of the total neutrino interaction cross section is charged current neutrino-nucleon scattering, and 40% is neutral current neutrino nucleon scattering, shown in figure 2.5. In a ν_μ (ν_e) charged current interaction, the final state contains at least one μ^- (e^-) and some combination of neutrons, protons, and pions. In neutral current interactions, the final state contains the original neutrino, with a different energy in the interaction was inelastic, as well as nucleons and possibly pions. The existing cross section measurements in MiniBooNE's energy range are also superimposed in figure 2.5. The measurements that exist for exclusive channels have large error bars, and inclusive measurements are particularly scarce,

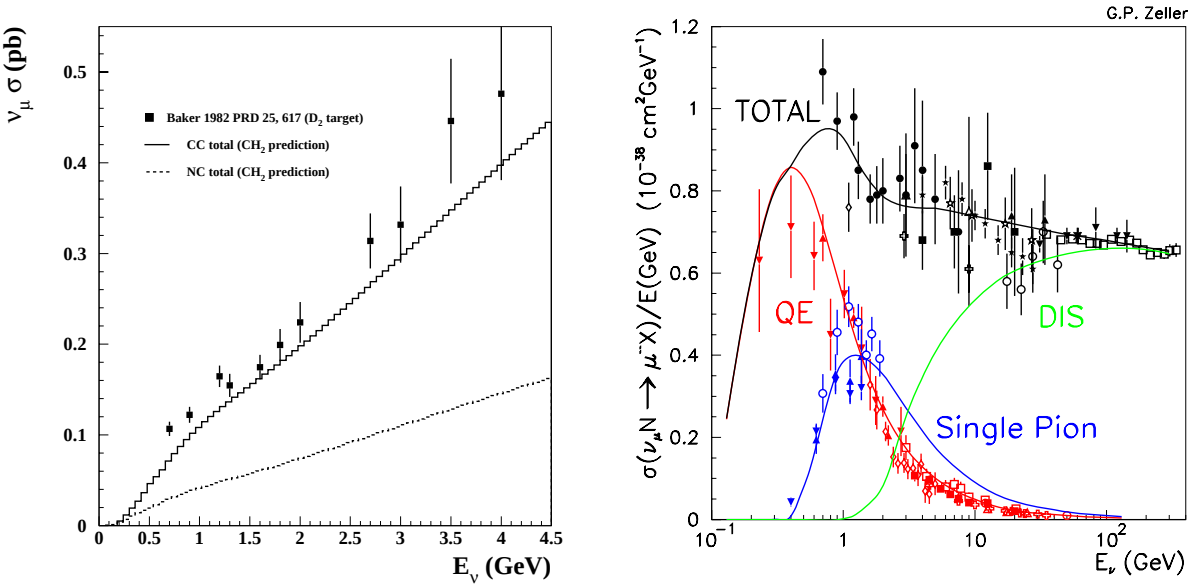

Figure 2.5: *Left: total charged and neutral current neutrino cross sections (GeV) vs. neutrino energy (GeV). Right: components of the charged current neutrino cross section divided by neutrino energy (pb/GeV) vs. neutrino energy (GeV). The solid lines in both panels show the NUANCE cross section Monte Carlo prediction for ν-D_2 scattering. This figure is from reference [46].*

for example, there are no measurements of the total neutral current cross section around $E_\nu \sim 1\ GeV$. A further difficulty with interpreting past data is that different neutrino flux and nuclear target corrections are applied by different experiments.

For the ν_e appearance oscillation analysis, the signal channel is charged current quasi-elastic (CCQE) scattering, $\nu_e n \rightarrow e^- p$, and the dominant background channel is neutral current resonant single pion production $\nu_\mu n(p) \rightarrow \pi^0 n(p)$. For the ν_μ disappearance oscillation analysis, the signal channel is also CCQE scattering, $\nu_\mu n \rightarrow \mu^- p$, while the most important background channel is charged current resonant single pion production, $\nu_\mu n(p) \rightarrow \pi^- \mu^+ p(n)$. The neutrino interaction cross section simulation is discussed in detail in chapter 3. In general, neutrino interaction cross sections on nu-

clear targets have large uncertainties around $E_\nu = 1\ GeV$ due to poor statistics from or a lack of previous measurements. MiniBooNE can measure the quasi-elastic and resonance production channels with high statistics; constraints on the cross section prediction using MiniBooNE data are described in chapter 6.

Given the dominant neutrino interaction cross sections, understanding the detector response to muons, electrons, pions, and nucleons in the $E_\nu < 1\ GeV$ range is most important for MiniBooNE. When charged particles travel through the oil, they produce photons by Cherenkov and scintillation emission processes. Cherenkov emission occurs when a particle travels faster than the phase velocity of light in a material, with relativistic $\beta > \beta_C = c/n$ where n is the index of refraction of the material and c is the speed of light in vacuum. This condition produces a shock wave of photons, which are radiated in a cone with a characteristic opening angle with respect to the particle track, $cos(\theta_C) = 1/(\beta n)$ [47]. Scintillation photons are a by-product of ionization energy loss, in which particles electromagnetically interact with, and excite, the molecules in the detector oil along their path. The amount of ionization energy lost by a particle depends on the particle's velocity and the specific properties of the medium. This energy loss is transferred to molecules in the detector medium along the particle's trajectory, and at some later time, these molecules may isotropically emit de-excitation photons. The number of scintillation photons is related to dE/dx by Birks' law [48]. Neutral particle detection is more difficult: neutral pions are detected via the electromagnetic interactions of their $\pi^0 \rightarrow \gamma\gamma$ decay products, and neutrons are detected via de-excitation photons resulting from neutron-nucleus scattering.

As photons propagate from the emission point to detection at the PMT sphere, they may be attenuated, and/or scattered. Attenuation decreases the number of photons as a function of distance x from the emission point as $N(x) = N_0 exp[-x/\lambda_A]$,

where N_0 is the initial number of photons, and λ_A is the attenuation length. With a 2 m long tester filled with the MiniBooNE detector oil, the transmission is measured to rise from 0% at 240 nm to 95% at 320 nm. Transmission is defined in this experiment to be the intensity of photons detected divided by the intensity of photons emitted, for a source with a fixed emission wavelength. These transmission measurements as a function of incident photon wavelength (λ_γ) are used to extrapolate to $\lambda_A = 25.2 \pm 3.1$ m at $\lambda_\gamma = 460$ nm; the attenuation length wavelength dependence is determined empirically to be an approximately linear function above threshold [49]. For photons produced at $\lambda_\gamma = 460$ nm at the center of the MiniBooNE detector, approximately 19% are attenuated before reaching the PMT sphere. The total scattering length in the MiniBooNE oil is measured with goniometry to be 51.7 ± 7 m and 114.5 ± 15.4 m at $\lambda_\gamma = 442$ and 532 nm respectively [50]. In this measurement, the scattering length is determined by measuring the number of photons detected at a non-zero angle with respect to the beam direction divided by the number of photons detected at 0^o. For $\lambda_{scattering}$ of 51.7 m, approximately 10% of photons produced at $\lambda_\gamma = 442$ nm at the center of the MiniBooNE detector undergo a scattering interaction before reaching the PMT sphere. In general, $\lambda_\gamma \sim 450$ nm is chosen as a reference wavelength for comparing optical parameters because it is approximately where the peak of the detection efficiency vs. wavelength is located.

Once the photons reach the PMT sphere, the detection probability depends on the properties of the PMTs, which convert the number of incident photons into an electric charge. PMTs employ several properties of the photo-electric effect [51]: (i) when a photon strikes a metal, an electron may be instantaneously knocked loose (the emitted electron is termed a photo-electron (p.e.)), (ii) this process can only occur if the wavelength of the incident light is less than a threshold value, and (iii) for a given incident photon wavelength, the number of emitted photo-electrons is proportional to

the number of incident photons. PMTs amplify the current of photo-electrons using a multi-stage dynode chain, which can provide many orders of magnitude of signal gain.

MiniBooNE uses Hamamatsu PMTs with an 8" diameter surface which have a $\sim$20% quantum efficiency for emitting a photo-electron given an incident photon with $\lambda_\gamma < \lambda_{threshold} = 550\ nm$ [52]. In practice the quantum efficiency is a smooth function of wavelength that rises steeply from zero below 300 nm to the plateau value, and falls steeply above 500 nm. The MiniBooNE PMTs are operated with $\sim$+2000 V on the dynode chain, resulting in a gain of 10^8. The intrinsic time resolution of the PMTs is $\sim$1 ns, and the intrinsic charge resolution is $\sim$15% at 1 p.e [53]. The charge resolution is further smeared by the signal processing electronics, however, the dominant contribution to the resolutions is from the intrinsic PMT properties.

Data Acquisition

MiniBooNE uses the LSND PMT electronics [54], which have one channel per PMT. The time (t) and charge (q) signals from each PMT are digitized by 8-bit ADCs synchronously on a 10 MHz clock. The t and q ADC values are stored in a 2 kB circular FIFO buffer, which stores 220 μs of data, indexed by the GPS time stamp of each clock tick. If a PMT registers $q > 2\ mV$, a discriminator fires, registering a hit. The PMT base resistors are set such that 2 mV corresponds to $\sim$0.1 photo-electrons ($p.e.$). The number of hit PMTs is summed on each clock tick and broadcast to the trigger. The PMT electronics consist of a series of op-amps, capacitors, and resistors which integrate the PMT voltage with an RC constant of $\sim$1100-1400 ns, depending on the channel. The digitized value of this voltage at each 10 MHz clock tick is used to reconstruct the total charge deposited. The t channel circuit has a fixed time ramp initiated by the discriminator, and a relatively fast return to baseline ($\sim$200

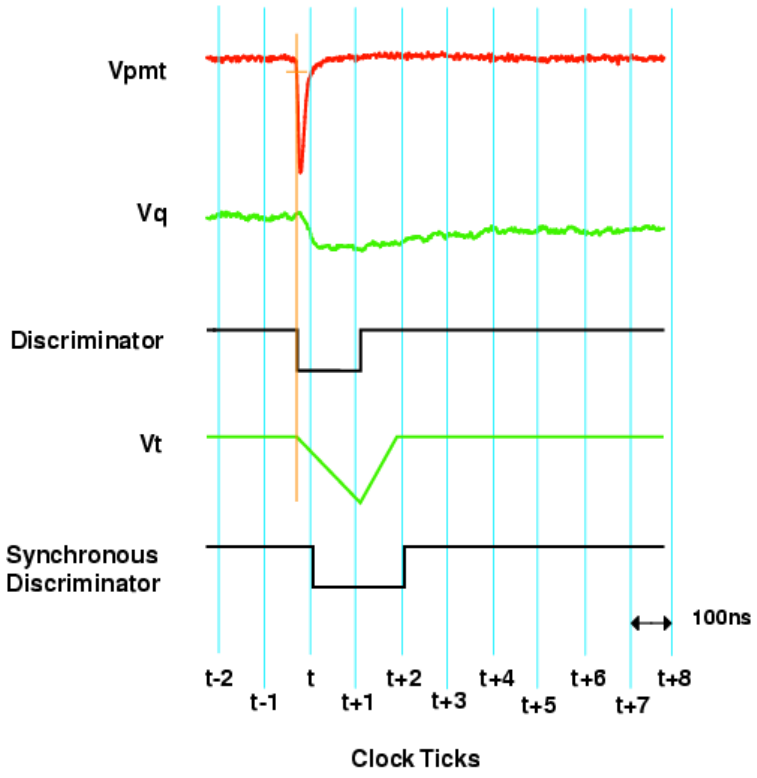

Figure 2.6: *Example of the MiniBooNE data acquisition electronics for a single PMT hit.*

ns). The delay before the discriminator for a given PMT can fire again is 200 ns. This sequence is illustrated in figure 2.6.

In the data acquisition software, a PMT hit consists of the digitized q and t ADC values, recorded over four 100 ns clock ticks. The four q and four t values form a data "quad". Data are retrieved from the FIFO buffers only if a trigger condition is satisfied. In this case the entire detector is read out for 19.2 μs. The PMT data are zero suppressed and assembled into "quads" as an event and written to disk.

The MiniBooNE trigger hardware has four external inputs for NIM signals, named $(E1)$, $(E2)$, $(E3)$, and $(E4)$, and seven comparator settings which are used to decide whether to read out the detector on a given clock tick. The trigger table is constructed

in software using combinations of the hardware triggers and trigger activity timing information. When a trigger fires, PMT information is collected for 192 subsequent clock ticks (19.2 μs) [1]. The trigger hardware external inputs are used for (in order of precedence): ($E1$) the beam-on-target trigger, which is a logical AND of the Booster accelerator 1D and 1F events, ($E2$) a 2.01 Hz strobe trigger (which is triggered by a pulser), ($E3$) the calibration trigger, which has a different NIM pulse length (CALIB_LASER, CALIB_CUBE, or CALIB_TRACKER) depending on whether it is a laser, cube, or tracker calibration event, and ($E4$) a NIM hardware OR of the previous three conditions. A hold-off is always applied after the beam trigger ($E1$) such that 20 μs pass before the trigger can register new activity. Only the E1 trigger input is used for the beam events in the analysis described in this thesis, however, a subset of the comparators are used for the analysis of electron calibration data. These are: $DET2$ (# of tank PMT hits $\geq$ 24), $DET4$ (# of tank PMT hits $\geq$ 200), and $VETO1$ (# of veto PMT hits $\geq$ 6). The relevant trigger table, listed in order of precedence, is shown in table 2.2. The total trigger rate is typically 25-30 Hz, of which up to 5 Hz is due to beam triggers.

PMT Calibration

The PMT q and t ADC values are converted into times in ns and charges in units of photo-electrons ($p.e.$) by the MiniBooNE PMT calibration algorithm. The calibration takes as inputs the raw ADC data for each hit (a "quad"), the trigger time stamp, and the calibration constants (charge $gain$, time $offset$, and time $slew$) for each PMT. The calibration includes the following steps.

1. The charge calibration: for PMT i, the voltage vs. time function for the charge integrator, $Vq(t)_i$, is fit to the four q ADC values in a "quad" for the overall

[1] The lengths of the calibration triggers may differ.

Table 2.2: *The MiniBooNE trigger types and rates relevant for this analysis.*

Trigger Name	*Trigger Condition*	*Rate (Hz)*
Beam	E1	3 - 5
Strobe	E2	2.01
Michel	.not.Veto1.and.DET2.and.	1.23
	3 μs $\leq$ time since (DET4.and.VETO1) $\leq$ 15 μs	
Laser	E3.and.CALIB_LASER	3.33
Cube	E3.and.CALIB_CUBE	1.19
Tracker	E3.and.CALIB_TRACKER	0.65

normalization. The best-fit normalization, $RawQ$, is corrected by the PMT $gain$ to produce the calibrated hit charge $Q = RawQ/gain$ in units of $p.e.$. The $RawQ$ value is approximately the difference between the third and first q ADC values.

2. The time calibration: for PMT i, the voltage vs. time function for the time ramp $Vt(t)_i$ is used to extrapolate back to the time when the discriminator fired, $RawT$. A further $offset$ correction for the signal transit time from the PMT face to the electronics is applied. Additionally, the start of the time ramp with respect to the start of the PMT signal depends on $RawQ$. This is called time $slewing$. The calibrated hit time $T = RawT$ + the $offset$ correction + the $slew$ correction in units of ns.

The calibration constants are extracted from laser calibration data. The laser calibration system consists of a 397 nm laser attached to a switching box, which can direct laser light down a set of optical fibers which are piped into four 10 cm diameter

spherical glass flasks filled with Ludox[2]. The flasks are located at the center of the detector and various off-axis positions. The purpose of the Ludox is to scatter the laser light such that it is emitted isotropically. The laser intensity, frequency, and emission flask can be varied; for the purpose of the calibrations described here, the laser is pulsed at 3.3 Hz, and light is emitted only from the central flask.

To extract the PMT *gain* constants, the laser is pulsed at low intensity such that the average number of detector PMTS which record a hit is <10% of the total (1280). The goal is to never have more than 1 photon incident on a PMT. For each PMT, a distribution is formed of *RawQ*, and the mean of this distribution, after zero-suppression, should correspond to the charge for 1 *p.e.*. The PMT *gain* is the constant needed to scale the mean of the *RawQ* distribution such that it equals 1.0. The calculated *gain* is adjusted for the Poisson probability of getting >1 *p.e.*.

To extract the PMT time $offset$ constant, the laser is pulsed at low intensity, and a distribution is formed for all PMTs of the *RawT* values with respect to the laser trigger time. The time $offset$ for each PMT is the time difference between the PMT time and the average time of the distribution of all PMTs. The time *slew* correction is derived by pulsing the laser over the full range of intensities and binning the $offset$ distribution in *RawQ*. The *slew* tables for each PMT are set such that the $offset$ is independent of *RawQ*.

Data Reduction

To select neutrino candidate events, two important forms of data reduction are applied. These are: (*i*) data quality requirements and (*ii*) cosmic ray rejection.

The purpose of the data quality cuts is to ensure that the experiment apparatus is functioning properly. This includes both beam line and detector. The only

[2]Ludox is a colloid of silica crystals suspended in water.

Table 2.3: *Data quality cuts and fraction of total protons on target that fail each cut. Toroid 875 measures the proton spill intensity 5 m upstream of the target face. Toroid 860 is located 150 m upstream of Toroid 875.*

Cut	*Fail Fraction(%)*
Detector DAQ .not.Latent	0.05
Toroid 875 > 0.1E12 protons per spill	0.00
$2 \times \frac{\lvert Toroid875 - Toroid860\rvert}{(Toroid875 + Toroid860)} < 10\%$	1.07
Horn Current > 165 kA	5.29
targeting efficiency > 95%	3.75
(Beam - Detector) GPS Time Stamp < 33 ms	0.01

contribution to the data quality cut failure rate from the detector is latent events, which occur when the circular PMT FIFO buffers have filled up, and hit information requested by a trigger has been overwritten. The trigger flags these hits, and events containing any latent hits are cut by the data quality analysis software. The most important data quality cuts related to the beam line are: (i) horn current within 5 kA of the expected value, (ii) 95% of the beam passes through the entire length of the target, and (iii) agreement between the toroids, which measure the number of protons per spill, to better than 10%. The fraction of data cut by these data quality requirements is $\sim$ 10%, most of which occured early in the MiniBooNE run. The data quality cuts and their individual efficiencies are summarized in table 2.3.

Once quality cuts have been applied, the largest source of background to beam-induced neutrino events comes from cosmic rays, since the MiniBooNE detector is located on the surface with only 3 m of dirt overburden. The through-going (stopping) cosmic ray rate has been measured to be 10 (2) kHz [55]. However, the short spill

length of the Booster accelerator (1.6 μs), and the high efficiency of the MiniBooNE detector veto region ($> 99\%$), enable cosmic ray rejection of better than 1000:1.

The cosmic ray rejection cuts rely on basic event identification, which employs only calibrated PMT hit times. Within the 19.2 μs beam trigger window, a simple cluster-finding algorithm groups calibrated hits in the detector by time. The algorithm loops over all hits in the beam window, and at each iteration accumulates all hits within a time window of width ΔT starting at time T_{min}. On the first iteration $T_{min} = 0.0$. If the time between contiguous hits is less than 10 ns, the window ΔT is extended to include the latest hit and the iteration continues on to examine the next PMT hit. However, if the time between contiguous hits is greater than 10 ns, then the cluster is finished and the time of the next hit becomes the new T_{min}. If a cluster includes more than 10 hit PMTs, then the cluster is tagged as a "'sub-event". If multiple sub-events occur in an event, they are numbered in time order.

To remove cosmic rays, the following cuts are applied:

1. that there be at least one sub-event, and
2. that the average time of the PMT hits in the first sub-event be within the beam spill window (4400 $ns <$ average time $<$ 6400 ns with respect to the beam trigger start), and
3. that the first sub-event have fewer than 6 hit PMTs in the veto region of the detector, and
4. that the first sub-event have greater than 200 hit PMTs in the main tank region of the detector.

The first two cuts require detector activity in time with the beam spill. Environmental backgrounds tend to have fewer than 10 hits contiguous in this time window. The

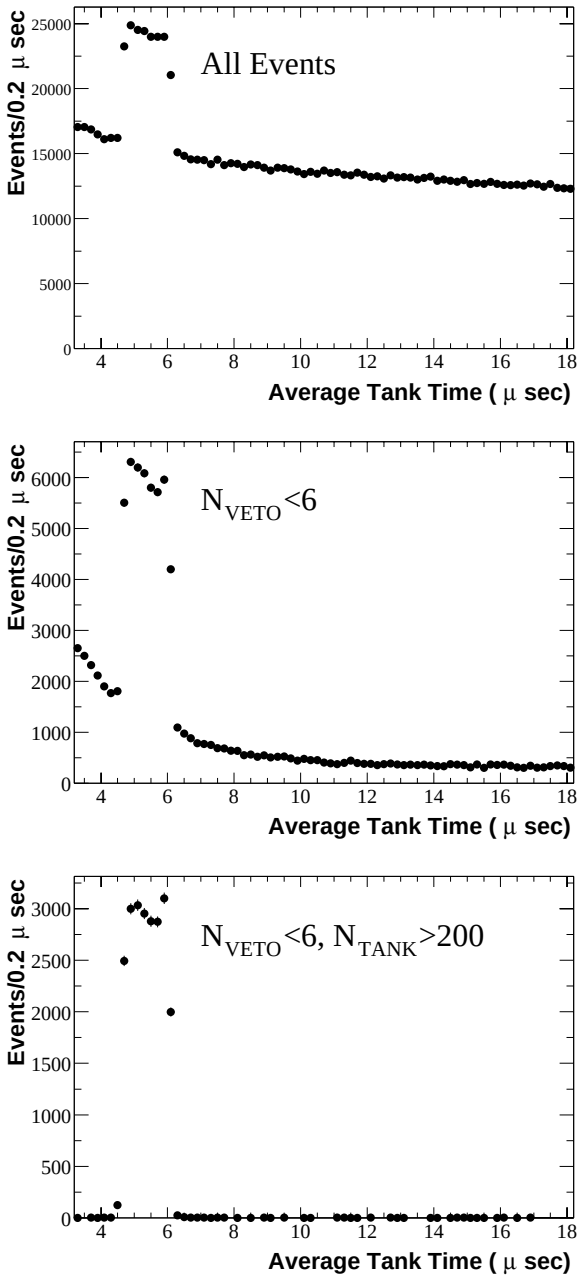

Figure 2.7: *Number of hits in the MiniBooNE beam trigger window vs. time (ns) since the trigger start, in the first sub-event. Top: events passing cosmic ray cut #1. Middle: events passing cosmic ray cuts #1 and #2. Left: events passing cosmic ray cuts #1, #2, and #3. See text for cut explanation.*

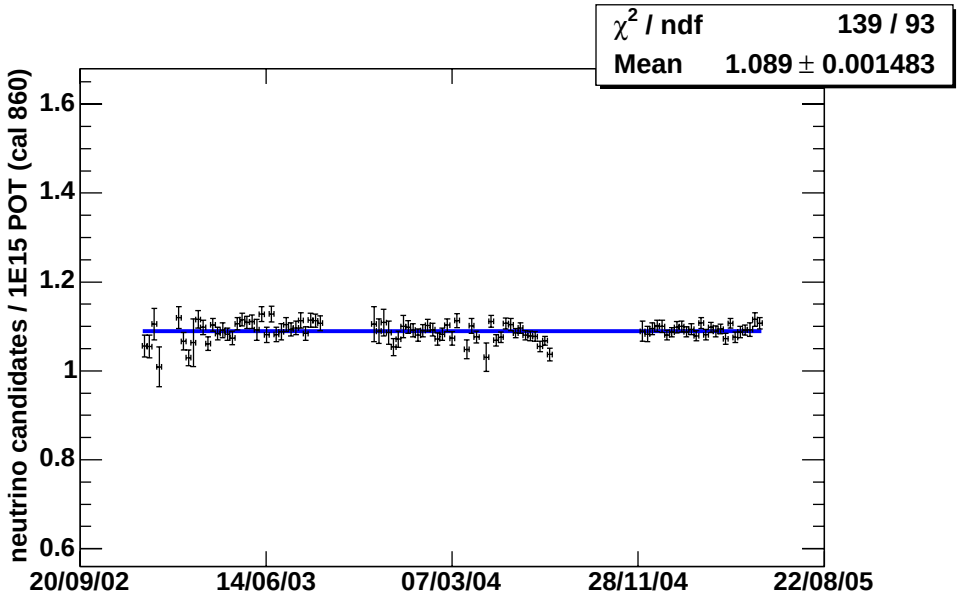

Figure 2.8: *Number of events per proton on target after data reduction cuts vs. time for the MiniBooNE ν mode data set.*

third cut eliminates charged particles entering the detector from outside the veto region, however, electrons from stopped cosmic ray muon decays inside the detector volume will still pass the third cut. On average these decay electrons produce ∼100 PMT hits, and therefore the fourth cut eliminates this background. The data are shown after each cut is applied, sequentially, in figure 2.7. The efficiency of these cuts in beam data is approximately 0.3%, however it depends on the neutrino beam rate, that is, the ratio of spills with to without neutrino-induced interactions.

After the data quality and cosmic ray cuts are applied, the remaining events are termed "neutrino candidates." MiniBooNE measures $\sim$ 1 neutrino candidate event per 1×10^{15} protons on target. The stability of the data acquisition, beamline, and detector can be monitored with the rate of neutrino events per proton on target as a function of time. This distribution, shown in figure 2.8, is consistent with being flat, within errors. It has been verified that the variations are consistent with the

expectation from Poisson statistics[3].

Event Reconstruction

For each sub-event of a neutrino candidate event, the MiniBooNE reconstruction algorithm calculates the event vertex, direction, and energy using a maximum likelihood method, which is the procedure of finding the value of one or more parameters for a given statistic which makes a known likelihood distribution a maximum. The reconstruction algorithm contains a model of light emission, propagation, and detection which is used to predict the q and t each PMT should observe in a given sub-event. A `MINUIT` [56] minimization program is used to find the unknown particle vertex and direction that maximize the charge and time likelihood functions. A conceptual sketch is given here, more information may be found in reference [57].

The time likelihood function is a Gaussian, with mean $\mu = 0.0$ and r.m.s. $\sigma = 1.8\ ns$ = the time resolution of the PMTs measured with laser calibration data. For PMT i located at (x_i, y_i, z_i), the probability for measuring light at time t_i which was emitted at time t_0 and location (x_0, y_0, z_0) is

$$P(t_i|x_0, y_0, z_0, t_0) \ = \ \frac{1}{\sqrt{2\pi}\sigma} exp\Big[-\frac{(t_i - t_0 - r_i/c_n)^2}{2\sigma^2}\Big] \tag{2.4}$$

where c_n is the speed of light in material with refractive index n, and

$$r_i \ = \ \sqrt{(x_i - x_0)^2 \ + \ (y_i - y_0)^2 \ + \ (z_i - z_0)^2}. \tag{2.5}$$

For an ensemble of $N \ = \ 1280$ PMTs, the probability to measure a set of times (t_i) is the product of the likelihood functions for the individual PMTs,

$$P((t_i)|x_0, y_0, z_0, t_0) \ = \ \prod_{i=1}^{N} \frac{1}{\sqrt{2\pi}\sigma} exp\Big[-\frac{(t_i - t_0 - r_i/c_n)^2}{2\sigma^2}\Big]. \tag{2.6}$$

[3]Poisson statistics are used because the number of events in any given run may be small.

Subtleties that modify this simple Gaussian likelihood function include the presence of PMT hits where more than one photon was observed, and the different time constants of the Cherenkov and scintillation emission mechanisms. These tend to couple the time likelihood function to the predicted charge.

The charge likelihood function is a Poisson distribution, where the predicted charge μ_i at each PMT is modified by light attenuation, the solid angle subtended by the PMT, and the PMT quantum efficiency. The probability to measure a set of (n_i) photo-electrons at an ensemble of $N = 1280$ PMTs is the product of the charge likelihoods for each PMT,

$$P((n_i)|x_0, y_0, z_0, \Phi_0) = \prod_{i=1}^{N} \frac{1}{n_i!} \mu_i^{n_i} exp[-\mu_i] \tag{2.7}$$

where Φ_0 is the flux of emitted photons, which are assumed to originate from a point source. The predicted charge at each PMT is

$$\mu_i = \Phi_0 \times \epsilon_i \times F(cos\theta_i) \times e^{(-r_i/\lambda_{eff})} \times \frac{f_L(cos\eta_i)}{r_i^2} \tag{2.8}$$

where ϵ_i is the quantum efficiency of PMT i, $F(cos\theta_i)$ is the angular distribution of the emitted light, $e^{(r_i/\lambda_{eff})}$ accounts for the attenuation of light with effective attenuation length[4] λ_{eff}, and $\frac{f_L(cos\eta_i)}{r_i^2}$ is the product of the PMT solid angle and its response as a function of incident photon angle η_i. Including the angular distribution of light emission introduces dependence on the particle track direction into the likelihood function. This picture is further complicated by the fact that all of the parameters of the charge likelihood function depend on the photon emission mechanism.

The product of the time and charge likelihood functions are maximized iteratively with respect to the original light emission vertex and time, and the particle track direction. Once the best-fit parameters are found, the energy is estimated from the

[4]The attenuation length is an effective one since it is an average over all wavelengths of emitted light.

total predicted charge in the event, corrected for attenuation and quantum efficiency. A subsequent fit is performed in which the event vertex, track direction, and energy are fixed to their best-fit values, and the Cherenkov and scintillation components are varied to find the best-fit emission flux composition.

Once the vertex and direction are found, one can calculate the corrected time and angle for each PMT hit. These quantities are interesting because they characterize the detected light at the emission point, rather than at the detection locations. The corrected time T_{corr} is defined as

$$T_{corr} \;=\; T_{PMT} - \frac{\sqrt{X^2 \;+\; Y^2 \;+\; Z^2}}{c_n} \tag{2.9}$$

where T_{PMT} is the calibrated PMT time of light detection, c_n is the speed of light in material with index of refraction n, and $\sqrt{X^2 \;+\; Y^2 \;+\; Z^2}$ is the distance from the PMT to the best-fit event vertex, e.g. $X \;=\; (X_{PMT} - X_0)$ where X_0 is the best-fit vertex X coordinate and X_{PMT} is the X coordinate of the PMT. The corrected angle θ_{corr} is given by

$$\theta_{corr} \;=\; \frac{UX_0 \times X \;+\; UY_0 \times Y \;+\; UZ_0 \times Z}{\sqrt{X^2 \;+\; Y^2 \;+\; Z^2}} \tag{2.10}$$

where (UZ_0, UY_0, UZ_0) are the best-fit track direction cosines.

The parameters of the likelihood functions are extracted from calibration data distributions of charge, corrected time, and corrected angle [58]. The list of parameters to be determined is: (i) the PMT time resolution σ, (ii) the relative PMT quantum efficiencies ϵ_i, (iii) the Cherenkov and scintillation emission time constants, (iv) the Cherenkov and scintillation fluxes Φ_C and Φ_S, (v) the Cherenkov and scintillation light emission angular distributions $F(cos\ \theta_i)_C$ and $F(cos\ \theta_i)_S$, (vi) the Cherenkov and scintillation light effective attenuation lengths λ_C and λ_S, (vii) the PMT angular response functions for Cherenkov and scintillation light $f_C(cos\ \eta_i)$ and $f_S(cos\ \eta_i)$, and $(viii)$ the conversion from Cherenkov and scintillation fluxes to energy. The first two

are determined from laser calibration data, and the rest are extracted from electron calibration data, which contains both Cherenkov and scintillation light.

Particle Calibration

MiniBooNE has an abundance of calibration particles from cosmic ray muons and their decay electrons, called "Michel" electrons. The most important function of the particle calibration data sets is to tune the Monte Carlo simulation of the experiment. Many comparisons between particle calibration data and the Monte Carlo are shown in chapter 3, section 3.3.

The cosmic ray muons useful for calibration span $200 < E_\mu < 800\ MeV$, are generally all pointed downwards, and are distributed as $\sim cos^3\theta$. The angular distribution of incoming cosmic rays differs from $cos^2\theta$ due to interactions and scattering in the detector overburden. Michel electrons range over $0.511 < E_e < \frac{m_\mu}{2}\ MeV$, are pointed isotropically (for depolarized muon decays at rest in the detector), and are produced uniformly in the x and z detector coordinates with a small asymmetry in y. The Michel electron (and $\overline{\nu}_\mu$) energy distribution in μ^+ decay is given by [59]

$$d\Gamma \;=\; \frac{G_F^2 m_\mu^5}{192\pi^3} 2\epsilon^2(3-2\epsilon) \tag{2.11}$$

and the ν_e energy distribution is

$$d\Gamma \;=\; \frac{G_F^2 m_\mu^5}{192\pi^3} 2\epsilon^2(6-6\epsilon) \tag{2.12}$$

where

$$\epsilon \;=\; \frac{E_e}{E_{max}}, \qquad E_{max} \;=\; \frac{m_\mu}{2}. \tag{2.13}$$

and G_F is Fermi's constant, m_μ is the muon mass.

Michel electrons possess a number of qualities useful for calibration purposes. First, although the cosmic ray muons are polarized, the Michel electrons are effectively

produced isotropically in the detector due to the distribution of cosmic ray arrival directions, which is $\propto \cos^2 \theta_{zenith}$, and the multiple scattering of muons in the soil berm above the detector. Therefore a high statistics sample of Michel electrons will tend to illuminate all of the PMTs. Second, Michel electrons produce both Cherenkov and scintillation light, in a ratio of ∼7:1, and therefore can be used to extract parameters describing both emission processes for the reconstruction. Third, the Michel electron energy endpoint, 52.8 MeV provides a "standard candle" calibration for the energy scale and resolution of the detector. Additionally, the data set of Michel electrons is virtually infinite, therefore the energy scale and resolution can be measured in bins of radius, track direction, PMT corrected time, and PMT corrected θ, for the purpose of tuning the Monte Carlo model of light propagation in the detector oil.

The energy resolution and scale at the Michel end-point are calculated by convolving the expected Michel electron energy distribution with a Gaussian, and fitting to the Michel data set in a 500 cm radius fiducial volume. The energy resolution and scale are extracted for the total light yield, and for the Cherenkov and scintillation flux components separately. The energy resolution is measured to be ∼13% for all light, and ∼13% (∼11%) for Cherenkov (scintillation) light only [60]. The best-fit mean energy is used to set the energy scale of the reconstruction. This is enforced by the conversion from Cherenkov (scintillation) flux to energy, which is calculated as the ratio of the theoretical value to the best-fit mean energy from the Cherenkov (scintillation) flux fit.

The drawback of Michel electrons is that they provide a calibration at low energy, while neutrino interactions in MiniBooNE may produce leptons up to ∼1 GeV. To verify the extrapolation from the Michel end-point to higher energies, MiniBooNE uses a cosmic ray muon calibration system, which consists of a muon tracker hodoscope and seven scintillator cubes.

The muon calibration system employs a hodoscope tracker, which is designed to measure precisely the incoming direction of cosmic ray muons, and seven scintillator cubes deployed inside the detector volume. The muon tracker has two sets of X and Y planes, located 2 and 3.5 m above and parallel to the top of the MiniBooNE detector sphere. The top (bottom) planes consists of 23 (28) scintillator strips which are 10 (6) cm wide, with a PMT at each end. The X and Y planes are oriented perpendicular to each other. The $CALIB\_TRACKER$ trigger requires an OR of all strips in a given plane, and an AND of the four planes. The trigger rate of 4-plane coincidences is $\sim 140\ Hz$, which is prescaled to 0.5 Hz. The scintillator cubes record the primary muon and its decay electron when a cosmic ray muon stops in one of the cubes. In combination with the tracker, the cubes provide a precise measurement of the muon track length. The parameters of the cubes are described in table 2.4. Each cube is attached to an optical fiber which carries the scintillation light to a PMT located outside the detector volume. The $CALIB\_CUBE$ trigger requires concidence of a cube PMT above threshold and a $CALIB\_TRACKER$ trigger, which results in a 1.2 Hz trigger rate. This trigger condition can be satisfied by a muon passing through, but not stopping in, a cube, and therefore further cuts on tank and veto PMT hits, and cube PMT charge and time, are applied to select stopping cosmic rays. The cubes are sensitive to muon kinetic energies ranging from $\sim$0.95 to 0.770 GeV.

The measured range from the muon calibration system is used to calculate the muon's energy independently of the reconstruction, via [61]

$$-\frac{dT}{dx} = 2\pi a_0^2 m_e c^2 n_e \frac{Z^2}{\beta^2}\Big[ln\Big(\frac{2m_e c^2\gamma^2\beta^2 W_{max}}{I^2}\Big) - 2\beta^2 - \delta - 2\frac{C}{Z}\Big]. \qquad (2.14)$$

where a_0 is the Bohr radius, c is the speed of light, I is the mean excitation potential of the medium through which the particle travels, β and γ are the usual relativistic factors, W_{max} is the maximum energy transfer possible in a single collision, and C and δ are empirical corrections for the nuclear energy shells and density respectively. A full

Table 2.4: *Scintillator cube calibration system description, including depths below the detector optical barrier, positions with respect to the detector axis, muon range and kinetic energy sensitivity, and intrinsic energy resolution.*

cube depth (cm)	x (cm)	y (cm)	z (cm)	$< Range >$ (g/cm^2)	$\delta Range$ (g/cm^2)	$< T_\mu >$ (MeV)	δT_μ (MeV)
31.3	-60.76	540.70	15.12	27.6	0.9	95.9	2.2
60.3	15.55	511.70	-57.62	54.1	1.0	155.9	2.2
100.5	57.89	471.50	-13.54	88.6	1.2	229.1	2.6
200.8	-18.64	371.20	59.20	173.9	1.9	407.2	4.0
298.1	40.82	273.90	44.50	256.4	3.6	580.2	7.6
401.9	40.82	170.10	44.50	344.2	4.3	767.8	9.2

Bethe-Block range calculation for muons in mineral oil, including straggling, is used to convert the muon calibration system range measurement into a muon energy [62]. The resulting uncertainty on the muon tracker range-energy measurement is $\sim$1%, due to range straggling.

The muon calibration system is used to measure the energy, vertex, and angle resolution of the reconstruction. For muons with 0.7 GeV kinetic energy, the reconstruction energy resolution is measured to be $\sim$6%, and the angular resolution is measured to be $\sim$6 *degrees*. The reconstruction's vertex resolution and drive (position bias) in the direction perpedicular to the muon track are measured to be 6.5 cm (11.7 cm), and 12.5 cm (9.8 cm) for the parallel direction. The intrinsic energy, angle, and vertex resolutions of the muon tracker system are $\sim$1%, 2 *degrees*, and (3.5 cm, 3.5 cm, 2.0 cm) for (x, y, z) [63].

Particle Identification

Particle identification in the MiniBooNE detector relies on hit timing, hit charge, and event topology. For the oscillation analyses, the most important particles for MiniBooNE to distinguish are muons, electrons, and neutral pions. The primary method for finding muons is via their decay electrons: $\sim$ 90% of muons followed by a decay electrons appear as two sub-events in the MiniBooNE detector. The average length of a muon sub-event is $\sim$50 ns, and so the probability of the decay electron getting "masked" by the primary muon (and as a result not creating its own sub-event) is 2%, and, 8% of μ^- capture in Carbon, and therefore do not create a second sub-event. To distinguish electrons from neutral pions, events are fit with a 1-ring and 2-ring hypothesis. While both particles produce one sub-event, cleanly reconstructed $\pi^0 \rightarrow \gamma\gamma$ events have a better likelihood value for the 2-ring fit, as well as a reconstructed invariant mass within $\sim$50 MeV of the π^0 mass. However, when π^0s are not cleanly reconstructed, they are the largest source of events mis-identified as electrons. Various sophisticated algorithms are trained to distinguish hard-to-identify π^0 events from electrons, which rely on comparing the likelihood values in bins of corrected PMT time and angle [64].

To identify a particular interaction channel, for example, $\nu_\mu n \rightarrow \mu^- p$, PMT corrected time, corrected angle, and charge distributions are examined for consistency with the expected final state, e.g., one muon-like ring. An example of this approach is the ν_μ charged current quasi-elastic event selection, which is described in detail in chapter 4.

Chapter 3

Simulation of the Experiment

3.1 Flux Prediction

The processes that contribute to the MiniBooNE ν_μ flux are $\pi^+ \to \mu^+\nu_\mu$ and $K^+ \to \mu^+\nu_\mu$; the processes that contribute to the intrinsic ν_e in the beam are $\mu^+ \to e^+\nu_e\overline{\nu}_\mu$, $K^+ \to \pi^0 e^+\nu_e$, and $K^0_L \to \pi^\pm e^\mp \nu_e$. Therefore the important components of predicting the MiniBooNE neutrino flux are understanding the π and K production cross sections in the MiniBooNE target, and accurately modeling meson propagation and decay. MiniBooNE predicts the meson production cross sections with global fits to data from past experiments. Meson propagation and decay are modeled in a Geant4 Monte Carlo simulation of the MiniBooNE target and decay region.

3.1.1 Particle Production Cross Sections

Historically, the particle production cross sections of relevance for MiniBooNE were not well known, and therefore are an important source of uncertainty for MiniBooNE. There are no published measurements of inclusive π or K production in proton-

beryllium interactions at 8.9 GeV/c incident proton momentum, although preliminary results are available from the HARP experiment. The relevant cross sections are not theoretically straightforward either, and as a result, different Monte Carlo hadron production simulations make wildly varying predictions [65], shown in figure 3.1. However, a number of past experiments measured the production cross sections in part or all of the meson kinematic phase space relevant for MiniBooNE, although not at the same incident proton beam momentum. Therefore, to obtain production cross sections for MiniBooNE we fit a parameterization of the meson production differential cross section, which is a function of incident proton momentum, meson momentum, and meson angle, to the available data. The best-fit differential cross section is then used to extrapolate to $p_{proton} = 8.9\ GeV/c$ and to the range of $(p_{meson},\ \theta_{meson})$ needed by MiniBooNE.

The modern meson production cross section data comes from experiments which typically have secondary proton beams incident on the production target, and scintillator counters which identify and trigger on each proton. The target is situated inside a time projection chamber, which is used to tag the secondary production vertex. Various particle ID detectors and a magnetic spectrometer with large acceptance identify mesons downstream and measure their momenta. The spectrometer acceptance, decay and absorption corrections, and track reconstruction and particle ID efficiency are determined from Monte Carlo simulations. The measured differential cross section is given by [66]

$$\frac{d^2\sigma_\alpha}{dp_i d\theta_j} = \frac{\frac{1}{N_{pot}}\frac{A}{N_A \rho t} M^{-1}_{ij\alpha,i'j'\alpha'} \left[N^{\alpha'}_{i'j'}(T) - N^{\alpha'}_{i'j'}(E) \right]}{\Delta p_i \Delta \theta_j} \tag{3.1}$$

where p_i, θ_j are the momentum and angle of particle type α (e.g. π^+) at production, N_{pot} is the number of incident protons on target, A is the atomic number, N_A is Avogadro's number, ρ is the target material density, t is the linear thickness of the

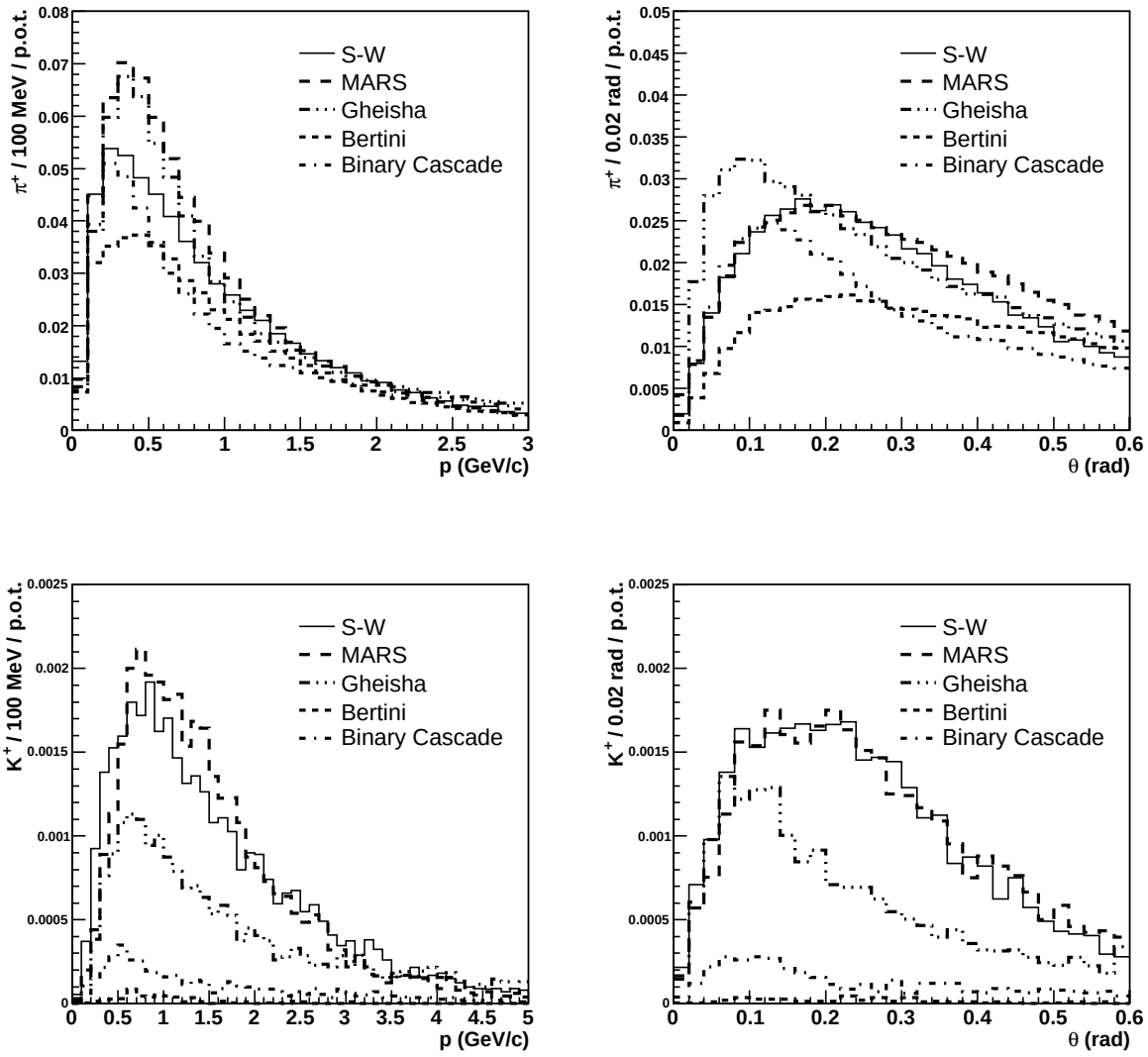

Figure 3.1: *Comparison of inclusive meson production normalization and kinematics in hadron production models from various Monte Carlo event generators. The same number of incident protons on target is simulated for each production model. Top left: number of π^+ vs. p_π (GeV/c) at production. Top right: number of π^+ vs. θ_π (radians) at production. Bottom left: number of K^+ vs. p_K (GeV/c) at production. Bottom right: number of K^+ vs. θ_K (radians) at production. Figure from reference [65].*

target, $M^{-1}_{ij\alpha,i'j'\alpha'}$ is an unfolding matrix that relates the measured momentum, angle, and particle type to the true values, corrected for efficiency, acceptance, and absorption, $N^{\alpha'}_{i'}(T)$ is the measured number of particles identified as type α' in (p,θ) bins (i',j') with the target in place, $N^{\alpha'}_{i'}(E)$ is the same quantity with the target removed, and $\Delta p_i \Delta\theta_j$ are the bin widths. Typical errors on a given data point are at the few percent level, the dominant sources of uncertainty come from the unsmearing and absorption corrections. Data is taken with the target removed to correct for noise and environmental backgrounds.

Sanford & Wang Parameterization

The Sanford & Wang parameterization describes the non-invariant double differential cross section in terms of the incident proton momentum (p_{proton}), the out-going meson momentum (p_{meson}), the out-going meson angle (θ_{meson}), and 9 free parameters c_i [67]:

$$\frac{d^2\sigma}{dpd\Omega} = c_1 {p_{meson}}^{c_2}(1 - \frac{p_{meson}}{p_{proton} - c_9}) \times \tag{3.2}$$

$$exp\Big[\frac{-c_3 {p_{meson}}^{c_4}}{{p_{proton}}^{c_5}} - c_6\theta_{meson}(p_{meson} - c_7 p_{proton} cos^{c_8}\theta_{meson})\Big]$$

The functional form comes from inspection of $p\ Be \rightarrow \pi^{\pm}\ X$, $p\ Be \rightarrow K^{\pm}\ X$, and $p\ Be \rightarrow p\ X$ data. The original fit parameters were tuned on the data of Lundy *et al.* [68], Dekkers *et al.* [69], Baker *et al.* [70], and Fitch *et al.* [71], with the normalization of [69]. This normalization condition assumes a total inelastic cross-section of 227 mb [72], which is roughly 10% higher than the currently accepted value 208 mb [73].

The data used by Sanford & Wang have incident proton momenta between 10 and 70 GeV/c, slightly above the MiniBooNE incident proton momentum of 8.89 GeV/c. Further, the majority of the data are from the 33 GeV Bevatron, and the only forward (0 degree) production data are from the Dekkers experiment. There

are several more recent fits which primarily use the data of Cho *et al.* (1971) [74], however, no published fit has extended the data to proton beam momenta below 10 GeV/c. We incorporate data at 3 and 6 GeV/c from the Piroue and E910 experiments since it is preferable to interpolate between data sets above and below MiniBooNE's beam momentum, rather than extrapolate based on higher energy data alone.

The motivation for the p_{proton} dependence of the Sanford & Wang parameterization is Feynman scaling [75], since the invariant cross section data vs. x_F becomes approximately independent of x_F above the kinematic threshold for producing a given meson, where

$$x_F \;=\; \left(\frac{p_z}{p_z^{max}}\right)_{CM}, \tag{3.3}$$

$(p_z)_{CM}$ is the longitudinal momentum of the π in the center of mass in the reaction $p\ Be \rightarrow \pi\ X$, and $p_z^{max} \;\simeq\; \sqrt{s}/2$. The angular and momentum dependences of the function, for forward production, are based on two other scaling relations [76]. By dropping the term $c_7 P_p cos^{c_8}\theta_\pi$ in equation 3.2, one can show that

$$\frac{d^2\sigma(P_p{}')}{dpd\Omega} \;=\; \sqrt{\frac{P_p{}'}{P_p}}\frac{d^2\sigma(P_p)}{dpd\Omega}, \tag{3.4}$$

where $P_p{}'$ and P_p are two different incident proton momenta. The second scaling law describes the angular dependence of the pion production

$$\theta' \;=\; \frac{P_p}{P_p{}'}\theta \tag{3.5}$$

at a fixed P_π, P_p, and pion transverse momentum $P_\perp$.

While these simple momentum scaling relations describe forward production data, a more complex functional form is allowed for other angles. The Sanford & Wang parametrization attempts to represent the data at different production angles by introducing three additional free parameters, $c6$, $c7$, and $c8$. The remainder of the parameters are related to either the change in cross-section with incident beam momentum, $c1$, $c3$, and $c5$, or to the variation with pion momentum, $c2$ and $c4$.

Production Cross Section Fits

The parameters c_1 through c_8 are determined from fits of the data to the Sanford-Wang parameterization. The production cross section fits minimize the following function for an experiment j:

$$\chi_j^2 \;=\; \Big[\sum_i \frac{(N_j \times SW_i - Data_i)^2}{\sigma_i^2}\Big] + \frac{(1-N_j)^2}{\sigma_{N_j}^2} \tag{3.6}$$

where i is the (P_{meson},θ_{meson}) bin index, $SW_i \;=\; \Big(\frac{d^2\sigma(p_{meson},\theta_{meson},p_{proton},c_k)}{dpd\Omega}\Big)$ is the parameterization prediction evaluated at a given $(p_{proton}, \theta_{meson}, p_{meson})$ and set of coefficients c_k with $k = (1, 8)$, $Data_i$ is the measurement at a given $(p_{proton}, \theta_{meson}, p_{meson})$, σ_i is the data systematic error on measurement i, N_j is the normalization pull term for experiment j, and σ_{N_j} is the normalization uncertainty experiment j. The total χ^2 for external data sets is the sum of the individual χ^2s for each experiment:

$$\chi^2 = \sum_j \chi_j^2. \tag{3.7}$$

To account for coarse binning in the measured data, or for bins in which the production cross section is changing rapidly, the data are bin center corrected at each iteration of the fit[1]. The bin center correction is calculated from the average value of the parameterization cross section in a data bin at a given iteration k, which is

$$\Big(\overline{\frac{d^2\sigma(p_{meson},\theta_{meson},p_{proton},c_k)}{dpd\Omega}}\Big)_k \;= \tag{3.8}$$

$$\frac{1}{\Delta p \Delta\Omega} \times \int_{p_{min}}^{p_{max}} \int_{\theta_{min}}^{\theta_{max}} \Big(\frac{d^2\sigma(p_{meson},\theta_{meson},p_{proton},c_k)}{dpd\Omega}\Big) dpd\Omega$$

where the data bin limits are $p_{min} < p_{meson} < p_{max}$ and $\theta_{min} < \theta_{meson} < \theta_{max}$, $\Delta p \;=\; p_{max} - p_{min}$, $\Delta\Omega \;=\; \Omega_{max} - \Omega_{min}$, and c_k are the values of the fit parameters

[1]The assumption is made that the data are reported at the center of the measurement bins.

at iteration k. The bin center correction $C(p_{meson}, \theta_{meson})_k$ is the ratio of the average parameterization value divided by the parameterization value at the center of the bin:

$$C(p_{meson}, \theta_{meson})_k \;=\; \frac{\left(\overline{\frac{d^2\sigma}{dpd\Omega}}\right)_k}{\left(\frac{d^2\sigma}{dpd\Omega}\right)_k} \tag{3.9}$$

This correction is applied multiplicatively to the data when calculating the χ^2 function.

Pion Production Results

The external inclusive π^+ production data in the range of interest to MiniBooNE are summarized in figure 3.2. Only modern experiments, as described in the previous section, are shown. These include E910[77] and HARP[78], which span a range of production phase space: $6.4 < p_{proton} < 12.3\ GeV/c$, $0 < p_\pi < 6.5\ GeV/c$, and $0 < \theta_\pi < 330\ mr$. These data are all reported in bins of double differential cross section vs. π^+ momentum and angle. Older experiments are discussed in appendix B.

To remove the effect of differing incident proton beam momenta, one can assume Feynman scaling and can compare the production phase space in the center of mass ($x_{Feynman}$, p_T). These parameters are defined as

$$p_T \;=\; \sqrt{(p_x^{LAB})^2 + (p_y^{LAB})^2}; \qquad x_{Feynman} \;=\; \frac{p_z^{CM}}{p_{z,\ MAX}^{CM}} \tag{3.10}$$

Figure 3.2 shows p_T vs. $x_{Feynman}$ for the relevant experiments, superimposed upon the MiniBooNE beam Monte Carlo prediction π^+ that decay to neutrinos in the MiniBooNE detector acceptance. The most important range for MiniBooNE is around $p_T = 0.2$ GeV/c and $x_F = 0.2$, and the E910 and HARP experiments have good coverage of the entire MiniBooNE phase space.

experiment	p_{proton} *(GeV/c)*	p_π *(GeV/c)*	θ_π	N_{DATA}	σ_{NORM}
E910 [77]	6.4, 12.3	1 - 5.5	0 - 20^o	101	5%
HARP [78]	8.9	1 - 5.5	0 - 11^o	72	4%

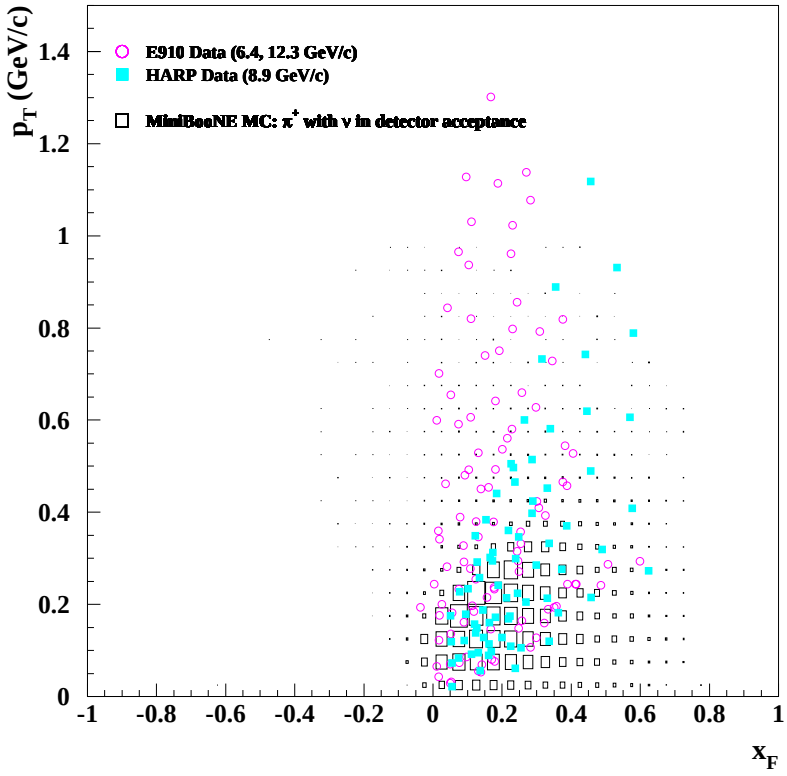

Figure 3.2: *Top: Summary of modern experiments which measure p Be* $\rightarrow \pi^+X$ *in a region of interest to MiniBooNE. Bottom: Transverse momentum (GeV) vs.* $x_{Feynman}$ *for* π^+ *production experiments, overlaid with the MiniBooNE beam Monte Carlo prediction for* π^+*-decay* ν *in the MiniBooNE detector acceptance.*

The HARP 8.9 GeV/c, E910 6.4 GeV/c, and E910 12.3 GeV/c data are fit by minimizing the χ^2 function of equation 3.6. The free parameters in the Sanford-Wang fit include the eight function constants $c1$ through $c8$, and the normalization pull terms n_i. However, each n_i has an associated penalty term (the second term in equation 3.6), and therefore does not change the number of degrees of freedom in the fit: $N_{Data} - 8$. Different normalization pull terms are used for the E910 6.4 and 12.3 GeV/c data because the data sets were recorded with different experimental settings [77]. Two χ^2 values are reported here: a "shape χ^2", which is the value of the χ^2 function with the normalization pull term penalty subtracted from the total, and a "total χ^2," which includes the penalty. Comparing these two χ^2 values tests the normalization compatibility of the different experiments included in the fit.

The best-fit Sanford-Wang parameters are shown in table 3.1, assuming uncorrelated errors for all data points. The χ^2/ndf of the HARP and E910 experiments individually are 1.10 and 1.21 respectively, while the combined fit χ^2/ndf is 1.52. Inspection of the shape vs. total χ^2 values and the data show that the tension between the two experiments is due to shape rather than normalization, in particular for the larger angles (if the 11^o bin in HARP were dropped from the fit, the combined χ^2/ndf would be $177/153 = 1.16$).

The E910 data are reported with uncorrelated errors, however, the preliminary HARP data are reported with correlated errors. The best-fit Sanford-Wang parameters using the correlated HARP errors are shown in table 3.2[2]. The fit quality is significantly worse than the uncorrelated result, although the best-fit cross section is very similar. The χ^2/ndf of the HARP data, fit with correlated errors, is 3.26, and the

[2]Following the recommendation of the HARP collaboration, the HARP data with correlated errors are fit using an average of the χ^2 shown in equation 3.6 and the corresponding Pearson χ^2 function.

Table 3.1: *Best-fit Sanford-Wang π^+ parameters, assuming uncorrelated errors for all data sets. The "E910 + HARP" fit combines HARP 8.9 GeV/c, E910 6.4 GeV/c, and E910 12.3 GeV/c data. The "E910 only" and "HARP only" fits are performed to check the consistency of the individual experiments with the Sanford-Wang hypothesis. Since HARP measures only one p_{proton} value, the parameter c5 is fixed in the Sanford-Wang function for the "HARP only" fit. Probability refers to the total χ^2/ndf.*

fit parameter	*E910 + HARP*	*E910 only*	*HARP only*
c1	242.8±12.85	219.9 ±38.40	460.9±95.830
c2	1.069±0.148	0.927 ±0.1391	1.782±0.2347
c3	2.838±0.929	5.324 ±7.548	1.017±0.0685
c4	1.684±0.142	3.000 ±1.582	0.7422±0.0628
c5	1.523±0.104	2.651 ±1.129	0.000±0.00
c6	5.479±0.690	5.067 ±0.4915	5.757±0.6302
c7	0.0833±0.015	0.0877±0.0239	0.1808±0.0246
c8	9.483±4.240	10.55 ±3.786	40.51±17.910
n_{HARP}	1.00±0.00	-	1.00±0.00
$n_{E910\ 6.4}$	1.04±0.07	1.03±0.07	-
$n_{E910\ 12.3}$	0.99±0.03	0.98±0.03	-
shape χ^2/ndf	247/165	110/93	71/64
total χ^2/ndf	250/165	113/93	71/64
probability	2.1×10^{-5}	0.078	0.26

Table 3.2: *Best-fit Sanford-Wang π^+ parameters, using correlated errors for the HARP data, and uncorrelated errors for the E910 data. The "E910 + HARP" fit combines HARP 8.9 GeV/c, E910 6.4 GeV/c, and E910 12.3 GeV/c data. The "HARP only" fit is performed to check the consistency of the individual experiments with the Sanford-Wang hypothesis. Since HARP measures only one p_{proton} value, the parameter c5 is fixed in the Sanford-Wang function for the "HARP only" fit. Probability refers to the total χ^2/ndf.*

fit parameter	*E910 + HARP*	*HARP only*
c1	266.5±31.44	380.9±6.843
c2	1.045±0.0512	1.433±0.1090
c3	1.846±0.1566	0.5762±0.0160
c4	1.482±0.1105	0.9469±0.0376
c5	1.171±0.0281	0.000±0.000
c6	5.026±0.2938	4.846±0.2182
c7	0.078±0.0063	0.1190±0.0175
c8	10.11±5.995	41.76±3.798
n_{HARP}	1.00±0.00	1.00±0.00
$n_{E910\ 6.4}$	1.02±0.06	-
$n_{E910\ 12.3}$	0.97±0.03	-
shape χ^2/ndf	368/165	209/64
total χ^2/ndf	371/165	209/64
probability	0.0	0.0

combined fit χ^2/ndf is 2.25. The data are compared with the best-fit Sanford-Wang cross section in figures 3.3 through 3.5.

The best-fit Sanford-Wang inclusive π^+ production cross section is evaluated at the MiniBooNE beam momentum and shown as a function of p_π for different θ_π values in the left-hand side of figure 3.6. The magnitude of the cross section falls very steeply as a function of both angle and momentum from a maximum at (p_π, θ_π) = $(2\ GeV/c, 0^o)$. The best-fit cross section is shown as a function of incident proton momentum in the right-hand side of figure 3.6, evaluated at the average (p_π, θ_π) for π^+ that decay to neutrinos in the MiniBooNE detector acceptance. The p_{proton} dependence of the best-fit Sanford-Wang cross section is approximately consistent with the $ln(s)$ behavior predicted by Feynman scaling (where $E_{CM} = \sqrt{s}$).

Similar fits are performed for π^- production. These are described in appendix B, section B.2.

The π^+ production fit in table 3.2, labelled "E910 + HARP", has been used to generate all of the Monte Carlo in this thesis. As will be shown in chapter 4, the energy distribution of the predicted ν_μ flux agrees very well in shape with the MiniBooNE data.

Kaon Production Results

Low-energy kaon production data in proton-beryllium interactions is even more sparse than pion production data. The most relevant K^+ production data in the (x_F, p_T) phase space of interest to MiniBooNE is summarized in figure 3.7. The most important range for MiniBooNE is around $p_T = 0.2$ GeV/c and $x_F = 0.3$. The experiments which cover this phase space have very different lab frame measurement parameters: p_{proton} varies from 9.5 to 24.0, p_{meson} from 0.5 and 16 GeV/c, and θ_{meson} from 0 to 40 degrees.

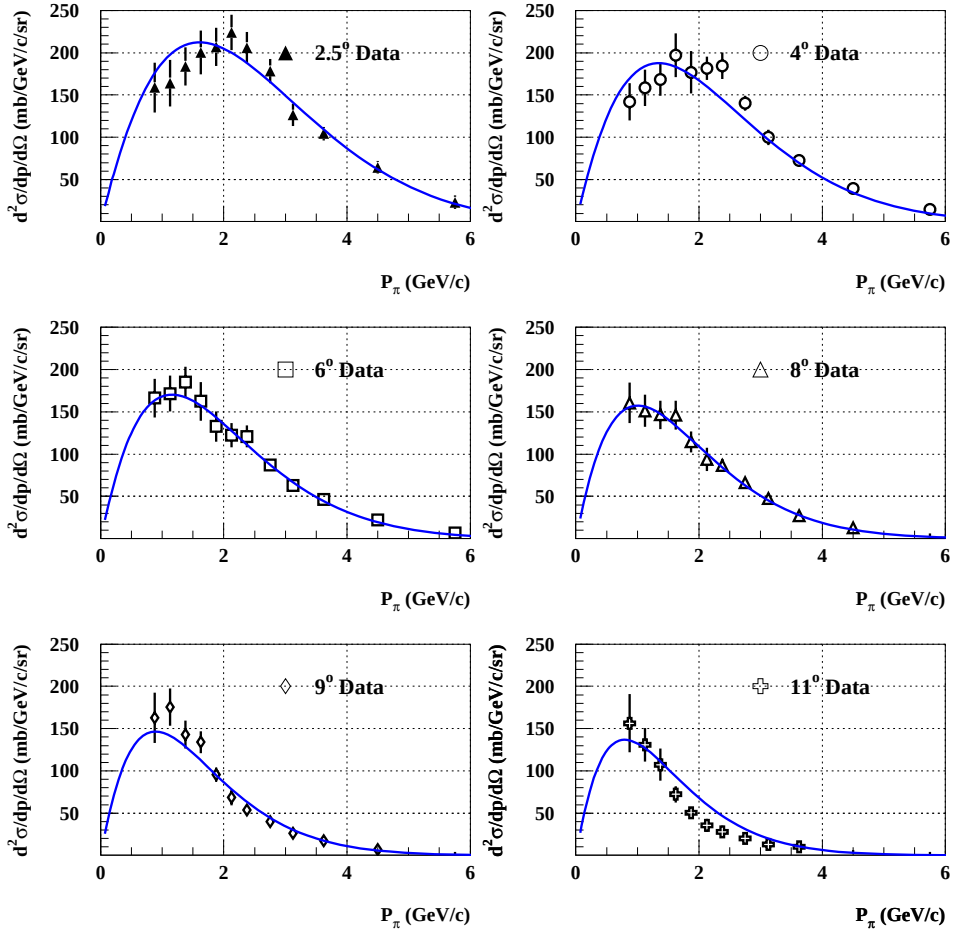

Figure 3.3: *HARP [78] experiment measured inclusive π^+ production cross section (milli-barns/GeV/c/steradian) in proton-beryllium interactions vs. π^+ momentum (GeV/c), at $p_{proton} = 8.9$ GeV/c. Error bars include statistics and systematics.*

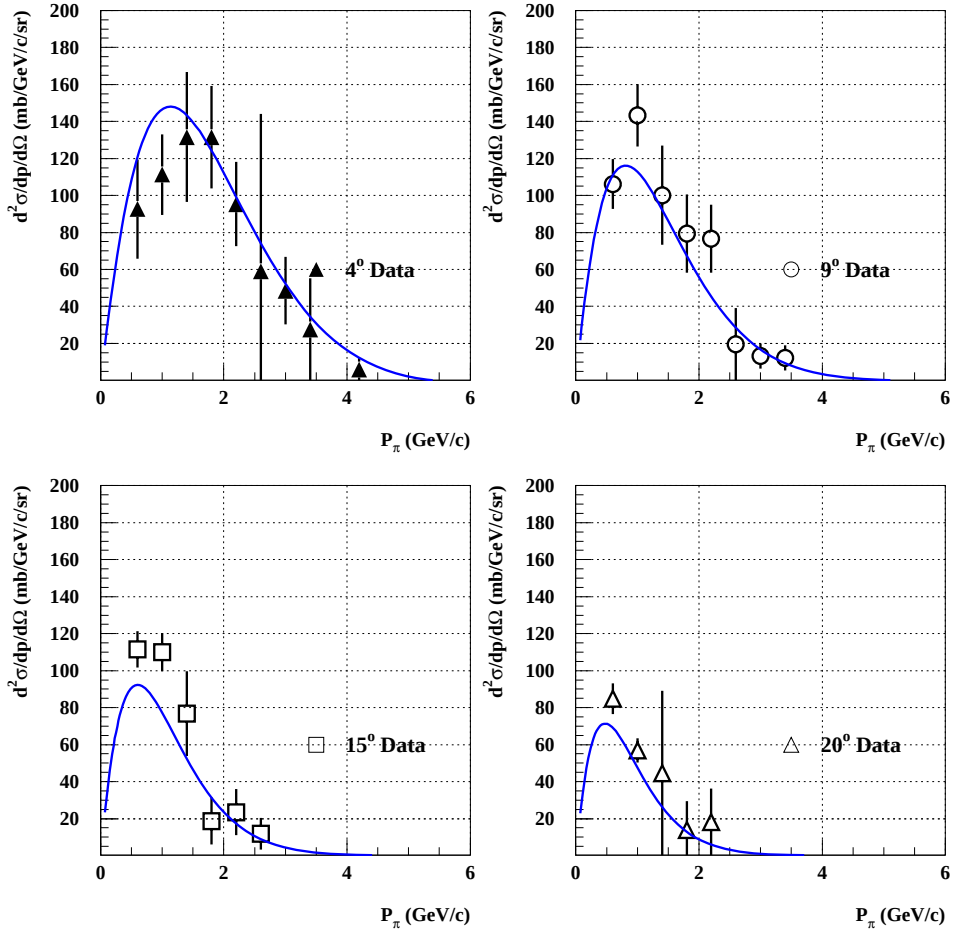

Figure 3.4: *E910 [77] experiment measured inclusive π^+ production cross section (milli-barns/GeV/c/steradian) in proton-beryllium interactions vs. π^+ momentum (GeV/c), at p_{proton} = 6.4 GeV/c. Error bars include statistics and systematics.*

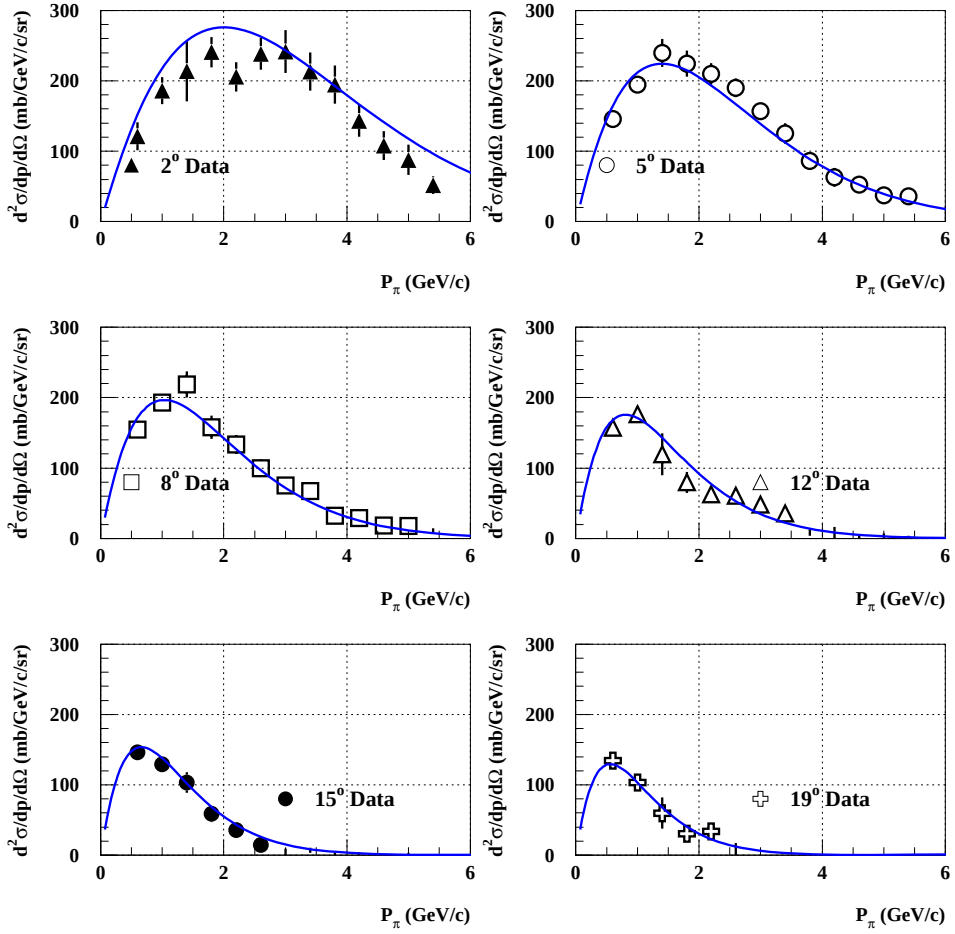

Figure 3.5: *E910 [77] experiment measured inclusive π^+ production cross section (milli-barns/GeV/c/steradian) in proton-beryllium interactions vs. π^+ momentum (GeV/c), at $p_{proton} = 12.3$ GeV/c. Error bars include statistics and systematics.*

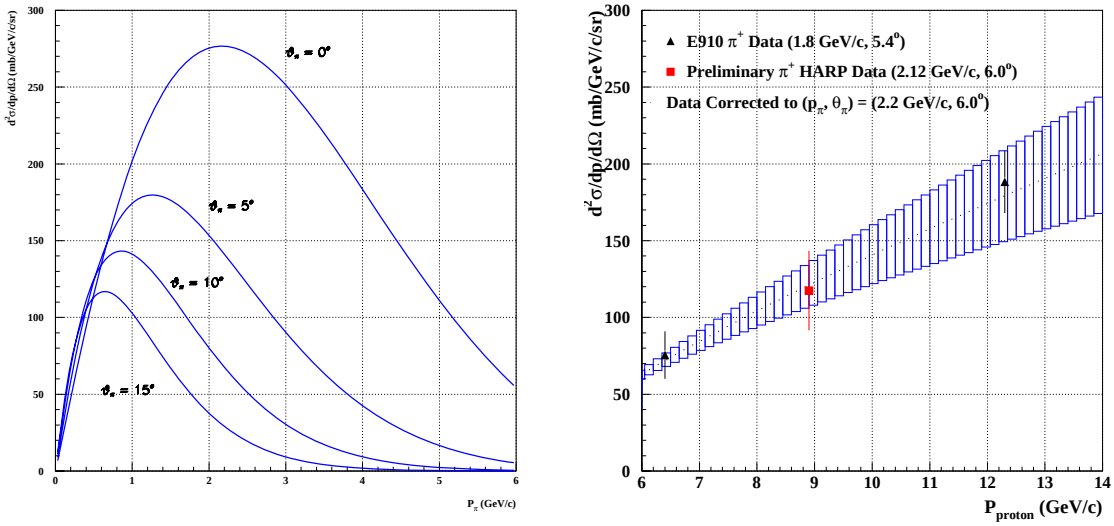

Figure 3.6: *Left: best-fit Sanford-Wang inclusive π^+ production cross section (milli-barns/GeV/c/steradian) vs. π^+ momentum (GeV/c) for various angles, at p_{proton} = 8.9 GeV/c. Right: best-fit Sanford-Wang inclusive π^+ production cross section (milli-barns/GeV/c/steradian) vs. proton momentum (GeV/c), evaluated at* $(p_\pi, \theta_\pi) = (1.8\ GeV/c, 5.4^o)$.

The data from all experiments except Vorontsov, Abbott, and Eichten are reported in bins of double differential cross section vs. kaon momentum and angle. For the purpose of this fit, the data from these experiments have been converted to double differential cross section. The Vorontsov data are reported as invariant cross section vs. kaon momentum and is converted to double differential cross section via

$$\frac{d^2\sigma}{dpd\Omega} \;=\; \Big(\frac{p_K^2}{E_K}\Big) \times E\frac{d^3\sigma}{d^3p} \tag{3.11}$$

The Abbott data are reported as invariant cross section vs. transverse kinetic energy (K_T) in bins of rapidity, where

$$K_T \;=\; m_T - m_K \;=\; \sqrt{m_K^2 + p_T^2} - m_K \tag{3.12}$$

and

$$m_T^2 \;=\; m_K^2 + p_T^2 \tag{3.13}$$

The conversion to double differential cross section vs. kaon momentum in bins of kaon production angle uses

$$E\frac{d^3\sigma}{d^3p} \;=\; \frac{d^2\sigma}{\pi dyd(p_T^2)}, \quad y \;=\; tanh^{-1}\Big(\frac{pz}{E}\Big), \tag{3.14}$$

$$p_Z \;=\; \sqrt{\frac{m_K^2 + p_T^2}{\Big(\frac{1}{tanh(y)}\Big)^2 - 1}}, \quad p_T \;=\; \sqrt{K_T^2 + 2m_K K_T}, \tag{3.15}$$

and

$$p_{total} \;=\; \sqrt{p_T^2 + p_Z^2}, \quad \theta \;=\; atan2(p_T, p_Z).$$

Unfortunately the Abbott data are reported in 7 rather large bins of rapidity ($\Delta y = 0.2$). The average rapidity in each bin is used to calculate p_Z, which introduces error into the conversion. The data are subsequently sorted into 7 bins of equal solid angle by requiring $\theta_{min} < \theta < \theta_{max}$ where θ_{min} and θ_{max} are the bin limits for a given bin in $d(cos(\theta))$. In the first (last) bin θ_{min} (θ_{max}) is arbitrarily set to a value smaller (larger)

experiment	p_{proton} (GeV/c)	p_K (GeV/c)	θ_K	N_{DATA}	σ_{NORM}
Abbott [79]	14.6	2-8	20 - 30^o	43	10%
Aleshin [80]	9.5	3-6.5	3.5^o	5	10%
Eichten [81]	24.0	4-18	0-6^o	56	20%
Piroue [82]	2.74	0.5-1	13,30^o	13	20%
Vorontsov [83]	10.1	1-4.5	3.5^o	13	25%

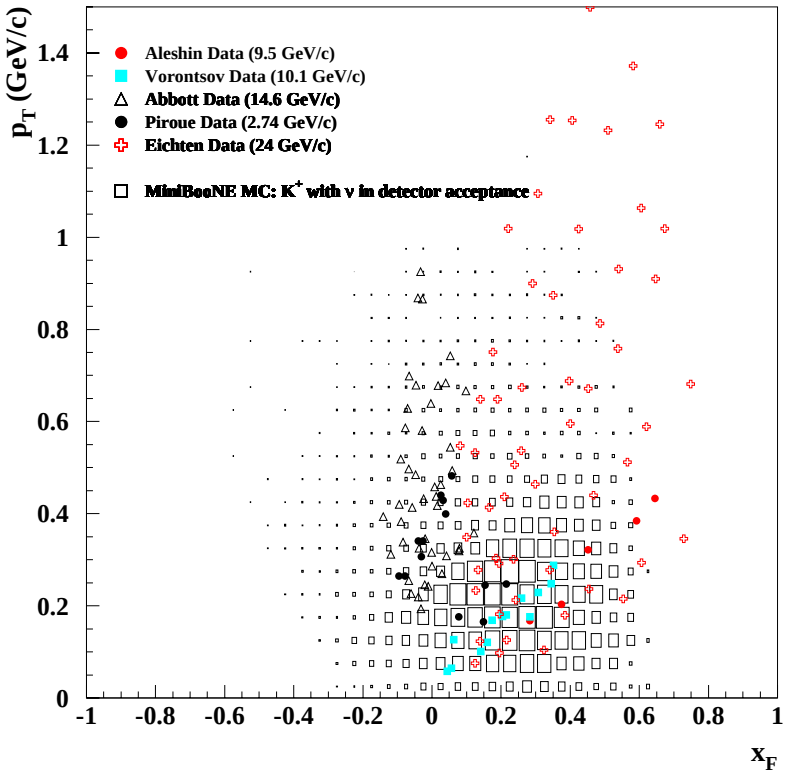

Figure 3.7: *Top: Summary of experiments which measure $pBe \rightarrow K^+X$ in a region of interest to MiniBooNE. Bottom: Transverse momentum (GeV) vs. $x_{Feynman}$ for K^+ production experiments, overlaid with the MiniBooNE beam Monte Carlo prediction for K^+-decay ν in the MiniBooNE detector acceptance.*

than the smallest (largest) angle reported in the data. The Eichten data are reported as invariant particle density vs. kaon momentum in bins of kaon production angle. The conversion from invariant particle density to double differential cross section is

$$\frac{d^2\sigma}{dpd\Omega} \;=\; \omega(p_K,\theta_K) \times \left(\frac{p_K^2}{2E_K}\right) \times \sigma_I \tag{3.16}$$

where $\omega(p_K,\theta_K)$ is the Lorentz invariant particle density, and σ_I is the inelastic proton-beryllium cross section, assumed here to be 204.5 mb.

The Abbott, Aleshin, Eichten, Piroue, and Vorontsov data are fit by minimizing the χ^2 function of equation 3.6, however, the Sanford-Wang function is modified such that the kinematic cutoff is a free parameter in the fit. The term $\left(1-\frac{p_{meson}}{p_{proton}-1}\right)$ in equation 3.2 becomes $\left(1-\frac{p_{meson}}{p_{proton}-c_9}\right)$, where c_9 is the ninth free parameter in the fit. The errors are assumed to be uncorrelated for all data points. The best-fit parameters for the Sanford-Wang K^+ production cross section are shown in table 3.3. The χ^2/ndf of the combined fit is 3.61. The contribution to the total fit χ^2 from each individual experiment is shown in table 3.5.

This K^+ fit differs from the π^+ fit in that each angle of each experiment is assigned a normalization pull term. In contrast, for the π^+ fit, one normalization pull term is used per experiment. The motivation for the difference is that in the K^+ experiments, the data at each angle were recorded with a different spectrometer location, unlike the modern π^+ experiments, which use fixed spectrometers with large acceptances. The best-fit pull term values are shown in table 3.4.

The data are compared with the best-fit Sanford-Wang K^+ production cross section in figures 3.8 through 3.11. By inspection one can see that there is tension in the fit for the Vorontsov and Piroue data, and in the lowest-angle bin data from the Eichten experiment.

The Vorontsov data are clearly incompatible with the shape of the Sanford-Wang

Table 3.3: *Best-fit Sanford-Wang K^+ parameters, assuming uncorrelated errors for all data sets. Probability refers to the total χ^2/ndf.*

fit parameter	*best-fit value ± error*
c1	6.083 ± 0.7136
c2	1.468 ± 0.06185
c3	10.04 ± 2.887
c4	3.085 ± 0.08379
c5	3.356 ± 0.0278
c6	5.718 ± 0.1523
c7	0.1274± 0.008995
c8	10.36 ± 1.662
c9	0.000 ± 0.2116
shape χ^2/ndf	426/121
total χ^2/ndf	438/121
probability	0.0

Table 3.4: *Best-fit Sanford-Wang K^+ pull-term parameters, assuming uncorrelated errors for all data sets.*

fit parameter	*best-fit value ± error*
n_1 (Aleshin)	1.19±0.28
n_1 (Vorontsov)	0.63±0.15
n_1 (Abbott)	1.003± 0.2898
n_2 (Abbott)	0.9958± 0.2404
n_3 (Abbott)	1.152± 0.2659
n_4 (Abbott)	0.9678± 0.2577
n_5 (Abbott)	0.9271± 0.2695
n_6 (Abbott)	1.034± 0.3169
n_7 (Abbott)	0.9562± 0.3694
n_1 (Piroue)	0.7798±0.2960
n_2 (Piroue)	1.146±0.4192
n_1 (Eichten)	0.7081±0.2295
n_2 (Eichten)	0.9877±0.2351
n_3 (Eichten)	1.084±0.2058
n_4 (Eichten)	1.046±0.1890
n_5 (Eichten)	1.001±0.1970
n_6 (Eichten)	0.9525±0.2264
n_7 (Eichten)	0.9078±0.2557

Table 3.5: *Compatibility of K^+ production experiments with best-fit Sanford-Wang K^+ production cross section prediction.*

experiment	χ^2_{shape}	χ^2_{total}	*ndf*	χ^2_{total} *probability*
Aleshin	47.47	49.08	-4	-
Vorontsov	122.2	124.4	4	0.000
Abbott	42.51	43.96	34	0.117
Piroue	37.38	39.12	4	0.000
Eichten	176.7	181.4	47	0.000

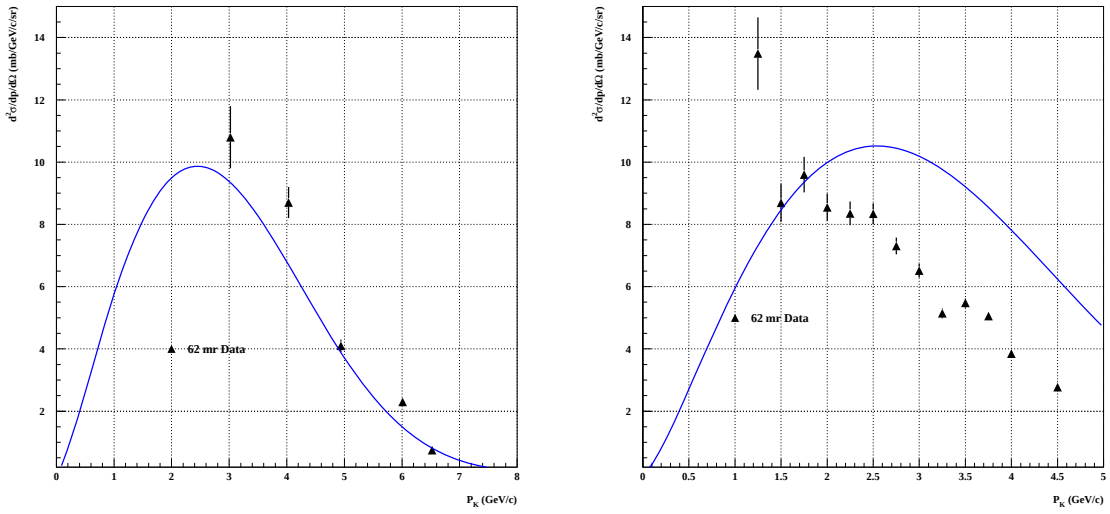

Figure 3.8: *Left: Aleshin [80] experiment measured inclusive K^+ production cross section (milli-barns/GeV/c/steradian) in proton-beryllium interactions vs. K^+ momentum (GeV/c), at p_{proton} = 9.5 GeV/c. Right: Vorontsov [83] experiment measured inclusive K^+ production cross section (milli-barns/GeV/c/steradian) in proton-beryllium interactions vs. K^+ momentum (GeV/c), at p_{proton} = 10.1 GeV/c. Error bars include statistics and systematics.*

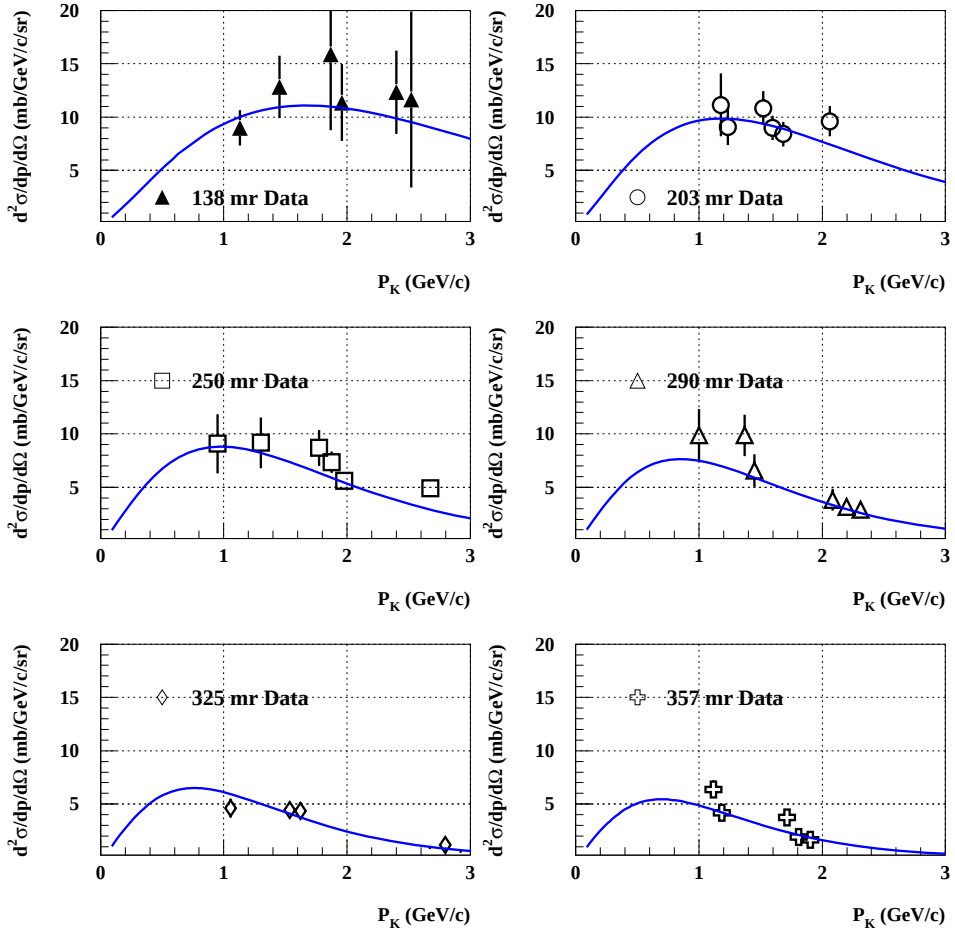

Figure 3.9: *Abbott [79] experiment measured inclusive K^+ production cross section (milli-barns/GeV/c/steradian) in proton-beryllium interactions vs. K^+ momentum (GeV/c), at $p_{proton} = 14.6$ GeV/c. Error bars include statistics and systematics.*

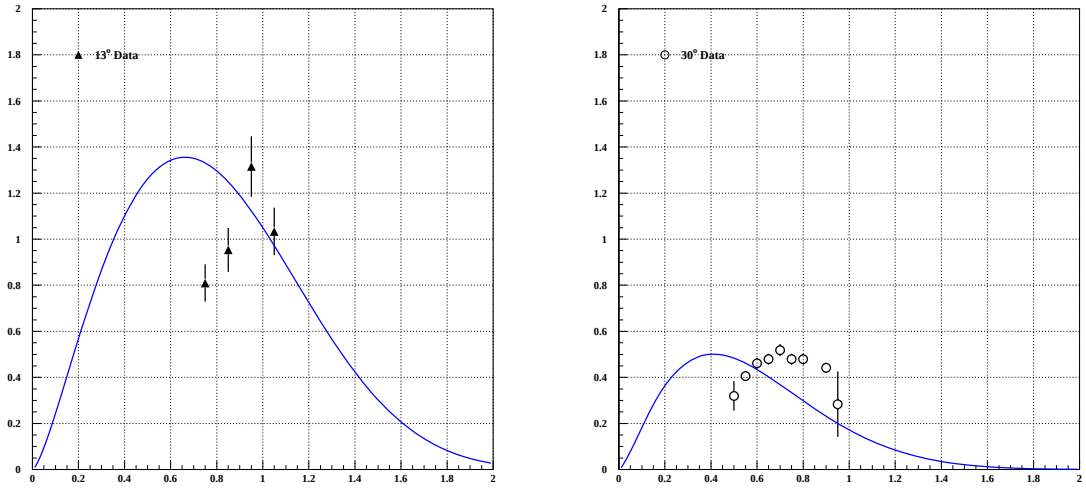

Figure 3.10: *Piroue [82] experiment measured inclusive K^+ production cross section (milli-barns/GeV/c/steradian) in proton-beryllium interactions vs. K^+ momentum (GeV/c), at p_{proton} = 2.74 GeV/c. Error bars include statistics and systematics.*

prediction, and with Aleshin data. The Aleshin and Vorontsov measurements are taken at the same production angle, similar production momenta, and similar incident proton beam momentum. The fact that the cross section results are so different between the two experiments may indicate an experimental problem. However, it is unclear which experiment is wrong, therefore both are included in the fit. The Piroue data are also incompatible in shape with the Sanford-Wang function, however, since this is the only experiment with an incident proton beam momentum less than MiniBooNE's, it is worth including this data in global fit.

The Eichten low-angle data disagreement with the Sanford-Wang function suggests a deficiency in the Sanford-Wang function extrapolation to low angles, however, it is also possible that this is due to the lack of bin-center corrections. None of the data in the combined K^+ fit is bin-center corrected, since the original bin limits are unknown. The cross section changes rapidly near $\theta = 0^o$, and therefore bin center

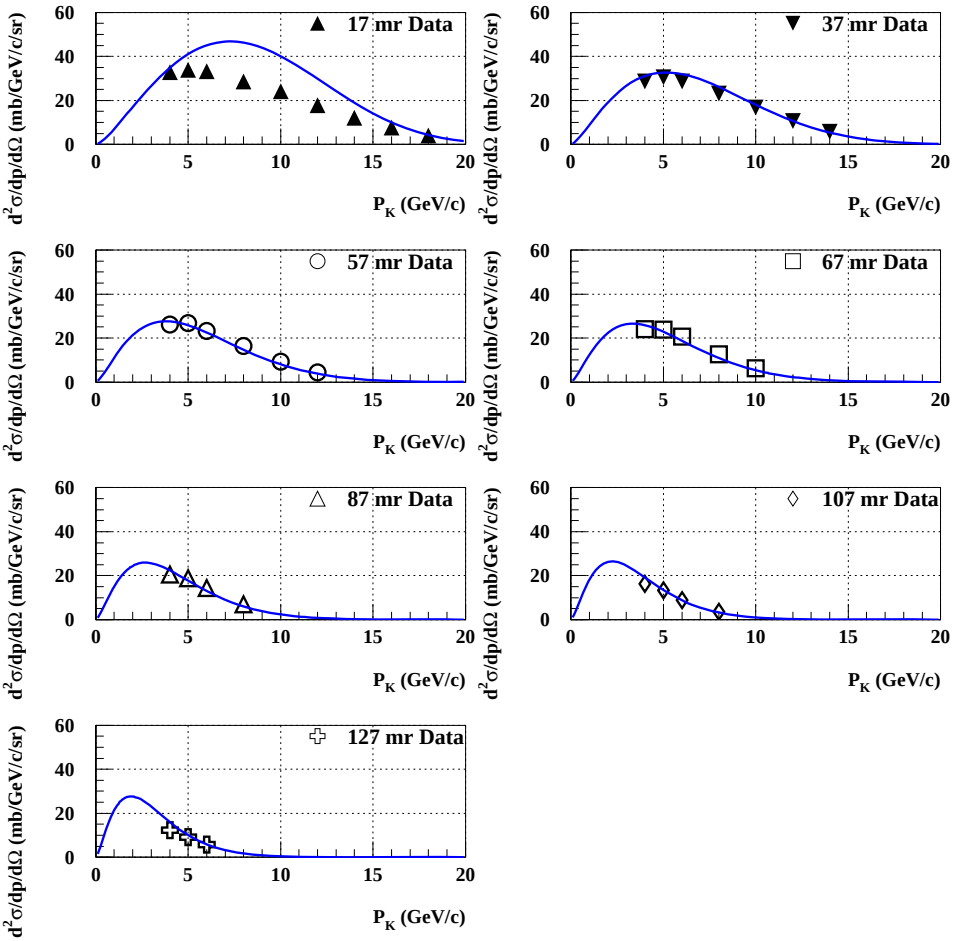

Figure 3.11: *Eichten [81] experiment measured inclusive K^+ production cross section (milli-barns/GeV/c/steradian) in proton-beryllium interactions vs. K^+ momentum (GeV/c), at $p_{proton} = 24.0$ GeV/c. Error bars include statistics and systematics.*

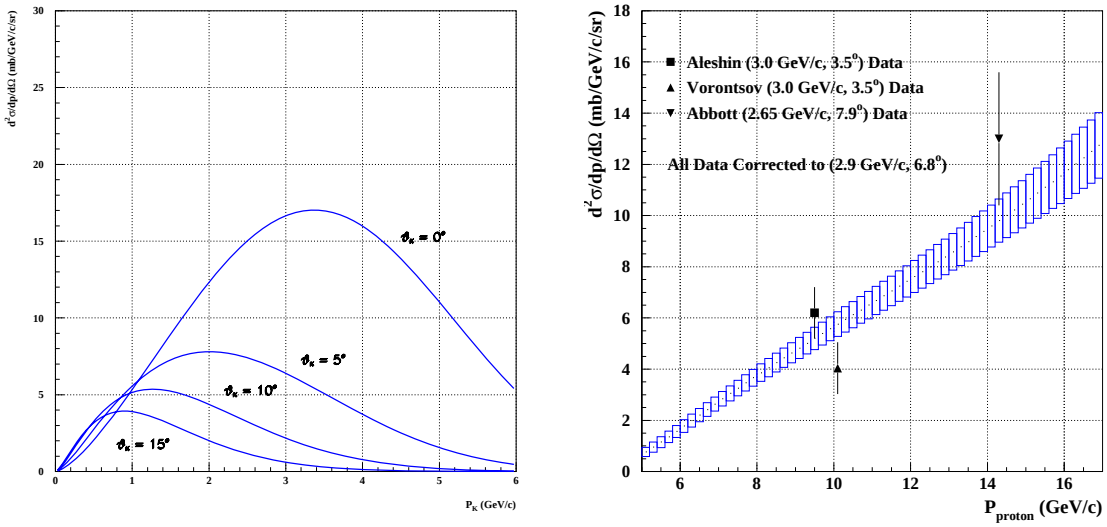

Figure 3.12: *Left: best-fit Sanford-Wang inclusive K^+ production cross section (millibarns/GeV/c/steradian) vs. K^+ momentum (GeV/c) for various angles, at p_{proton} = 8.9 GeV/c. Right: best-fit Sanford-Wang inclusive K^+ production cross section (millibarns/GeV/c/steradian) vs. proton momentum (GeV/c), evaluated at (p_K, θ_K) = (2.9 GeV/c, 6.8°).*

corrections may have a large effect here.

The K^+ production fit in table 3.3 has been used to generate all of the Monte Carlo in this thesis. Because of the poor fit quality, several efforts to measure neutrinos from kaon decay in the MiniBooNE data are underway. One of these is discussed in chapter 5.

3.1.2 MiniBooNE Beam Monte Carlo

A Geant4 [84] Monte Carlo simulation describes the MiniBooNE neutrino beam line, starting from protons incident on the target, and ending with the flux incident on the MiniBooNE neutrino detector. Only a brief summary is given here as this program has been described in detail elsewhere [85]. After meson production, described in

the previous sections, the most relevant processes to the MiniBooNE neutrino flux prediction are hadronic interactions, deflection in the focusing horn magnetic field, and meson decay.

The possible hadronic interactions can be categorized as elastic, quasi-elastic, and inelastic. In elastic interactions the projectile scatters coherently off of the target nucleus or nucleon, and only the direction of the projectile changes; its energy and the energy of the struck particle remain the same. In quasi-elastic interactions the projectile scatters incoherently off of the struck nucleon, and the total number of particles is conserved. However, momentum and quantum numbers can be exchanged. Examples of quasi-elastic interactions include target dissociation ($pd \rightarrow ppn$), and charge exchange ($\pi^- p \rightarrow \pi^0 n$). In inelastic interactions new particles are created, resulting in meson production. The kinematics of particles produced in inelastic interactions are simulated according to the differential Sanford-Wang cross section predictions described in the previous section.

Inelastic interactions are most important for producing the MiniBooNE neutrino beam. Historically there is much variation among measurements of the inelastic cross section on beryllium at MiniBooNE beam enerigies, which is in part responsible for the normalization differences among older π^+ production cross section measurements. Fits to data from the Gachurin [86] and Bobchenko [87] experiments are used in the MiniBooNE beam Monte Carlo to describe the inelastic cross section vs. p_{proton} in p-Be interactions. The π^+-Be (and π^--Be) inelastic cross section is based on a fit to data from the Gachurin [86], Allardyce [88], and Ashery [89] experiments. The resulting p-Be (π^+-Be) inelastic cross section is 212 mb (200 mb) at $p_{proton} = 8.9$ GeV/c ($p_\pi = 2.0$ GeV/c). These p-Be and π^+-Be inelastic cross section fits are shown in figure 3.13. The p-Be and π^+-Be quasi-elastic and elastic cross section models in the MiniBooNE beam Monte Carlo are based on Glauber model calculations [90].

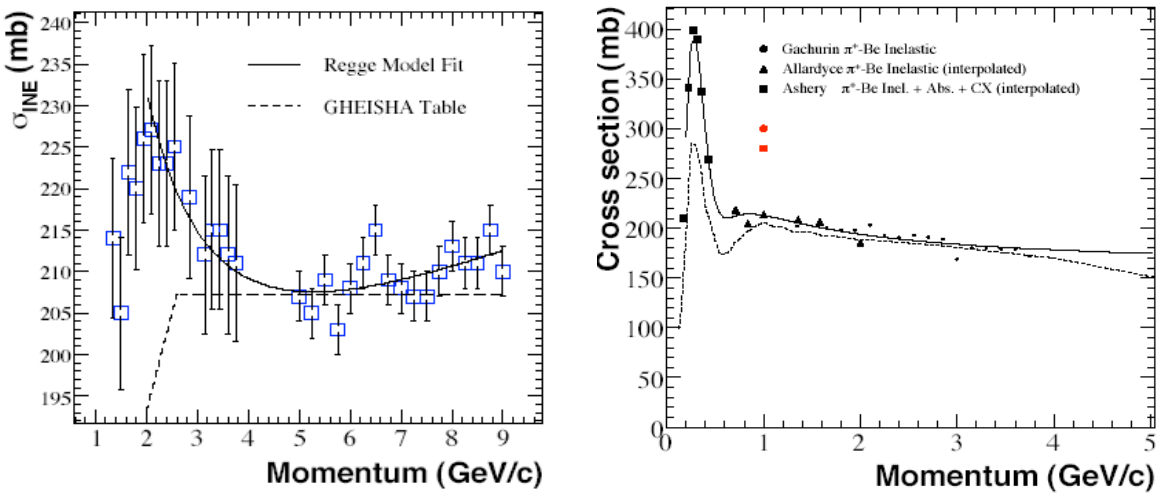

Figure 3.13: *Left: inelastic p-Be cross section data (mb) vs. incident proton momentum (GeV/c). Right: inelastic π^+-Be cross section data (mb) vs. incident π^+ momentum (GeV/c). The MiniBooNE beam Monte Carlo fit and the GHEISHA hadronic interaction model curves are overlaid. Figure from reference [90].*

From the Monte Carlo simulation, quasi-elastic interactions are responsible for ∼5% of the neutrino flux incident on the MiniBooNE detector, and elastic interactions contribute <1%.

Each time a proton on target is simulated, its inelastic interaction probability is determined by the interaction length $\lambda_{inelastic}$,

$$P_{inelastic} \;=\; (1 - exp[L_{target}/\lambda_{inelastic}]) \tag{3.17}$$

and

$$\frac{1}{\lambda_{inelastic}} \;=\; \frac{N_A\ \sigma_{inelastic}}{A_{Be}}. \tag{3.18}$$

If the proton interacts, the number of secondary mesons is determined by throwing against Poisson distributions with means equal to the average multiplicity for each secondary particle type. The multiplicity is calculated from the differential cross

sections via

$$< n_{\pi^+} > = \frac{\int (d^2\sigma_{\pi^+}/dpd\Omega) dpd\Omega}{\sigma_{inelastic}} \tag{3.19}$$

for example, where $(d^2\sigma_{\pi^+}/dpd\Omega)$ is the best-fit production cross section. If an event with greater than zero mesons has occured, then the kinematics are drawn from the meson production cross section tables, which are binned in p_T and p_Z. Neither energy nor the total cross section are required to be conserved on an event by event basis by this procedure, however, on average, energy is conserved, and the differential and inelastic cross sections equal their input values. The following secondary particle types are considered: π^+, π^-, K^+, K^0_L, n, and p. The differential cross sections for the first four come from Sanford-Wang model fits, while the latter two come from the MARS15 Monte Carlo. K^- production is not simulated since the probability of getting a ν in the detector from a K^- decay is a factor of 100 less than from a K^+. The K^0_L fits are described in reference [91].

Once a secondary particle has been generated, it is tracked through the simulation geometry, which contains a full description of the MiniBooNE neutrino beam line, as well as physics models for electromagnetic interactions, ionization energy loss, multiple coulomb scattering, and meson decay. On average, a π^+ travels 82 cm through the magnetic focusing horn field region, with a mean magnetic field of 0.71 $Tesla$. This changes the average momentum and angle of the π^+ beam from (2.2 GeV/c, 105 mr) before the horn to (2.1 GeV/c, 30 mr) afterwards, and increases the number of ν from π^+ decay in the detector acceptance by a factor of $\sim$5. The mean distance travelled by a π^+ through beam line material is 8.5 cm (5.9 cm) in beryllium (aluminum), resulting in a 21.5 (22.3) MeV energy loss, and an average multiple scattering angle of 1 (2) mr. The secondary mesons subsequently decay, producing the MiniBooNE neutrino beam, which has an average energy of 0.72 GeV (for neutrinos in the MiniBooNE detector acceptance). The most important decay

Table 3.6: *MiniBooNE Geant4 beam Monte Carlo meson decay parameters.*

Particle	Lifetime (ns)	Decay mode	Branching ratio (%)
π^+	26.03	$\mu^+\nu_\mu$	99.9877
		$e^+\nu_e$	0.0123
K^+	12.37	$\mu^+\nu_\mu$	63.17
		$\pi^+\pi^0$	21.2
		$\pi^+\pi^+\pi^-$	5.6
		$\pi^0 e^+\nu_e$	5.13
		$\pi^0\mu^+\nu_\mu$	3.2
		$\pi^+\pi^0\pi^0$	1.7
K^0_L	51.70	$\pi^0\pi^0\pi^0$	19.45
		$\pi^- e^+\nu_e$	20.4
		$\pi^+ e^-\bar{\nu}_e$	20.27
		$\pi^-\mu^+\nu_\mu$	13.55
		$\pi^+\mu^-\bar{\nu}_\mu$	13.46
		$\pi^0\pi^+\pi^-$	12.87
μ^+	2197.03	$e^+\nu_e\bar{\nu}_\mu$	100.0

modes and their Geant4 beam Monte Carlo simulation parameters are shown in table 3.6.

The predicted neutrino fluxes are shown as a function of neutrino energy in figures 3.14 through 3.15. According to the Monte Carlo, the neutrino beam composition is 92.7% ν_μ, 6.6% $\overline{\nu}_\mu$, 0.6% ν_e, and 0.1% $\overline{\nu}_e$. Of these, 86% come from decays of mesons produced in primary inelastic interactions (e.g. $p\ Be \rightarrow \pi^+ \rightarrow \nu_\mu$), secondary interactions (e.g. $p\ Be \rightarrow p\ Be \rightarrow \pi^+ \rightarrow \nu_\mu$) comprise the remaining 14%. The ν_μ

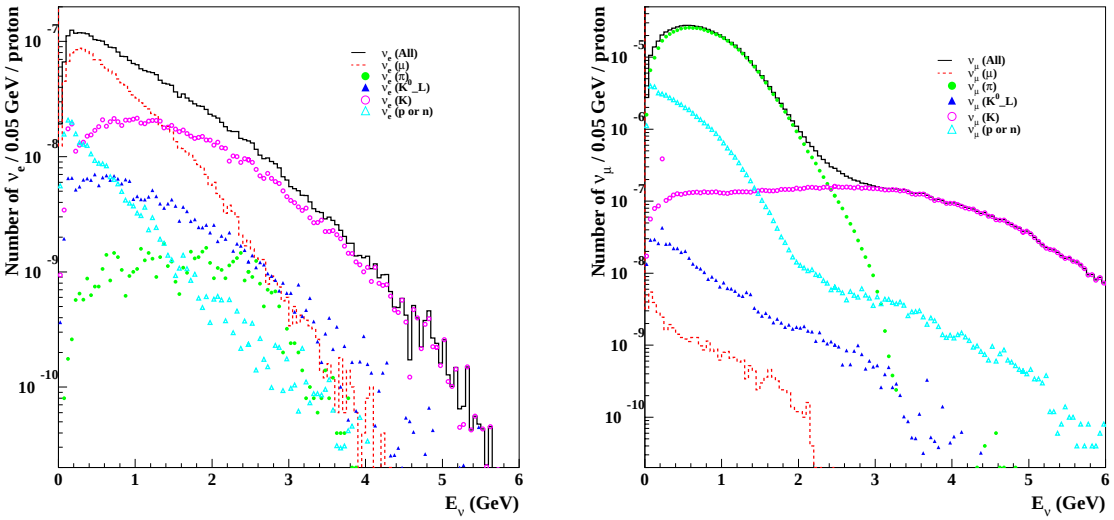

Figure 3.14: *Left: ν_e flux prediction by parent vs. Monte Carlo generated ν_e energy (GeV). Right: ν_μ flux prediction by parent vs. Monte Carlo generated ν_μ energy (GeV).*

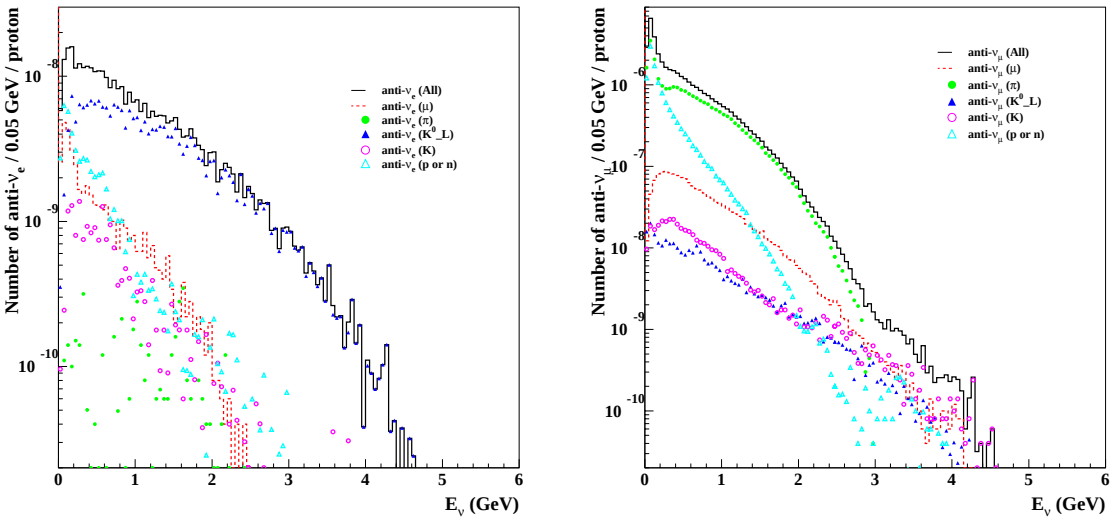

Figure 3.15: *Left: $\overline{\nu}_e$ flux prediction by parent vs. Monte Carlo generated $\overline{\nu}_e$ energy (GeV). Right: $\overline{\nu}_\mu$ flux prediction by parent vs. Monte Carlo generated $\overline{\nu}_\mu$ energy (GeV).*

Table 3.7: *MiniBooNE Geant4 beam Monte Carlo neutrino flux production modes.*

Neutrino Flavor	*Process*	*Fraction per Flavor (%)*
ν_μ	$p \to \pi^+ \to \nu_\mu$	86.1
	$p \to p \to \pi^+ \to \nu_\mu$	7.3
	$p \to K^+ \to \nu_\mu$	2.8
	$p \to n \to \pi^+ \to \nu_\mu$	1.9
	Other	1.9
$\bar{\nu}_\mu$	$p \to \pi^- \to \bar{\nu}_\mu$	55.0
	$p \to p \to \pi^- \to \bar{\nu}_\mu$	16.6
	$p \to n \to \pi^- \to \bar{\nu}_\mu$	12.0
	Other	16.4
ν_e	$p \to \pi^+ \to \mu^+ \to \nu_e$	47.6
	$p \to K^+ \to \nu_e$	32.7
	$p \to K^0_L \to \nu_e$	7.2
	$p \to p \to \pi^+ \to \mu^+ \to \nu_e$	5.0
	Other	7.5
$\bar{\nu}_e$	$p \to K^0_L \to \bar{\nu}_e$	65.5
	$p \to \pi^- \to \mu^- \to \bar{\nu}_e$	9.8
	Other	24.7

flux is 86% from primary π^+ decay, and 3% from primary K^+ decay. The ν_e flux from primary interactions is composed of 33% from K^+ decay, 7% from K^0_L decay, and 48% from μ^+ decay (via $p\ Be \rightarrow \pi^+ \rightarrow \mu^+ \rightarrow \nu_e$). The detailed meson parentage history of the flux by neutrino flavor is summarized in table 3.7.

3.1.3 Flux Prediction Uncertainties

The sources of uncertainty in the flux prediction include: proton beam focusing, hadronic cross sections, the differential Sanford-Wang meson production cross sections, the horn magnetic field, and the beam line geometry and interaction cross sections for secondary particles. Additional sources of normalization uncertainty related to the proton beam line are proton beam targeting efficiency, and the accuracy of the protons on target measurement. An estimate of the contribution of each of these components to the flux prediction uncertainty is summarized in table 3.8, and the production cross section uncertainty by meson type is shown in table 3.9.

The contribution to the neutrino flux uncertainty from proton beam focusing and hadronic cross sections is estimated to be less than 4% [92]. The constituents considered include perfect focusing and de-focusing, p-Be total, inelastic, and quasi-elastic cross section variations, and elastic and quasi-elastic scattering parameter variations.

The meson production cross section uncertainties come from the Sanford-Wang fits. The fit parameter errors in tables 3.2 and 3.3 for π^+ and K^+ respectively are combined with the parameter correlation matrix to calculate the predicted cross section uncertainty at a given $(p_{proton}, p_{meson}, \theta_{meson})$ as follows. The change in the Sanford-Wang predicted cross section function Δf_1 due to a change in parameter c_1

Table 3.8: *Summary of sources of neutrino flux uncertainty. "Quasi-elastic" is abbreviated as "QE" below. The quadrature sum assumes the parameters are uncorrelated.*

source	*MC parameter*	*default value*	*variation*	$\Delta\Phi_\nu$ *(%)*
beam focusing [92]	$\rho(\sigma_x, \sigma_y)$	0.0	± 1	0.8
p-Be σ_{total} [92]	σ_{TOT} (mb)	285.5	15	0.8
p-Be $\sigma_{inelastic}$ [92]	σ_{INEL} (mb)	212.4	5	1.2
p-Be σ_{QE} [92]	σ_{QE} (mb)	34.9	20	2.5
elastic scattering [92]	β_{EL} $(GeV/c)^{-2}$	-70	10	0.4
QE scattering [92]	β_{QE} $(GeV/c)^{-2}$	-10	3	1.7
horn current	horn current kA	174	5	2.0
target position [93]	z_{target} (cm)	3.5	4.0	4.0
horn length [93]	L_{horn} (cm)	180	8	3.7
$N_{p.o.t.}$ measurement	accuracy (%)	-	2.0	2.0
quadrature sum	-	-	-	6.99

Table 3.9: *Summary of meson production cross section uncertainty, for π^+, π^-, K^+, and K^0_L, evaluated at the average production parameters for mesons which decay to neutrinos in the MiniBooNE detector acceptance. All numbers are reported in percent (%).*

source	$\Delta\sigma(\pi^+)$	$\Delta\sigma(\pi^-)$	$\Delta\sigma(K^+)$	$\Delta\sigma(K^0_L)$
Differential cross section	12.0	12.0	8.5	25.0

is calculated as

$$\Delta f_1 \;=\; f(c_1 + \delta c_1, c_2, ..., c_n) - f(c_1, c2, ..., c_n) \tag{3.20}$$

where c_i are the best-fit Sanford-Wang function parameters, δc_1 is the best-fit parameter error for c_1, and $i \;=\; 1, 8$ (or $i \;=\; 1, 9$ for K^+ fits). Similarly, Δf_i are calculated for the other Sanford-Wang parameters. The set of Δf_i are combined with the parameter correlation matrix from the fit $P_{i,j}$ to form the error matrix $M_{i,j}$,

$$M_{i,j} \;=\; \Delta f_i \; P_{i,j} \; \Delta f_j. \tag{3.21}$$

The correlated error on the predicted Sanford-Wang cross section, evaluated at a given $(p_{proton}, p_{meson}, \theta_{meson})$ is

$$\Delta\Big(\frac{d^2\sigma(p_{proton}, p_{meson}, \theta_{meson})}{dpd\Omega}\Big) \;= \sum_{i,j} M_{i,j}. \tag{3.22}$$

The error bars shown in figures 3.6 and 3.12 are calculated in this way. The π^+ and K^+ Sanford-Wang fit correlation matrices are given in appendix F. The π^- and K^0_L differential production cross section uncertainties are also calculated in this way.

The error on the predicted π^+ cross section at the average phase space point for π^+ that decay to neutrinos in the MiniBooNE detector acceptance, $(p_{proton},\; p_{\pi^+},\; \theta_{\pi^+})$ = (8.9 GeV/c, 2.2 GeV/c, 0.105 mr), is 7.9%. One can take the fact that the χ^2/ndf is not equal to 1.0 into account by scaling the fit parameter errors by $\sqrt{\chi^2/ndf}$, and repeating the calculation above. For the π^+ fit, this results in a predicted π^+ cross section error of 12.0%. The predicted K^+ cross section error at the average phase space point for K^+ that decay to ν in the MiniBooNE detector acceptance, $(p_{proton}, p_{K^+}, \theta_{K^+})$ = (8.9 GeV/c, 2.9 GeV/c, 0.118 mr), is 4.4%, or 8.5% when scaled by $\sqrt{\chi^2/ndf}$ for the K^+ fit. These cross section errors are evaluated at one point in the production phase space, while the MiniBooNE neutrino flux samples a range

of production momenta and angles. Therefore, the meson production cross section uncertainties do not necessarily translate linearly into neutrino flux uncertainties.

The horn magnetic field uncertainty is set by the measurement accuracy of the horn current monitor, which is ±5 kA. Varying the horn current with respect to the central value by this amount, $174 \pm 5\ kA$, in the beam Monte Carlo produces a change in the total neutrino flux of 2%.

The beam line geometry uncertainties can be assessed by individually varying many parameters describing the elements of the beam line, two examples which affect the meson production and focusing are given in table 3.8. Their effects on the flux at the detector are estimated to be ∼5.5% [93] using the `ModelB` fast beam line simulation [94]. Uncertainties on the neutrino flux due to interactions of secondary particles with the beam line geometry are related to the secondary interaction cross sections assumed in the Monte Carlo. The HARP experiment provides a suite of measurements that are being used to tune the MiniBooNE beam Monte Carlo secondary interaction model. This process is ongoing, and therefore the systematic errors associated with secondary interactions and the beam line geometry are not yet known. These will be calculated once the tuning of the beam Monte Carlo is complete.

The effect of proton beam targeting on the flux prediction uncertainty is negligible, since data reduction cuts are applied to ensure that >99% of the proton beam transits the entire length of the target. The uncertainty on the measurement of protons on target is estimated to be 2%, discussed in detail in appendix A.

Only the uncertainties in table 3.9 are considered in this thesis, since the normalization uncertainties given in table 3.8 are either negligible when compared with the Sanford-Wang particle production uncertainties, or still under investigation.

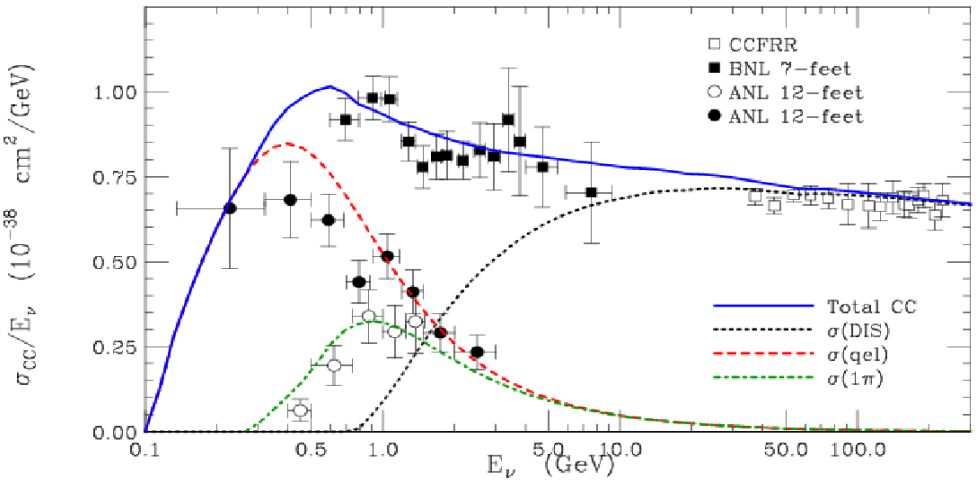

Figure 3.16: *Charged current neutrino cross section measurements divided by neutrino energy vs. E_ν (GeV); the curves are fit to the data to guide the eye. Figure from reference [95].*

3.2 Neutrino Cross Section Prediction

MiniBooNE operates in an interesting region for neutrino interaction cross sections, $E_\nu \sim 1\ GeV$, which is shown in figure 3.16. First, there is a dearth of data on nuclear targets in this energy range. Second, this region is complex theoretically since both charged current quasi-elastic ($\nu_\mu n \rightarrow \mu^- p$) and resonance (e.g. $\nu_\mu n \rightarrow \mu^- p \pi^+$) scattering processes contribute in roughly equal proportions. Finally, in this energy range deep-inelastic scattering interactions (e.g. $\nu_\mu n \rightarrow \mu^- p \pi^+ \pi^-$) are turning on, and therefore contribute non-negligibly to the total cross section for MiniBooNE's highest energy events. As a result, the simulation of neutrino interaction cross sections is a dominant source of uncertainty for MiniBooNE. However, MiniBooNE will accumulate more than 1×10^6 neutrino interactions on a nuclear target (CH_2), and can therefore make important contributions to constraining the cross section uncertainties in this regime.

3.2.1 MiniBooNE Cross Section Monte Carlo

MiniBooNE uses the NUANCE [96] Monte Carlo to simulate the neutrino interaction cross sections and final state kinematics. At MiniBooNE neutrino energies, the cross section has contributions from charged current quasi-elastic scattering (39% of the total event rate), charged current resonance production (25%), neutral current elastic scattering (16%), and neutral current π^0 production (8%).

For the $\nu_\mu \rightarrow \nu_e$ oscillation analysis, the most important processes are charged current quasi-elastic (CCQE) scattering, which affords a precise measurement of the neutrino energy, and neutral current π^0 production, which is a large background to a ν_e CCQE signal. Neutral current π^0 production at MiniBooNE has been described in detail elsewhere [40], therefore it will not be discussed here. For the ν_μ disappearance oscillation analysis, the most important processes are ν_μ CCQE scattering, and ν_μ charged current resonant single pion production (CC1π), which comprises the largest source of background after the ν_μ CCQE event selection, which is described in detail in chapter 4.

The free-nucleon theoretical inputs to the NUANCE Monte Carlo include the LLewellyn-Smith quasi-elastic cross section [97], the Rein-Sehgal resonance cross section model [98] for $W^2 < 2\ GeV$, and the standard deep inelastic scattering formula for $W^2 > 2\ GeV$, with the Bodek-Yang method for joining the resonance and deep inelastic scattering regions [99], where W^2 is the square of the mass of the hadronic system. Nuclear effects are included via the Smith-Moniz relativistic Fermi gas model for quasi-elastic and resonance interactions [100], and the treatment of final state nucleons. For final state mesons, NUANCE uses a π interaction model tuned on π electro-production data [101].

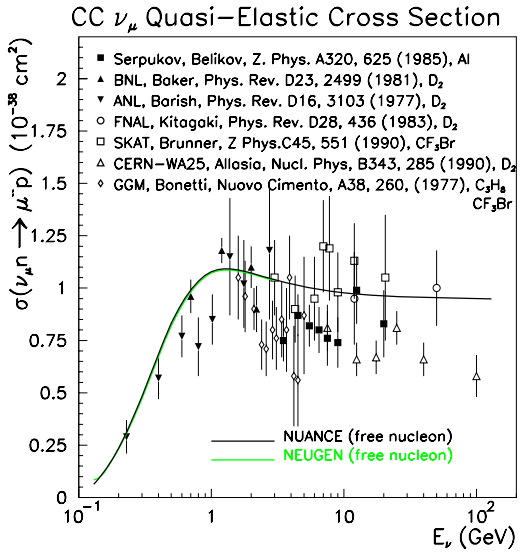

Figure 3.17: *NUANCE prediction compared with experimental data.* $\nu_\mu n \rightarrow \mu^- p$ *cross section (mb) vs.* E_ν (GeV). *Figure courtesy of [46]. Predictions assume* $m_V = 0.084$ GeV/c^2 *and* $m_A = 1.032$ GeV/c^2.

Charged Current Quasi-Elastic Cross Section

Charged current quasi-elastic interactions ($\nu_\mu n \rightarrow \mu^- p$) are fairly well measured in the MiniBooNE energy range on light targets, however the cross section on heavy targets is less well known. A summary of the existing data are shown in figure 3.17.

The Feynman diagram for CCQE scattering is shown in figure 3.18. The kinematics are defined by the four vectors

$$q_1 = (E_\nu, \vec{p}_\nu), \qquad q_2 = (E_{lepton}, \vec{p}_{lepton}), \tag{3.23}$$

$$p_1 = (M, 0), \qquad p_2 = (E, \vec{p}),$$

where E_ν (E_{lepton}) is the neutrino (lepton) energy, $\vec{p}_\nu$ ($\vec{p}_{lepton}$) is the neutrino (lepton) three momentum, M is the mass of the struck nucleon, and (E, $\vec{p}$) describe the outgoing nucleon's energy and three momentum. The CCQE cross section kinematics depend on the four-momentum transfer squared, Q^2, and the energy transfer, ω.

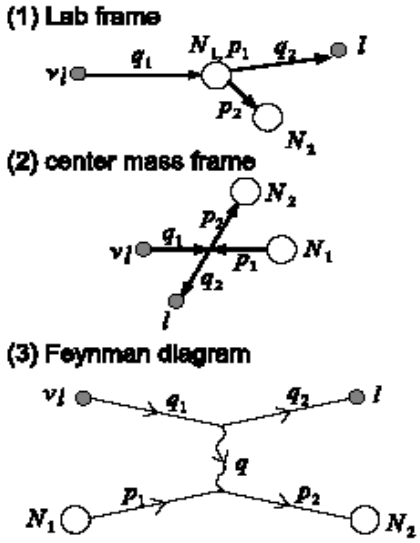

Figure 3.18: *Charged current quasi-elastic scattering diagrams.*

These are:

$$Q^2 \;=\; -(q_1 - q_2)^2 \;=\; -m^2_{lepton} + 2E_\nu(E_{lepton} - p_{lepton}cos(\theta_{lepton})) \tag{3.24}$$

where θ_{lepton} is the angle between the lepton and neutrino directions, and $Q^2 \;>\; 0$, and,

$$\omega \;=\; E_\nu - E_{lepton}. \tag{3.25}$$

Charged current quasi-elastic scattering is the most important neutrino interaction for MiniBooNE because its the most numerous, and, two-body kinematics enable a precise determination of the neutrino energy. Neglecting corrections for the motion of the target nucleon and the binding energy, the neutrino energy can be calculated from the measured energy and angle of the final state lepton:

$$E^{QE}_\nu \;=\; \frac{1}{2}\frac{2ME_{lepton} - m^2_{lepton}}{M - E_{lepton} + \sqrt{(E^2_{lepton} - m^2_{lepton})}cos\theta_{lepton}} \tag{3.26}$$

where M is the recoil nucleon mass, m_{lepton} is the lepton mass, E_{lepton} is the lepton energy, and θ_{lepton} is the lepton angle with respect to the beam direction. The energy resolution achievable by MiniBooNE for CCQE interactions is $\sim$10% at $E_\nu = 1\ GeV$.

The differential cross section for CCQE scattering off of a free nucleon is given by [97]

$$\frac{d\sigma}{dQ^2 dE_\nu} = \Big(\frac{M^2 G_F^2 V_{ud}^2}{8\pi(\hbar c)^2}\Big)\Big(\frac{1}{E_\nu^2}\Big)\Big(A(Q^2) \mp B(Q^2)\frac{(s-u)}{M^2} + C(Q^2)\frac{(s-u)^2}{M^4}\Big) \quad (3.27)$$

The first factor contains the normalization, where M is the mass of the struck nucleon, G_F is Fermi's constant, V_{ud} is the Cabibbo angle, and $(\hbar c)$ is $2\pi\times$ Planck's constant multiplied by the speed of light c. The sign convention for the second factor is positive for $\overline{\nu}$ and negative for ν scattering. The second factor contains the explicit neutrino energy (E_ν) dependence, and the neutrino energy also enters via the energy transfer given in terms of the Mandelstam variables $(s-u)$, where

$$s = (p_1+q_1)^2 = (p_2+q_2)^2 = M^2 + 2ME_\nu, \quad (3.28)$$

$$u = (q_2-p_1)^2 = (p_2-q_1)^2 = M^2 + m_{lepton}^2 - 2ME_\nu.$$

The third factor contains the terms A, B, and C, which parameterize the structure of the nucleon in terms of Q^2,

$$A(Q^2) = \frac{(m_{lepton}^2+Q^2)}{M^2}\Big[(1+z)F_A^2 - (1-z)F_1^2 + z(1-z)F_2^2 + 4zF_1F_2 \quad (3.29)$$
$$-\frac{m_{lepton}^2}{4M^2}\Big((F_1+F_2)^2 + (F_A+2F_P)^2 - \Big(\frac{Q^2}{M^2}+4\Big)F_P^2\Big)\Big],$$

$$B(Q^2) = \frac{Q^2}{M^2}F_A(F_1+F_2), \quad (3.30)$$

and

$$C(Q^2) = \frac{1}{4}(F_A^2 + F_1^2 + zF_2^2) \quad (3.31)$$

where

$$z = \frac{Q^2}{4M^2}. \quad (3.32)$$

These functions are written in terms of the axial (F_A), pseudoscalar (F_P), and vector (F_1 and F_2) form factors. The Fourier transforms of the axial and vector form factors describe the weak and electromagnetic charge distributions within the nucleon

respectively. These are given by the following formulae under the dipole assumption[3]:

$$F_1 = \frac{1+z(1+\mu_p-\mu_n)}{(1+z)\left(1+\frac{Q^2}{m_V^2}\right)^2}, \qquad F_2 = \frac{(\mu_p-\mu_n)}{(1+z)\left(1+\frac{Q^2}{m_V^2}\right)^2} \tag{3.33}$$

$$F_A = \frac{g_A}{\left(1+\frac{Q^2}{m_A^2}\right)^2}, \qquad F_P = \frac{2M^2}{m_\pi^2+Q^2}F_A(Q^2)$$

where $\mu_p = 1.793\mu_N$ and $\mu_n = -1.913\mu_N$ are the anomalous magnetic moments of the proton and neutron, $g_A = -1.267$ is the value of the axial form factor at $Q^2 = 0$ [45], $m_V = 0.84GeV/c^2$ is the vector mass, and $m_A = 1.03GeV/c^2$ is the axial mass [102]. With the exception of m_A, all of these constants are measured very precisely and so do not contribute to the uncertainty in the cross section predictions.

The dipole assumption has been checked in detail for the vector form factors, which are extracted from high-statistics electron scattering data. For Q^2 values above $\sim 0.2\ GeV^2$ the assumption is a good one, however, there are deviations at $Q^2 > 1\ GeV^2$. NUANCE uses the most recent non-dipole electromagnetic form factor fit results [103]. The axial form factor is most precisely measured in ν scattering data, which has had prohibitively small statistics until recently. The axial mass and the functional form of $F_A(Q^2)$ are therefore the dominant uncertainties on MiniBooNE's free nucleon CCQE cross section prediction.

Since the MiniBooNE neutrino target is CH_2, which has 6 bound (and no free) neutrons, the relevant experimental cross section for MiniBooNE is the bound nucleon CCQE scattering cross section. MiniBooNE uses the Smith-Moniz formalism to describe this process. This formalism parameterizes the nucleons inside a nucleus as a Fermi gas, with binding energy and Fermi momentum. The differential bound

[3]The dipole form factor assumption corresponds to a spatial charge distribution $\propto \rho(r) = exp(-r)$.

nucleon CCQE cross section is given by [100]:

$$\frac{d^2\sigma}{dp_{lepton}dcos(\theta_{lepton})} = \frac{2\pi(\hbar c G_F V_{ud})^2/M}{(1+Q^2/m_W^2)^2} \times \Big(\frac{p_{lepton}}{2\pi}\Big)^2 cos^2(\chi/2) \times \tag{3.34}$$

$$\Big(w_2 + 2w_1 + w_a\Big(\frac{m_{lepton}}{M}\Big)^2 tan^2(\chi/2) + (w_b + w_8)\frac{m_{lepton}^2}{ME_{lepton}cos^2(\chi/2)} -$$

$$2\Big(\frac{w_8}{M}\Big)tan(\chi/2)sec(\chi/2) \times \sqrt{Q^2cos^2(\chi/2) + |Q|^2sin^2(\chi/2) + m_{lepton}^2}\Big).$$

where p_{lepton}, E_{lepton}, and $cos(\theta_{lepton})$ describe the outgoing muon. The scattering kinematics are included via the four-momentum transfer squared Q^2, the magnitude of the three momentum transfer $|q|$, and the factors

$$cos^2(\chi/2) = \frac{E_{lepton} + p_{lepton}cos(\theta_{lepton})}{2E_{lepton}},\ sin^2(\chi/2) = \frac{E_{lepton} - p_{lepton}cos(\theta_{lepton})}{2E_{lepton}},$$

$$tan(\chi/2) = \sqrt{\frac{sin^2(\chi/2)}{cos^2(\chi/2)}},\ tan^2(\chi/2) = \frac{sin^2(\chi/2)}{cos^2(\chi/2)},\ sec(\chi/2) = \sqrt{\frac{1}{cos^2(\chi/2)}}. \tag{3.35}$$

The nuclear environment is described by the form factors w_i,

$$w_1 = a_1t_1 + (a_2 - a_3)t_2/2,\ w_2 = (a_4 + 2\omega\frac{a_5}{q} + \omega^2\frac{a_3}{q^2} + Q^2\frac{a_2 - a_3}{2q^2}) \times t_2 \tag{3.36}$$

$$w_a = (1.5a_3 - a_2/2)t_2\Big(\frac{M^2}{q^2}\Big) + a_1\Big(\frac{M}{m_{recoil}}^2\Big)t_a + 2a_6t_b\Big(\frac{M^2}{m_{recoil}q}\Big),$$

$$w_b = \Big(\frac{M}{m_{recoil}}\Big)(a_7 + \omega a_6/q)t_b + \Big(\frac{M}{q}\Big) \times \Big(a_5 + \Big(\frac{\omega}{q}\Big)(1.5a_3 - a_2/2)\Big)t_2,$$

$$w_8 = \Big(\frac{M}{m_{recoil}}\Big)(a_7 + \omega\Big(\frac{a_6}{q}\Big) \times t_8)$$

The w_i are written in terms of a set of functions t_i, which depend on the free nucleon vector and axial form factors, and a set of constants a_i which depend on the lepton kinematics and the Fermi gas model parameters.

The free nucleon form factors enter the Smith-Moniz cross section via the constants t_i, which are

$$t_1 = \frac{Q^2}{2}(F_1 + 2MF_2)^2 + (2M^2 + \frac{Q^2}{2})F_A^2,\ t_2 = 2M^2(F_1^2 + Q^2F_2^2 + F_A^2), \tag{3.37}$$

$$t_a \;=\; -\Big(\frac{M^2}{Q^2}\Big)t_1 + \frac{t_2}{4} + \Big(\frac{M^2}{2Q^2}\Big)(2MF_A - Q^2F_P)^2,\; t_b \;=\; \frac{-t_2}{2},$$
$$t_8 \;=\; 2M^2F_A(F_1 + 2MF_2).$$

The binding energy of the nucleus, E_B, is included via effective kinematic parameters,

$$\omega_{eff} \;=\; \omega - E_B, \qquad q^2_{eff} \;=\; q^2 - \omega^2_{eff} + m^2_{recoil} - M^2. \tag{3.38}$$

The a_i are given by

$$a_1 = b_0,\; a_2 = b_2 - b_0, \tag{3.39}$$
$$a_3 = \Big(\frac{-\omega_{eff}}{q}\Big)^2 b_2 + 2\Big(\frac{-\omega_{eff}}{q}\Big)\Big(\frac{q^2_{eff}}{2qM}\Big)b_1 + \Big(\frac{q^2_{eff}}{2qM}\Big)^2 b_0$$
$$a_4 = b_2 - \Big(\frac{2E_B}{M}\Big)b_1 + \Big(\frac{E_B^2}{M^2}\Big)b_0$$
$$a_5 = \Big(\frac{-\omega_{eff}}{q}\Big)b_2 + \Big[\frac{q^2_{eff}}{2qM} - E_B\frac{(-\omega_{eff}/q)}{M}\Big]b_1 - E_B\Big(\frac{q^2_{eff}}{2qM}\Big)\Big(\frac{1}{M}\Big)b_0$$
$$a_6 = \Big(\frac{-\omega_{eff}}{q}\Big)b_1 + \Big(\frac{q^2_{eff}}{2qM}\Big)b_0,\; a_7 = b_1 - \frac{E_B}{M}b_0$$

where the functions b_0, b_1, and b_2 implement the Fermi gas model via the implicit limits of integration E_{high} and E_{low},

$$E_{high} \;=\; \sqrt{k_F^2 + M^2}, \tag{3.40}$$

$$E_{low} \;=\; max\Big[M\Big(\frac{\Big(\frac{-\omega_{eff}}{q}\Big) * \Big(\frac{q^2_{eff}}{2qM}\Big) + \sqrt{1 - \Big(\frac{-\omega_{eff}}{q}\Big)^2 + \Big(\frac{q^2_{eff}}{2qM}\Big)^2}}{1 - \Big(\frac{-\omega_{eff}}{q}\Big)^2}\Big), E_{high} - \omega_{eff}\Big]$$

where k_F is the Fermi momentum. The set of constants b_i are given by

$$b_0 \;=\; \Big(\frac{M\omega}{q4\pi^2}\Big) \times \Big(f(E_{high}) - f(E_{low})\Big);\quad f(E) = E + E_B log(E - E_B), \tag{3.41}$$

$$b_1 \;=\; \Big(\frac{M\omega}{q4\pi^2 M}\Big) \times \Big(f(E_{high}) - f(E_{low})\Big);\quad f(E) = \frac{E^2}{2} + E_B\Big(E + E_B log(E - E_B)\Big),$$
$$b_2 \;=\; \Big(\frac{M\omega}{q4\pi^2 M^2}\Big) \times \Big(f(E_{high}) - f(E_{low})\Big);$$

$$f(E) = \frac{E^3}{3} + E_B\Big(\frac{E^2}{2} + E_B E + E_B^2 log(E - E_B)\Big)$$

For CH_2, the default NUANCE values of the binding energy E_B and the Fermi momentum k_F are 25 MeV and 220 MeV/c respectively [104]. These Fermi gas model constants are the dominant contribution to the bound nucleon CCQE cross section simulation uncertainty, and therefore MiniBooNE extracts effective values of these parameters by fitting the CCQE data, described in chapter 6. This analysis also provides Fermi gas model parameter errors and correlations.

When integrated over the MiniBooNE flux, the bound nucleon ν_μ CCQE cross section differs from the free nucleon prediction in both rate and kinematics of the final state particles. Figure 3.19 shows the number of events at MiniBooNE calculated with the free and bound nucleon CCQE cross sections. The total number of CCQE interactions is $\sim$20% lower, and while the reduction is approximately independent of final-state lepton momentum, it is a strong function of Q^2. This occurs because the bound target nucleons are not at rest, and can impart up to k_F of momentum to the total initial state momentum of the system. This affects low Q^2 events more than high Q^2 events because the fractional change (with respect to the free nucleon case) is largest at low Q^2. The bound nucleon cross section also suppresses events at low neutrino energy because for the reaction to occur, the energy transfer must exceed the binding energy E_B. Finally, Pauli blocking requires that there must be an unoccupied fermion state available to the recoil nucleon, which accounts for $\sim$5% of the total rate suppression, and affects only Q^2 values less than $\sim k_F^2$.

The Smith-Moniz relativistic Fermi gas model also has an important effect on the neutrino energy reconstruction resolution for CCQE events. In the absence of the Fermi motion of the target nucleon, the lepton momentum is completely specified by E_ν and Q^2. The effect of the Fermi gas model is to smear the final-state muon momentum away from the value it would have if the target nucleon were at rest. The

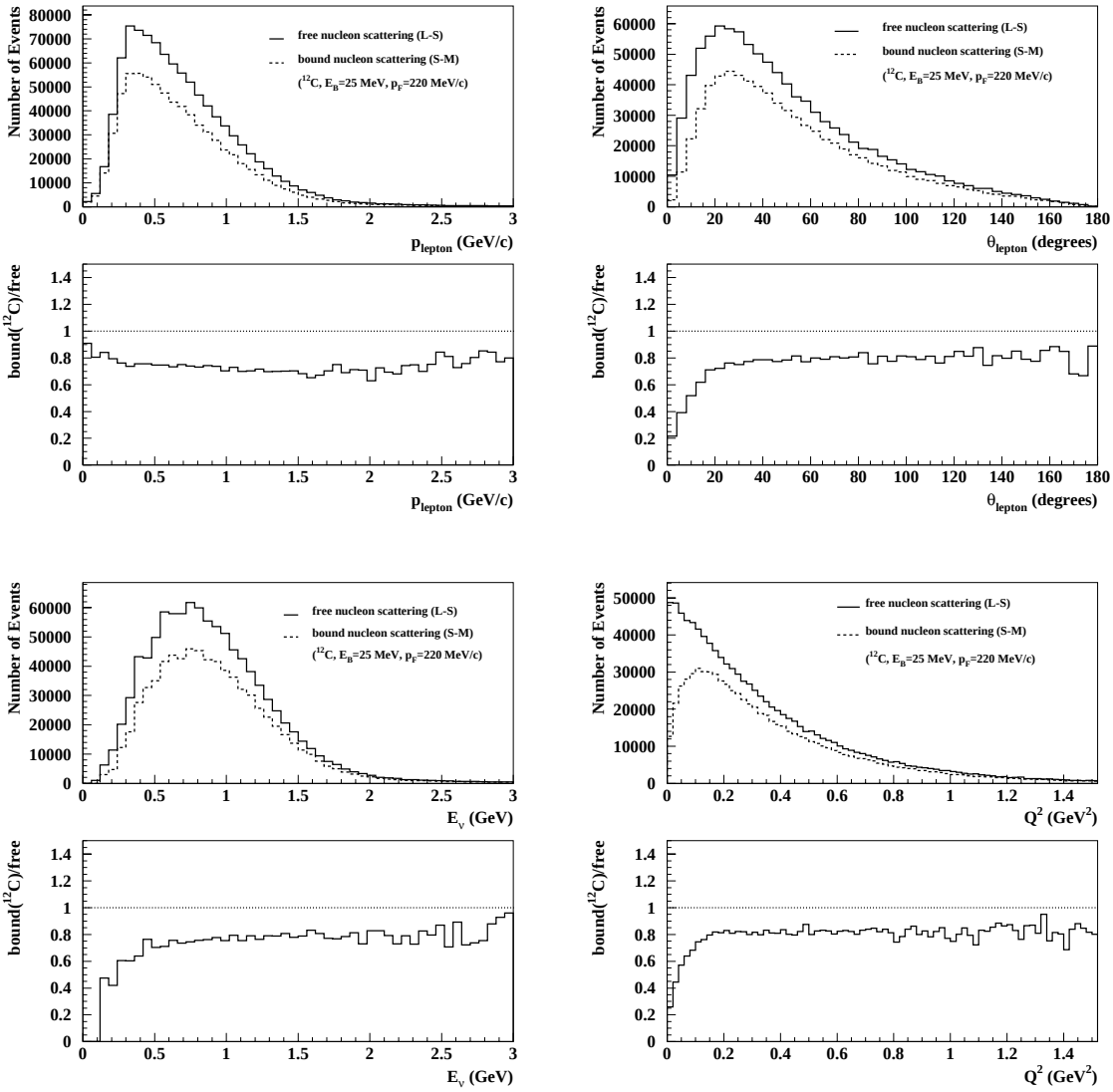

Figure 3.19: *Comparison of absolute numbers of events calculated using the MiniBooNE neutrino flux for bound (dashed) vs. free (solid) ν_μ CCQE scattering, for an arbitrary number of p.o.t.. Top left: number of events vs. p_μ (GeV/c). Top right: number of events vs. θ_μ (degrees). Bottom left: number of events vs. E_ν (GeV). Bottom right: number of events vs. Q^2 (GeV^2).*

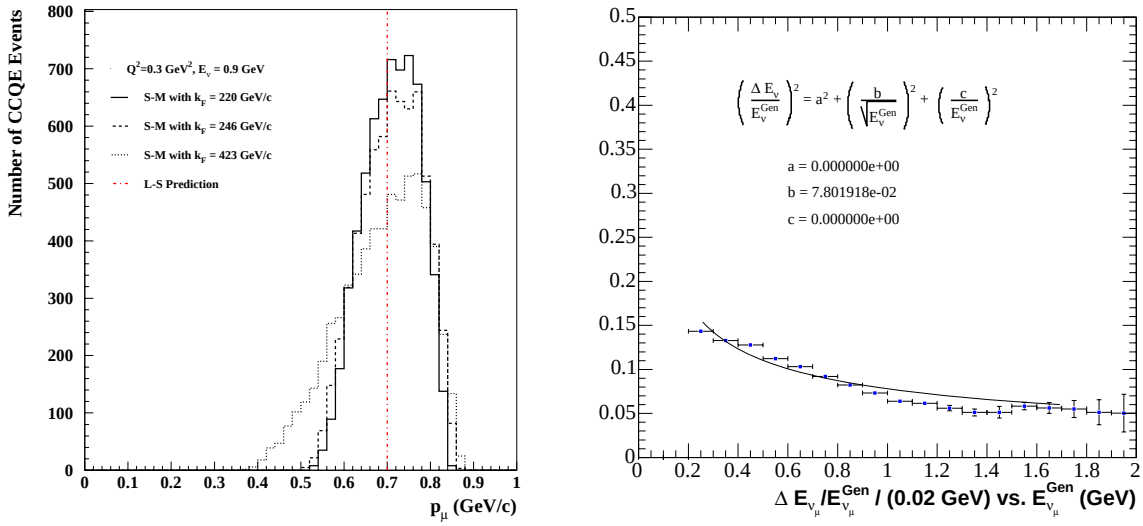

Figure 3.20: *Final-state muon momentum smearing due to the Smith-Moniz bound nucleon CCQE cross section model. Left: muon momentum (GeV/c) for MiniBooNE CCQE events generated at the average* $(E_\nu, Q^2) = (0.9\ GeV,\ 0.3\ GeV^2)$ *after event selection cuts for different values of the Fermi momentum* k_F *(GeV/c). The dashed line shows the free nucleon cross section value. Right: quasi-elastic neutrino energy resolution vs. true Monte Carlo neutrino energy (GeV).* E_ν^{QE} *is calculated from 2-body kinematics using the generated* p_μ, $cos(\theta_\mu)$.

size of this effect as a function of k_F is shown in the left panel of figure 3.20. This muon momentum smearing sets a lower limit on the resolution of the quasi-elastic neutrino energy calculation in equation 3.26. For CCQE events at MiniBooNE, this minimum E_ν resolution is 7.8% at $E_\nu = 1\ GeV$, shown in the right panel of figure 3.20.

The largest source of background to ν_μ CCQE interactions is from charged current resonant single pion (CC1π) production, since the pion may be absorbed inside the nucleus. This occurs in $\sim$20% of CC1π interactions at MiniBooNE energies. In this case, the final state particles that appear in the detector are one nucleon and one lepton, which is exactly the same final state particle content as in a CCQE interaction. These events are termed "CCQE-like." The free parameters in the cross section simulation related to this background are the axial mass in the free nucleon resonant cross section, $m_A^{1\pi}$, and the pion absoption cross section. In principle, since the axial mass describes the nucleus, $m_A^{1\pi}$ and m_A^{QE} should be the same, however, the data favor different values for the two constants and therefore they are usually treated separately. Both $m_A^{1\pi}$ and the pion absorption cross section have large experimental errors, and therefore are important sources of uncertainty for the MiniBooNE cross section model.

The dominant CC1π reactions at MiniBooNE are $\nu_\mu n \rightarrow \mu^- n\pi^+$, $\nu_\mu p \rightarrow \mu^- p\pi^+$, and the coherent charged current scattering process $\nu_\mu A \rightarrow \mu^- A\pi^+$. The NUANCE prediction for the resonant channels is shown with the low energy experimental data in figure 3.21. Combined, these three channels account for 25% of the total events at MiniBooNE, compared with 40% for CCQE. The underlying process is Δ production (the Δ decays inside the nucleus), and 94% of the dominant CC1π interactions come from decays of the Δ 1232 (MeV). The CC1π processes therefore have a higher neutrino energy threshold than CCQE interactions. Because of their cross section,

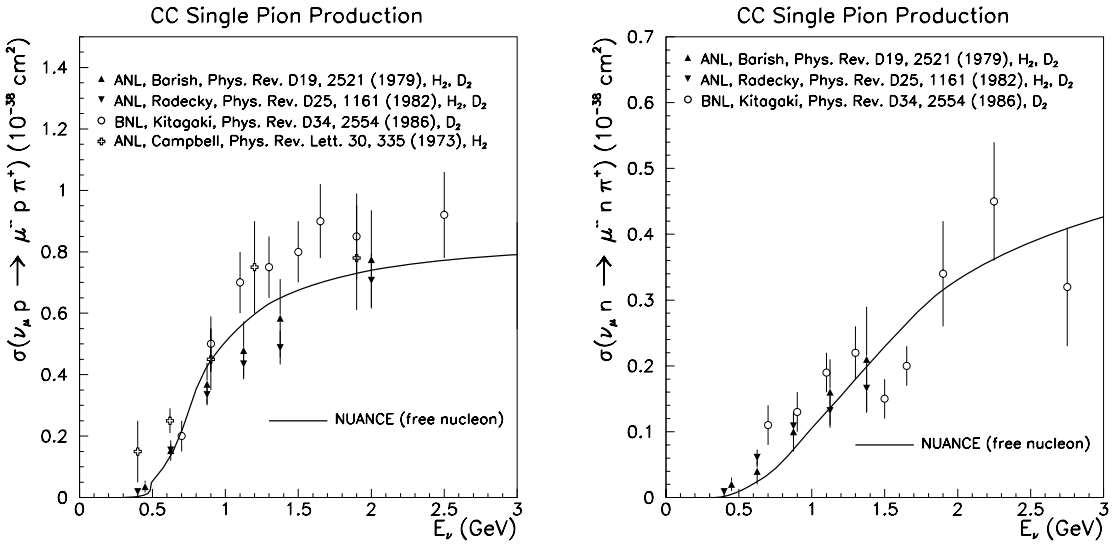

Figure 3.21: *NUANCE prediction compared with experimental data. Left:* $\nu_\mu p \rightarrow \mu^- p \pi^+$ *cross section* (cm^2) *vs.* E_ν (GeV). *Right:* $\nu_\mu n \rightarrow \mu^- n \pi^+$ *cross section* (cm^2) *vs.* E_ν (GeV). *Figure courtesy of [46].*

the average E_ν for these CC1π interactions is 1.3 GeV, compared with 1.0 GeV for CCQE events. The average CC1π (CCQE) muon momentum is 0.61 (0.72) GeV, the average final state nucleon momentum is 0.64 (0.61) GeV, and the average π momentum is 0.44 GeV.

3.2.2 Cross Section Prediction Uncertainties

The MiniBooNE cross section simulation input parameters and their 1σ uncertainties are summarized in table 3.10. The free nucleon cross section simulation input parameters are the axial masses assumed for CCQE, CC1π, and multi-pion scattering, the normalization of the CC and NC coherent scattering cross sections, and the component of the strange spin Δs carried by the valence quarks in the NC cross sections. The bound nucleon cross section simulation inputs are the Fermi gas model parameters. While the bound and free nucleon cross sections affect the total predicted

Table 3.10: *Summary of sources of neutrino cross section uncertainty. The last column shows the change in the total number of neutrino interactions, integrated over the MiniBooNE flux. Modifications to final state particle interactions affect kinematics rather than the total number of events. The quadrature sum assumes the parameters are uncorrelated.*

source	*MC parameter*	*default value*	*variation*	ΔN_ν *(%)*
σ_{CCQE} m_A	m_A^{QE} (GeV)	1.25	1.49	10.0
binding energy	E_B (GeV)	0.034	0.060	5.9
Fermi momentum	k_F (GeV/c)	0.246	0.423	19.4
coherent σ_{NC+CC}	normalization	0.5	0.75	1.0
σ_{NC} Δs	Δs	0.0	0.10	0.2
$\sigma_{CC1\pi}$ m_A	$m_A^{1\pi}$ (GeV)	1.10	1.32	6.4
$\sigma_{CCN\pi}$ m_A	$m_A^{N\pi}$ (GeV)	1.30	1.755	1.5
$\Delta \rightarrow N\gamma$	normalization	1.0	1.25	-
Δ decay width	$\Gamma\Delta$ (MeV)	120	125	-
π absorption σ	normalization	1.0	1.25	-
π charge exchange σ	normalization	1.0	1.30	-
$\Delta N \rightarrow NN$	normalization	1.0	0.5	-
quadrature sum	-	-	-	23.5

number of events, there are also processes that affect the final state particle content or kinematics, but not the overall normalization. These include the pion absorption and charge exchange cross sections, the Δ re-scattering cross section (for $\Delta N \rightarrow NN$), the decay width, the $\Delta \rightarrow N\gamma$ branching ratio, and the nuclear de-excitation model.

The cross section model parameter uncertainties are generally derived from comparing the NUANCE event generator prediction with external data, as described in reference [105]. The exceptions to this rule are the m_A^{QE}, p_F, and E_B uncertainties. These parameters are extracted from MiniBooNE data, which is described in detail in chapter 6. The MiniBooNE measured values are 1-2σ away from the world-average parameters, which are (m_A, p_F, E_B) = (1.03 GeV/c^2, 0.220 GeV, 0.025 GeV), as discussed in the previous section. The uncertainties on m_A, p_F, and E_B in table 3.10 are designed to generously cover the difference, although, they are not far from the uncertainties estimated from considering external data alone. The range of m_A measurements from light to heavy target data, not including MiniBooNE, spans 20% of the world-average value of 1.03 GeV/c^2 [37], which is consistent with the parameter variation given in table 3.10. The Fermi Gas model parameter uncertainties are estimated from external data in reference [105] to have 100% and 13% uncertainties for E_B and p_F respectively. The assumed E_B uncertainty here is similar, although the p_F uncertainty is significantly larger.

An important piece of information that the MiniBooNE cross section parameter extraction analysis provides is the correlations between m_A, p_F, and E_B. Without correlations, the total cross section uncertainty is $\sim$25%, as shown in table 3.10; with correlations, the uncertainty is $\sim$15%. The correlation matrix for the cross section simulation input parameters in table 3.10 is given in appendix F.

The systematic errors calculated in chapter 6 on the MiniBooNE measurement for m_A, p_F, and E_B are smaller than those assumed in table 3.10. However, the error

analysis in chapter 6 is not yet finalized, and therefore the MiniBooNE parameter errors are not yet used when estimating the impact of cross section simulation input parameter uncertainties on the oscillation search.

3.3 Neutrino Detector Simulation

The MiniBooNE detector simulation models the propagation of final state leptons, mesons, and nucleons from ν-CH_2 interactions through the detector volume. These final state particles emit prompt Cherenkov light, or delayed scintillation light. The subsequent photons may scatter, or get absorbed and potentially re-emitted, as they travel to the edge of the detector volume. The detector is instrumented with 1280 inward-facing 8" photo-multipler tubes (PMTs) at a radius of 550 cm for 10% photo-cathode coverage. The important components of predicting the MiniBooNE detector response are light emission by these low energy final state particles, the optical model for photon propagation in CH_2, and the PMT response. The quality of the detector simulation is determined by the level of agreement between the simulation and the MiniBooNE detector calibration data.

3.3.1 MiniBooNE Detector Monte Carlo

MiniBooNE uses a Geant3-based [106] Monte Carlo to simulate particle propagation in the detector. The input to this simulation is the output from the NUANCE cross section Monte Carlo, which consists of the final state particles from neutrino interactions in CH_2. The detector Monte Carlo tracks these particles, simulates energy loss, multiple scattering, and decay, generates infrared, optical, and ultra-violet wavelength photons, and propagates the photons to the PMT cathode.

The geometry of the Geant3 simulation includes the oil-filled main tank, the optical barrier and PMT support structure, the veto region, the evacuated PMT volumes, the iron detector sphere, the detector vault and electronics room, the dirt regions above and around the detector, and the calibration flasks, cubes, and the muon tracker. The neutrino events generated by the NUANCE cross section Monte Carlo are distributed throughout the detector volume by the detector Monte Carlo, which chooses the vertex locations weighted by the local density[4]. This procedure results in >96% of the neutrino events generated by NUANCE in the detector originating in the detector oil.

Two other important classes of events are also simulated: events originating from neutrino interactions in the dirt, and cosmic ray muons incident on the detector. For every neutrino interaction in the detector volume, there are ∼8 neutrino interactions in the material (mostly dirt) upstream of the detector. Density weighting is used to throw the dirt neutrino interaction vertices, using NUANCE events generated assuming a CH_2 target. The majority of events originating in the dirt that enter the detector generate light in the veto region, and can therefore be eliminated with a cut on the number of veto PMT hits. However, ∼0.25% of dirt events entering the detector can fake the signature of a final state particle from a beam neutrino-induced interaction [107].

The cosmic ray background is simulated by mixing each Monte Carlo generated neutrino event with real data from the $CALIB\_STROBE$ trigger. The strobe trigger is identical to the beam trigger in every way except that it does not contain any beam neutrino events. The uncalibrated hits from the strobe data and from the detector Monte Carlo neutrino event are concatenated prior to PMT hit calibration and event reconstruction. The resulting Monte Carlo sample contains beam-induced neutrino

[4]The detector Monte Carlo disregards the NUANCE generated event vertex.

events and cosmic ray backgrounds (and uncorrelated PMT noise) in the correct proportions for beam triggers with a neutrino interaction. However, this procedure does not include the class of beam triggers in the data where no neutrino interaction occured, or PMT noise correlated with a neutrino interaction.

MiniBooNE uses the standard Geant3 settings to simulate most physics processes, with a few exceptions. These include a custom model for light propagation in the detector oil, the GCALOR hadronic interaction model, and lowered tracking thresholds for photons (0.1 MeV), electrons (0.1 MeV), neutrons (1.0 MeV), hadrons (1.0 MeV), muons (1.0 MeV), and protons (1.0 MeV).

The MiniBooNE model for light propagation in the detector oil is referred to as the "optical model". It comprises photon emission via Cherenkov and scintillation processes, and photon propagation, during which the photon may be absorbed and re-emitted, attenuated, and/or scattered. The optical model describes the wavelength, time, and angular dependence of all of these processes.

The number of Cherenkov photons emitted per unit path length in the detector Monte Carlo simulation is given by [47]

$$\frac{d^2N}{dxd\lambda} \;=\; 2\pi\alpha\Big(\frac{1}{\lambda^2}\Big)\Big(1-\frac{1}{\beta^2n^2(\lambda)}\Big) \tag{3.42}$$

where $\alpha \;=\; \frac{1}{137}$, the wavelengths are measured in vacuum, and the second term determines the Cherenkov emission angle,

$$sin^2(\theta_C) \;=\; \Big(1-\frac{1}{\beta^2n^2(\lambda)}\Big). \tag{3.43}$$

Cherenkov emission is prompt in time. In the wavelength acceptance of the MiniBooNE PMTs, $340 < \lambda < 540\ nm$, the number of Cherenkov photons emitted is $\sim$500 $\times sin^2(\theta_C)$ [52]. The Cherenkov emission also depends on the wavelength dependence of the index of refraction. This is measured to be $n_D \;=\; n(\lambda = 589.3\ nm) = 1.4684 \pm$

Table 3.11: *Cherenkov threshold momentum (MeV/c) for particles of interest in the MiniBooNE detector oil, evaluated at* $n_D(\lambda = 589.3\ nm) = 1.46$.

	p	n	$\mu^{\pm}$	$e^{\pm}$	$\pi^{\pm}$	π^0
$p_{threshold}\ MeV/c$	872	874	98	0.5	128	126

0.0002 at $T_0 = 20^o\ C$, and is empirically determined to have the following wavelength dependence [108]:

$$n(\lambda, T) = \Big[n_D + B\Big(\frac{1}{\lambda^2} - \frac{1}{\lambda_D^2}\Big)\Big] \times \Big[1 - \beta(T - T_0)\Big] \tag{3.44}$$

where λ is the wavelength in air, $\lambda_D = 589.3\ nm$, T is the temperature, and from a fit to the data, $B = (4240 \pm 157) nm^2$, and $\beta = (3.66 \pm 0.04)\dot{1}0^{-4}(^oC)^{-1}$. Using the measured value $n_D(\lambda = 589.3\ nm)$, the Cherenkov angle at threshhold is 47 degrees, and the Cherenkov threshold momenta for some particles of interest is summarized in table 3.11.

The number of scintillation photons produced per unit length in the detector Monte Carlo is governed by Birk's law, which relates the scintillation yield to the energy loss via [48]

$$\frac{dL}{dx} = S\Big(\frac{dE}{dx}\Big)\Big(\frac{1}{1 + k_B(dE/dx)}\Big). \tag{3.45}$$

where S and k_B parameterize the scintillation efficiency of the medium[5], and the energy loss is given by equation 2.14. Scintillation light is produced isotropically. The scintillation properties of the MiniBooNE oil have been measured with 180 MeV kinetic energy protons at the Indiana University cyclotron [109]. The measured scintillation light output is $4.7 \pm 0.1 \pm 0.7\ p.e./MeV$ [6]. The time distribution of the

[5]MiniBooNE assumes $kB = 0.0146 gm/cm^2/MeV$, which is the measured value for anthracene.

[6]The first error is due to systematic error in the fit to determine the average number of photons producedd, while the second error is due to systematic uncertainty on the energy loss and PMT

scintillation light is exponential, with a time constant of 18.6 ± 1.0 ns. In the MiniBooNE detector Monte Carlo the wavelength dependence of the scintillation production is linearly proportional to the measured wavelength dependence of flourescence emission [110].

As the Cherenkov and scintillation photons propagate, they may be attenuated and/or scattered. Several exclusive processes have been measured in test samples of the MiniBooNE oil to understand the details of the time, angle, and wavelength dependence. The most important components are Rayleigh scattering, Raman scattering, and flourescence.

Rayleigh scattering occurs when photons scatter off of density perturbations in the oil, which changes the direction but not the wavelength of the interacting photon. This process has a characteristic angular dependence for the scattered light of $\sim (1+cos^2\theta)$ for $\perp$ photon polarization, and isotropic for $\parallel$ polarization. In Raman scattering, the photon interacts with an oil molecule, transferring some its energy into exciting a vibrational or rotational mode, which increases the wavelength of the original photon. The probability of both Raman and Rayleigh scattering depend on wavelength as $\sim 1/\lambda^4$, and occur promptly in time. The ratio of Raman to Rayleigh scattering contributions is measured to be ∼1:25 [50].

Flourescence occurs when the interacting photon excites the electronic levels of a struck molecule, gets absorbed in the process, and is later re-emitted, isotropically, at a different wavelength. This process can shift ultra-violet photons into the wavelength acceptance of the MiniBooNE PMTs, and similarly, shift optical photons above λ = 540 nm. The excitation and emission wavelengths and the time constant of re-emission are characteristic of the fluorescent molecule species. In the MiniBooNE oil, the dominant flourophores have time constants of 12 and 17 ns, and the flourescence

solid angle in the test setup.

Table 3.12: *Wavelength dependence of several detector Monte Carlo optical model parameters.* $\epsilon^{PC}/\epsilon^{max}$ *is the PMT photo-cathode efficiency normalized to the maximum value,* $\epsilon^{max} = 0.231$.

λ (nm)	$\epsilon^{PC}/\epsilon_{max}$	$\lambda^{attenuation}$ (cm)	$\lambda^{absorption}$ (cm)	$\lambda^{Rayleigh}$ (cm)	λ^{Raman} (cm)	$\lambda^{flourescence}$ (cm)
250.0	0.000	5.6	7.2	280.1	4690.1	28.0
300.0	0.266	8.2	9.2	659.1	9725.3	90.0
350.0	0.924	622.7	1386.2	1320.1	18017.3	13988.5
400.0	0.982	1812.7	10281.2	2370.4	30736.8	99999.0
450.0	0.807	3577.8	199731.0	3934.2	49234.4	99999.0
500.0	0.541	5919.4	99999.0	6151.5	75041.0	99999.0
550.0	0.234	8837.5	99999.0	9179.3	109867.5	99999.0
600.0	0.061	12332.2	99999.0	13190.6	155605.0	99999.0

probability is maximal at $\lambda \sim 295nm$ [110]. At this wavelength, the flourescence strength is $\sim$1/20 of the Rayleigh scattering strength [111].

The simulation of these physical processes in the MiniBooNE detector Monte Carlo is described in detail in reference [112]. Some of the optical model simulation parameter values are taken from external measurements, and the rest are tuned on MiniBooNE calibration data. The detector Monte Carlo values for a set of parameters which are important to photon attenuation as a function of wavelength are listed in table 3.12. The detector Monte Carlo also models the PMT quantum efficiency, which is angle and wavelength dependent. The angular dependence is measured externally to vary by $\sim\pm5\%$ across the PMT face, and the wavelength dependence is taken from the PMT specifications provided by the manufacturer [53]. The detector Monte

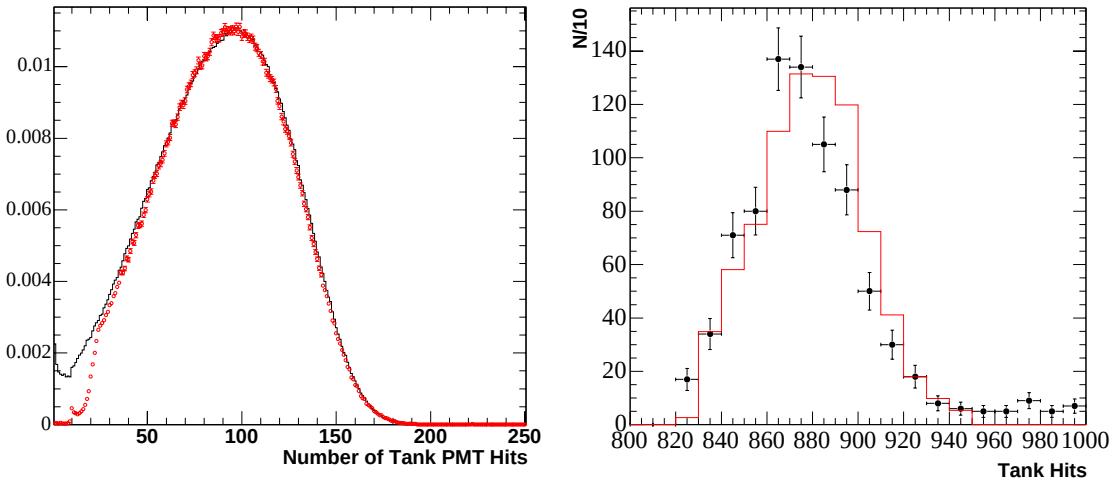

Figure 3.22: *Left: number of tank hits for Michel electrons. Right: number of tank hits for muons tagged by the external muon tracker and stopping in the scintillator cube with* $T_\mu \sim 0.8\,GeV$*. Data is shown by points, Monte Carlo is the solid histogram.*

Carlo does not simulate the PMT dynode chain or the signal processing electronics, however, smearing to account for these effects is included in the Monte Carlo analysis chain before PMT hit calibration and event reconstruction. This is described in detail in reference [113].

Particle calibration data is used to measure the performance of the detector response simulation. This includes Michel electrons, which come from the Michel trigger, and cosmic ray muons from from the $CALIB\_CUBE$ trigger, which have a detector entry point tagged by the muon tracker hodoscope, and a stopping point tagged by one of the scintillator cubes. The most basic test of event-level agreement between data and Monte Carlo is to compare the number of tank PMT hits. This measurement does not involve event reconstruction, and so achieving agreement means getting the total number of photo-electrons correct, but not necessarily the hit charge, time or spatial distribution of the photons. Therefore, the number of tank hits in the Monte Carlo depends primarily on the PMT threshhold and quantum

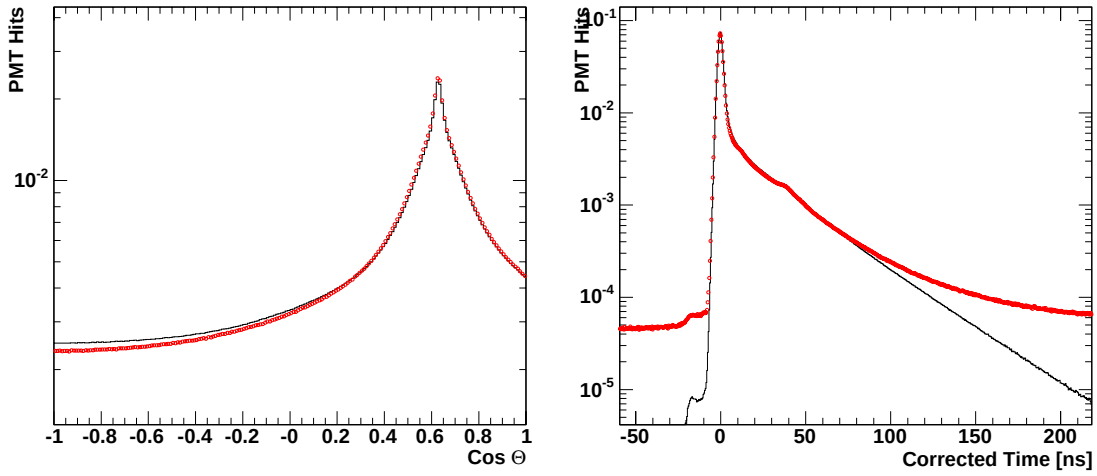

Figure 3.23: *Left: corrected angle for Michel electrons. Right: corrected time for Michel electrons. Data is shown by points, Monte Carlo is the solid histogram.*

efficiency model, on the PMT noise, and on the photon attenuation simulation. The left panel of figure 3.22 shows the distribution of tank hits in data and Monte Carlo for Michel electron calibration events, which have $T_e \sim 0.05\ GeV$. These events have fewer than 200 tank PMTs registering hits, and show excellent agreement between data and Monte Carlo above ∼30 tank hits. Below 30 hits, effects that are not simulated in the Monte Carlo such as long-lived decays (e.g. ^{12}B) and correlated PMT noise become important. These events are used extensively to tune the detector simulation. The right panel of figure 3.22 shows the distribution of tank hits in data and Monte Carlo for muon calibration events with kinetic energy ∼0.8 GeV; this sample is not used to tune the Monte Carlo, and shows reasonable agreement.

A higher-level test of the detector simulation is to compare the corrected time and angle distributions, defined in equations 2.9 and 2.10. These require the reconstructed event vertex and position, which depend primarily on the time likelihood minimization. Achieving agreement between data and Monte Carlo means simulating the location and time of arrival of the optical photons correctly. Therefore, these dis-

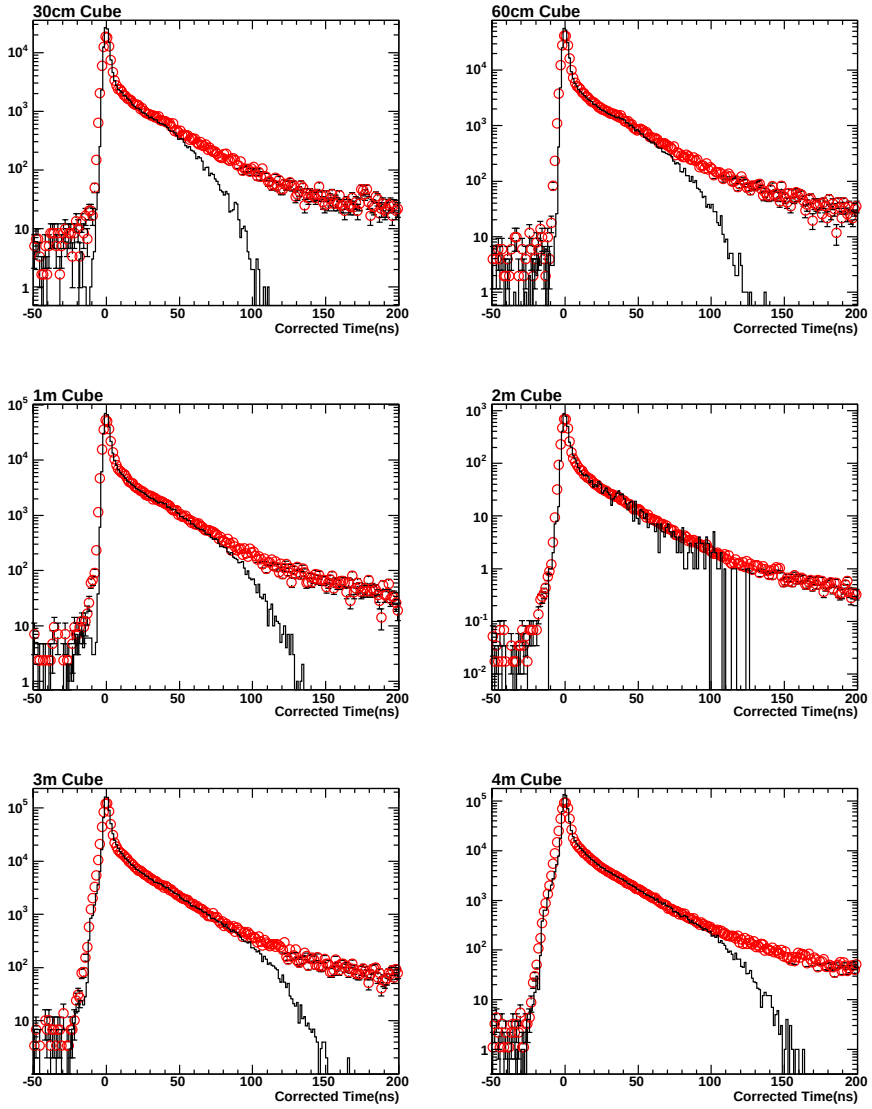

Figure 3.24: *Corrected time distributions of tank PMT hits for stopping muon events in the six deepest cubes. The event vertex and time are measured using the cubes and muon tracker. Data is shown by points, Monte Carlo is the solid histogram.*

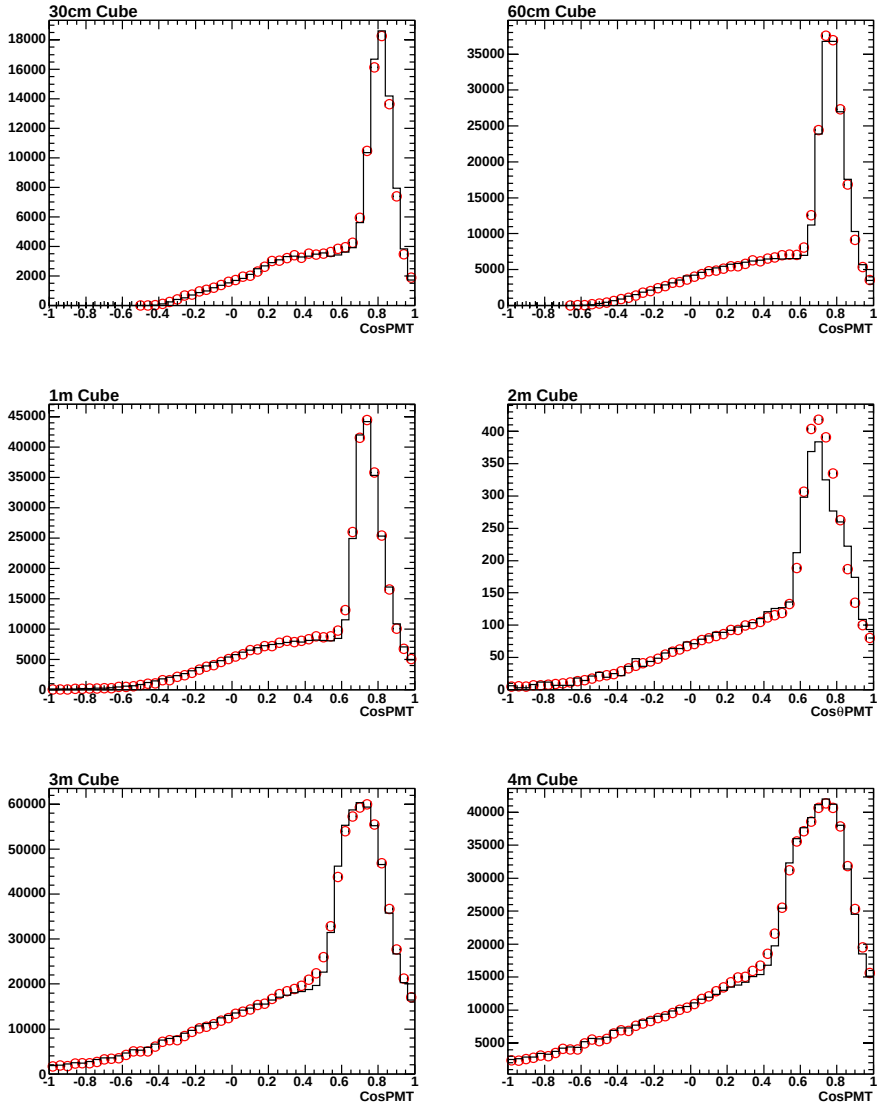

Figure 3.25: *Corrected angle distributions of tank PMT hits for stopping muon events in the six deepest cubes. The event vertex and time are measured using the cubes and muon tracker. Data is shown by points, Monte Carlo is the solid histogram.*

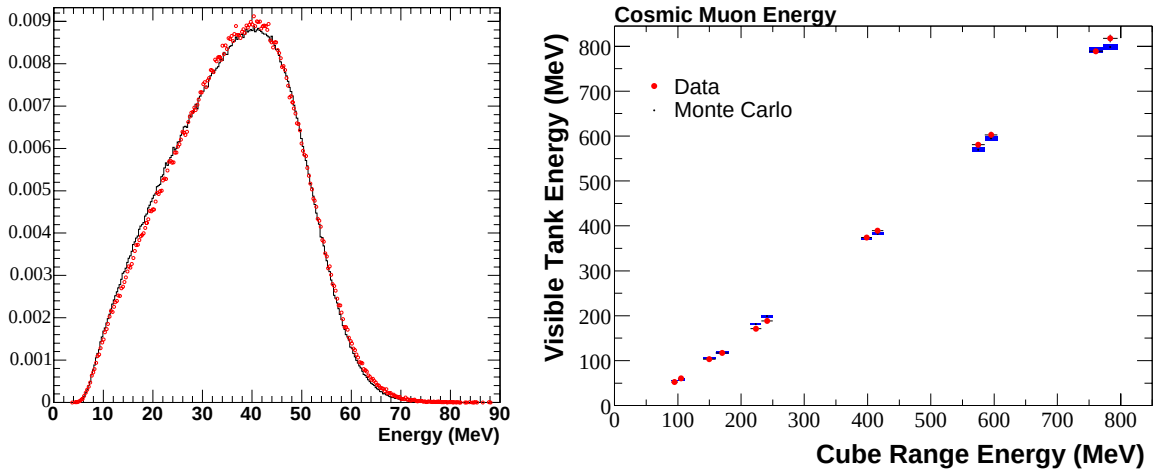

Figure 3.26: *Left: reconstruced Michel electron energy (MeV). Right: muon energy as determined by the reconstruction vs. cube range energy calculated from the muon path determined using the external muon tracker and the scintillator cubes inside the tank. Data is shown by points, Monte Carlo is the solid histogram.*

tributions are also sensitive to the optical model of scintillation, photon scattering, absorption, and re-emission. The reconstructed corrected time and angle distributions for Michel electron calibration events are shown in figure 3.23 for data and Monte Carlo. The corrected time distribution shows good agreement between data and Monte Carlo for the prompt Cherenkov peak and the subsequent 75 ns, over which the number of hits drops by 3 orders of magnitude. However, before the peak and for times later than 75 ns, data has many more hit PMTs. These differences occur primarily because cosmic ray and PMT noise backgrounds are not simulated for calibration events, however, there may also be a contribution from un-modeled late light production via scintillation or flourescence. The corrected angle distribution shows good agreement between data and Monte Carlo around the Cherenkov peak, however, the late-time difference shows up at the <1% level in the flat, isotropic component, as expected. The reconstructed corrected time and angle distributions for muon calibration events are shown in data and Monte Carlo for each cube in figures

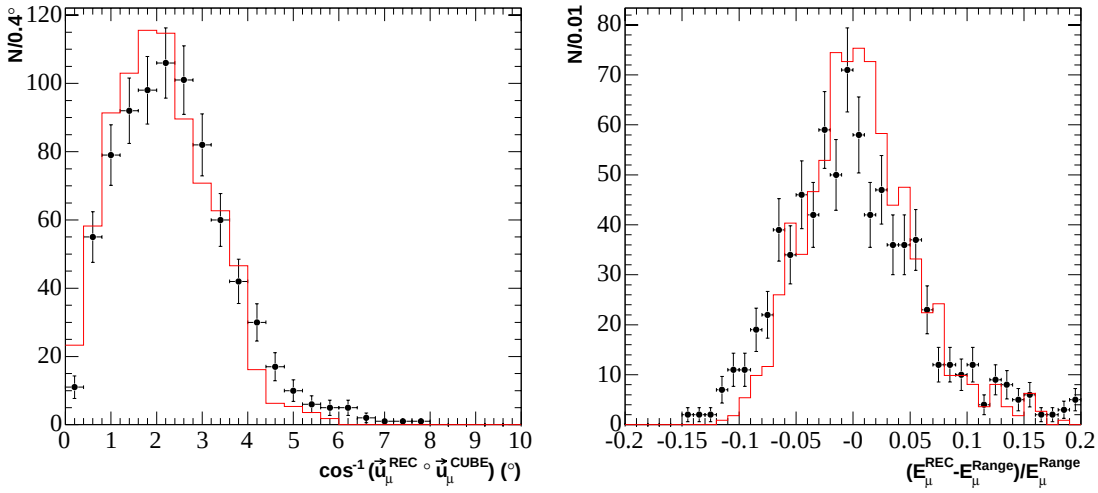

Figure 3.27: *Left: angular resolution from the scintillator cube system, for* T_μ = *0.770 GeV. Right: Energy resolution from the scintillator cube system, for* T_μ = *0.770 GeV. Data is shown by points, Monte Carlo is shown by the solid histogram.*

3.24 and 3.25. The muon data and Monte Carlo agree well for corrected times less than $\sim$75 ns, and the corrected muon angle distributions also show good agreement.

The most important test of the detector simulation for oscillation analyses is to compare reconstructed energy distributions in data and Monte Carlo. Reconstructing the lepton energy depends on both the time and charge likelihood minimizations. Therefore achieving agreement between data and Monte Carlo here tests the PMT charge response simulation and the whole optical model, since the Monte Carlo must predict the correct number of *p.e.* detected by each phototube as a function of time. The reconstructed energy for Michel electron calibration events is compared in data and Monte Carlo in the left panel of figure 3.26. There is good agreement between data and Monte Carlo over the full range of reconstructed Michel electron energies, 0 to 0.07 GeV. This distribution is used to measure the energy scale of the detector and the reconstruction energy resolution for electrons at the Michel endpoint. The reconstructed energy for muon calibration events is compared in data and Monte Carlo

with the energy calculated from the muon range, independently of the reconstruction, in the right panel of figure 3.26. There is good agreement between data and Monte Carlo over the full range of muon energies, 0.1 to 0.8 GeV.

The neutrino energy is inferred from the measured lepton energy and angle. Therefore, modeling the measurement resolution correctly in Monte Carlo is important. The muon tracker and cube callibration system can measure both the angular and lepton energy resolutions of the recontruction. A comparison of these in data and Monte Carlo is shown in figure 3.27, for muons with T_μ $\sim$0.8 GeV. Fitting the angular resolution with a projection of a 2D Gaussian function gives an r.m.s. of 1.9^o in data and 1.7^o in Monte Carlo. Fitting the energy resolution with a Gaussian function results in 5.4% in data, and 4.4% in Monte Carlo. This level of agreement approaches the intrisic resolution of the muon tracker and cube calibration system, shown in table 2.4, and demonstrates good reconstruction performance for typical ν_μ CCQE final-state muon energies.

3.3.2 Detector Response Simulation Uncertainties

The method for estimating the detector response simulation uncertainties is still under development, however, at present, the systematic error sources include the parameters of the optical model and the parameterization of the PMT response. The MiniBooNE detector simulation parameters and their uncertainties are summarized in tables 3.13 and 3.14. The terminology is as follows: MiniBooNE models light production in the detector response simulation with Cherenkov emission and scintillation excitation, as well as additional excitation by Cherenkov photons with $\lambda > 250$ nm ($\lambda < 250$ nm) which is termed flourescence (UV-flourescence). An excited oil molecule can radiate via four emission spectra, which are termed "sci 1-4", "flu 1-4", and "uvf 1-4" depending on the excitation process, with time constants "tau 1-4". In general,

Table 3.13: *Summary of sources of detector simulation uncertainty which are constrained by calibration data. The $\Delta\langle E_{michel}\rangle$ column shows the change in the average Michel electron energy. The last column shows the 1σ error in the simulation parameter as a fraction of the variation.*

source	*default value*	*variation*	$\Delta\langle E_{michel}\rangle$	1σ
Birk's Law k_B	0.014	0.028	-0.3561$\times10^{-1}$	0.3771
Cherenkov Normalization	1.1064	1.0564	-0.3561$\times10^{-1}$	0.1660
Extinction Length	40 m	45 m	0.4331$\times10^{-1}$	0.1111
(at λ=460 nm)				
PMT Angular Response FWHM	0.63365	0.71404	-0.6679$\times10^{-2}$	0.2591
Optical Barrier Reflection	0.95	0.925	0.1881$\times10^{-1}$	0.0771
Scattering lengths	3.566 m	4.279 m	-0.3564$\times10^{-1}$	0.0771
(at λ = 460 nm)	11.887 m	14.264 m		
	35.658 m	42.789 m		
Sci2 γ/MeV	0.0	51.4	0.1637$\times10^{-1}$	0.2721
Sci3 γ/MeV	0.0	4.2	0.7072$\times10^{-2}$	0.2703
Sci4 γ/MeV	31.64	22.15	-0.2888$\times10^{-1}$	0.1177
τ_4	34.0 ns	30.0 ns	0.2137$\times10^{-2}$	0.0076
UV extinction length	2.390 m	1.929 m	0.1444$\times10^{-1}$	0.3164
(at λ=320 nm)				
UVF2 Normalization	0.0	0.328	0.4610$\times10^{-1}$	0.1206
UVF3 Normalization	0.0	0.0267	0.1991$\times10^{-1}$	0.1767
UVF4 Normalization	0.074	0.111	0.4982$\times10^{-1}$	0.0936
Flu1	1	0	-0.2160$\times10^{-2}$	0.3180
Flu2	1	0	-0.2325$\times10^{-2}$	0.3069
Flu3	1	0	-0.7101$\times10^{-2}$	0.2531
Flu4	1	0	-0.1851$\times10^{-1}$	0.0866

Table 3.14: *Summary of sources of detector simulation uncertainty which are not constrained by calibration data. The $\Delta\langle E_{michel}\rangle$ column shows the change in the average Michel electron energy. The last column shows the 1σ error in the simulation parameter as a fraction of the "variation" value. "Old" and "New" refer to the two kinds of MiniBooNE PMTs.*

source	*default value*	*variation*	$\Delta\langle E_{michel}\rangle$	1σ
Scattering $\parallel$, $\perp$ lengths	3.566 m	4.279 m	0.9077×10^{-3}	1.0
(at λ=460 nm)	11.887 m	7.641 m		
τ_1	33.0 ns	29.0 ns	-0.1477×10^{-3}	1.0
τ_2	14.0 ns	5.0 ns	0.8212×10^{-3}	1.0
τ_3	1.0 ns	0.3 ns	-0.3752×10^{-3}	1.0
PMT time response smearing	0.0 ns (r.m.s.)	0.5 ns	-0.2781×10^{-3}	1.0
Veto albedo	0.905	0.955	0.8826×10^{-3}	1.0
PMT discriminator thresholds	0.1 $p.e.$	0.2 $p.e.$	-0.6275×10^{-1}	1.0
Qlin (Old/New)	18/9	999/999	-0.1727×10^{-2}	1.0
Qtcorr (Old/New)	0.08/0.08	0.0/0.0	0.6649×10^{-1}	1.0
Time slew (Old/New)	6.51/0.93	3.00/1.12	-0.7756×10^{-3}	1.0

variations in the optical model do not change the total number of neutrino interactions. However, these parameters can have a large effect on the number of PMT hits and the magnitude of PMT charges, and therefore on the detector energy scale. Tables 3.13 and 3.14 show the change in the average energy of Michel electrons due to each source of uncertainty. Further, varying the optical model parameters may change the energy scale as a function of radius, direction, and/or time. As a result, the detector simulation uncertainties can contribute a significant error on the total number of events passing a set of selection cuts, if those cuts depend on any of the above quantities. In practice, this is always the case.

The parameter variations in tables 3.13 and 3.14 do not always represent 1σ errors, since these are still under investigation. Some of the detector simulation uncertainties are taken from external measurements, such as the flourescence time constants and normalization, the PMT angular response full width at half max, and the PMT prepulse amplitude. However, the majority of the uncertainties can be determined with much greater precision from MiniBooNE's own calibration data.

Parameter uncertainties and correlations are currently extracted from fits which minimize the energy scale difference between Monte Carlo and data, binned in radius, track direction, and corrected time, with pull terms for each source of detector simulation uncertainty. Timing and number of PMT hit distributions from neutrino neutral current elastic scattering data, which contains low energy protons and neutrons, are also used. This approach yields 1σ errors which are typically 10-50% of the variations given in table 3.13. The resulting parameter correlation matrix is given in appendix F. The limitation of this procedure is that it can only constrain the uncertainties on the parameters which affect the calibration data included in the fit in a non-degenerate way; table 3.14 lists the sources of uncertainty which are not currently constrained by calibration data. In this case, the 1 σ uncertainty is assumed to

be the current size of the parameter variation. Work is ongoing to include additional calibration data sets which are sensitive to the remaining unconstrained parameters.

Chapter 4

ν_μ Charged Current Quasi-Elastic Events in MiniBooNE

The ν_μ charged current quasi-elastic (CCQE) fraction of all beam-induced ν_μ interactions in the MiniBooNE detector is approximately 40%. The goal of the ν_μ CCQE event selection is to maximize the number of $\nu_\mu n \to \mu^- p$ events accepted by the cuts, while minimizing background contamination, with good neutrino energy resolution for the accepted events. The motivation for studying this class of events is that they are numerous, the cross section is relatively straightforward, the particle content of the final state is limited, and the neutrino energy can be reconstructed by measuring only the muon's kinematics because it is a 2-body scattering interaction. Further, several important experimental parameters can be determined using the MiniBooNE ν_μ CCQE data set: constraints on the neutrino flux prediction and its uncertainties are described in chapter 5, and constraints on the CCQE cross section and its uncertainties are described in chapter 6. Finally, the search for neutrino oscillations described in chapter 7 employs the ν_μ CCQE data set described here.

4.1 Selection Cuts

There are two levels of ν_μ CCQE event selection cuts. The first level consists of a few cuts on quantities that do not require the reconstruction, to reduce the cosmic-ray and non-ν_μ-charged-current backgrounds, and a more sophisticated cut to select events with a well-reconstructed muon decay. These cuts are referred to as "pre-cuts" in the following. The second level imposes a simple particle identification algorithm via a Fisher discriminant to eliminate non-ν_μ-CCQE backgrounds.

With no cuts, the MiniBooNE data consists mostly of cosmic rays passing through or stopping in the detector. At the most basic level, the MiniBooNE data are characterized by the number of tank and veto PMTs that register a hit in a given beam trigger event, which is 19.2 μs long. The proton beam spill duration is 1.6 μs, and it begins 4.6 μs after the beam trigger start, shown in figure 2.7. Clusters of tank PMT hits that are contiguous in time, with less than 10 ns between hits, are referred to as sub-events. The number of sub-events and veto PMT hits are shown in data and Monte Carlo, with no cuts, in figure 4.1. The MiniBooNE detector simulation models cosmic ray backgrounds for events in which there is a neutrino interaction, however, it does not model the beam spills which have cosmic rays *without* neutrino interactions, which occur at $\sim$200$\times$ the neutrino interaction rate. These excess cosmic rays in the data are clearly evident in figure 4.1; through-going cosmic rays typically have one sub-event with between 30 and 60 veto PMT hits, and stopping cosmic rays have between 10 and 30 veto PMT hits, which indicates a single veto penetration, and two sub-events, where the second sub-event is due to the Michel electron from the stopping cosmic ray muon's decay.

The "pre-cuts" are designed to eliminate the cosmic-ray background, and to select beam neutrino-induced charged current events that are contained in the detector

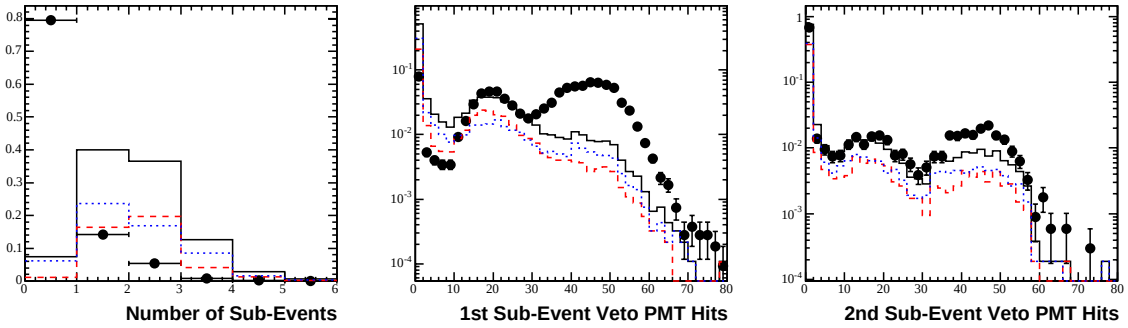

Figure 4.1: *Variables that are used in the ν_μ CCQE selection "pre-cuts". Left: the number of sub-events; middle: the number of veto PMT hits in the first sub-event; right: the number of veto PMT hits in the second sub-event. Data with statistical errors (black points) are compared with the Monte Carlo total (solid black line), Monte Carlo signal (dotted red line), and Monte Carlo background (dotted blue line) predictions. Data and the total Monte Carlo curves are normalized to unit area. No cuts are applied.*

fiducial volume and well-reconstructed. The "pre-cuts" require:

1. that the 1st sub-event occur within the proton-spill time window: $4500 < \bar{t}_{tank\ PMT} < 6200\ ns$,
2. that the number of veto hits in the 1st sub-event be less than 6,
3. that there be 2 sub-events,
4. that the number of veto hits in the 2nd sub-event be less than 6, and
5. that the distance ΔR between the muon (1st subevent) endpoint and the Michel (2nd subevent) vertex be less than 100 cm.

The first and second cuts reject cosmic rays and Michel electrons from cosmic rays which decayed before the beam trigger start. The veto inefficiency is measured to

be <0.1% using strobe trigger data, which results in a rejection factor for cosmic-ray muons from these two cuts of $\sim 1.6\mu s/19.2\mu s \times 0.001 \;=\; 8.3 \times 10^{-5}$. The rejection factor for Michel electrons is less, $\sim 8.3 \times 10^{-2}$, since if the muon decay occurs inside the detector fiducial volume, the Michel electron sub-event will pass the veto hits cut. However, if the Michel electron is produced in the veto region, which comprises roughly half of the detector oil volume, it will fail the veto hits cut. The third cut selects events that have muons that decay in the fiducial volume in the 19.2 μs beam trigger window, which in combination with the first two cuts eliminates most ν_μ non-charged-current interactions. The fourth cut eliminates interactions where the Michel electron is not contained in the fiducial volume, or non-charged-current neutrino-induced events which have a coincident cosmic ray follower. The third and fourth cuts together also reject secondaries produced in beam-neutrino interactions outside of the detector, e.g. in the dirt upstream.

The fifth cut requires that the first and second sub-events have a reconstructed spatial relationship consistent with a single muon decay. Poorly reconstructed ν_μ CCQE events will fail this cut, as will some of the background charged current interactions [1]. The Michel distance variable ΔR is calculated as:

$$\Delta R \;=\; \sqrt{(X_1 - X_2)^2 + (Y_1 - Y_2)^2 + (Z_1 - Z_2)^2} \tag{4.1}$$

where the electron track vertex, (X_2, Y_2, Z_2), is given by the reconstructed track-center coordinates of the second sub-event (which makes the approximation that the Michel electron track is a point), and the muon track endpoint coordinates are given by

$$X_1 \;=\; \mathtt{X^R(1)} + \mathtt{UX^R(1)} \times \Big(\frac{Range(\mathtt{E^R_\mu(1)})}{2} \Big) \tag{4.2}$$

[1] For example, in a $\nu_\mu p \rightarrow \mu^- p \pi^+$ interaction the μ^- may be absorbed before decaying, and therefore the second sub-event would be due to the e^+ from the π^+-decay μ^+. In this case, the distance between the Michel electron vertex and the μ^- endpoint may be large.

and similarly for Y_1 and Z_1. $\mathtt{X^R(1)}$ is the reconstructed track-center x coordinate for the first sub-event, *Range* is calculated from a look-up table for polyethylene [114], and $\mathtt{E^R_\mu(1)}$ is the reconstructed energy of the first sub-event assuming a muon hypothesis. The variables that go into calculating ΔR are shown in data and Monte Carlo after the first four "pre-cuts" in figure 4.2. At this point, data and Monte Carlo agree very well, which indicates that the first four "pre-cuts" effectively eliminate the non-neutrino-induced backgrounds.

The individual and combined efficiencies of the "pre-cuts" are shown as a function of Monte Carlo generated neutrino energy in figure 4.3. Below $\sim$0.2 GeV there are very few events, and therefore the cutoff in efficiency below this point is artificial. Above 0.2 GeV, the cuts on the number of veto hits and sub-events have the strongest energy dependence, particularly the 1st sub-event veto hits cut. This is the case because high energy charged current neutrino interactions tend to produce high energy muons, and the probability that a muon will penetrate the veto region increases with energy. Similarly, if the muon exits the detector fiducial volume the event will fail the cut on the number of sub-events. In contrast, the efficiency of the cuts on the time and Michel distance are nearly independent of energy.

The efficiencies of the "pre-cuts," integrated over energy, are shown in table 4.1 for the Monte Carlo. The efficiency of the first four pre-cuts is 21.7% for all events, and 33.7% for ν_μ CCQE interactions. After these cuts the signal purity is 66.8%. All of the "pre-cuts" together result in an efficiency of 16.8% (29.2%) for all (signal) events, with a resulting ν_μ CCQE purity of 74.6%. The majority of the non-ν_μ CCQE events remaining after the "pre-cuts" are due to charged current resonant single pion production. Of the 25.4% background remaining after the "pre-cuts," 17% comes from charged current resonant pion production (13.4% from $\nu_\mu p \rightarrow \mu^- p\pi^+$, 3.0% from $\nu_\mu n \rightarrow \mu^- n\pi^+$, 1.0% from $\nu_\mu A \rightarrow \mu^- A\pi^+$, 3.5% from $\nu_\mu p \rightarrow \mu^- p\pi^0$), and 3.0%

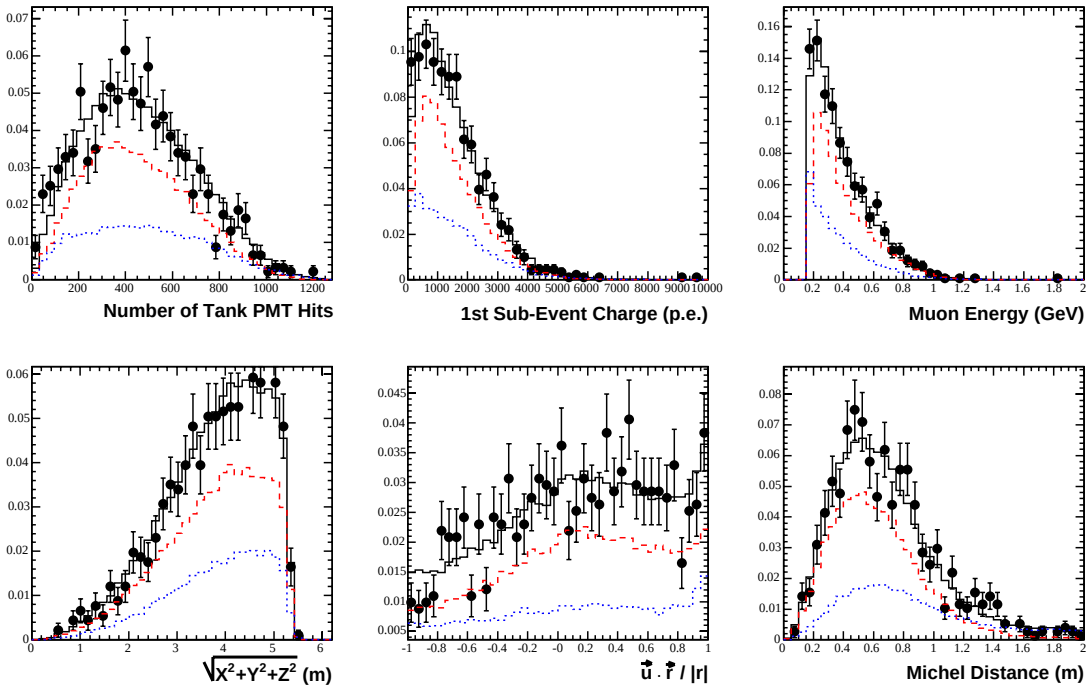

Figure 4.2: *Variables that are used in the ν_μ CCQE selection Michel distance "pre-cut" for the first sub-event. Top left: the number of tank PMT hits; top middle: the total charge in the first sub-event; top right: the reconstructed muon energy (GeV). Bottom left: the reconstructed radius of the track center (m); bottom middle: the reconstructed track direction; bottom right: the reconstructed Michel distance (m). Data with statistical errors (black points) are compared with the Monte Carlo total (solid black line), Monte Carlo signal (dotted red line), and Monte Carlo background (dotted blue line) predictions. Data and the total Monte Carlo curves are normalized to unit area. The first four "pre-cuts" are applied.*

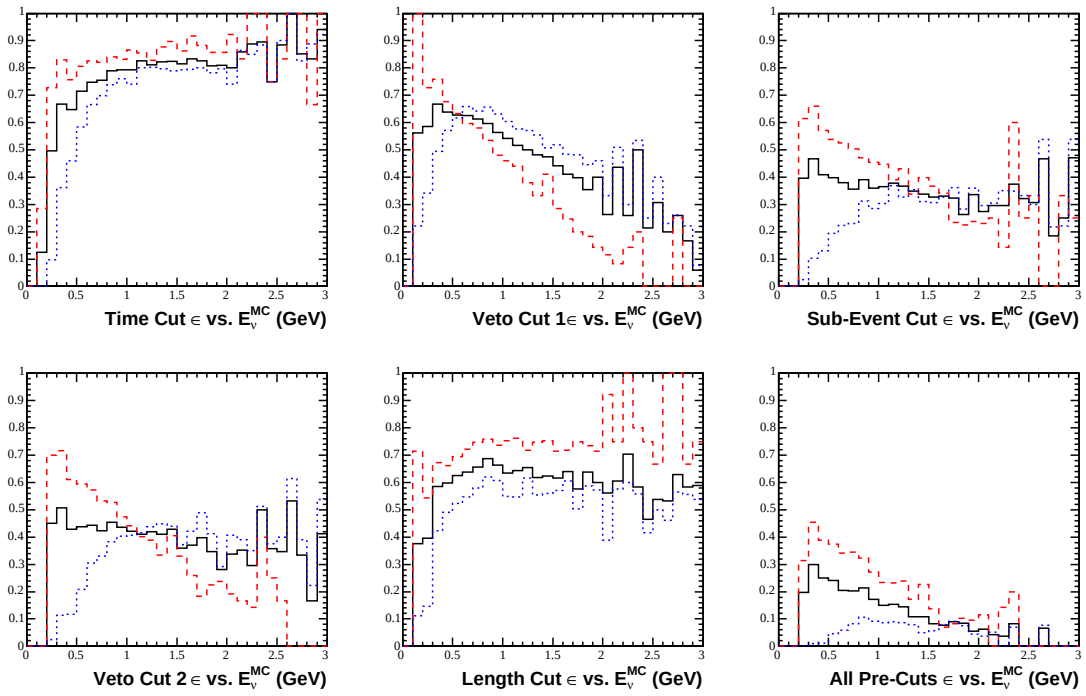

Figure 4.3: *Efficiencies of the ν_μ CCQE selection "pre-cuts" vs. Monte Carlo neutrino energy (GeV). The first five panels from top left to bottom right show the efficiency of each "pre-cut" individually. The bottom right panel shows the efficiency of all "pre-cuts" combined. The efficiency is shown for all Monte Carlo events (solid black line), Monte Carlo signal (dotted red line), and Monte Carlo background (dotted blue line) predictions.*

Table 4.1: *Monte Carlo ν_μ CCQE selection cut efficiencies (ϵ) and signal purity. Relative efficiency is defined to be the number of events passing a given cut divided by the number passing the previous cut.*

cut	ϵ	*relative* ϵ	*signal* ϵ	*signal purity*
no cuts	1	1	1	0.429881
in-spill time	0.779931	0.779931	0.824764	0.454592
Veto(1) Hits < 6	0.505858	0.648593	0.48815	0.414832
2 sub-events	0.241842	0.478084	0.355188	0.631355
Veto(2) Hits < 6	0.217188	0.898058	0.337357	0.667729
$\Delta R < 100\ cm$	0.168085	0.773911	0.291771	0.746213
Fisher > 0.425	0.081069	0.482312	0.17164	0.910143

comes from neutral current resonant π^+ production.

The second level of cuts employ a Fisher discriminant [115] to identify ν_μ CCQE interactions. The Fisher discriminant method produces an output variable (the Fisher decision axis) which is a linear combination of input variables, where the coefficients are chosen such that the difference between two classes of events (signal and background) is maximized in the output variable. For example, for a vector of 5 variables $\vec{x}_i$ describing each event i, the mean $\vec{\mu}_x$ for each class k is

$$\vec{\mu}_{x,k} \;=\; \frac{1}{N_k}\sum_{i=1}^{N}\vec{x}_{i,k}. \tag{4.3}$$

The scatter matrix between the classes is given by

$$S_B \;=\; \sum_{k=1}^{K} N_k(\vec{\mu}_{x,k}-\vec{\mu}_x)(\vec{\mu}_{x,k}-\vec{\mu}_x)^T \tag{4.4}$$

and the scatter matrix within each class is

$$S_W \;=\; \sum_{k=1}^{K}\sum_{i=1}^{N}(\vec{x}_i-\vec{\mu}_{x,k})(\vec{x}_i-\vec{\mu}_{x,k})^T \tag{4.5}$$

where K is the total number of classes (here $K = 2$) and N is the total number of events. The eigenvectors of the product $S_B S_W^{-1}$ with the largest set of eigenvalues $\vec{w}$ maximize the Fisher criterion for the transformation that produces the greatest separation between classes,

$$J(\vec{w}) \;=\; \frac{det(W^T S_B W)}{det(W^T S_W W)} \tag{4.6}$$

where W is the matrix of eigenvectors of S_B and S_W. The Fisher discriminant output variable y_i is related to the input variables $\vec{x}_i$ by

$$y_i \;=\; \vec{w} \cdot \vec{x}_i. \tag{4.7}$$

To produce an effective Fisher discriminant, the Fisher input variables $\vec{x}$ should have maximally different means for the signal and background distributions. After the "pre-cuts", the background is mostly CC1π events, which differ from the signal CCQE by having an extra π in the final state. The distinguishing characteristics of these two classes of events that are used in this analysis include the following. First, the extra π will produce more late, isotropic scintillation light integrated over the duration of the event, while the CCQE final state will have a greater fraction of prompt, Cherenkov light. Second, the Cherenkov emission from pions tends to be less "ring-like" than for muons because the pion has a larger cross section for scattering hadronically. Finally, a single muon will have a reconstructed track length consistent with the muon range calculated from the reconstructed energy, which is not necessarily the case for an event with an extra pion. Five Fisher input variables are constructed with these characteristics in mind, which are:

1. the Michel distance ΔR, defined in equation 4.2,

2. the muon length hypothesis, $(R - L)/E$, where R is the muon range calculated from the reconstructed muon energy E, and L is the reconstructed track length, based on the reconstruction charge and time likelihoods,

3. the fraction of PMT hits transverse to the track direction, defined by

$$\frac{\sum_{PMT} hits[|cos(\theta_{vertex,PMT})| < 0.25]}{\sum_{PMT} hits} \tag{4.8}$$

   where $cos(\theta_{vertex,PMT})$ is the corrected angle defined in equation 2.10,

4. The fraction of very late PMT hits, where "very late" is defined to be corrected time $> 5\ ns$, and the corrected time is given by equation 2.9, and

5. the fraction of hits from Cherenkov vs. total light emission, where the Cherenkov and total fluxes are determined by the reconstruction.

These variables are shown in data and Monte Carlo after the five "pre-cuts" in figure 4.4, with Monte Carlo predictions for the ν_μ CCQE signal and background overlaid. The first two variables are related to the question of whether the event has a track length consistent with the muon range. On average, the background events tend to have larger distances between the reconstructed Michel electron vertex and the muon endpoint, as expected if the Michel electron is uncorrelated with the primary muon. The value of $(R - L)/E$ is smaller for signal events, indicating that the reconstructed track length for the CCQE final state is closer to the expectation for the range of a single muon track. The third variable, the transverse fraction, is related to the Cherenkov ring topology. It has been scaled up by a factor of ten so that its numerical range is similar that of the other variables. The annulus with $|cos\theta_{PMT}| < 0.25$ is located upstream of where the Cherenkov ring is expected to be ($cos\theta_{PMT} > 0.5$) with respect to the track direction. Therefore, this variable is sensitive to the fraction of the PMT hits that are *not* located in the Cherenkov ring. A lower bound on $cos\theta_{PMT}$ is chosen so that the variable depends less on the exact details of photon scattering in the detector Monte Carlo optical model. The fourth and fifth variables pertain to the scintillation vs. Cherenkov properties of signal and

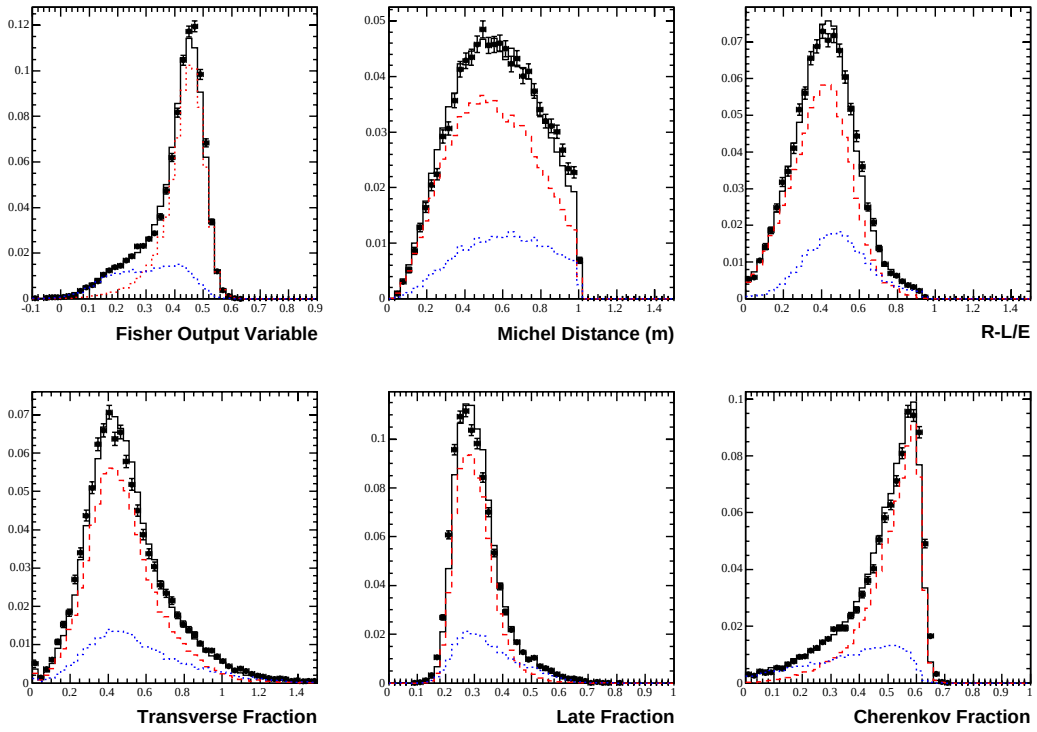

Figure 4.4: *Variables that are used in the ν_μ CCQE selection Fisher discriminant cut. Top left: the Fisher discriminant output variable; all other panels: Fisher discriminant input variables. Data with statistical errors (black points) are compared with the Monte Carlo total (solid black line), Monte Carlo signal (dotted red line), and Monte Carlo background (dotted blue line) predictions. Data and the total Monte Carlo curves are normalized to unit area. The five "pre-cuts" are applied.*

background events, and show that signal events have a greater fraction of prompt Cherenkov light than background.

The transverse fraction and the Michel distance do not show any dramatic separation between signal and backgound, however, there are useful correlations between variables that are exploited by the Fisher discriminant method. The correlations are shown for the five Fisher input variables described above for signal and background in the Monte Carlo in figure 4.5. Both the Michel distance and the transverse fraction are correlated with the Cherenkov fraction in such a way that a "diagonal" cut on a linear combination of these variables provides good separation between the signal and background populations.

The Fisher discriminant coefficients $\vec{w}$ are determined with Monte Carlo training samples of ν_μ CCQE events and ν_μ non-CCQE background events after the "pre-cuts". The resulting Fisher discriminant output variable is shown in the top left panel of figure 4.4. The second level event selection cut is applied on this Fisher output variable, and the position of the cut is optimized to maximize ν_μ CCQE signal and minimize background, while maintaining reasonable signal efficiency. The signal purity and efficiency are shown as a function of the Fisher output variable cut value in figure 4.6. The cut value is chosen to be > 0.425, which results in a ν_μ CCQE purity of $\sim$90% and a signal efficiency of $\sim$50% with respect to the number of events passing the "pre-cuts". In the Monte Carlo, the remaining background comes entirely from charged current resonant single pion production events (5.5% from $\nu_\mu p \rightarrow \mu^- p \pi^+$, 1.1% from $\nu_\mu n \rightarrow \mu^- n \pi^+$, and 1.2% from $\nu_\mu p \rightarrow \mu^- p \pi^0$).

The efficiency of the Fisher cut as a function of Monte Carlo generated energy is shown in figure 4.7 relative to events passing the "pre-cuts". Between 0.4 and 1.7 GeV, the efficiency is approximately independent of energy. The combination of the "pre-cuts" and the Fisher cut will be called the CCQE selection cuts hereafter. The

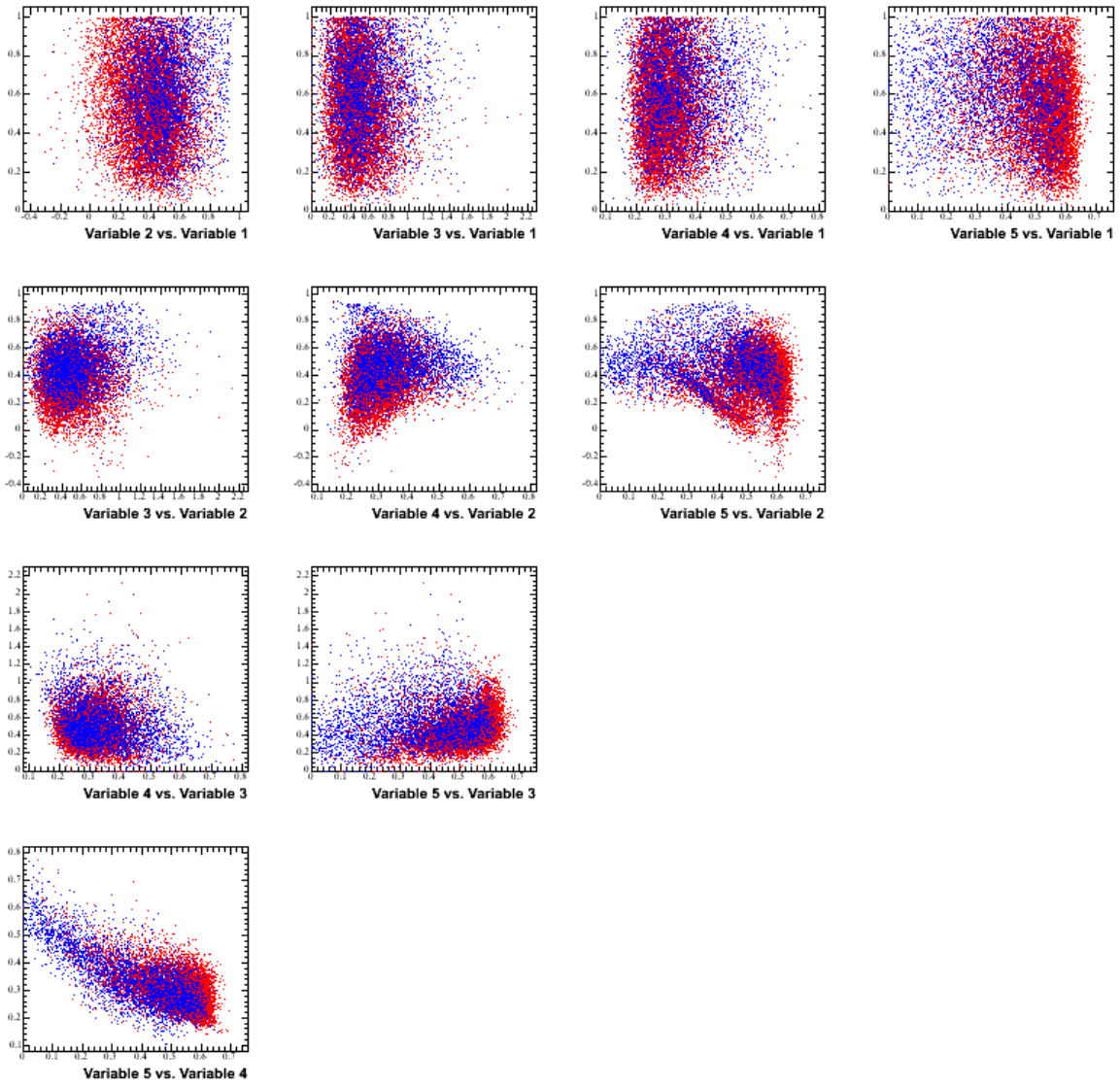

Figure 4.5: *Correlations of the Fisher discriminant input variables in Monte Carlo for signal (red) and background (blue). Only unique combinations of variables are shown.*

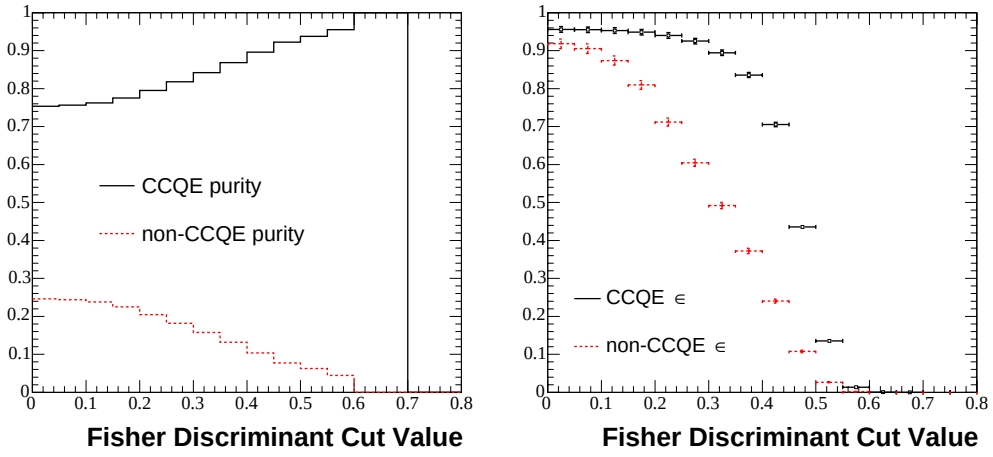

Figure 4.6: *Optimization of the Fisher discriminant cut. Left: Monte Carlo prediction for the signal (black solid line) and background (red dashed line) fractions remaining after a cut on the Fisher output variable > the abcissa value. Right: Monte Carlo prediction for the signal (black solid line) and background (red dashed line) cut efficiencies after a cut on the Fisher output variable > the abcissa value.*

efficiency as a function of energy for the full CCQE selection relative to no cuts is shown in the middle panel of figure 4.7. The energy dependence of this efficiency comes primarily from the "pre-cuts" on the number of veto hits and sub-events. The right panel shows the signal and background fractions as a function of energy after all CCQE selection cuts. The neutrino energy threshold for CC1π production is higher than for CCQE because there must be enough energy in the center of mass to produce the resonance, therefore, below $\sim$0.6 GeV the events passing the CCQE selection cuts are almost entirely ν_μ CCQE interactions. At high energy, CC1π produce lower energy μ than a CCQE event with the same E_ν, and therefore, for a fixed E_ν, a high energy CC1π event is more likely to pass the veto hit cut than a CCQE event.

The efficiency of the CCQE selection cuts in data is shown in table 4.2. The efficiency of the first four "pre-cuts," which primarily eliminate cosmic rays and non-ν_μ-charged-current interactions, is 1.6%. The efficiency of all of the "pre-cuts" together

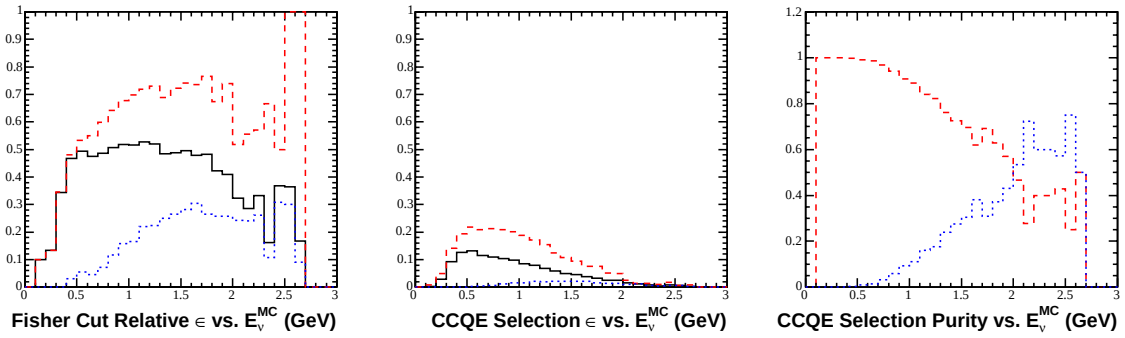

Figure 4.7: *Efficiency and resulting purity of the ν_μ CCQE selection cuts vs. Monte Carlo neutrino energy (GeV). Left: efficiency of the Fisher cut relative to events that pass the "pre-cuts"; middle: efficiency of all ν_μ CCQE selection cuts relative to no cuts; right: ν_μ CCQE signal and background after all selection cuts. Distributions are shown for all Monte Carlo events (solid black line), Monte Carlo signal (dotted red line), and Monte Carlo background (dotted blue line) predictions.*

is 1.2%, and the percentage of events in data passing all of the CCQE selection cuts is 0.6%. These numbers are dramatically smaller than in the Monte Carlo because of the 200:1 ratio of cosmic rays to beam ν_μ induced events in data, while neutrino-less events are not simulated in the Monte Carlo.

However, one can compare the relative efficiencies of each cut, that is, the number of events that pass a given cut divided by the number that passed the previous cut. The ratio of relative efficiencies in data to Monte Carlo is shown in the last column of table 4.2. The first two cuts have very different relative efficiencies in data and Monte Carlo, as expected given the cosmic ray backgrounds. After this point, the relative cut efficiencies are similar in data and Monte Carlo, and in fact the product of the last four relative efficiencies is 0.986. This product is equivalent to the ratio in data to Monte Carlo of the number of events passing all cuts relative to the number that pass the first two cuts. Therefore, after neutrino-less events are eliminated in the data, the CCQE selection cut efficiency agrees between data and Monte Carlo to

Table 4.2: *Data ν_μ CCQE selection cut efficiencies (ϵ). Relative efficiency is defined to be the number of events passing a given cut divided by the number passing the previous cut. The denominator of the (data/MC) relative efficiency ratio is taken from column 2 of table 4.1.*

cut	ϵ	*relative* ϵ	*(data/MC) relative* ϵ
no cuts	1	1	1
in-spill time	0.167475	0.167475	0.21473
Veto(1) Hits < 6	0.0385013	0.229893	0.354449
2 sub-events	0.0172044	0.446852	0.934674
Veto(2) Hits < 6	0.0156945	0.91224	1.01579
$\Delta R < 100\ cm$	0.0116815	0.744304	0.961743
Fisher > 0.425	0.00607915	0.520408	1.07899

within 2%.

After cosmic rays are eliminated, one can also compare the efficiency as a function of energy between data and Monte Carlo. Unfortunately the true neutrino energy is not available in the data, therefore the abcissa must be the reconstructed neutrino energy. The left panel of figure 4.8 shows the efficiency of the Michel distance cut relative to events passing the first four "pre-cuts" in data and Monte Carlo. The right panel shows the efficiency of the Fisher output variable cut relative to events passing all of the "pre-cuts." In general, the agreement between data and Monte Carlo is good, which builds confidence that the CCQE selection cuts affect data and Monte Carlo in the same way.

The event sample composition in the Monte Carlo after all of the ν_μ CCQE selection cuts have been applied is summarized in tables 4.3 through 4.5. The vast

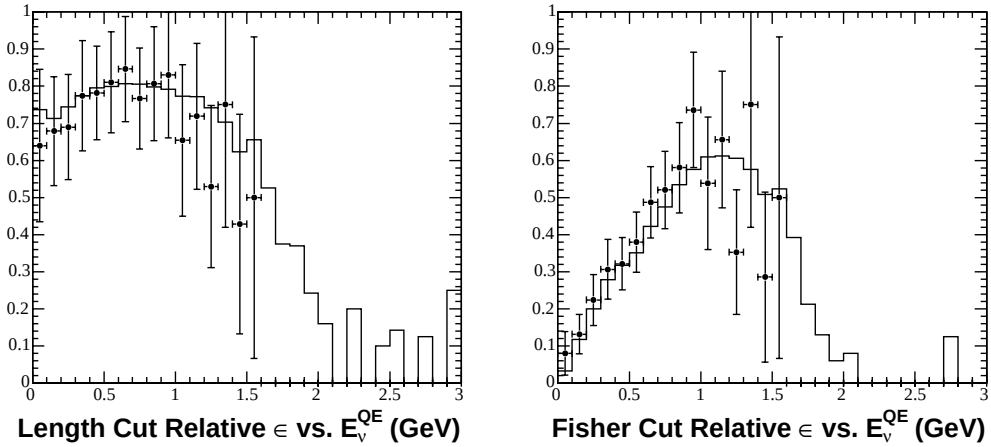

Figure 4.8: *ν_μ CCQE selection cut efficiencies vs. reconstructed neutrino energy (GeV) in data (black points with statistical errors) and Monte Carlo (solid black line). Right: efficiency of the Michel distance cut relative to events passing the first four "pre-cuts". Left: efficiency of the Fisher output variable cut relative to events passing all "pre-cuts".*

majority, 97.2%, of the neutrinos passing the CCQE selection cuts come from π^+ decay, while π^- and K^+ decay contribute 1.7% and 0.9% of the neutrino flux respectively. As a result, 98.2% of the flux is ν_μ while only 1.8% is $\overline{\nu}_\mu$. Of the events passing the CCQE cuts, 91% are signal $\nu_\mu n \rightarrow \mu^- p$ interactions, and most of the background comes from charged current resonant single π^+ production. Of the background events, 38% have the same particle content in the final state as ν_μ CCQE interactions because the pion was absorbed inside of the nucleus.

The final state kinematics of the events passing cuts are very similar between signal and background. The average Monte Carlo generated muon momentum is 0.66 (0.73) GeV for signal (background), and the average nucleon momentum is 0.51 (0.53) GeV. For background events with a pion in the final state the average pion momentum is 0.28 GeV. In contrast, the generated neutrino energy is typically much higher for background events, 1.24 GeV compared with 0.86 GeV for signal events, because the

Table 4.3: *Monte Carlo sample composition by neutrino interaction channel after ν_μ CCQE selection cuts. Only interactions that account for >0.005 of the total are included.*

ν interaction type	*fraction*
$\nu_\mu n \rightarrow \mu^- p$	0.9053
$\nu_\mu p \rightarrow \mu^- p \pi^+$	0.0576
$\nu_\mu n \rightarrow \mu^- p \pi^0$	0.0126
$\nu_\mu n \rightarrow \mu^- n \pi^+$	0.0116
$\nu_\mu n \rightarrow \nu_\mu n \pi^0$	0.0036
$\overline{\nu}_\mu p \rightarrow \mu^+ n$	0.0011
$\nu_\mu A \rightarrow \mu^- \pi^+ A$	0.0058

background events come from higher-threshold resonance production processes.

4.2 CCQE Data Set

The ν_μ CCQE selection cuts described in the previous section are applied to the MiniBooNE data, and the resulting ν_μ CCQE sample contains 98,381 events, corresponding to 4.23747×10^{20} incident protons on target (*p.o.t.*), or 2.32169×10^{-16} interactions in the detector per *p.o.t.*. The number of *p.o.t.* in the data is calculated from the beam toroid measurement, corrected for events that do not pass the data quality cuts described in chapter 2. The data taking time period spans runs 3539 to 12417, which were recorded between August 2002 and October 2005. The Monte Carlo statistics after the ν_μ CCQE selection cuts comprise 414,004 events, which correspond to 2.346×10^{21} simulated *p.o.t.* [2]. The number of *p.o.t.* is calculated as

[2]The May 2006 baseline Monte Carlo is used for all studies in this thesis.

Table 4.4: *Monte Carlo sample composition by parent meson type after ν_μ CCQE selection cuts. Fraction 1 is the fraction of the total events where the source meson is produced in the primary proton-Be interaction. Fraction 2 is the fraction of the total events where the source meson is the particle which decays to the neutrino, which is not necessarily produced in the primary $p - Be$ interaction.*

meson type	*fraction 1*	*fraction 2*
μ^+	0.0000	0.0012
μ^-	0.0000	0.0001
π^+	0.9259	0.9723
π^-	0.0146	0.0167
K_L^0	0.0007	0.0004
K^+	0.0096	0.0091
K^-	0.0002	0.0002
p	0.0092	0.0000
n	0.0396	0.0000

Table 4.5: *Monte Carlo sample composition by neutrino type, after the ν_μ CCQE selection cuts.*

	ν_e	$\overline{\nu}_e$	ν_μ	$\overline{\nu}_\mu$
fraction	0.00002	0.00000	0.98168	0.01829

$p.o.t.^{MC} = N^{MC}_{no\ cuts}/(MC\ events\ per\ p.o.t.)$, where $N^{MC}_{no\ cuts}$ is the number of generated events considered, 8.0×10^6, and $(MC\ events\ per\ p.o.t.)$ is the total cross section, flux, and target nucleon weighted conversion of 2.19738×10^{-15} events (of all neutrino interaction types) per *p.o.t.* in the 610 *cm* radius detector volume. The conversion factor $(MC\ events\ per\ p.o.t.)$ gets a multiplicative correction for density weighting of event vertices in the detector Monte Carlo of 1.04. The number of events $N^{MC}_{no\ cuts}$ gets a multiplicative correction of $\sim$0.67 for the probability that a neutrino will interact in the detector given the pathlength of detector material it traverses, which is determined by its position and angle at production in the neutrino beam line. When normalized to the same number of *p.o.t.* as the data, the Monte Carlo comprises 74,546 events in the 610 *cm* radius detector volume, which corresponds to 1.75921×10^{-16} events after cuts per *p.o.t.*.

Once a ν_μ CCQE data set is isolated, one can compare the kinematics of ν_μ CCQE events in data and Monte Carlo to measure the level of agreement. The most interesting kinematic distribution is the reconstructed neutrino energy, E^{QE}_ν, since this is used to search for oscillations. Two types of comparisons between data and Monte Carlo are considered here: relatively normalized distributions, which test the level of agreement in the predicted and observed shapes, and absolutely normalized rates. Relatively normalized comparisons are most useful for the ν_μ disappearance analysis, where MiniBooNE's sensitivity to oscillations comes primarily from the shape distortion of the neutrino energy spectrum. However, for the ν_e appearance analysis, normalization and the energy spectrum contribute to the oscillation sensitivity in roughly equal proportions, therefore understanding the absolute normalization of data relative to Monte Carlo is important as well.

The neutrino energy is reconstructed from the measured muon direction and energy according to two body kinematics, with a few corrections derived from Monte

Carlo to reduce bias and smearing. The neutrino energy reconstruction algorithm is described in detail in reference [116], so only a brief summary is given here. Quasi-elastic scattering is a two-body interaction, and therefore the kinematics are speficied by:

$$E_\nu^{QE} = \frac{1}{2}\frac{2m_N E_\mu - m_\mu^2}{m_N - E_\mu + p_\mu cos(\theta_\mu)} \tag{4.9}$$

where E_μ, p_μ, and $cos(\theta_\mu)$ are the reconstructed muon's energy, momentum, and direction cosine with respect to the neutrino beam direction, m_N is the target neutron mass, and m_μ is the final state lepton mass, under a ν_μ scattering hypothesis. A ν_e scattering hypothesis would replace the muon mass with the electron mass. In a CCQE interaction on carbon, as in the MiniBooNE detector, the target nucleon is bound, and is changed into a proton by the charged current. Taking these considerations into account modifies equation 4.9 via

$$E_\nu^{QE} = \frac{1}{2}\frac{2(m_N + E_B)E_\mu - (\Delta M^2 + 2m_N E_B + E_B^2 + m_\mu^2)}{(m_N + E_B) - E_\mu + p_\mu cos(\theta_\mu)} \tag{4.10}$$

where E_B is the binding energy of the target neutron, and $\Delta M^2 = m_N^2 - m_P^2$ where m_P is the proton mass. Reconstruction bias is corrected with a few calibrations derived empirically from Monte Carlo. First, the measured muon kinetic energy, T_μ, is corrected towards the "true" Monte Carlo value via

$$T_\mu^{corr} = a_1 \cdot T_\mu + a_2 \tag{4.11}$$

where (a_1, a_2) = (0.8867, 0.0927) under a ν_μ hypothesis, and (0.9942, 0.0113) under a ν_e hypothesis. The corrected kinetic energy is used to calculate the momentum and energy for use in equation 4.10 to calculate E_ν^{QE}, and the four-momentum transfer squared,

$$Q_{QE}^2 = 2E_\nu^{QE} E_\mu (1 - \beta cos(\theta_\mu)) - m_\mu^2. \tag{4.12}$$

The E_ν^{QE} value calculated using T_μ^{corr} and equation 4.10 is further corrected towards

the "true" Monte Carlo generated neutrino energy by a polynomial in Q^2_{QE},

$$(E_\nu^{QE})^{corr} \;=\; E_\nu^{QE} - \Big(b_1 + b_2 Q^2_{QE} + b_3 (Q^2_{QE})^2 + b_4 (Q^2_{QE})^3\Big) \tag{4.13}$$

The constants b_i are (-0.0777, 0.1189, 0.1777, -0.0291) and (-0.1472, 0.2788, 0.0898, -0.0196) under a ν_μ and ν_e hypothesis respectively. The four-momentum transfer squared is recalculated, substituting $(E_\nu^{QE})^{corr}$ into equation 4.12. The form of this E_ν^{QE} correction was determined empirically, however the fact that a Q^2-dependent correction works better than an E_ν^{QE}-dependent correction is probably because the dominant source of smearing in the neutrino energy reconstruction comes from nuclear effects. As seen in chapter 3, the Fermi Gas nuclear model produces E_ν^{QE} smearing of $\sim$7%, and its effects have a much stronger dependence on Q^2 than on E_ν.

Relatively normalized comparisons of the reconstructed direction, muon energy, neutrino energy, and four-momentum transfer squared are shown in figure 4.9. The shapes of the signal and background distributions from the Monte Carlo are also overlaid. For the reconstructed muon and neutrino energies, the background and signal shapes are very similar, however, the background is significantly more peaked near $cos(\theta) \;\sim\; 1$ and $Q^2 \;\sim\; 0$. This is due to mis-reconstruction of background events, rather than the true kinematics. In general the background events have higher values of the true E_ν and Q^2, since a Δ resonance must be produced.

The measurement resolution for each of these kinematic quantities is calculated by projecting a profile histogram of the difference between the Monte Carlo generated and reconstructed variable into bins of the generated quantity, e.g. $(E_\nu^{MC} - E_\nu^{QE})$ vs. E_ν^{MC} for $0 < E_\nu^{MC} < 100\ MeV$. The projection is fit with a gaussian function, and the r.m.s. of the best fit gaussian divided by the bin center is taken to be the resolution in that bin. For the oscillation analysis, the most important resolution is that of the neutrino energy measurement, which is shown as a function of generated Monte Carlo neutrino energy in figure 4.10. At $E_\nu = 1\ GeV$, the resolution is 10.6%. The

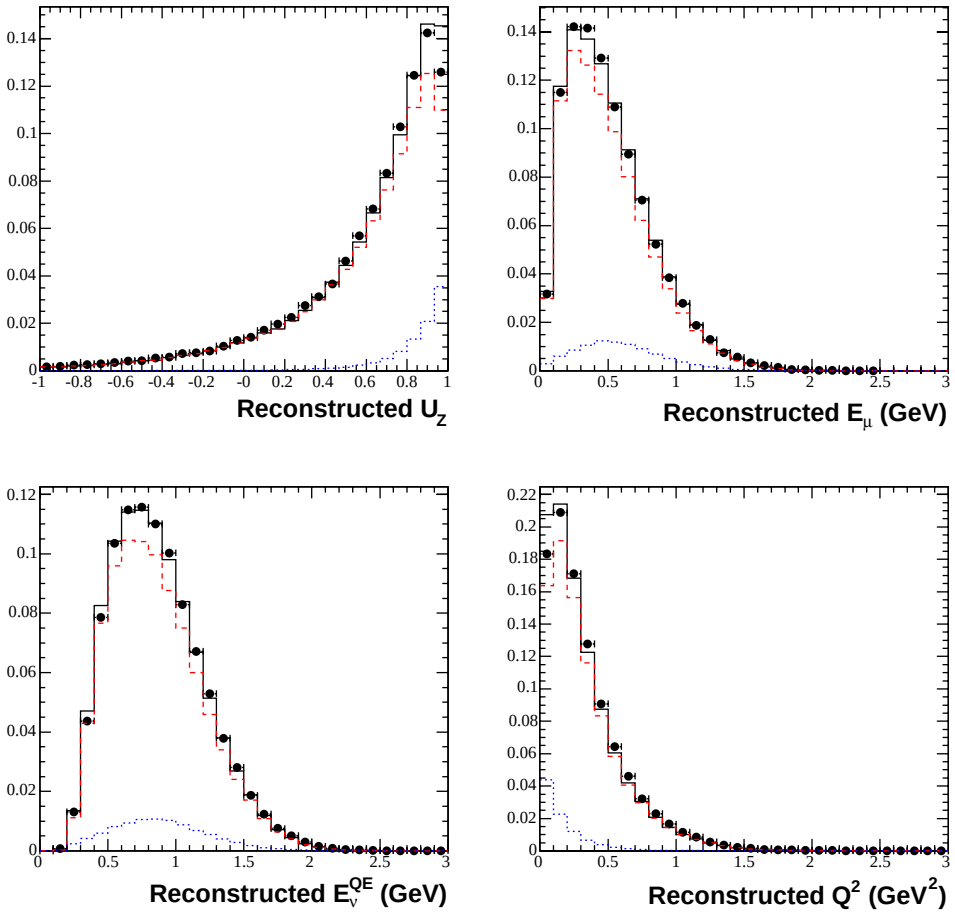

Figure 4.9: *Comparison of kinematic variables after the ν_μ CCQE selection cuts. Top left: reconstructed track angle with respect to the beam direction; top right: reconstructed energy under a muon hypothesis (GeV); bottom left: reconstructed neutrino energy assuming 2-body kinematics (GeV); bottom right: reconstructed four-momentum transfer squared (GeV^2). Data with statistical errors (black points) are compared with the Monte Carlo total (solid black line), Monte Carlo signal (dotted red line), and Monte Carlo background (dotted blue line) predictions. Data and the total Monte Carlo curves are normalized to unit area.*

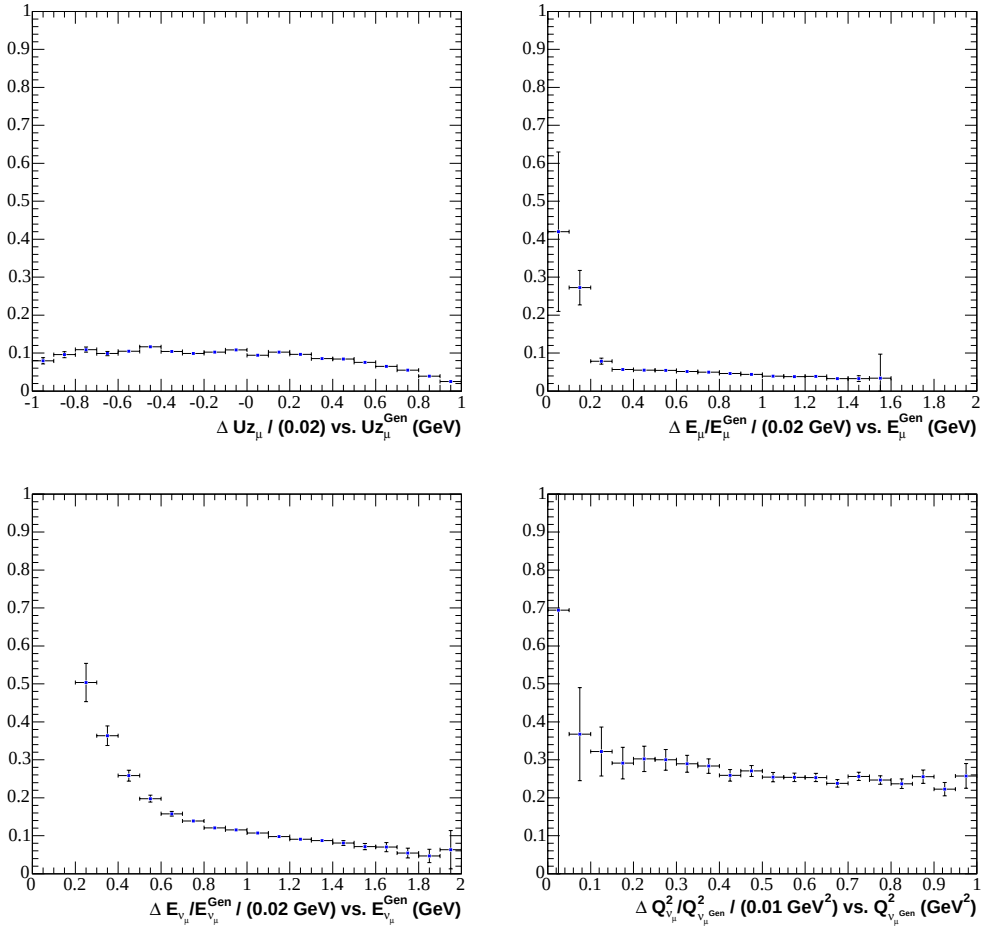

Figure 4.10: *Measurement resolution as a function of kinematic variables, for Monte Carlo events passing the ν_μ CCQE selection cuts. Top left: reconstructed - generated difference vs. generated primary track angle with respect to the beam direction; top right: (reconstructed - generated) / generated vs. generated muon energy (GeV); bottom left: (reconstructed - generated) / generated vs. generated neutrino energy (GeV); bottom right: (reconstructed - generated) / generated vs. generated four-momentum transfer squared (GeV^2). Error bars are the r.m.s. of a gaussian fit to the residual distributions.*

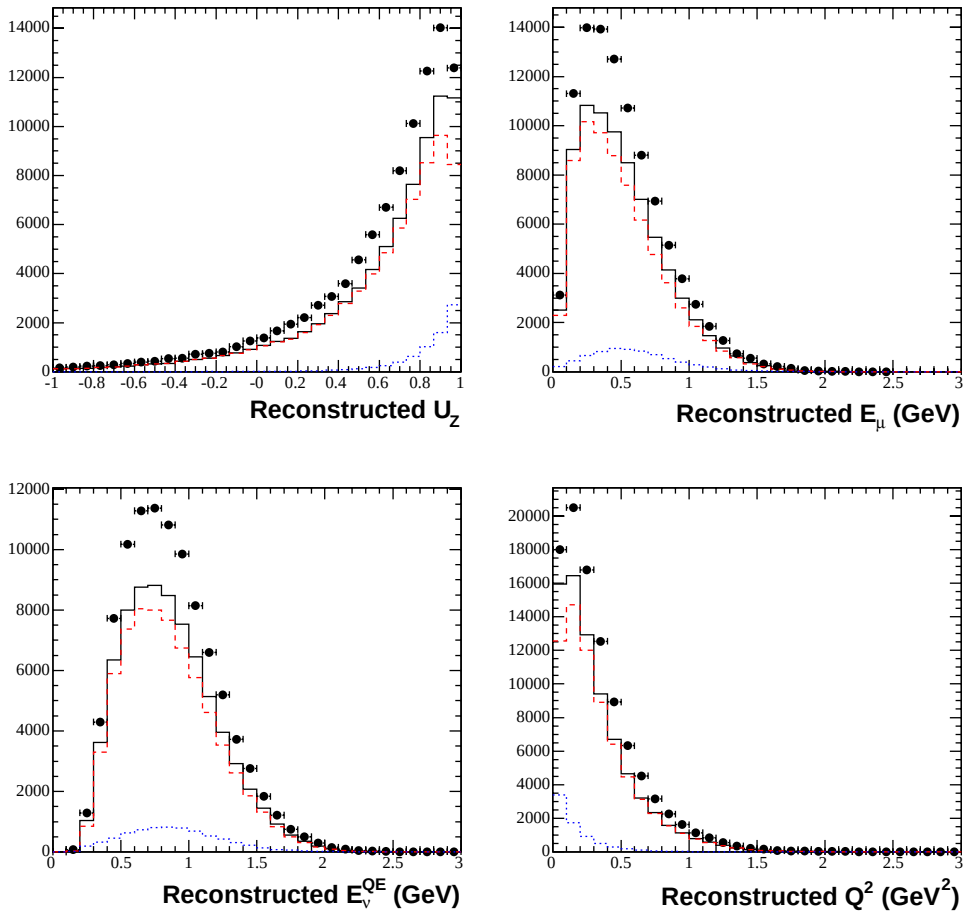

Figure 4.11: *Comparison of kinematic variables after the ν_μ CCQE selection cuts, absolutely normalized to protons on target. Top left: reconstructed track angle with respect to the beam direction; top right: reconstructed energy under a muon hypothesis (GeV); bottom left: reconstructed neutrino energy assuming 2-body kinematics (GeV); bottom right: reconstructed four-momentum transfer squared (GeV^2). Data with statistical errors (black points) are compared with the Monte Carlo total (solid black line), Monte Carlo signal (dotted red line), and Monte Carlo background (dotted blue line) predictions.*

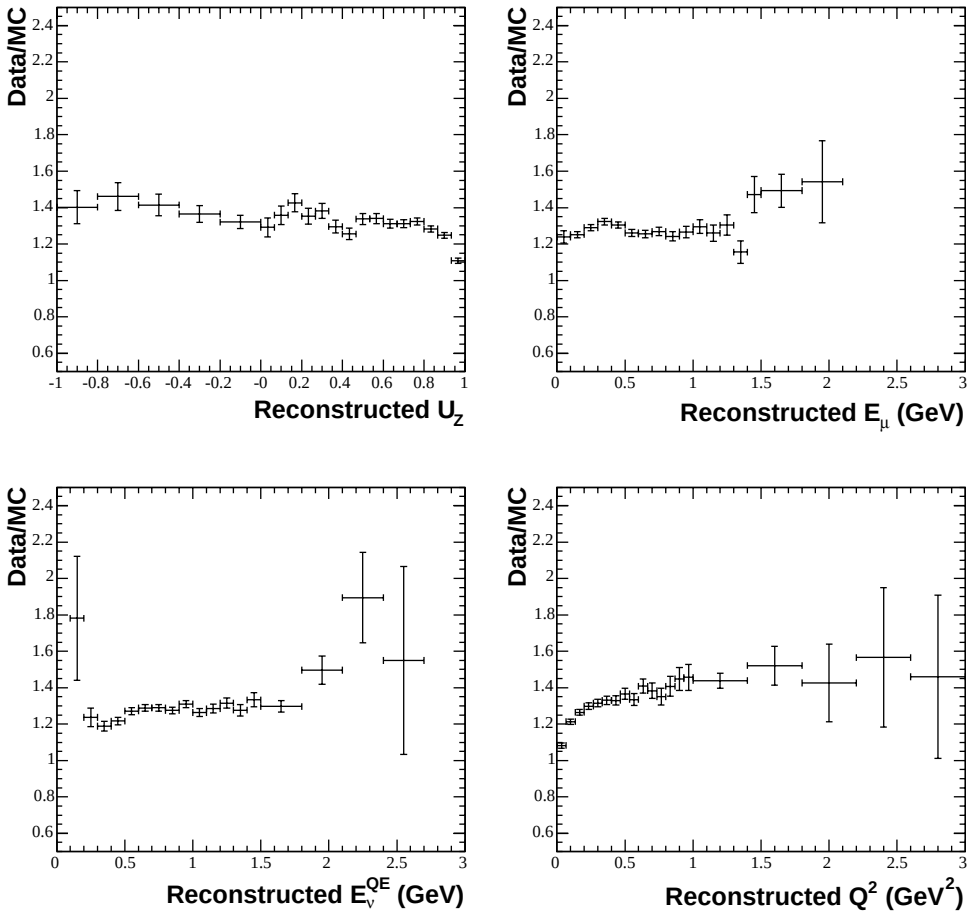

Figure 4.12: *Ratio of data to Monte Carlo after ν_μ CCQE selection cuts as a function of kinematic variables, absolutely normalized to protons on target. Top left: reconstructed track angle with respect to the beam direction; top right: reconstructed energy under a muon hypothesis (GeV); bottom left: reconstructed neutrino energy assuming 2-body kinematics (GeV); bottom right: reconstructed four-momentum transfer squared (GeV^2). Error bars include data and Monte Carlo statistics only.*

background remaining after the CCQE selection cuts does not significantly degrade the energy resolution; without background contamination the resolution is 10.4%, according to the Monte Carlo.

The corresponding absolutely normalized kinematic distributions are shown in figure 4.11. The absolutely normalized rates do not agree between data and Monte Carlo: the ratio of the total number of events in data to Monte Carlo after the ν_μ CCQE selection cuts is 1.28±0.006, with statistical errors only. The source of this normalization discrepancy has been a subject of much study, and is not yet understood [85].

The ratio of data to Monte Carlo for each of the four kinematic variables discussed here is shown in figure 4.12. The ratio is fairly flat below $E_\nu \sim 1.5\ GeV$, however, it does show a systematic variation at high u_z ($cos\theta_\mu$ with respect to the neutrino beam direction) and low Q^2. It is unlikely that the source of the kinematic distribution shape differences is the event reconstruction since the behavior of the ratio has persisted through many reconstruction versions, and because the muon calibration system data do not show the same effect. The Q^2 dependence strongly implies that the shape difference is due to a simulation deficiency in the neutrino interaction cross section Monte Carlo, most likely in the treatment of the nuclear environment. This hypothesis is analyzed in detail in chapter 6.

4.3 Systematic Errors

The uncertainty on the Monte Carlo prediction for events passing the ν_μ CCQE selection cuts is calculated by propagating the uncertainties on the underlying simulation parameters, using the standard method for transforming an error matrix from one basis to another [117]. The error propagation calculations described here use the

simulation parameter uncertainties described in chapter 3, sections 3.1.3, 3.2.2, and 3.3.2, and the simulation parameter correlation matrices given in appendix F.

Any error matrix can be calculated in an arbitrary number of bins i of an output variable O given an input covariance matrix with an arbitrary number j of input parameters P. For example, the input parameters P_j could be the Sanford-Wang π^+ production cross section coefficients ($\sum_j = 8$), with the output variable bins O_i as 30 bins of the generated neutrino energy, E_ν^{MC}, from 0 to 3 GeV ($\sum_i = 30$). The input parameter covariance matrix $\mathcal{P}$, with dimension $j \times j$, comes from the Sanford-Wang fits. To propagate the Sanford-Wang parameter errors to an uncertainty on the E_ν^{MC} distribution a matrix of first derivatives is employed. The first derivative matrix $\mathcal{F}(O)_{i,j}$ is computed as the change in the number of events in each bin i of the output variable O with respect to each input parameter variation j:

$$\mathcal{F}(O)_{i,j} \;=\; \frac{(N(O)_0 - N(O)_j)_i}{C_j - U_j} \tag{4.14}$$

where $(N(O)_j)_i$ is the number of events in bin i of the generated energy distribution from the Sanford-Wang beam Monte Carlo run where parameter j was varied by 1σ. $(N(O)_0)_i$ is the number of events in bin i of the generated energy distribution from a Monte Carlo run where all parameters j are set to their central values. This is referred to as "central value" Monte Carlo hereafter. The parameters C_j and U_j are the values used to generate the central value and "unisim" Monte Carlo samples respectively. The output variable error matrix $\mathcal{M}(O)_{m,n}$ is then given by the product

$$\mathcal{M}(O)_{m,n} \;=\; \mathcal{F}(O)^T_{m,j}\; \mathcal{P}_{j,k}\; \mathcal{F}(O)_{n,k} \tag{4.15}$$

where $\mathcal{F}(O)^T_{m,j}$ is the transpose of the first derivative matrix. The output variable error matrix $\mathcal{M}(O)_{m,n}$ has dimension $i \times i$.

Several quantities are used in the following discussions to extract information from the error matrix $\mathcal{M}(O)$.

1. $\mathcal{F}^{scaled}(O)$: the scaled first derivative measures the fractional change in the number of events in a given energy bin with respect to the central value Monte Carlo due to a 1σ variation of an input parameter. The scaled first derivative is defined to be

$$\mathcal{F}^{scaled}(O)_{i,j} \;=\; \frac{C_j}{(N(O)_0)_i} \times \mathcal{F}(O)_{i,j}. \tag{4.16}$$

2. $\sigma(O)_i$: the square root of the diagonal elements of $\mathcal{M}(O)$ (the errors typically displayed on an output variable distribution).

$$\sigma(O)_i \;=\; \sqrt{\mathcal{M}(O)_{i,i}} \tag{4.17}$$

3. $\delta(O)$: the average of the error bars on the output variable distribution. $\delta(O)$ samples only the diagonal elements of the error matrix but is sensitive to the shape distortion as well as the total normalization change due to a given source of uncertainty. This quantity includes correlations between simulation input parameters, but not correlations between output variable bins.

$$\delta(O) \;=\; \frac{\sqrt{\sum_i \sigma(O)_i^2}}{\sum_i N(O)_i} \;=\; \frac{\sqrt{\sum_i \mathcal{M}(O)_{i,i}}}{\sum_i N(O)_i} \tag{4.18}$$

where $N(O)_i$ is the number of events in bin i of the output variable O distribution (where all input parameters j are set to their central values).

4. $\delta\mathcal{M}$: the fractional output variable error matrix, defined as

$$\delta\mathcal{M}(O)_{i,k} \;=\; \frac{\mathcal{M}(O)_{i,k}}{N(O)_i N(O)_k} \tag{4.19}$$

5. $\Delta_N(O)$: the error on the total number of events in the output variable O distribution, computed using the full fractional error matrix $\delta\mathcal{M}$ including correlations between output variable bins and simulation input parameters.

$$\Delta_N(O) \;=\; \sqrt{\sum_i N(O)_i \left(\sum_k \delta\mathcal{M}(O)_{i,k}\; N(O)_k\right)} \;=\; \sqrt{\sum_{i,k} \mathcal{M}(O)_{i,k}} \tag{4.20}$$

The components of an example error calculation propagating the π^+ flux simulation input parameter uncertainties to error bars on an output variable distribution, E_ν^{MC}, for events passing the ν_μ CCQE selection cuts, are shown in figure 4.13. First, a set of j Monte Carlo distributions is produced where Sanford Wang π^+ production cross section parameter j has been varied by $+1$ σ. These are shown in the top left panel of figure 4.13, and referred to as "unisims" hereafter. The "unisims" may be produced either by reweighting the Monte Carlo event-by-event, or by generating a new Monte Carlo sample with the desired simulation input parameter varied. The "unisims" are used to calculate the first derivative matrix in equation 4.14. Each row of the matrix comes from the variation of one Sanford-Wang π^+ production cross section parameter, and each column comes from one bin of the output variable. The rows of the scaled first derivative matrix are shown in the bottom eight panels of figure 4.13. The first derivative matrix and the Sanford-Wang parameter error matrix are combined as in equation 4.15 to produce an error matrix in bins of the output variable E_ν^{MC}. The square root of the diagonal elements of this matrix are shown as the error bars on the central value Monte Carlo prediction in the top middle panel of figure 4.13. These error bars include correlations between the Sanford-Wang parameters, and therefore may be either smaller or larger than the spread in the "unisims". The fractional uncertainty is shown in the top left panel of figure 4.13. In bins where there are no events the fractional uncertainty is set to 1.0, and at the peak of the E_ν^{MC} distribution the fractional uncertainty is $\sim$7%. The two error estimators discussed above, $\delta(O)$ and $\Delta_N(O)$, are 5.5% and 1.8% respectively.

To estimate the flux simulation contribution to the uncertainty on the Monte Carlo prediction for events passing the ν_μ CCQE selection cuts, the 8 variations of the Sanford-Wang parameters (one variation per parameter) for the π^+ production cross section are considered. The simulation parameter values and their excursions

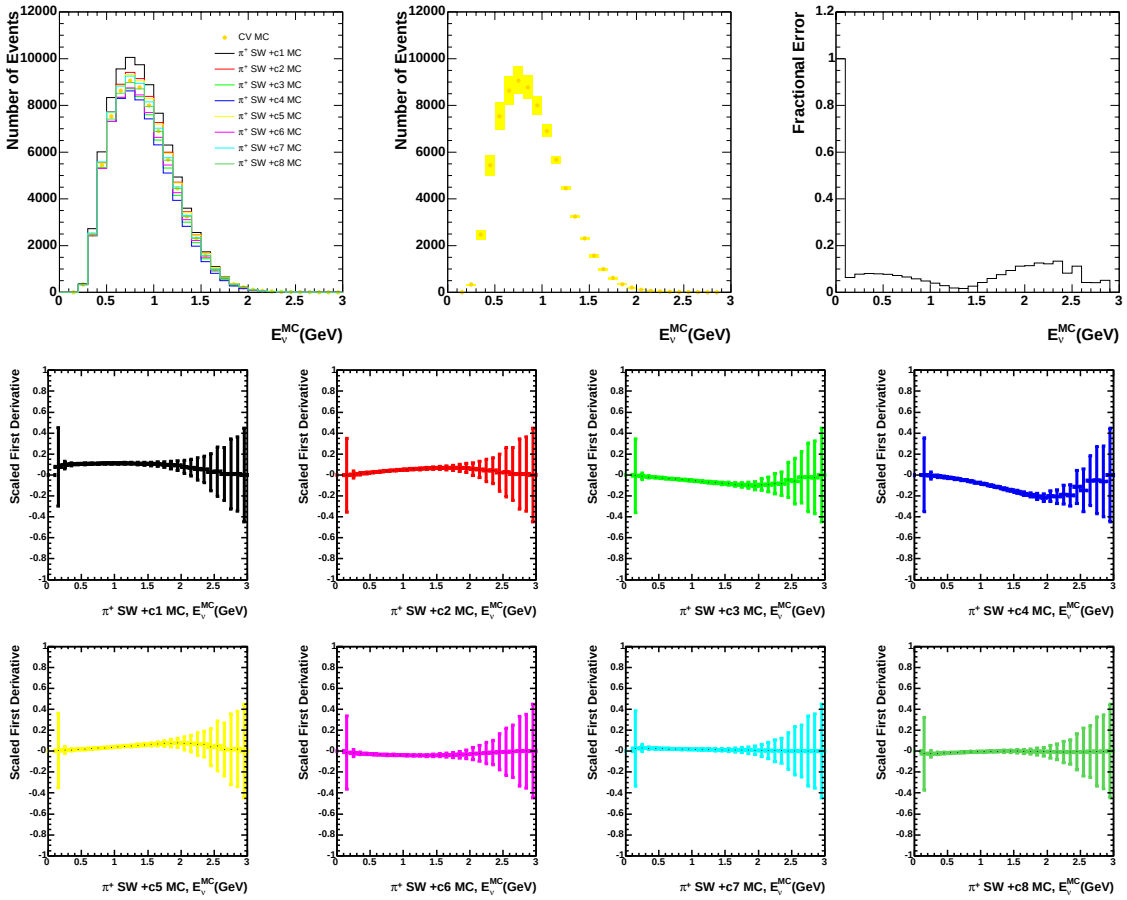

Figure 4.13: *Components of the calculation for propagating the errors on the Sanford-Wang π^+ flux prediction parameters to the distribution of E_ν^{MC} for events passing the ν_μ CCQE selection cuts. Top left: distribution of "unisims," top middle: central value Monte Carlo number of events vs. E_ν^{MC} with errors from the π^+ flux prediction, top right: fractional error vs. E_ν^{MC}. Bottom eight panels show the rows of the first derivative matrix.*

are summarized in the "E910+HARP" column of table 3.2. This error analysis does not include every source of flux prediction uncertainty given in table 3.9 since it neglects (*i*) 8 variations of the Sanford-Wang parameters for the π^- flux prediction cross section, (*ii*) 9 variations of the Sanford-Wang parameters for the K^+ production cross section, (*iii*) 9 variations of the Sanford-Wang parameters for the K^0_L production cross section, (*iv*) a set of variations for the hadronic interactions of secondary particles, and (*v*) uncertainties related to the beam line geometry. The fraction of events after cuts coming from the decay of mesons other than π^+ is estimated from Monte Carlo to be ∼2% from table 4.4, therefore the Sanford-Wang parameter variations for π^-, K^+, and K^0_L are neglected. The fraction of events after cuts produced by neutrinos from secondary interactions is ∼5% from table 4.4, and therefore this uncertainty should perhaps be considered in a full error analysis. It is not included here because the uncertainty on the hadronic interactions of secondary particles is currently not well understood. The scale of this uncertainty has been estimated by switching hadronic interaction models from GFLUKA to GHEISHA in the MiniBooNE beam Monte Carlo, which produces a ∼5% change in the total number of events passing the CCQE selection cuts. Measurements from the HARP experiment are expected to set the uncertainties on the secondary interaction cross sections in the near future. Uncertainties associated with the simulation geometry are correlated with the secondary interaction model, and will be investigated in detail when the beam Monte Carlo tuning, using HARP results, is complete.

To estimate the neutrino interaction cross section simulation contribution to the uncertainty on the Monte Carlo prediction for events passing the ν_μ CCQE selection cuts, the following simulation input parameter variations are considered: (*i*) the axial masses for the CCQE, CC1π, CC multi-π, and coherent neutrino-nucleon scattering cross sections (m_A^{QE}, $m_A^{1\pi}$, $m_A^{N\pi}$, m_A^{coh}), (*ii*) the Fermi Gas model Fermi momentum p_F

and binding energy E_B, (iii) the component of the nucleon spin carried by the strange sea quarks Δs, which impacts the neutral current cross sections, and (iv) the radiative Δ decay branching fractions, and (v) variations in the final state particle interaction cross sections inside the nucleus, including the pion absoroption and change exchange cross sections, and the probability for losing a final state pion due to Δ resonance re-interaction. The values of the cross section parameter variations is given in table 3.10. The treatment of the final state pion interaction cross section uncertainties in item (v) above is not handled consistently in the sense that these pion cross section variations are not considered for interactions that occur outside of the nucleus, in the detector oil. These should be considered in a full error analysis, and this task is currently underway. The magnitude of this uncertainty is probably comparable to the systematic error estimated using the simulation parameter variations in (v).

To estimate the detector simulation contribution to the uncertainty on the Monte Carlo prediction for events passing the ν_μ CCQE selection cuts, a subset of the simulation input parameters discussed in chapter 3, section 3.3.2 are varied. The list of parameters considered here is given in table 4.8; their values and excursions are given in table 3.13. As discussed in chapter 3, the values of and method for calculating the detector response uncertainties is still under investigation. Further, not all of the "unisim" Monte Carlo sets are currently available due to CPU limitations. As a result, the impact of the simulation parameter variations that are not considered here is unknown, and in this respect, the error analysis in this thesis is incomplete.

Reweighting is used to construct all of the flux "unisims", and the first 9 neutrino interaction cross section "unisims" listed in table 4.7 as well. The remainder of the "unisims" are produced by re-running the Monte Carlo simulation with one input parameter varied with respect to its nominal value. One advantage of producing the "unisims" by reweighting is that the statistical error on the first derivatives comes only

from the Monte Carlo statistics of the central value distribution, and while the error on the first derivatives does not enter the error matrix calculation, the elements of the error matrix can be unreliable where the first derivative errors are large. The statistics of the Monte Carlo used for this analysis comprise (i) 8×10^6 central value Monte Carlo events (which are also used to produce the flux and 9 neutrino interaction cross section "unisims") before cuts, (ii) 4×10^6 events before cuts in each of the 3 neutrino interaction cross section simulated "unisims", and (iii) 1.6×10^6 events before cuts in each of the 22 available detector response Monte Carlo simulated "unisims". These samples correspond to ∼430,000, ∼215,000, and ∼86,000 events after the ν_μ CCQE selection cuts for (i), (ii), and (iii) respectively.

The distributions of "unisims" for events passing the ν_μ CCQE selection cuts in the reconstructed variables E_μ, $cos(\theta_\mu)$, E_ν^{QE}, and Q^2 are shown for the π^+ flux, neutrino interaction cross section, and detector response uncertainties in figures 4.14, 4.15, and 4.16. The fractional changes in the numbers of events passing the ν_μ CCQE selection cuts for each of the "unisims" are summarized in tables 4.6, 4.7, and 4.8 respectively. The π^+ Sanford-Wang $c1$ parameter, the Fermi Gas Model neutrino interaction cross section parameter variations (E_B and p_F), and the detector response parameters related to UV flourescence and late time scintillation cause the largest changes in the output variable distribution normalizations for events passing the ν_μ CCQE selection cuts. However, recall that the "unisim" distributions do not reflect the correlations between simulation input variables, which can be large, and therefore the resulting correlated error may be either larger or smaller than the spread of the "unisims".

The error matrices $\mathcal{M}(O)_\Phi$, $\mathcal{M}(O)_\sigma$, and $\mathcal{M}(O)_{detector}$ are calculated separately for each of the sources of uncertainty, then added together to construct the total error matrix $\mathcal{M}(O)_{total}$. This procedure assumes that the various sources are uncor-

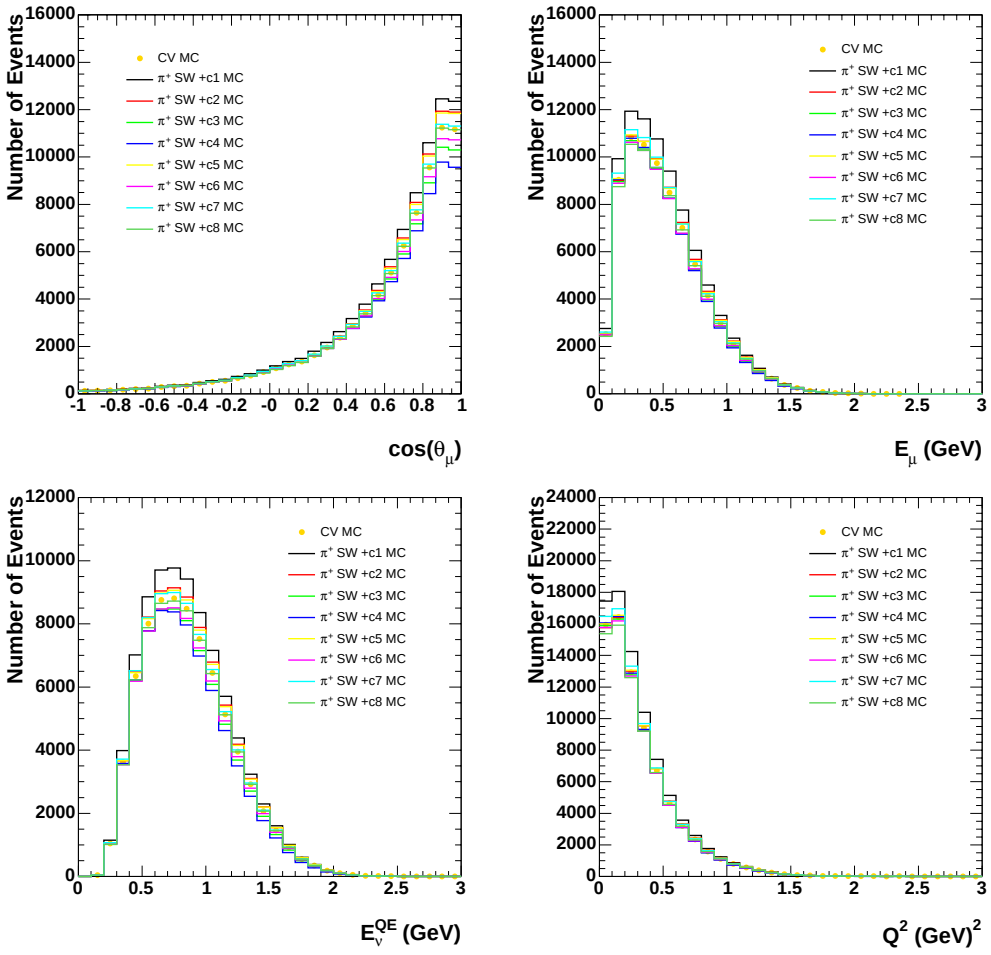

Figure 4.14: *Unisim distributions for π^+ flux simulation uncertainties after the ν_μ CCQE selection cuts, absolutely normalized to protons on target. Top left: reconstructed track direction cosine with respect to the beam direction; top right: reconstructed energy under a muon hypothesis (GeV); bottom left: reconstructed neutrino energy assuming 2-body kinematics (GeV); bottom right: reconstructed four-momentum transfer squared (GeV^2).*

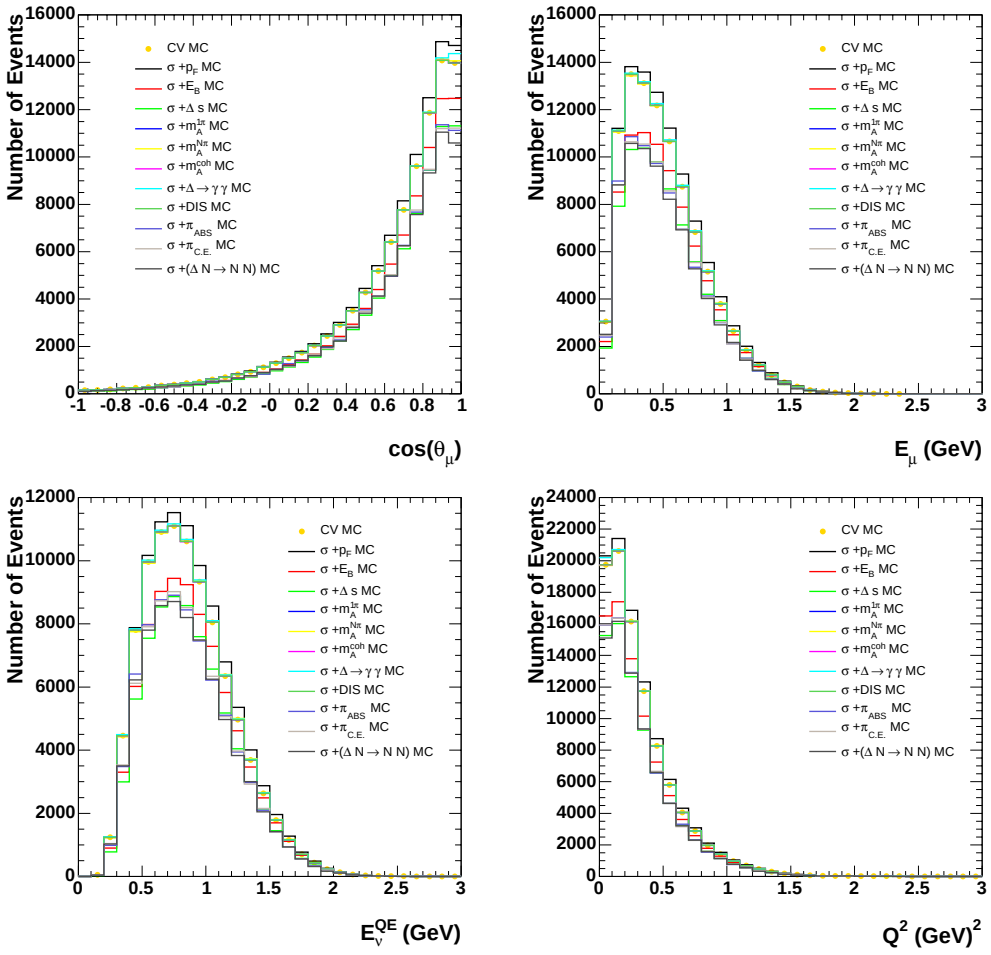

Figure 4.15: *Unisim distributions for neutrino interaction cross section simulation uncertainties after the ν_μ CCQE selection cuts, absolutely normalized to protons on target. Top left: reconstructed track direction cosine with respect to the beam direction; top right: reconstructed energy under a muon hypothesis (GeV); bottom left: reconstructed neutrino energy assuming 2-body kinematics (GeV); bottom right: reconstructed four-momentum transfer squared (GeV^2).*

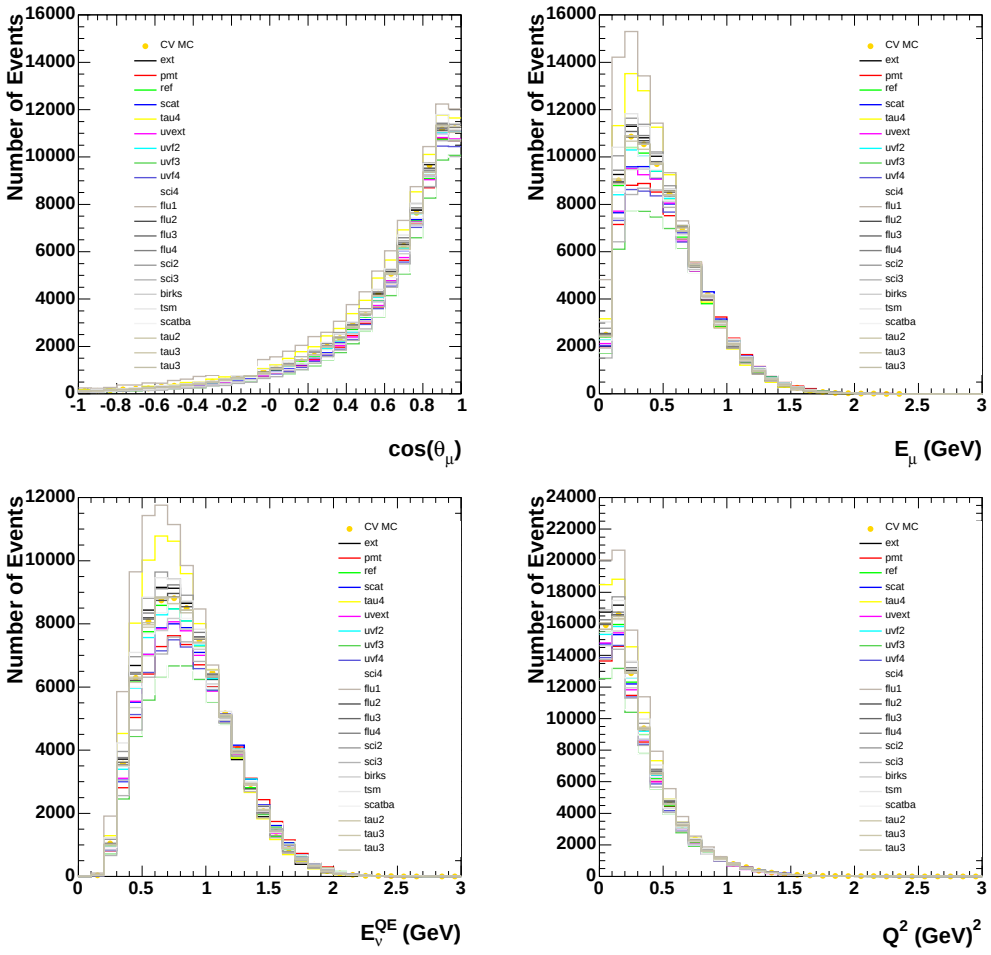

Figure 4.16: *Unisim distributions for detector response simulation uncertainties after the ν_μ CCQE selection cuts, absolutely normalized to protons on target. Top left: reconstructed track direction cosine with respect to the beam direction; top right: reconstructed energy under a muon hypothesis (GeV); bottom left: reconstructed neutrino energy assuming 2-body kinematics (GeV); bottom right: reconstructed four-momentum transfer squared (GeV^2).*

Table 4.6: *Fractional change in the total number of events passing the ν_μ CCQE selection cuts in each π^+ prediction "unisim" Monte Carlo set, for kinematic distributions of interest.*

"unisim"	E_ν^{QE}	E_μ	Q^2	$cos(\theta_\mu)$	E_ν^{MC}
π^+ flux SW +c1	0.1079	0.1044	0.1014	0.1082	0.1082
π^+ flux SW +c2	0.0412	0.0214	0.0088	0.0474	0.0430
π^+ flux SW +c3	-0.0455	-0.0264	-0.0170	-0.0542	-0.0473
π^+ flux SW +c4	-0.0661	-0.0285	-0.0126	-0.0866	-0.0670
π^+ flux SW +c5	0.0339	0.0196	0.0129	0.0407	0.0353
π^+ flux SW +c6	-0.0345	-0.0265	-0.0207	-0.0362	-0.0351
π^+ flux SW +c7	0.0120	0.0255	0.0287	0.0182	0.0195
π^+ flux SW +c8	-0.0094	-0.0186	-0.0253	-0.0075	-0.0086

related. The square roots of the diagonal elements of $\mathcal{M}(O)_{total}$ are shown for the reconstructed kinematic distributions $cos(\theta_\mu)$, E_μ, E_ν^{QE}, and Q^2, in figure 4.17, with the data superimposed. The contribution to the fractional error from each of the sources is shown in figure 4.18. The two error estimators, $\delta(O)$ and $\Delta_N(O)$, are summarized for each uncertainty source in table 4.9. The total normalization uncertainty is $\sim$14%, with the domininant contribution coming from uncertainties in the neutrino interaction cross sections. Therefore, the Monte Carlo prediction disagrees with the data, as discussed above, by $\sim 2\sigma$.

Given the overall normalization difference between data and the Monte Carlo prediction, it is desirable to do analyses where the Monte Carlo can be normalized relatively to the data, rather than absolutely normalized to the number of incident protons on target. In the relatively normalized case, the systematic errors, by def-

Table 4.7: *Fractional change in the total number of events passing the ν_μ CCQE selection cuts in each neutrino interaction cross section "unisim" Monte Carlo set, for kinematic distributions of interest.*

"unisim"	E_ν^{QE}	E_μ	Q^2	$cos(\theta_\mu)$	E_ν^{MC}
σ_ν $+m_A^{QE}$	0.0184	-0.0154	-0.0406	0.0250	0.0211
σ_ν $+p_F$	-0.0656	-0.0663	-0.0662	-0.0655	-0.0655
σ_ν $+E_B$	-0.2357	-0.2955	-0.3406	-0.2253	-0.2310
σ_ν $+\Delta s$	0.0000	0.0000	0.0000	0.0000	0.0000
σ_ν $+m_A^{1\pi}$	-0.0001	0.0000	0.0003	0.0000	0.0000
σ_ν $+m_A^{N\pi}$	0.0000	0.0000	0.0000	0.0000	0.0000
σ_ν $+m_A^{coh}$	0.0058	0.0060	0.0060	0.0056	0.0058
σ_ν $+\Delta \rightarrow \gamma\gamma$	0.0000	0.0000	0.0000	0.0000	0.0000
σ_ν $+\sigma^\pi_{absorption}$	-0.0031	-0.0031	-0.0031	-0.0031	-0.0031
σ_ν $+\sigma^\pi_{charge\ exchange}$	-0.0029	-0.0028	-0.0029	-0.0028	-0.0028
σ_ν $+\Delta N \rightarrow NN$	-0.0187	-0.0187	-0.0188	-0.0187	-0.0187

Table 4.8: *Fractional change in the total number of events passing the ν_μ CCQE selection cuts in detector response "unisim" Monte Carlo sets, for kinematic distributions of interest.*

"unisim"	E_ν^{QE}	E_μ	Q^2	$cos(\theta_\mu)$	E_ν^{MC}
cher	-0.0017	-0.0017	-0.0017	-0.0017	-0.0017
ext	0.0962	0.0962	0.0962	0.0962	0.0962
pmt	0.0437	0.0437	0.0437	0.0437	0.0437
ref	0.0565	0.0565	0.0566	0.0565	0.0565
scat	-0.1143	-0.1143	-0.1141	-0.1143	-0.1143
tau4	0.0829	0.0829	0.0829	0.0829	0.0829
uvext	0.0273	0.0273	0.0274	0.0273	0.0273
uvf2	0.1820	0.1820	0.1820	0.1820	0.1820
uvf3	0.1184	0.1184	0.1184	0.1184	0.1184
uvf4	0.1768	0.1768	0.1768	0.1768	0.1768
sci4	-0.2136	-0.2136	-0.2134	-0.2136	-0.2136
flu1	0.0004	0.0004	0.0005	0.0004	0.0004
flu2	-0.0011	-0.0011	-0.0011	-0.0011	-0.0011
flu3	-0.0211	-0.0211	-0.0210	-0.0211	-0.0211
flu4	-0.0375	-0.0375	-0.0374	-0.0375	-0.0375
sci2	0.1283	0.1283	0.1283	0.1283	0.1283
sci3	0.0751	0.0751	0.0751	0.0751	0.0751
birks	-0.0562	-0.0562	-0.0560	-0.0562	-0.0562
tsm	0.0362	0.0362	0.0363	0.0362	0.0362
scatba	0.0015	0.0015	0.0017	0.0015	0.0015
tau2	0.0113	0.0113	0.0114	0.0113	0.0113
tau3	0.0059	0.0059	0.0059	0.0059	0.0059

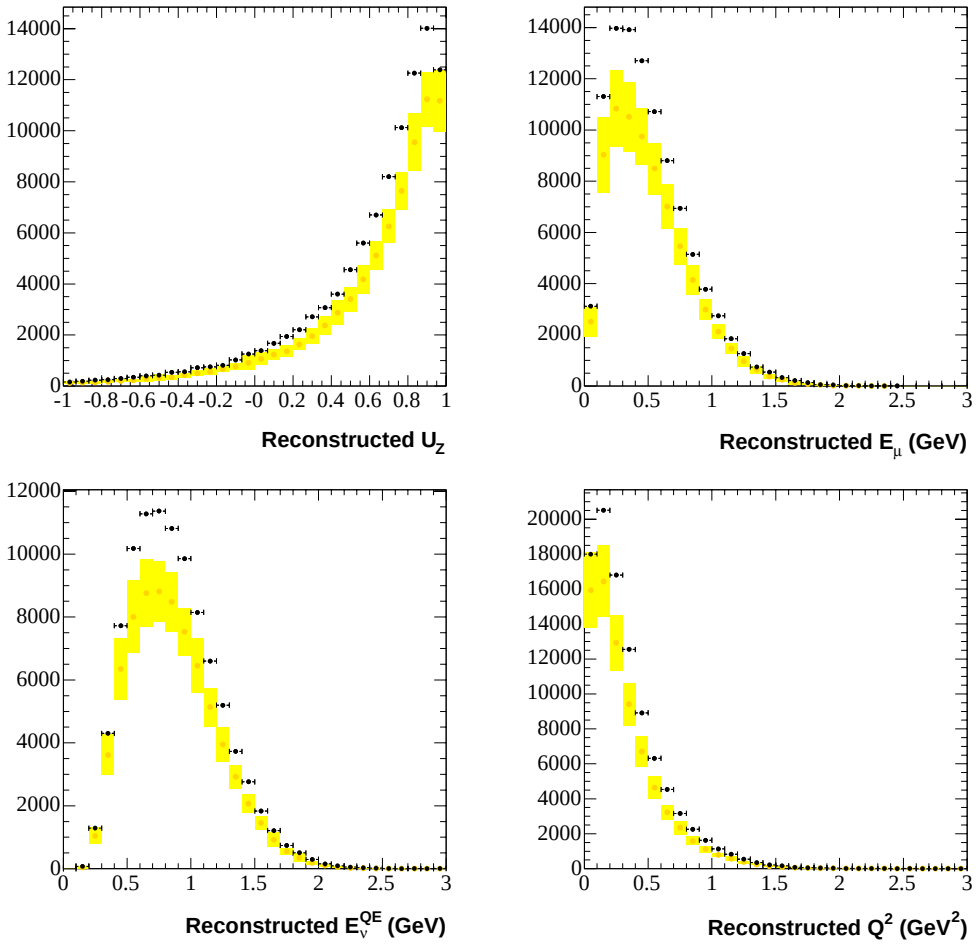

Figure 4.17: *Uncertainty on the Monte Carlo prediction for the number of events after the ν_μ CCQE selection cuts, absolutely normalized to protons on target, from the π^+ flux simulation and the neutrino interaction cross section simulation. Top left: reconstructed track direction cosine with respect to the beam direction; top right: reconstructed energy under a muon hypothesis (GeV); bottom left: reconstructed neutrino energy assuming 2-body kinematics (GeV); bottom right: reconstructed four-momentum transfer squared (GeV^2). The data (black points) with statistical errors is superimposed.*

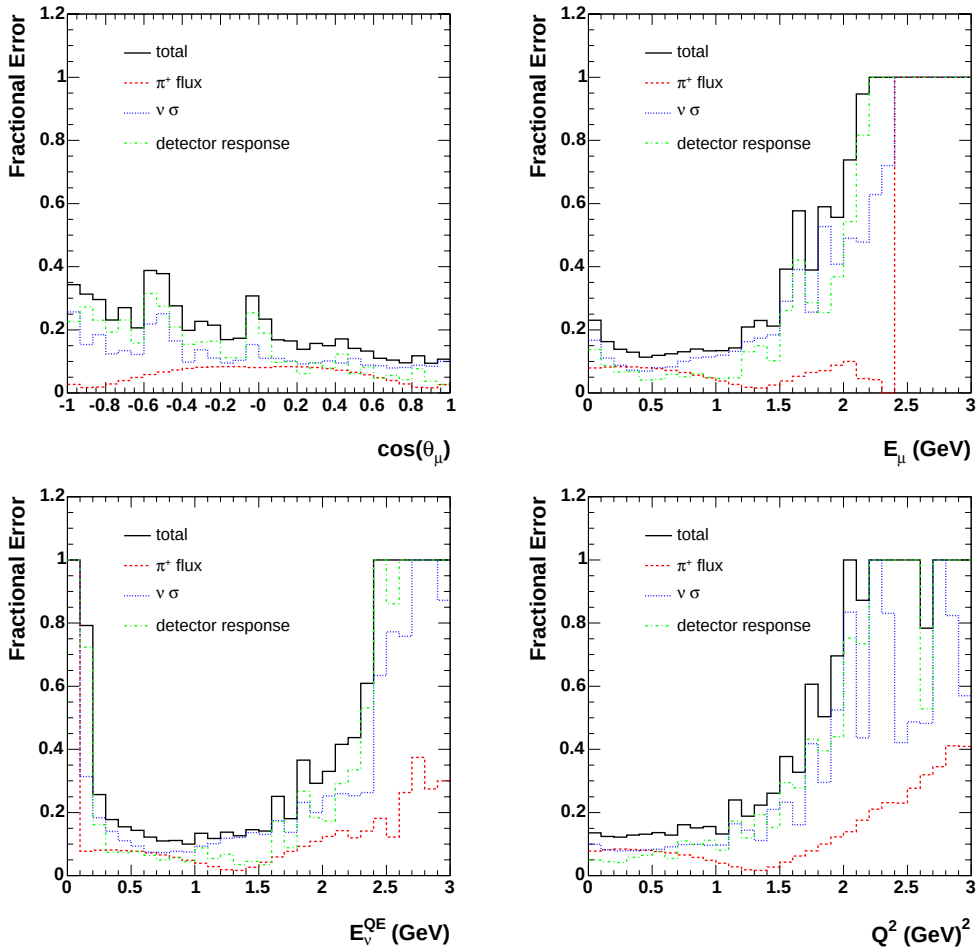

Figure 4.18: *Contribution to the fractional error on the Monte Carlo prediction for the number of events after the ν_μ CCQE selection cuts, absolutely normalized to protons on target, from the π^+ flux simulation, and the neutrino interaction cross section simulation. Top left: reconstructed track direction cosine with respect to the beam direction; top right: reconstructed energy under a muon hypothesis (GeV); bottom left: reconstructed neutrino energy assuming 2-body kinematics (GeV); bottom right: reconstructed four-momentum transfer squared (GeV^2).*

Table 4.9: *Correlated error contributions by source for events passing the ν_μ CCQE selection cuts, for kinematic distributions of interest.*

	E_ν^{QE}	E_μ	Q^2	$cos(\theta_\mu)$	E_ν^{MC}
π^+ flux $\delta(O)$	0.0181	0.0249	0.0309	0.0101	0.0176
π^+ flux $\Delta N(O)$	0.0570	0.0725	0.0777	0.0421	0.0551
σ_ν $\delta(O)$	0.0262	0.0281	0.0334	0.0269	0.0265
σ_ν $\Delta N(O)$	0.0974	0.0959	0.0887	0.0944	0.0974
detector response $\delta(O)$	0.0187	0.0203	0.0193	0.0168	0.0177
detector response $\Delta N(O)$	0.0663	0.0652	0.0584	0.0692	0.0630
total $\delta(O)$	0.0369	0.0427	0.0494	0.0333	0.0364
total $\Delta N(O)$	0.1309	0.1368	0.1316	0.1244	0.1284

Table 4.10: *Fractional change in the distribution mean for events passing the ν_μ CCQE selection cuts in each π^+ production "unisim" Monte Carlo set, for unit-area normalized kinematic distributions of interest.*

"unisim"	E_ν^{QE}	E_μ	Q^2	$cos(\theta_\mu)$	E_ν^{MC}
π^+ flux SW +c1	0.0002	0.0012	0.0035	0.0005	0.0000
π^+ flux SW +c2	0.0058	0.0106	0.0152	0.0086	0.0052
π^+ flux SW +c3	-0.0079	-0.0010	-0.0132	-0.0104	-0.0073
π^+ flux SW +c4	-0.0182	-0.0192	-0.0239	-0.0231	-0.0171
π^+ flux SW +c5	0.0057	0.0071	0.0093	0.0073	0.0052
π^+ flux SW +c6	-0.0018	-0.0046	-0.0070	-0.0032	-0.0015
π^+ flux SW +c7	-0.0018	-0.0031	-0.0039	-0.0027	-0.0017
π^+ flux SW +c8	0.0024	0.0056	0.0078	0.0040	0.0021

Table 4.11: *Fractional change in the distribution mean for events passing the ν_μ CCQE selection cuts in each neutrino interaction cross section "unisim" Monte Carlo set, for unit-area normalized kinematic distributions of interest.*

"unisim"	E_ν^{QE}	E_μ	Q^2	$cos(\theta_\mu)$	E_ν^{MC}
σ_ν $+m_A^{QE}$	0.0077	0.0203	0.0300	0.0134	0.0065
σ_ν $+p_F$	0.0003	0.0004	-0.0005	0.0006	0.0002
σ_ν $+E_B$	0.0172	0.0510	0.0746	0.0323	0.0142
σ_ν $+\Delta s$	0.0000	0.0000	0.0000	0.0000	0.0000
σ_ν $+m_A^{1\pi}$	-0.0007	-0.0006	-0.0014	0.0001	0.0005
σ_ν $+m_A^{N\pi}$	0.0004	0.0010	0.0010	0.0014	0.0009
σ_ν $+m_A^{coh}$	-0.0004	-0.0024	0.0060	-0.0063	-0.0061
σ_ν $+\Delta \rightarrow \gamma\gamma$	0.0000	0.0000	0.0000	0.0000	0.0000
σ_ν $+\sigma^\pi_{absorption}$	-0.0007	-0.0006	-0.0014	0.0001	0.0005
σ_ν $+\sigma^\pi_{charge\ exchange}$	0.0004	0.0010	0.0010	0.0014	0.0009
σ_ν $+\Delta N \rightarrow NN$	-0.0004	-0.0024	0.0059	-0.0063	-0.0061

Table 4.12: *Fractional change in the distribution mean for events passing the ν_μ CCQE selection cuts in detector response "unisim" Monte Carlo sets, for unit-area normalized kinematic distributions of interest.*

"unisim"	E_ν^{QE}	E_μ	Q^2	$cos(\theta_\mu)$	E_ν^{MC}
cher	-0.0221	-0.0269	-0.0434	0.0067	0.0021
ext	0.0517	0.0766	0.0464	0.0296	0.0097
pmt	-0.0065	-0.0088	-0.0102	0.0004	-0.0014
ref	0.0331	0.0504	0.0266	0.0234	0.0137
scat	-0.0496	-0.0746	-0.0343	-0.0321	-0.0135
tau4	0.0141	0.0282	-0.0176	0.0301	0.0095
uvext	0.0153	0.0230	0.0127	0.0113	0.0033
uvf2	0.0626	0.0977	0.0332	0.0479	0.0242
uvf3	0.0327	0.0551	0.0025	0.0355	0.0129
uvf4	0.0619	0.0960	0.0381	0.0422	0.0190
sci4	-0.0733	-0.1142	-0.0347	-0.0832	-0.0232
flu1	-0.0018	-0.0026	-0.0014	0.0021	-0.0007
flu2	-0.0015	-0.0030	0.0016	-0.0035	0.0000
flu3	-0.0069	-0.0133	0.0065	-0.0075	-2.4929
flu4	-0.0246	-0.0346	-0.0271	-0.0102	-0.0068
sci2	0.0456	0.0756	0.0054	0.0603	0.0198
sci3	0.0219	0.0385	-0.0048	0.0371	0.0092
birks	-0.0181	-0.0291	-0.0054	-0.0231	-0.0080
tsm	0.0041	0.0099	-0.0129	0.0128	0.0044
scatba	-0.0007	-0.0015	0.0009	0.0000	-0.0009
tau2	0.0004	0.0001	0.0024	0.0024	0.0013
tau3	0.0005	0.0002	0.0022	-0.0001	-0.0002

Table 4.13: *Correlated shape error contributions by source for events passing the ν_μ CCQE selection cuts, for unit-area normalized kinematic distributions of interest.*

	E_ν^{QE}	E_μ	Q^2	$cos(\theta_\mu)$	E_ν^{MC}
π^+ flux $\delta(O)$	0.0082	0.0043	0.0024	0.0120	0.0085
π^+ flux $\Delta N(O)$	0.0310	0.0153	0.0085	0.0374	0.0317
σ_ν $\delta(O)$	0.0143	0.0143	0.0110	0.0111	0.0152
σ_ν $\Delta N(O)$	0.0552	0.0507	0.0300	0.0425	0.0571
detector response $\delta(O)$	0.0100	0.0103	0.0090	0.0136	0.0088
detector response $\Delta N(O)$	0.0403	0.0393	0.0299	0.0542	0.0351
total $\delta(O)$	0.0193	0.0181	0.0144	0.0213	0.0195
total $\Delta N(O)$	0.0750	0.0660	0.0432	0.0784	0.0741

inition, affect only the shape of a Monte Carlo predicted distribution, and not the normalization. To calculate the error matrix for relatively normalized Monte Carlo, the "unisim" Monte Carlo sets are first normalized to have the same total number of events as the central value Monte Carlo, via

$$(N'(O)_j)_i \;=\; \frac{\sum_i (N(O)_0)_i}{\sum_i (N(O)_j)_i} (N(O)_j)_i \tag{4.21}$$

where $(N(O)_j)_i$ is the absolutely normalized number of events in bin i of the output variable distribution O for "unisim" j, and $(N(O)_0)_i$ is the number of events in bin i of the central value Monte Carlo distribution. The relatively normalized first derivative matrix is subsequently calculated from the difference between the relatively normalized "unisim" and the central value Monte Carlo in each bin:

$$\mathcal{F}'(O)_{i,j} \;=\; \frac{(N(O)_0 - N'(O)_j)_i}{C_j - U_j} \tag{4.22}$$

similarly to the absolutely normalized case in equation 4.14. The effect of a relatively normalized "unisim" is to change the shape of a distribution with respect to

the central value Monte Carlo prediction. The fractional changes in the means of various kinematic distributions of interest are summarized for the π^+ flux, neutrino interaction cross section, and detector response uncertainties in tables 4.10, 4.11, and 4.12 respectively.

The simulation input parameter errors are propagated to the relatively normalized output variable error matrix as in equation 4.15, via

$$\mathcal{M}'(O)_{m,n} \;=\; \mathcal{F}'(O)^{T}_{m,j}\;\mathcal{P}_{j,k}\;\mathcal{F}'(O)_{n,k}. \tag{4.23}$$

The relatively normalized error matrices $\mathcal{M}'(O)_{\Phi}$, $\mathcal{M}'(O)_{\sigma}$, and $\mathcal{M}(O)'_{detector}$ are calculated separately for each of the sources of uncertainty, then are added together to construct the total relatively normalized error matrix $\mathcal{M}'(O)_{total}$. The square root of the diagonal elements of the relatively normalized total error matrix $\mathcal{M}'(O)_{total}$ are shown for the reconstructed kinematic distributions $cos(\theta_{\mu})$, E_{μ}, E_{ν}^{QE}, and Q^2, in figure 4.19, with the data superimposed. The contribution to the fractional relatively normalized error from each source is shown in figure 4.20. The two error estimators, $\delta(O)$ and $\Delta_N(O)$, are summarized for the relatively normalized distributions of each uncertainty source in table 4.13. In general, the relatively normalized errors on the output variable distributions are much smaller than the absolutely normalized errors, and the three sources of uncertainty contribute in roughly equal proportions. Given these errors, data and Monte Carlo disagree in shape at the 1-2σ level in the lowest Q^2 and highest $cos(\theta_{\mu})$ bins; everywhere else, they agree very well.

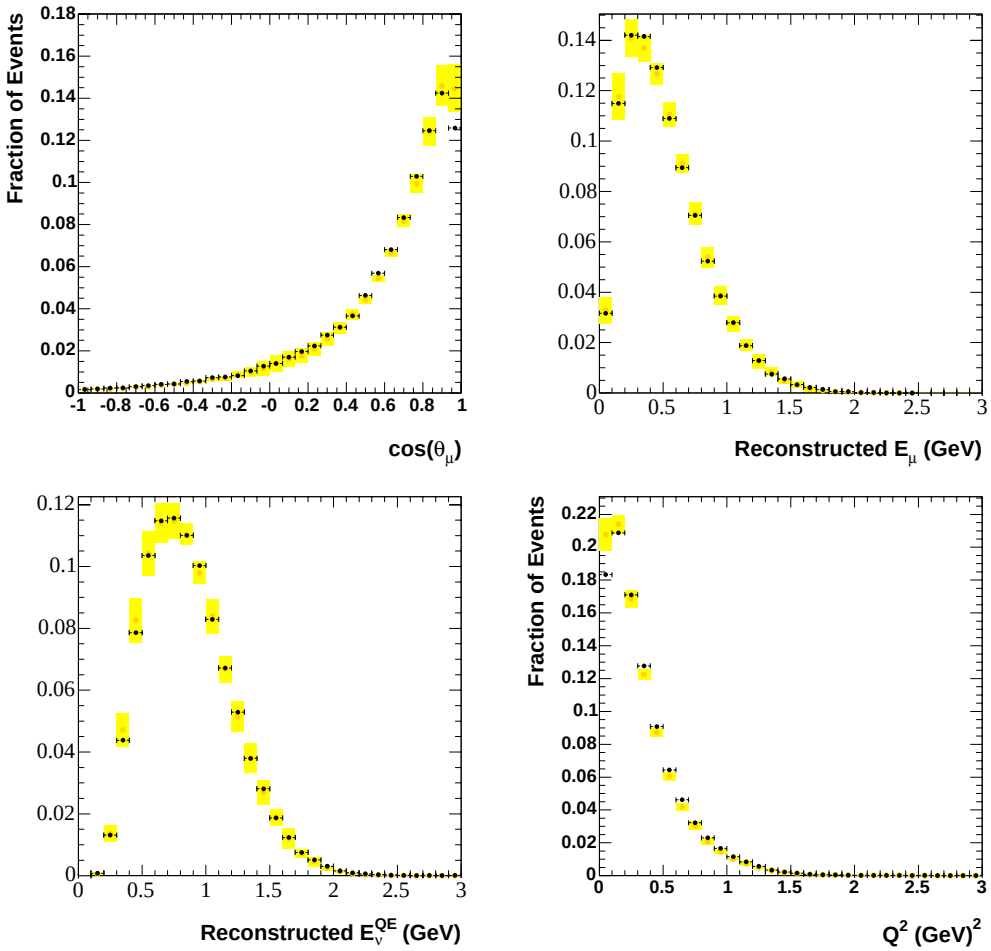

Figure 4.19: *Uncertainty on the Monte Carlo prediction for the fraction of events after the ν_μ CCQE selection cuts, normalized to unit-area, from the π^+ flux simulation and the neutrino interaction cross section simulation. Top left: reconstructed track direction cosine with respect to the beam direction; top right: reconstructed energy under a muon hypothesis (GeV); bottom left: reconstructed neutrino energy assuming 2-body kinematics (GeV); bottom right: reconstructed four-momentum transfer squared (GeV^2). The data (black points) with statistical errors is superimposed.*

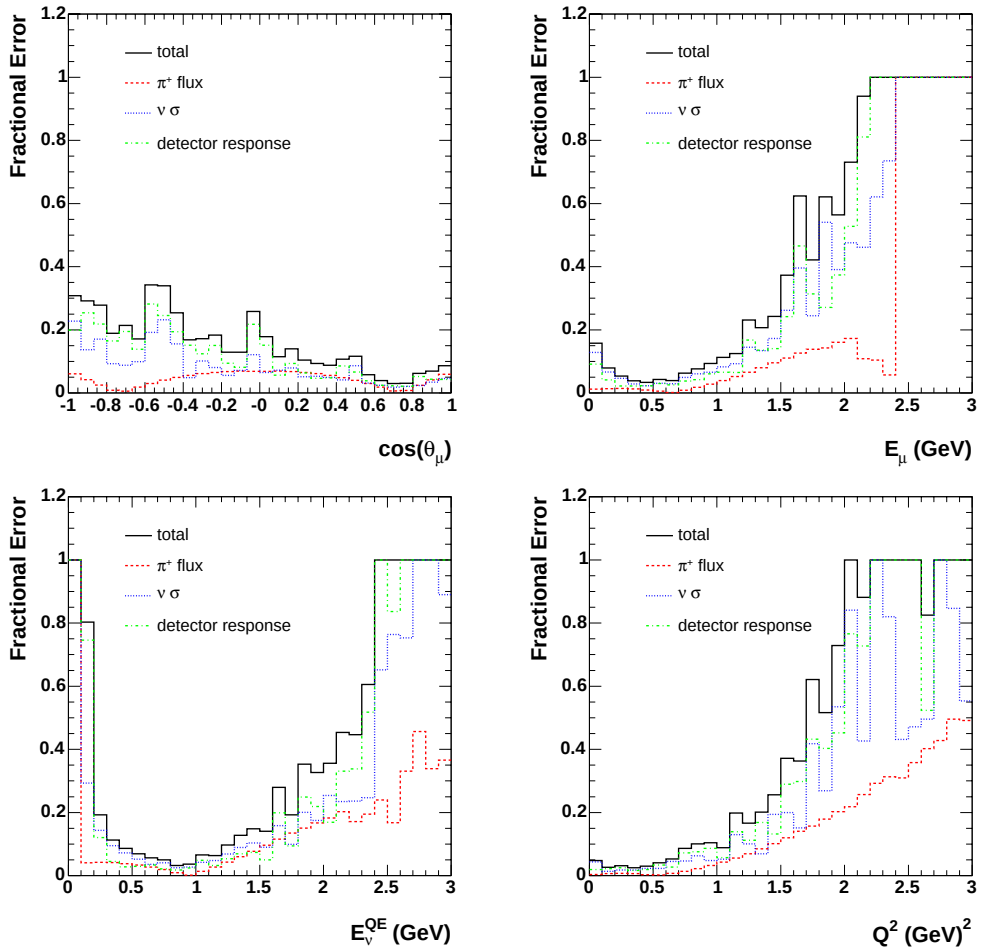

Figure 4.20: *Contribution to the fractional error on the Monte Carlo prediction for the fraction of events after the ν_μ CCQE selection cuts, normalized to unit-area, from the π^+ flux simulation and the neutrino interaction cross section simulation. Top left: reconstructed track direction cosine with respect to the beam direction; top right: reconstructed energy under a muon hypothesis (GeV); bottom left: reconstructed neutrino energy assuming 2-body kinematics (GeV); bottom right: reconstructed four-momentum transfer squared (GeV^2).*

Chapter 5

Constraining the Flux Predictions with ν_μ Data

The high statistics ν_μ data set at MiniBooNE affords important constraints on the neutrino flux prediction. The measured ν_μ spectrum is used to constrain the predicted rate and energy distribution of ν_e events from μ^+ decay, and ν_μ events from π^+ decay, in the MiniBooNE beam line. For the ν_e appearance analysis, μ^+-decay ν_e events comprise $\sim$1/2 of the intrinsic beam ν_e background, and therefore the uncertainty on the prediction of this background source is an important factor in the oscillation sensitivity of MiniBooNE. Nearly all of the ν_e from μ^+ decay come from the production chain $p\ Be \rightarrow \pi^+ X$, $\pi^+ \rightarrow \mu^+ \nu_\mu$, $\mu^+ \rightarrow e^+ \nu_e\ \overline{\nu}_\mu$. Therefore, the uncertainty on the prediction of the μ^+-decay ν_e flux comes primarily from the π^+ production cross section. Fortunately, since the μ^+ come from $\pi^+ \rightarrow \mu^+ \nu_\mu$ decay, the MiniBooNE ν_μ data provide a strong constraint on the π^+ spectrum and therefore also on the μ^+-decay ν_e. The MiniBooNE ν_μ CCQE data set described in chapter 4 is employed for this analysis; it comprises $\sim$100,000 events after cuts, with a ν_μ CCQE purity of $\sim$92%.

5.1 Method

The μ^+-decay ν_e analysis uses the measured ratio of data to Monte Carlo ν_μ events, after the ν_μ CCQE selection cuts, to adjust the Monte Carlo predicted spectrum such that the ν_μ agree in data and Monte Carlo. The reweighting function is

$$\mathcal{R} \;=\; \frac{N_{DATA}^{after\ CCQE\ cuts}(E_\nu^{QE})}{N_{MC}^{after\ CCQE\ cuts}(E_\nu^{QE})} \tag{5.1}$$

which can be written in terms of the constituent factors

$$\mathcal{R} \;=\; \frac{\Phi_{Data}(E_\nu) \times \sigma^{CCQE}(E_\nu) \times \epsilon^{CCQE\ cuts}(E_\nu) \times \mathcal{M}(E_\nu|E_\nu^{QE}) \times N_{targets} \times N_{p.o.t.}}{\Phi_{MC}(E_\nu) \times \sigma^{CCQE}(E_\nu) \times \epsilon^{CCQE\ cuts}(E_\nu) \times \mathcal{M}(E_\nu|E_\nu^{QE}) \times N_{targets} \times N_{p.o.t.}}$$

where Φ is the neutrino flux in units of $(\nu/cm^2/proton)$, σ is the ν_μ CCQE cross section in units of cm^2, ϵ is the efficiency of the CCQE selection cuts, $\mathcal{M}$ is a smearing matrix that relates the "true" neutrino energy E_ν to the reconstructed energy E_ν^{QE}, $N_{targets}$ is the number of target nucleons, and $N_{p.o.t.}$ is the number of incident protons on target. The ansatz of the analysis is that all predictions of the Monte Carlo are correct, meaning identical to the data, except for the flux, and therefore the reweighting function in equation 5.1 reduces to

$$\mathcal{R} \;=\; \frac{\Phi_{Data}(E_\nu)}{\Phi_{MC}(E_\nu)}. \tag{5.2}$$

The uncertainty on the reweighting function is assessed by propagating the uncertainties on the Monte Carlo assumptions.

The measured ν_μ flux can be used to infer the π^+ energy distribution because of the strong correlation between the "parent" π^+ and the "daughter" ν_μ in the MiniBooNE neutrino beam. This is the case because the MiniBooNE detector subtends a very small angle, 11 mr, when viewed from the target, and since the angular divergence of the pion beam is limited by the 90 cm radius of the decay pipe to be small. Therefore, any π^+ that decays to a ν_μ which passes through the detector oil must

have very little angle with respect to the beam direction at its decay vertex. In a two body decay, the ν_μ energy is related to the π^+ energy via

$$E_\nu^{LAB} \;=\; \gamma E_\nu^{CM}(1+\beta\ cos\theta) \tag{5.3}$$

where $\gamma \;=\; E_\pi^{LAB}/m_\pi$, $\beta \;=\; p_\pi^{LAB}/E_\pi^{LAB}$, θ is the angle between the π^+ and the ν_μ, and $E_\nu^{CM} \;=\; (m_\pi^2 - m_\mu^2)/(2m_\pi)$. Therefore,

$$E_\nu^{LAB} \;=\; E_\pi^{LAB} \times 0.215 \times (1+\beta\ cos\theta).$$

If one assumes that the π^+ is relativistic, and pointed straight at the detector at its decay vertex, and that the decay angle of the π^+ with respect to the beam direction is zero, then the ν_μ energy in the lab frame is related to the π^+ energy by a constant:

$$E_\nu^{LAB} \;=\; 0.43 \times E_\pi^{LAB}. \tag{5.4}$$

In this analysis the particle kinematics from the Monte Carlo are used, with no assumptions about divergence, etc. as in the formula above, however, the simple relation in equation 5.4 is a fairly good description. The correlation in the MiniBooNE beam Monte Carlo between the π^+ and ν_μ energies is shown in figure 5.1, with a line of slope 0.43 superimposed. The majority of π^+-decay ν_μ events exhibit the maximum possible correlation, and as a result, the measured ν_μ spectrum can be used to infer the π^+ spectrum with good resolution.

The MiniBooNE beam Monte Carlo allows one to track the entire history of each neutrino, and therefore on an event-by-event basis one can reweight a ν_μ, its parent π^+, the π^+-decay μ^+, and the subsequent μ^+-decay ν_e, all with the same weight. The relation between the energy of a π^+ and its subsequent μ^+-decay ν_e is shown in the right panel of figure 5.1. This distribution is not cross section weighted, however, after weighting by the ν_e CCQE cross section, the mean energy of μ^+-decay ν_e is $\sim$

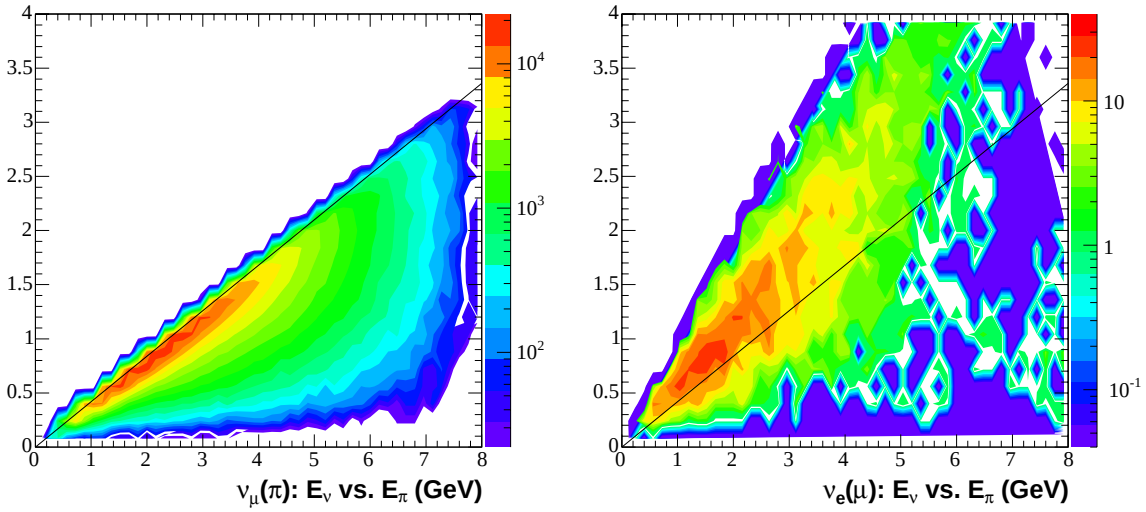

Figure 5.1: *Left: E_ν (GeV) vs. E_π (GeV) for ν_μ from π^+ decay, in the MiniBooNE detector acceptance. Reft: E_ν (GeV) vs. E_π (GeV) for ν_e from μ^+ from π^+ decay, in the MiniBooNE detector acceptance. A line with slope 0.43 is super-imposed to indicate the maximum available energy to the ν_μ in a 2 body π^+ decay.*

0.6 GeV. From the right panel of figure 5.1, for E_{ν_e} ∼0.6 GeV, E_π ∼1.5 GeV, with a distribution that is tightly peaked about the mean.

This flux constraint analysis does two useful things: first, it fixes the normalization and energy distribution of the μ^+-decay ν_e to be consistent with the observed ν_μ data; second, it reduces the flux uncertainty on μ^+-decay ν_e to be of the order of the statistical error on the measured ν_μ energy spectrum. The error reduction occurs because uncertainties in the π^+ production prediction affect all π^+-decay particles identically. Therefore, using this method, the uncertainty on the μ^+-decay ν_e is given by the *relative* uncertainty with respect to the π^+-decay ν_μ, rather than the *absolute* π^+ prediction uncertainty. The relative uncertainty is of the order of the fluctuations in the reweighting function, which are mostly due to statistical error on the measured ν_μ. This argument about error reduction is valid in general for any source of uncertainty that affects the π^+-decay ν_μ and μ^+-decay ν_e in the same way.

In practice, the reduction in error is calculated by replacing the denominator in equation 5.2 with "fake data" (central value Monte Carlo), and the numerator with "unisim" Monte Carlo, via

$$\mathcal{R} \;=\; \frac{N_{CVMC}^{after\ CCQE\ cuts}(E_\nu^{QE})}{N_{\text{“}unisim''\ MC}^{after\ CCQE\ cuts}(E_\nu^{QE})}. \tag{5.5}$$

The function $R_j(E_\nu^{QE})$ depends on "unisim" j, and is a function of reconstructed neutrino energy E_ν^{QE}. The "unisim" Monte Carlo is then modified by reweighting to match the central value Monte Carlo using $R_j(E_\nu^{QE})$ as the reweighting function, and the set of modified "unisims" are used to calculate the error matrix for the μ^+-decay ν_e, as described in chapter 4.

This procedure is illustrated with "fake data" in figures 5.2 and 5.3 for the Sanford-Wang π^+ prediction "unisims" and the central value Monte Carlo. The left panel of figure 5.2 shows the reconstructed energy distributions in "unisim" and central value Monte Carlo for events passing the ν_μ CCQE selection cuts. Each π^+-decay ν_μ event from "unisim" j is assigned a weight based on its reconstructed E_ν^{QE}, given the reweighting function $R_j(E_\nu^{QE})$. The reweighting function is binned in 0.1 GeV-wide reconstructed neutrino energy bins, and all events in a given E_ν^{QE} bin are assigned the same weight. This weight applies to the ν_μ-parent π^+ and all of the π^+ descendents. The right panel shows the "unisim" distributions that have been modified by the $\mathcal{R}$ reweighting for only ν_μ from π^+ decay, where the π^+ was produced in the primary $p\ Be \rightarrow \pi^+\ X$ interaction, compared with the central value Monte Carlo for all events passing the ν_μ CCQE selection cuts. The normalization difference between the central value Monte Carlo and the set of modified "unisims" is due to the $\sim$8% of ν_μ produced by secondary interactions, discussed in chapter 4 and summarized in table 4.4. The corresponding distributions for the ν_μ "parent" (and ν_e "grandparent") π^+ in Monte Carlo are shown in the top panels of figure 5.3. The generated energy distributions of the μ^+ "sister" and ν_e "niece" to the ν_μ are

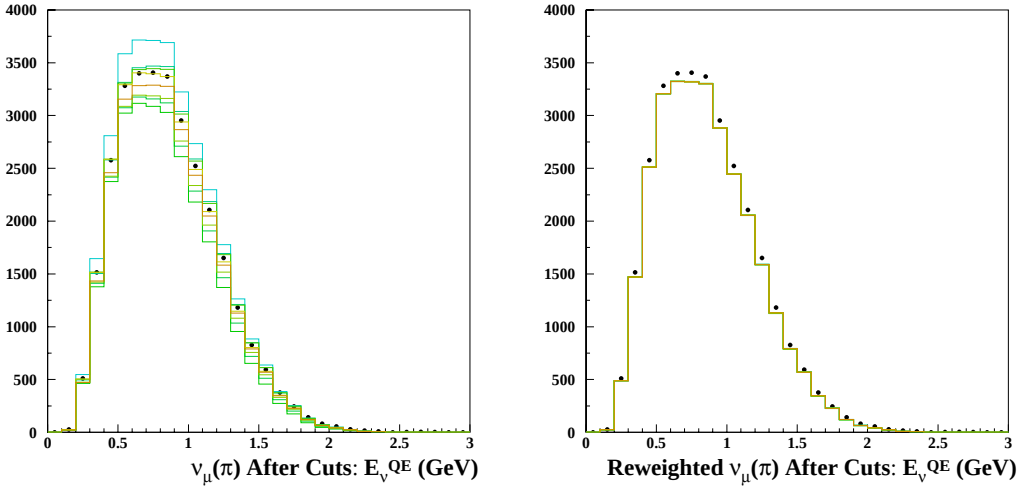

Figure 5.2: *Left: number of events vs. reconstructed neutrino energy (GeV) for events passing the ν_μ CCQE selection cuts. Right: reweighted number of events vs. reconstructed neutrino energy (GeV) for events passing the ν_μ CCQE selection cuts. Central value Monte Carlo is indicated by the points, Sanford-Wang π^+ prediction "unisim" Monte Carlo is shown by the lines.*

shown before and after the reweighting modification in the middle and bottom panels of figure 5.3 respectively.

By construction, the reweighting modification works perfectly for the E_ν^{QE} distribution for π^+-decay ν_μ events, that is, the spread in the "unisims" is zero after reweighting. The finite π^+ energy resolution can be seen by the fact that the reweighting works well but not perfectly for the π^+, and therefore the μ^+ and ν_e distributions. The resolution degrades with increasing π^+ energy because the E_{ν_μ}-E_π correlation decreases, as can be seen in the left panel of figure 5.1. As the π^+ energy increases, π^+ with angles relative to the beam axis greater than zero at decay can still produce a ν_μ in the detector acceptance due to the greater available Lorentz boost, and therefore a larger range of ν_μ energies is allowed for a given π^+ energy.

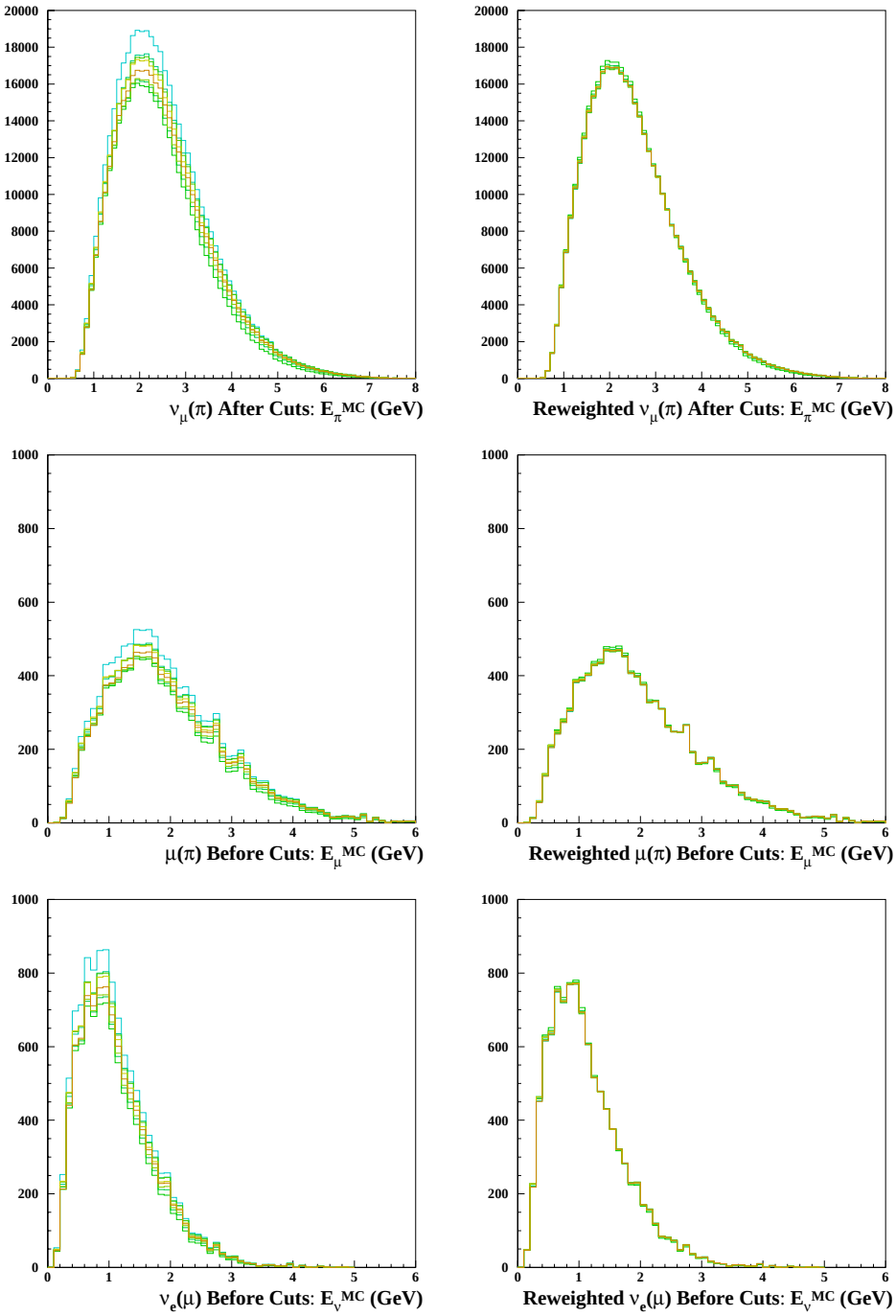

Figure 5.3: *Left: generated Monte Carlo energy distributions. Right: reweighted Monte Carlo energy distributions. Top: number of events vs. π^+ energy (GeV). Middle: number of events vs. μ^+ energy (GeV). Bottom: number of events vs. ν_e energy (GeV).*

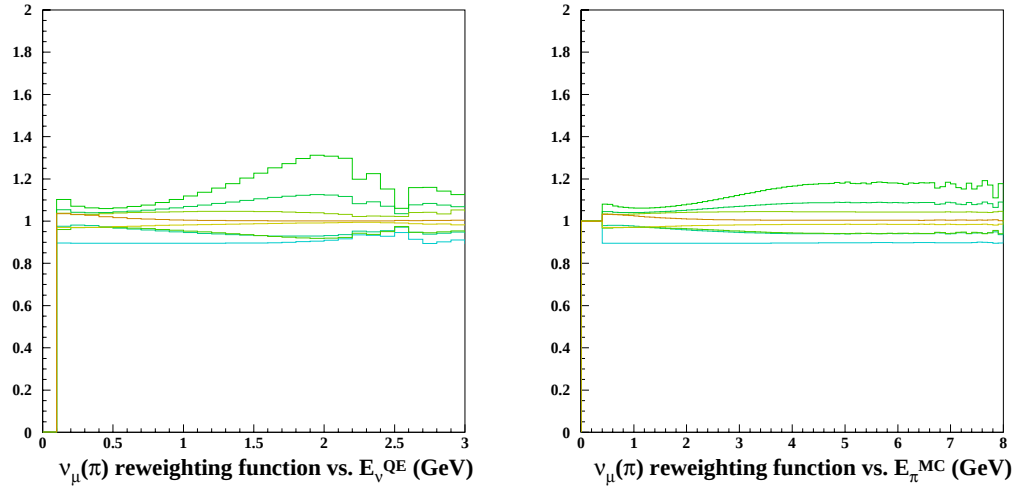

Figure 5.4: *Ratio of Sanford-Wang π^+ prediction "unisims" to central value Monte Carlo for events passing the ν_μ CCQE selection cuts. Left: reweighting functions vs. reconstructed ν_μ energy (GeV). Right: reweighting functions vs. generated π^+ energy (GeV).*

The reweighting function in equation 5.2 is calculated using events passing the ν_μ CCQE selection cuts because good neutrino energy measurement resolution is desired. However, the efficiency of the selection cuts is not very high, and while generating a large Monte Carlo set of π^+-decay ν_μ is easy, obtaining high statistics for μ^+-decay ν_e is not. This is because the μ^+ decays have 3-body kinematics and therefore the probability that the ν_e is not pointed at the detector, which subtends only 11 mr at the MiniBooNE target, is much larger than for the ν_μ products of 2-body π^+ decays. Therefore, to increase the statistics of μ^+-decay ν_e events, the reweighting procedure is done in two steps, taking advantage of the fact that in Monte Carlo one knows both the reconstructed E_ν and generated E_π for every π^+-decay ν_μ event. First, the ratio of data to Monte Carlo, $\mathcal{R}_1$, is formed as a function of reconstructed E_ν^{QE}, for events passing the ν_μ CCQE selection cuts. $\mathcal{R}_1(E_\nu^{QE})$ is shown in the left panel of figure 5.4 for the Sanford-Wang π^+ "unisims". $\mathcal{R}_1(E_\nu^{QE})$ is used event-by-event to reweight

the generated E_π^{MC} distribution for events passing the ν_μ CCQE selection cuts. A second ratio $\mathcal{R}_2$ is formed, which is the ratio of the reweighted to the original E_π^{MC} distributions, for events passing the ν_μ CCQE selection cuts. $\mathcal{R}_2(E_\pi^{MC})$ is shown in the right panel of figure 5.4. $\mathcal{R}_2(E_\pi^{MC})$ is then used as a look-up table to find the weight for any ν_μ event with a π^+ parent, or ν_e event with a π^+ grandparent, whether the neutrino passes the ν_μ CCQE selection cuts or not. This works because the ν_μ CCQE selection cuts do not change the energy of a given π^+, which is all that R_2 depends on. In this way, one can use all of the Monte Carlo π^+ events to form the associated μ^+-decay ν_e distributions, both before and after reweighting, instead of only those with an associated ν_μ that passes the ν_μ CCQE selection cuts. The transformation from $\mathcal{R}_1$, which is a function of reconstructed E_ν^{QE}, to $\mathcal{R}_2$, which is a function of generated E_π^{MC}, is necessary because not every event has a reasonable E_ν^{QE} value. Only cleanly-reconstructed ν_μ CCQE events can be expected to have E_ν^{QE} values near the true E_ν^{MC}, however, all π^+-decay Monte Carlo events have the correct E_π^{MC} value. This two-step procedure was used to produce all of the reweighted distributions in figures 5.2 through 5.4. This method passes the closure test, which is that all of the reweighted "unisim" E_ν^{QE} distributions agree perfectly with the "fake data" π^+-decay ν_μ spectrum, as is shown in the right panel of figure 5.2.

To achieve the simulation statistics for μ^+-decay ν_e shown in figure 5.4, two enhancement schemes are employed in the MiniBooNE beam Monte Carlo [118]. First, the $p\ Be \rightarrow \pi^+\ X$ cross section is weighted according to an exponential function to increase the statistics for high p_Z events. The primary motivation for this is to decrease the statistical error on the prediction of the high energy ν_μ flux. Second, and more importantly for this analysis, every time a π^+ decays, 20 identical copies of the resulting μ^+ are produced and subsequently tracked through the beam Monte Carlo. A new random number seed is chosen each time a muon decays, and therefore

the 20 resulting μ^+-decay ν_e are independent. Both of these techniques contribute to the weight for each μ^+-decay ν_e event; the distribution of weights has a mean of 0.00637 and an r.m.s of 0.00864. The resulting beam Monte Carlo histogram for the predicted flux of neutrinos from $p\ Be \rightarrow \pi^+ \rightarrow \mu^+ \rightarrow e^+\ \nu_e\ \overline{\nu}_\mu$ has 6.5×10^6 entries, and the statistical error on the flux prediction is <1% in each E_ν^{MC} bin.

However, many fewer events are sampled from this distribution when neutrino interactions are simulated. This is because the Monte Carlo is generated with all components of the flux in their weighted proportions, shown in figure 3.14 and table 3.7. The total neutrino interaction Monte Carlo set, before any selection cuts, comprises 8×10^6 events, which is 5×10^6 events in the detector volume, and corresponds to 2.2×10^{21} simulated protons on target. The vast majority of these events are π^+-decay ν_μ interactions, with only 12,658 from μ^+-decay ν_e interactions. These 12,658 events comprise the Monte Carlo μ^+-decay ν_e sample used for this analysis.

5.2 Results

The reweighting method described above may change the shape, normalization, and uncertainty on the predicted μ^+-decay ν_e distribution. To separate these different effects, the μ^+-decay ν_e error matrix is calculated in bins of E_ν^{MC} for three cases:

1. with no reweighting modification (the reweighting function is taken to be 1.0 in all energy bins), so the error matrix comes directly from the Sanford-Wang π^+ production cross section parameter errors with no reference to the data;

2. with reweighting modifications, where the numerator of the reweighting function is "fake data" (central value Monte Carlo), so this tests the effect of the reweighting method on the uncertainties only;

3. with reweighting modifications, where the numerator of the reweighting function is the ν_μ CCQE data set described in chapter 4.

The reweighting procedure is applied to the central value Monte Carlo, and to each of the Sanford-Wang π^+ flux "unisims" described in chapter 4, section 4.3. The "unisims", which have been modified by $\mathcal{R}$ in equation 5.5, are used to calculate the first derivative matrices and propagate the simulation input parameter errors, as described in chapter 4, to the uncertainties on the predicted E_ν^{MC} distribution for μ^+-decay ν_e and π^+-decay ν_μ events, with no selection cuts applied. The ratio of the modified "unisims" to the original central value Monte Carlo for each of the three cases is shown as a function of E_ν^{MC} in figure 5.5. For case 1, with no reweighting, the spread in the (modified "unisim" / original central value) ratios is $\sim$10% about a value of 1.0 at $E_\nu = 1\ GeV$ for both μ^+-decay ν_e and π^+-decay ν_μ. For case 2, where the "unisims" have been modified via reweighting to match the "fake data," the spread is $\sim$2% about 1.0 at $E_\nu = 1\ GeV$. This reduction in the spread of the ratios translates directly into a reduction in the predicted uncertainty on the E_ν^{MC} distribution. For case 3, the spread in the ratios is nearly identical to case 2, as expected, however, the value of the ratio is $\sim$1.3 at $E_\nu = 1\ GeV$. The 20% increase in the ratio in the 0.1 to 0.2 GeV bin relative to its value above 0.2 GeV is an artifact of low statistics; the statistical error on the data to Monte Carlo ratio in this bin, shown in figure 4.12, is $\sim$30%. The value of the ratio in case 3 is the same normalization difference between the ν_μ CCQE data set and the predicted Monte Carlo spectrum which was first discussed in chapter 4, section 4.2. In this way, the case 3 reweighting procedure ties the normalization and energy spectrum of the π^+-decay ν_μ and μ^+-decay ν_e spectra to the observed rate in the data.

These modified "unisims" are used to propagate the simulation input parameter uncertainties to the E_ν^{MC} distribution for μ^+-decay ν_e events. For case 1, the scaled

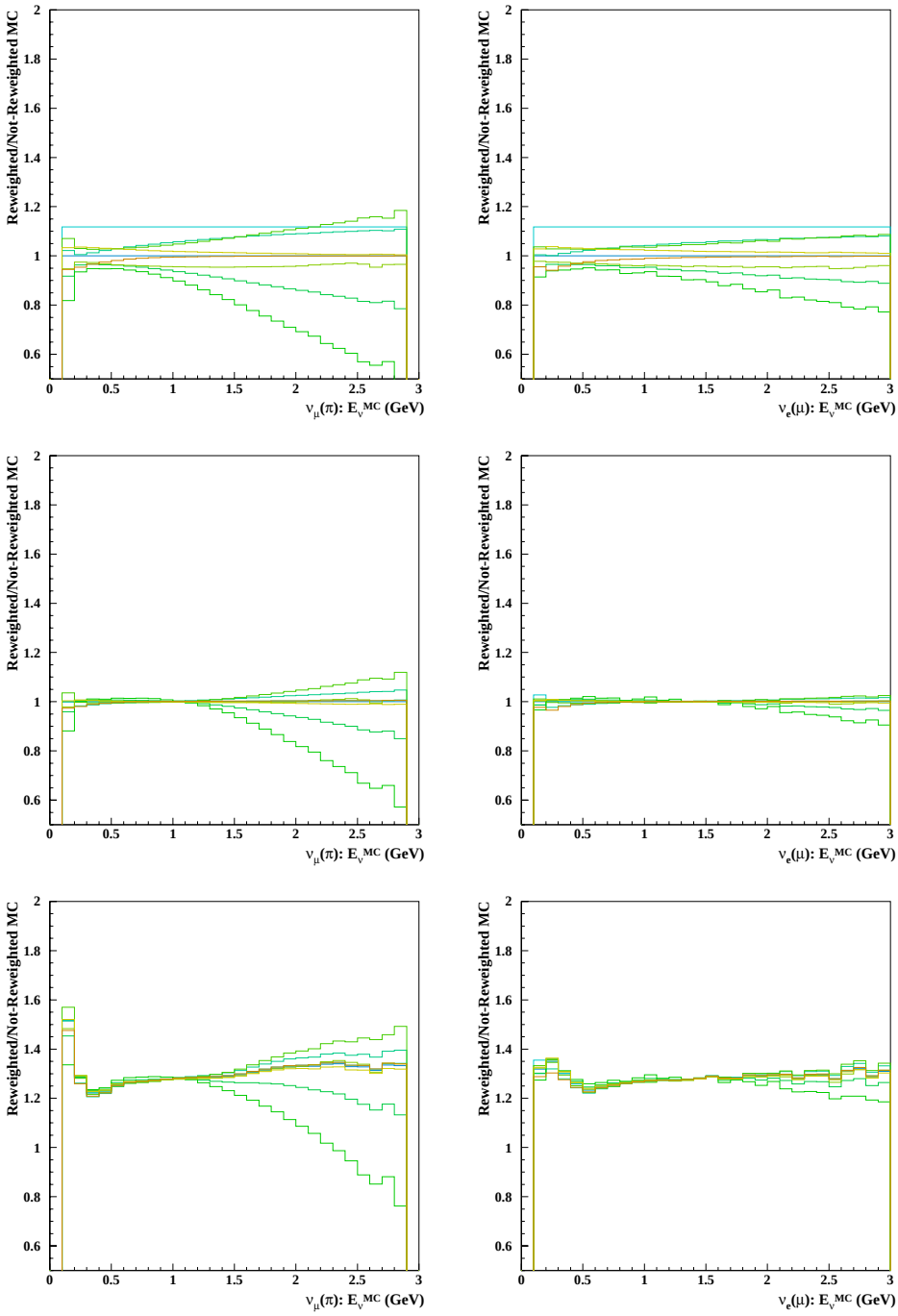

Figure 5.5: *Ratio of Sanford-Wang π^+ prediction "unisims" to original central value Monte Carlo vs. E_ν^{MC} (GeV), with no selection cuts applied. Left: predicted π^+-decay ν_μ energy spectra. Right: predicted μ^+-decay ν_e energy spectra.*

first derivatives are shown as a function of generated neutrino energy E_ν^{MC} for each of the eight Sanford-Wang π^+ flux prediction parameter variations in the top eight panels of figure 5.6. The scaled first derivatives are defined in chapter 4, equation 4.16; they describe the fractional change in the number of events in a given bin with respect to a 1σ change in a simulation input parameter. The values of the scaled first derivatives are typically fairly small, and the errors on the scaled first derivatives are relatively large. In many bins the fractional error is greater than 100%. The error on the first derivatives does not enter into the error matrix calculation, however, statistical fluctuations on the first derivatives can increase (or decrease) particular elements of the error matrix.

To address the issue of statistical fluctuations, the μ^+-decay ν_e scaled first derivative histograms are fit with a polynomial function $f(E_\nu) = a_1 + a_2 \cdot E_\nu^{MC} + a_3 \cdot (E_\nu^{MC})^2$, shown superimposed on the scaled first derivatives in the top eight panels of figure 5.6. Fitting the first derivatives to a function, and using that function value in place of the first derivative in the error matrix calculation, does not on average change the total error on the number of events, but serves to smooth statistical fluctuations on a given element of the error matrix. In general, a polynomial function is a good fit to the scaled first derivatives vs. E_ν^{MC}; the χ^2/ndf values of the fit are all much less than 1.0 because of the large statistical errors on central value Monte Carlo prediction [1]. The second degree polynomial fit, which is superimposed on the un-fit derivatives, results in much smaller errors on the scaled first derivatives, shown in figure 5.6. The fit error bars are calculated from the fit covariance matrix, and by construction the fit error bars change smoothly as a function of E_ν. The fit coefficients for the μ^+-decay ν_e case 3 scaled first derivatives are summarized for each

[1] The statistical errors on the scaled first derivatives effectively come only from the central value Monte Carlo statistics, since the "unisims" are all produced by reweighting central value Monte Carlo, and the variance of the weights in any E_ν^{MC} bin is less than 1.0.

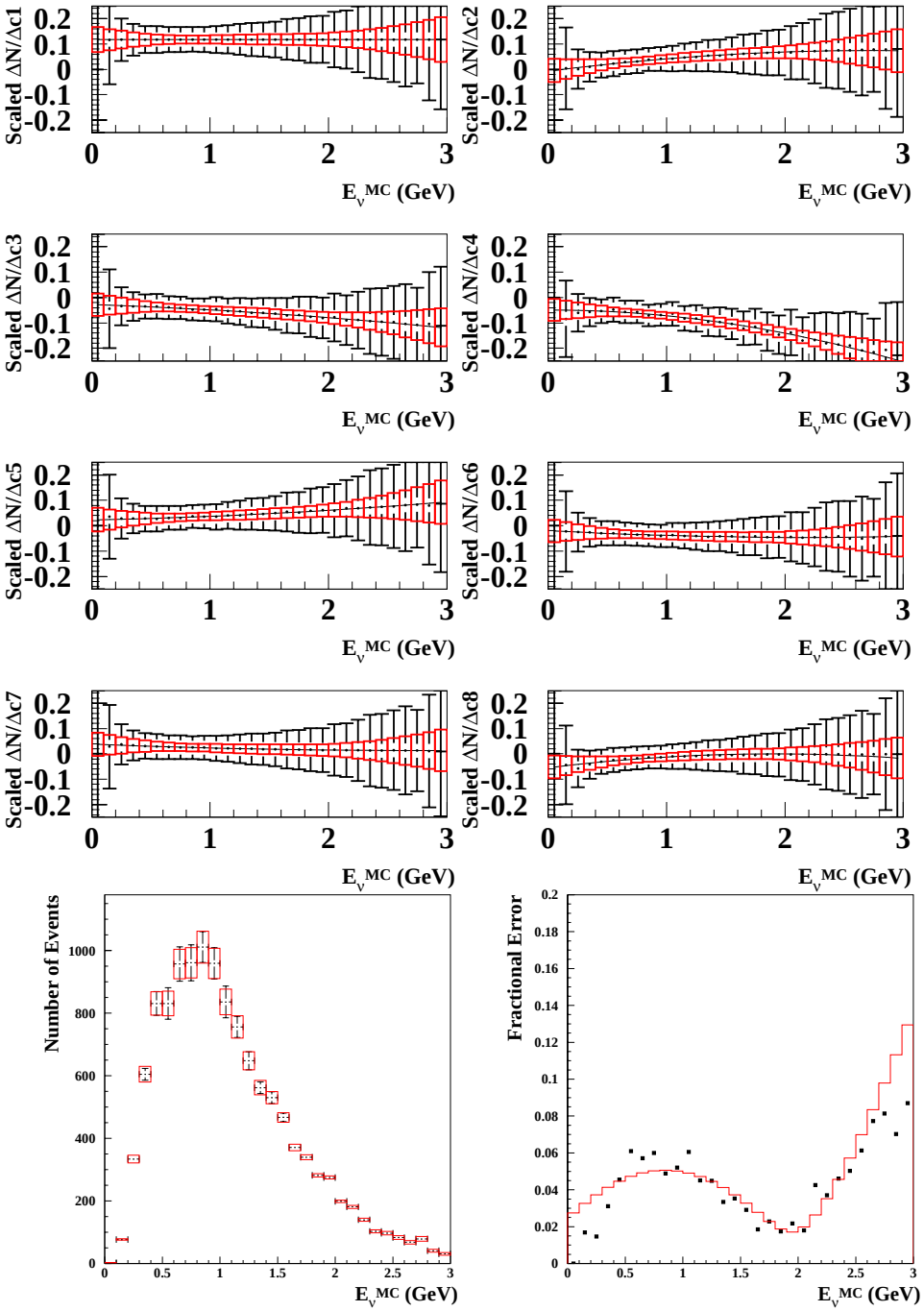

Figure 5.6: *Error on μ^+-decay ν_e E_ν^{MC} spectrum from Sanford-Wang π^+ prediction uncertainties. Top eight panels: scaled first derivatives (defined in equation 4.16) vs. E_ν^{MC}. Bottom left: predicted number of events vs. E_ν^{MC} (GeV) with π^+ prediction systematic errors for 2.2 $\times 10^{21}$ protons on target. Bottom right: fractional error vs. E_ν^{MC} (GeV). Red solid lines (black points) show the (un-) fit error calculation.*

"unisim" in table 5.3.

The fit scaled first derivatives are used to calculate the output variable error matrix $\mathcal{M}$ in bins of E_ν^{MC}. The square roots of the diagonal elements of $\mathcal{M}$ are shown as the error bars on the central value Monte Carlo predicted E_ν^{MC} distribution for μ^+-decay ν_e events in the bottom left panel of figure 5.6. The fractional error as a function of E_ν^{MC} is shown in the bottom right panel of figure 5.6. For comparison, the error bars and fractional error vs. E_ν^{MC} calculated without fitting the scaled first derivatives are also shown. The error bars produced with fitting can be either larger or smaller than those calculated without fitting the scaled first derivatives, however, the fitted fractional errors show a much smoother dependence on E_ν^{MC}.

For case 2, the scaled first derivatives are shown as a function of generated neutrino energy E_ν^{MC} for each of the eight Sanford-Wang π^+ flux prediction parameter variations in the top eight panels of figure 5.7. In this case the scaled first derivatives are all close to zero because of the "unisims" have been modified by the ("fake data"/"unisim") reweighting function. The modified "unisims" are propagated to the error matrix in bins of E_ν^{MC}, and the square roots of the diagonal elements of $\mathcal{M}$ are shown as the error bars on the central value Monte Carlo predicted E_ν^{MC} distribution for μ^+-decay ν_e events in the bottom left panel of figure 5.7. The fractional error as a function of E_ν^{MC} is shown in the bottom right panel of figure 5.7. Between $\sim$0.2 and 2 GeV, the error bars are smaller in all E_ν^{MC} bins than in case 1, where the "unisims" were not reweighted to match the central value Monte Carlo. The energy range where the errors can be reduced using this method is not unlimited because the reweighting modification is only effective where the ν_μ CCQE data set has reasonable statistics; above 2 GeV and below 0.2 GeV the selection cut efficiencies are very low, as is shown in figure 4.7.

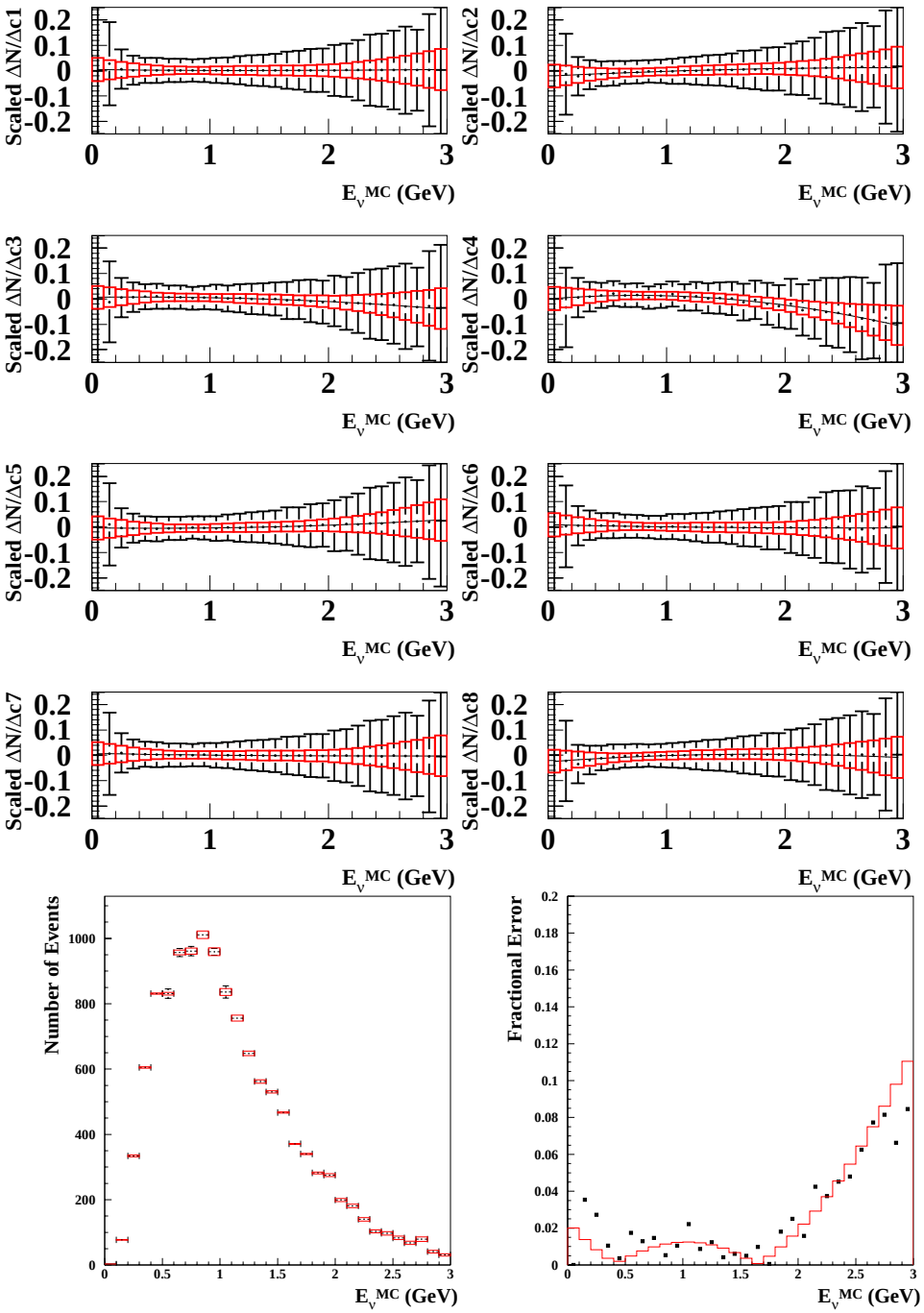

Figure 5.7: *Error on μ^+-decay ν_e E_ν^{MC} spectrum from "fake data"-reweighted Sanford - Wang π^+ prediction uncertainties. Top eight panels: scaled first derivatives (defined in equation 4.16) vs. E_ν^{MC}. Bottom left: predicted number of events vs. E_ν^{MC} (GeV) with π^+ prediction systematic errors for 2.2 $\times 10^{21}$ protons on target. Bottom right: fractional error vs. E_ν^{MC} (GeV). Red solid lines (black points) show the (un-) fit error calculation.*

Table 5.1: *Summary of number of and uncertainty on μ^+-decay ν_e in the detector acceptance for the three reweighting scenarios described in the text. The Monte Carlo set corresponds to 2.2×10^{21} simulated protons on target.*

Reweighting Ratio	$N\ \nu_e(\mu^+)$	ΔN *(un-)fit value (%)*	δN *(un-)fit value (%)*
1.0	12,658	(4.455) 4.383	(1.158) 1.079
"fake data" / "unisim"	12,658	(1.438) 1.166	(0.320) 0.252
data / "unisim"	16,095	(1.595) 1.167	(0.353) 0.251

For case 3, the scaled first derivatives are shown as a function of generated neutrino energy E_ν^{MC} for each of the eight Sanford-Wang π^+ flux prediction parameter variations in the top eight panels of figure 5.8. As in case 2, the scaled first derivatives are all close to zero because of the reweighting procedure, but the total number of events is increased by a factor of ∼1.3, as can be seen by comparing the vertical scale of the predicted number of events vs. E_ν^{MC} in the bottom left panel of figure 5.8 with that of figure 5.7. The fractional error as a function of E_ν^{MC} is shown in the bottom right panel of figure 5.8, and is nearly identical to the case 2 fractional error distribution, as expected.

To compare the three scenarios, the total number of predicted μ^+-decay ν_e events and the two error estimators δN and Δ_N, which are defined in equations 4.18 and 4.20, are summarized in table 5.1. With the out-of-the-box Sanford-Wang π^+ flux prediction uncertainties, implemented as described in chapter 4, section 4.3, the μ^+-decay ν_e flux error is estimated to be 4.4% without fitting the scaled first derivatives, and 3.6% with fitting. The bulk of this error comes from normalization rather than shape uncertainty; the fitted (un-fitted) shape uncertainty estimator δN is 0.9% (1.1%). With the case 2 reweighting, where the "unisims" are reweighted to match the central value

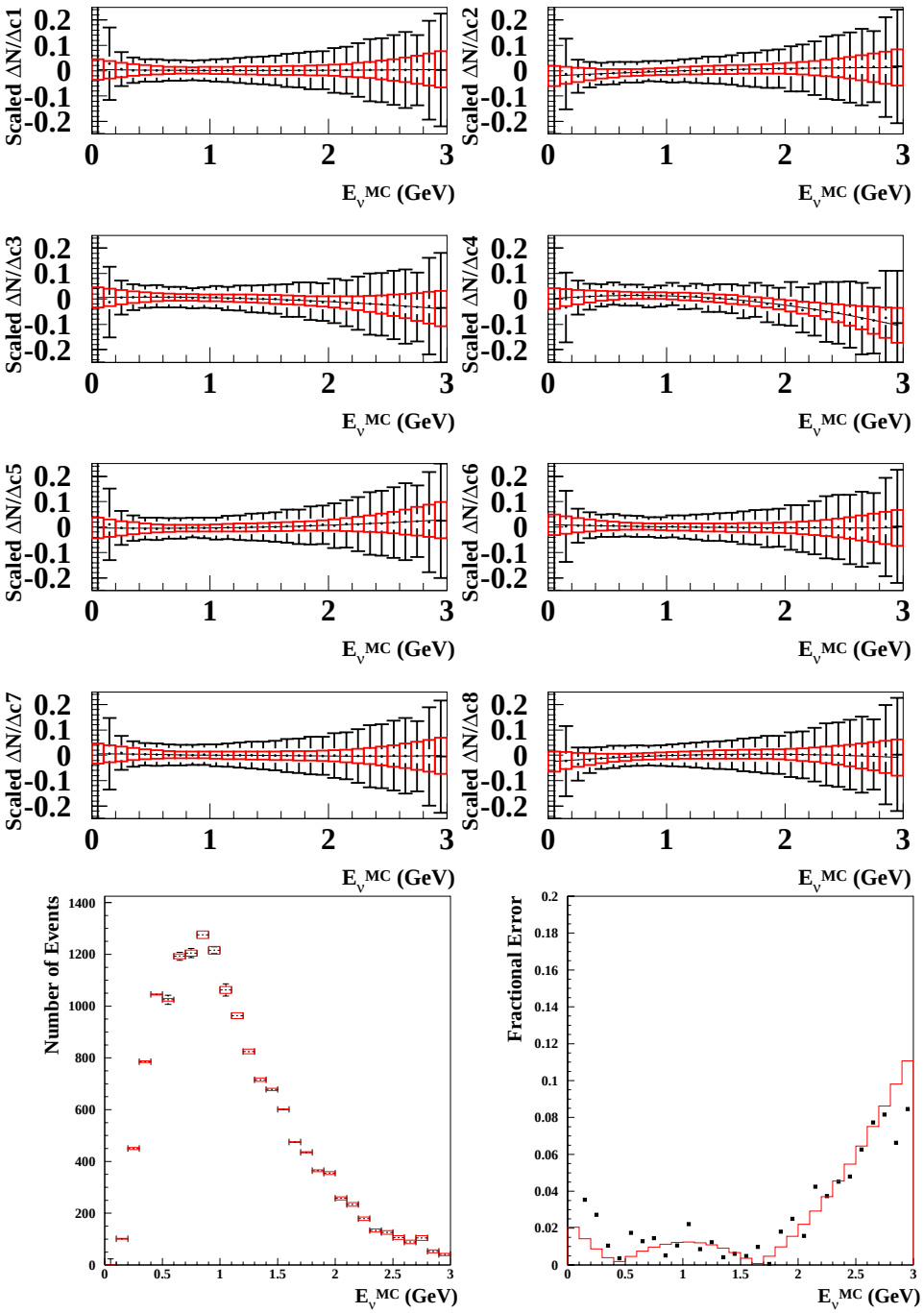

Figure 5.8: *Error on μ^+-decay ν_e E_ν^{MC} spectrum from data-reweighted Sanford - Wang π^+ prediction uncertainties. Top eight panels: scaled first derivatives (defined in equation 4.16) vs. E_ν^{MC}. Bottom left: predicted number of events vs. E_ν^{MC} (GeV) with π^+ prediction systematic errors for 2.2 $\times 10^{21}$ protons on target. Bottom right: fractional error vs. E_ν^{MC} (GeV). Red solid lines (black points) show the (un-) fit error calculation.*

Monte Carlo "fake data", the fitted (un-fitted) normalization error is reduced to 0.9% (1.9%), and the shape error is 0.2% (0.5%). For case 3, where the Monte Carlo is reweighted to match the ν_μ CCQE data set, the fitted (un-fitted) normalization error is 0.9% (2.0%), and the shape error is 0.2% (0.5%).

This result can be used in the oscillation analysis in two ways. First, the μ^+-decay ν_e prediction for the background to the ν_e appearance analysis can be directly tied to data using this method. When performing an oscillation search, one would apply the case 3 ratio to the predicted μ^+-decay ν_e background spectrum. This would effectively convert a background prediction, which relies on external data and the Monte Carlo, into an indirect in-situ background measurement. Second, the flux uncertainty associated with the μ^+-decay ν_e background prediction is greatly reduced, as table 5.1 shows, because the high statistics π^+-decay ν_μ data set strongly constrains the allowable variations in the simulation input parameters describing the π^+-decay flux production. To implement this error reduction in the oscillation analysis one would use the error matrix calculated in case 3, instead of the case 0 matrix, to parameterize the uncertainty on the μ^+-decay ν_e background coming from the π^+ flux prediction. The one serious complication with using this result in the oscillation fit is how to include the systematic errors on the flux and flux uncertainty constraint, which come from the cross section and detector response assumptions discussed in connection with equation 5.2. This question is addressed in detail in chapter 7.

This analysis can be used to constrain the π^+-decay ν_μ prediction in exactly the same way as for the μ^+-decay ν_e flux. The ratio of the modified "unisims" to the original central value Monte Carlo for each of the three cases discussed above is shown as a function of E_ν^{MC} for π^+-decay ν_μ events in the left-side panels of figure 5.5, with no selection cuts applied. The modified "unisims" are used to propagate the simulation input parameter uncertainties to the E_ν^{MC} distribution for π^+-decay ν_μ events. The

Table 5.2: *Summary of number of and uncertainty on π^+-decay ν_μ in the detector acceptance for the three reweighting scenarios described in the text. The Monte Carlo set corresponds to 2.43×10^{20} simulated protons on target.*

Reweighting Ratio	*N $\nu_\mu(\pi^+)$*	*ΔN (un-)fit value (%)*	*δN (un-)fit value (%)*
1.0	552,493	(5.658) 5.664	(1.462) 1.460
"Unisim" / CV MC	552,493	(2.556) 2.492	(0.714) 0.591
Data / CV MC	705,633	(2.508) 2.504	(0.618) 0.601

scaled first derivatives are shown as a function of generated neutrino energy E_ν^{MC} for each of the eight Sanford-Wang π^+ flux prediction parameter variations in the top eight panels of figures 5.9, 5.10, and 5.11 for cases 1, 2, and 3. The predicted E_ν^{MC} distributions for π^+-decay ν_μ events with systematic errors from the π^+ flux prediction, and the fractional errors vs. E_ν^{MC}, are shown in the bottom panels of figures 5.9, 5.10, and 5.11. The fit coefficients for the π^+-decay ν_μ case 3 scaled first derivatives are summarized for each "unisim" in table 5.3.

To compare the three scenarios, the total number of predicted π^+-decay ν_μ events and the two error estimators δN and Δ_N, which are defined in equations 4.18 and 4.20, are summarized in table 5.2. With the out-of-the-box Sanford-Wang π^+ flux prediction uncertainties, the π^+-decay ν_μ flux error is estimated to be 5.7%, both with and without fitting the scaled first derivatives. As for the μ^+-decay ν_e flux, the bulk of this error comes from normalization rather than shape uncertainty; the fitted (un-fitted) shape uncertainty estimator δN is 1.46% (1.46%). With the case 2 reweighting, where the "unisims" are modified by reweighting such that they match the central value Monte Carlo "fake data", the fitted (un-fitted) normalization error is reduced to 2.5% (2.6%), and the shape error is 0.6% (0.7%). For case 3, where the Monte Carlo

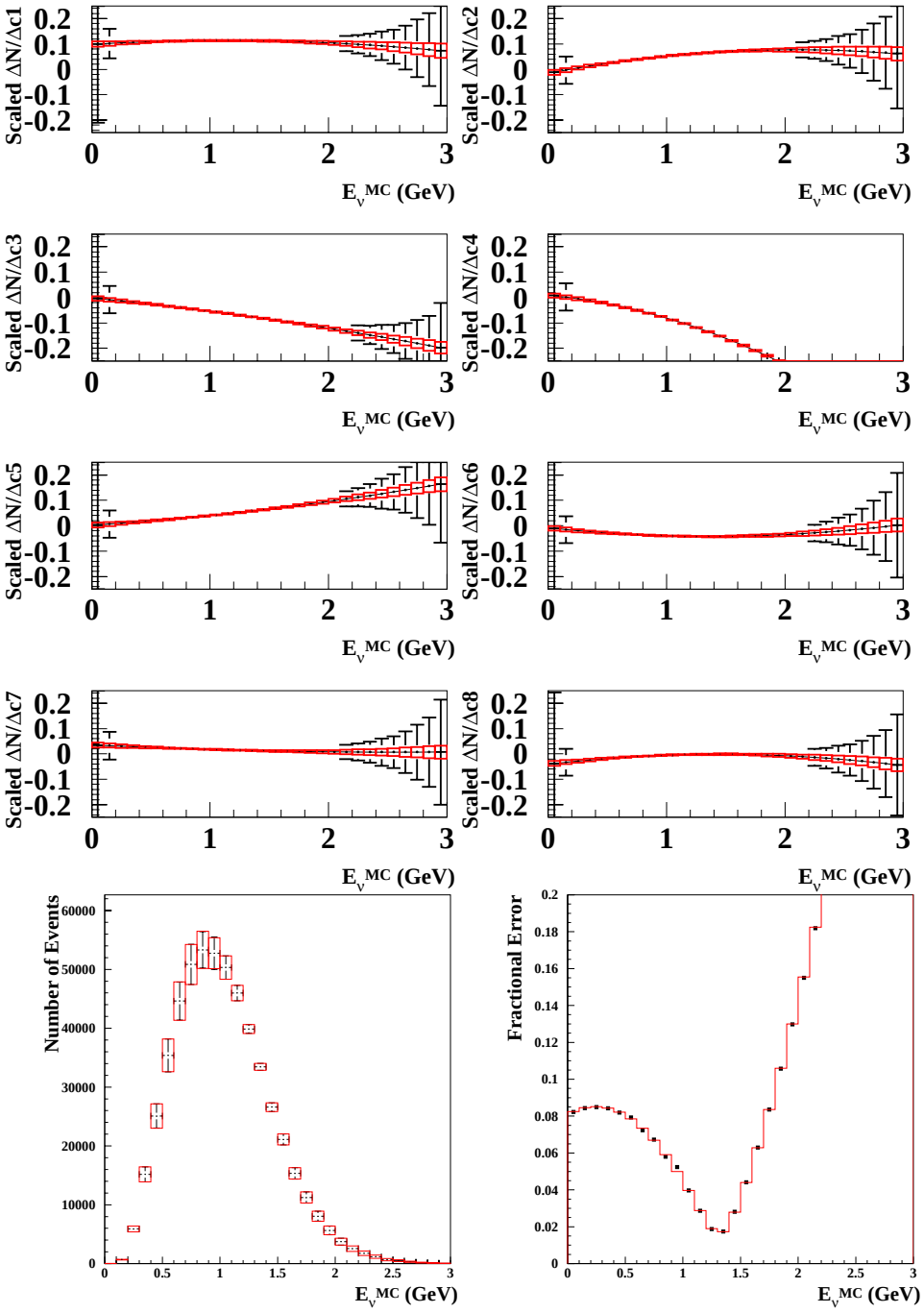

Figure 5.9: *Error on π^+-decay ν_μ E_ν^{MC} spectrum from Sanford-Wang π^+ prediction uncertainties. Top eight panels: scaled first derivatives (defined in equation 4.16) vs. E_ν^{MC}. Bottom left: predicted number of events vs. E_ν^{MC} (GeV) with π^+ prediction systematic errors for 2.43 $\times 10^{20}$ protons on target. Bottom right: fractional error vs. E_ν^{MC} (GeV). Red solid lines (black points) show the (un-) fit error calculation.*

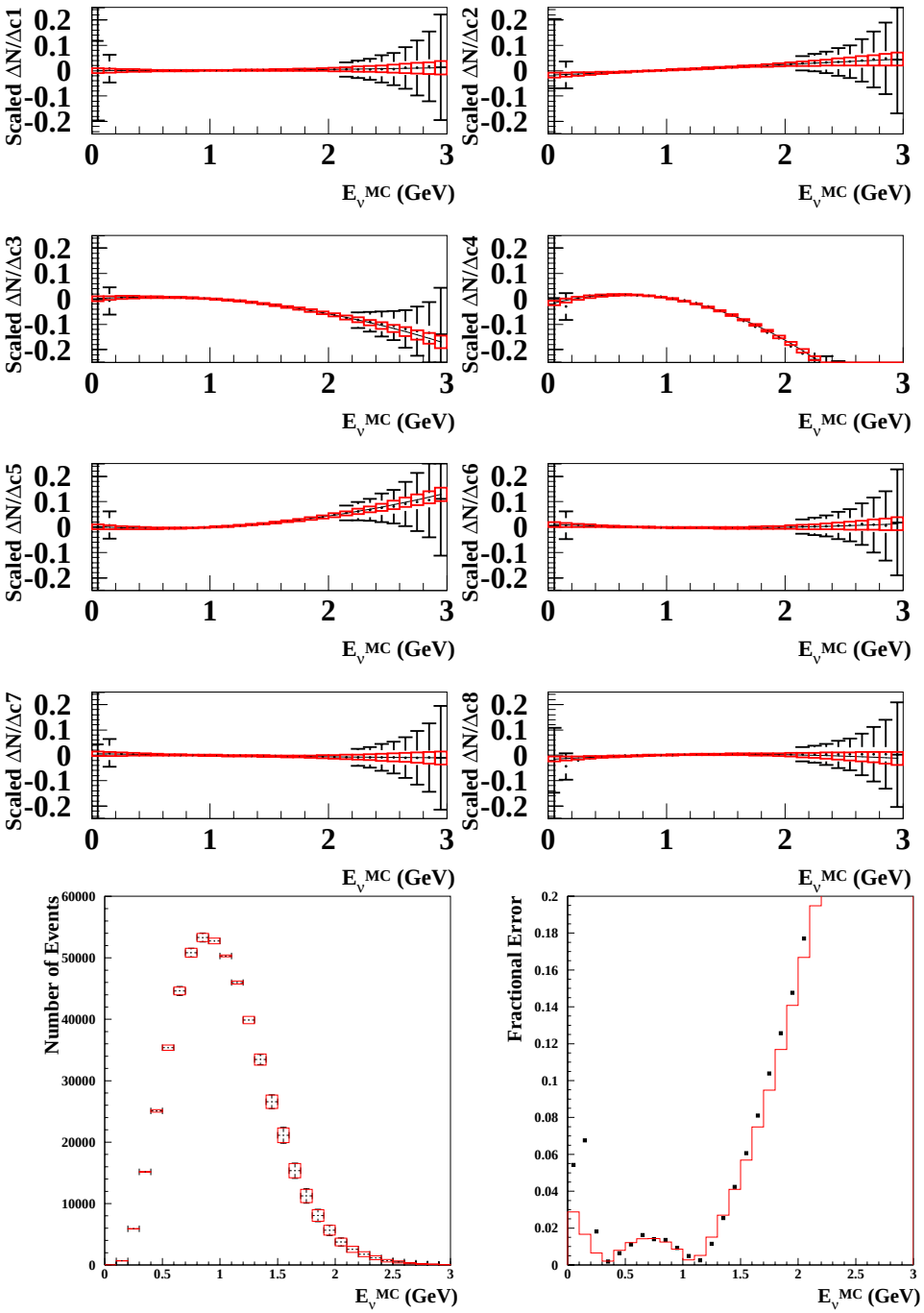

Figure 5.10: *Error on π^+-decay ν_μ E_ν^{MC} spectrum from "fake data"-reweighted Sanford-Wang π^+ prediction uncertainties. Top eight panels: scaled first derivatives (defined in equation 4.16) vs. E_ν^{MC}. Bottom left: predicted number of events vs. E_ν^{MC} (GeV) with π^+ prediction systematic errors for 2.43 $\times 10^{20}$ protons on target. Bottom right: fractional error vs. E_ν^{MC} (GeV). Red solid lines (black points) show the (un-) fit error calculation.*

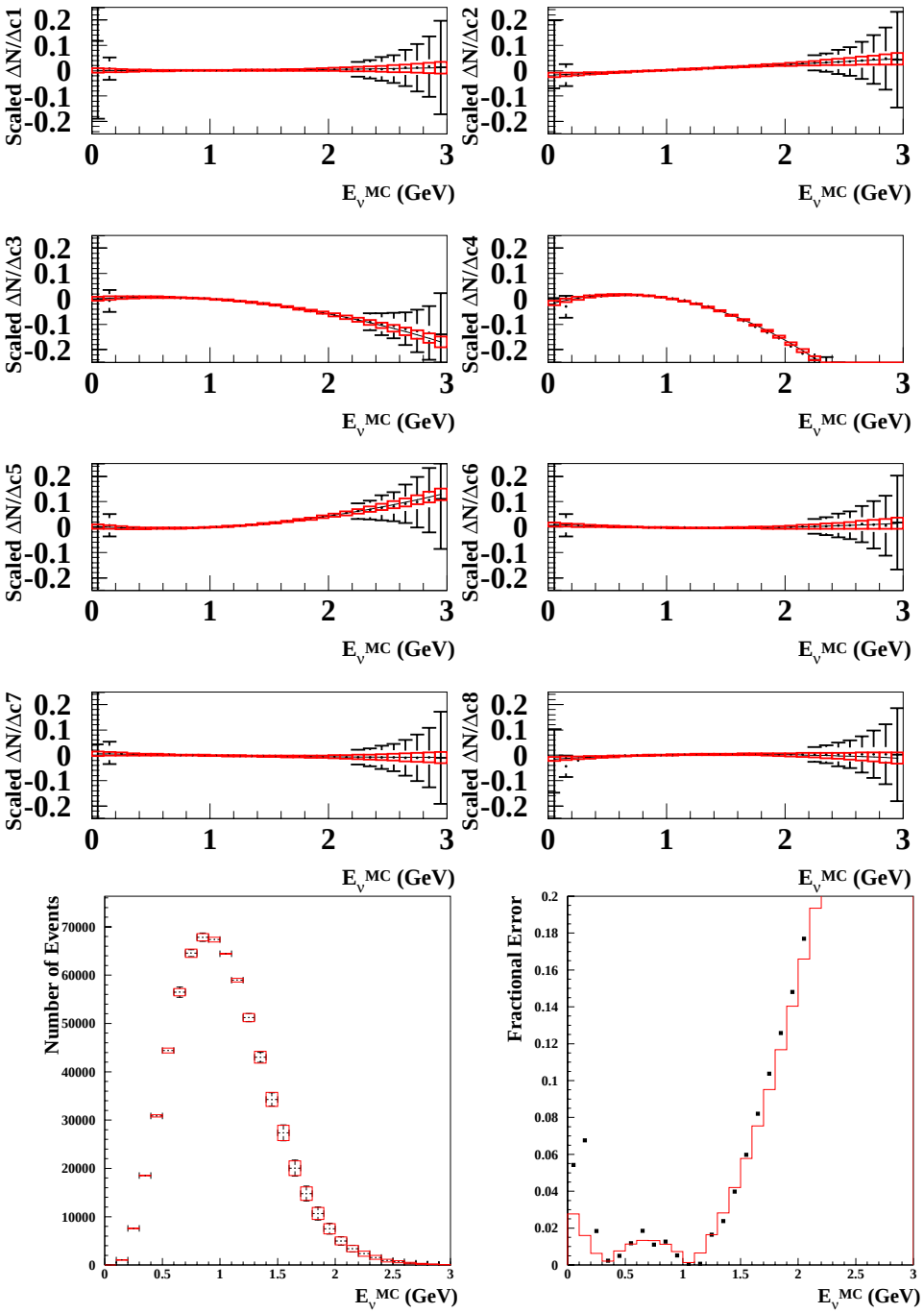

Figure 5.11: *Error on π^+-decay ν_μ E_ν^{MC} spectrum from data-reweighted Sanford-Wang π^+ prediction uncertainties. Top eight panels: scaled first derivatives (defined in equation 4.16) vs. E_ν^{MC}. Bottom left: predicted number of events vs. E_ν^{MC} (GeV) with π^+ prediction systematic errors for 2.43 $\times 10^{20}$ protons on target. Bottom right: fractional error vs. E_ν^{MC} (GeV). Red solid lines (black points) show the (un-) fit error calculation.*

Table 5.3: *Summary of scaled first derivative fit coefficients for the data-reweighted Sanford-Wang π^+ prediction unisims. The fit function is $a_1 + a_2 \cdot E_\nu^{MC} + a_3 \cdot (E_\nu^{MC})^2$. All coefficients have been multiplied by 10^2.*

reweigted *"unisim"*	$\nu_\mu(\pi^+)$ a_1	$\nu_\mu(\pi^+)$ a_2	$\nu_\mu(\pi^+)$ a_3	$\nu_e(\mu^+)$ a_1	$\nu_e(\mu^+)$ a_2	$\nu_e(\mu^+)$ a_3
SW π^+ $c1$	0.077	-0.174	0.183	0.446	-0.549	0.196
SW π^+ $c2$	-1.788	1.924	0.086	-2.182	2.310	-0.394
SW π^+ $c3$	-0.099	3.058	-2.967	0.558	0.615	-0.713
SW π^+ $c4$	-2.186	0.121	-9.579	-0.009	3.644	-2.433
SW π^+ $c5$	0.333	-2.797	2.399	-0.314	-0.576	0.550
SW π^+ $c6$	1.117	-2.083	0.748	0.955	-1.056	0.216
SW π^+ $c7$	0.689	-0.855	0.112	0.731	-0.813	0.171
SW π^+ $c8$	-1.571	2.495	-0.790	-2.572	3.420	-0.960

is reweighted to match the ν_μ CCQE data set, the fitted (un-fitted) normalization error is 2.5% (2.5%), and the shape error is 0.6% (0.7%). As before, reweighting the Monte Carlo to match the data increases the total number of predicted events by a factor of 1.28. In general, the π^+-decay ν_μ errors tend to be larger than the μ^+-decay ν_e errors because of the high E_ν^{MC} contribution; for $E_\nu < 1.5\ GeV$ the fractional errors are comparable [2].

One notable difference between the π^+-decay ν_μ and μ^+-decay ν_e constraints is that for the π^+-decay ν_μ events, fitting the scaled first derivatives does not change the error matrix appreciably with respect to the un-fit calculation. This is the case

[2]The Sanford-Wang π^+ production cross section uncertainty increases with E_ν^{MC} because a 1.5 GeV π^+-decay ν_μ comes from a 4.0 GeV π^+, while a 1.5 GeV μ^+-decay ν_e comes from a 2.5 GeV π^+, from figure 5.1, and the π^+ production cross section uncertainty also grows p_π.

because the majority of the neutrino-interaction Monte Carlo set is comprised of π^+-decay ν_μ events, and so the statistical fluctuations in the E_ν^{MC} distribution for these events are negligible.

The applicability of the flux and flux uncertainty constraints derived here is analysis-dependent. For the $\nu_\mu \rightarrow \nu_e$ oscillation search, the constraints in this chapter can be used, since the appearance analysis compares the total number of ν_e events to the background ν_e event expectation. Relating both signal and background to the observed ν_μ event rate, rather than just the signal component, reduces the systematic errors significantly and builds confidence in the oscillation analysis. However, the ν_μ disappearance oscillation search compares an observed ν_μ signal with a predicted ν_μ signal. Therefore, the prediction must come from information external to the observed event rate in MiniBooNE, and so these constraints cannot be used.

Cross section measurements are another class of MiniBooNE analyses where the constraints derived here can be applied in some situations but not in others. The neutrino interaction cross sections for all processes that contribute to the event sample passing the ν_μ CCQE selection cuts are assumed when deriving the flux constraint here, and therefore this constraint cannot be used for a measurement of the contributing cross sections. However, for other neutrino interaction cross section measurements the flux constraint derived here is applicable. For example, MiniBooNE's first two cross section measurements, of neutral current resonant π^0 [40] and charged current resonant π^+ [119] production, are normalized to the ν_μ CCQE data observed event rate using the technique of this analysis.

5.3 Extensions of this Analysis

The application of this analysis to constraining the uncertainties associated with the MiniBooNE simulation predictions effectively uses the ν_μ CCQE data set as a calibration source. When viewed in this way, the ν_μ CCQE data set could also be applied to constraining any source of uncertainty it has in common with the ν_e oscillation data set. As long as a source systematic uncertainty affects the ν_e and ν_μ data sets in similar ways, the high statistics of the ν_μ CCQE data can provide a strong constraint on the allowable variations of simulation parameters. The first candidate for this treatment is the CCQE cross section prediction uncertainties, since these are based on external data, and the MiniBooNE ν_μ CCQE data set contains an order of magnitude more CCQE events than all previous measurements in MiniBooNE's energy range combined. The application of the method described here to constraining the cross section simulation uncertainties is described in appendix C.

Along the same lines, the observed high energy ν_μ events can be used to provide a constraint on the rate of charged kaon decays in the MiniBooNE beam line. Above $E_\nu \sim 2.0\ GeV$, the majority of ν_μ come from K^+, rather than π^+, decays, therefore a measurement of the number of events in this region normalizes the K^+ contribution to the neutrino flux. The high energy ν_μ measurement can be used to validate the K^+ production cross section fit result of chapter 3, in combination with the in-situ constraint from the little muon counter (LMC) system in the neutrino beam line. A sketch of a method for incorporating these data sets to produce a constraint on the K^+ flux prediction is given in appendix D.

Chapter 6

Constraining the Cross Section Predictions with ν_μ Data

Cross sections in the $E_\nu \sim 1\ GeV$ range have sizable uncertainties from both theory and experiment. The theoretical description of the nuclear environment is a simple approximation in most neutrino interaction simulations [120], and the existing data in MiniBooNE's energy range comprises a total of ∼10,000, events from all previous experiments combined [41]. The high statistics MiniBooNE ν_μ CCQE data set can add significantly to the understanding of this important neutrino interaction, and additionally constrain the simulation at MiniBooNE to match the observed ν_μ data. Two measurements are described here. First, the axial mass (m_A), the Fermi momentum (p_F), and the binding energy (E_B) are extracted simultaneously from fitting the MiniBooNE ν_μ CCQE data set assuming the Smith-Moniz bound nucleon CCQE cross section formalism. The results provide constraints on the parameter values, their uncertainties, and their correlations for the MiniBooNE neutrino interaction simulation. Second, the functional dependence of the axial form factor on the four-momentum transfer squared, $F_A(Q^2)$, is measured in the MiniBooNE data, along

with p_F and E_B. This is the first measurement of its kind on Carbon in MiniBooNE's energy range.

6.1 CCQE Cross Section Parameter Measurement

Charged current quasi-elastic neutrino interactions are the signal channel for both the $\nu_\mu \rightarrow \nu_e$ and ν_μ disappearance oscillation searches, therefore it is desirable to constrain the CCQE cross section prediction using MiniBooNE data. However, for the oscillation analyses it is important that any constraints be derived in a flux-independent way so as not to bias the result. Historically, this is how the majority of CCQE cross section parameter measurements have been made, because accurate predictions of neutrino fluxes have not been available [121, 122, 123, 124, 125] due to the dearth of comprehensive meson production data in p-N collisions.

In the Smith-Moniz formalism [100] described in chapter 3, the free parameters in the CCQE cross section are the Fermi gas model parameters p_F and E_B, and the form factor parameters m_A, $F_A(Q^2)$, m_V, and $F_V(Q^2)$. The vector parameters m_V and $F_V(Q^2)$ are measured very precisely in electron scattering experiments [103], and therefore contribute negligibly to the neutrino interaction cross section uncertainties at MiniBooNE. However, of the axial parameters, only g_A, the value of $F_A(Q^2 = 0)$, has a small uncertainty [41]. The remaining CCQE cross section parameters are not well constrained by past measurements, and therefore are an important contribution to MiniBooNE's CCQE cross section prediction uncertainty [105].

The axial form factor parameterizes the distribution of the weak charge within the nucleus in neutrino scattering, and m_A is sometimes called the "charge radius". This form factor is usually assumed to have a dipole form as a function of momentum

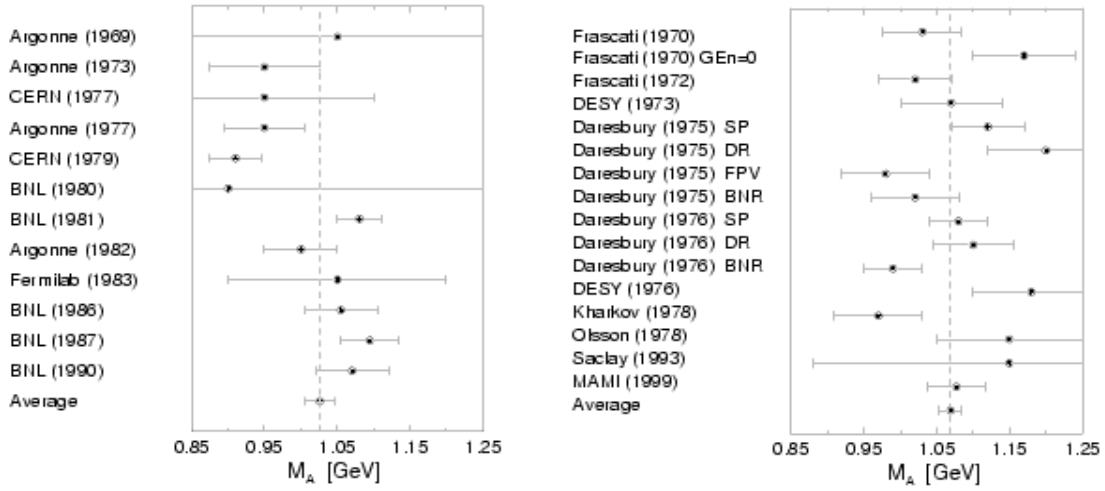

Figure 6.1: *Measurements of m_A from neutrino scattering (left) and pion electroproduction (right) experiments, assuming a dipole form for $F_A(Q^2)$. This figure is from reference [102]*

transfer squared (Q^2):

$$F_A(Q^2) \;=\; \frac{-g_A}{\left(1+\frac{Q^2}{m_A^2}\right)^2}. \tag{6.1}$$

The Fourier transform of this functional form gives an exponential charge density distribution with radius m_A. The dipole assumption historically comes from equating the Q^2 dependence of the vector and axial form factors, which is equivalent to assuming identical distributions of electromagnetic and weak charge within the nucleus. A number of experiments have measured m_A under the dipole assumption; their results are summarized in figure 6.1.

In general, neutrino scattering experiments extract m_A by fitting the Q^2 distribution of ν_μ CCQE events. The world-average value from neutrino scattering experiments is 1.026 $\pm$ 0.021 GeV/c^2 [102]. However, the average of the bubble-chamber experiments which measure m_A on Freon (Propane-Freon) is 0.84 $\pm$ 0.08 (0.88 $\pm$0.07) [102], which has a much larger uncertainty, $\sim$10%. The discrepancy

may be due to nuclear corrections to the CCQE cross section: since m_A is a parameter of the free nucleon cross section, heavy target experiments must include a simulation of or correction for nuclear effects, which can be quite large and may be treated differently in each experiment. For this reason, the most straightforward measurements to interpret are those on deuterium, which have an average m_A value of 1.05 ± 0.03. The axial mass can also be measured in pion electro-production data, using $ep \rightarrow ep\pi^0$ and $ep \rightarrow en\pi^+$ at threshold, however this requires additional assumptions beyond the dipole form for $F_A(Q^2)$ to address radiative corrections and the contributions of multiple resonances [126]. The electroproduction world-average m_A value is $1.069 \pm 0.016\ GeV/c^2$ [102].

The parameters in the Smith-Moniz CCQE cross section formalism which include the effects of the bound target nucleon are the Fermi gas model parameters E_B and p_F. The values of these parameters for a Carbon target can be extracted from electron scattering data; the most recent published measurement dates from 1971, and is used as input to the MiniBooNE simulation [104]. The Fermi gas model prediction agrees with quasi-elastic neutrino scattering cross section measurements at the 10% level for projectile energies above 1 GeV, however, it overpredicts the cross section below 1 GeV. Therefore, the external-data based uncertainties assumed by MiniBooNE on E_B and p_F are inflated with respect to past measurements such that the MiniBooNE neutrino interaction Monte Carlo prediction covers the LSND measurement of the ν_μ CCQE cross section at $E_\nu = 0.150\ GeV$ within errors [105]. The resulting Fermi gas model parameters are $E_B = 0.025 \pm 0.025\ GeV$ and $p_F = 0.220 \pm 0.030\ GeV$.

In recent years there have been several surprises in CCQE cross section parameter measurements. The K2K experiment, which is a neutrino oscillation experiment very similar to MiniBooNE at $E_\nu \sim 1.2\ GeV$ with a CH_2 target, measures a value of $m_A = 1.20 \pm 0.12\ (GeV/c^2)$ [37]. This is very interesting for MiniBooNE because the

reconstructed Q^2 distribution disagreement between data and Monte Carlo at low Q^2 is quite similar to the K2K observation [37, 120]. Another surprising development is that the most recent measurements of the vector form factor reveal non-dipole dependence on Q^2 [103]. Both of these results are in conflict with theoretical expectations, and therefore motivate closer study of the parameters of the CCQE cross section and their uncertainties.

6.1.1 Method

To measure the CCQE cross section parameters at MiniBooNE, a histogram of the reconstructed Q^2 distribution for data passing the ν_μ CCQE event selection cuts is fit with m_A, p_F, and E_B as free parameters in the fit, assuming the dipole form for $F_A(Q^2)$. The fit uses the MiniBooNE Monte Carlo to propagate the underlying CCQE free nucleon cross section parameters to a histogram of events vs. reconstructed Q^2, which is subsequently compared with the data. The procedure is as follows:

1. the ν_μ CCQE data set described in chapter 4 is histogrammed in reconstructed Q^2 bins.

2. A file of Monte Carlo events is created which contains the generated and reconstructed E_ν and Q^2, the generated muon momentum p_μ and angle $cos(\theta_\mu)$, and a weight for each event. The weight is a function of m_A, p_F, and E_B.

3. The Monte Carlo weights are summed to histogram the Monte Carlo in Q^2_{REC} bins, with the same histogram definition as the data.

4. The fit minimizes a χ^2 formed between data and Monte Carlo with respect to the parameters (m_A, p_F, E_B),

$$\chi^2 \;=\; \sum_i \Big(\frac{N_{DATA,i} - N_{MC,i}(m_A, p_F, E_B)}{\sqrt{N_{DATA,i}}} \Big)^2 \tag{6.2}$$

where i indexes Q^2_{REC} bins, $N_{DATA,i}$ is the number of events in the data in bin i, $\sqrt{N_{DATA,i}}$ is the statistical error on the data, $N_{MC,i}(m_A, p_F, E_B)$ is the number of Monte Carlo events in bin i and is a function of (m_A, p_F, E_B) via the Monte Carlo weights. The `MINUIT` program is employed to perform the minimization with the `MINOS` error analysis option [56]. The initial values of the parameters are the world-average values, $E_B = 0.025\ GeV$, $p_F = 0.220\ GeV$, and $m_A = 1.03\ GeV/c^2$, and the parameters are unbounded in the fit.

The Monte Carlo weights are calculated from the Smith-Moniz relativistic Fermi gas model CCQE cross section, which is given in chapter 3, equations 3.34 through 3.41, and implemented identically in the MiniBooNE neutrino interaction cross section Monte Carlo. The initial weight of each event is set to the value of the Smith-Moniz CCQE cross section under the dipole $F_A(Q^2)$ assumption with the world-average CCQE cross section parameter values, and the generated E_ν, p_μ and $cos(\theta_\mu)$ of the event.

At each iteration in the fit, as m_A, p_F, and E_B are varied, the cross section is recalculated and each event is given a weight equal to the current value of the cross section divided by the initial value. One attractive feature of fitting for all three of the free parameters in the Smith-Moniz CCQE cross section simultaneously is that the fit returns a covariance matrix for the parameters. This matrix not only gives the parameter errors, but also their correlations ρ. The ρ can be large, and should be included when propagating errors from underlying simulation parameters to output variable distributions such as E_ν^{QE}, used for oscillation analyses.

The events are re-binned at each iteration of the fit, and compared with the data. Ideally, the Q^2 bin widths would be as small as possible, however, the Q^2 reconstruction resolution and, to a lesser extent the statistical error, sets a lower limit on the bin size. The reconstructed Q^2 bin widths are chosen to be approximately twice

the Q^2 resolution in the lowest Q^2 bin, which is the most restrictive, as figure 4.10 shows. Stated another way, the reconstructed Q^2 bin widths are chosen such that the average Monte Carlo generated Q^2 in each reconstructed Q^2 bin lies in the same reconstructed Q^2 bin. This constraint results in 16 bins between 0.0 and 1.0 GeV^2. The cutoff at 1.0 GeV^2 is chosen to minimize statistical error. This reconstructed Q^2 range includes 96% of the events in the ν_μ CCQE data set.

According to the Monte Carlo, 9.5% of the events that pass the ν_μ CCQE selection cuts are due to non-CCQE background interactions. Since the Smith-Moniz cross section is valid only for CCQE events it cannot be used to calculate the weights for background events. Therefore these weights are treated as independent of the fit parameters, that is, the weight for background events is a constant equal to 1.0 at each iteration in the fit. Fortunately, the reconstructed Q^2 distributions of background and signal are quite different, as is shown in figure 4.9 in chapter 4. The background is much more peaked at low reconstructed Q^2, and therefore one can test the impact of the background events on the fit results by fitting above a minimum Q^2 value. Above $Q^2 = 0.2\ GeV^2$, the fraction of background events in any bin is $< 1\%$, and the total background fraction is reduced to 5%.

This kind of analysis can be done with either absolutely or relatively normalized Q^2 distributions, since m_A (and E_B and p_F) affect both $d\sigma/dQ^2$ and the overall normalization of the CCQE cross section. Given the disagreement between the data and Monte Carlo predicted rates at MiniBooNE, the CCQE parameter extraction analysis here uses only the shape of the data Q^2 distribution. This is accomplished by normalizing the Monte Carlo such that the total number of events is equal to the number in data. The relatively normalized total number of Monte Carlo events, before any fitting, is given by

$$N_R^{MC} \;=\; \frac{\sum_i N_i^{DATA}}{\sum_i N_i^{MC}} N^{MC} \;=\; N^{DATA} \tag{6.3}$$

where i indexes events passing the ν_μ CCQE selection cuts.

In practice this analysis is performed with weighted events to start with, since the Monte Carlo was generated with different values of the CCQE cross section parameters from the world-averages. The events are reweighted by a factor

$$w = \frac{\sigma_{CCQE}(E_B, p_F, m_A | E_\nu^{MC}, p_\mu^{MC}, cos(\theta_\mu)^{MC})}{\sigma_{CCQE}(E'_B, p'_F, m'_A | E_\nu^{MC}, p_\mu^{MC}, cos(\theta_\mu)^{MC})} \tag{6.4}$$

where σ_{CCQE} is the Smith-Moniz ν_μ CCQE cross section, E_B, p_F, and m_A are the world-average values given above, and E'_B, p'_F, and m'_A are the original values used when the Monte Carlo events were generated. The event kinematics are specified by E_ν^{MC}, p_μ^{MC}, and $cos(\theta_\mu)^{MC}$. It has been verified that the (p_μ^{MC}, $cos(\theta_\mu)^{MC}$) kinematic phase space overlap between the world-average and original CCQE cross section parameter Monte Carlo sets is 99.98%, that is, the problem of trying to reweight events that do not exist occurs for <0.02% of the events. The variance of the weights is small relative to the sum of the weights: $\sum_i (w_i - \overline{w})^2 / \sum_i w_i \ < \ 1\%$, and therefore the effect of Monte Carlo statistics will be small, however, the error on the number of weighted events is a function of Q^2 and therefore it is included in the χ^2 definition via

$$\chi^2 \ = \ \sum_i \Big(\frac{N_{DATA,i} - N_{MC,i}(m_A, p_F, E_B)}{\sqrt{N_{DATA,i} + \sigma^2_{MC,i}}} \Big)^2 \tag{6.5}$$

where $\sigma^2_{MC,i}$ is the variance in bin i of the Monte Carlo weights, evaluated before the fit changes the CCQE cross section parameters [1]

6.1.2 Results

The analysis method is first verified by several "fake data" studies, where "fake data" is central value Monte Carlo. The "fake data" set in this case has the statistics of

[1] The variance is not updated during the fit to avoid having fit parameters in the denominator, which causes well-known problems [127] with minimizers like `MINUIT`.

Table 6.1: *Fake data fit results with statistically identical "fake data" and Monte Carlo sets; both have the statistics of the data. The fake data is generated with E_B = 0.025 GeV, p_F = 0.220 GeV, and m_A = 1.03 GeV/c^2.*

N^{MC}	χ^2	E_B (GeV)	p_F (GeV)	m_A (GeV/c^2)
98,381	0.0000	0.0250±0.0053	0.2200±0.0056	1.030±0.0297

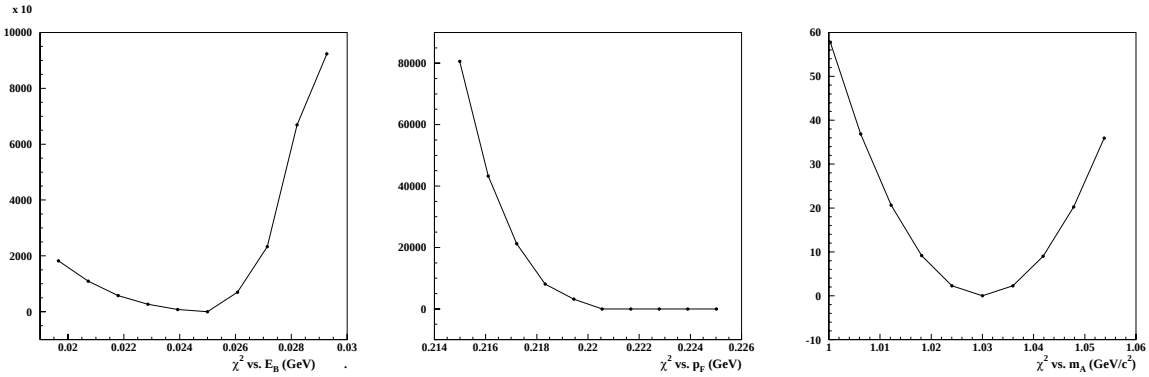

Figure 6.2: χ^2 *function value vs. fit parameter value for a fit with statistically identical "fake data" and Monte Carlo samples. Left:* χ^2 *vs.* E_B *(GeV). Middle:* χ^2 *vs.* p_F *(GeV). Right:* χ^2 *vs.* m_A *(GeV/*c^2*).*

the data, 98,381 events, and is statistically independent from the Monte Carlo used in fitting, unless noted otherwise.

The first check of the method is that fitting statistically identical "fake data" and Monte Carlo results in $\chi^2 = 0.0$ at the minimum, and returns the Monte Carlo CCQE cross section parameters. The fit passes this test, and the best-fit parameters and errors are shown in table 6.1. The errors on the fit parameters are determined by the "fake data" and Monte Carlo statistics, which correspond here to $\sim 2 \times 10^6$ Monte Carlo events before event selection cuts. The χ^2 functions about the parameter minima are shown in figure 6.2. These are one-dimensional scans in the sense that while one parameter is varied by ± 1 σ the other two parameters are fixed to their

Table 6.2: *"Fake data" fit results as a function of the number of Monte Carlo events. The "fake data" is central value Monte Carlo with the statistics of the data, 98,381 events, and is statistically independent from the Monte Carlo event samples.* N^{MC} *is the number of Monte Carlo events after the* ν_μ *CCQE event selection cuts and the requirement that* $Q^2_{REC} < 1.0\ GeV^2$.

$N^{MC}_{no\ cuts}$	$N^{MC}_{after\ cuts}$	χ^2	ndf	$E_B\ (GeV)$	$p_F\ (GeV)$	$m_A\ (GeV/c^2)$
1×10^6	46,969	56.8041	13	0.0248	0.2213	1.032
2×10^6	103,413	23.7028	13	0.0249	0.2200	1.031
3×10^6	150,252	23.7183	13	0.0250	0.2200	1.028
4×10^6	197,162	18.0740	13	0.0250	0.2200	1.030
5×10^6	244,047	16.6362	13	0.0250	0.2200	1.029
6×10^6	290,933	14.6538	13	0.0250	0.2200	1.029
7×10^6	337,657	12.0116	13	0.0250	0.2200	1.030
8×10^6	374,929	12.0167	13	0.0250	0.2204	1.029

best-fit values. These distributions show that while the χ^2 function is very symmetric about the minimum for m_A, it is highly asymmetric about the minima for E_B and p_F [2]

In practice, one would like the Monte Carlo statistical error to be negligible, and therefore the Monte Carlo statistics should be much larger than the data statistics. One test for determining when the Monte Carlo statistics are sufficiently large is to examine the value of the χ^2 at the best-fit point for a "fake data" fit as a function of the Monte Carlo statistics. When the value of the χ^2 is equal to the number of degrees

[2]The values of the χ^2 function for the points sampled above the best-fit p_F value only appear to be zero because of the scale of the figure; the coordinates of these points range from (p_F, χ^2) = (0.221, 0.452) to (0.226, 11.459).

of freedom, and does not change with increasing Monte Carlo statistics, then the fit result is stable and the Monte Carlo statistics are sufficient. The results of this test are shown in table 6.2. The stable point occurs when the Monte Carlo statistics are $\sim$4 times larger than the data statistics. Another interesting feature of this study is that the best-fit parameter values are fairly independent of the number of Monte Carlo events used, only the value of the χ^2 function at the minimum changes significantly. This builds confidence that the parameter determination is unbiased with respect to Monte Carlo statistics. For all subsequent fits described here, the Monte Carlo set with the maximum number of events shown in this table is used, which is 374,929 events after cuts, corresponding to 8×10^6 generated events. As discussed in chapter 4, approximately 1/3 of the generated events are thrown away due to the correlation between neutrino direction and interaction length, therefore 8×10^6 generated events corresponds to $\sim$5.4 $\times10^6$ events generated in the detector volume. After cuts, this Monte Carlo set has 274,929 events, which is $\sim$4$\times$ larger than the data statistics.

The reconstructed Q^2 distribution is shown before and after the fit with the "fake data" superimposed in the left panel of figure 6.3. The Monte Carlo sample is 8 $\times10^6$ events before ν_μ CCQE selection cuts. As expected, Monte Carlo and "fake data" agree well, both before and after the fit. The contribution to the χ^2 at the best-fit point from each reconstructed Q^2 bin is shown in the right panel of figure 6.3.

It is important to verify that this analysis is insensitive to neutrino oscillations since oscillations could bias the CCQE cross section parameter results, or, tuning the Monte Carlo based on fits to data with an oscillation signal could bias the oscillation analysis. To check the sensitivity of this method to oscillations, the maximum allowed ν_μ disappearance signal under a 3+1 model [36] is introduced into the "fake data" set, which has the statistics of the data without oscillations [3]. The parameters are (Δm^2,

[3]Since the efficiency of the ν_μ CCQE selection cuts is neglible for ν_e events, the presence of

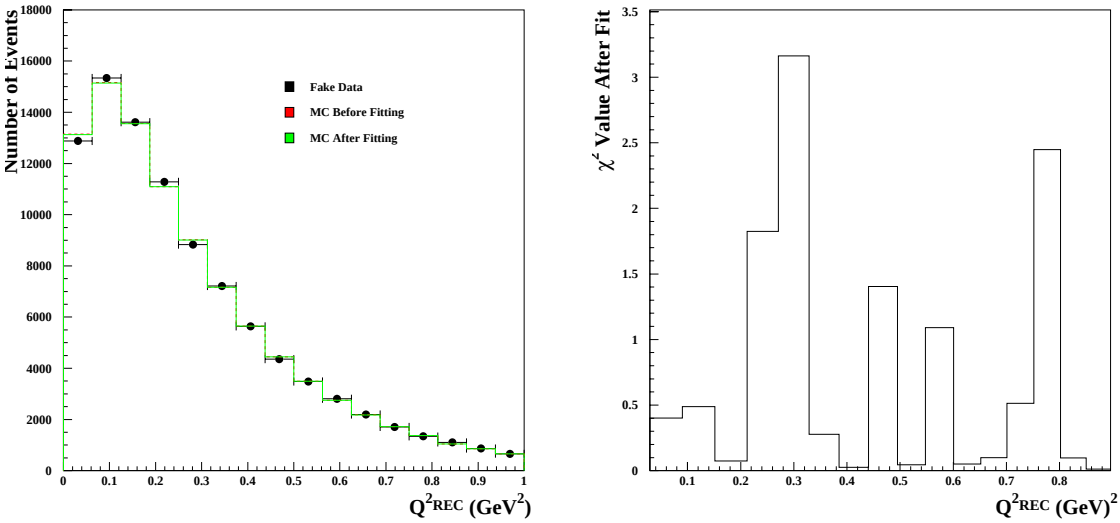

Figure 6.3: *Left: number of events before (dashed, red line) and after (solid, green line) fitting "fake data" with Monte Carlo vs. reconstructed Q^2 (GeV^2). Right: χ^2 value vs. reconstructed Q^2 (GeV^2) at the best-fit point.*

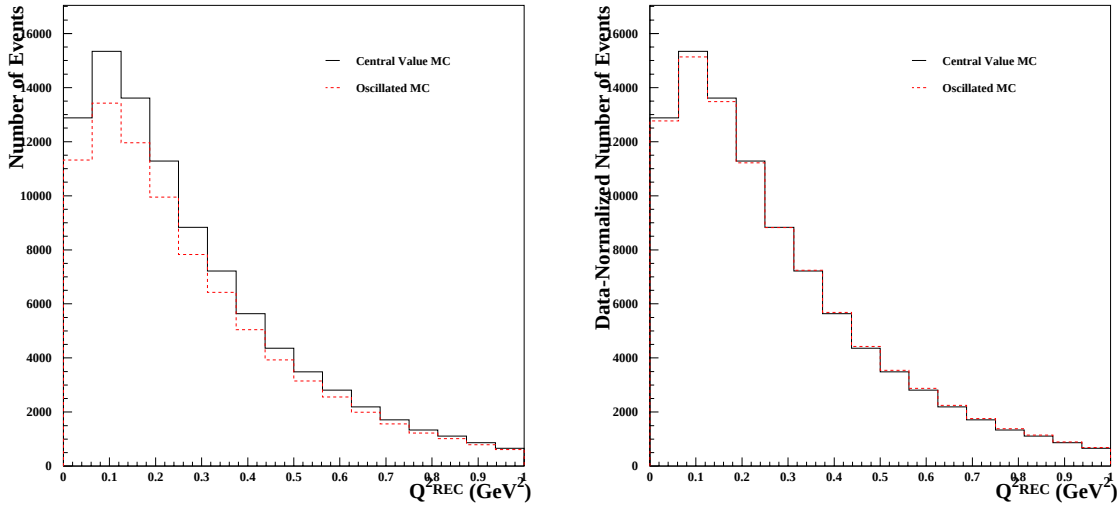

Figure 6.4: *Number of events vs. reconstructed Q^2 (GeV^2) for oscillated (red, dashed line) and un-oscillated (black, solid line) "fake data" with the statistics of the data. Left: number of events absolutely normalized to protons on target. Right: number of events normalized to the data.*

$sin^2 2\theta) = (1.eV^2,\ 0.2)$, and the oscillated spectrum is produced by weighting the central value Monte Carlo (un-oscillated) events by the survival probability $P(\nu_\mu \rightarrow \nu_\mu) = 1 - sin^2 2\theta sin^2\left(\frac{1.27\Delta m^2 0.541(km)}{E_\nu^{MC}(GeV)}\right)$. The reconstructed Q^2 distribution is shown in figure 6.4, compared with the no-oscillation case. The left panel shows the number of events vs. Q^2, and the effect of the oscillation signal is clearly visible. However, this analysis normalizes the Monte Carlo to the data (or "fake data"), and therefore the normalization component of the oscillation signal is lost. The right panel of figure 6.4 shows the oscillated and un-oscillated "fake data" sets, normalized to the same number of events. Here, the oscillation signal is much less apparent. A fit to the oscillated "fake data" using the Monte Carlo sample from 8 $\times 10^6$ generated events before cuts results in best-fit CCQE paramters that are very similar to the un-oscillated "fake data" fit result. The best-fit parameter values are $E_B = 0.0240\ GeV$, $p_F = 0.2286\ GeV$, and $m_A = 1.037\ GeV/c^2$; the χ^2 value at the best-fit point is 11.1, and the fit has 13 degrees of freedom. The comparable un-oscillated "fake data" fit results are summarized in the last row of table 6.2. These two cases agree within the systematic errors on the fit parameters, which are summarized in table 6.6. A lower Δm^2 signal might produce more of a spectrum distortion, which would have a larger affect the m_A fit, however, regions with $\Delta m^2 < \sim 1.0\ eV^2$ are excluded by the atmospheric data [36].

An important assumption of this analysis method is that the background can be treated as noise in the sense that the background normalization does not change during the fit. The Monte Carlo predicted distribution of the background as a function of reconstruction Q^2 is shown in figure 6.5, and one can see that the relative signal and background fractions change significantly as a function of Q^2. To test the impact of background on the fit results, one can restrict the range of Q^2 values used in

$\nu_\mu \rightarrow \nu_e$ oscillations at the LSND-predicted level would have no impact on this analysis.

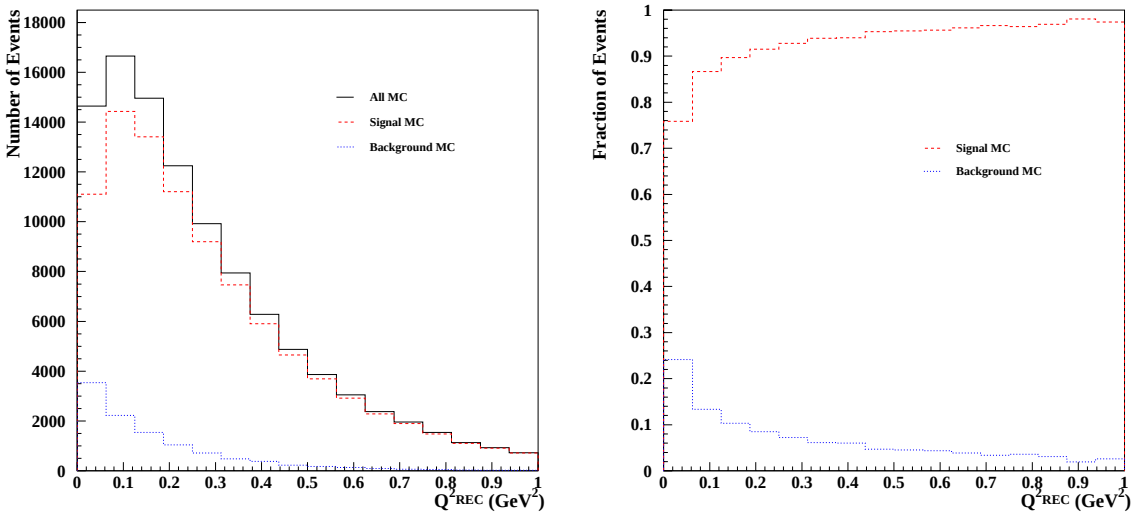

Figure 6.5: *Left: number of events vs. reconstructed Q^2 (GeV^2) in "fake data" for all neutrino interaction types (black, solid line), ν_μ CCQE events (red, dashed line), and backgound events (blue, dotted line). Right: fraction of ν_μ CCQE (red, dashed line) and background (blue, dotted line) events vs. reconstructed Q^2 (GeV^2).*

Table 6.3: *"Fake data" fit results as a function of the minimum reconstructed Q^2 value used in the fit. The "fake data" is central value Monte Carlo with the statistics of the data, 98,381 events, and is statistically independent from the Monte Carlo event sample, which corresponds to 8×10^6 events before selection cuts.*

Q^2_{min} (GeV^2)	χ^2	*ndf*	*bgnd/total*	E_B (GeV)	p_F (GeV)	m_A (GeV/c^2)
0.0000	12.0167	13	0.1013	0.0250	0.2204	1.0290
0.0625	10.6889	12	0.0790	0.0250	0.2200	1.0251
0.1250	9.6668	11	0.0670	0.0250	0.2209	1.0239
0.1875	10.8390	10	0.0581	0.0251	0.2244	1.0288
0.2500	7.2560	9	0.0512	0.0252	0.2316	1.0313

Table 6.4: *Data fit results. The Monte Carlo set corresponds to 8×10^6 events before selection cuts, or ∼4× the data statistics after cuts. The probability for χ^2/ndf = 3.67/13 is 99.4%.*

N^{Data}	χ^2/ndf	E_B (GeV)	p_F (GeV)	m_A (GeV/c^2)
98,381	3.6712/13	0.0341±0.0013	0.2830±0.0069	1.2542±0.0204

the fit thereby changing the total fraction of background events. The Monte Carlo is normalized to the total number of "fake data" events, with no Q^2 cuts, in all cases. The results of this study are summarized in table 6.3. For each fit, a minimum reconstructed Q^2 cut is applied to "fake data" and the statistically independent Monte Carlo sample corresponding to 8 $\times 10^6$ events before cuts. The resulting best-fit parameters are all in good agreement with the default $Q^2 > 0.0$ case, which builds confidence that the presence of background events at low Q^2 does not bias the fit results under this analysis method. Note however that this study assumes that the Q^2 distribution of background events is known perfectly. A similar study can be done with the data, and if the fit results depend on the minimum reconstructed Q^2 value, it may indicate that the assumed Q^2 distribution of the background events is incorrect.

Having determined the necessary Monte Carlo statistics, verified that the analysis is insensitive to oscillations, and checked that the presence of background does not bias the fit results, one can apply this analysis to the actual ν_μ CCQE data set. The minimization converges successfully with MINUIT fit status parameter `ISTAT` equal to 3.0. The resulting best-fit parameters and their fit errors are summarized in table 6.4. The best-fit parameters are quite different from the world-average values: the binding energy E_B is 0.034±0.0013 GeV compared with the world-average value of 0.025 GeV, the Fermi momentum p_F is 0.283±0.0069 GeV compared with 0.220

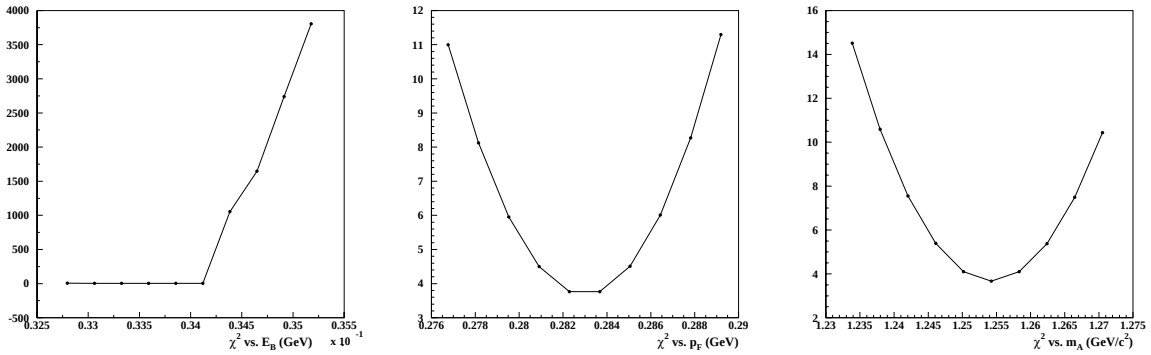

Figure 6.6: χ^2 *function value vs. fit parameter value for a fit to data. Left:* χ^2 *vs.* E_B *(GeV). Middle:* χ^2 *vs.* p_F *(GeV). Right:* χ^2 *vs.* m_A *(GeV/*c^2*).*

GeV, and the axial mass m_A is 1.25±0.02 GeV/c^2 compared with 1.03 GeV/c^2. The correlations between parameters, from the fit covariance matrix, are $\rho_{1,2} = \rho_{2,1} =$ -0.060, $\rho_{1,3} = \rho_{3,1} = 0.500$, and $\rho_{2,3} = \rho_{3,2} = 0.617$, where parameter #1 is E_B, #2 is p_F, and #3 is m_A. The value of the χ^2 as a function of the fit parameters about their mimina is shown in figure 6.6. As in the "fake data" case, the χ^2 is symmetric about the best-fit m_A value and asymetric about E_B [4]. Here the χ^2 is also symmetric about the best-fit p_F value.

The reconstructed Q^2 distribution is shown before and after the fit with the data points superimposed in the left panel of figure 6.7. Before the fit, data and Monte Carlo disagree significantly for $Q^2_{REC} < 0.2\ GeV^2$; after the fit, the Monte Carlo reproduces the data well. The contribution to the χ^2 at the best-fit point from each reconstructed Q^2 bin is shown in the right panel of figure 6.7.

Given the large differences between the starting and ending values of the CCQE cross section parameters, one might worry about how other kinematic distributions

[4]The values of the χ^2 function for the points sampled below the best-fit E_B value only appear to be zero because of the scale of the figure; the coordinates of these points range from (E_B, χ^2) = (0.034, 3.695) to (0.0328, 5.801).

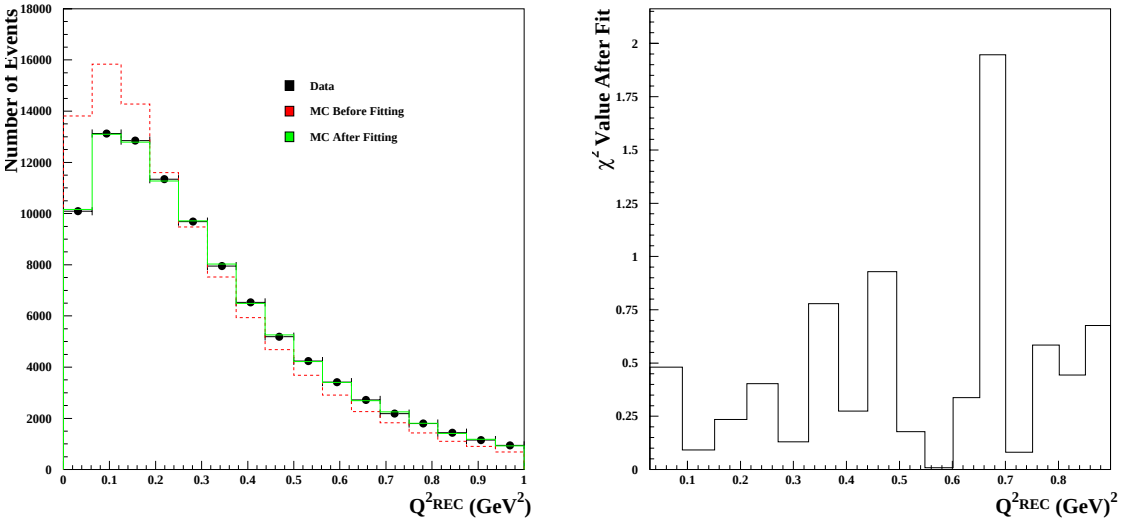

Figure 6.7: *Left: number of events before (dashed, red line) and after (solid, green line) fitting data with Monte Carlo vs. reconstructed Q^2 (GeV^2). Right: χ^2 value vs. reconstructed Q^2 (GeV^2) at the best-fit point.*

are affected. Figures 6.8 and 6.9 show the reconstructed E_ν^{QE} distribution in each Q^2_{REC} bin before and after the fit compared with the ν_μ CCQE data set. These show that after the fit the Monte Carlo prediction agrees much better with the data, even though these E_ν^{QE} distributions are not included in the fit, since only the total number of events in each Q^2_{REC} bin is considered. It is also very encouraging that the E_ν^{QE} distributions agree equally well for all E_ν^{QE} values, because this indicates that the CCQE parameter fitting has not introduced a bias as a function of E_ν^{QE}, which is the important variable for the oscillation analyses. In general, figures 6.8 and 6.9 demonstrate excellent agreement between the Monte Carlo prediction after the fit and the data over $0 < Q^2_{REC} < 1\ GeV^2$ and $0 < E_\nu^{QE} < 3\ GeV$, which is nearly all of the MiniBooNE (Q^2, E_ν^{QE}) parameter space.

To check the background reconstructed Q^2 distribution assumption, the data have been fit with a series of minimum reconstructed Q^2 cuts, ranging from 0.00 to 0.25

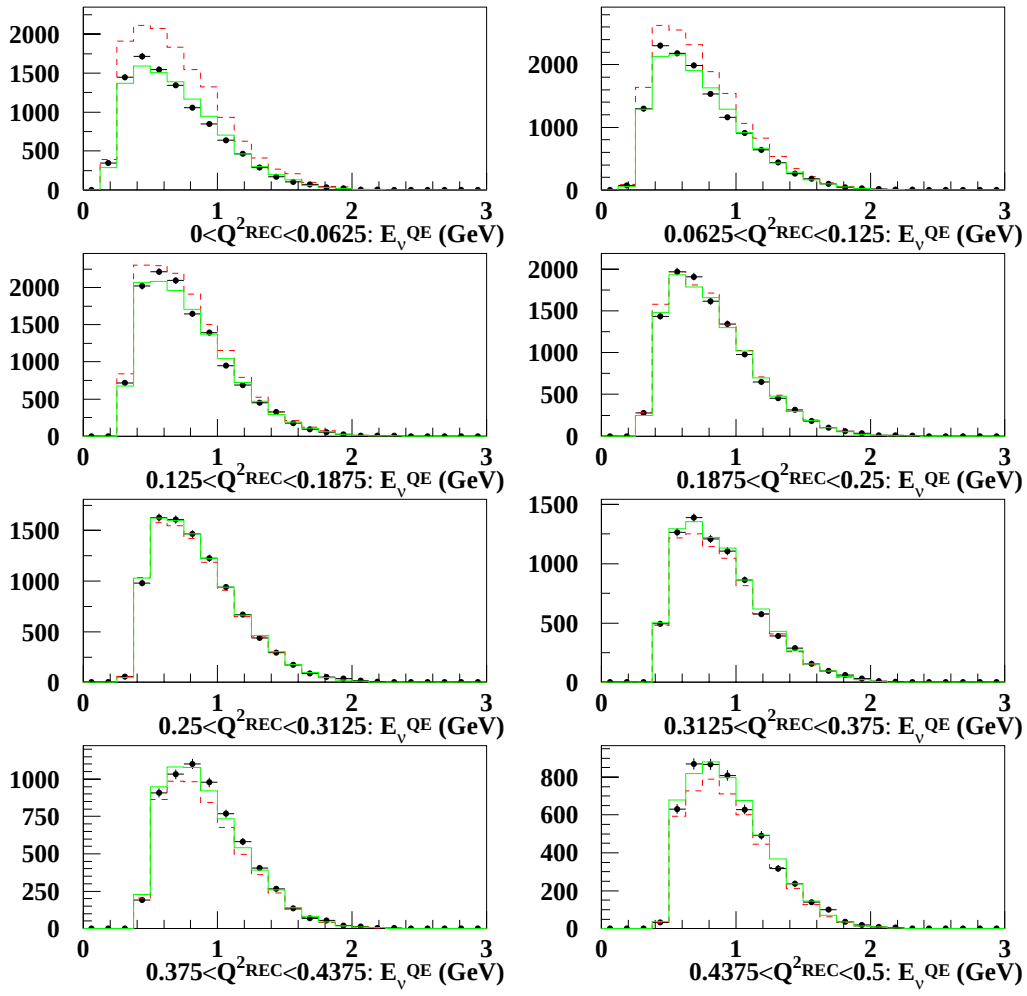

Figure 6.8: *Number of events vs. reconstructed neutrino energy (GeV) in each reconstructed Q^2 bin before (red, dashed line) and after (green, solid line) fitting for CCQE cross section parameters. The ν_μ CCQE data (black points) with statistical errors are superimposed.*

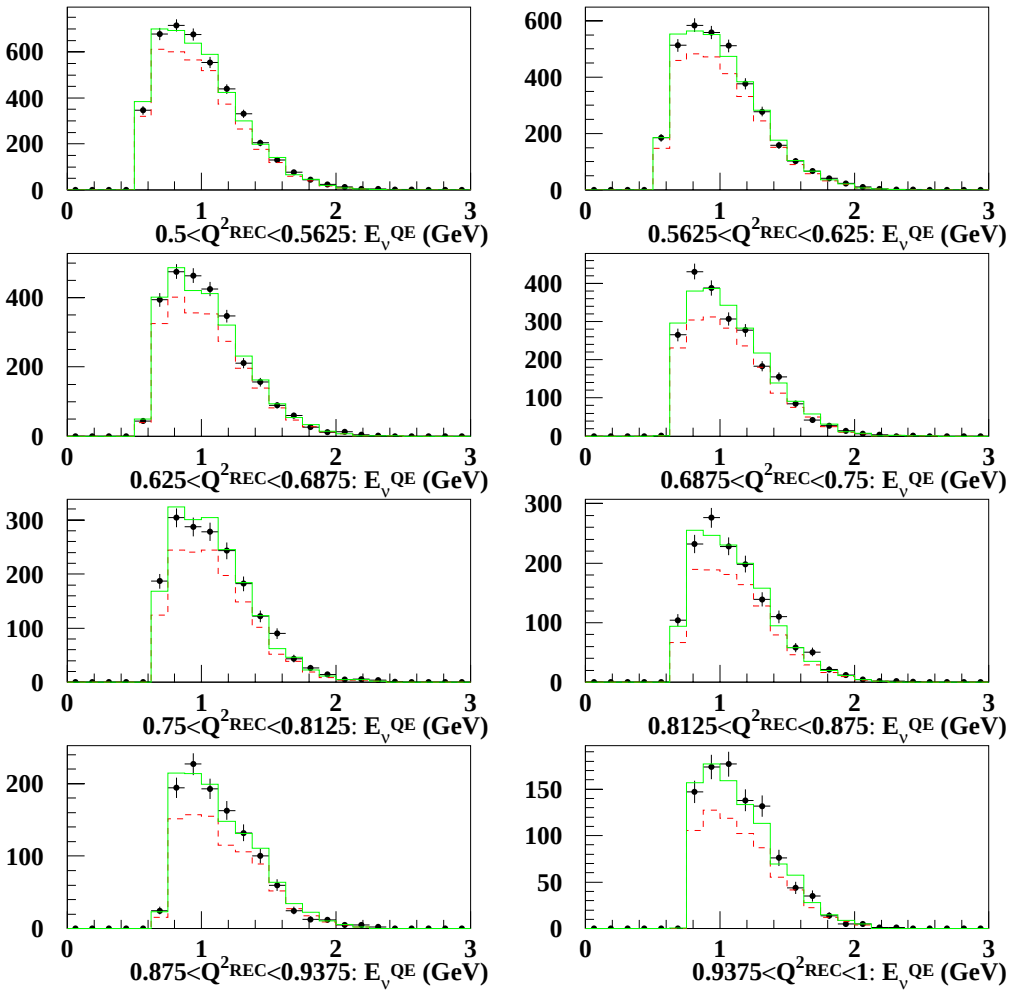

Figure 6.9: *Number of events vs. reconstructed neutrino energy (GeV) in each reconstructed Q^2 bin before (red, dashed line) and after (green, solid line) fitting for CCQE cross section parameters. The ν_μ CCQE data (black points) with statistical errors are superimposed.*

Table 6.5: *Data fit results as a function of the minimum reconstructed Q^2 value used in the fit. The Monte Carlo event sample corresponds to 8×10^6 events before selection cuts.*

Q^2_{min} (GeV^2)	χ^2	ndf	E_B (GeV)	p_F (GeV)	m_A (GeV/c^2)
0.0000	3.6712	13	0.0341	0.2830	1.2542
0.0625	3.5723	12	0.0321	0.2856	1.2493
0.1250	3.5827	11	0.0287	0.2903	1.2427
0.1875	3.4296	10	0.0317	0.2866	1.2487
0.2500	3.4868	9	0.0289	0.2916	1.2458

GeV^2. The results of this study are summarized in table 6.5. As with the "fake data" study, the Monte Carlo is normalized to have the same total number of events as the data with no Q^2 cuts, and so the normalization is identical in all cases. The best-fit value of m_A varies by $< 1\%$ with respect to the $Q^2 > 0.0$ fit result, which agrees within statistical errors. However, p_F and E_B have larger variations, 3% and 15% respectively. These parameter excursions are covered by the systematic errors, which are summarized in table 6.6, however, they indicate that fits with Q^2_{min} cutoffs may be less sensitive to the values of the Fermi Gas model parameters. This is not a surprise since the effects of non-zero E_B and p_F are largest at low Q^2, as discussed in chapter 3, although this is interesting because the Fermi gas model parameters are quite correlated with m_A, and previous measurements extract m_A with fixed values for p_F and E_B.

The systematic errors on the fit parameters are evaluated by fitting "fake data" with a "unisim" Monte Carlo sample, in which one underlying simulation parameter, e.g. the Sanford-Wang π^+ production cross section parameter c_1, has been varied by

1σ. The sources of systematic error discussed in chapter 4, section 4.3 are considered here. These include: (i) the π^+ flux prediction Sanford-Wang parameter uncertainties, (ii) the neutrino interaction cross section uncertainties, and (iii) a set of detector response uncertainties.

A fit for (m_A, p_F, E_B) is done for each of j "unisims" where the "unisim" j is used as the Monte Carlo in the fit, and the "fake data," which is really central value Monte Carlo, is used as the data. The difference between the best-fit parameters $\vec{p}_j = (m_A, E_B, p_F)_j$ and the central value parameters $\vec{p}_0$ is taken to be the systematic error contribution to the uncertainty on the fit parameters from source j. In this case, the "fake data" is generated with the full available central value Monte Carlo set, which is 8×10^6 events with no cuts, rather than the statistics of the real data. The reason for this is to eliminate statistical uncertainties in the determination of $\vec{p}_j$, since including them in each of the j "unisim" fits, by having "fake data" with the data statistics, would effectively count the statistical error j times. Instead, the statistical error for each unisim is included via the variance of the weights, which is small, and the contribution to the fit parameters is estimated using the central value Monte Carlo fit to the real data, shown in table 6.4. This fit error, which comes dominantly from the data statistics, is added in quadrature once with the j systematic errors. For "unisims" produced via reweighting, the statistical error in the determination of $\vec{p}_j$ is negligible with this method. In contrast, the currently available simulated "unisim" Monte Carlo sets, described in chapter 4, section 4.3, have roughly the same statistics as the data, and therefore their statistical error is not negligible.

Because this is a measurement of the CCQE cross section parameters, the neutrino interaction cross section "unisims" must be handled with care. To estimate the contribution from these cross section uncertainties, only the variation of the background in each of the CCQE parameter "unisims" is considered. Therefore, although

Table 6.6: *Systematic error contributions to CCQE parameters. The δ are calculated as the "unisim" best-fit parameters minus the central value Monte Carlo values, (E_B, p_F, m_A) = (0.025 GeV, 0.220 GeV, 1.03 GeV/c^2). Numbers in percent are quoted with respect to the central value parameters.*

source	δE_B (GeV)	δp_F (GeV)	δm_A (GeV/c^2)
SW π^+ quadrature sum	0.0011 (4.38%)	0.0076 (3.45%)	0.0072 (0.70%)
σ_ν quadrature sum	0.0031 (12.48%)	0.0087 (3.96%)	0.0475 (4.61%)
detector response	0.0021 (8.27%)	0.0150 (6.79%)	0.0626 (6.08%)
total	0.0039 (15.60%)	0.0189 (8.58%)	0.0789 (7.66%)

the changes in the CCQE parameters are quite large in these "unisims," as is discussed in chapter 4, their impact on this analysis is small because only the background events, which comprise ∼10% of the total, are affected.

The difference between the best-fit parameters for central value and each "unisim" fit, $\Delta\vec{p}_j$, are shown in tables E.1, E.2, and E.3 in appendix E. The total systematic error is calculated in the usual way by propagating the $\Delta\vec{p}_j$ with the simulation input parameter correlation matrix for each source, as described in chapter 4. In this case, because the $\Delta\vec{p}_j$ due to the π^+ and CCQE parameter errors are negligible, the Sanford-Wang π^+ production and neutrino interaction cross section simulation parameter correlations have been neglected. The detector response correlation matrix given in appendix F is used to propagate the the detector response $\Delta\vec{p}_j$. The resulting CCQE parameter systematic errors are summarized in table 6.6. As for the m_A fit, the detector response uncertainties contribute the most to the m_A systematic error.

The values for the CCQE parameter uncertainties assumed in the MiniBooNE simulation, which are based on past, external data, are 20%, 76%, and 72% for m_A,

E_B, and p_F respectively, as discussed in chapter 3. The MiniBooNE measurement uncertainties summarized in table 6.6 are significantly smaller than the assumed values, at 8%, 9%, and 16%. Although the error analysis here is not complete since the detector response systematic errors are still under development, the MiniBooNE measurement is very competitive and likely will remain so when a full error analysis is included.

The best-fit values from the data fit described in table 6.4 have been used to generate all of the Monte Carlo in this thesis, with the exception of the p_F value, where 0.246 GeV was used instead of 0.283 GeV [5]. These changes to the CCQE cross section parameters with respect to the world-average values are not small, and they impact both the total number of predicted events, and their kinematics. Further, the changes to m_A and the Fermi Gas model parameters (E_B, p_F) have rather different effects. Increasing m_A from 1.03 GeV/c^2 to 1.25 GeV/c^2 changes the total number of events passing the selection cuts by +15%, while changing (E_B, p_F) from (0.025 GeV, 0.220 GeV) to (0.034 GeV, 0.246 GeV) decreases the predicted rate by -7%. The effects of these variations on the reconstructed Q^2 and E_ν^{QE} distributions are shown in figure 6.10, both absolutely and relatively normalized. Increasing m_A tends to steepen the roll-over at low Q^2 more than changing the Fermi Gas model parameters, however, the trend is in the same direction, and for both, most of the change to the Q^2 shape occurs below $Q^2_{REC} = 0.2\ GeV^2$. None of the parameter changes have as dramatic an impact on the E_ν^{QE} distribution, but the cumulative effect is to shift the spectrum slightly towards higher energy.

[5] The difference in the p_F values comes from a change in the treatment of fit parameter limits that post-dates the Monte Carlo generation. A fit to the data with the E_B parameter limited to be $0.0 < E_B < 1.0$ results in a best-fit p_F value of 0.246 GeV with best-fit $E_B = 0.034\ GeV$ and $m_A = 1.25\ GeV/c^2$. The fitting method was changed here to use unbounded parameters, which is the recommended procedure and generally gives more reliable results [56].

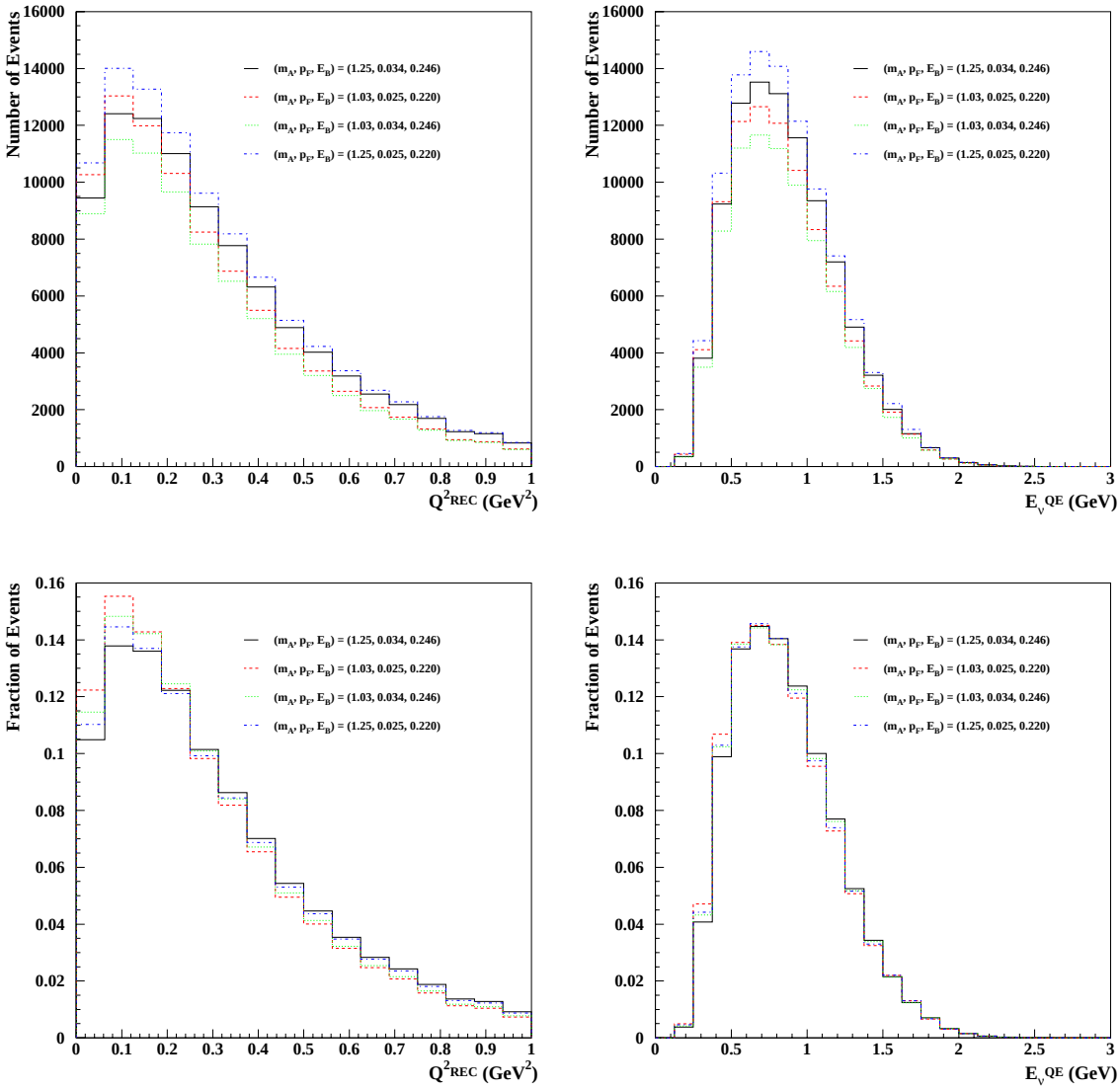

Figure 6.10: *Impact of CCQE parameter changes in Monte Carlo for events passing the ν_μ CCQE selection cuts. Left: number of events (top), fraction of events (bottom) vs. reconstructed Q^2 (GeV^2). Right: number of events (top), fraction of events (bottom) vs. reconstructed E_ν^{QE} (GeV).*

Table 6.7: *Iteration test data fit results. The Monte Carlo set corresponds to 8×10^6 events before selection cuts, or ∼4× the data statistics after cuts, and is generated with the best-fit CCQE parameters: m_A = 1.254 GeV/c^2, E_B = 0.034 GeV, and p_F = 0.283 GeV. The probability for χ^2/ndf = 4.718/13 is 98.09%.*

N^{Data}	χ^2/ndf	E_B (GeV)	p_F (GeV)	m_A (GeV/c^2)
98,381	4.718/13	0.0341±0.0029	0.2879±0.0091	1.2221±0.0140

Table 6.8: *Summary of uncertainties on the CCQE parameter measurement. Statistical errors are from table 6.7, and the systematic errors are from table 6.6.*

source	δE_B (GeV)	δp_F (GeV)	δm_A (GeV/c^2)
statistical errors	8.5%	2.4%	1.6%
systematic errors	15.6%	8.6%	7.7%
total	17.8%	8.9%	7.9%

A final check of the validity of the analysis method is to iterate the measurement using Monte Carlo that has been generated with the best-fit CCQE parameters. The result of this study, using the same central value Monte Carlo statistics as before, is summarized in table 6.7. The iteration test fit converges successfully with MINUIT fit status parameter `ISTAT` equal to 3.0. The best-fit parameter values are very similar to the previous result: the binding energy E_B is 0.0341±0.0029 GeV compared with the previous best-fit value of 0.0341GeV, the Fermi momentum p_F is 0.288±0.009 GeV compared with 0.283 GeV, and the axial mass m_A is 1.22±0.014 GeV/c^2 compared with 1.25 GeV/c^2. The correlations between parameters, from the fit covariance matrix, are $\rho_{1,2} = \rho_{2,1}$ = -0.924, $\rho_{1,3} = \rho_{3,1}$ = -0.205, and $\rho_{2,3} = \rho_{3,2}$ = 0.430, where parameter #1 is E_B, #2 is p_F, and #3 is m_A.

To estimate the total uncertainty on the MiniBooNE measurement of the CCQE cross section parameters, the statistical and systematic errors are added in quadrature, which is summarized in table 6.8. Note that errors considered in this work are preliminary, and the method for simulating the detector response uncertainties is still under investigation. However, with the error analysis described here, the MiniBooNE measurement is $E_B = 0.034 \pm 0.0.006\ GeV$, which is 1.7σ from the world-average value of $0.025\ GeV$, $p_F = 0.288 \pm 0.026\ GeV$, which is 2.6σ from the world-average value of $0.220\ GeV$, and $m_A = 1.22 \pm 0.10\ GeV/c^2$, which is 1.9σ away from the world-average value of $1.03\ GeV/c^2$.

At this point it is worth noting that the difference with respect to the world-average values may be due to nuclear effects. The world-average value for m_A comes from light nuclear target data. On the other hand, this measurement agrees within errors with the recent K2K m_A value of $1.20 \pm 0.12\ GeV/c^2$ [37], which was also measured on a CH_2 target. This large and systematic difference between the modern heavy-target measurements and the older light-target data suggests that there may be an interesting, and as yet not understood, physical explanation.

6.2 CCQE Axial Form Factor Measurement

One component that previous analyses have in common is the dipole axial form factor assumption, and as a result, the functional form of the axial form factor is not well constrained by past experiments. Previous measurements of F_A vs. Q^2 are shown for neutrino scattering and pion electroproduction experiments in figure 6.11. The uncertainties on the neutrino scattering measurements are very large, and therefore provide little information on the Q^2 dependence of the form factor, and the electroproduction measurements are model-dependent. Also, there is scant electroproduction data be-

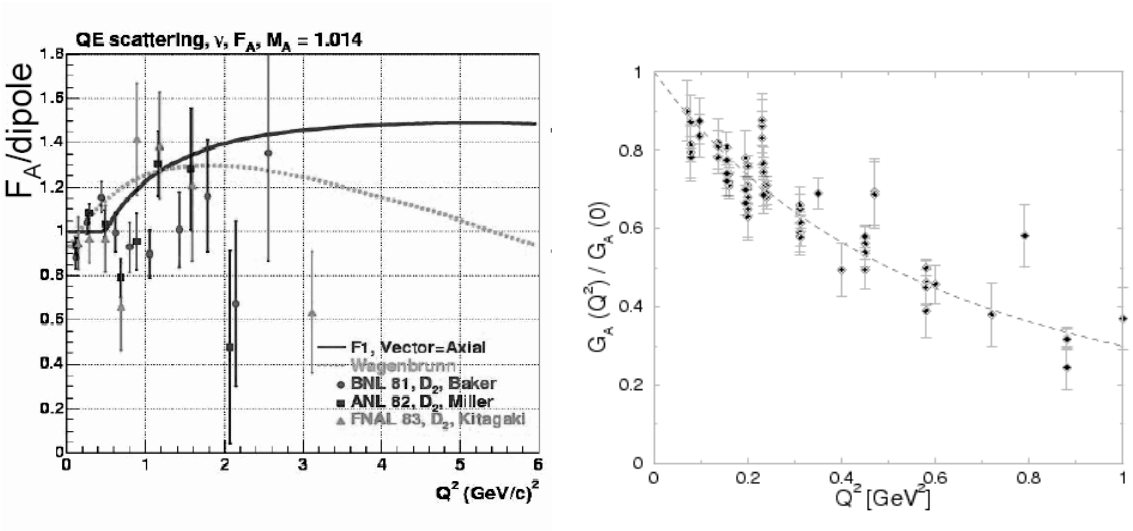

Figure 6.11: *Left: measurements of F_A vs. Q^2 from neutrino scattering data divided by the dipole assumption, with predictions from lattice gauge theory (dashed line) and a duality-based model (solid line); figure from reference [128]. Right: measurements of F_A vs. Q^2 from pion electroproduction data; figure from reference [102].*

low $Q^2 = 0.1\ GeV^2$. This is an important region for MiniBooNE because ∼20% of the events have $Q^2 < 0.1\ GeV^2$, and because both the MiniBooNE and K2K experiments observe disagreement between data and Monte Carlo in this region [37, 120].

The functional form of $F_A(Q^2)$ at low Q^2 can have a large effect on both the normalization and the Q^2 dependence of the CCQE cross section. For example, a shape that is a dipole above and flat below Q^2 of 0.25, with the same value of $F_A(Q^2 = 0)$, results in 15% more CCQE events passing the ν_μ CCQE selection cuts when integrated over the MiniBooNE neutrino flux, and a 10% decrease of the number of events below $Q^2 = 0.1\ GeV^2$. The number of CCQE events passing the selection cuts vs. reconstructed Q^2 and E_ν^{QE} are shown for this alternative form compared with the usual dipole dependence in figure 6.12. This type of variation is not excluded by past measurements, as figure 6.11 shows.

6.2.1 Method

The analysis to extract $F_A(Q^2)$ from the MiniBooNE data is very similar to the m_A measurement, however, when fitting, the free parameters in the Smith-Moniz cross section calculation are the Fermi Gas model parameters E_B and p_F, and the value of F_A in each Q^2 bin. Fitting for the value of $(F_A)_i$ in each reconstructed Q^2 bin i enables the determination of the functional form of F_A vs. Q^2 with no assumptions about the Q^2 dependence. This approach is completely independent of the usual dipole form since it no longer appears in the CCQE cross section calculation. Instead, the whole axial form factor is wrapped up as one free parameter in the fit, e.g. $F_A(Q^2) = g_A/\left(1+\frac{m_A^2}{Q^2}\right)^2$ is replaced by $(F_A)_i$ in the Smith-Moniz CCQE cross section calculation. With 16 reconstructed Q^2 bins, this procedure leads to 18 free parameters in the fit, and therefore more data bins are required to constrain the fit parameters than in the m_A fit, which had 3 free parameters and 16 reconstructed Q^2 bins as the data points. The additional data points in this fit are the 24 reconstructed E_ν bins, from 0 to 3 GeV, in each of 16 reconstructed Q^2 bins from 0 to 1 GeV/c^2, as shown in figures 6.8 and 6.9.

The χ^2 for this fit is given by

$$\chi^2 = \sum_i \sum_j \left(\frac{N_{DATA,i,j} - N_{MC,i,j}((F_A)_i, E_B, p_F)}{\sqrt{N_{DATA,i,j}}} \right)^2 \tag{6.6}$$

where i indexes reconstructed Q^2 bins, j indexes reconstructed neutrino energy bins, $N_{DATA,i,j}$ is the number of events in the data in bin (i, j), $\sqrt{N_{DATA,i,j}}$ is the statistical error on the data, $N_{MC,i,j}((F_A)_i, E_B, p_F)$ is the number of Monte Carlo events in bin (i,j), and is a function of $(F_A)_i$, E_B, and p_F via the Monte Carlo weights. This χ^2 function is minimized with respect to $(F_A)_i$ in each Q^2_{REC} bin, and the Fermi Gas model parameters E_B and p_F. The latter two are global parameters in the sense that there is one value for all Q^2 and E_ν bins. The mechanics of the fit, e.g.

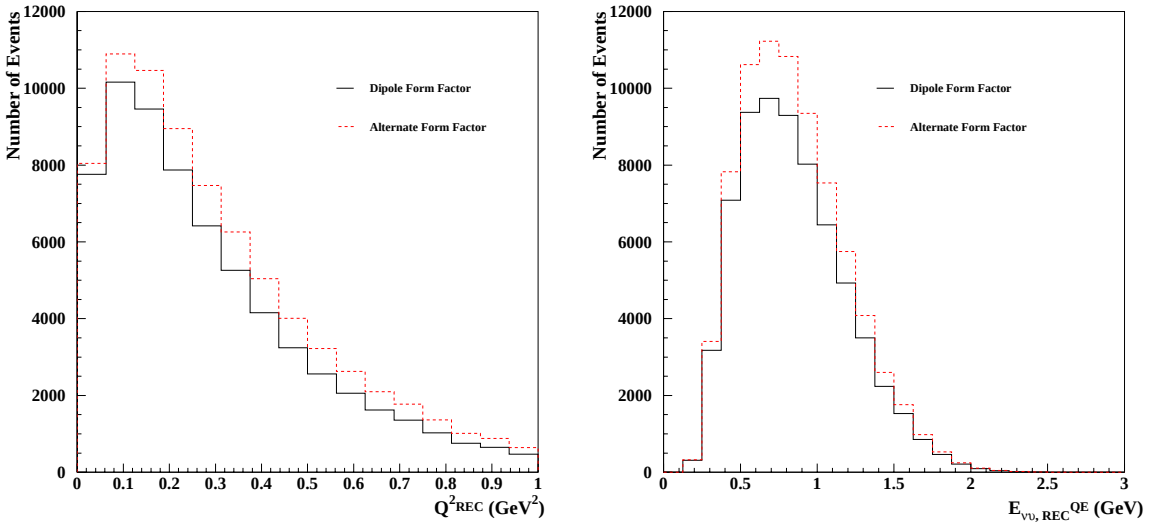

Figure 6.12: *Impact of changing the axial form factor functional dependence on Q^2 in Monte Carlo for events passing the ν_μ CCQE selection cuts. The "dipole form" (black, solid line) and "alternative form" (red, dashed line) are explained in the text. Both use (m_A, E_B, p_F) = (1.03 GeV/c^2, 0.025 GeV, 0.220 GeV). Left: number of events vs. reconstructed Q^2 (GeV^2). Right: number of events vs. reconstructed E_ν^{QE} (GeV).*

the Monte Carlo weight calculation, the Monte Carlo normalization, the treatment of background, etc., are identical to the m_A analysis. The initial values of the parameters in the fit are the world-average E_B, 0.025 GeV, and p_F, 0.220 GeV, values, and F_A evaluated at the average generated Q^2 in each reconstructed Q^2 bin assuming the dipole form with the world-average values for g_A, 1.2671, and m_A, 1.03 GeV/c^2.

6.2.2 Results

As with the m_A analysis, "fake data" studies are employed to verify the analysis procedure. First, "fake data" is fit with statistically identical Monte Carlo, both with the statistics of the ν_μ CCQE data set after cuts, 98,371 events. The resulting best-fit parameters and their fit errors are summarized in table 6.9. In all cases the best-fit parameters are identical to the parameters the "fake data" was generated with, and the value of the χ^2 function at the minimum is 0.0, for 366 degrees of freedom. The number of degrees of freedom is calculated as (16 Q^2 bins) $\times$ (24 E_ν bins) - (18 fit parameters) = 366, however, unlike the m_A fit, not all $E_{\nu,REC}$ bins are occupied. Of the 384 (Q^2_{REC},$E_{\nu,REC}$) bins, 251 are occupied and therefore contribute to the χ^2. As a result, the expected number of degrees of freedom is more like (251 bins) - (18 fit parameters) = 233. The χ^2 functions about the parameter minima are shown in figure 6.13. These distributions look as expected from previous experience with the m_A fits: for E_B and p_F the χ^2 function is highly asymmetric about the minima, and for $(F_A)_i$ the χ^2 function is very well behaved.

Smearing is somewhat more important here than for the m_A measurement because this analysis seeks to determine the functional form of F_A vs. "true", or un-smeared, Q^2. The effect of Q^2 smearing is that the average reconstructed Q^2 is different from the average "true" Monte Carlo generated Q^2 for events in a Q^2_{REC} bin. The second two columns of table 6.10 compare these two quantities. In all of the following studies, the

Table 6.9: *Fake data fit results with statistically identical "fake data" and Monte Carlo sets; both have the statistics of the data. The χ^2 value at the minimum is 0.0000 for 366 degrees of freedom. "$F_A(Q_1^2)$" refers to the value of F_A in reconstructed Q^2 bin #1.*

parameter	*MC value*	*best-fit value*	*fit error*
E_B (GeV)	0.0250	0.0250	0.0024
p_F (GeV)	0.2200	0.2200	0.0103
$F_A(Q_1^2)$	-1.1371	-1.1371	0.05194
$F_A(Q_2^2)$	-1.0289	-1.0289	0.03669
$F_A(Q_3^2)$	-0.9321	-0.9320	0.02442
$F_A(Q_4^2)$	-0.8456	-0.8456	0.01952
$F_A(Q_5^2)$	-0.7747	-0.7747	0.01792
$F_A(Q_6^2)$	-0.7131	-0.7131	0.01857
$F_A(Q_7^2)$	-0.6614	-0.6614	0.01964
$F_A(Q_8^2)$	-0.6104	-0.6104	0.02024
$F_A(Q_9^2)$	-0.5715	-0.5715	0.02124
$F_A(Q_{10}^2)$	-0.5354	-0.5354	0.02283
$F_A(Q_{11}^2)$	-0.5005	-0.5005	0.02403
$F_A(Q_{12}^2)$	-0.4726	-0.4726	0.02560
$F_A(Q_{13}^2)$	-0.4485	-0.4485	0.02842
$F_A(Q_{14}^2)$	-0.4243	-0.4243	0.02975
$F_A(Q_{15}^2)$	-0.4020	-0.4020	0.03154
$F_A(Q_{16}^2)$	-0.3794	-0.3794	0.03336

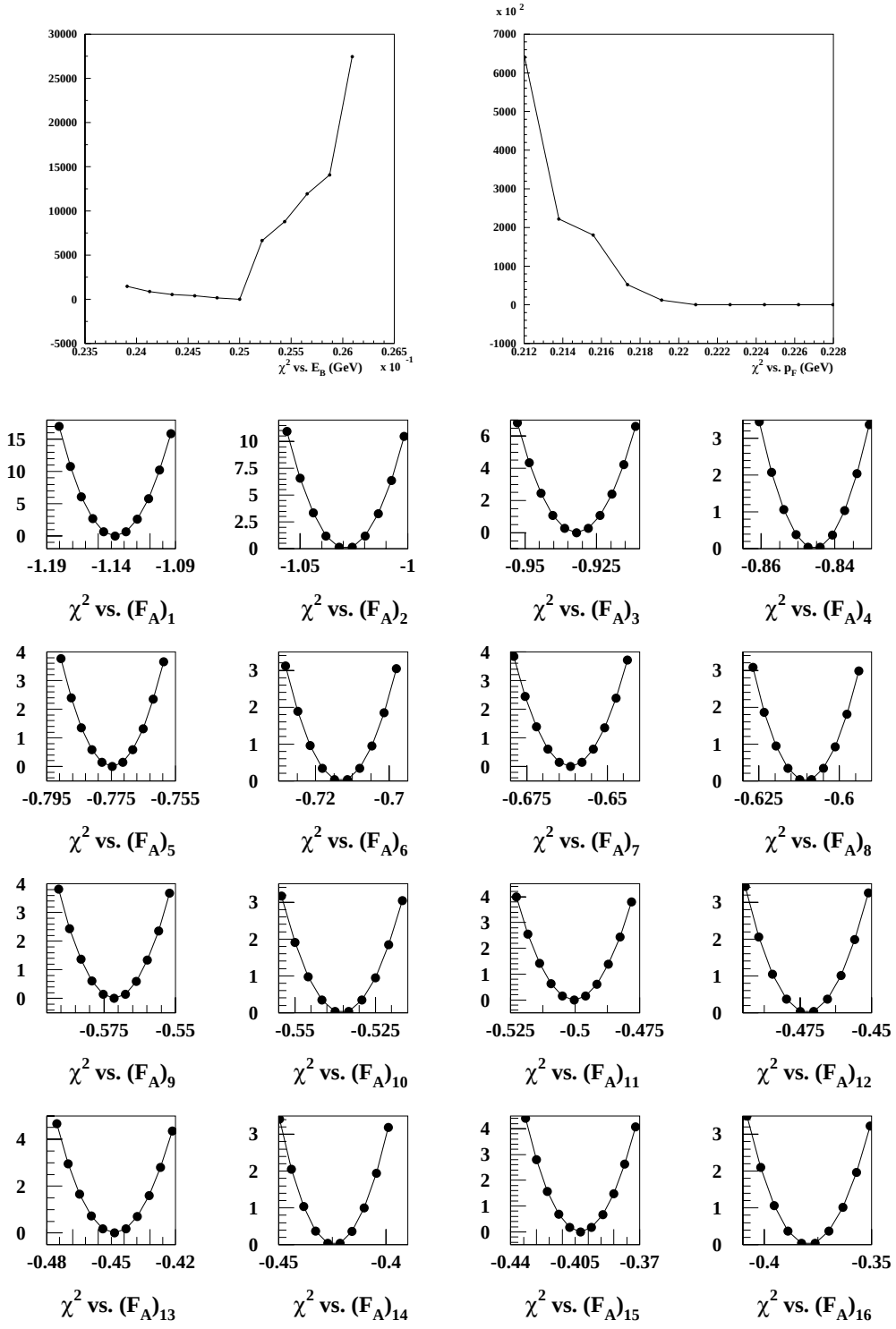

Figure 6.13: *χ^2 function value vs. fit parameter value for a fit with statistically identical "fake data" and Monte Carlo samples. Top left: χ^2 vs. E_B (GeV). Top right: χ^2 vs. p_F (GeV). Bottom: χ^2 vs. F_A in Q^2 bins.*

Table 6.10: *Effect of Q^2 reconstruction smearing after a "fake data" fit with statistically identical "fake data" and Monte Carlo sets; both have the statistics of the data. $\overline{Q^2_{REC}}$ and $\overline{Q^2_{GEN}}$ are the average reconstructed and generated Q^2 in each Q^2_{REC} bin respectively. $F_A(\overline{Q^2_{GEN}})$ is the dipole-assumption value of F_A evaluated at the average Q^2_{GEN} in each Q^2_{REC} bin, and $\overline{F_A}(Q^2_{GEN})$ is the average of all of the F_A values, calculated at the Q^2_{GEN} of each event, in a given Q^2_{REC} bin.*

Q^2_{REC} *bin #*	$\overline{Q^2_{REC}}$	$\overline{Q^2_{GEN}}$	*r.m.s.* Q^2_{GEN}	$F_A(\overline{Q^2_{GEN}})$	$\overline{F_A}(Q^2_{GEN})$	$\frac{\overline{F_A}(Q^2_{GEN})}{F_A(\overline{Q^2_{GEN}})}$
1	0.031	0.060	0.085	-1.137	-1.145	1.009
2	0.094	0.121	0.076	-1.029	-1.028	1.007
3	0.156	0.181	0.068	-0.932	-0.932	1.008
4	0.219	0.243	0.080	-0.846	-0.847	1.010
5	0.281	0.300	0.090	-0.775	-0.779	1.012
6	0.344	0.357	0.097	-0.713	-0.718	1.013
7	0.406	0.411	0.108	-0.661	-0.668	1.015
8	0.469	0.471	0.118	-0.610	-0.618	1.016
9	0.531	0.522	0.124	-0.571	-0.579	1.017
10	0.594	0.573	0.134	-0.535	-0.544	1.019
11	0.656	0.629	0.139	-0.500	-0.509	1.019
12	0.719	0.678	0.151	-0.473	-0.482	1.021
13	0.781	0.724	0.149	-0.449	-0.457	1.020
14	0.844	0.773	0.168	-0.424	-0.434	1.024
15	0.906	0.824	0.161	-0.402	-0.410	1.021
16	0.969	0.878	0.168	-0.379	-0.388	1.021

best-fit values of F_A are reported at the average generated Q^2 in each reconstructed Q^2 bin. This quantity is calculated at each iteration of the fit, since the CCQE cross section parameters which are varied in the course of minimization can affect dN/dQ^2.

Both event reconstruction and nuclear interactions contribute to the Q^2 smearing. The event reconstruction smearing in angle and lepton energy can be measured in data and compared with Monte Carlo using the muon tracker calibration system, as shown in figure 3.27. Nuclear interactions contribute to the smearing because F_A is part of the free-nucleon CCQE cross section, and therefore interactions of outgoing particles within the nucleus may change the kinematics. This analysis provides a gross check of the MiniBooNE nuclear model in that the χ^2/ndf measures the overall level of agreement between the simulation and the data in terms of high-level reconstructed quantities, however, there is no analogous calibration source to the muon tracker for nuclear interactions. As a consequence, this $F_A(Q^2)$ (and m_A) measurement *assumes* the MiniBooNE model for nuclear effects, and uses the MiniBooNE Monte Carlo to calculate the mapping from the generated event kinematics to a reconstructed Q^2. Fortunately, Q^2 smearing has a small impact on this measurement, as is shown by the success of the fits to "fake data" in extracting the CCQE cross section parameters used to generate the "fake data".

Another worrysome possibility with smearing is that it may be asymetric, for example, in the case of a steeply changing F_A distribution, smearing may push more events into a bin than out of it. To quantify the importance of this effect, table 6.10 compares the value of $F_A(Q^2)$ evaluated at the average generated Q^2 ($\overline{Q^2_{GEN}}$) in each Q^2_{REC} bin with $F_A(Q^2_{GEN})$ averaged over all events in a given Q^2_{REC} bin. The difference between these two is at the level of a few % for all Q^2_{REC} bins. Therefore, this effect is neglected in the following.

The next closure test of the analysis method is to fit statistically independent

Table 6.11: *Statistically independent "fake data fit" results as a function of the number of Monte Carlo events. "$F_A(Q_1^2)$" refers to the value of F_A in reconstructed Q^2 bin #1; the "MC value" column lists the value of each parameter used to generate the "fake data"; the "2M best-fit" column shows the best-fit parameter values for a Monte Carlo set corresponding to 2×10^6 events with no cuts.*

parameter name	*MC value*	*2M best-fit*	*4M best-fit*	*6M best-fit*	*8M best-fit*	*oscillated 8M best-fit*
E_B (GeV)	0.0250	0.0250	0.0250	0.0250	0.0251	0.0250
p_F (GeV)	0.2200	0.2200	0.2200	0.2200	0.2202	0.2200
$F_A(Q_1^2)$	-1.1371	-1.1057	-1.1099	-1.1159	-1.1203	-1.0926
$F_A(Q_2^2)$	-1.0289	-1.0621	-1.0650	-1.0602	-1.0519	-1.0279
$F_A(Q_3^2)$	-0.9321	-0.9354	-0.9298	-0.9318	-0.9352	-0.9057
$F_A(Q_4^2)$	-0.8456	-0.8607	-0.8682	-0.8668	-0.8632	-0.8572
$F_A(Q_5^2)$	-0.7747	-0.7592	-0.7582	-0.7573	-0.7581	-0.7534
$F_A(Q_6^2)$	-0.7131	-0.7150	-0.7138	-0.7172	-0.7174	-0.7123
$F_A(Q_7^2)$	-0.6614	-0.6515	-0.6533	-0.6551	-0.6565	-0.6573
$F_A(Q_8^2)$	-0.6104	-0.5992	-0.5944	-0.5948	-0.5977	-0.6028
$F_A(Q_9^2)$	-0.5715	-0.5695	-0.5669	-0.5675	-0.5690	-0.5766
$F_A(Q_{10}^2)$	-0.5354	-0.5423	-0.5387	-0.5387	-0.5447	-0.5541
$F_A(Q_{11}^2)$	-0.5005	-0.5056	-0.5074	-0.5065	-0.5017	-0.5141
$F_A(Q_{12}^2)$	-0.4726	-0.4466	-0.4569	-0.4597	-0.4657	-0.4790
$F_A(Q_{13}^2)$	-0.4485	-0.4198	-0.4318	-0.4288	-0.4295	-0.4446
$F_A(Q_{14}^2)$	-0.4243	-0.4531	-0.4401	-0.4412	-0.4450	-0.4603
$F_A(Q_{15}^2)$	-0.4020	-0.4056	-0.3972	-0.3980	-0.4041	-0.4202
$F_A(Q_{16}^2)$	-0.3794	-0.3701	-0.3800	-0.3753	-0.3742	-0.3905
χ^2	N/A	438	277	257	222	313

"fake data," and to determine what number of Monte Carlo statistics are sufficient. The results of this study are summarized in table 6.11. As with the m_A analysis, the Monte Carlo set corresponding to 8×10^6 events before cuts appears to have sufficient statistics since the χ^2/ndf has approximately the expected value once the number of Monte Carlo events exceeds 6×10^6. The resulting best-fit parameters are in good agreement with those used to generate the "fake data," therefore one can conclude that the closure test is successful and the analysis method is reasonably free of bias.

The best fit values of F_A vs. $\overline{Q^2_{GEN}}$ obtained from fitting the 8×10^6 Monte Carlo event set to statistically independent "fake data," with the statistics of the real data, are shown in the left panel of figure 6.14, compared with the Monte Carlo input F_A vs. $\overline{Q^2_{GEN}}$ values. The χ^2/ndf of the fit is 222/233, which has a probability of 68.6%. Fitting the dipole form to the fake data best fit F_A vs. $\overline{Q^2_{GEN}}$ results in $F_A(Q^2 = 0) = -1.2674$ and $m_A = 1.043$ with a χ^2/ndf of 1.29/14. The total χ^2 in each Q^2_{REC} bin i, which is a sum of the χ^2 contribution from each $E_{\nu,REC}$ bin j in Q^2_{REC} bin i, is shown in the right panel of figure 6.14. The $E_{\nu,REC}$ distributions in each Q^2_{REC} bin, which are used in the fit χ^2 function, are shown in figures 6.15 and 6.16 before and after the fit, compared with the ν_μ CCQE "fake data" points with statistical errors.

Since the F_A fits use the $E_{\nu,REC}$ distribution, it is especially important to determine the sensitivity of the analysis to an oscillation signal in the data. Further, the F_A fit results are not used to tune the MiniBooNE Monte Carlo to avoid any possibility of introducing bias to the oscillation analyses. This study is done in exactly the same way as for the m_A analysis: the maximum allowed ν_μ disappearance signal is introduced into the "fake data," which is fit with the high statistics central value Monte Carlo set. The $E_{\nu,REC}$ distribution in each Q^2_{REC} bin is shown in figure 6.17, compared with the no-oscillation case, absolutely normalized. The effect of the oscil-

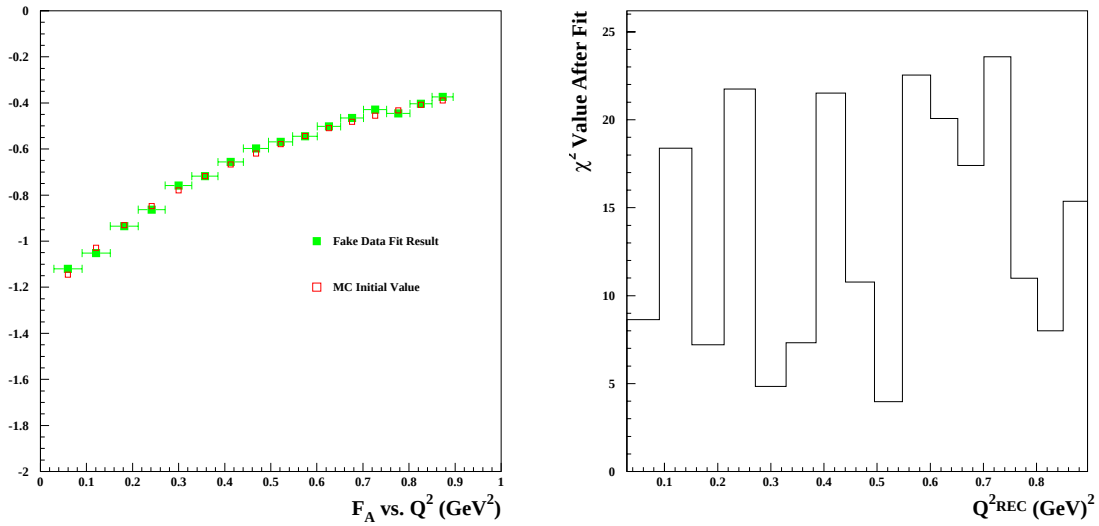

Figure 6.14: *Left: F_A before (red, open squares) and after (green, solid squares) fitting "fake data" with Monte Carlo vs. Q^2 (GeV^2). Right: χ^2 value vs. reconstructed Q^2 (GeV^2) at the best-fit point.*

lation signal is clearly visible, however, as for m_A, once the Monte Carlo is normalized to the data (or "fake data"), the difference between the oscillated and un-oscillated spectra is negligble. Figure 6.18 shows this comparison. The best-fit parameters for the oscillated case are compared with the un-oscillated "fake data" result in the last two columns of table 6.11. These two cases agree within the systematic errors on the fit parameters, shown in table 6.14, and therefore the conclusion of this study is that oscillations do not bias this analysis.

Finally, the ν_μ CCQE data set is fit with the high statistics central value Monte Carlo set. The resulting best-fit parameters and their fit errors are summarized in the first two columns of table 6.12. The χ^2 value at the minimum is 269, to be compared with the 366 degrees of freedom, of which 233 contribute to the χ^2 function. The probability for $\chi^2/ndf = 269/233$ is 0.053. The χ^2 functions about the parameter minima are shown in figure 6.20. These distributions are roughly

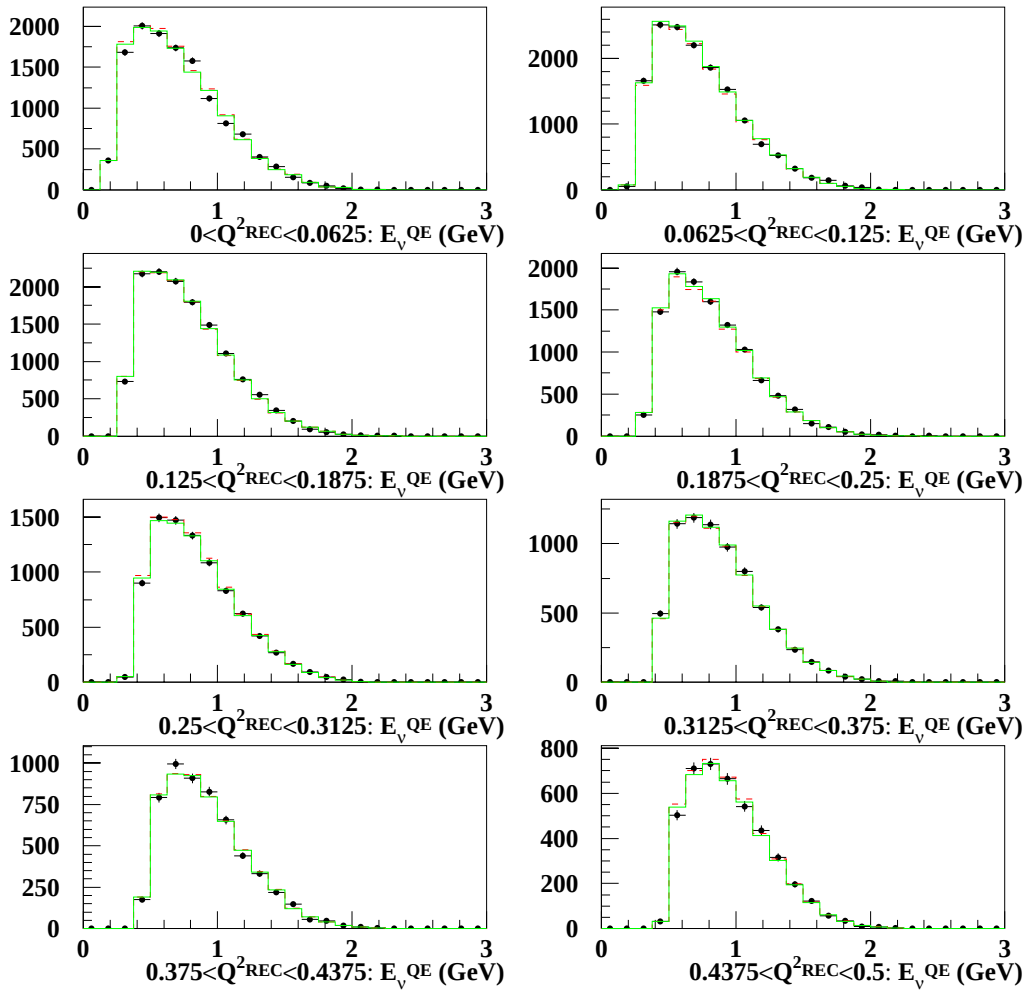

Figure 6.15: *Number of events vs. reconstructed neutrino energy (GeV) in each reconstructed Q^2 bin before (red, dashed line) and after (green, solid line) fitting for CCQE cross section parameters. The ν_μ CCQE "fake data" (black points) with statistical errors are superimposed.*

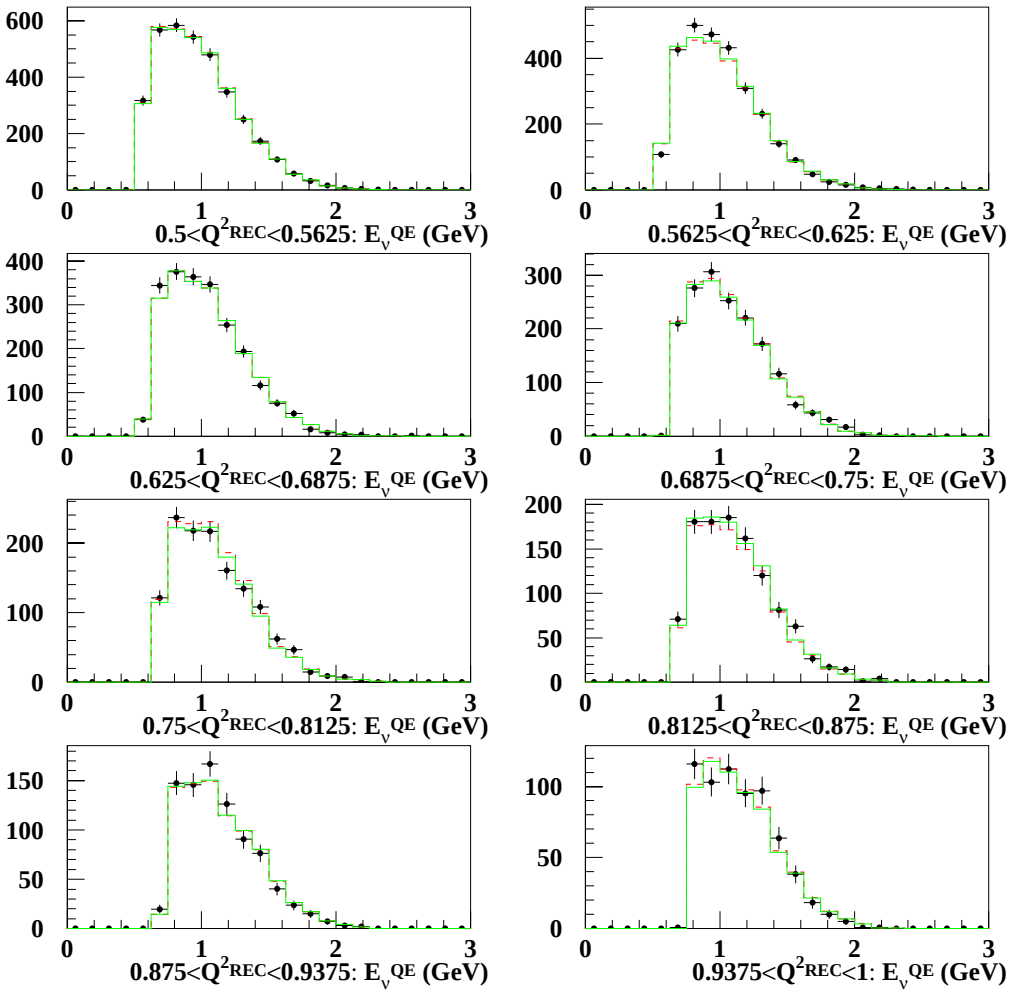

Figure 6.16: *Number of events vs. reconstructed neutrino energy (GeV) in each reconstructed Q^2 bin before (red, dashed line) and after (green, solid line) fitting for CCQE cross section parameters. The ν_μ CCQE "fake data" (black points) with statistical errors are superimposed.*

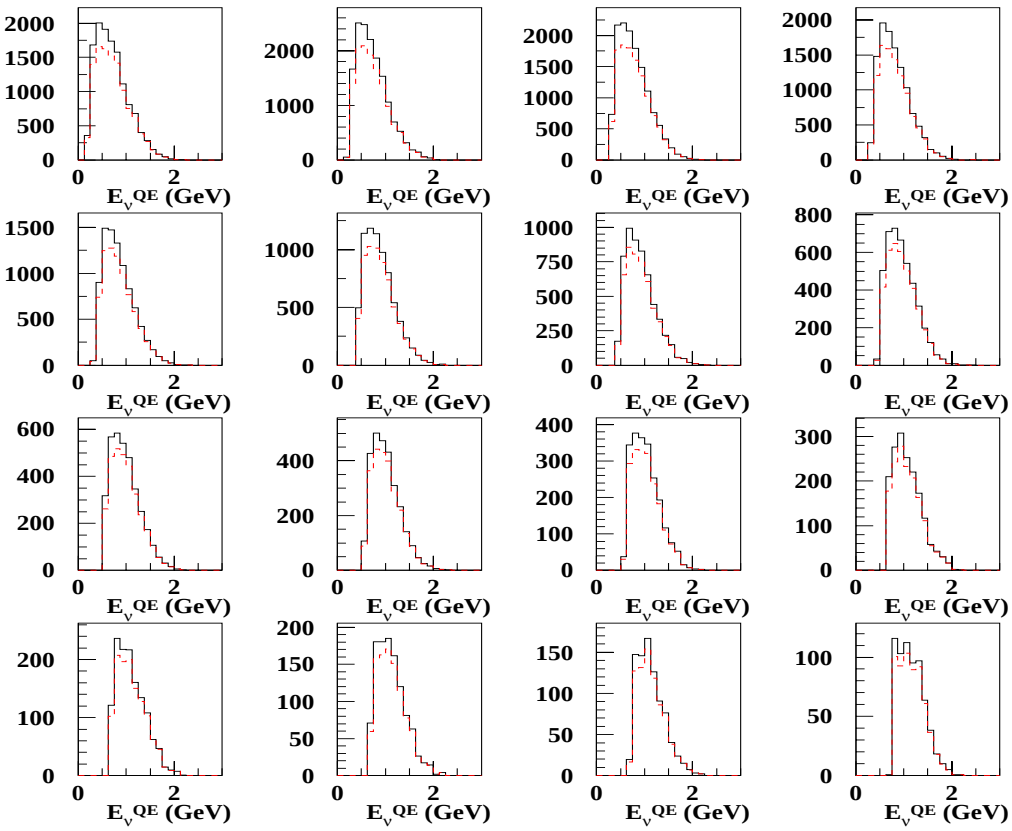

Figure 6.17: *Number of Monte Carlo events vs. reconstructed E_ν (GeV) in each Q^2_{REC} bin for oscillated (red, dashed line) and un-oscillated (black, solid line) "fake data" with the statistics of the data. The number of Monte Carlo events is absolutely normalized to protons on target.*

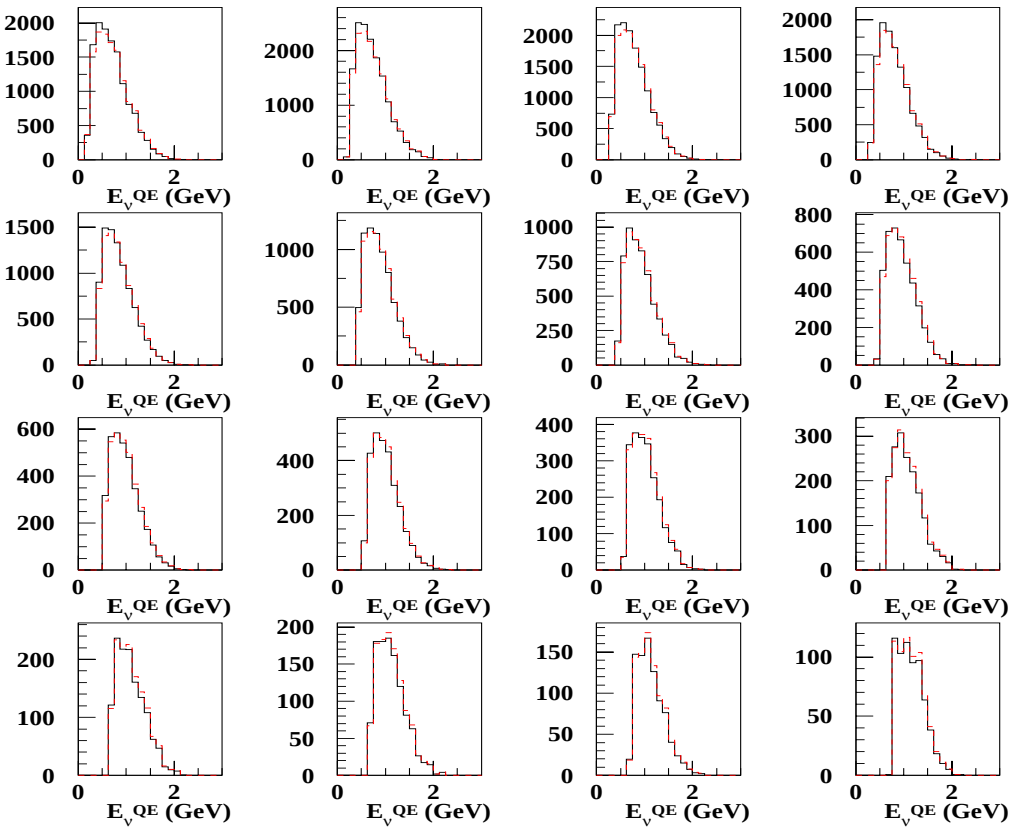

Figure 6.18: *Number of Monte Carlo events vs. reconstructed E_ν (GeV) in each Q^2_{REC} bin for oscillated (red, dashed line) and un-oscillated (black, solid line) "fake data" with the statistics of the data. The number of Monte Carlo events is normalized to the "fake data."*

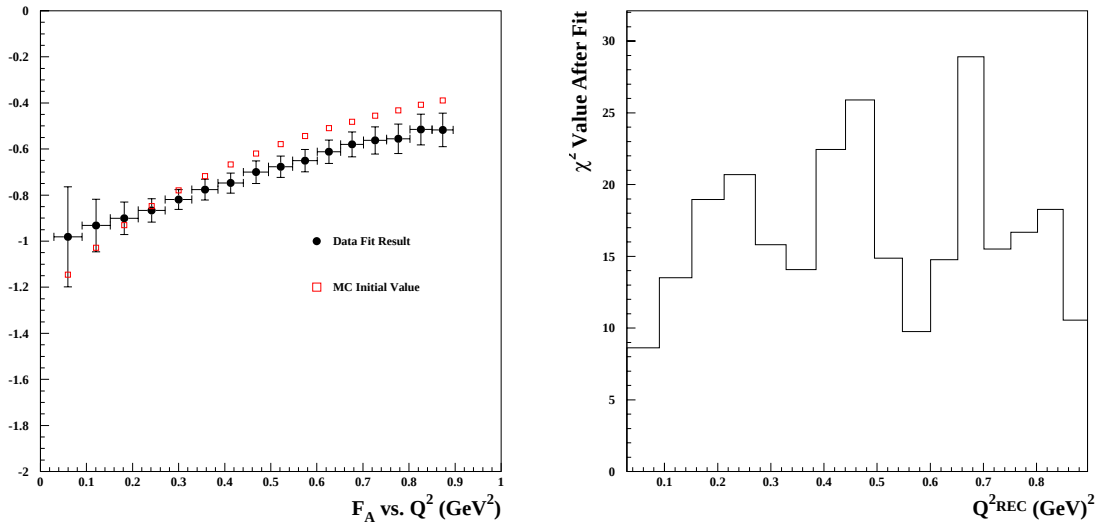

Figure 6.19: *Left: F_A before (red, open squares) and after (black, filled circles) fitting data with Monte Carlo vs. Q^2 (GeV^2). Right: χ^2 value vs. reconstructed Q^2 (GeV^2) at the best-fit point.*

parabolic for all parameters, which a good sign, however, the MINUIT fit convergence status parameter `ISTAT` equals 2 for the data fit, rather than 3 which is the sign of convergence with an accurate parameter covariance matrix. `ISTAT` equal to 2 indicates that the fit converged, however, the parameter covariance matrix at the minimum has been forced to be positive-definite by the addition of a constant to the diagonal elements. This often indicates that the fit errors may be unreliable due to a non-quadratic dependence of the χ^2 on the parameter errors at the minimum, or, parameters which are 100% correlated. In this case, the problem is that the correlation between E_B and p_F is 99.9%. In a fit where E_B is fixed to the best-fit value, 0.034 GeV, and the remaining 17 parameters are free in the fit, the resulting fit status is 3 and the fit converges to the same minimum, as is shown in the third column of table 6.12. The latter fit, with `ISTAT` equals 3, is used as the data result in the following.

Table 6.12: *Data fit results with 8 $\times 10^6$ Monte Carlo events before cuts. Case 1 has all parameters free in the fit, case 2 has E_B fixed to the best-fit value from case 1. "$F_A(Q_1^2)$" refers to the value of F_A in reconstructed Q^2 bin #1. The probability for χ^2/ndf = 269/233 is 0.053.*

parameter	*case 1 best-fit value*	*case 2 best-fit value*
E_B	0.0342 ± 7.6522	0.0341 ± N/A
p_F	0.2521 ± 0.0003	0.2518 ± 0.0180
$F_A(Q_1^2)$	-0.9856 ± 1.5002×10^{-5}	-0.9811 ± 0.2173
$F_A(Q_2^2)$	-0.9340 ± 1.5073×10^{-5}	-0.9320 ± 0.1140
$F_A(Q_3^2)$	-0.9020 ± 2.0358×10^{-5}	-0.9007 ± 0.0706
$F_A(Q_4^2)$	-0.8678 ± 3.4495×10^{-5}	-0.8667 ± 0.0509
$F_A(Q_5^2)$	-0.8203 ± 2.0989×10^{-5}	-0.8195 ± 0.0431
$F_A(Q_6^2)$	-0.7771 ± 1.5090×10^{-5}	-0.7765 ± 0.0452
$F_A(Q_7^2)$	-0.7484 ± 5.4379×10^{-5}	-0.7478 ± 0.0434
$F_A(Q_8^2)$	-0.7010 ± 4.9480×10^{-5}	-0.7005 ± 0.0492
$F_A(Q_9^2)$	-0.6777 ± 1.7115×10^{-5}	-0.6772 ± 0.0464
$F_A(Q_{10}^2)$	-0.6510 ± 1.8061×10^{-5}	-0.6506 ± 0.0480
$F_A(Q_{11}^2)$	-0.6125 ± 1.5010×10^{-5}	-0.6121 ± 0.0510
$F_A(Q_{12}^2)$	-0.5803 ± 1.6423×10^{-5}	-0.5799 ± 0.0544
$F_A(Q_{13}^2)$	-0.5631 ± 2.2581×10^{-5}	-0.5628 ± 0.0593
$F_A(Q_{14}^2)$	-0.5563 ± 1.5114×10^{-5}	-0.5559 ± 0.0638
$F_A(Q_{15}^2)$	-0.5156 ± 1.6700×10^{-5}	-0.5153 ± 0.0668
$F_A(Q_{16}^2)$	-0.5176 ± 1.5138×10^{-5}	-0.5173 ± 0.0724
χ^2	269	269
`ISTAT`	2	3

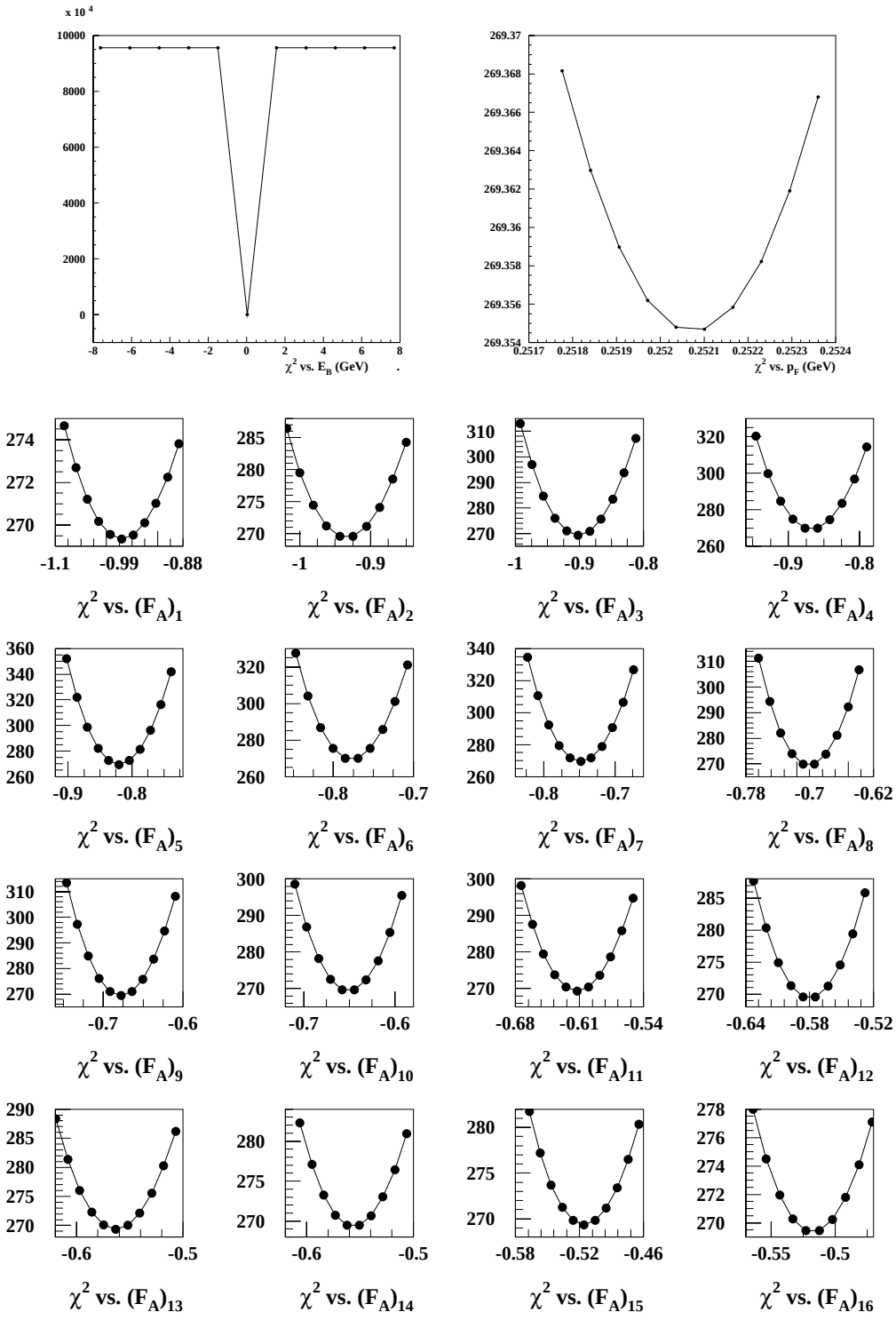

Figure 6.20: *χ^2 function value vs. fit parameter value for a fit to data. Top left: χ^2 vs. E_B (GeV). Top right: χ^2 vs. p_F (GeV). Bottom: χ^2 vs. F_A in Q^2 bins.*

The best fit values of F_A vs. $\overline{Q^2_{GEN}}$ obtained from fitting the ν_μ CCQE data are shown in the left panel of figure 6.19, compared with the Monte Carlo input F_A vs. $\overline{Q^2_{GEN}}$ values. Fitting the dipole form to the fake data best fit F_A vs. $\overline{Q^2_{GEN}}$ results in $F_A(Q^2 = 0) = -1.0942$ and $m_A = 1.3755$ with a χ^2/ndf of 0.4379/14. The total χ^2 in each Q^2_{REC} bin i, which is a sum of the χ^2 contribution from each $E_{\nu,REC}$ bin j in Q^2_{REC} bin i, is shown in the right panel of figure 6.19. The $E_{\nu,REC}$ distributions in each Q^2_{REC} bin, which are used in the fit χ^2 function, are shown in figures 6.21 and 6.22 before and after the fit, compared with the ν_μ CCQE data with statistical errors.

The normalization of the Monte Carlo in the fit is arbitrary, because at the start it is scaled to have the same total number of events as the data. This makes the overall normalization scale of the best-fit F_A values arbitrary as well, because the fit χ^2 function is balancing two effects: (i) the initial normalization of the data and Monte Carlo which is such that the $\chi^2 = 0$ when $m_A = 1.03$ and g_A = -1.2671, and, (ii) the increase in the number of events in the Monte Carlo as the slope of F_A is decreased (which corresponds to m_A being increased) as the fit attempts to match the data Q^2 distribution. Hence, as the slope of $F_A(Q^2)$ is decreased the best-fit $F_A(Q^2 = 0)$ is increased to preserve the same total number of events in data and Monte Carlo.

However, the normalization of F_A at $Q^2 = 0.0\ GeV^2$ is very precisely measured in neutron beta decay to be g_A = -1.2671 $\pm$ 0.0035 [45]. This constraint is not included in the F_A fits here because of the Monte Carlo normalization condition, and therefore the result in table 6.12 must be corrected by a scale factor to recover a physical value for $F_A(Q^2 = 0)$. This issue does not similarly affect the m_A fits because the value of $F_A(Q^2 = 0) = -1.2671$ is explicitly included via the dipole form factor and g_A. The ratio of the measured g_A to the best-fit $F_A(Q^2 = 0)$ is -1.2671/-1.0942 =

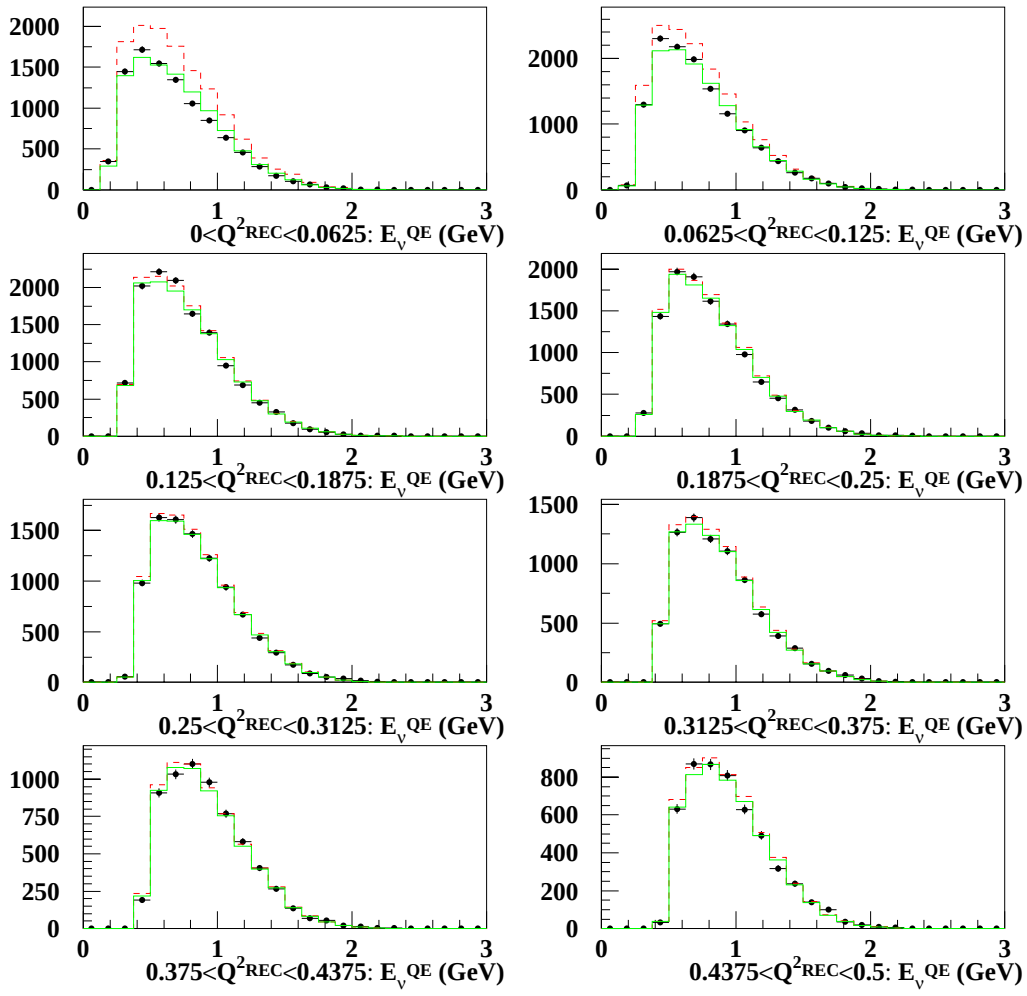

Figure 6.21: *Number of events vs. reconstructed neutrino energy (GeV) in each reconstructed Q^2 bin before (red, dashed line) and after (green, solid line) fitting for CCQE cross section parameters. The ν_μ CCQE data (black points) with statistical errors are superimposed.*

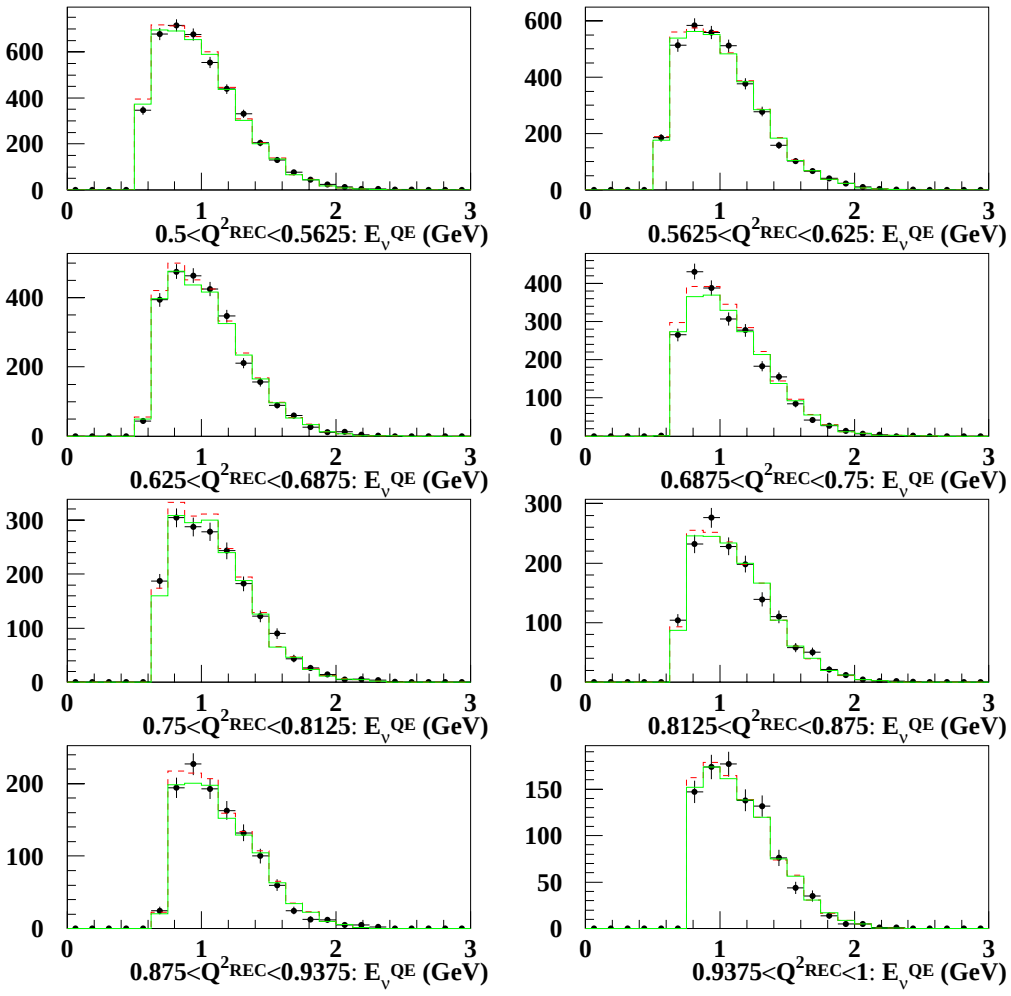

Figure 6.22: *Number of events vs. reconstructed neutrino energy (GeV) in each reconstructed Q^2 bin before (red, dashed line) and after (green, solid line) fitting for CCQE cross section parameters. The ν_μ CCQE data (black points) with statistical errors are superimposed.*

1.1580. The extrapolation to $Q^2 = 0.0$ uses the coefficients from the dipole fit to the best-fit F_A vs. Q^2 described above. It is interesting that this constant, which is based on a fit to the shapes of the kinematic distributions, goes in same direction as the normalization difference between data and the MiniBooNE Monte Carlo prediction discussed in chapter 4. The MiniBooNE F_A vs. Q^2 measurement in data is corrected by this scale factor, 1.158, in the following.

The systematic errors on the fit parameters are evaluated by fitting "fake data" with a "unisim" Monte Carlo sample, with a procedure identical to that of the m_A analysis. The difference between the best-fit parameters for central value Monte Carlo and each "unisim" fit are shown in tables E.4, E.5, and E.7 for the π^+ flux, neutrino interaction cross section, and detector response uncertainties respectively. These do not include parameter correlations. The systematic errors are summarized by source in table 6.13, as before including correlations between detector response simulation parameters but neglecting π^+ and neutrino interaction cross section parameter correlations. The contributions of the π^+ flux and neutrino interaction cross section uncertainties, which come primarily from the pion final state interaction model variations, are of similar sizes, ∼1-5%, and the detector response systematic error contribution is a bit larger, ∼5-10%. The total systematic error ranges from ∼10-15%; for comparison, the statistical errors contribute ∼5-10%.

The MiniBooNE $(F_A)_i$ result, which has been scaled to have $F_A(Q^2 = 0) = g_A$, is given in table 6.14. The total error is calculated by adding the systematic errors from the variations of simulation input parameters in quadrature with the statistical error from the data fit. The total F_A vs. Q^2 measurement uncertainty ranges from ∼10-20%, which the largest uncertainties for the lowest and highest Q^2 values.

The implications of the measurements in this chapter are that the Smith-Moniz CCQE cross section formalism, together with the dipole axial form factor and the

Table 6.13: *Systematic error contributions by source to the CCQE cross section parameters that are varied in the ($F_A(Q^2)$, E_B, p_F) fit. Errors are given as a percentage of the Monte Carlo values, in parentheses.*

parameter	*MC value*	π^+ *flux*	σ_ν	*detector response*
E_B	0.02500	0.00397 (15.869)	0.00667 (26.684)	0.00685 (27.401)
p_F	0.22000	0.00743 (3.378)	0.02996 (13.617)	0.03599 (16.359)
$F_A(Q_1^2)$	-1.13710	0.03215 (2.827)	0.13709 (12.056)	0.14371 (12.638)
$F_A(Q_2^2)$	-1.02890	0.02438 (2.370)	0.05337 (5.187)	0.09690 (9.418)
$F_A(Q_3^2)$	-0.93205	0.01561 (1.674)	0.04418 (4.740)	0.06894 (7.397)
$F_A(Q_4^2)$	-0.84561	0.01400 (1.656)	0.00982 (1.161)	0.06490 (7.675)
$F_A(Q_5^2)$	-0.77466	0.01313 (1.695)	0.01144 (1.477)	0.04965 (6.410)
$F_A(Q_6^2)$	-0.71310	0.01532 (2.148)	0.01605 (2.250)	0.05702 (7.996)
$F_A(Q_7^2)$	-0.66141	0.01713 (2.590)	0.02530 (3.825)	0.04442 (6.716)
$F_A(Q_8^2)$	-0.61044	0.02410 (3.949)	0.01699 (2.783)	0.05422 (8.882)
$F_A(Q_9^2)$	-0.57146	0.02306 (4.035)	0.01932 (3.381)	0.03364 (5.887)
$F_A(Q_{10}^2)$	-0.53542	0.02627 (4.906)	0.03093 (5.776)	0.04769 (8.906)
$F_A(Q_{11}^2)$	-0.50046	0.02710 (5.415)	0.02939 (5.873)	0.03843 (7.679)
$F_A(Q_{12}^2)$	-0.47262	0.02821 (5.969)	0.03961 (8.381)	0.03608 (7.634)
$F_A(Q_{13}^2)$	-0.44851	0.02540 (5.663)	0.03066 (6.835)	0.04547 (10.138)
$F_A(Q_{14}^2)$	-0.42434	0.02709 (6.384)	0.03513 (8.279)	0.05668 (13.358)
$F_A(Q_{15}^2)$	-0.40203	0.02739 (6.812)	0.02784 (6.925)	0.05398 (13.427)
$F_A(Q_{16}^2)$	-0.37942	0.03092 (8.150)	0.04978 (13.119)	0.05430 (14.311)

Table 6.14: *Data fit results and error analysis summary for E_B, p_F, and $(F_A)_i$ measurement. The data fit results $F_A \pm \delta(F_A)_{total}$ are normalized to g_A = -1.2671. The total error is the quadrature sum of the statistical and systematic errors.*

parameter	$F_A \pm \delta(F_A)_{total}$	*stat. error (%)*	*sys. error (%)*	*total error (%)*
E_B	0.0341 ± 0.0141	N/A	41.4086	41.4086
p_F	0.2518 ± 0.0572	7.1366	21.5511	22.7020
$F_A(Q_1^2)$	-1.1361 ± 0.2988	22.1486	14.1869	26.3026
$F_A(Q_2^2)$	-1.0792 ± 0.1696	12.2317	9.8716	15.7182
$F_A(Q_3^2)$	-1.0430 ± 0.1140	7.8383	7.6280	10.9373
$F_A(Q_4^2)$	-1.0036 ± 0.0988	5.8728	7.9094	9.8514
$F_A(Q_5^2)$	-0.9489 ± 0.0812	5.2593	6.7510	8.5578
$F_A(Q_6^2)$	-0.8991 ± 0.0923	5.8209	8.4653	10.2735
$F_A(Q_7^2)$	-0.8659 ± 0.0824	5.8036	7.5454	9.5192
$F_A(Q_8^2)$	-0.8111 ± 0.0986	7.0235	9.9241	12.1580
$F_A(Q_9^2)$	-0.7841 ± 0.0798	6.8517	7.5266	10.1782
$F_A(Q_{10}^2)$	-0.7533 ± 0.0964	7.3778	10.4631	12.8026
$F_A(Q_{11}^2)$	-0.7088 ± 0.0907	8.3319	9.7169	12.8000
$F_A(Q_{12}^2)$	-0.6715 ± 0.0922	9.3809	10.0301	13.7334
$F_A(Q_{13}^2)$	-0.6517 ± 0.1048	10.5366	12.1597	16.0897
$F_A(Q_{14}^2)$	-0.6437 ± 0.1229	11.4768	15.2597	19.0939
$F_A(Q_{15}^2)$	-0.5967 ± 0.1205	12.9633	15.4981	20.2049
$F_A(Q_{16}^2)$	-0.5990 ± 0.1307	13.9957	16.7426	21.8219

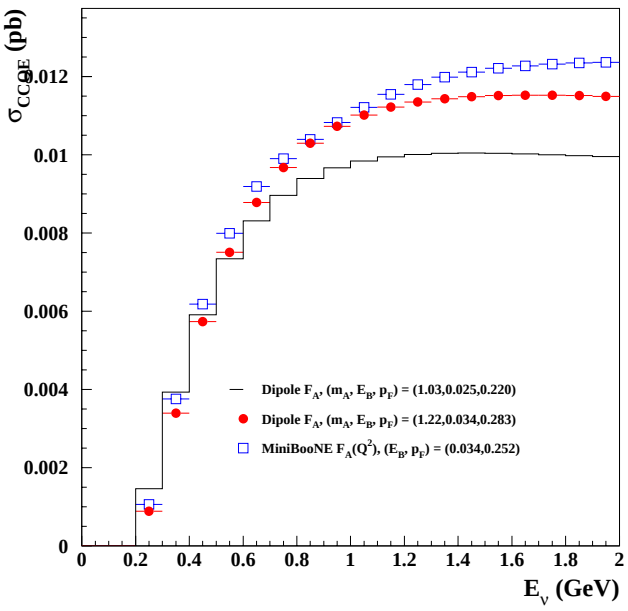

Figure 6.23: *Smith-Moniz CCQE cross section calculated with the world-average parameters, compared with calculations using the two MiniBooNE measurements. No uncertainties are shown.*

Fermi Gas model, describes the MiniBooNE data well, although different parameters from those measured with light-target data are preferred. The best-fit F_A vs. Q^2 prefer a much shallower slope than the dipole form evaluated with the world-average (m_A, E_B, p_F) values. A shallower slope corresponds to higher m_A values, in agreement with the trend of the m_A fit results.

The Smith-Moniz CCQE cross section calculated using the world-average CCQE parameters is compared in figure 6.23 with calculations using the two MiniBooNE measurements: (i) the best-fit (m_A, E_B, p_F) values, and (ii) the g_A-normalized best-fit ($(F_A)_i$, E_B, p_F) values. At the average MiniBooNE neutrino beam energy of 0.8 GeV, the cross sections calculated using the MiniBooNE measurements are in good agreement, and are $\sim$10% larger than the prediction using the world-average light-target values for m_A, E_B, and p_F.

Chapter 7

Oscillation Search

Two kinds of oscillation searches are possible at MiniBooNE: ν_μ disappearance, via $\nu_\mu \rightarrow \nu_x$ where $x \neq \mu$, and ν_e appearance, via $\nu_\mu \rightarrow \nu_e$. Theoretically, these two channels may probe different oscillation transitions, as in 3+1 or 3+2 models, where the LSND observation is posited to be a combination of $\nu_\mu \rightarrow \nu_s$ and $\nu_s \rightarrow \nu_e$ flavor oscillations. In the 3+1 case, the ν_e appearance search probes the product of the probabilities for these two processes, $P_{osc} \sim |U_{e4}|^2|U_{\mu 4}|^2$. In contrast, the ν_μ disappearance analysis is sensitive to $P_{osc} \sim |U_{\mu 4}|^2$, and therefore combining the two can add information about the underlying oscillation parameters. Experimentally, combining information from the ν_μ data set with the ν_e appearance analysis provides some reduction of the systematic errors for the ν_e search. As in chapter 5, the ν_μ data in MiniBooNE can be used to measure the ν_μ flux and constrain the uncertainty on the flux prediction for the intrinsic ν_e background. Similarly, the ν_μ CCQE data set can be used to extract information about the ν_e CCQE cross section, as in chapter 6. However, care must be taken to account for the possibility of ν_μ disappearance. A straightforward way to address this and incorporate the ν_μ experimental constraints on the systematic errors for the ν_e appearance search is to perform a combined oscil-

lation fit for ν_μ disappearance and ν_e appearance in MiniBooNE.

7.1 Method

The analysis described here focuses on the second aspect of the combined ν_e and ν_μ fit, which is to reduce the systematic errors associated with the ν_e appearance search. For this purpose, a general two-neutrino model is employed, in which the $\nu_\mu \rightarrow \nu_e$ and $\nu_\mu \rightarrow \nu_x$ oscillation parameters are completely independent and specified by four experimental parameters, $(\Delta m^2_A,\ sin^2 2\theta_{\mu e})$ and $(\Delta m^2_D,\ sin^2 2\theta_{\mu x})$. For simplicity, the subscript on Δm^2 is dropped in the following. Because of these model assumptions, this analysis seeks to measure "effective" oscillation parameters which describe the MiniBooNE data under this hypothesis, rather than the true, fundamental mass splittings and mixing angles found in nature.

To search for oscillations, the neutrino energy distribution is compared in data and Monte Carlo, where the Monte Carlo contains an oscillation hypothesis. In this two-neutrino model, the number of detected ν_μ events $N^{det}_{\nu_\mu}$ in Monte Carlo as a function of true neutrino energy E_ν depends on the oscillation parameters as

$$\begin{aligned} N^{det}_{\nu_\mu}(E_\nu) &= N^{prod}(E_\nu) \times P(\nu_\mu \rightarrow \nu_\mu) = N^{prod}(E_\nu) \times \Big[1 - P(\nu_\mu \rightarrow \nu_x)\Big] \\ &= N^{prod}(E_\nu) \times \Big[1 - sin^2 2\theta_{\mu x}\ sin^2\Big(\frac{1.27\Delta m^2 L_\nu}{E_\nu}\Big)\Big] \end{aligned} \quad (7.1)$$

where $N^{prod}(E_\nu)$ is the number of ν_μ events that would be detected if the ν_μ flux at the detector were equal to the ν_μ flux at production (before oscillations may occur), L_ν is the distance traveled by the ν_μ between production and detection in km, and E_ν is the energy of the ν_μ in GeV. For ν_e appearance, the number of detected ν_e Monte Carlo events $N^{det}_{\nu_e}$ as a function of neutrino energy E_ν depends on the oscillation parameters as

$$N^{det}_{\nu_e}(E_\nu) = N^{prod}(E_\nu) \times P(\nu_\mu \rightarrow \nu_e) \quad (7.2)$$

$$= N^{prod}(E_\nu) \times sin^2 2\theta_{\mu e}\ sin^2\Big(\frac{1.27\Delta m^2 L_\nu}{E_\nu}\Big).$$

The oscillation signal is at a maximum when

$$\Big(\frac{1.27\Delta m^2 L_\nu}{E_\nu}\Big) = \frac{\pi}{2} \tag{7.3}$$

which occurs when

$$\Delta m^2 = \frac{\pi}{2} \times \Big(\frac{E_\nu}{1.27 L_\nu}\Big). \tag{7.4}$$

For MiniBooNE, with $\langle E_\nu \rangle \sim 0.8\ GeV$ and $\langle L_\nu \rangle \sim 0.54\ km$, this occurs at $\sim$1.8 eV^2.

Since the true neutrino energy is unknown in the data, the χ^2 function must compare the data and Monte Carlo as a function of reconstructed neutrino energy, E_ν^{QE}. Finite energy resolution will diminish the oscillation sensitivity of the experiment because above some Δm^2 value, the oscillation frequency is too high for the experiment to resolve individual oscillation peaks in the detected neutrino energy spectrum. The distance between oscillation maxima is

$$\lambda = \frac{2\pi E_\nu}{1.27\Delta m^2}. \tag{7.5}$$

For MiniBooNE, the neutrino energy resolution is $\sim$10% at 1.0 GeV for signal events, shown in figure 4.10, and therefore the experiment loses sensitivity to the energy spectrum distortion due to oscillations when the distance between oscillation maxima is less than 0.1 GeV, which occurs at $\Delta m^2 \sim 50\ eV^2$. In practice, this threshold is lower because there are systematic errors which affect the energy spectrum.

A basic oscillation fit minimizes this function:

$$\chi^2 = \sum_i \Big(\frac{N_i^{Data} - N_i^{MC}(\Delta m^2, sin^2 2\theta)}{\sigma_i}\Big)^2 \tag{7.6}$$

where i indexes E_ν^{QE} bins, N_i^{Data} is the number of events in the data in reconstructed neutrino energy bin i, $N_i^{MC}(\Delta m^2, sin^2 2\theta)$ is the number of events predicted in the

Monte Carlo under an oscillation hypothesis with $(\Delta m^2, sin^2 2\theta)$, and σ_i is the uncertainty on the predicted number of events with no oscillations. The uncertainty σ_i is defined in this way to minimize the effects of Poisson statistics. In the sensitivity calculations here, the data are really "fake data" with no oscillation signal, that is, $N_i^{Data} = N_i^{prod}$ calculated in the Monte Carlo.

The limiting cases of high and low Δm^2 can be used to verify oscillation sensitivity fit results. This kind of calculation seeks to address the question of what oscillation parameter space an experiment can exclude when no signal is present, given its systematic and statistical uncertainties. Therefore, the data are assumed to have no signal, and the experimental systematic errors are assesed on the Monte Carlo prediction. In this case, the value of $sin^2 2\theta$ at the best-fit point is 0.0, the value of the χ^2 function at the minimum equals 0.0, and the 1σ limit value $sin^2 2\theta_{limit}$ occurs when $\Delta\chi^2 = \chi - \chi^2_{min} = 1$:

$$\Delta\chi^2 \;=\; \left(\frac{N_i^{prod} - N_i^{det}(\Delta m^2, sin^2 2\theta)}{\sigma_i^{prod}}\right)^2 = 1 \tag{7.7}$$

At high Δm^2, the oscillatory term $sin^2\left(\frac{1.27\Delta m^2 L_\nu}{E_\nu}\right)$ averages to $\frac{1}{2}$, and so the oscillation probability reduces to $P_{osc} \simeq sin^2 2\theta \times \frac{1}{2}$. At low Δm^2, the frequency term is very small, and the Taylor expansion of $sin^2\left(\frac{1.27\Delta m^2 L_\nu}{E_\nu}\right) \simeq \left(\frac{1.27\Delta m^2 L_\nu}{E_\nu}\right)^2$. In this case, the oscillation probability is $P_{osc} \simeq sin^2 2\theta \times \left(\frac{1.27\Delta m^2 L_\nu}{E_\nu}\right)^2$.

For ν_μ disappearance, N^{det} is simply related to N^{prod} via $N^{det} = N^{prod} \times (1 - P_{osc})$. This is because to first order there is no background to the ν_μ disappearance analysis since the beam is composed of 99.5% ν_μ flavor neutrinos. Making this substitution, and summing over all energy bins i:

$$\Delta\chi^2 \;=\; \chi^2 - \chi^2_{\rm min} = = \chi^2 \;=\; \left(\frac{N^{prod} - N^{prod} \times [1 - P_{osc}]}{\sigma^{prod}}\right)^2 \tag{7.8}$$

The sum over all energy bins makes this a "counting-only" experiment, since no information about the energy spectrum is used. Assuming a fractional normalization

systematic error on N^{prod} of $\Delta f^{prod} = \frac{\delta N^{prod}}{N^{prod}}$, the uncertainty σ^{prod} is the quadrature sum of the statistical and systematic errors,

$$(\sigma^{prod})^2 = (\sqrt{N^{prod}})^2 + (\Delta f^{prod} \times N^{prod})^2.$$

Now,

$$\Delta\chi^2 = \frac{(N^{prod} - N^{prod} \times [1 - P_{osc}])^2}{N^{prod} + (\Delta f^{prod} \times N^{prod})^2} = \frac{(N^{prod})^2}{(N^{prod})^2} \frac{(1 - [1 - P_{osc}])^2}{(\frac{1}{N^{prod}} + (\Delta f^{prod})^2)} \quad (7.9)$$

Making the approximation that the statistical error is much smaller than the systematic error, $\frac{1}{N^{prod}} \ll (\Delta f^{prod})^2$,

$$\Delta\chi^2 = \frac{(P_{osc})^2}{(\Delta f^{prod})^2} \quad (7.10)$$

So, the limit value of $sin^2 2\theta$ at high Δm^2 occurs at

$$sin^2 2\theta_{limit} = 2 \times \Delta f^{prod}, \quad (7.11)$$

For example, a normalization uncertainty of 10% would result in a $sin^2 2\theta_{limit}$ value of 0.2. The "counting" experiment sensitivity at high Δm^2 is the true sensitivity, since no energy spectrum deformation due to oscillations is present when the oscillation probability averages to $sin^2 2\theta \times \frac{1}{2}$. At low Δm^2 this is not the case, because energy spectrum distortion adds information. For the "counting" experiment at low Δm^2, $P_{osc} \sim sin^2 2\theta \times \left(\frac{1.27\Delta m^2 L_\nu}{E_\nu}\right)^2$, and so the "counting-only" experiment limit value is

$$sin^2 2\theta_{limit} = \frac{\Delta f^{prod}}{\left(\frac{1.27\Delta m^2 L_\nu}{E_\nu}\right)^2} \quad (7.12)$$

At $\Delta m^2 = 1.0\ eV^2$, which is allowed for $0.05 < sin^2 2\theta < 0.35$ in the models with one sterile neutrino shown in figure 1.2, the MiniBooNE limit value would be $sin^2 2\theta_{limit} = 0.14$, for $\Delta f^{prod} = 10\%$ and $E_\nu = 0.8\ GeV$. So, with 10% normalization uncertainty, a MiniBooNE disappearance search would have sensitivity to a part of this allowed

region, $0.14 < sin^2 2\theta_{\mu x} < 1.0$. The minimum Δm^2 value that a "counting" experiment is sensitive to is determined by when $sin^2 2\theta_{limit}$ approaches 1.0. Substituting $sin^2 2\theta_{limit} = 1.0$ and solving for Δm^2, the limit value is

$$\Delta m^2_{min} \;=\; \sqrt{\Delta f^{prod} \times \Big(\frac{E_\nu}{1.27 L_\nu}\Big)^2} \tag{7.13}$$

In the test case described above, $\Delta m^2_{limit} = 0.37\ eV^2$. However, since the energy spectrum at low Δm^2 adds information to the fit, a "counting" +"energy fit" analysis can have a lower Δm^2_{limit} value.

For the case of ν_e appearance, N^{det} is a sum of the oscillation signal events *and* unoscillated background events. So, N^{det} is related to N^{prod} via $N^{det} = N^{prod} P_{osc} + N^{bgnd}$. The expected number of events in the absence of oscillations, N^{Data}, is just N^{bgnd}, and so the error on the null expectation is $\sigma \;=\; \sqrt{N^{bgnd} + (\Delta f^{prod} \times N^{bgnd})^2}$. Making these substitutions into the χ^2 formula in equation 7.6, and summing over all energy bins i for a "counting-only" experiment:

$$\begin{aligned} \Delta\chi^2 \;&=\; \chi^2 - \chi^2_{\min} \;=\; \chi^2 \;=\; \Big(\frac{N^{bgnd} - (N^{prod} \times P_{osc} + N^{bgnd})}{\sigma^{bgnd}}\Big)^2 \\ &=\; \frac{(-N^{prod} \times P_{osc})^2}{N^{bgnd} + (\Delta f^{prod} \times N^{bgnd})^2} \;=\; \frac{(-N^{prod})^2}{(N^{bgnd})^2} \frac{P^2_{osc}}{\frac{1}{N^{bgnd}} + (\Delta f^{prod})^2} \end{aligned} \tag{7.14}$$

When $\Delta\chi^2 = 1$,

$$P_{osc} \;=\; \frac{\sqrt{\frac{1}{N^{bgnd}} + (\Delta f^{prod})^2}}{(N^{prod}/N^{bgnd})}$$

In the high Δm^2 limit, $P_{osc} = sin^2 2\theta \times \frac{1}{2}$, and so

$$sin^2 2\theta_{limit} \;=\; 2 \times \frac{\sqrt{\frac{1}{N^{bgnd}} + (\Delta f^{prod})^2}}{(N^{prod}/N^{bgnd})} \tag{7.15}$$

As expected, the smaller N^{bgnd} and the error are, the better the sensitivity. For a test case with $\Delta f^{prod} = 10\%$, $(N^{bgnd}/N^{prod}) = 1\%$, and $N^{bgnd} = 500$ events, the limit value would be $sin^2 2\theta_{limit} = 0.002$. For the "counting" experiment at low Δm^2,

$$sin^2 2\theta_{limit} \;=\; \frac{1}{\Big(\frac{1.27 \Delta m^2 L_\nu}{E_\nu}\Big)^2} \times \frac{\sqrt{\frac{1}{N^{bgnd}} + (\Delta f^{prod})^2}}{(N^{prod}/N^{bgnd})} \tag{7.16}$$

which would be $sin^2 2\theta_{limit} = 0.008$ at $\Delta m^2 = 0.4\ eV^2$. This sensitivity would cover the region of oscillation parameter space allowed by the LSND result. The minimum accessible Δm^2 in the ν_e appearance "counting" experiment is

$$\Delta m^2_{min} \;=\; \sqrt{\Big(\frac{E_\nu}{1.27 L_\nu}\Big)^2 \times \frac{\sqrt{\frac{1}{N^{bgnd}} + (\Delta f^{prod})^2}}{(N^{prod}/N^{bgnd})}} \tag{7.17}$$

which is $0.037\ eV^2$. As for the ν_μ disappearance, the smaller (E_ν/L_ν) is, the lower Δm^2_{min} can be.

In practice, the systematic errors are much more complicated than a simple normalization uncertainty like Δf^{prod}. To include uncertainties that are correlated as a function of energy, an error matrix $\mathcal{M}$ is introduced into the χ^2 function:

$$\chi^2 \;=\; \sum_i \sum_j \Big(N_i^{Data} - N_i^{MC}(\Delta m^2, sin^2 2\theta)\Big) \mathcal{M}^{-1}_{i,j} \Big(N_j^{Data} - N_j^{MC}(\Delta m^2, sin^2 2\theta)\Big) \tag{7.18}$$

where i and j index E_ν bins. The error matrix $\mathcal{M}_{i,j}$ is the total output variable systematic error matrix calculated in chapter 4, where the term "output variable" refers to the fact that the matrix is calculated in bins of neutrino energy rather than simulation input parameters, such as the Sanford-Wang π^+ prediction c_i. If $\mathcal{M}_{i,j}$ has no off-diagonal elements correlating different energy bins, then the χ^2 reduces to the form in equation 7.6. Correlations between energy bins can either increase or decrease the total systematic error, depending on the effect of each systematic source.

Both the ν_e appearance and ν_μ disappearance analyses here use 30 reconstructed neutrino energy bins from 0.0 to 3.0 GeV. When an "appearance-only" or "disappearance-only" fit is described, the dimension of $\mathcal{M}_{i,j}$ is 30×30 and the vector $\Big(N_i^{Data} - N_i^{MC}(\Delta m^2, sin^2 2\theta)\Big)$ has 30 elements. For the "combined" fit, the dimension of $\mathcal{M}_{i,j}$ is 60×60, and the first 30 elements of the vector $\Big(N_i^{Data} - N_i^{MC}(\Delta m^2, sin^2 2\theta)\Big)$ are the ν_e bins and the second 30 elements are the ν_μ bins. The `MINUIT` [56] minimization

program is used to perform the fits, with the MINOS error estimation option, and in all cases normal convergence is required with status parameter ISTAT equal to 3.0.

7.2 Event Selection

The ν_μ disappearance analysis here uses the event selection cuts described in chapter 4. The data set after cuts has ∼90% ν_μ CCQE purity according to the Monte Carlo, and the background is composed almost entirely of ν_μ resonant single π^+ production, summarized in table 7.1. The efficiency of the selection cuts for signal ν_μ CCQE events is 17.16%, from table 4.1, for a fiducial volume of radius 610 cm, which is the entire detector. For 5×10^{20} protons on target, the number of Monte Carlo predicted ν_μ events after cuts in the presence of an oscillation signal with (Δm^2, $sin^2 2\theta_{\mu x}$) = (1 eV^2, 0.2) would be ∼85,000, compared with ∼92,000 in the absence of oscillations. Example reconstructed neutrino energy distributions in Monte Carlo for all events passing the selection cuts are shown with and without oscillations, for $0.1 < \Delta m^2 < 7\ eV^2$ and $sin^2 2\theta_{\mu x} = 0.2$, in figure 7.1. The neutrino energy of events passing the ν_μ CCQE selection cuts is reconstructed under a muon hypothesis, assuming the muon mass for the final state lepton.

The ν_e appearance analysis uses event selection cuts based on a particle identification algorithm described in reference [64]. The event selection development is still in progress, and therefore the results given here are not final and may improve. The composition of the background to a ν_e appearance signal after the oscillation ν_e event selection cuts have been applied are summarized in table 7.2. The efficiency of the selection cuts for signal ν_e CCQE events events is 24.50%, and the efficiency for background is 0.07%, for a fiducial volume of radius 610 cm, which is the entire detector. The largest sources of ν_e and ν_μ background come from intrinsic beam

Table 7.1: *Fractional composition in Monte Carlo of background after oscillation ν_μ selection cuts, which are described in detail in chapter 4. The total number of events predicted by the Monte Carlo after cuts, with no oscillations, for 5×10^{20} protons on target, is ∼91,000.*

source	*all*	ν_e	$\overline{\nu_e}$	ν_μ	$\overline{\nu_\mu}$
total	1.000	0.000	0.000	0.981	0.019
π^+ parent	0.926	0.000	0.000	0.943	0.068
π^- parent	0.014	0.000	0.000	0.001	0.761
K^0_L parent	0.001	0.000	0.000	0.001	0.013
K^+ parent	0.010	0.000	0.000	0.010	0.002
K^- parent	0.000	0.000	0.000	0.000	0.009
p parent	0.010	0.000	0.000	0.008	0.057
n parent	0.039	0.000	0.000	0.038	0.085
CCQE	0.906	0.000	0.000	0.907	0.866
CC1π^+	0.068	0.000	0.000	0.070	0.000
CC1π coherent	0.000	0.000	0.000	0.000	0.019
CC1π^0	0.012	0.000	0.000	0.012	0.000

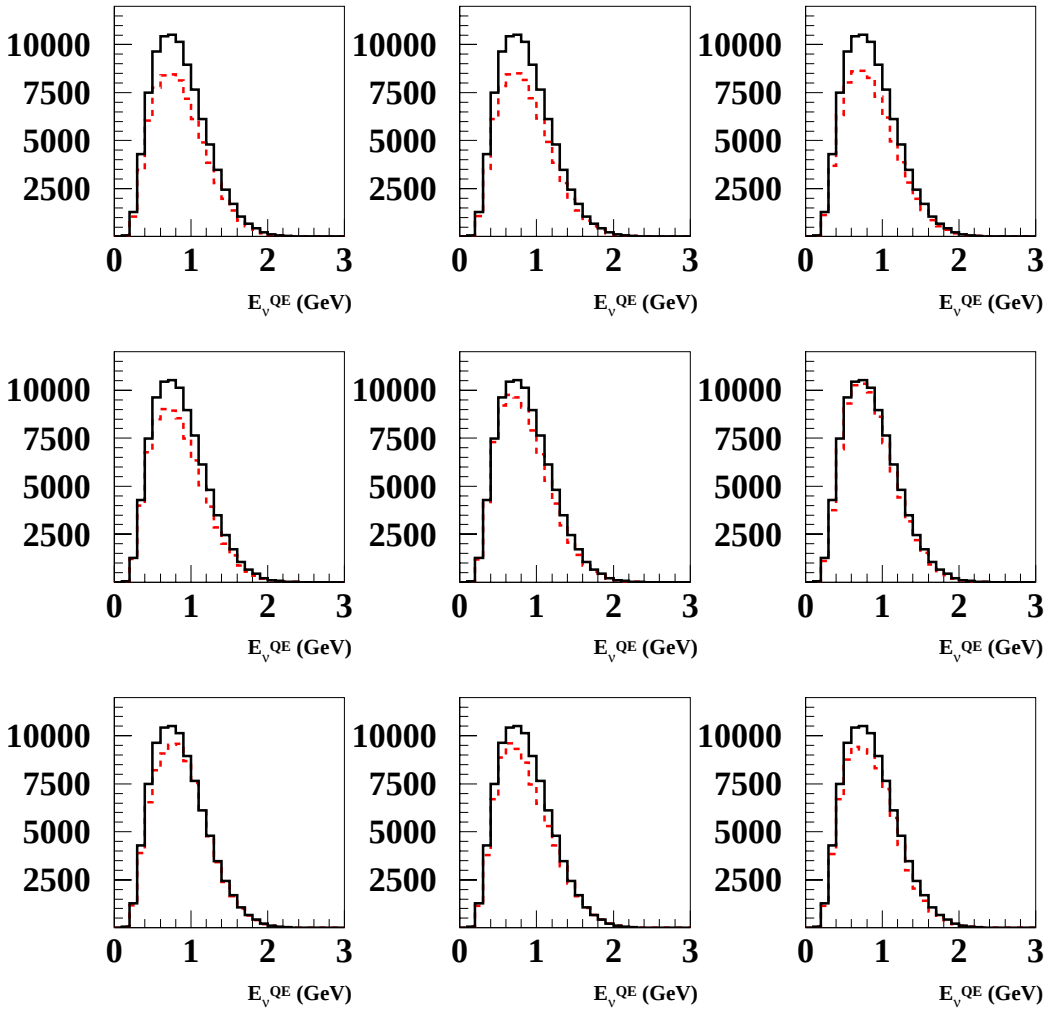

Figure 7.1: *Example ν_μ disappearance signal at MiniBooNE after event selection cuts, for $sin^2 2\theta_{\mu,x} = 0.2$ and 5×10^{20} p.o.t.. Panels show the number of events vs. reconstructed neutrino energy E_ν^{QE} (GeV) for Δm^2 = (0.13, 0.22, 0.36, 0.59, 0.97, 1.58, 2.58, 4.24, 6.95) eV^2 (top left to bottom right) with (red, dashed line) and without (black, solid line) oscillations.*

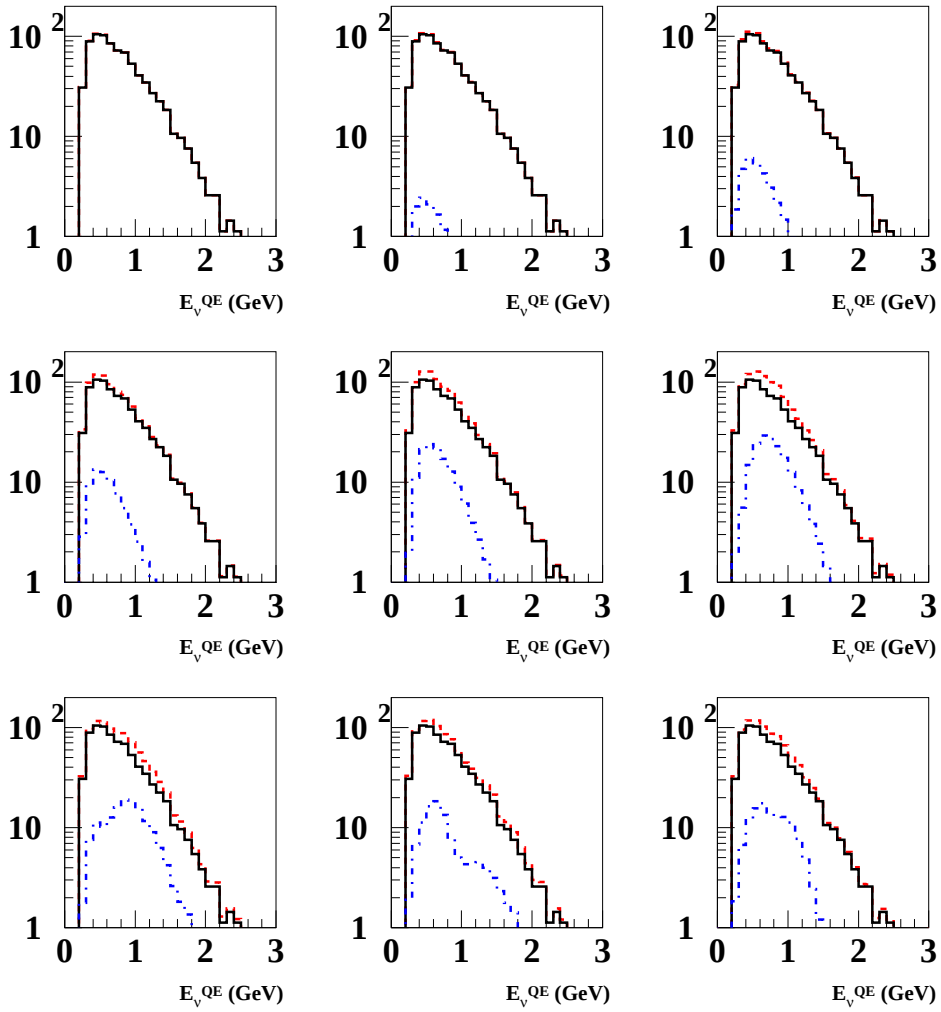

Figure 7.2: *Example ν_e appearance signal at MiniBooNE after event selection cuts, for $sin^2 2\theta_{\mu,e} = 0.002$ and 5×10^{20} p.o.t.. Panels show the number of events vs. reconstructed neutrino energy E_ν^{QE} (GeV) for Δm^2 = (0.13, 0.22, 0.36, 0.59, 0.97, 1.58, 2.58, 4.24, 6.95) eV^2 (top left to bottom right) with (red, dashed line) and without (black, solid line) oscillations, and signal only (blue, dotted line).*

Table 7.2: *Fractional composition in Monte Carlo of background after oscillation ν_e selection cuts, which are* `YBoost23_COMBINED` $>$ *7.1 and* `Stancu_UZ` $<$ *0.9. Note that for ν_e from π^+ decay, 95.2% come from the decay chain $\pi^+ \to \mu^+\nu_\mu$, $\mu^+ \to e^+\nu_e\overline{\nu_\mu}$, and 4.8% come from $\pi^+ \to e^+\nu_e$. The total number of events predicted by the Monte Carlo after cuts, with no oscillations, for 5×10^{20} protons on target, is ∼800.*

source	*all*	ν_e	$\overline{\nu_e}$	ν_μ	$\overline{\nu_\mu}$
total	1.000	0.606	0.035	0.355	0.005
π^+ parent	0.620	0.528	0.007	0.843	0.238
π^- parent	0.007	0.001	0.091	0.000	0.714
K^0_L parent	0.077	0.081	0.796	0.000	0.000
K^+ parent	0.248	0.332	0.000	0.131	0.000
K^- parent	0.001	0.000	0.028	0.000	0.000
p parent	0.011	0.012	0.042	0.006	0.048
n parent	0.036	0.046	0.035	0.020	0.000
CCQE	0.569	0.860	0.810	0.056	0.048
NC1π^0	0.179	0.000	0.000	0.502	0.000
$\Delta \to \gamma\gamma$	0.077	0.000	0.000	0.212	0.238
CC1π^+	0.067	0.104	0.021	0.000	0.000
NCπ^0 coherent	0.023	0.000	0.000	0.062	0.190
CC1π^0	0.017	0.020	0.000	0.014	0.000
νe elastic	0.016	0.000	0.000	0.042	0.000
NC DIS	0.010	0.000	0.000	0.028	0.028

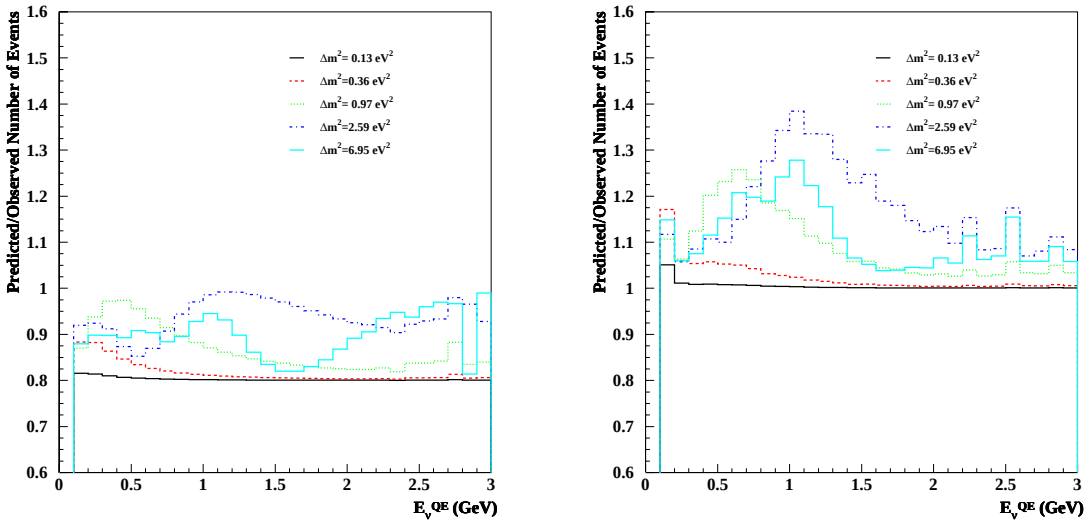

Figure 7.3: *Example oscillation signals at MiniBooNE after event selection cuts for* 5×10^{20} *p.o.t.. Left: ratio of number of events for a predicted* ν_μ *disappearance oscillation signal to the number observed without oscillations vs.* E_ν^{QE} *(GeV) with* $sin^2 2\theta_{\mu x} = 0.2$*. Right: ratio of number of events for a predicted* ν_e *appearance oscillation signal to the number observed without oscillations vs.* E_ν^{QE} *(GeV) with* $sin^2 2\theta_{\mu e} = 0.002$*.*

μ^+-decay ν_e and mis-identified ν_μ neutral current π^0 interactions. The total Monte Carlo predicted number of background and signal events in the presence of oscillations would be ∼800 and ∼160 for (Δm^2, $sin^2 2\theta_{\mu e}$) = (1 eV^2, 0.002), for a data set with 5×10^{20} protons on target. Example reconstructed neutrino energy distributions in Monte Carlo for all events passing the selection cuts are shown with and without oscillations, for $0.1 < \Delta m^2 < 7\ eV^2$ and $sin^2 2\theta_{\mu e} = 0.002$, in figure 7.2. The neutrino energy of events passing the ν_e CCQE selection cuts is reconstructed under a electron hypothesis, assuming the electron mass for the final state lepton.

The power of the oscillation fit comes from both the normalization and the distortion of the reconstructed energy spectrum due to oscillations. Figure 7.3 illustrates the dependence of the spectral distortion on Δm^2 for both appearance and disappearance searches. In the event of a positive signal, MiniBooNE's ability to measure the value of Δm^2 comes from distinguishing the spectral distortions for different oscillation parameters.

7.3 Systematic Errors

In the following, the sources of systematic error considered include the π^+ and K^+ flux predictions, and the neutrino interaction cross section predictions. This list is incomplete because it does not include the neutrino cross section final state interaction uncertainties or the detector response errors, and therefore, the studies in this chapter only use "fake data," that is, central value Monte Carlo with no oscillation signal. Hereafter, the term data always refers to "fake data." The Monte Carlo statistics are currently insufficient to calculate error matrices with 30 energy bins for the systematic sources that are not included here, however, both final state interaction cross sections and detector response errors are expected to contribute at the <10% level each to the

total systematic uncertainty.

The error matrix $\mathcal{M}_{total}$ used for the oscillation fits is constructed via

$$\mathcal{M}_{total} \;=\; \mathcal{M}_{\pi^+} + \mathcal{M}_{K^+} + \mathcal{M}_{\sigma} + \mathcal{M}_{stat} \tag{7.19}$$

where $\mathcal{M}_{\pi^+}$, $\mathcal{M}_{K^+}$, $\mathcal{M}_{\sigma}$, and $\mathcal{M}_{stat}$ are the π^+, K^+, neutrino interaction cross section, and statistical error matrices respectively. The statistical error matrix is diagonal, with elements equal to the number of events in each reconstructed neutrino energy bin. The systematic error matrices are calculated as described in chapter 4, using first derivative matrices to propagate the simulation input parameter errors and correlations to the reconstructed neutrino energy distributions for events passing the selection cuts. The first derivative matrices are calculated assuming no oscillations, and the reconstructed neutrino energy uses a muon hypothesis, that is, assuming the muon mass for the final state lepton, for the ν_μ event sample, and an electron hypothesis for the ν_e sample.

The π^+ flux prediction errors come from the Sanford-Wang fit to external π^+ production data discussed in chapter 3, and are calculated as described in chapter 4, section 4.3. To construct $\mathcal{M}_{\pi^+}$ for the ν_μ disappearance fit,

$$(\mathcal{M}^{\nu_\mu}_{\pi^+})_{i,j} \;=\; (\mathcal{F}^{\nu_\mu})^T_{i,k}(\mathcal{P}_{\pi^+})_{k,l}(\mathcal{F}^{\nu_\mu})_{l,j} \tag{7.20}$$

where i, j index reconstructed neutrino energy bins and k, l index Sanford-Wang π^+ parameters c_1 through c_8. The dimensions of $(\mathcal{M}^{\nu_\mu}_{\pi^+})_{i,j}$, $(\mathcal{P}_{\pi^+})_{k,l}$ and $(\mathcal{F}^{\nu_\mu})_{l,j}$ are (30×30), (8×8), and (8×30) respectively. The matrix $(\mathcal{P}_{\pi^+})_{k,l}$ is the covariance matrix of the Sanford-Wang π^+ prediction parameters from the external data fit, given in appendix F. The matrix $(\mathcal{F}^{\nu_\mu})_{l,j}$ is the first derivative matrix that describes the change in the number of events passing the ν_μ CCQE selection cuts in reconstructed neutrino energy bin j, under a ν_μ hypothesis, given a $+1\sigma$ change in Sanford-Wang π^+

parameter l. Similarly, for the ν_e appearance analysis, the error matrix is constructed as

$$(\mathcal{M}^{\nu_e}_{\pi^+})_{i,j} \;=\; (\mathcal{F}^{\nu_e})^T_{i,k}(\mathcal{P}_{\pi^+})_{k,l}(\mathcal{F}^{\nu_e})_{l,j} \tag{7.21}$$

where $(\mathcal{F}^{\nu_e})_{l,j}$ is the matrix of first derivatives for events passing the ν_e selection cuts as a function of reconstructed neutrino energy, under a ν_e hypothesis, given a $+1\sigma$ change in Sanford-Wang π^+ parameter l. The dimensions of the matrices are identical to the ν_μ case. For the combined fit, the error matrix is calculated via

$$(\mathcal{M}^{\nu_e\nu_\mu}_{\pi^+})_{i,j} \;=\; (\mathcal{F}^{\nu_e\nu_\mu})^T_{i,k}(\mathcal{P}_{\pi^+})_{k,l}(\mathcal{F}^{\nu_e\nu_\mu})_{l,j} \tag{7.22}$$

where $(\mathcal{F}^{\nu_e\nu_\mu})_{l,j}$ is an (8×60) matrix, where the first 30 elements in any row are the ν_e derivatives, and the last 30 elements are the ν_μ derivatives. To account for the fact that the χ^2/ndf of the Sanford-Wang π^+ fit to external data is not equal to 1.0, the parameter errors, and therefore the first derivatives are scaled up by the $\sqrt{\chi^2/ndf}$, which is $\sqrt{2.2} = 1.5$. As expected, the largest source of normalization uncertainty comes from the error on the Sanford-Wang π^+ c_1 parameter, shown in table F.1.

Like the π^+ systematic errors, the K^+ flux prediction uncertainties come from the Sanford-Wang K^+ fit to external production data described in chapter 3. To construct $\mathcal{M}_{K^+}$ for the ν_μ disappearance fit,

$$(\mathcal{M}^{\nu_\mu}_{K^+})_{i,j} \;=\; (\mathcal{F}^{\nu_\mu})^T_{i,k}(\mathcal{P}_{K^+})_{k,l}(\mathcal{F}^{\nu_\mu})_{l,j} \tag{7.23}$$

where i, j index reconstructed neutrino energy bins and k, l index Sanford-Wang K^+ parameters c_1 through c_9. The dimensions of $(\mathcal{M}^{\nu_\mu}_{K^+})_{i,j}$, $(\mathcal{P}_{K^+})_{k,l}$ and $(\mathcal{F}^{\nu_\mu})_{l,j}$ are (30 $\times$ 30), (9×9), and (9×30) respectively. The matrix $(\mathcal{P}_{K^+})_{k,l}$ is the covariance matrix of the Sanford-Wang K^+ prediction parameters from the external data fit, given in appendix F. The matrix $(\mathcal{F}^{\nu_\mu})_{l,j}$ is the first derivative matrix that describes the change in the number of events passing the ν_μ CCQE selection cuts in reconstructed

neutrino energy bin j, under a ν_μ hypothesis, given a $+1\sigma$ change in Sanford-Wang K^+ parameter l. Similarly, for the ν_e appearance analysis, the error matrix is constructed as

$$(\mathcal{M}^{\nu_e}_{K^+})_{i,j} \;=\; (\mathcal{F}^{\nu_e})^T_{i,k}(\mathcal{P}_{K^+})_{k,l}(\mathcal{F}^{\nu_e})_{l,j} \tag{7.24}$$

where $(\mathcal{F}^{\nu_e})_{l,j}$ is the matrix of first derivatives for events passing the ν_e selection cuts as a function of reconstructed neutrino energy, under a ν_e hypothesis, given a $+1\sigma$ change in Sanford-Wang K^+ parameter l. The dimensions of the matrices are identical to the ν_μ case. For the combined fit, the error matrix is calculated via

$$(\mathcal{M}^{\nu_e\nu_\mu}_{K^+})_{i,j} \;=\; (\mathcal{F}^{\nu_e\nu_\mu})^T_{i,k}(\mathcal{P}_{K^+})_{k,l}(\mathcal{F}^{\nu_e\nu_\mu})_{l,j} \tag{7.25}$$

where $(\mathcal{F}^{\nu_e\nu_\mu})_{l,j}$ is a (9×60) matrix, where the first 30 elements in any row are the ν_e derivatives, and the last 30 elements are the ν_μ derivatives. To account for the fact that the χ^2/ndf of the Sanford-Wang K^+ fits to external data is not equal to 1.0, the first derivatives are scaled up by the $\sqrt{\chi^2/ndf}$, which is $\sqrt{3.6} = 1.9$. As for the π^+ flux, the largest source of normalization uncertainty comes from the error on the Sanford-Wang K^+ c_1 parameter, shown in table F.2.

The neutrino interaction cross section errors come from the estimates based on past data described in chapter 3, and are calculated as described in chapter 4, section 4.3 with one important difference: only the neutrino interaction cross section uncertainties are considered. The final state cross section errors, which comprise the last three rows of table 4.7, are not included. With the exception of the CCQE parameters, the neutrino interaction cross section sources systematic error are assumed to be uncorrelated. The correlations between the axial mass for CCQE interactions, m_A, and the Fermi Gas model parameters, E_B and p_F, are taken from the m_A analysis of chapter 6. In the future, the relevant parameter errors will also use the MiniBooNE measurement, however, these are not used now because the contribution of

the detector response uncertainties is still under investigation. Note that since the CCQE cross section parameter analysis is flux-independent, these constraints derived from MiniBooNE data can be applied to both the ν_e and ν_μ oscillation analyses; if the (m_A, E_B, p_F) parameter measurement were sensitive to variations of the neutrino flux due to oscillations, then this constraint could only be applied to the ν_e appearance analysis and *not* to the ν_μ disappearance search.

To construct $\mathcal{M}_\sigma$ for the ν_μ disappearance fit,

$$(\mathcal{M}_\sigma^{\nu_\mu})_{i,j} \;=\; (\mathcal{F}^{\nu_\mu})^T_{i,k}(\mathcal{P}_\sigma)_{k,l}(\mathcal{F}^{\nu_\mu})_{l,j} \tag{7.26}$$

where i, j index reconstructed neutrino energy bins and k, l index neutrino interaction cross section sources of uncertainty. The sources considered here include the first 9 elements of table 3.10. Notable exceptions are the final state interaction parameters. A complete analysis would include these, however, they are still under investigation at this time. The dimensions of $(\mathcal{M}_\sigma^{\nu_\mu})_{i,j}$, $(\mathcal{P}_\sigma)_{k,l}$ and $(\mathcal{F}^{\nu_\mu})_{l,j}$ are (30×30), (9×9), and (9×30) respectively. The matrix $(\mathcal{P}_\sigma)_{k,l}$ is the covariance matrix of the neutrino interaction cross section prediction parameters, given in appendix F. The matrix $(\mathcal{F}^{\nu_\mu})_{l,j}$ is the first derivative matrix that describes the change in the number of events passing the ν_μ CCQE selection cuts in reconstructed neutrino energy bin j, under a ν_μ hypothesis, given a $+1\sigma$ change in neutrino interaction cross section parameter l. Similarly, for the ν_e appearance analysis, the error matrix is constructed as

$$(\mathcal{M}_\sigma^{\nu_e})_{i,j} \;=\; (\mathcal{F}^{\nu_e})^T_{i,k}(\mathcal{P}_\sigma)_{k,l}(\mathcal{F}^{\nu_e})_{l,j} \tag{7.27}$$

where $(\mathcal{F}^{\nu_e})_{l,j}$ is the matrix of first derivatives for events passing the ν_e selection cuts as a function of reconstructed neutrino energy, under a ν_e hypothesis, given a $+1\sigma$ change in neutrino interaction cross section parameter l. The dimensions of the matrices are identical to the ν_μ case. For the combined fit, the error matrix is

calculated via

$$(\mathcal{M}_{\sigma}^{\nu_e\nu_\mu})_{i,j} \;=\; (\mathcal{F}^{\nu_e\nu_\mu})^{T}_{i,k}(\mathcal{P}_{\sigma})_{k,l}(\mathcal{F}^{\nu_e\nu_\mu})_{l,j} \tag{7.28}$$

where $(\mathcal{F}^{\nu_e\nu_\mu})_{l,j}$ is a (9×60) matrix, where the first 30 elements in any row are the ν_e derivatives, and the last 30 elements are the ν_μ derivatives. The largest sources of normalization uncertainty come from the errors on the Fermi Gas model parameters and the value of m_A for coherent pion production, shown in table F.3.

The contribution of each of the above sources to the normalization uncertainty for the ν_μ and ν_e event samples passing selection cuts is summarized in table 7.3. The normalization uncertainty is calculated by summing over all elements of the error matrix $\mathcal{M}$, which takes into account correlations between energy bins. The contributions to the normalization systematic errors for each constituent simulation parameter are summarized in tables F.1 through F.4 in appendix F.

The difference in normalization between the Monte Carlo prediction and the measured rate in data, discussed in chapter 4, is not taken into account in the uncertainty estimates here. A number of approaches to this problem are under investigation. One way to handle the discrepancy is to choose a source and assign a larger systematic error such that the normalization of Monte Carlo agrees with data within errors. Examples of this could include increasing the uncertainty on the Sanford-Wang π^+ c_1 parameter, which sets the overall normalization of the π^+ production cross section, or, increasing the uncertainty on the neutrino interaction CCQE cross section m_A value. Another way to deal with the discrepancy is to add parameters to the oscillation fit, such that it would become a combined fit for Δm^2, $sin^2 2\theta$, n_π, and n_K, where the n are normalization pull terms for the π^+ and K^+ event rates respectively.

Of the analyses described previously in this thesis which seek to reduce the uncertainties with respect to external data, only the cross section analysis results can be applied to the ν_μ disappearance search. However, the addition of the cross sec-

Table 7.3: *Summary of fractional normalization systematic errors Δf^{prod} for ν_μ and ν_e events after their respective event selection cuts, and for the combined data sets. The constrained uncertainties use the reduction in systematic errors from the analysis of chapter 5. The neutrino interaction cross section uncertainties with correlations among CCQE parameters, ρ_{CCQE}, come from chapter 6.*

source	ν_μ	ν_e	*combined*
statistics	0.0033	0.0354	0.0033
π^+ flux prediction	0.0738	0.0388	0.0735
K^+ flux prediction	0.0023	0.0640	0.0028
σ_ν predictions	0.2606	0.2692	-
σ_ν predictions + ρ_{CCQE}	0.0799	0.0720	0.0796
constrained π^+ prediction	N/A	0.0016	N/A
constrained σ_ν predictions	N/A	0.0563	N/A

tion parameter correlations has a big effect because the assumed CCQE simulation parameter uncertainties are very large. Without correlations, Δf^{prod} due to cross sections is 26%, from table 7.3, and with the correlations taken from the final data (m_A, E_B, p_F) fit in chapter 6, Δf^{prod} is reduced to 8%.

In contrast, the constraints on the π^+-decay ν_μ and μ^+-decay ν_e fluxes and the cross section uncertainties from chapter 5 *can* be applied to the ν_e appearance search, since these depend only on the observed ν_μ distribution. In fact, the dependence of these constraints on the measured ν_μ spectrum is precisely why they cannot be used in the ν_μ disappearance analysis. The constrained π^+ simulation parameter errors, derived from the analysis in chapter 5, reduce the ν_e sample normalization systematic error contribution of the π^+ flux prediction uncertainty from 3.9% to <1%. The reason the constraint is so effective is that ∼30% of the total events passing the ν_e selection cuts are μ^+-decay ν_e, and another ∼30% are π^+-decay ν_μ, both of which are directly related to the ν_μ data set. The constraints on the ν_e neutrino interaction cross section simulation parameter uncertainties, from the same analysis, reduce the normalization uncertainty contribution from 7.2% to 5.6%. This reduction in uncertainty is somewhat smaller because the ν_μ data set constrains only the CCQE cross section simulation parameter uncertainties, which comprise 1/3 of the systematic errors, and while ∼60% of all events passing the ν_e selection cuts are CCQE interactions, the cross section uncertainty has large contributions from other interaction channels, such as single π^0 production and radiative Δ decay, which are not reduced by parameter correlations.

7.4 ν_e Appearance and ν_μ Disappearance Sensitivities

The MiniBooNE ν_μ disappearance and ν_e appearance oscillation sensitivities are shown for a variety of systematic error assumptions in figures 7.4 and 7.5. The event selection criteria are described above, and the systematic error assumptions all come from external data, with the exception of the CCQE cross section parameter correlations, which are based on the measurement in chapter 6. In these figures, the left panels show the 90% confidence level limit for ν_μ disappearance, under a two-neutrino (μ, x) hypothesis, along with the allowed regions of (Δm^2, $sin^2 2\theta_{\mu x}$) parameter space in models with one sterile neutrino [36], at 90% (light blue) and 99% (dark blue) confidence level. The right panels in figures 7.4 and 7.5 show the 90% confidence level limit for ν_e appearance in MiniBooNE, under a two-neutrino (μ, e) hypothesis, along with the allowed regions of (Δm^2, $sin^2 2\theta_{\mu e}$) reported by the LSND experiment [31], at 90% (light blue) and 99% (dark blue) confidence level.

The systematic error assumptions shown in figures 7.4 and 7.5 include: (i) statistical errors only, (ii) statistical and π^+ flux prediction errors only, (iii) statistical and K^+ flux prediction errors only, (iv) statistical and neutrino interaction cross section errors only, and (v) all of the above combined. For both ν_μ disappearance and ν_e appearance the most restrictive source of systematic error comes from neutrino interaction cross sections. Both are dominated by contributions from the CCQE cross section simulation parameter uncertainties. Currently the errors on the Fermi Gas Model parameters are quite large, of order 70% as discussed in chapter 3, and will be reduced significantly by using the MiniBooNE measurement in chapter 6, which is *not* used here to set the magnitudes of the simulation parameter uncertainties.

The next most important sources of uncertainty in limiting the MiniBooNE os-

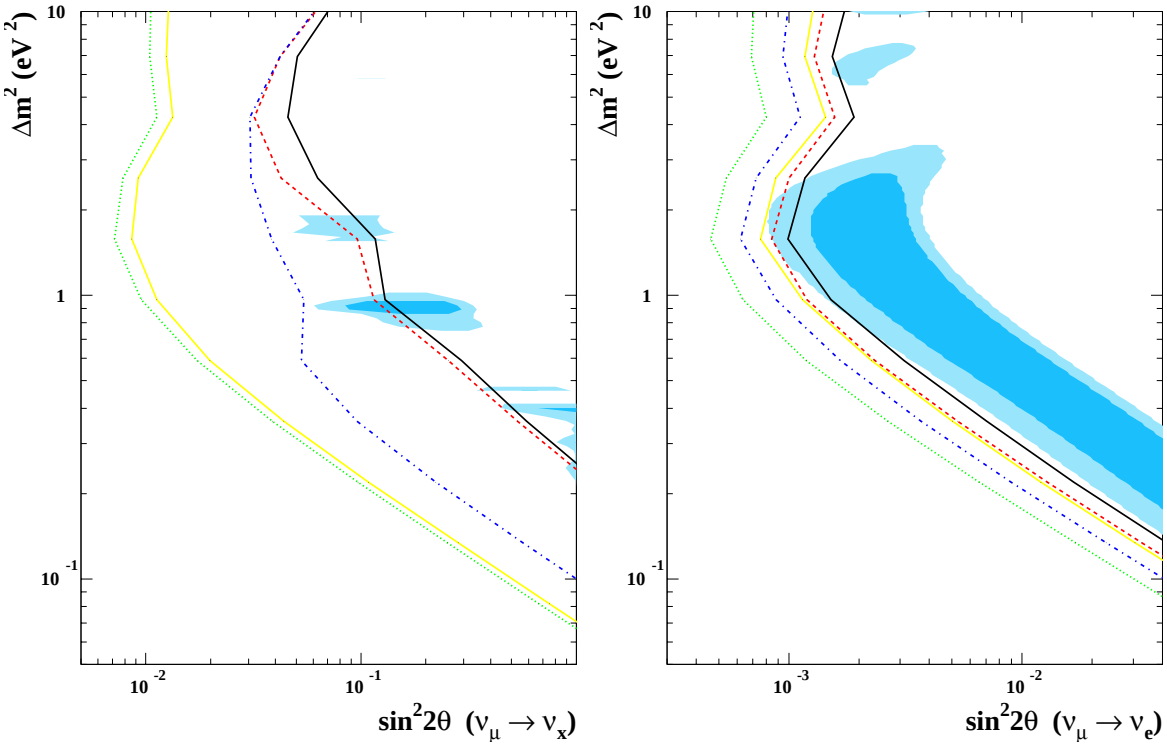

Figure 7.4: *MiniBooNE oscillation sensitivity at 90% confidence level. Left:* Δm^2 *(*eV^2*) vs.* $sin^2 2\theta_{\mu x}$*, with 3+1 allowed regions at 90% (light blue) and 99% (dark blue) confidence level. Right:* Δm^2 *(*eV^2*) vs.* $sin^2 2\theta_{\mu e}$*, with LSND allowed regions at 90% (light blue) and 99% (dark blue) confidence level. Systematic error assumptions include (i) statistical errors only (green, dotted line), (ii)* K^+ *flux and statistical errors only (yellow, solid line), (iii)* π^+ *flux and statistical errors only (blue, dashed line), (iv)* σ_ν *and statistical errors only (red, dash-dotted line), and (v) all of the above combined (black, solid line).*

Table 7.4: *Comparison of expected and best-fit limit values of $sin^2 2\theta$ at Δm^2 = 100 eV^2. Limits are stated at $\Delta\chi^2$ = 1.0 (not 1.64 as in the plots with 90% confidence level curves), and expected values are calculated from the errors given in table 7.3 and equations 7.11 and 7.15 for ν_μ disappearance and ν_e appearance respectively.*

source	ν_μ *expected*	ν_μ *limit*	ν_e *expected*	ν_e *limit*
statistics	0.0066	0.0066	4.547×10^{-4}	4.567×10^{-4}
π^+ flux	0.1476	0.1477	6.741×10^{-4}	6.773×10^{-4}
K^+ flux	0.0080	0.0080	9.403×10^{-4}	9.434×10^{-4}
σ_ν + ρ_{CCQE}	0.1598	0.1597	10.306×10^{-4}	10.339×10^{-4}
all	0.2176	0.2175	14.090×10^{-4}	14.145×10^{-4}

cillation sensitivity are the π^+ and K^+ flux predictions, for the ν_μ disappearance and the ν_e appearance searches respectively. The number of neutrinos from K^+ decay is actually larger in the ν_μ sample, $\sim$1500 after the ν_μ cuts compared with $\sim$200 passing the ν_e cuts, however, the fraction of K^+-decay neutrino induced events is much smaller, $\sim$2%, in the ν_μ sample than in the ν_e set, $\sim$25%. Therefore, the K^+ uncertainty contributes almost nothing to the ν_μ sample total systematic error, and very significantly to the total ν_e systematic error.

The value of $sin^2 2\theta$ at high Δm^2, where the sensitivity comes from the "counting experiment" alone, can be compared with the simple limits derived in equations 7.11 and 7.15 to verify that the oscillation fit results are sensible. The expected and best-fit $sin^2 2\theta_{\mu x}$ and $sin^2 2\theta_{\mu e}$ limits are compared in table 7.4 for ν_μ disappearance and ν_e appearance respectively. In general, the best-fit limit values are in excellent agreement with the expected values, which builds confidence in the oscillation fit method and implementation.

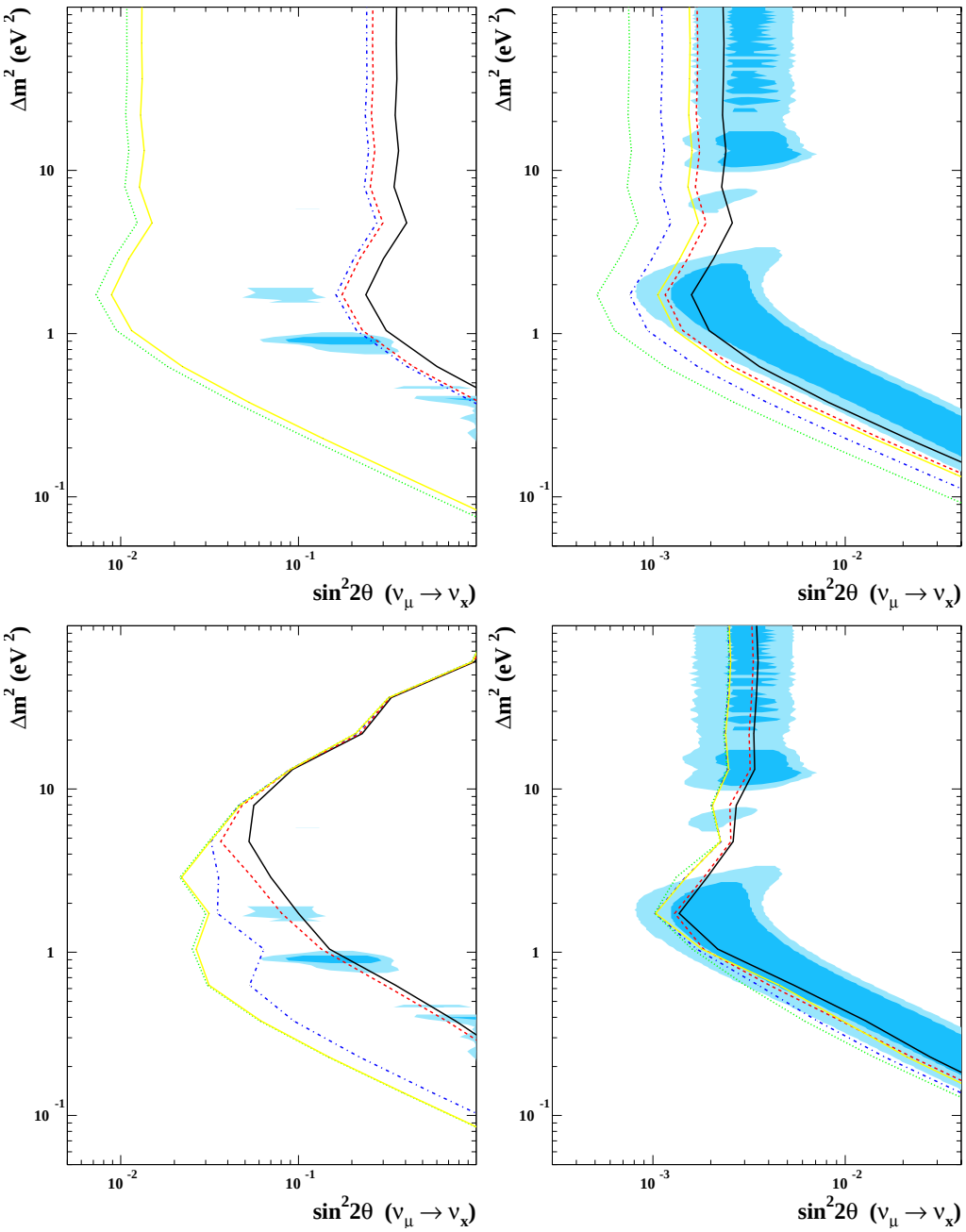

Figure 7.5: *MiniBooNE oscillation sensitivity at 90% confidence level from normalization only (top) and E_ν^{QE} shape only (bottom). Left: Δm^2 (eV^2) vs. $sin^2 2\theta_{\mu x}$. Right: Δm^2 (eV^2) vs. $sin^2 2\theta_{\mu e}$. Systematic errors include (i) statistical (green, dotted line), (ii) K^+ flux (yellow, solid line), (iii) π^+ flux (blue, dashed line), (iv) σ_ν (red, dash-dotted line), and (v) all of the above combined (black, solid line). Allowed regions are described in figure 7.4.*

The importance of the "counting" experiment is rather different in the ν_e and ν_μ searches. For ν_e appearance, the "counting" experiment is the dominant contribution to the oscillation sensitivity, while for ν_μ disappearance the distortion of the reconstructed neutrino energy spectrum contains most of the useful information for the oscillation fit. This is illustrated in figure 7.5, in which the top two panels show the ν_μ and ν_e oscillation sensitivities calculated using only the total number of events, with no information about the reconstructed neutrino energy spectrum. The sensitivities calculated using E_ν^{QE} distribution shape information only are shown in the bottom panels of figure 7.5. To separate the shape and normalization components, two different forms of the χ^2 function are used. For normalization-only sensitivities, the χ^2 function in equations 7.8 and 7.14 are used for the ν_μ disappearance and ν_e appearance limit calculations respectively. For the shape-only sensitivity calculation, the basic χ^2 function is slightly modified such that the predicted total number of events in the absence of oscillations is normalized to be the same as the observed total number of events. The χ^2 function is given by

$$\chi^2 \;=\; \sum_i \sum_j \Big(N_i^{Data} - k N_i^{MC}(\Delta m^2, sin^2 2\theta)\Big)(\mathcal{M}'_{i,j})^{-1}\Big(N_j^{Data} - k N_j^{MC}(\Delta m^2, sin^2 2\theta)\Big) \tag{7.29}$$

where the constant k normalizes the total number of Monte Carlo events to be equal to the number of data events, via

$$k \;=\; \frac{\sum_i N_i^{Data}}{\sum_i N_i^{MC}} \tag{7.30}$$

where i indexes bins of E_ν^{QE}. The error matrix $\mathcal{M}'$ is calculated using first derivatives similarly normalized such that only the differences in the E_ν^{QE} spectrum shape contribute to the uncertainty; e.g. in E_ν^{QE} bin i for systematic source j, the element of the first derivative matrix would be

$$\mathcal{F}'_{i,j} \;=\; \frac{\frac{\sum_i N_i^0}{\sum_i N_i^j} N_i^j - N_i^0}{\Delta p_j} \tag{7.31}$$

where N_i^0 is the number of events in bin i predicted by the central value Monte Carlo, and N_i^j is the number of events in bin i predicted by a Monte Carlo set in which parameter j has been varied with respect to its nominal value by Δp_j.

Experimentally, the fact that the ν_μ and ν_e oscillation sensitivities depend rather differently on the systematic errors is quite useful. The high statistics ν_μ data set can provide a normalization constraint on several of the important background sources for the ν_e appearance search, and because the appearance sensitivity depends largely on measuring a rate rather than shape difference, adding normalization information from the ν_μ data set has a big impact on the ν_e search. The converse is that adding the ν_e data does not help the ν_μ disappearance sensitivity significantly because the ν_e statistics are relatively small, and do not provide a strong constraint on the ν_μ energy spectrum. The impact on the oscillation search of three kinds of constraints, all derived from the ν_μ CCQE data set of chapter 4, are described in the following: (*i*) the CCQE cross section parameter measurement of chapter 6, (*ii*) the π^+ flux constraint method of chapter 5, and (*iii*) a combined oscillation fit to the ν_μ and ν_e data sets.

The results of the CCQE cross section parameter measurement described in chapter 6 can be applied to both the appearance and the disappearance search, because the measurement is flux-independent. The CCQE (m_A, p_F, E_B) analysis produces two kinds of information: (*i*) the correlations between the CCQE simulation parameters m_A, E_B, and p_F, and (*ii*) the uncertainties on those parameters. The impact of adding the correlations between m_A, E_B, and p_F is illustrated in 7.6. The uncertainties assumed on the CCQE parameters are large: 20% for m_A, 72% for p_F, and 76% for E_B. Conservatively, the CCQE parameter extraction in chapter 6 will measure p_F and E_B at least twice as well as this. The impact of adding both correlations *and* reducing the p_F and E_B simulation parameter uncertainties by 50% is also shown

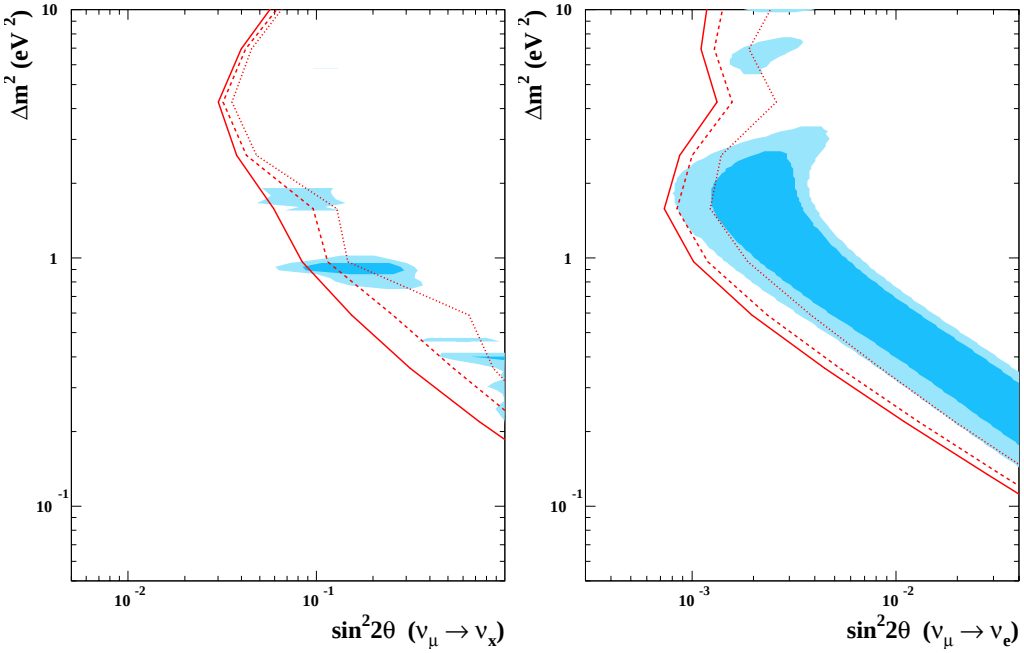

Figure 7.6: *MiniBooNE 90% confidence level sensitivity with σ_ν systematic errors, from external sources (red, dotted line), with MiniBooNE-measured correlations (red, dashed line), and with MiniBooNE-measured correlations and projected parameter errors (red, solid line). Left: Δm^2 (eV^2) vs. $sin^2 2\theta_{\mu x}$. Right: Δm^2 (eV^2) vs. $sin^2 2\theta_{\mu e}$. Allowed regions are described in figure 7.4.*

in figure 7.6. Incorporating both of these results improves the oscillation sensitivity for both ν_μ disappearance and ν_e appearance by $>1\sigma$ at low Δm^2. However, since detector response uncertainties are not yet included in the (m_A, p_F, E_B) measurement, in the following, only the CCQE parameter correlations measured in chapter 6 are applied, and the large parameter uncertainties based on external data are used, rather than MiniBooNE-measured values.

The method used to derive constraints on the simulation parameter uncertainties in chapter 5 uses the measured ν_μ rate, and therefore cannot be applied to the ν_μ disappearance analysis. However for the ν_e appearance it can be applied in two ways: (i) by assuming the cross section predictions, and deriving constraints on the

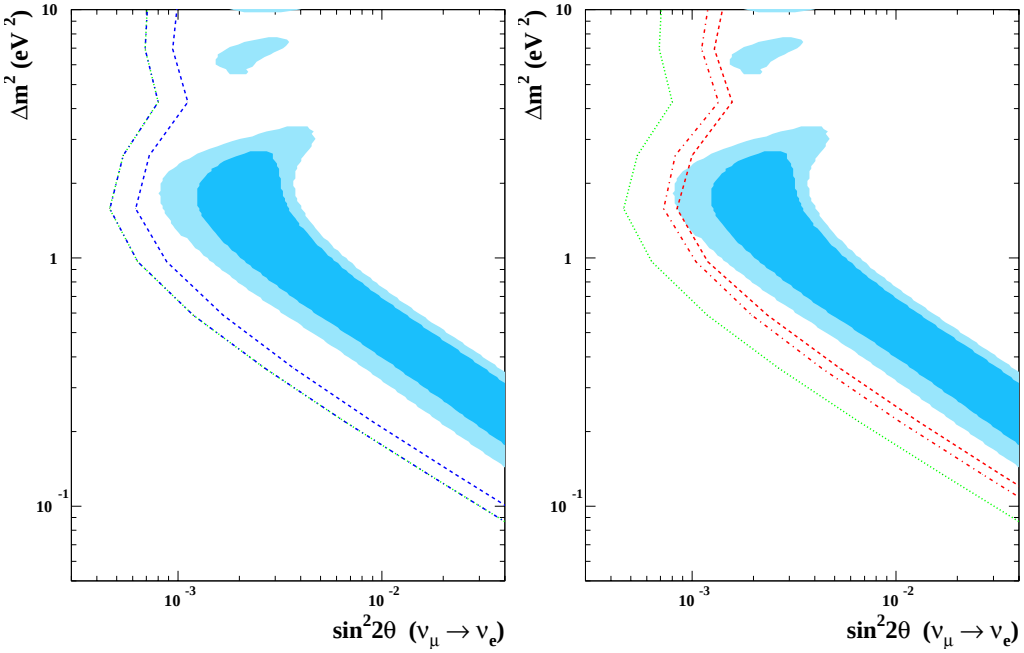

Figure 7.7: *MiniBooNE 90% confidence level sensitivity with statistical errors (green, dotted line), errors derived from external sources (dashed line), and errors constrained by the ν_μ data (dash-dotted line), as discussed in the text. Left: Δm^2 (eV^2) vs. $sin^2 2\theta_{\mu x}$ with systematic errors from π^+ flux prediction and statistical errors. Right: Δm^2 (eV^2) vs. $sin^2 2\theta_{\mu e}$ with systematic errors from σ_ν and statistical errors. Allowed regions are described in figure 7.4.*

uncertainties in the π^+ flux simulation, as discussed in chapter 5, and (*ii*) by assuming the flux prediction, and deriving constraints on the uncertainties in the neutrino interaction cross section simulation, which is described in appendix C. The results of these two approaches are shown in the left and right panels of figure 7.7 respectively. The flux constraint, as expected, translates directly into a reduction of the π^+ flux prediction uncertainty on the π^+-decay ν_μ and μ^+-decay ν_e sources of background after the ν_e selection cuts. In fact, the resulting uncertainties, summarized in tables 5.1 and 5.2, are smaller than the statistical error on the ν_e sample after selection cuts, which is 3.5% on the total number of events and larger for individual E_ν^{QE} bins. The

cross section constraint is somewhat less effective, because only CCQE interactions are constrained by the ν_μ data set, however, it still represents an improvement of $\sim 0.5\sigma$ over the un-constrained case. Note that for the constrained cross section sensitivity calculation here, only the π^+-decay neutrinos have had the CCQE cross section uncertainty reduction applied. This is a conservative choice since, in principle, the CCQE cross section constraints derived by this analysis are applicable to all neutrinos.

A combined oscillation fit to the ν_μ and ν_e data sets has the advantage of incorporating the constraints from the ν_μ sample while solving several complexities associated with using "off-line" ν_μ information, like the constraints described above, in a ν_e appearance fit. First, a combined fit avoids double counting of uncertainties, which most likely affects any constraint derived from the ν_μ sample. For example, using the m_A error derived from the analysis in chapter 6, which includes contributions from flux, background cross sections, and detector response errors, to determine the ν_e cross section error matrix, and then additionally using a detector response error matrix in the ν_e fit, probably double counts the contribution of any detector response systematics that affect the ν_e and ν_μ events similarly. Sorting out the correlations would be messy and difficult. However, a combined fit simply uses the cross section error matrix derived from external data together with the detector response error matrix, and automatically deals with the correlations of all uncertainties when mapping out the χ^2 space. Second, the constraints on the flux and cross section derived using the observed ν_μ spectrum in chapter 5 assume no oscillations. However, if there is ν_μ disappearance, it can be as large as $\sim 10\%$, which could lead to an under-estimate of the number of μ^+-decay ν_e. This would happen because the analysis of chapter 5 would use the oscillated ν_μ events to infer the π^+ spectrum, and consequently infer too few π^+ and therefore predict few μ^+-decay ν_e. To first order, a disappearance

signal would probably not affect the constraint on the simulation uncertainties, which is how the chapter 5 results are used in the discussion above, however, if the analysis were used to set the normalization of the μ^+-decay ν_e prediction in the fit, it would be incorrect. Therefore, ν_μ disappearance would be a source systematic error in determining the π^+ flux and CCQE cross section constraints in the analysis of chapter 5. One might address this by iterating the ν_e fit with and without assuming disappearance, however, the combined fit handles this kind of difficulty transparently because it estimates the ν_e and ν_μ oscillation parameter values and errors simultaneously, including their correlations. Finally, a combined fit is a straightforward way to include the ν_μ data in the ν_e appearance analysis, and is therefore much easier to understand and explain.

The combined fit results are shown in figures 7.8 through 7.11 with statistical and π^+ flux errors, statistical and K^+ flux errors, statistical and σ_ν errors, and all of the above respectively. A comparison of the 90% confidence level, 3σ, and 5σ sensitivity curves is shown for the combined fit vs. the appearance-only or disappearance-only fits using errors based on external data (with the CCQE parameter correlations from MiniBooNE) in figure 7.12. In general, the combined fit represents an improvement of 1-1.5σ over the appearance-only fit with systematic errors estimates from external data.

The combined fit result for ν_e appearance, with uncertainties from the π^+ flux prediction, agrees very well with the result in figure 7.7 which used the π^+ flux constraint method of chapter 5. This is shown in figure 7.8. The ν_μ sensitivity with π^+ errors is identical in the disappearance-only and combined fits. Similarly, for the neutrino interaction cross section errors, the combined fit appearance sensitivity is consistent with the sensitivity shown in figure 7.7, which uses the constrained CCQE cross section errors derived in chapter 5. The combined fit ν_e result, shown in figure

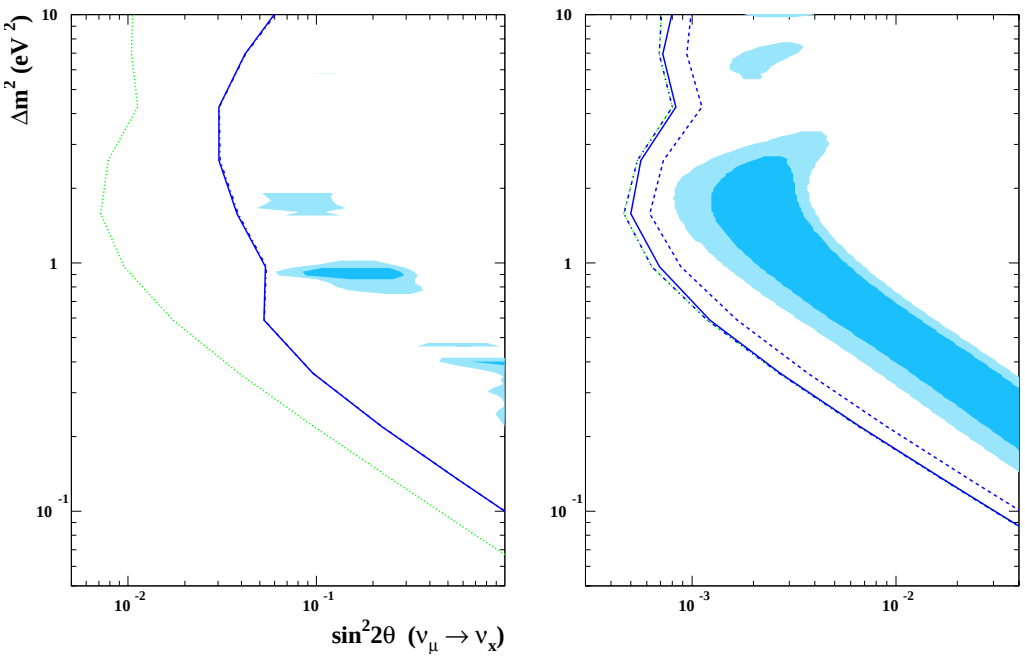

Figure 7.8: *MiniBooNE 90% confidence level sensitivity with statistical errors (green, dotted line), and π^+ flux prediction systematic errors from external sources (blue, dashed line), from the constrained π^+ errors in chapter 5 (blue, dash-dotted line), and from the combined fit (blue, solid line). Left: Δm^2 (eV^2) vs. $sin^2 2\theta_{\mu x}$. Right: Δm^2 (eV^2) vs. $sin^2 2\theta_{\mu e}$. Allowed regions are described in figure 7.4.*

7.9, is slightly improved with respect to this limit at high Δm^2, where high energy neutrinos from kaons are more important. This is likely because only π^+-decay neutrinos were constrained in figure 7.7, while the error reduction is properly applicable to all neutrinos with CCQE interactions. For ν_μ disappearance, the sensitivity is identical for all but Δm^2 of 1.58 eV^2, where the combined-fit result is slightly better than the disappearance-only fit. This Δm^2 is very close to the first oscillation maximum, and as figure 7.3 shows, the ν_e sample does contribute spectral information at this point, that is, the energy spectrum exhibits deformation due to oscillations. The `MINUIT` fit at this Δm^2 shows every sign of normal convergence, and so this may be a case where the ν_e data helps the ν_μ fit.

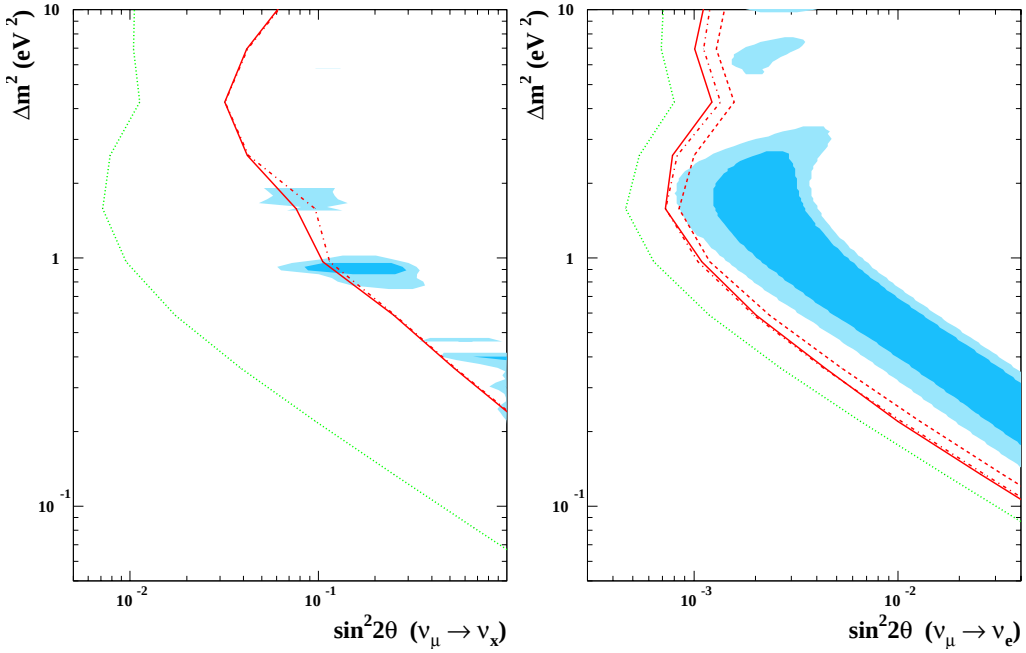

Figure 7.9: *MiniBooNE 90% confidence level sensitivity with statistical errors (green, dotted line), and σ_ν prediction systematic errors from external sources (red, dashed line), from the constrained σ_ν errors in chapter 5 (red, dash-dotted line), and from the combined fit (red, solid line). Left: Δm^2 (eV^2) vs. $sin^2 2\theta_{\mu x}$. Right: Δm^2 (eV^2) vs. $sin^2 2\theta_{\mu e}$. Allowed regions are described in figure 7.4.*

For the π^+ and neutrino interaction cross section uncertainties, the combined fit result can be compared with appearance-only fits using "off-line" constraints from the ν_μ data. The agreement between the combined fit results and the "off-line" expectations build confidence in the combined fit procedure. For the K^+ errors, no such "off-line" analysis is available here. The combined fit ν_e appearance and ν_μ disappearance sensitivities with statistical and K^+ errors are shown in figure 7.10. The improvement in the ν_e sensitivity over the appearance-only fit is significant. It is not surprising that the ν_μ data set provides a strong constraint because there are $\sim$8$\times$ more K^+-decay events after cuts in the ν_μ sample than in the ν_e data set. However, the combined-fit result for the disappearance sensitivity is slightly worse than the

disappearance-only fit result. This is because although the number of K^+-induced events is larger in the ν_μ sample, the number of K^+ induced events in the ν_e sample is of the same order of magnitude, and therefore has power in the fit. In fact, the total correlated normalization error is actually increased in the combined fit, to 0.28%, with respect to the disappearance-only fit, where the normalization error coming from K^+ systematics is 0.23%. For all other sources of systematic error considered here, the combined-fit normalization error is approximately equal to the disappearance-only fit value, as table 7.3 shows. The difference between the high Δm^2 $sin^2 2\theta_{\mu x}$ limit values in the disappearance-only and combined fits is 0.0007, which is roughly the expected value, $\sim$2 $\times$ (0.0028-0.0023), from equation 7.11. However, the relation in 7.11 is not strictly valid for the combined fit because the oscillation parameters $sin^2 2\theta_{\mu x}$ and $sin^2 2\theta_{\mu e}$ are slightly correlated by the common systematics. From the fit, the correlation coefficient is $\rho = 0.062$.

Finally, the combined fit results for statistical, π^+ flux prediction, K^+ flux prediction, and neutrino interaction cross section errors combined are shown in figure 7.11. For ν_e appearance, the sensitivity calculated using the "off-line" constraints for the π^+ and neutrino cross section uncertainties, together with the statistical and external K^+ errors, is also shown. The combined fit is slightly improved with respect to this limit due to the additional K^+ error constraint, for which there is no "off-line" analogue here. For ν_μ disappearance, the combined-fit and disappearance-only sensitivities are identical for all points other than $\Delta m^2 = 1.58\ eV^2$, where the improvement is due to the marginal reduction in cross section uncertainties seen in figure 7.9.

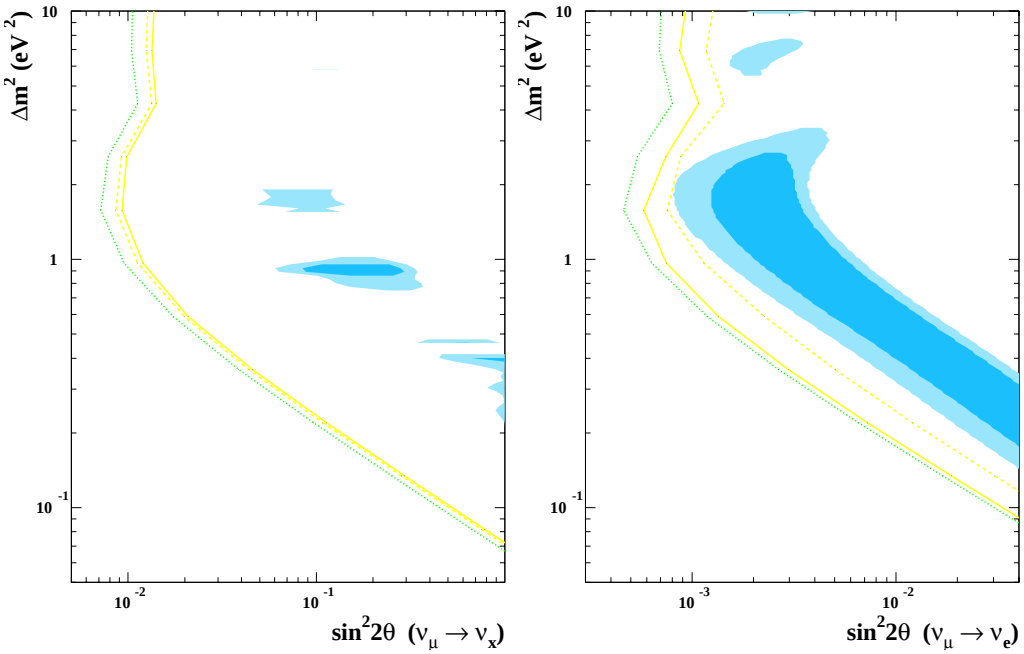

Figure 7.10: *MiniBooNE 90% confidence level sensitivity with statistical errors (green, dotted line), and K^+ prediction systematic errors from external sources (yellow, dashed line), and from the combined fit (yellow, solid line). Left: Δm^2 (eV^2) vs. $sin^2 2\theta_{\mu x}$. Right: Δm^2 (eV^2) vs. $sin^2 2\theta_{\mu e}$. Allowed regions are described in figure 7.4.*

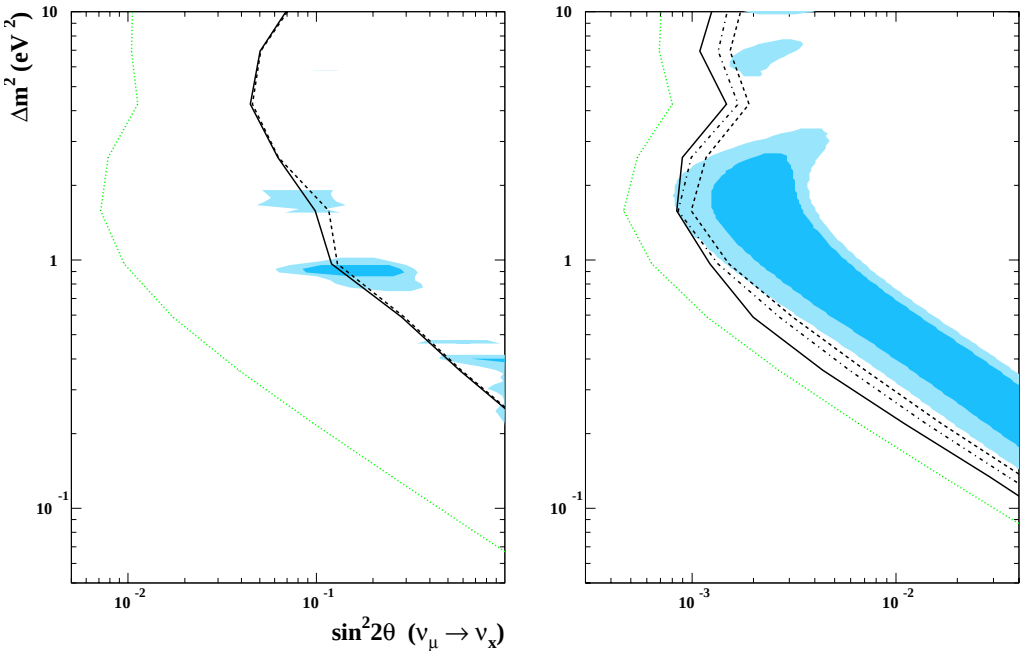

Figure 7.11: *MiniBooNE 90% confidence level sensitivity with statistical errors (green, dotted line), and π^+, K^+, and σ_ν prediction systematic errors from external sources (black, dashed line), from the constrained errors in chapter 5 (black, dash-dotted line), and from the combined fit (black, solid line). eft: Δm^2 (eV^2) vs. $sin^2 2\theta_{\mu x}$. Right: Δm^2 (eV^2) vs. $sin^2 2\theta_{\mu e}$. Allowed regions are described in figure 7.4.*

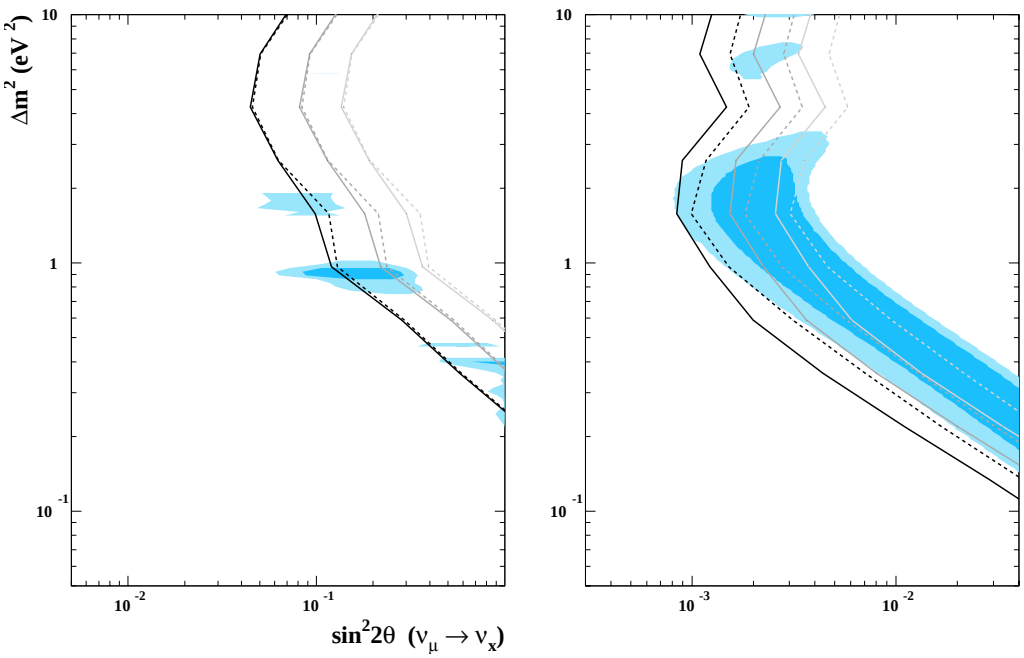

Figure 7.12: *MiniBooNE sensitivity with statistics, π^+, K^+, and ν cross section prediction systematic errors at 90% confidence level (black), 3σ (medium grey), and 5σ (light grey) for the combined fit (solid lines) and appearance-only or disappearance-only (dashed lines), using external systematic errors. Left: Δm^2 (eV^2) vs. $sin^2 2\theta_{\mu x}$. Right: Δm^2 (eV^2) vs. $sin^2 2\theta_{\mu e}$. Allowed regions are described in figure 7.4.*

7.5 Conclusions

The ν_μ data set in MiniBooNE provides a powerful constraint on several important sources of systematic error for the ν_e appearance oscillation analysis, notably the π^+ flux prediction, the K^+ flux prediction, and the neutrino interaction CCQE cross section model. A variety of approaches to incorporating information from the ν_μ data into the ν_e analysis have been pursued, and are found to be consistent with each other.

The 90% confidence level, 3σ, and 5σ sensitivity curves are shown for ν_e appearance and ν_μ disappearance in figure 7.12, comparing the combined-fit result with the

appearance-only and disappearance-only fits including statistical and π^+ flux prediction, K^+ flux prediction, and neutrino interaction cross section prediction systematic errors. For ν_e appearance, the combined fit improves the experiment sensitivity by 1.2-1.5 σ depending on the value of Δm^2, relative to an appearance-only fit. For ν_μ disappearance, the combined fit sensitivity is similar to a disappearance-only fit.

The systematic errors considered in this work are not yet complete since they do not include uncertainties on the detector response or final state interaction cross sections, which will degrade the oscillation sensitivity. However, there are also sources of systematic error which will be reduced by using MiniBooNE measurements to set their uncertainties. Examples include the CCQE parameter errors, and the neutral current π^0 cross section uncertainties. Both of these will improve MiniBooNE's reach significantly since the neutrino interaction cross sections are currently the limiting sources of systematic error. On balance, the MiniBooNE sensitivity will most likely be somewhat improved with respect the analysis described here.

For both the ν_μ disappearance and the ν_e appearance, the 90% confidence level sensitivity curves calculated here cover interesting regions of oscillation parameter space. For some limited (Δm^2, $sin^2 2\theta_{\mu x}$) combinations, with these systematic errors, MiniBooNE has 3σ coverage in ν_μ disappearance. For the ν_e appearance search, MiniBooNE has 3-5σ discovery potential over most of the LSND (Δm^2, $sin^2 2\theta_{\mu e}$) allowed region using the combined fit developed here.

Whether MiniBooNE confirms or rules out the LSND signal, the most important criterion is that the result be unambiguous. The LSND signal raises many fascinating possibilities, and for progress to be made in understanding what neutrino oscillations tell us about the Standard Model, these questions must be resolved by a definitive measurement. MiniBooNE is a difficult experiment because it operates in a proton beam and neutrino interaction energy regime where few experiments have gone before.

Therefore, constraining systematic errors and background predictions using in-situ neutrino data is both interesting in its own right and a relevant part of making the MiniBooNE measurement conclusive. This is what I have tried to accomplish and describe in my thesis analysis.

Bibliography

[1] B. Kayser, F. Gibrat-Debu, and F. Perrier, *The Physics of Massive Neutrinos*. Singapore: World Scientific (1989).

[2] E. Majorana, *Nuovo Cimiento*. **14**, 171 (1937).

[3] F. Boehm and P. Vogel, *The Physics of Massive Neutrinos*, University of Cambridge, Great Britian: University Press (1992).

[4] V. Gribov and B. Pontecorvo, *Phys. Lett.,* **B28**, 493 (1969); Z. Maki, N. Nakagawa, S. Sakata, Prog. Theor. Phys. **28**, 870 (1962).

[5] B. Kayser, arXiv:hep-ph/0211134.

[6] J. Patti and A. Salam, *Phys. Rev.,* **D10**, 275 (1974).

[7] C. Quigg, *Gauge Theories of the Strong, Weak, and Electromagnetic Interactions*, USA: Westview Press (1997).

[8] G. Gell-Mann, P. Ramond, and R. Silensky in *Supergravity*, ed. D. Freeman and P. van Nieuwenhuizen, North Holland, Amsterdam (1979).

[9] Y. Fukuda *et al.* [Super-Kamiokande Collaboration], Phys. Rev. Lett. **82**, 2644 (1999) [arXiv:hep-ex/9812014].

[10] C. Caso *et al.* [Particle Data Group], Eur. Phys. J. C **3**, 1 (1998).

[11] http://cupp.oulu.fi/neutrino/nd-mass.html

[12] C. Weinheimer, , *Prepared for 3rd International Conference on Dark Matter in Astro and Particle Physics (Dark 2000), Heidelberg, Germany, 10-16 Jul 2000.*

[13] H. Ejiri *et al.*, Phys. Rev. C **63**, 065501 (2001).

[14] K. Assamagan *et al.*, Phys. Rev. D **53**, 6065 (1996).

[15] R. Barate *et al.* [ALEPH Collaboration], Eur. Phys. J. C **2**, 395 (1998).

[16] S. Hannestad, JCAP 0305, 004 (2003) [astro-ph/0303076]; O. Elgaroy, O. Lahav, JCAP 0304, 004 (2003) [astro-ph/0303089].

[17] D. N. Spergel, *et al.*, astro-ph/0302209.

[18] KATRIN experiment, http://www-ik.fzk.de/ katrin

[19] L. Baudis *et al.*, Phys. Rev. Lett. **83**, 41 (1999) [arXiv:hep-ex/9902014].

[20] H. V. Klapdor-Kleingrothaus, A. Dietz, H. L. Harney and I. V. Krivosheina, Mod. Phys. Lett. A **16**, 2409 (2001) [arXiv:hep-ph/0201231].

[21] C. E. Aalseth *et al.*, Mod. Phys. Lett. A **17**, 1475 (2002) [arXiv:hep-ex/0202018].

[22] GENUIS experiment, http://www.mpi-hd.mpg.de/non_acc/descr1.html; NEMO3 experiment, http://http://nemo.web.lal.in2p3.fr/

[23] T. Adams *et al.* [NuTeV Collaboration], Int. J. Mod. Phys. A **16S1B**, 761 (2001) [arXiv:hep-ex/0009007].

[24] A. G. Doroshkevich, Y. B. Zeldovich, R. A. Syunyaev, M. Y. Khlopov, Pisma Astron. Zh. **6**, 457 (1980) [Sov. Astron. Lett. 6, 252 (1980)].

[25] W. Hu, D. J. Eisenstein, M. Tegmark, Phys. Rev. Lett. **80**, 5255 (1998) [astro-ph/9712057].

[26] Y. Ashie *et al.* [Super-Kamiokande Collaboration], Phys. Rev. D **71**, 112005 (2005) [arXiv:hep-ex/0501064].

[27] R. J. Davis, D. S. Harmer and K. C. Hoffman, Phys. Rev. Lett. **20**, 1205 (1968).

[28] Q. R. Ahmad *et al.* [SNO Collaboration], Phys. Rev. Lett. **87**, 071301 (2001) [arXiv:nucl-ex/0106015].

[29] B. Aharmim *et al.* [SNO Collaboration], Phys. Rev. C **72**, 055502 (2005) [arXiv:nucl-ex/0502021].

[30] K. Eguchi *et al.* [KamLAND Collaboration], Phys. Rev. Lett. **90**, 021802 (2003) [arXiv:hep-ex/0212021].

[31] A. Aguilar *et al.* [LSND Collaboration], Phys. Rev. D **64**, 112007 (2001) [arXiv:hep-ex/0104049].

[32] N. Tagg [MINOS Collaboration], arXiv:hep-ex/0605058.

[33] M. H. Ahn [K2K Collaboration], arXiv:hep-ex/0606032.

[34] H. Murayama, for the 2006 Particle Data Group review. [http://hitoshi.berkeley.edu/neutrino/]

[35] G. Fogli, E. Lisi, A. Marrone, and A. Pallazo, [hep-ph/0506083].

[36] M. Sorel, J. M. Conrad and M. Shaevitz, Phys. Rev. D **70**, 073004 (2004) [arXiv:hep-ph/0305255].

[37] R. Gran *et al.* [K2K Collaboration], arXiv:hep-ex/0603034.

[38] J. Monroe, NuFact 2005 conference presentation;

[39] M. O. Wascko, arXiv:hep-ex/0602050.

[40] J. L. Raaf, "A measurement of the neutrino neutral current pion cross section at MiniBooNE," UMI-31-90981 (2005).

[41] G. P. Zeller, NuFact03 AIP Conf. Proc. **721**, 375 (2004).

[42] T. Kobilarcik, J. DeVoy, C. Moore, Particle Accelerator Conference Proceedings **5**, 2934 (2003).

[43] C. Moore, J. Anderson Jr., R. Ducar, R. Ford, T. Kobilarcik, E. J. Prebys, A. Russell, R. Stefanski, J. Monroe, Particle Accelerator Conference Proceedings **3**, 1652 (2003).

[44] L. Bugel, M. Sorel, MiniBooNE Technical Note #34.

[45] D. E. Groom *et al.*, (Particle Data Group) Eur. Phys. J **C5** 1, (2001).

[46] G. P. Zeller, arXiv:hep-ex/0312061.

[47] J. D. Jackson, *Classical Electrodynamics*, 3rd edition, (John Wiley & Sons), New York, 1998).

[48] J. B. Birks, *The Theory and Practice of Scintillation Counting*, (Macmillan, New York, 1964).

[49] J. L. Raaf *et al.*, IEEE Trans. Nucl. Sci. **49** 957 (2002).

[50] A. O. Bazarko, P. D. Meyers, R. B. Patterson, F .C. Shoemaker, H. A. Tanaka, MiniBooNE Technical Note #144.

[51] A. Einstein, Annalen der Physik, **17** pp. 132-148 (1905).

[52] B. C. Brown, MiniBooNE Detector Memo #8.

[53] S. J. Brice, "Photomultiplier Tubes for the MiniBooNE Experiment," accepted for publication in NIM (2006).

[54] C. Athanassopoulos, *et al.*, Nucl. Instrum. Methods Phys. Res., Sect. A 388, 149 (1997).

[55] L. Bugel and M. Sharp, *private communication*; H. C. Kim, MiniBooNE Technical Note #132.

[56] F. James and M. Roos, Comput. Phys. Commun. **10**, 343 (1975) [http://wwwasdoc.web.cern.ch/wwwasdoc/minuit/minmain.html].

[57] I. Stancu, MiniBooNE Techical Note #50.

[58] I. Stancu (and Y. Liu), MiniBooNE Technical Notes #36, 50, 77, 100, 115, 125, 126.

[59] L. Michel, Proc. Phys. Soc. A **63**, 514 (1950).

[60] Y. Liu, I. Stancu, MiniBooNE Technical Note #126.

[61] B. Rossi, *High Energy Particles*, Prentice-Hall, Inc., Englewood Cliffs, NJ (1952).

[62] R. Imlay, B. Metcalf, S. Ouedraogo, M. Sung, and M. Wascko, MiniBooNE Technical Note #106.

[63] R. Imlay *et al.*, NIM, 2006, in preparation; M. O. Wascko, *private communication.*

[64] B. P. Roe, H. J. Yang, J. Zhu, Y. Liu, I. Stancu and G. McGregor, Nucl. Instrum. Meth. A **543**, 577 (2005), and H. J. Yang, B. P. Roe and J. Zhu, Nucl. Instrum. Meth. A **555**, 370 (2005).

[65] D. Schmitz, Neutrino Beams and Instrumentation 2005, Conference Presentation [http://www.hep.utexas.edu/nbi2005/transparencies/beamMChadprod/dschmitz-harp-nbi2005.pdf] (Unpublished).

[66] M. G. Catanesi *et al.* [HARP Collaboration], Nucl. Phys. B **732**, 1 (2006) [arXiv:hep-ex/0510039].

[67] J. R. Sanford and C. L. Wang, BNL AGS internal report # BNL11299 and # BNL11479, (1967).

[68] R. A. Lundy, *et al.*, Phys. Rev. Lett. **14**, 504 (1965).

[69] D. Dekkers, *et al.*, Phys. Rev. **137**, B962 (1965).

[70] W. F. Baker, *et al.*, Phys. Rev. Lett. **7**, 101 (1961).

[71] V. L. Fitch, *et al.*, Phys. Rev. **126** 1849 (1962).

[72] G. Belletini, *et al.*, CERN Report PS/5037/KL (1965). (Unpublished)

[73] NEED A REFERENCE FOR MODERN XSEC VALUE 208 MB (Unpublished)

[74] Y. Cho, *et al.*, Phys. Rev. D **4**, 1967 (1971).

[75] R. P. Feynman, Phys. Rev. Lett. **23**, 1415 (1969).

[76] C. L. Wang, Phys. Rev. Lett. **25**, 1068 (1970).

[77] J. Link, *et al.*, to be submitted to Phys. Rev. C (2006).

[78] D. Schmitz, Private Communication (2006).

[79] T. Abbott, *et al.*, Phys. Rev. D, **45**, 3906 (1992). Data from BNL data base entry #H0001001,940628

[80] Aleshin *et al.*, ITEP-77-80 (1977).

[81] T. Eichten *et al.*, Nuclear Physics **B44** 333 (1972).

[82] P. A. Piroue *et al.*, Phys. Rev. **148** 4 (1966).

[83] I. A. Vorontsov, *et al.*, ITEP-85-1983 and ITEP-88-11.

[84] The Geant4 collaboration: `http://geant4.web.cern.ch/geant4/`.

[85] M. Sorel, "Search for Sterile Neutrinos Using the MiniBooNE Beam," FERMILAB-THESIS-2005-07.

[86] V. V. Gachurin *et al.*, ITEP-59-1985.

[87] Bobchenko *et al.*, Sov. J. Nucl. Phys. **30** 805 (1979), Yad. Fiz. **30** 1553 (1979).

[88] B. W. Allardyce *et al.*, Nucl. Phys. A **209**, 1 (1973).

[89] D. Ashery *et al.*, Phys. Rev. C **23** 2173 (1981).

[90] H. A. Tanaka, *private communication.*

[91] M. H. Shaevitz, MiniBooNE Technical Note #188.

[92] H. A. Tanaka, MiniBooNE Technical Note #122.

[93] J. M. Conrad, *private communication.*

[94] M. H. Shaevitz, MiniBooNE Technical Note #185.

[95] P. Lipari, Nucl. Phys. B Proc. Suppl. **112**:274 (2002).

[96] D. Casper, Nucl. Phys. B Proc. Suppl. **112**:161 (2002).

[97] C. H. Llewellyn Smith, Phys. Rep. **3C**:261 (1972).

[98] D. Rein and L. M. Sehgal, Annals of Physics **133**:79 (1981).

[99] A. Bodek and J. L. Ritchie, submitted to Nucl. Phys. Proc. Suppl., arXiv:hep-ex/0308007.

[100] R. A. Smith and E. J. Moniz, Nucl. Phys. **B43**:605 (1972); erratum: Nucl. Phys. **B101**, 574 (1975).

[101] E. A. Hawker, Nucl. Phys. Proc. Suppl. **139**, 260 (2005).

[102] V. Bernard *et al.*, J. Phys. **G28**, R1 (2002).

[103] H. Budd, A. Bodek and J. Arrington, Nucl. Phys. Proc. Suppl. **139**, 90 (2005) [arXiv:hep-ex/0410055].

[104] E. J. Moniz *et al.*, PRL **26**, 445 (1971).

[105] G. P. Zeller *et al.*, MiniBooNE Technical Note #102.

[106] R. Brun, M. Caillat, M. Maire, G. N. Patrick and L. Urban, CERN-DD/85/1.

[107] T. Katori, MiniBooNE Technical Note #176.

[108] H. O. Meyer, MiniBooNE Technical Note #90.

[109] P. Ockerse, S. Breitzmann, C. Cox, T. Katori, S. McKenney, H.-O. Meyer, J. L. Raaf, R. Tayloe, N. Walbridge, MiniBooNE Technical Note #74.

[110] D. Toptygin, MiniBooNE Technical Note #122.

[111] B. C. Brown, S. Maza, A. Pla-Dalmau, H. A. Tanaka, MiniBooNE Technical Note #145.

[112] S. Brice, B. Fleming, P. Meyers, R. Patterson, H. Tanaka, M. Wascko, MiniBooNE Technical Note #95.

[113] R. B. Patterson, MiniBooNE Technical Note #83.

[114] Page written and maintained by Don Groom, [http://pdg.lbl.gov/AtomicNuclearProperties].

[115] R. A. Fisher, Annals of Eugenics, vol. 7, part II, pp. 179-188, (1936).

[116] A. Aguilar-Arevalo, MiniBooNE Technical Note #97.

[117] L. Lyons, "Statistics for nuclear and particle physicists" (Cambridge Univ. Press, 1986).

[118] M. Wilking, MiniBooNE Collaboration Meeting Presentation (May 18, 2006).

[119] M. O. Wascko [MiniBooNE Collaboration], arXiv:hep-ex/0602050.

[120] J. Monroe [MiniBooNE Collaboration], Nucl. Phys. Proc. Suppl. **139**, 59 (2005) [arXiv:hep-ex/0408019].

[121] N. J. Baker, Phys. Rev. **D23**:2499 (1981).

[122] Barish *et al.*, Phys. Rev. **D16**, 3103 (1977).

[123] Kitagaki *et al.*, Phys. Rev. **D28**, 436 (1983).

[124] K. L. Miller, "A Study Of The Weak Axial Vector Form-Factor In The Quasielastic Reaction Muon-Neutrino D → Mu- P P(S)," UMI-82-09392.

[125] A. K. Mann, Print-78-0933 (PENN) *Presented at 19th Int. Conf. on High Energy Physics, Tokyo, Japan, Aug 23-30, 1978.*

[126] Y. Nambu and M. Yoshimura, Phys. Rev. Lett. **24** 25 (1970).

[127] V. Blobel, eConf **C030908**, MOET002 (2003).

[128] A. Bodek and H. Budd, [http://arxiv.org/abs/hep-ex/0410055] and [http://conferences.jlab.org/neutrino/talks/bodek_a.pdf]

[129] J. Monroe, D. Finley, T. Kobilarcik, H.-O. Meyer, MiniBooNE Technical Note #87.

[130] Pearson Electronics, [http://www.pearsonelectronics.com]

[131] A. Tollestrop (FNAL), *private communication*, 2004.

[132] MiniBooNE Beam Line Technical Design Report, [http://www-boone.fnal.gov]; A. Russell (FNAL), *private communication*, February 6, 2003.

[133] Measured by J. Monroe and D. Finley, February 7, 2003.

[134] B. Fellenz, *private communication*, February 4, 2003.

[135] B. Webber, FERMILAB-Conf-94/333 (1994).

[136] J. Crisp, Fermilab Instrumentation Group Memo, "Evaluation of Toroid Calibration Procedure" (2001).

[137] J. Crisp, Fermilab Instrumentation Group Memo, "Evaluation of Magnetic Fields and Pearson Toroids" (2001).

[138] A. Cadorna, Fermilab Instrumentation Group Memo, "Noise Analysis of Torroid Integrator" (2001).

[139] J. Crisp, *private communication*, January 21, 2003.

[140] A. Cadorna, *private communication*, February 6, 2003.

[141] G. Federwitz, *private communication*, February 6, 2003.

[142] R. Ford, *private communication*, December 24, 2002.

[143] A. Cadorna, Fermilab Instrumentation Group Memo, "Evaluation of Wave Form Generator Used for All Toroid Calibrations at FNAL" (2003).

[144] H. Anderson and G. Federwitz, Fermilab Interlock Group Memo, "Electronic Berm Interlock Module Functional Description" (2002) [http://www-bd.fnal.gov/icfa/workshops/20/overheads.html]; J. Anderson, Fermilab Interlock Group Memo, "Toroid Integrator Calibration Module" (2001).

[145] Calibration modules built and commissioned by Bill Sippach and Li Zhang, Nevis Laboratory, Columbia University.

[146] A. Cadorna, *private communication*, February 27, 2003.

[147] T. Kobilarcik, author of the MiniBooNE ACNET data acquisition program.

[148] J. V. Allaby *et al.*, CERN Report 70-12 (1970). (Unpublished)

[149] J. G. Asbury *et al.*, Phys. Rev. 178, 2086 (1969).

[150] G. J. Marmer *et al.*, Phys. Rev. D **3** 5 (1971), and kaon production data from G. J. Marmer Dissertation, Ohio State University (1968). (Unpublished)

[151] R. G. Van de Water, MiniBooNE Technical Note #128; J. Conrad, MiniBooNE Technical Note #149; J. Conrad, MiniBooNE Technical Note #150; K. Mahn, MiniBooNE Technical Note #168; K. Mahn, MiniBooNE Technical Note #175.

Appendix A

Protons on Target Measurement

The measurement of the number of protons on incident on the MiniBooNE target, abbreviated as *p.o.t.* hereafter, comes from two toroids, located 5 and 50 m upstream of the target respectively. The calibration of the toroids is the dominant contribution to the systematic error, which is $\sim$1%. The evolution of this analysis is described in detail in [129], the current status is summarized here.

A.1 Hardware

Toroids provide the primary measure of the total charge per Booster proton beam pulse in the MiniBooNE beam line. MiniBooNE uses two Pearson 3100 toroids, with a 3.5" aperture [130]. The toroids are essentially transformers, with the beam current acting as a one turn primary winding. The signal is transmitted from the beam enclosure to the MI10 service building where electronics condition and monitor the signal. The toroid calibration system is also located in the same building. The toroids each have two cable connections: one for signal pulse output, and one for calibration pulse input. The calibration loop of the toroid is simply a wire that passes through

the toroid, to simulate a one turn primary winding. The signal cable is RG108, and the calibration cable is 3/8" heliax. The calibration cable characteristics are such that the input pulse charge loss is less than 0.01% [131].

Toroid TOR875 is located 5 meters upstream of the MiniBooNE target, and toroid 860 is located 194.162 meters upstream of toroid 875 along the beam path [132]. Both are located quite far from the service building, and the time for the calibration signal to make a round trip from the MI10 service building to TOR875 and back is measured with an oscilloscope to be 1500 +- 250 ns [133] and calculated from time delay reflectometry [134] measurements on nearby BPM cables to be 1671 +- 40 ns. Schematics of the toroid locations and associated cables are shown in figure A.1.

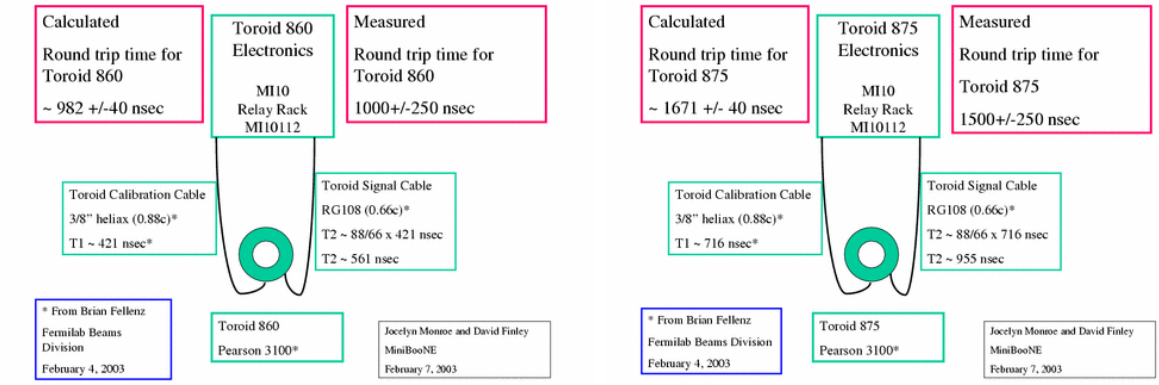

Figure A.1: *Left: toroid 860 location and cable transit time schematic. Right: toroid 875 location and cable transit time schematic.*

The toroids work like transformers: the beam or calibration pulse acts as the primary turn, and induces current in the many secondary turns wound about a circular ferrite core. When the proton beam passes through the toroid aperture, a voltage is induced in the toroid windings proportional to the mutual inductance of the transformer, and the change in the beam current with time [135]. The output voltage is integrated by an FNAL-built integrator, and the signal is digitized by an MADC.

The ideal response of the toroid + integrator + MADC system is,

$$N_{p.p.p.} = \frac{V_{out}\Delta t}{eR_g} \tag{A.1}$$

where $N_{p.p.p.}$ is the number of protons per pulse passing through the toroid, V_{out} is the voltage output of the toroid, Δt is the length of the beam pulse in seconds, e is the charge of a beam particle, and R_g is the termination resistance.

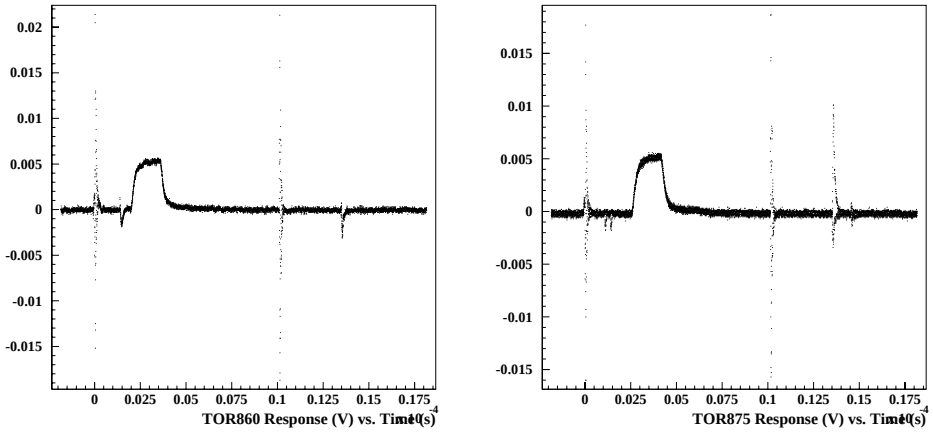

Figure A.2: *Left: toroid 860 beam pulse output voltage (V) vs. time (s). Right: toroid 875 beam pulse output voltage (V) vs. time (s).*

The toroids output 0.5 $Volts$ per *Ampere* of beam current, when terminated into 50 Ω. The voltage output of the toroid can be calculated using a simple transformer model [136], where the output voltage is related to the beam voltage by

$$V_{out} = V_{in} \times k\frac{R_L}{NR_g} \tag{A.2}$$

$$k = \frac{M}{\sqrt{L_1 L_2}} \tag{A.3}$$

where k is the coupling coefficient of the transformer (for and ideal transformer, $k = 1$) in terms of the mutual inductance M and the inductances of the primary, L_1, and secondary, L_2, loops, R_L is the load resistance of the transformer circuit, N is the turns ratio, and R_g is the termination resistance at the toroid, which is 50Ω. At

MiniBooNE beam intensities, the typical V_{out} is a few mV. The shorting mechanism that starts and ends the integrator gate causes noise fluctuations of this scale, as can be seen in figure A.2, however, since the toroid is electrically isolated from the beam pipe, the noise level in the toroid circuit is much smaller within the integrator gate [137]. Typical toroid signals are shown in figure A.2. As expected for a Booster proton beam pulse, the width of the toroid output voltage pulse is $1.6\mu s$. Comparison of TOR860 and TOR875 output voltage times shows that the TOR875 signal starts later, which is due to both the difference in cable length and distance between the two toroids.

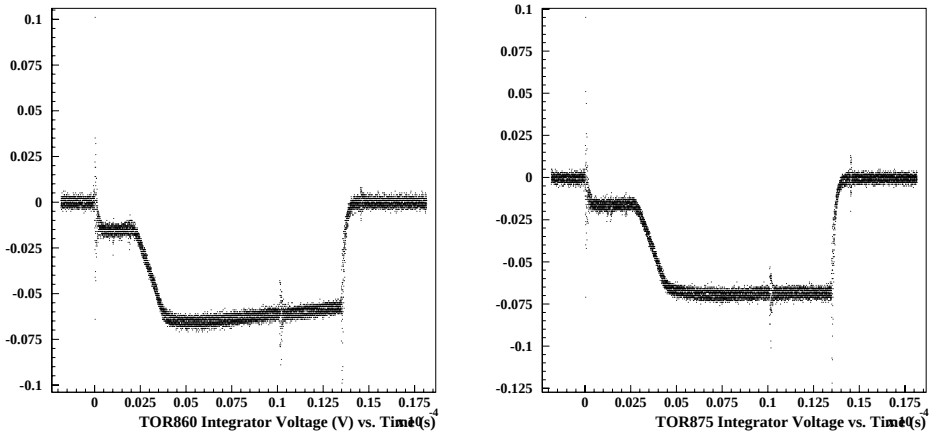

Figure A.3: *Left: toroid 860 beam pulse integrated voltage (V) vs. time (s). Right: toroid 875 beam pulse integrated voltage (V) vs. time (s).*

The integrator gate width, $10\mu s$, is much longer than the Booster pulse length, $1.6\mu s$, to account for reflections in the signal cables [138]. The integrator signal is shown for a Booster proton beam pulse in figure A.3. The integrators are triggered approximately $2\mu s$ before the beam transits the toroids, and the baseline of the integrators is non-zero, as can be seen from the time the integrator gate opens ($t = 0$ in figure A.3) to the time when the beam-induced voltage integration starts. The non-zero baseline value of the integrators requires the calibration correction of the

MADC pedestal. The integrator voltage level decays after the beam pulse has gone by, which requires calibration of the MADC gain to recover the full beam pulse voltage. Additionally, the decay constants are different between the TOR860 and TOR875 integrators, which necessitates careful timing of the integrator triggers with respect to the beam arrival time at each of the toroids. At the end of the gate, $10\mu s$ after the start, there is a $2.5\mu s$ sample-and-hold, when the integrator signal is digitized by the MADC, after which the integrator resets.

The integrator trigger time with respect to the Booster proton beam arrival affects the measured *p.o.t.* value because the integrators for TOR860 and TOR875 have different voltage decay constants. Additionally, since the toroids are separated by $\sim$200 m, the time of arrival of the beam with respect to a common integrator gate start time differs by $\sim$1 μs. Calibrations were done using a Hewlett Packard 8112A pulse generator to send a 1 V, 1.6 μs square pulse through the calibration loop of both toroids, and the start time of the calibration pulse was varied from 1 to 9 μs after the start of the integrator gate (this time is referred to as the delay in the following), preserving the toriod output pulse integrator time difference. Figure A.4 shows the measured number of protons per pulse as a function of delay with respect to a common start time of the integrator gate for the two toroids. The measured values differ by a few percent for delays less than 5μs, after which the ratio of TOR860/TOR875 changes rapidly as the delay approaches the end of the gate. The delay is currently set to occur at 2 μs, and this difference in gain between the two toroids is corrected for in the *p.o.t.* analysis.

In the initial beam line configuration, both integrators were triggered at the same time, with respect to the injection of beam into the Booster from the Linac [1]. This

[1]Both integrators were triggered on the 1D event + 33.45 ms + 319.6 μs. with respect to the 1D accelerator event, which corresponds to injection of beam from the Linac into the Booster. The 1D

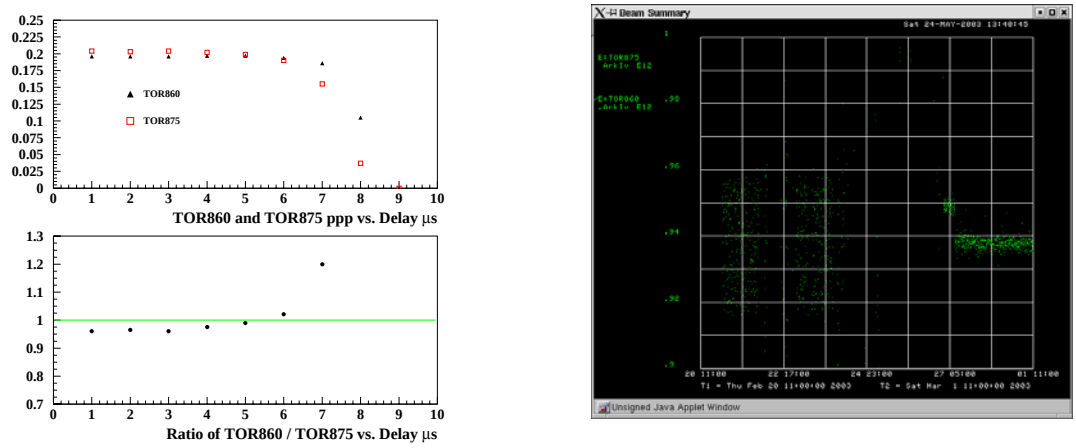

Figure A.4: *Left top: toroid 860 (Black) and 875 (Red) output (V) vs. delay after integrator gate start (μs). Left bottom: ratio of 860 / 875 output vs. delay after integrator gate start. Right: ratio of toroid 875 to toroid 860 number of protons per pulse vs. time, before and after the integrator trigger timing change described in the text.*

was problematic because the Booster extraction time with respect to injection can vary by up to 1.6 μs, because the extraction is synchronized with a notch created in the beam to minimize radiation due to particle losses at extraction. The placement of the notch is asynchronous with the extraction signal, and so the extraction trigger waits until the notch is in the appropriate location in the Booster. The length of one Booster turn in time, at the extraction beam energy, is 1.6 μs. Therefore as a result of triggering the integrators with respect to injection, rather than extraction, the time of arrival of the beam within the integrator gate could vary by up to 1.6 μs at both toroids.

The integrator trigger was changed at 4 $p.m.$ on February 26, 2003, such that the

event is the signal for beam to be injected into the Booster from the Linac, the acceleration time is approximately 33 ms, and the transit time of beam to the MiniBooNE beam line is approximately 319 μs.

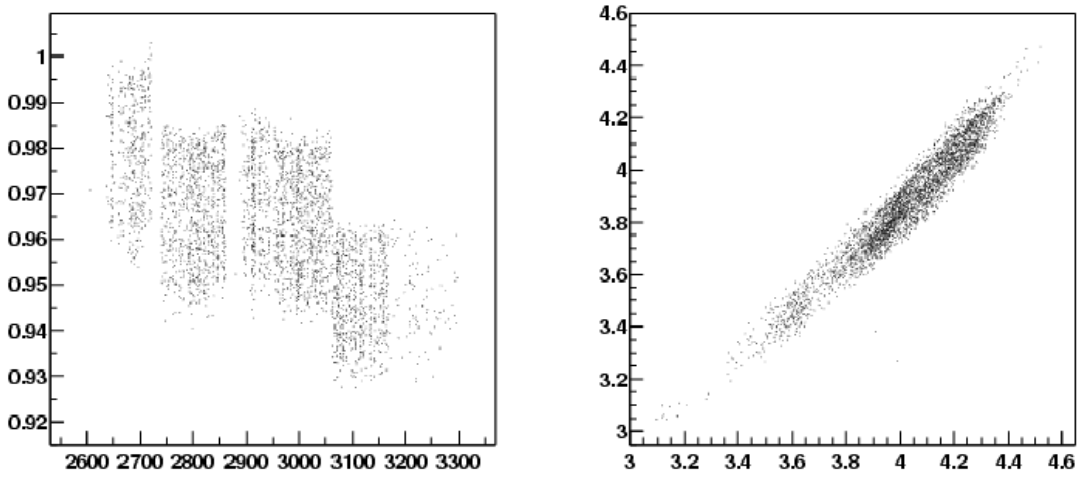

Figure A.5: *Left: ratio of toroid 875 to toroid 860 measured number of protons per pulse vs. run number. Right: toroid 875 vs. toroid 860 measured number of protons per pulse.*

trigger times are now with respect to the Booster extraction event [2], which ensures that there is no variation in the beam time of arrival with respect to the Booster notch, and such that the beam arrives 2 μs after the integrator gate start at TOR860, and approximately 3 μs after the integrator gate start at TOR875. The result of the change is shown in the right panel of figure A.4. Before the trigger timing change, the ratio of the two toroids varied by about $\pm$ 2% since the integrator triggers were set at 5 μs, where a $\pm$1.6 μs variation in the beam time-of-arrival has a few percent effect. After the trigger timing change one can see from figure A.4 that the variation is less than 0.5%.

The best intrinsic measurement resolution of the Pearson 3100 toroids is approximately 0.1% [139], however, this value is from benchtop measurements, and does not include the response of the associated integrating electronics or cables. In situ, the toroids are observed to have significant drift as a function of time [140]. This phenomenon is widely observed at FNAL, and the cause is not understood. The

[2]The new integrator trigger is the 1F event + 318.5 μs, for both toroids.

working hypothesis is that the drift is due to changes in the terminating resistance of the toroid, the integrator gain stages, and/or the MADC internal resistance [141]. Figure A.5 shows the ratio of the number of protons per pulse measured by TOR860 to TOR875 as a function of MiniBooNE run number. There are clear steps, as large as 1% in magnitude, where the relative calibration of the two toroids has changed [3]. However, it is not clear which of the toroids is drifting, and therefore calibration information is required.

A.2 Calibration

Two kinds of calibrations are employed to address the issue of toroid drift. Absolute calibrations are done approximately twice yearly by the FNAL Beams Division Instrumentation Group to measure the absolute ratio of voltage input to voltage output. The calibration of the two toroids relative to each other (called relative calibrations hereafter) is measured at 5 Hz by a custom calibration module designed and built at Nevis Laboratories. The relative calibration data is read out by the MiniBooNE beam line data acquisition system, and applied in the *p.o.t.* analysis software.

Absolute Calibration

The absolute calibration of the toroids addresses the issues of integrator gain and resistance changes. The absolute calibration employs a high precision wave form

[3] Since toroid 875 is considerably farther downstream in the beam line than toroid 860, one might ask whether the difference between the two measurements can be due to beam loss. This possibility has been ruled out by controlled loss measurements using a bayonet SWIC, in which a foil of a known thickness is inserted into the beam, and the loss monitors are tracked. A loss of 1% of the MiniBooNE beam would produce loss monitor readings approximately a factor of 10 higher than the nominal operating values [142].

generator, whose output voltage is calibrated to 0.6% [143]. It generates a series of 1.6 μs long pulses (Δt_{WFG}), which range from 0.0 to 4.0 V (V_{WFG}), which are run through the toroid calibration loop. The test pulse is timed to occur 2 μs after the start of the integrator gate. The wave form generator resistance, R_{WFG}, is measured to be 50.54 Ω. The absolute calibration of the toroid + integrator + MADC system gain and pedestal is done by comparing the measured value of the toroid integrator output with the predicted value, for each test pulse voltage. The ideal toroid integrator output is

$$N_{p.p.p.} = \frac{V_{WFG} \times \Delta t_{WFG}}{((R_{toroid} + R_{WFG})/2) \times e} \tag{A.4}$$

where $N_{p.p.p.}$ is the number of protons per pulse, R_{toroid} is the load resistance of the toroid + integrator system, and e is the charge of the proton. The gain is defined to be the constant of proportionality between the measured and predicted $N_{p.p.p}$, and the pedestal is defined to be the correction needed to make the measured $N_{p.p.p.} = 0$ when $V_{WFG} = 0$.

The gain and pedestal corrections are found by a linear regression on the measured and predicted $N_{p.p.p.}$ [143]. The ideal gain, G_{ideal}, is 1.0, and the ideal pedestal, P_{ideal} is 0.0. The gain correction is

$$G_{correction} = \frac{G_{ideal}}{G_{LSF}} \tag{A.5}$$

where G_{LSF} is the 1st coefficient in the linear regression. The pedestal correction is

$$P_{correction} = \frac{(P_{ideal} - P_{LSF})}{G_{LSF}} \tag{A.6}$$

where P_{LSF} is the 2nd coefficient in the linear regression. Typical values of the gain and pedestal corrections are 0.85 and 0.0, respectively.

Absolute calibrations of the toroids have been done several times; table A.1 shows the calibration date, gain, and percentage change. The pedestal corrections are not shown as the correction is typically of order 0.001, and is usually neglected. The error

Table A.1: *Gains from absolute calibrations as a function of time.*

Date	*860 Gain*	*% Gain Change*	*875 Gain*	*% Gain Change*
09.01.03	0.8300	-	0.8680	-
02.06.03	0.8713	4.97	0.8574	-1.24
02.27.03	0.8198	-6.00	0.8713	1.62
02.28.03	0.8263	0.79	0.9354	7.36
03.07.03	0.8209	-0.66	0.8210	-13.93
11.29.04	0.8259	+0.60	0.844	+2.61

Table A.2: *Errors on absolute calibration constants. The calibration equipment errors are propagated to find the uncertainty on the toroid gain.*

Cause	*Error (%)*	*Gain Change (%)*
Toroid Termination Resistance	0.47	0.26
Calibration Voltage	0.6	0.87
Toroid Drift (before 02.27.03) [4]	2.86	2.86
Toroid Drift (after 02.27.03)	1.45	1.45
Total Error (before 02.27.03)	-	3.00
Total Error (after 02.27.03)	-	1.71

on the absolute calibration constants of the toroids is determined by the measured uncertainties on the wave form generator output voltage, the measured termination resistance of the toroid, and the drift of the toroid gains between calibrations. These errors are summarized in table Appendices:::Protons::table:abscalerrs.

Relative Calibration

The calibration constants of the toroids change fairly often, as was seen in the previous section, and the changes can be large. Also, the toroids drift as a function of time. For these reasons, a un-used safety system, the E-Berm [144], has been modified such that it can be used to measure the calibration constants of the toroids on each beam pulse. The E-Berm consists of the two MiniBooNE toroids and a comparator module, used in conjunction with two toroid calibration modules [145]. The comparator module is designed to calculate the difference between the two toroids for each pulse, and for the sum of the previous ten pulses. The instantaneous and integrated losses are designed to be output to the radiation safety interlock system, which could automatically inhibit the next beam pulse if the per-pulse losses are greater than 6%, or if the average losses are greater than 2%. This system was never used for beam line safety, and therefore was available as a calibration monitor.

The E-Berm trigger was modified to measure the relative toroid calibration at $5Hz$. The calibration sequence consists of a series of 10 current pulses that are sent through a toroid calibration loop and read back through an integrator. The calibration occurs simultaneously for both toroids, over the full dynamic range (0.5E11 to 5E12 *p.p.p.*) of the beam intensity, which corresponds to an input voltage of 0.5 to 25 V. A linear regression is performed on the measured and ideal values of the integrated toroid output in the calibration module hardware. Gain and pedestal corrections are obtained for each toroid, and, for the purposes of monitoring the

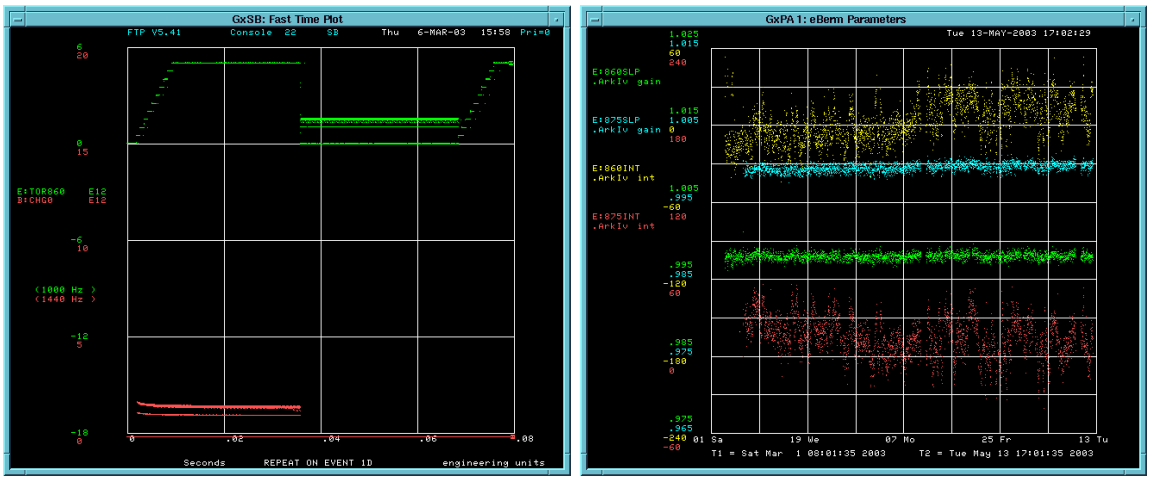

Figure A.6: *Left: E-Berm calibration sequence on toroid 860 (green) shown with the Booster charge (red) vs. time (s). The calibration sequence starts 1 ms. after the 0C event, and beam transits the toroids 330 μs after Booster extraction. The constant value of the toroid after Booster extraction is the measured beam intensity. Right: E-Berm calibration constants vs. time. Green: TOR860 E-Berm gain, Blue: TOR875 E-Berm gain, Yellow: TOR860 E-Berm raw pedestal, Red: TOR875 E-Berm raw pedestal.*

relative calibration of the toroids on each pulse, the gain and pedestal corrections are output to the MiniBooNE beam line data acquisition system. The calibration sequence is shown in figure A.6.

The internal resistance of the toroid integrator is different from the design values assumed when the Nevis calibration modules were made. As a result, the E-Berm system is used as a relative rather than absolute calibration, and, the relative calibration constant calculation is slightly different from that of the absolute calibration. The relative calibration of the toroids is given by [146]

$$N_{p.p.p.}^{corrected} = G_{E-Berm} \times N_{p.p.p} + P_{E-Berm}^{*} \tag{A.7}$$

where $N_{p.p.p.}^{corrected}$ is the number of protons per pulse, corrected by the relative calibra-

tion factor calculated by the E-Berm, G_{E-Berm}, and $N_{p.p.p.}$ is the number of protons per pulse calculated using the absolute calibration constants discussed in the previous section. The pedestal value calculated by the E-Berm, P^{RAW}_{E-Berm}, is the raw MADC pedestal, and so must be corrected according to the Acnet MADC scaling functions to obtain the pedestal correction, P^{*}_{E-Berm}, used to determine the number of protons per pulse.

$$P^{*}_{E-Berm} = \frac{P^{RAW}_{E-Berm}}{3267.8} \times G_{E-Berm} \times G_{Abs.\ Cal.} \tag{A.8}$$

where $G_{Abs.\ Cal.}$ is the gain from the absolute calibration, and 3267.8 is the factor needed to turn the raw MADC data into a voltage level. The noise level of the E-Berm gain calculation appears to be at the level of 0.1 - 0.2%, which is consistent with the best accuracy measured by the Beams division instrumentation group for the Pearson 3100 toroid. The E-Berm calibration constants have changed by less than 0.5% since March 7, 2003, when the E-Berm calibration data entered the MiniBooNE data stream. The calibration constants are shown as a function of time in the right panel of figure A.6.

A.3 Data Acquisition

The beam line data is acquired as follows. Data from beam line devices is collected by rack-mounted internet devices (IRMs), which time stamp the data when is arrives at the IRM. The data collection trigger occurs once per Booster pulse. The time-stamped and time-ordered data is read out of the IRMs by the AcnetDAQ software package [147] once every 3 seconds. The AcnetDAQ assembles the data for each event and concatenates the data from all events in a given detector (TankDAQ) run. When the run ends, the AcnetDAQ data for that run is shipped to the central data acquisition engine (UberDAQ), and subsequently merged by the NearLine program

with all of the other MiniBooNE data streams, such as detector, resistive wall monitor, and slow monitoring. The merging process merges events from all data streams which have GPS time stamps within 13 ms of the TankDAQ beam trigger time.

Data acquisition does not contribute to the systematic error on the *p.o.t.* measurement because events without *p.o.t.* information are eliminated by the analysis data quality cuts. Therefore data loss due to failure of the data acquisition system affects the efficiency of the data quality cuts. Historically, beam line data acquisition was problematic during the initial few months of MiniBooNE operations, however since March of 2003 the efficiency of the data quality cut that requires toroid information has been >95%. A description of the beam line data acquisition system commisioning can be found in reference [129].

A.4 Systematic Errors

Uncertainties on the *p.o.t.* measurement come from the calibration of the toroids and the timing of the beam within the integrator gate. When calculating the systematic error on the *p.o.t.* measurement, three distinct periods of toroid data taking are considered: (1) pre-2/27/03, before E-Berm calibration information was available and before the integrator trigger timing change, (2) 2/27/03 - 3/7/03 after the integrator trigger timing change and before E-Berm calibration information was available, and (3) post-3/7/03, when E-Berm data became available. The systematic errors for these three periods, summarized in table A.3, are different due primarily to the measured changes in the toroid gains.

The following systematic error sources are included:

- Toroid calibration constants: the systematic error on the toroid calibration constants before the E-Berm data became available is estimated by taking the

Table A.3: *Summary of systematic errors (%) in the three periods of toroid data taking: (1) pre-2/27/03, before E-Berm calibration information was available and before the integrator trigger timing change, (2) 2/27/03 - 3/7/03 after the integrator trigger timing change and before E-Berm calibration information was available, and (3) post-3/7/03, when E-Berm data became available.*

Cause	*Phase 1*	*Phase 2*	*Phase 3*
Toroid Calibration Constants	3.00	1.71	0.5
Toroid Pedestal	0.05	0.05	0.05
Integrator Gate Timing	2.00	0.5	0.5
Total	3.64	1.85	0.86

ratio of the measured gain on a given date to the previously measured value. From table A.1, before February 27, 2003, the error is estimated to be 3.00%, and between February 27 and March 7, the error is estimated to be 1.71%. After March 7, when the E-Berm relative calibration measurements began, the toroid gains have changed by less than 0.5%, shown in figure BLAH.

- Toroid pedestal: the pedestal value is not corrected for in the calibration, and is not subtracted from the beam-on reading. The pedestal contributes approximately -0.05% to the normalization of each beam pulse.

- Integrator gate timing: before the integrator trigger timing change on 2/26/03, the systematic error due to the timing is estimated from the variation in the toroid ratio shown in figure A.4, which is 2%. After the timing change, the uncertainty is estimated in the same way to be 0.5%.

Added in quadrature, the total estimated error is 3.64% on the protons on target sum

before February 27, 2003. Between February 27 and March 7, the total estimated error is 1.85%, and since March 7, the total estimated error is 0.86%.

Appendix B

Particle Production Fits

B.1 π^+ Production Fit Result Compared with Past Data

A number of experiments measured inclusive pion production in the phase space of interest to MiniBooNE prior to 1990. These older experiments typically have scintillator counters to trigger on the proton beam incidence on target, and a magnetic spectrometer with small acceptance which sits at a specific angle with respect to the incident proton beam. Therefore the meson yield is measured at a one production angle, and the entire apparatus is moved to measure production at a different angle. Cherenkov chambers are usually used for particle identification. The chambers are calibrated with radioactive foils with an accuracy of about 5%, beam-off running is done to subtract noise and background, and the spectrometer acceptance is determined geometrically. For these types of experiments, the measured cross section is typically given by (e.g. [74])

$$\frac{d^2\sigma}{dpd\Omega} = \frac{n \times (correction\ factor)}{N(N_0/A)\rho L \Delta\Omega \Delta p}$$

where n is the measured pion yield, the *correction factor* accounts for the efficiency of the spectrometer as a function of pion momentum, N is the number of incident protons, N_0 is Avogadro's number, A is the atomic number of the material, ρ is the density of the material in g/cm^3, L is the length of the target in cm, and $\Delta\Omega$ and Δp are the acceptances of the spectrometer in $sr.$ and GeV/c respectively. Typical acceptances are $3.5\%/(GeV/c)$ and 5.0 μsr, and the correction factor is usually folded into the yield if it is published [74]. Another method employed by older experiments without precise proton beam intensity or targeting efficiency monitors is to measure a meson yield in angle and momentum bins, and covert it into a differential cross section measurement by assuming a value for the total inelastic cross section, e.g.

$$\frac{d^2\sigma}{dpd\Omega} \;=\; \sigma_T \frac{d^2N}{dpd\Omega}.$$

where σ_T is the total inelastic cross section. The value of the inelastic proton-beryllium cross section has varied somewhat as a function of time, which contributes to the normalization discrepancy between older experiments. Typical reported errors on a data point are ∼5-10%, and the dominant sources of uncertainty come from statistics, the repeatability of measurements, and corrections for absorption and meson decay. Published normalization uncertainties are ∼5-20%.

Figure B.1 shows p_T vs. $x_{Feynman}$ for these experiments, superimposed upon the MiniBooNE beam Monte Carlo prediction for the phase space of π^+ that decay to neutrinos in the MiniBooNE detector acceptance. These data are reported in bins of $\frac{d^2\sigma}{dpd\Omega}$ or $E\frac{d^3\sigma}{d^3p}$ vs. pion momentum and angle. The most relevant cross section measurements are from the Cho[74] and Vorontsov[83] experiments, which are compared with the best-fit Sanford-Wang cross section described in Chapter 3 section 6 in Figures B.2 through B.4. The χ^2 between the older data in figure B.1 and the best-fit Sanford-Wang π^+ cross section prediction is shown in table B.1.

experiment	p_{BEAM} *(GeV/c)*	p_π *(GeV/c)*	θ_π	N_{DATA}	σ_{NORM}
Allaby[148]	19.2	6 - 10	0 - 7^o	21	15%
Asbury[149]	12.4	3 - 5	12, 15^o	6	15%
Cho[74]	12.4	1 - 5	0 - 12^o	53	5-8%
Dekkers[69]	18.8,23.1	4 - 12	0,5^o	30	(20%)
Marmer[150]	12.4	0.5 - 1	0 - 10^o	14	20%
Vorontsov 1983[83]	10.1	1 - 4.5	3.5^o	14	25%
Vorontsov 1988[83]	10.1	1 - 4.5	3.5^o	14	25%

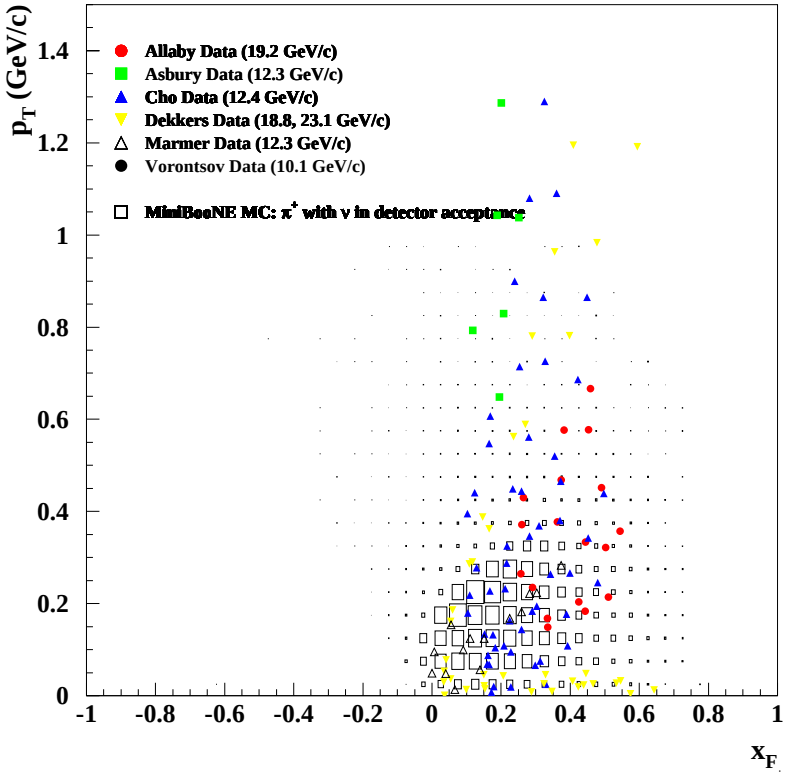

Figure B.1: *Top: Summary of experiments which measure* $pBe \rightarrow \pi^+ X$ *in a region of interest to MiniBooNE. Bottom: Transverse momentum (GeV) vs.* $x_{Feynman}$ *for* π^+ *production experiments, overlaid with the MiniBooNE beam Monte Carlo prediction for* π^+*-decay* ν *in the MiniBooNE detector acceptance.*

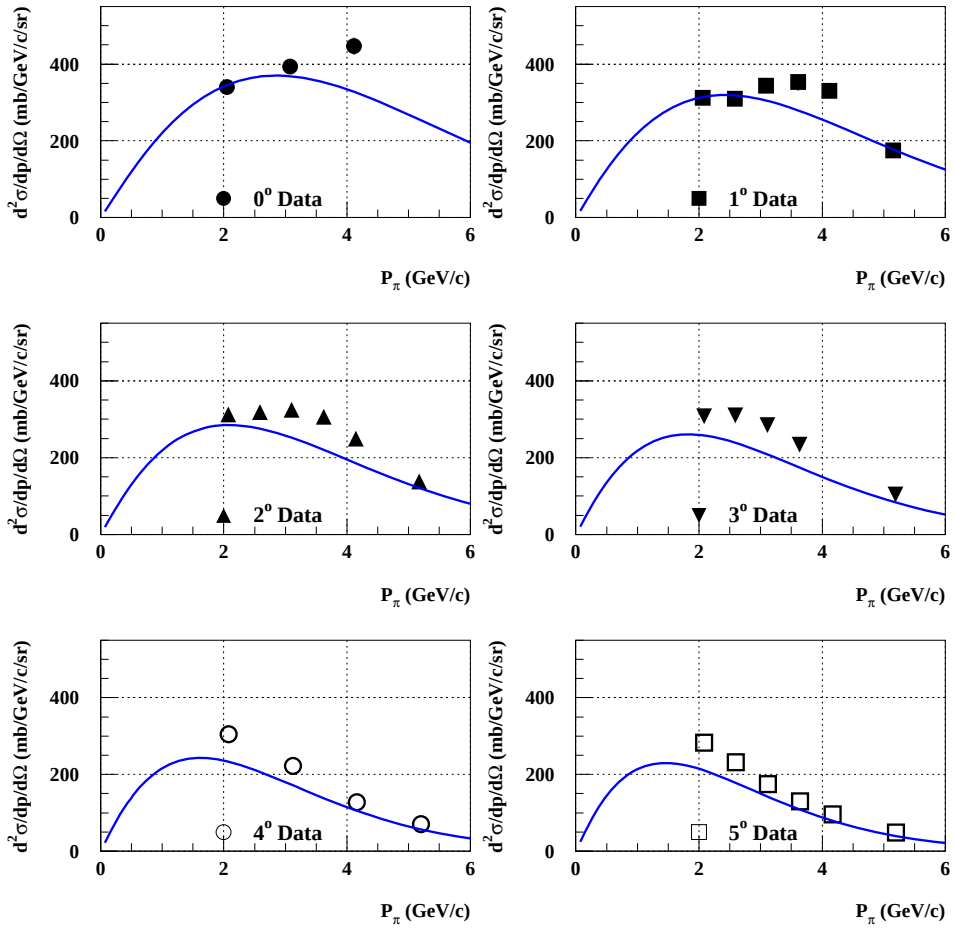

Figure B.2: *Cho[74] experiment measured inclusive π^+ production cross section (milli-barns/GeV/c/steradian) in proton-beryllium interactions vs. π^+ momentum (GeV/c), at p_{proton} = 12.3 GeV/c. Error bars include statistics and systematics.*

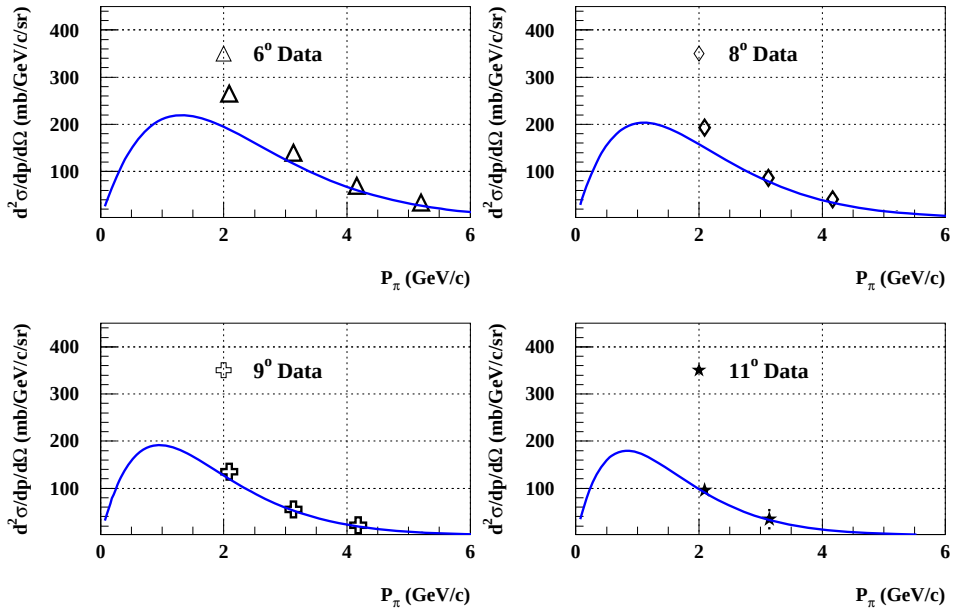

Figure B.3: *Cho[74] experiment measured inclusive π^+ production cross section (milli-barns/GeV/c/steradian) in proton-beryllium interactions vs. π^+ momentum (GeV/c), at p_{proton} = 12.3 GeV/c. Error bars include statistics and systematics.*

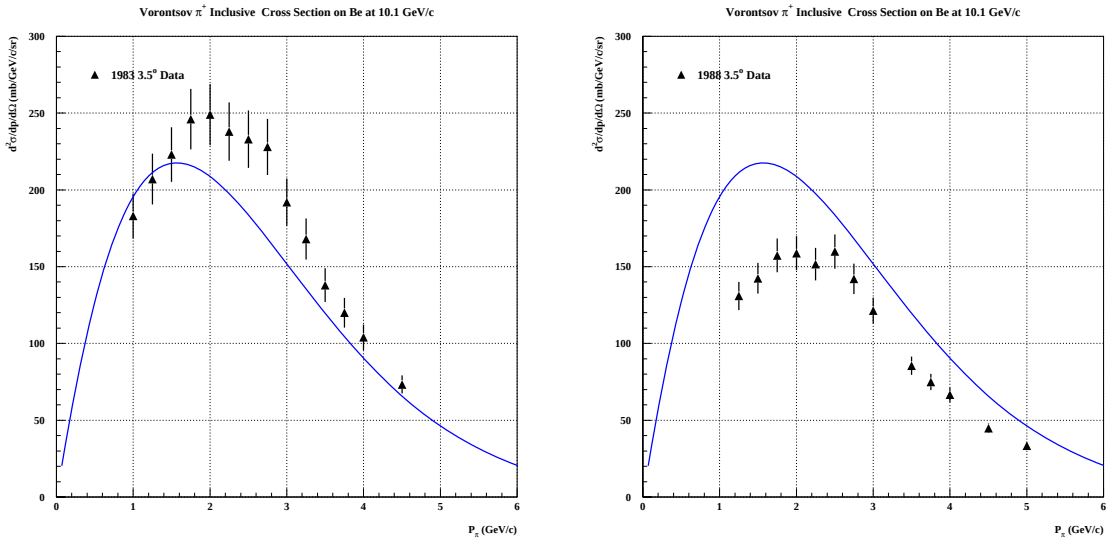

Figure B.4: *Vorontsov[83] experiment measured inclusive π^+ production cross section (milli-barns/GeV/c/steradian) in proton-beryllium interactions vs. π^+ momentum (GeV/c), at p_{proton} = 10.1 GeV/c. Error bars include statistics and systematics.*

Table B.1: *Compatibility of older π^+ production experiments with best-fit Sanford-Wang π^+ production cross section prediction.*

experiment	χ^2_{shape}	χ^2_{total}	*ndf*
Allaby	246	281	13
Asbury	95	99	-2
Cho	165	246	45
Dekkers	91	92	22
Marmer	83	116	6
Vorontsov	19	21	6

B.2 π^- Production Fit

Similar fits to those described in chapter 3 are performed for inclusive π^- production data from the E910 and HARP experiments. The results, assuming uncorrelated errors, are summarized in table B.2. The data are compared with the best-fit Sanford-Wang cross section in Figures B.6 through B.8. The χ^2/ndf of the combined fit is 1.30.

B.3 K^+ Production Fit Result Compared with Past Data

Several older experiments which have measured $pBe \rightarrow K^+X$ are not included in the Sanford-Wang K^+ cross section fit described in chapter 3. These experiments generally have worse coverage of the phase space of interest to MiniBooNE, shown in figure B.9, or are missing necessary information such as the normalization uncertainty

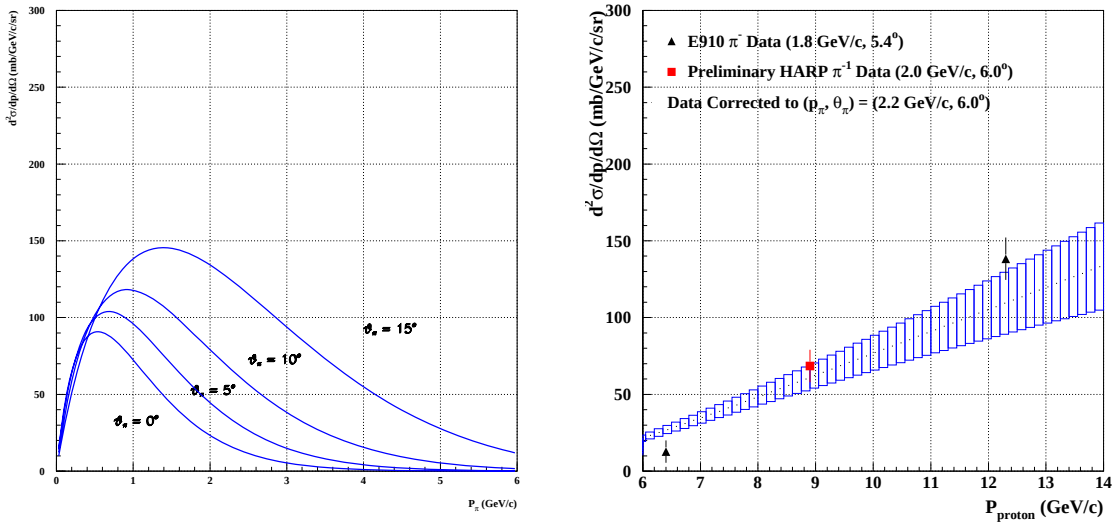

Figure B.5: *Left: best-fit Sanford-Wang inclusive π^- production cross section (milli-barns/GeV/c/steradian) vs. π^- momentum (GeV/c) for various angles, at p_{proton} = 8.9 GeV/c. Right: best-fit Sanford-Wang inclusive π^- production cross section (milli-barns/GeV/c/steradian) vs. proton momentum (GeV/c) at $(p_\pi, \theta_\pi) = (1.8\ GeV/c, 5.4^o)$.*

Table B.2: *Best-fit Sanford-Wang π^- parameters, assuming uncorrelated errors for all data sets. The "E910 + HARP" fit combines HARP 8.9 GeV/c, E910 6.4 GeV/c, and E910 12.3 GeV/c data. The "E910 only" and "HARP only" fits are performed to check the consistency of the individual experiments with the Sanford-Wang hypothesis. Since HARP measures only one p_{proton} value, the parameter c5 is fixed in the Sanford-Wang function for the "HARP only" fit.*

fit parameter	*E910 + HARP*	*E910 only*	*HARP only*
c1	226.2 ±35.72	235.0 ±39.83	379.6± 26.61
c2	0.8726±0.1355	1.005 ±0.1878	1.398± 0.3072
c3	6.096 ±0.6343	3.199 ±0.8616	1.142± 0.2193
c4	1.236 ±0.1571	1.150 ±0.2467	0.8453± 0.0657
c5	1.289 ±0.0835	1.017 ±0.1637	0.000± 0.000
c6	4.232 ±0.6759	5.004 ±1.103	3.796± 0.2960
c7	0.0661±0.0185	0.0635±0.0154	0.1521± 0.0751
c8	9.820 ±10.13	6.182 ±5.212	23.16± 63.68
n_{HARP}	1.00±0.00	-	
$n_{E910\ 6.4}$	1.00±0.07	1.00±0.07	-
$n_{E910\ 12.3}$	1.00±0.03	1.00±0.03	-
shape χ^2/ndf	174/135	117/93	10/34
total χ^2/ndf	175/135	117/93	10/34
total χ^2/ndf probability	0.011	0.047	0.999

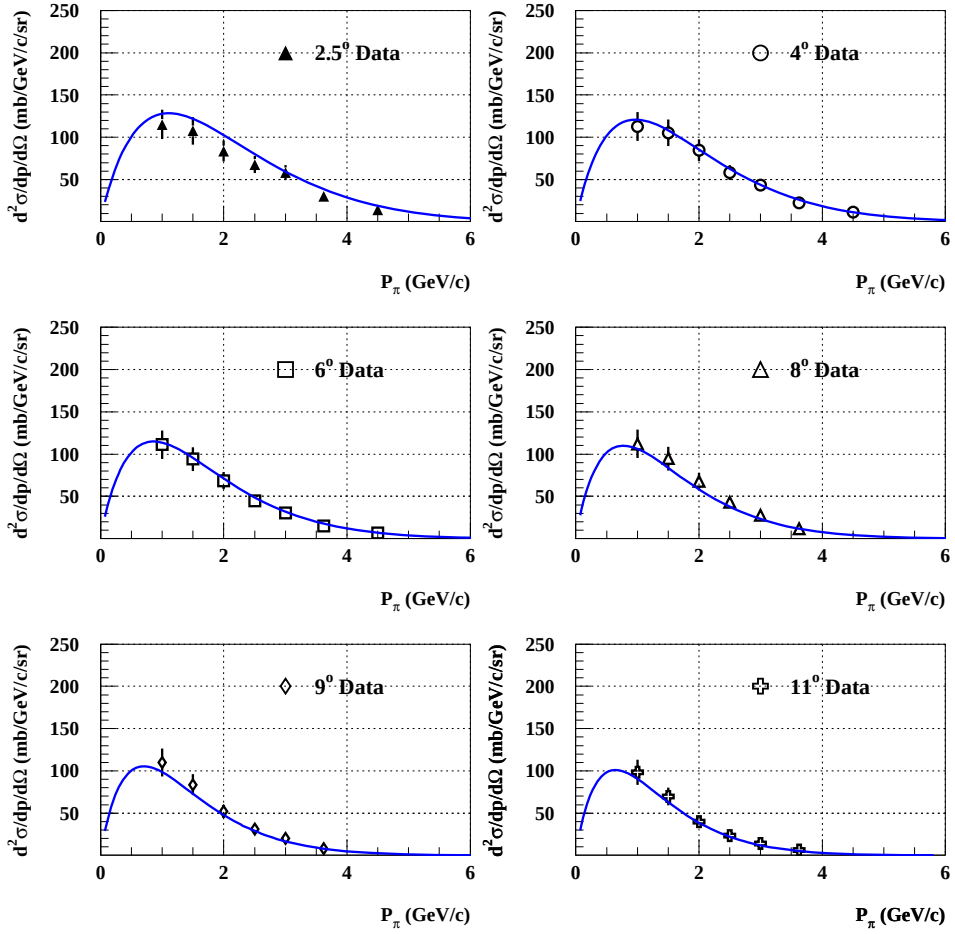

Figure B.6: *HARP[78] experiment measured inclusive π^- production cross section (milli-barns/GeV/c/steradian) in proton-beryllium interactions vs. π^- momentum (GeV/c), at $p_{proton} = 8.9$ GeV/c. Error bars include statistics and systematics.*

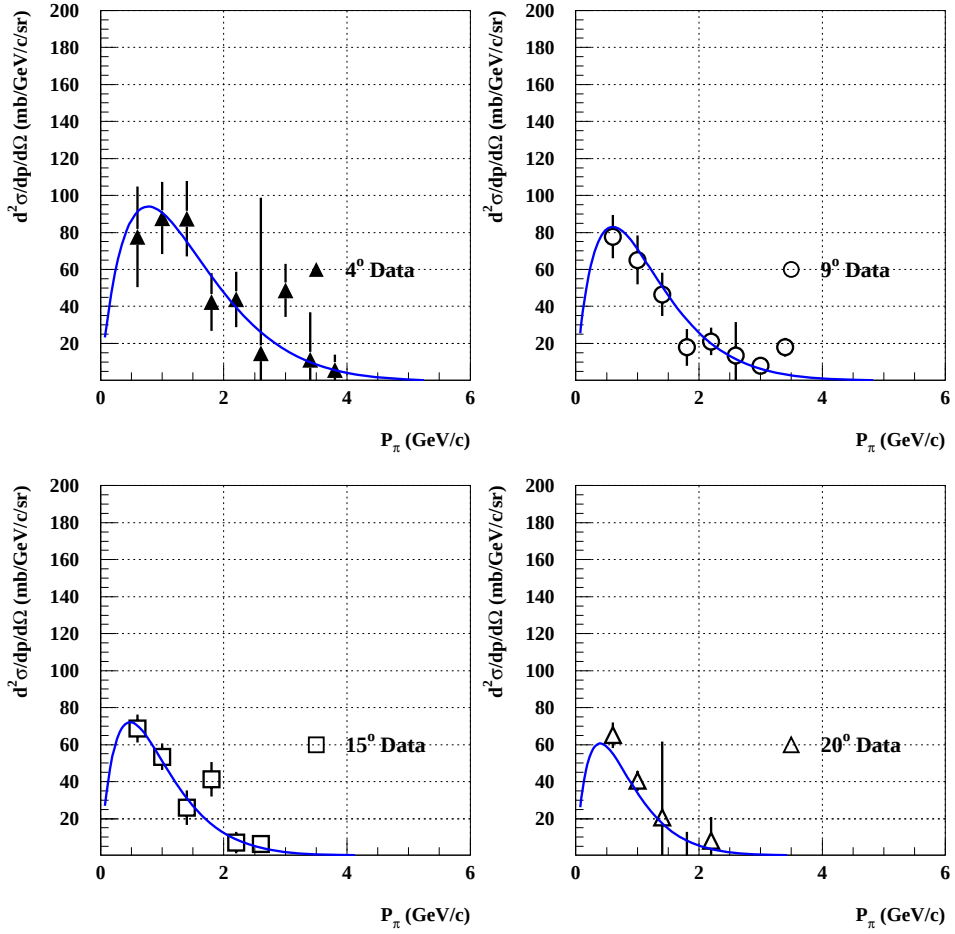

Figure B.7: *E910[77] experiment measured inclusive π^- production cross section (milli-barns/GeV/c/steradian) in proton-beryllium interactions vs. π^- momentum (GeV/c), at p_{proton} = 6.4 GeV/c. Error bars include statistics and systematics.*

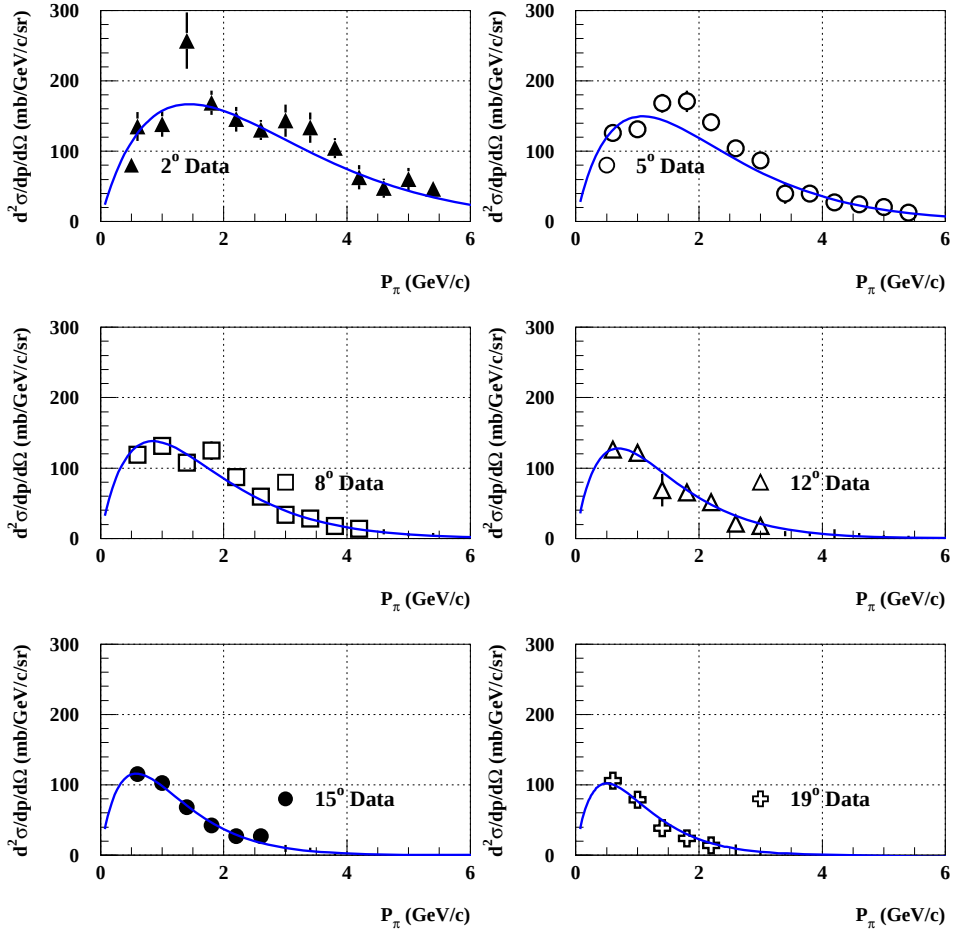

Figure B.8: *E910[77] experiment measured inclusive π^- production cross section (milli-barns/GeV/c/steradian) in proton-beryllium interactions vs. π^- momentum (GeV/c), at p_{proton} = 12.3 GeV/c. Error bars include statistics and systematics.*

Table B.3: *Compatibility of older K^+ production experiments with best-fit Sanford-Wang K^+ production cross section prediction.*

experiment	χ^2_{shape}	χ^2_{total}	*ndf*
Allaby	664	681	42
Dekkers	161	179	11
Lundy	52	71	10
Marmer	67	83	0

(Dekkers and Lundy). Of these experiments, the most relevant are Allaby and Lundy, which are compared with the best-fit Sanford-Wang K^+ production cross section in figures B.10 and B.11. The χ^2 between the data in figure B.1 and the best-fit Sanford-Wang K^+ cross section prediction is shown in table B.3.

experiment	p_{BEAM} *(GeV/c)*	p_K *(GeV/c)*	θ_K	N_{DATA}	σ_{NORM}
Allaby[148]	19.2	6-16	0 - 7^o	51	15%
Dekkers[69]	18.8, 23.1	4-12	$0{,}5^o$	20	(20%)
Lundy[68]	13.4	3-6	$2{,}4{,}8^o$	19	(20%)
Marmer[150]	12.3	0.5-1	$0{,}5{,}10^o$	9	20%

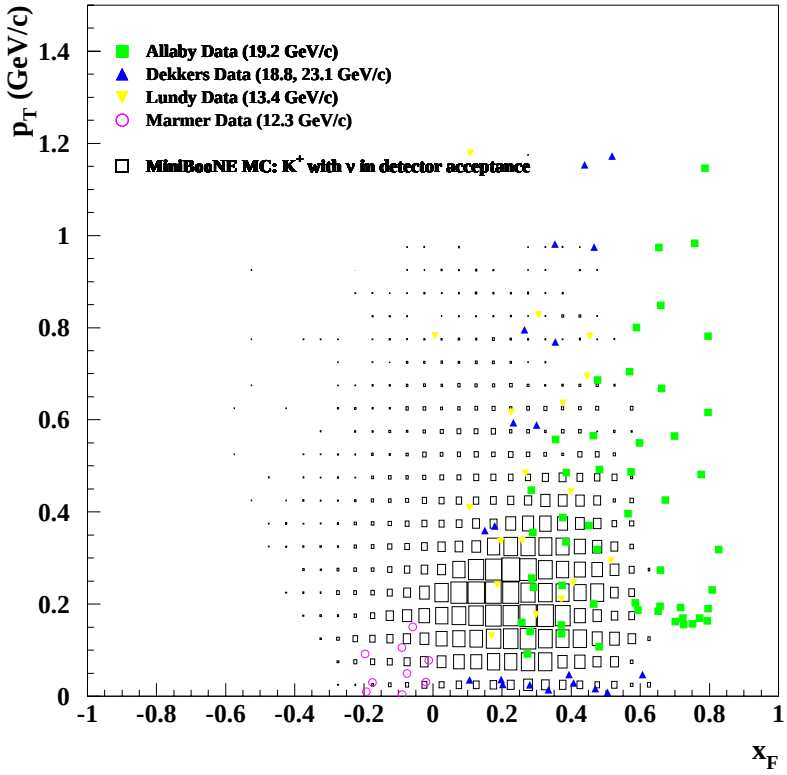

Figure B.9: *Top: Summary of experiments which measure p Be* $\rightarrow K^+X$ *in a region of interest to MiniBooNE. Bottom: Transverse momentum (GeV) vs.* $x_{Feynman}$ *for* K^+ *production experiments, overlaid with the MiniBooNE beam Monte Carlo prediction for* K^+*-decay* ν *in the MiniBooNE detector acceptance.*

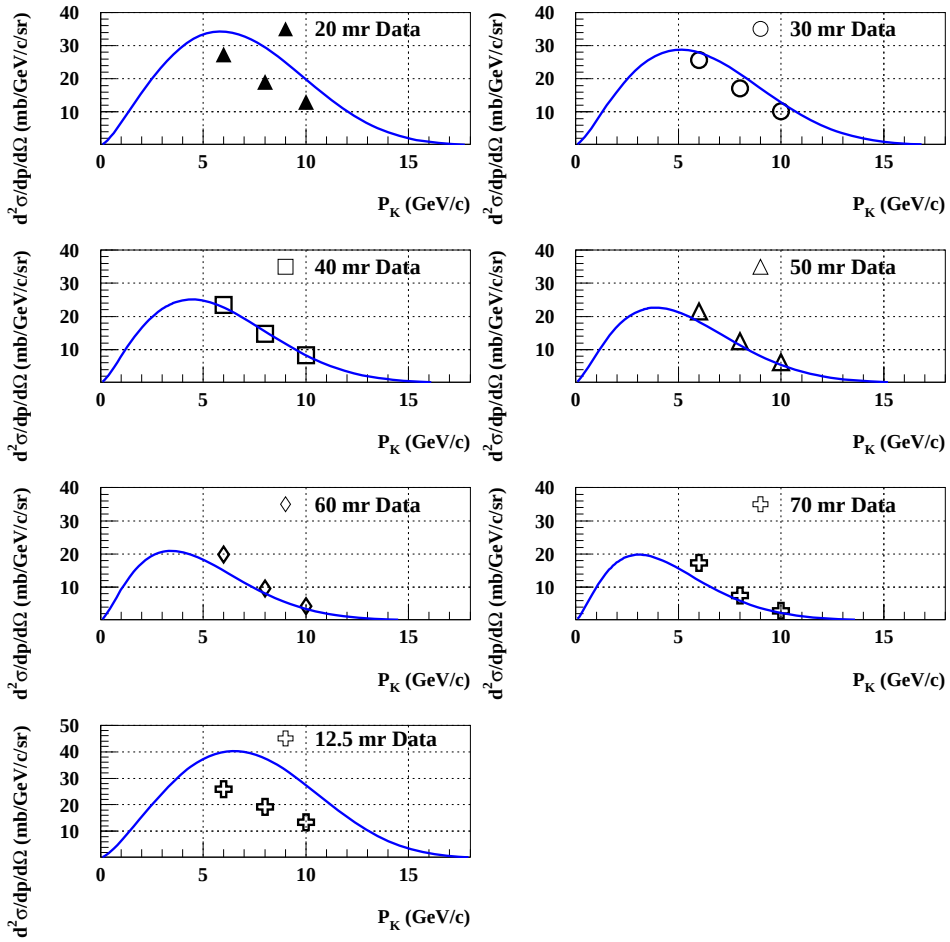

Figure B.10: *Allaby[148] experiment measured inclusive K^+ production cross section (milli-barns/GeV/c/steradian) in proton-beryllium interactions vs. K^+ momentum (GeV/c), at $p_{proton} = 19.2$ GeV/c. Error bars include statistics and systematics.*

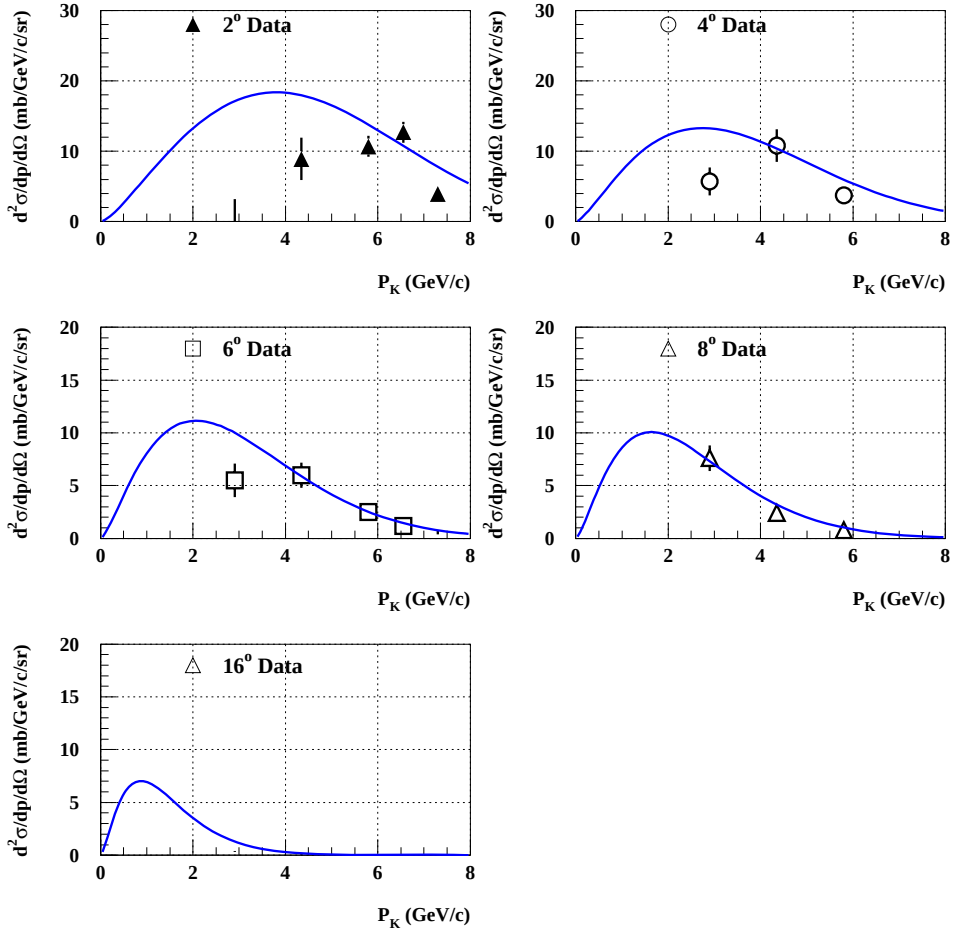

Figure B.11: *Lundy[68] experiment measured inclusive K^+ production cross section (milli-barns/GeV/c/steradian) in proton-beryllium interactions vs. K^+ momentum (GeV/c), at p_{proton} = 13.4 GeV/c. Error bars include statistics and systematics.*

Appendix C

Chapter 5 Cross Section Uncertainty Calculation

The method discussed in chapter 5 for constraining the simulation parameter uncertainties using the MiniBooNE ν_μ CCQE data set can be applied to the cross section predictions as well. Here, the ansatz would be that the flux is known, and therefore the ratio of data to Monte Carlo in equation 5.1 reduces to

$$\mathcal{R} \;=\; \frac{N_{DATA}^{after\ CCQE\ cuts}(E_\nu^{QE})}{N_{MC}^{after\ CCQE\ cuts}(E_\nu^{QE})} \;=\; \frac{\sigma_{Data}^{CCQE}(E_\nu)}{\sigma_{MC}^{CCQE}(E_\nu)}. \tag{C.1}$$

To use this ratio as a reweighting function for constaining the uncertainties on the cross section simulation parameters, one would replace $N_{DATA}^{after\ CCQE\ cuts}(E_\nu^{QE})$ with "fake data", which is really central value Monte Carlo, and correspondingly replace $N_{MC}^{after\ CCQE\ cuts}(E_\nu^{QE})$ with "unisim" Monte Carlo, in which some cross section simulation parameter has been varied. The cross section simulation parameter variations considered here include the first 9 sources in table 4.7, which are (i) the axial masses for the CCQE, CC1π, CC multi-π, and coherent neutrino-nucleon scattering cross sections (m_A^{QE}, $m_A^{1\pi}$, $m_A^{N\pi}$, m_A^{coh}), (ii) the Fermi Gas model Fermi momentum p_F and

binding energy E_B, (iii) the component of the nucleon spin carried by the strange sea quarks Δs, which impacts the neutral current cross sections, and (iv) the radiative Δ decay branching fractions. The final state pion interaction cross section simulation parameter variations are not included here because they cannot be produced by reweighting central value Monte Carlo, and therefore the statistics of the μ^+-decay ν_e are insufficient for this analysis at present.

The reconstructed neutrino energy distributions before and after modification by reweighting via equation C.1, for "fake data" and cross section "unisim" Monte Carlo events passing the ν_μ CCQE selection cuts, are shown in the figure C.1. Exactly the same reweighting approach is employed as in chapter 5: the ν_μ spectrum is used to infer the π^+, μ^+, and ν_e energy distributions. This is not a particularly meaningful way to relate the ν_e and ν_μ predictions in the case of cross section simulation parameter uncertainties, and in fact any sample of ν_e Monte Carlo could be used. However, the μ^+-decay ν_e energy spectrum is quite similar to that of a potential ν_e oscillation signal. Therefore, using the μ^+-decay ν_e as the ν_e sample here provides a useful measure of how well the ν_μ CCQE calibration approach can work in the ν_e appearance analysis. The inferred π^+, μ^+, and ν_e distributions are shown before and after modification by reweighting in figure C.2. As in the π^+ case, by construction, the reweighting modification works perfectly for the E_ν^{QE} distribution, and is only applied to π^+-decay ν_μ events. In principle, all events passing the ν_μ CCQE selection cuts could be used, including the non-π^+-decay ν_μ.

The effectiveness of this method in constraining the cross section simulation uncertainties is evaluated by comparing three cases:

1. with no reweighting modification (the reweighting function is taken to be 1.0 in all energy bins), so the error matrix comes directly from the assumptions in chapter 3,

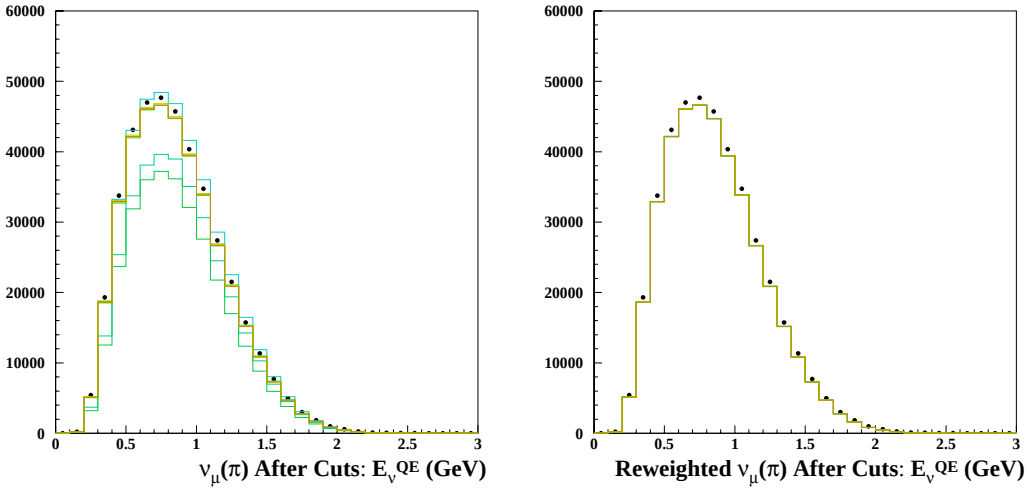

Figure C.1: *Left: number of events vs. reconstructed neutrino energy (GeV) for events passing the ν_μ CCQE selection cuts. Right: reweighted number of events vs. reconstructed neutrino energy (GeV) for events passing the ν_μ CCQE selection cuts. Central value Monte Carlo is indicated by the points, σ_ν prediction "unisim" Monte Carlo by the lines.*

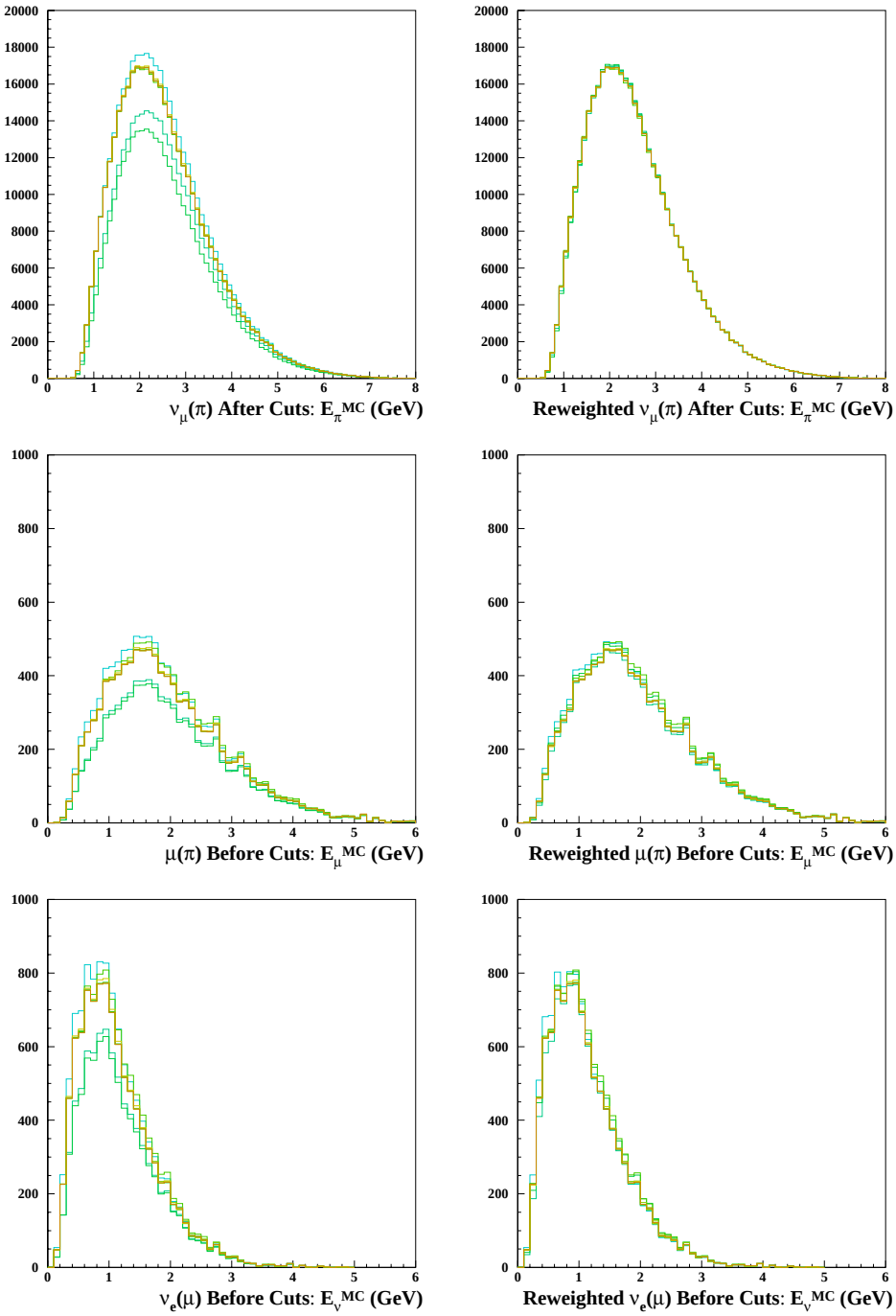

Figure C.2: *Left: generated Monte Carlo energy distributions. Right: reweighted Monte Carlo energy distributions. Top: number of events vs. π^+ energy (GeV). Middle: number of events vs. μ^+ energy (GeV). Bottom: number of events vs. ν_e energy (GeV).*

2. with reweighting modifications, where the numerator of the reweighting function is "fake data" (central value Monte Carlo), which tests the effect of the reweighting method on the uncertainties only;

3. with reweighting modifications, where the numerator of the reweighting function is the ν_μ CCQE data set described in chapter 4.

The reweighting modification procedure is applied to the central value Monte Carlo, and to each of the first nine ν interaction cross section "unisims" listed in table 3.10. The modified "unisims" are used to calculate the first derivative matrices and propagate the simulation input parameter errors, as described in chapter 4, to the uncertainties on the predicted E_ν^{MC} distribution for μ^+-decay ν_e and π^+-decay ν_μ events, with no selection cuts applied. The ratio of the modified "unisims" to the original central value Monte Carlo for each of the three cases is shown as a function of E_ν^{MC} in figure C.3. For case 1, with no modification, the spread in the (reweighted "unisim" / original central value) ratios is $\sim$20% about a value of 1.0 at $E_\nu = 1\ GeV$ for both μ^+-decay ν_e and π^+-decay ν_μ. This is dominated by the Fermi Gas model parameter variations, which lower the predicted number of events by sim20-30%. For case 2, where the "unisims" have been modified via reweighting to match the "fake data," the spread is $\sim$5% about 1.0 at $E_\nu = 1\ GeV$. This reduction in the spread of the ratios comes almost entirely from the change in the Fermi Gas model parameter "unisims", the rest are hardly affected, which makes sense because the ν_μ CCQE data set should only constrain the error on the CCQE cross section and the Fermi Gas model parameters. For case 3, the spread in the ratios is nearly identical to case 2, as expected, and the value of the ratio is $\sim$1.3 at $E_\nu = 1\ GeV$.

The modified "unisims" are used to construct the first derivative matrix, which in combination with the cross section parameter correlation matrix, is used to propagate the simulation input parameter uncertainties to the E_ν^{MC} distribution for π^+-decay ν_μ

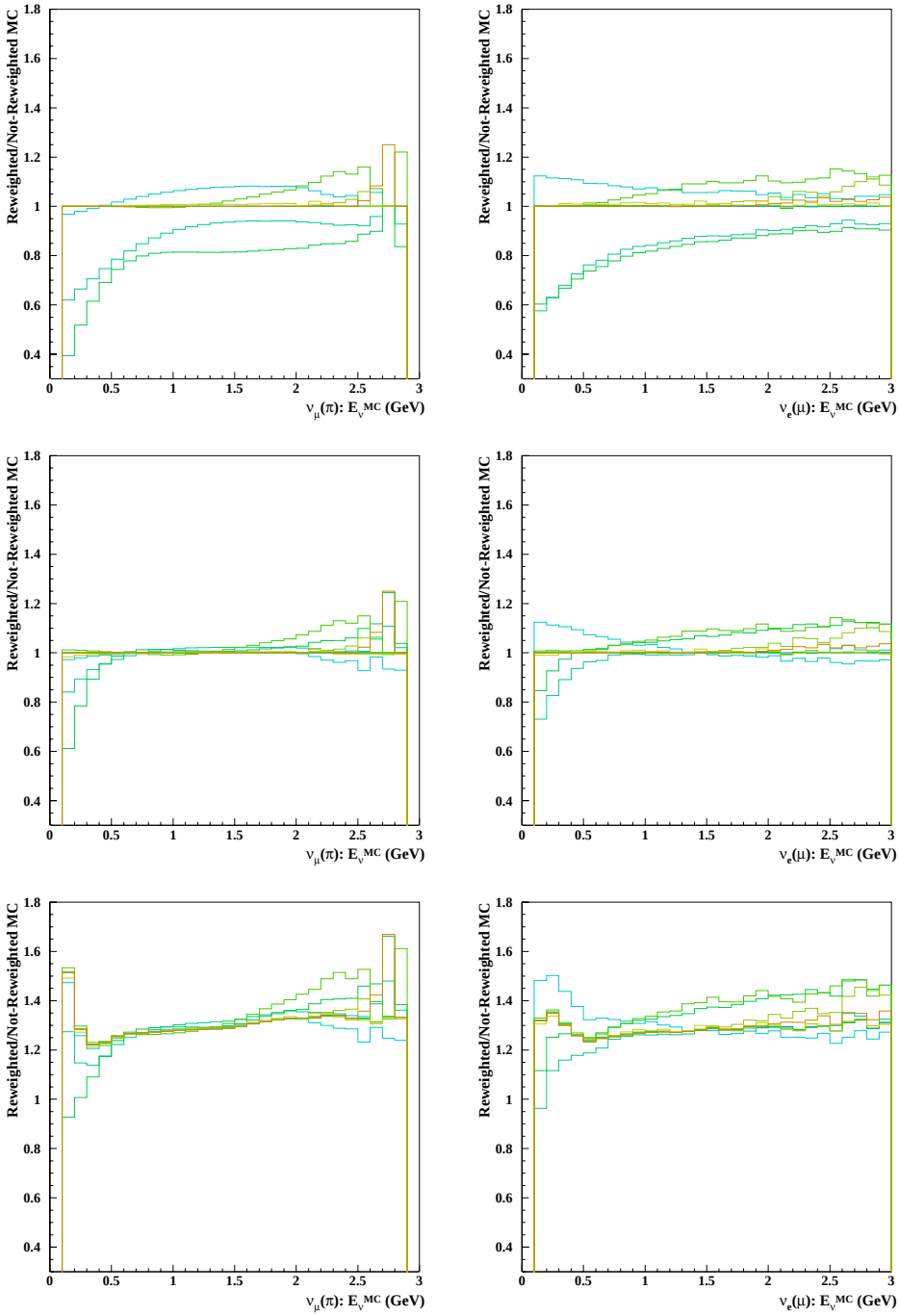

Figure C.3: *Ratio of σ_ν prediction "unisims" to original central value Monte Carlo vs. E_ν^{MC} (GeV), with no selection cuts applied. Left: predicted π^+-decay ν_μ spectra. Right: predicted μ^+-decay ν_e spectra.*

Table C.1: *Summary of the uncertainty on μ^+-decay ν_e in the detector acceptance for the three reweighting scenarios described in the text. The Monte Carlo set corresponds to 2.2×10^{21} simulated protons on target.*

Reweighting Ratio	$N\ \nu_e(\mu^+)$	ΔN *(%)*	δN *(%)*
1.0	12,658	9.527	2.085
"fake data" / "unisim"	12,658	8.410	1.893
data / "unisim"	16,095	8.437	1.893

and μ^+-decay ν_e events. The cross section parameter correlation matrix is discussed in detail in chapter 6 and given in Appendix F. Adding the parameter correlations greatly reduces the uncertainties due to the Fermi Gas model parameters, which account for the two largest "unisim" excursions, because they are highly anti-correlated. The central value Monte Carlo predicted E_ν^{MC} distribution for μ^+-decay ν_e events, with no selection cuts applied, is shown with neutrino interaction cross section errors, calculated for cases 1, 2, and 3, in the left-hand panels of figure C.4; the fractional errors as a function of E_ν^{MC} are shown in the right-hand panels. The corresponding distributions for π^+-decay ν_μ events are shown in figure C.5.

To compare the three scenarios, the total number of predicted μ^+-decay ν_e events and the two error estimators δN and Δ_N are summarized in table C.1. The error estimators are defined in equations 4.18 and 4.20; they describe the fully correlated normalization error and an estimate of the shape uncertainty respectively. Table C.1 contains the corresponding information for π^+-decay ν_μ events. The total neutrino interaction cross section uncertainty for the ν_e events is reduced from 9.5% to 8.4%, and from 9.4% to 1.8% for the ν_μ events.

The difference in the effectiveness of this method for constraining the neutrino

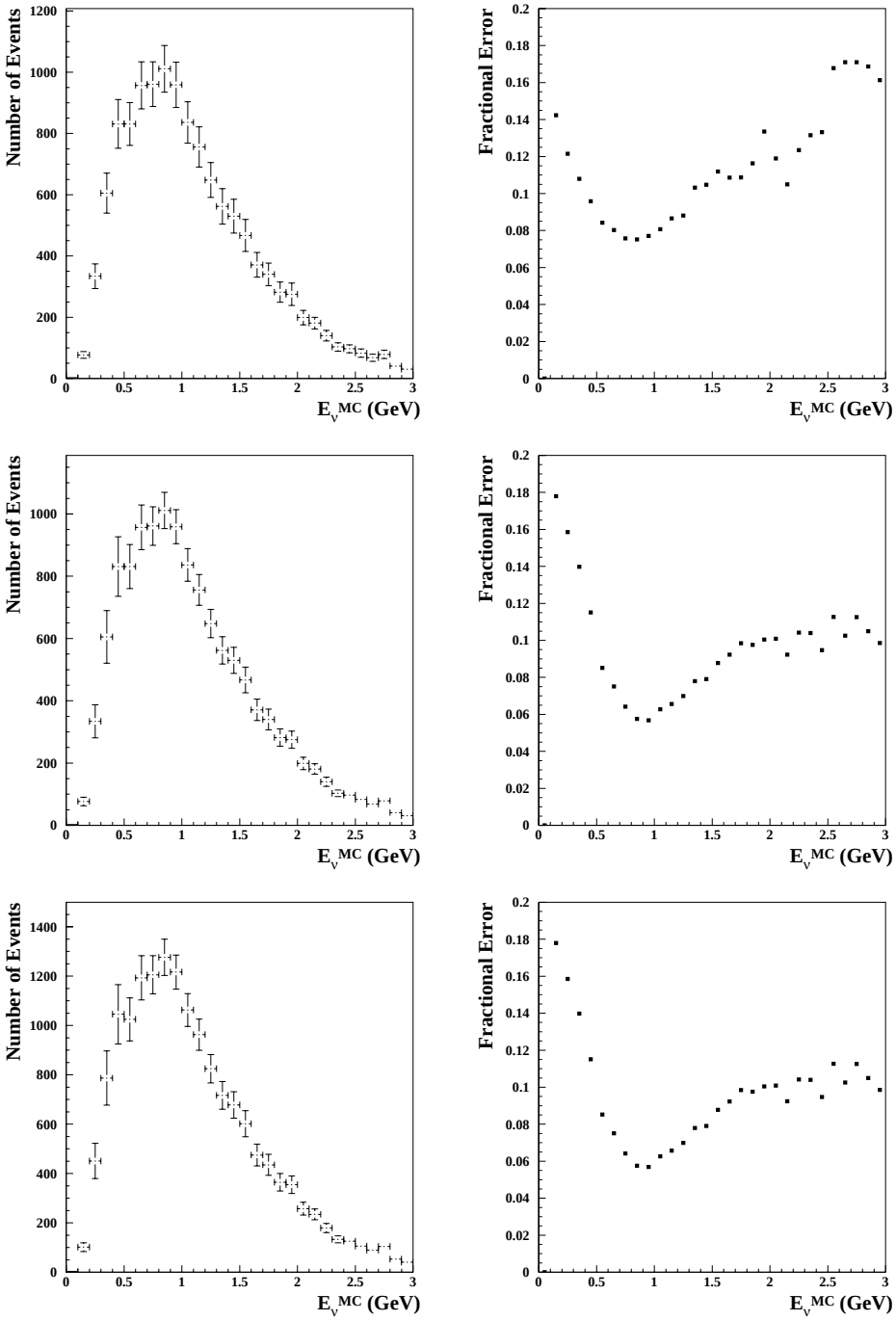

Figure C.4: *Error on μ^+-decay ν_e E_ν^{MC} spectrum from σ_ν prediction uncertainties, in reweighting cases 1 (top), 2 (middle), and 3 (bottom). Left: predicted number of events vs. E_ν^{MC} (GeV) for 2.2 $\times 10^{21}$ protons on target. Right: fractional error vs. E_ν^{MC} (GeV).*

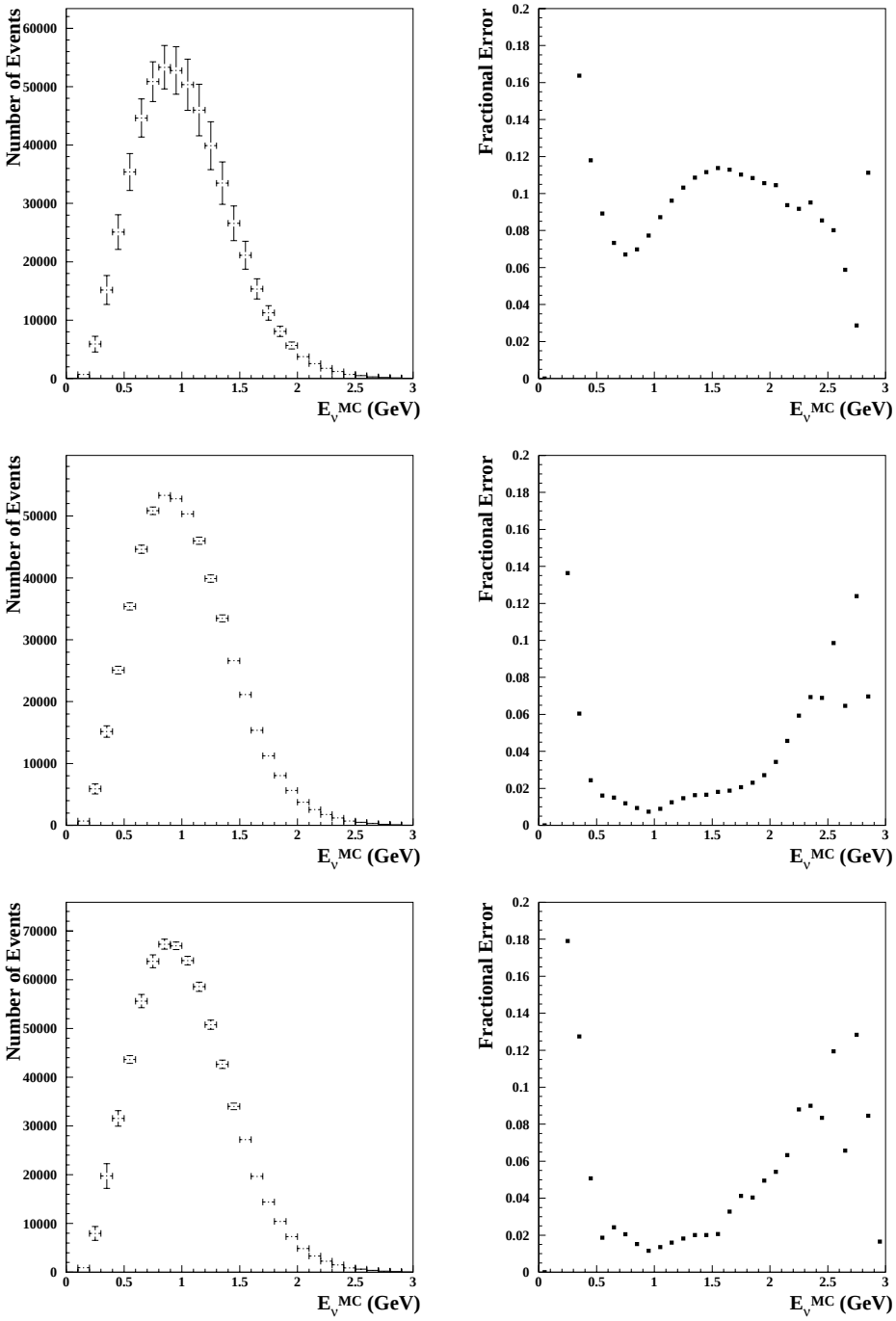

Figure C.5: *Error on π^+-decay ν_μ E_ν^{MC} spectrum from σ_ν prediction uncertainties, in reweighting cases 1 (top), 2 (middle), and 3 (bottom). Left: predicted number of events vs. E_ν^{MC} (GeV) for 0.243 $\times 10^{21}$ protons on target. Right: fractional error vs. E_ν^{MC} (GeV).*

Table C.2: *Summary of the uncertainty on π^+-decay ν_μ in the detector acceptance for the three reweighting scenarios described in the text. The Monte Carlo set corresponds to 2.43×10^{20} simulated protons on target.*

Reweighting Ratio	$N\ \nu_\mu(\pi^+)$	ΔN *(%)*	δN *(%)*
1.0	552,493	9.426	2.353
"Unisim" / CV MC	552,493	1.755	0.413
Data / CV MC	705,633	2.701	0.671

interaction cross section uncertainties for ν_μ and ν_e events likely occurs because the correlation between the ν_μ and π^+ energy is much tighter than the correlation between the ν_e and π^+ energy, as is shown in figure 5.1. For the pi^+ error reduction described in chapter 5, the ν_e (or ν_μ) and ancestor π are correlated on an event-by-event basis, however, for the neutrino interaction cross section analysis, they are not. Therefore the average correlation in each neutrino energy bin determines the effectiveness of the constraint method described here, and so the larger the spread of neutrino energies in each pion energy bin, the less effective the constraint will be.

Appendix D

Kaon Prediction Constraint Method

The ν_e background from K^+ decay comprises approximately 1/3 of the intrinsic beam ν_e background to the $\nu_\mu \rightarrow \nu_e$ analysis, and therefore must be well understood. The MiniBooNE prediction for K^+ meson production in the target, described in chapter 3, comes from a fit to data from past experiments, termed "external" data in the following. However, the fit requires extrapolation to the MiniBooNE proton beam momentum, has large errors, and the fit quality is poor. Therefore it is critical to check the prediction with "internal" data from MiniBooNE. The available in-situ cross checks for the K^+ production prediction include the little muon counter system (LMC) and the MiniBooNE detector high energy ν_μ data set (HE data). The LMC and HE data (x_F, p_T) coverage of the MiniBooNE K^+ production phase space of interest is shown in figure D.1; for comparison with the "external" data see figure 3.7.

The LMC is a muon spectrometer situated downstream of the MiniBooNE target at an angle of 7^o with respect to the decay pipe axis. The spectrometer accepts $\sim$0.5 - 2.0 GeV muons, which come from $K^+ \rightarrow \mu^+\nu_\mu$ decays in the MiniBooNE neutrino

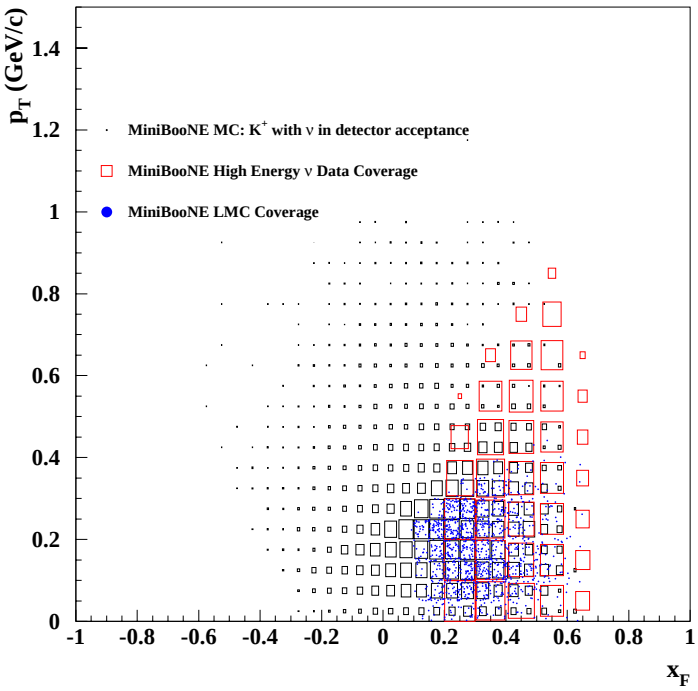

Figure D.1: *Transverse momentum (GeV) vs.* $x_{Feynman}$ *for the HE data and the LMC, overlaid with the MiniBooNE beam Monte Carlo prediction for* K^+*-decay* ν *in the MiniBooNE detector acceptance.*

beam line decay pipe. Muons from π^+ decay in this E_μ range are produced at smaller decay angles due to 2-body decay kinematics, and so do not contribute appreciably. However, there is a large background from secondary beam interactions in the material surrounding the LMC detector, which is measured to fall off exponentially with increasing muon momentum. At 7^o, the average K^+-decay μ^+ momentum is 1.8 GeV/c, compared with the average π^+-decay μ^+ momentum of 0.3 GeV/c. By measuring the number of muons as a function of momentum, the LMC can be used to infer the normalization of the K^+ spectrum in the MiniBooNE decay pipe, and potentially give some information on the shape as well.

The LMC analysis is still under development, and so only LMC "fake data" (which is really Monte Carlo) is considered here, shown in table D.1. The total number of events with K^+-decay μ^+ detected by the LMC is expected to be ∼45,000. This includes the muon detection efficiency, which is assumed to be 60% within the spectrometer momentum acceptance, and a cut at $p_\mu > 1\ GeV/c$ to eliminate the p_μ region dominated by background.

The HE data set is selected from neutrino interactions in the MiniBooNE detector. The right panel of figure 3.14 shows that above E_ν ∼2 GeV, the ν_μ flux comes dominantly from K^+ decays, therefore with a minimum E_ν cut MiniBooNE can obtain an in-situ K^+-decay ν_μ data set with good purity. The HE data event selection and analysis is described in detail in reference [151], and comprises ∼10,000 events. Of these, further cuts are applied to select four sub-sets: ν_μ CCQE events which are fully contained in the fiducial volume, ν_μ CCQE events where the μ^+ exits, ν_μ CC1π^+ contained, and ν_μ CC1π^+ exiting. These particular interaction channels are selected to minimize the uncertainty associated with predicting the neutrino interaction cross sections in this complex region [1]. The numbers of events and data

[1]For $E_\nu > 2\ GeV$, the cross section has non-negligible contributions from multi-pion production

Table D.1: *LMC "fake data" (Monte Carlo prediction) for the ν_μ from K^+ decay analysis. $N_\mu^{K,LMC}$ is the number of μ^+ from K in the LMC, while $N_{\mu,all}^{LMC}$ includes μ^+ from π^+-decay and background events as well. This "fake data" set corresponds to 1$\times 10^{17}$ protons on target.*

bin	$\overline{p}_\mu^{LMC}$ *(GeV)*	$N_\mu^{K,LMC}$	$N_{\mu,all}^{LMC}$	K^+ *fraction*	$\langle p_K \rangle (GeV/c)$	$\langle \theta_K \rangle (rad.)$
1	0.125	0.0	120269.27	0.00	-	-
2	0.375	4.28	62290.06	0.00	0.37	0.262
3	0.625	62.17	32319.09	0.00	0.69	0.188
4	0.875	561.40	17266.60	0.03	1.71	0.133
5	1.125	2301.97	10952.84	0.21	2.13	0.101
6	1.375	7470.59	11949.49	0.63	2.34	0.086
7	1.625	13847.90	16164.27	0.86	2.78	0.066
8	1.875	21088.28	22281.97	0.95	3.70	0.050

Table D.2: *High energy box data used for the ν_μ from K^+ decay analysis. The MiniBooNE detector Monte Carlo is used to estimate the K^+ purity and production kinematics. σ-channel fraction refers to, for example, the fraction of CCQE events in CCQE Contained sub-set. This data set corresponds to 3.2 $\times 10^{20}$ p.o.t.*

HEBox Sample	*CCQE Contained*	*CCQE Exiting*	*CCPI Contained*	*CCPI Exiting*
data	1269	1719	53	455
MC K^+ fraction	0.27	0.72	0.55	0.80
MC $\langle p_K \rangle$ (GeV/c)	2.81	3.82	3.15	3.96
MC $\langle \theta_K \rangle$ (GeV/c)	0.085	0.063	0.077	0.061
MC σ-channel fraction	0.67	0.65	0.76	0.69

sub-set compositions after cuts are summarized in table D.2.

To combine the "internal" and "external" constraints, the LMC and HE in-situ measurements and the external K^+ production data are all included in a fit for the K^+ production cross section. The ansatz of the K^+-decay ν_μ analysis is that the simulation of the entire experiment other than the K^+ production cross section is correct, and therefore one can fit the various data sets with the Sanford-Wang K^+ production cross section parameters as the only degrees of freedom. The uncertainties on the in-situ data sets therefore should include uncertainties for all of the experimental assumptions, specifically the neutrino interaction cross section predictions and the detector response simulation. The analysis of the in-situ K^+ data is still in progress, and therefore a sketch of a method for validating the K^+ production cross section prediction is described here, without the final in-situ data sets or a full error anal-

and deep inelastic scattering.

ysis. At this stage, the goal is to check the minimum criteria for verifying that the $p\ Be \rightarrow K^+\ X$ cross section prediction based on a fit to "external" data is consistent with the MiniBooNE data. These are: (1) that the fit prediction agrees with the in-situ K^+ measurements within errors, and (2) that the "external" data fit prediction agrees with the result of a combined fit to "external" and "internal" data within errors.

As described in chapter 3, the K^+ production cross section prediction is obtained by fitting the Sanford-Wang parameterization to measurements of the double differential $pBe \rightarrow K^+X$ cross section from past experiments. The fit minimizes the following function for an "external" experiment j:

$$\chi^2_j \ = \ \Big[\sum_i \frac{(N_j \times SW_i - Data_i)^2}{\sigma_i^2}\Big] + \frac{(1-N_j)^2}{\sigma^2_{N_j}} \tag{D.1}$$

where i is the (p_{meson},θ_{meson}) bin index, SW_i is the parameterization prediction evaluated at a given (p_{proton}, θ_{meson}, p_{meson}), $Data_i$ is the measurement at a given (p_{proton}, θ_{meson}, p_{meson}), σ_i is the data systematic error on measurement i, N_j is the normalization pull term for experiment j, and σ_{N_j} is the normalization uncertainty experiment j. The total χ^2 for external data sets is the sum of the individual χ^2s for each experiment:

$$\chi^2 = \sum_j \chi^2_j. \tag{D.2}$$

Similarly, one can form χ^2 terms for internal data. For the LMC,

$$\chi^2_{LMC} \ = \ \Big[\sum_i \frac{(N \times (N_\mu^{Predicted})_i - (N_\mu^{Observed})_i)^2}{\sigma_i^2}\Big] + \frac{(N-1)^2}{\sigma_N^2} \tag{D.3}$$

where i is the LMC muon energy bin index, $(N_\mu^{Observed})_i$ is the number of observed μ^+ in LMC E_μ bin i, σ_i is the error on each data point (for now, just $\sqrt{(N_\mu^{Observed})_i}$), N is the LMC normalization pull term, σ_N is the LMC normalization error, which for now is assumed to be 10%, and $(N_\mu^{Predicted})_i$ is the predicted number of muons

in LMC E_μ bin i given Sanford-Wang parameters c_1 ... c_N. For now we use "fake data" (Monte Carlo) for $(N_\mu^{Observed})_i$ since we do not yet have LMC results, and no systematic error is included in σ_i.

For each sub-set of the HE data, e.g. "CCQE Contained,"

$$\chi^2_{HEBox} = \frac{(N \times N_\nu^{Predicted} - N_\nu^{Observed})^2}{\sigma^2} + \frac{(N-1)^2}{\sigma_N^2} \tag{D.4}$$

where $(N_\nu^{Observed})_i$ is the number of observed ν in the HE data sub-set, σ is the statistical error ($\sqrt{N_\nu^{Observed}}$), σ_N is the HE data sub-set normalization uncertainty which includes systematic errors from the event selection and reconstruction (assumed to be 10% for now), and $N_\nu^{Predicted}$ is the predicted number of ν events in HE data given Sanford-Wang parameters c_1 ... c_N.

The prediction for the numbers of events in the LMC and the HE data relies on reweighting Monte Carlo at each iteration of the fit. For simplicity the procedure is illustrated with the LMC. The reweighting is done using a file of events from the `ModelB` Monte Carlo [94] which has one line for each K^+ event that decays to a μ^+ in the LMC acceptance. Each line contains p_K, θ_K, E_μ, $weight$, and $SW(p_K, \theta_k, c_i^{MC})$. The momentum and angle are evaluated at production, and $SW(p_K, \theta_K, c_i^{MC})$ is the value of the Sanford-Wang function in the Monte Carlo that was used to generate the event. The $weight$ is equal to the N_μ^{LMC} per proton on target for μ^+ from K^+ produced at (p_K, θ_K). The Monte Carlo predicted number of μ^+ in LMC E_μ bin i is $\sum_{events} weight_{event}$.

The fit varies the Sanford-Wang coefficients c_i^{FIT} to minimize, e.g.,

$$\chi^2_{LMC} = \Big[\sum_i \frac{(N \times (N_\mu^{Predicted})_i - (N_\mu^{Observed})_i)^2}{\sigma_i^2}\Big] + \frac{(N-1)^2}{\sigma_N^2} \tag{D.5}$$

where $(N_\mu^{Predicted})_i$ depends on c_i^{FIT} as follows. Each time the c_i^{FIT} change (at each iteration of the fit) $N_{\mu,i}^{Predicted}$ is recalculated by reweighting the Monte Carlo E_μ

distribution by R for each event:

$$R_{event} \;=\; \frac{SW(p_K, \theta_K, c_i^{FIT})}{SW(p_K, \theta_k, c_i^{MC})} \tag{D.6}$$

The constant R is the ratio of the current value of the Sanford-Wang K^+ cross section prediction, given the c_i^{FIT}, to the original value of the Sanford-Wang function that was used in generating the Monte Carlo event file. The reweighted events are summed in each E_μ bin i to find the predicted number of events for the Sanford-Wang function coefficients c_i^{FIT}

$$N_{\mu,i}^{Predicted} \;=\; \sum_{events} weight_{event} \;\times\; R_{event}. \tag{D.7}$$

This procedure is done similarly for each HE data sub-set, with the substitution of the reconstructed E_ν for the reconstructed E_μ. The Monte Carlo event files are produced with the MiniBooNE detector Monte Carlo, and contain p_K, θ_K, E_μ, $weight$, and $SW(p_K, \theta_k, c_i^{MC})$ for each event that passes the HE data sub-set selection cuts.

To combine "external" and "internal" data, the fit minimizes

$$\chi^2_{total} \;=\; \chi^2_{production\ data} + \chi^2_{LMC} + \chi^2_{HE}, \tag{D.8}$$

where $\chi^2_{production\ data}$ is a sum over all of the "external" K^+ production data sets described in chapter 3, and χ^2_{HE} is a sum over the four HE data sub-sets.

The most general cross-check is whether the fit to "external" K^+ production data only correctly predicts the HE data sub-sets. A comparison of the predicted and measured numbers of events is shown in table D.3. The reweighting procedure described above is used to make the prediction. The uncertainty on the measured numbers of events is from statistics only, while the uncertainty on the predicted number events in each HE data sub-set is assumed to be the Monte Carlo statistical error added in quadrature with a 10% systematic error. Eventually the systematic error will include the uncertainty from the π^+ flux prediction, the ν interaction cross

Table D.3: *Comparison of measured and predicted numbers of events in the MiniBooNE HE data sub-sets for 3.2 $\times 10^{20}$ protons on target. The statistical error is listed first for the predicted events, followed by the systematic error estimate. Statistical errors only are shown for the data. The prediction comes from the Sanford-Wang fits to external K^+ data, described in chapter 3.*

HEBox Sample	ν_μ *CCQE Contained*	ν_μ *CCQE Exiting*	ν_μ *CC1*π^+ *Contained*	ν_μ *CC1*π^+ *Exiting*
Predicted Total	731±12±73	1594±16±159	54±3±5	586±10±59
Data Total	1269±36	1719±42	53±7	455±21
Data/Predicted Total	1.74±0.19	1.08±0.11	0.98±0.18	0.78±0.09

section model, and the detector response simulation. The statistical error, ∼2%, is similar in data and Monte Carlo.

For the "ν_μ CCQE contained" sub-set, the prediction is 3.9 σ away from the data, for the "ν_μ CCQE exiting" and "ν_μ CC1π^+ contained" event samples the prediction is less than 1.0 σ away from the data, and for the "ν_μ CC1π^+ exiting" sub-set the prediction is 2.4 σ away from the data. The compositions of the various sub-sets are all different, and the "ν_μ CCQE contained" sub-set has a much lower K^+ fraction, 0.20, than the others, and therefore will not be considered further for a constraint on the K^+ flux prediction here. The background in the sub-sets consists of both meson decay backgrounds and neutrino interaction backgrounds. The normalization of the π^+-decay ν_μ background is taken from the ν_μ CCQE (data / Monte Carlo) measurement discussed in chapter 4. The neutrino interaction backgrounds come primarily from resonant single pion production for the CCQE sub-sets, and from CCQE and charged current deep inelastic scattering for the CC1π^+ sub-sets.

The error coming from the "external" data fit itself, which is 9% at the average (p_K, θ_K) for MiniBooNE, is not included in the prediction error in table D.3. This fit error covers the difference between the predictions and the measurements at the 1-2 σ level [2]. Therefore, the conclusion at this stage is that the prediction for the $p\ Be \rightarrow K^+\ X$ production cross section based in "external" data alone is in fair agreement with the in-situ MiniBooNE HE data, within the assumed uncertainties.

The second cross-check is whether the "external" data fit predicted K^+ production cross section agrees with the result of a combined fit to "internal" + "external" data. This fit is performed with the "external" data described in chapter 3, and the "ν_μ CCQE exiting," "ν_μ CC1π^+ contained," and "ν_μ CC1π^+ exiting" HE data sub-sets. The results are summarized in table D.4. By comparing the total predicted numbers of events in tables D.3 and D.4 one sees that the "internal" + "external" data combined fit agrees with the "external"-only fit to 2%, which is well within the "external" data fit uncertainty of 9%. This check verifies that including or excluding the in-situ data sets does not change the resulting best-fit Sanford-Wang K^+ production cross section significantly.

The HE data verify the criteria discussed in the previous section for demonstrating consistency between the "external" data fit and the MiniBooNE data, which builds confidence in the K^+-decay ν_e background prediction for the $\nu_\mu \rightarrow \nu_e$ oscillation search. The logical next step is to try to constrain the K^+ prediction uncertainty using in-situ measurements. The result of adding the HE data to the K^+ production fit is an error on the best-fit cross section at the average (p_K, θ_K) for MiniBooNE of 8.5%, which is not appreciably smaller than the "external"-only result, 9%. This occurs because the HE data has relatively large systematic errors, assumed to be 10% here,

[2]The error estimate from the "external" data fit has been scaled up by the $\sqrt{\chi^2/ndf}$ to attempt to account for the poor fit quality as discussed in chapter 3.

Table D.4: *Comparison of measured and predicted numbers of events in the MiniBooNE HE data sub-sets. The statistical error is listed first for the predicted events, followed by the systematic error estimate. Statistical errors only are shown for the data. The prediction comes from the combined Sanford-Wang fit to external K^+ data and the "CCQE Exiting" and both "CCPI" HE data sub-sets.*

HEBox Sample	*CCQE Contained*	*CCQE Exiting*	*CCPI Contained*	*CCPI Exiting*
Predicted K^+	-	1119	28	458
Predicted Total	-	1560±25±156	51±4±5	572±10±57
Data Total	-	1719±42	53±7	455±21
Data/Predicted Total	-	1.10±0.11	1.04±0.19	0.79±0.09

compared with the "external" production experiments, which did not have to contend with neutrino interaction cross section or detector optical model uncertainties.

To reduce the K^+ production uncertainty with respect to the "external" data fit, a more direct in-situ K^+ measurement is needed. This is the purpose of the LMC. Currently only "fake data" LMC studies have been done, in which LMC signal Monte Carlo with the expected data statistics is generated assuming the best-fit K^+ production cross section from the Sanford-Wang fits in chapter 3. A fit to this LMC "fake data" alone, which has $\chi^2 = 0.0$ by construction, results in an error on the best-fit cross section of 10%, while, for comparison, a fit to HE data sub-sets alone gives 18%. Note that this comparison is not very meaningful since the LMC fits include no systematic errors, while the HE data fits do. That said, the LMC measurement will not have uncertainties from neutrino interaction cross sections, and therefore the systematic errors are expected to be less than 10%. Fitting the LMC "fake data" in

combination with the "external" data results in a fit error at the average (p_K, θ_K) for MiniBooNE of 4%; adding in the HE data as well does not further reduce the K^+ production cross section fit error. This result is highly dependent on the systematic error assumptions and the degree of agreement between the "external" fit prediction and the LMC measurement, however, it demonstrates the potential of the LMC to reduce the K^+ flux prediction uncertainty.

Like the HE data set, the LMC can be used to measure the normalization of the K^+-decay ν flux. An important difference is that the LMC measures the K^+-decay μ^+, not the ν_μ, and therefore it can break the degeneracy between neutrino flux and cross section that exists for an event rate measurement, which is only sensitive to the product of the two. To demonstrate the normalization constraint potential of the LMC, a "fake data" study is performed with both LMC and HE Monte Carlo sets generated assuming the K^+ production cross section from the Sanford-Wang fit to "external" data only. The statistics of the HE "fake data" set corresponds to 5 $\times 10^{20}$ simulated *p.o.t.*, and the LMC "fake data" set corresponds to 1 $\times 10^{17}$ *p.o.t.*, which is the total sample expected. Combinations of the "external" data, HE "fake data," and LMC "fake data" are fit for the Sanford-Wang K^+ production parameters, and an overall normalization factor is applied to the K^+ "fake data" in either the HE sample, the LMC sample, or both. The ability of each "fake data" set to change the normalization of the best-fit K^+ production cross section is evaluated by comparing the best-fit cross section at the average (p_K, θ_K) for MiniBooNE.

The results of this study are summarized in table D.5, which shows that if a normalization factor of 1.6 is applied to either the HE sample or the LMC, and the "fake data" are fit with the "external" data, the best-fit K^+ cross section is correspondingly increased [3]. This demonstrates that both the HE box and the LMC

[3]The amount of the increase in the best-fit K^+ cross section at the average (p_K, θ_K) for Mini-

have the ability to constrain the normalization of the K^+ production cross section, under the given systematic error assumptions. However, the LMC provides a stronger constraint when both "fake data" sets are fit together with the "external" data and have different normalization factors. In a fit to all three, when the LMC normalization factor is increased but the HE normalization is not, the resulting best-fit K^+ cross section normalization reflects the LMC "fake data" rate. In contrast, when the HE "fake data" normalization is increased and the LMC is not, the resulting cross section still has the normalization of the LMC, although the incompatibility is reflected by the increase in the χ^2/ndf of the fit.

As before, the conclusions depend on the assumptions made here, however, this study shows that at the very least the MiniBooNE in-situ data can provide a valuable cross-check of the K^+ production prediction, and potentially can correct the normalization if the prediction based on "external" data only is incorrect.

BooNE does not have to be the same as the "fake data" normalization increase. This is because the acceptance of the HE and LMC samples are different, and integrated over a region of production phase space, while the best-fit cross section is evaluated at one point.

Table D.5: *Normalization constraint study for "external" p Be → K^+ X data (labelled ExData below), HE "fake data," and LMC "fake data" under various normalization scenarios. The normalization factor is only applied to the K^+-decay "fake data." The best-fit cross section σ, and fit error $\delta\sigma$ are evaluated at the average (p_K, θ_K) for MiniBooNE.*

case	*normalization factor*	σ	$\delta\sigma$	χ^2/ndf	$\sqrt{\frac{\chi^2}{ndf}} \times \left(\frac{\delta\sigma}{\sigma}\right)$
ExData	N/A	5.63	0.28	3.62	9.46%
ExData & LMC	1.0	5.63	0.13	3.39	4.34%
ExData & LMC	1.6	8.08	0.16	3.64	3.76%
ExData & HE	1.0	5.85	0.26	3.66	8.66%
ExData & HE	1.6	7.31	0.31	3.82	8.46%
ExData & HE & LMC	1.0 & 1.0	5.66	0.13	3.38	4.34%
ExData & HE & LMC	1.6 & 1.0	5.84	0.13	3.84	4.47%
ExData & HE & LMC	1.0 & 1.6	8.04	0.16	3.64	3.74%
ExData & HE & LMC	1.6 & 1.6	8.16	0.16	3.66	3.77%

Appendix E

Chapter 6 Systematic Error Calculation Details

Table E.1: *Systematic error contributions to CCQE parameters from π^+ flux prediction simulation parameter uncertainties. The δ are calculated as the "unisim" best-fit parameters minus the central value Monte Carlo values, (E_B, p_F, m_A) = (0.025 GeV, 0.220 GeV, 1.03 GeV/c^2). Numbers in percent are quoted with respect to the central value parameters.*

source	δE_B (GeV)	δp_F (GeV)	δm_A (GeV/c^2)
SW π^+ c_1	0.2839×10^{-5}	-0.4351×10^{-5}	-0.4333×10^{-3}
SW π^+ c_2	0.1667×10^{-5}	-0.5990×10^{-5}	-0.3391×10^{-2}
SW π^+ c_3	-0.4428×10^{-3}	0.3095×10^{-2}	0.2060×10^{-2}
SW π^+ c_4	-0.9874×10^{-3}	0.6811×10^{-2}	0.4953×10^{-2}
SW π^+ c_5	0.1820×10^{-5}	-0.5722×10^{-5}	-0.2741×10^{-2}
SW π^+ c_6	-0.1336×10^{-3}	0.1009×10^{-2}	0.9012×10^{-3}
SW π^+ c_7	-0.9949×10^{-4}	0.6990×10^{-3}	0.4516×10^{-3}
SW π^+ c_8	0.1637×10^{-5}	-0.6005×10^{-5}	-0.1556×10^{-2}
SW π^+ quadrature sum	0.0011 (4.38%)	0.0076 (3.45%)	0.0072 (0.70%)

Table E.2: *Systematic error contributions to CCQE parameters from neutrino interaction simulation parameter uncertainties. The δ are calculated as the "unisim" best-fit parameters minus the central value Monte Carlo values, (E_B, p_F, m_A) = (0.025 GeV, 0.220 GeV, 1.03 GeV/c^2). Numbers in percent are quoted with respect to the central value parameters.*

source	δE_B (GeV)	δp_F (GeV)	δm_A (GeV/c^2)
σ_ν $+m_A^{QE}$	-0.9464$\times10^{-5}$	0.3120$\times10^{-4}$	0.3898$\times10^{-4}$
σ_ν $+p_F$	-0.2006$\times10^{-4}$	-0.9775$\times10^{-5}$	-0.3765$\times10^{-2}$
σ_ν $+E_B$	-0.2003$\times10^{-3}$	0.9283$\times10^{-5}$	-0.2053$\times10^{-1}$
σ_ν $+\Delta s$	-0.1524$\times10^{-5}$	0.3278$\times10^{-6}$	-0.4530$\times10^{-5}$
σ_ν $+m_A^{1\pi}$	0.4319$\times10^{-5}$	-0.2265$\times10^{-5}$	-0.4515$\times10^{-2}$
σ_ν $+m_A^{N\pi}$	0.7277$\times10^{-5}$	0.1833$\times10^{-5}$	-0.1228$\times10^{-4}$
σ_ν $+m_A^{coh}$	0.1676$\times10^{-7}$	0.1490$\times10^{-7}$	0.1192$\times10^{-6}$
σ_ν +DIS	-0.3306$\times10^{-5}$	-0.2310$\times10^{-5}$	-0.1395$\times10^{-4}$
σ_ν $+\Delta \rightarrow \gamma\gamma$	-0.2161$\times10^{-5}$	-0.2474$\times10^{-5}$	-0.1132$\times10^{-4}$
σ_ν $+\sigma^{\pi}_{absorption}$	0.2865$\times10^{-2}$	0.8066$\times10^{-2}$	-0.2107$\times10^{-1}$
σ_ν $+\sigma^{\pi}_{charge\ exchange}$	0.0000	0.0000	0.0000
σ_ν $+\Delta N \rightarrow NN$	0.1220$\times10^{-2}$	0.3262$\times10^{-2}$	-0.3679$\times10^{-1}$
σ_ν quadrature sum	0.0031 (12.48%)	0.0087 (3.96%)	0.0475 (4.61%)

Table E.3: *Systematic error contributions to CCQE parameters from detector response simulation parameter uncertainties. The δ are calculated as the "unisim" best-fit parameters minus the central value Monte Carlo values, (E_B, p_F, m_A) = (0.025 GeV, 0.220 GeV, 1.03 GeV/c^2). Numbers in percent are quoted with respect to the central value parameters.*

source	δE_B (GeV)	δp_F (GeV)	δm_A (GeV/c^2)
cher	-0.3872×10^{-2}	0.3171×10^{-1}	0.5255×10^{-2}
ext	0.6405×10^{-4}	-0.3725×10^{-6}	-0.6327×10^{-1}
pmt	0.0000	0.0000	0.0000
ref	0.1578×10^{-3}	0.1522×10^{-3}	-0.4431×10^{-1}
scat	0.5654×10^{-2}	0.1970×10^{-1}	0.2736×10^{-1}
tau4	0.1035×10^{-2}	0.1306×10^{-1}	-0.2167×10^{-1}
uvext	0.1905×10^{-4}	0.6855×10^{-6}	-0.4289×10^{-1}
uvf2	0.9656×10^{-4}	0.1532×10^{-4}	-0.6020×10^{-1}
uvf3	0.2599×10^{-4}	0.5012×10^{-2}	-0.3914×10^{-1}
uvf4	0.1844×10^{-3}	-0.1252×10^{-5}	-0.9656×10^{-1}
sci4	0.3449×10^{-4}	0.2688×10^{-4}	-0.2462×10^{-1}
flu1	0.3152×10^{-2}	0.8310×10^{-2}	-0.1712×10^{-1}
flu2	-0.7212×10^{-5}	0.7674×10^{-5}	-0.3967×10^{-1}
flu3	0.2326×10^{-2}	0.6058×10^{-2}	-0.2964×10^{-1}
flu4	-0.2289×10^{-3}	0.2168×10^{-1}	-0.6941×10^{-2}
sci2	0.3491×10^{-5}	-0.1922×10^{-5}	-0.8214×10^{-1}
sci3	0.4486×10^{-4}	0.2237×10^{-4}	-0.3988×10^{-1}
birks	0.1056×10^{-2}	0.8836×10^{-2}	-0.2839×10^{-1}
tsm	0.0000	0.0000	0.0000
veto	-0.5588×10^{-7}	-0.4470×10^{-7}	-0.8122×10^{-1}
scatba	0.5880×10^{-3}	0.1187×10^{-1}	-0.1956×10^{-1}
tau2	-0.3947×10^{-3}	0.4994×10^{-2}	-0.3908×10^{-1}
tau3	0.8665×10^{-3}	0.2875×10^{-2}	-0.3851×10^{-1}
quadrature sum	0.0081 (32.46%)	0.0492 (22.35%)	0.2146 (20.84%)

Table E.4: *Systematic error contributions to CCQE parameters from Sanford-Wang π^+ flux prediction variations. The fit parameter variations δ are calculated as the "unisim" best-fit parameters minus the central value Monte Carlo values.*

	$+c_1$	$+c_2$	$+c_3$	$+c_4$	$+c_5$	$+c_6$	$+c_7$	$+c_8$
E_B	0.0000	0.0000	0.0036	0.0016	0.0000	0.0001	0.0002	0.0000
p_F	0.0000	0.0000	0.0068	0.0030	0.0001	0.0001	0.0003	0.0000
$\delta F_A(Q_1^2)$	-0.3143×10^{-2}	-0.7198×10^{-2}	-0.2894×10^{-1}	0.6851×10^{-2}	-0.6154×10^{-2}	0.4019×10^{-2}	0.4604×10^{-3}	-0.5737×10^{-2}
$\delta F_A(Q_2^2)$	-0.9923×10^{-3}	-0.5626×10^{-2}	-0.2236×10^{-1}	0.3459×10^{-2}	-0.5252×10^{-2}	0.3278×10^{-2}	0.1159×10^{-2}	-0.3184×10^{-2}
$\delta F_A(Q_3^2)$	0.5157×10^{-3}	0.1199×10^{-2}	-0.1418×10^{-1}	0.4773×10^{-2}	-0.2781×10^{-2}	0.2483×10^{-2}	0.1648×10^{-2}	0.1231×10^{-2}
$\delta F_A(Q_4^2)$	-0.1132×10^{-2}	-0.1087×10^{-2}	-0.1350×10^{-1}	-0.5196×10^{-3}	-0.2500×10^{-2}	-0.8026×10^{-3}	-0.1315×10^{-2}	-0.1543×10^{-2}
$\delta F_A(Q_5^2)$	-0.1978×10^{-3}	-0.5584×10^{-3}	-0.1282×10^{-1}	-0.2283×10^{-2}	-0.9724×10^{-3}	-0.7216×10^{-3}	-0.9478×10^{-3}	-0.2780×10^{-3}
$\delta F_A(Q_6^2)$	0.9845×10^{-3}	0.1483×10^{-2}	-0.1434×10^{-1}	-0.4824×10^{-2}	0.9054×10^{-3}	-0.6066×10^{-3}	-0.1565×10^{-3}	0.1122×10^{-2}
$\delta F_A(Q_7^2)$	0.1817×10^{-2}	0.3444×10^{-2}	-0.1485×10^{-1}	-0.6601×10^{-2}	0.2701×10^{-2}	0.3181×10^{-3}	0.1194×10^{-3}	0.2596×10^{-2}
$\delta F_A(Q_8^2)$	-0.1564×10^{-2}	0.1310×10^{-2}	-0.1913×10^{-1}	-0.1364×10^{-1}	0.6779×10^{-3}	-0.3577×10^{-2}	-0.3387×10^{-2}	-0.8899×10^{-4}
$\delta F_A(Q_9^2)$	0.7136×10^{-3}	0.4075×10^{-2}	-0.1781×10^{-1}	-0.1330×10^{-1}	0.3183×10^{-2}	-0.1779×10^{-2}	-0.1668×10^{-2}	0.2067×10^{-2}
$\delta F_A(Q_{10}^2)$	0.3670×10^{-3}	0.4365×10^{-2}	-0.1906×10^{-1}	-0.1673×10^{-1}	0.3804×10^{-2}	-0.2522×10^{-2}	-0.1805×10^{-2}	0.1849×10^{-2}
$\delta F_A(Q_{11}^2)$	-0.5798×10^{-3}	0.3897×10^{-2}	-0.1939×10^{-1}	-0.1759×10^{-1}	0.3194×10^{-2}	-0.2882×10^{-2}	-0.3636×10^{-2}	0.1407×10^{-2}
$\delta F_A(Q_{12}^2)$	-0.6954×10^{-3}	0.3992×10^{-2}	-0.1941×10^{-1}	-0.1913×10^{-1}	0.3374×10^{-2}	-0.3600×10^{-2}	-0.3348×10^{-2}	0.1087×10^{-2}
$\delta F_A(Q_{13}^2)$	0.1677×10^{-2}	0.6748×10^{-2}	-0.1610×10^{-1}	-0.1681×10^{-1}	0.6216×10^{-2}	-0.7849×10^{-3}	-0.1131×10^{-2}	0.3834×10^{-2}
$\delta F_A(Q_{14}^2)$	0.1873×10^{-2}	0.7029×10^{-2}	-0.1628×10^{-1}	-0.1885×10^{-1}	0.6744×10^{-2}	-0.1129×10^{-2}	-0.7178×10^{-3}	0.3659×10^{-2}
$\delta F_A(Q_{15}^2)$	0.1760×10^{-2}	0.7042×10^{-2}	-0.1594×10^{-1}	-0.1952×10^{-1}	0.6816×10^{-2}	-0.1215×10^{-2}	-0.1259×10^{-2}	0.3574×10^{-2}
$\delta F_A(Q_{16}^2)$	-0.1826×10^{-2}	0.3568×10^{-2}	-0.1852×10^{-1}	-0.2323×10^{-1}	0.3436×10^{-2}	-0.4798×10^{-2}	-0.4767×10^{-2}	0.9057×10^{-4}

Table E.5: *Systematic error contributions to CCQE parameters from neutrino interaction cross section variations. The fit parameter variations δ are calculated as the "unisim" best-fit parameters minus the central value Monte Carlo values. This table is continued in E.6.*

	$+m_A^{QE}$	$+p_F$	$+E_B$	$+\Delta s$	$+m_A^{1\pi}$	$+m_A^{N\pi}$
E_B	0.1487×10^{-4}	-0.2251×10^{-4}	-0.2480×10^{-4}	0.1380×10^{-5}	-0.2853×10^{-3}	0.1522×10^{-5}
p_F	0.3894×10^{-4}	0.8999×10^{-4}	0.8629×10^{-4}	0.4485×10^{-5}	0.3508×10^{-2}	0.1618×10^{-4}
$\delta F_A(Q_1^2)$	0.8531×10^{-3}	-0.1361×10^{-1}	-0.4744×10^{-1}	-0.1293×10^{-2}	-0.2887×10^{-1}	-0.1643×10^{-2}
$\delta F_A(Q_2^2)$	0.8868×10^{-3}	-0.3113×10^{-2}	-0.1114×10^{-1}	0.3654×10^{-3}	-0.1307×10^{-1}	0.2975×10^{-3}
$\delta F_A(Q_3^2)$	0.7937×10^{-3}	0.3619×10^{-3}	0.6089×10^{-3}	0.9202×10^{-3}	-0.4417×10^{-2}	0.9241×10^{-3}
$\delta F_A(Q_4^2)$	-0.1160×10^{-2}	-0.2314×10^{-3}	0.3917×10^{-2}	-0.1059×10^{-2}	-0.9447×10^{-4}	-0.1022×10^{-2}
$\delta F_A(Q_5^2)$	-0.5291×10^{-3}	0.1273×10^{-2}	0.7701×10^{-2}	-0.4035×10^{-3}	0.2854×10^{-2}	-0.3757×10^{-3}
$\delta F_A(Q_6^2)$	0.3980×10^{-3}	0.2778×10^{-2}	0.1034×10^{-1}	0.5115×10^{-3}	0.5347×10^{-2}	0.5565×10^{-3}
$\delta F_A(Q_7^2)$	0.1289×10^{-2}	0.3829×10^{-2}	0.1193×10^{-1}	0.1415×10^{-2}	0.7152×10^{-2}	0.1454×10^{-2}
$\delta F_A(Q_8^2)$	-0.1935×10^{-2}	0.8742×10^{-3}	0.9166×10^{-2}	-0.1843×10^{-2}	0.4301×10^{-2}	-0.1807×10^{-2}
$\delta F_A(Q_9^2)$	-0.4828×10^{-5}	0.2954×10^{-2}	0.1122×10^{-1}	0.1040×10^{-3}	0.6532×10^{-2}	0.1634×10^{-3}
$\delta F_A(Q_{10}^2)$	-0.3488×10^{-3}	0.2577×10^{-2}	0.1063×10^{-1}	-0.2457×10^{-3}	0.6710×10^{-2}	-0.2017×10^{-3}
$\delta F_A(Q_{11}^2)$	-0.1029×10^{-2}	0.1945×10^{-2}	0.9830×10^{-2}	-0.9305×10^{-3}	0.6011×10^{-2}	-0.8872×10^{-3}
$\delta F_A(Q_{12}^2)$	-0.1343×10^{-2}	0.1748×10^{-2}	0.9422×10^{-2}	-0.1255×10^{-2}	0.6138×10^{-2}	-0.1156×10^{-2}
$\delta F_A(Q_{13}^2)$	0.1307×10^{-2}	0.4148×10^{-2}	0.1149×10^{-1}	0.1388×10^{-2}	0.1012×10^{-1}	0.1452×10^{-2}
$\delta F_A(Q_{14}^2)$	0.1198×10^{-2}	0.4074×10^{-2}	0.1118×10^{-1}	0.1274×10^{-2}	0.9800×10^{-2}	0.1312×10^{-2}
$\delta F_A(Q_{15}^2)$	0.1058×10^{-2}	0.4013×10^{-2}	0.1081×10^{-1}	0.1128×10^{-2}	0.8876×10^{-2}	0.1165×10^{-2}
$\delta F_A(Q_{16}^2)$	-0.2457×10^{-2}	0.4207×10^{-3}	0.6905×10^{-2}	-0.2396×10^{-2}	0.6321×10^{-2}	-0.2357×10^{-2}

Table E.6: *Systematic error contributions to CCQE parameters from neutrino interaction cross section variations. The fit parameter variations δ are calculated as the "unisim" best-fit parameters minus the central value Monte Carlo values.*

	$+m_A^{coh}$	$+\sigma_{DIS}$	$+\Delta \rightarrow \gamma\gamma$	$+\sigma_{ABS}^{\pi}$	$+\sigma_{C.E.}^{\pi}$	$+\Delta N \rightarrow NN$
E_B	-0.7360×10^{-4}	-0.1129×10^{-5}	-0.1093×10^{-5}	0.4432×10^{-2}	0.4977×10^{-2}	0.0000
p_F	0.5665×10^{-3}	0.2399×10^{-5}	-0.6706×10^{-5}	0.2486×10^{-1}	0.1634×10^{-1}	0.0000
$\delta F_A(Q_1^2)$	0.3257×10^{-1}	-0.1310×10^{-2}	-0.1350×10^{-2}	-0.1019	-0.6383×10^{-1}	-0.6877×10^{-3}
$\delta F_A(Q_2^2)$	-0.5083×10^{-2}	0.3679×10^{-3}	0.3763×10^{-3}	-0.4292×10^{-1}	-0.2592×10^{-1}	-0.1764×10^{-2}
$\delta F_A(Q_3^2)$	-0.5830×10^{-2}	0.9385×10^{-3}	0.9386×10^{-3}	-0.3957×10^{-1}	-0.1788×10^{-1}	-0.2810×10^{-2}
$\delta F_A(Q_4^2)$	-0.6650×10^{-2}	-0.1025×10^{-2}	-0.1039×10^{-2}	0.6554×10^{-3}	0.5423×10^{-2}	-0.1128×10^{-2}
$\delta F_A(Q_5^2)$	-0.5187×10^{-2}	-0.4030×10^{-3}	-0.3909×10^{-3}	-0.5783×10^{-2}	0.6089×10^{-3}	-0.4279×10^{-3}
$\delta F_A(Q_6^2)$	-0.3686×10^{-2}	0.5130×10^{-3}	0.5156×10^{-3}	0.6767×10^{-2}	0.6896×10^{-2}	-0.2455×10^{-2}
$\delta F_A(Q_7^2)$	-0.2457×10^{-2}	0.1419×10^{-2}	0.1421×10^{-2}	-0.8414×10^{-2}	0.1838×10^{-1}	0.2709×10^{-2}
$\delta F_A(Q_8^2)$	-0.5369×10^{-2}	-0.1839×10^{-2}	-0.1829×10^{-2}	0.4879×10^{-2}	0.9274×10^{-2}	-0.5436×10^{-2}
$\delta F_A(Q_9^2)$	-0.3049×10^{-2}	0.1091×10^{-3}	0.1085×10^{-3}	0.3254×10^{-2}	0.1325×10^{-1}	0.7728×10^{-3}
$\delta F_A(Q_{10}^2)$	-0.3089×10^{-2}	-0.2262×10^{-3}	-0.2354×10^{-3}	0.2485×10^{-1}	0.1282×10^{-1}	0.9078×10^{-4}
$\delta F_A(Q_{11}^2)$	-0.3544×10^{-2}	-0.9247×10^{-3}	-0.9272×10^{-3}	0.2438×10^{-1}	-0.1077×10^{-1}	0.5203×10^{-3}
$\delta F_A(Q_{12}^2)$	-0.3513×10^{-2}	-0.1249×10^{-2}	-0.1225×10^{-2}	0.3390×10^{-1}	-0.1612×10^{-1}	-0.3201×10^{-2}
$\delta F_A(Q_{13}^2)$	-0.5961×10^{-3}	0.1394×10^{-2}	0.1387×10^{-2}	0.4179×10^{-2}	0.2570×10^{-1}	0.6345×10^{-4}
$\delta F_A(Q_{14}^2)$	-0.5912×10^{-3}	0.1303×10^{-2}	0.1285×10^{-2}	0.1494×10^{-1}	0.2766×10^{-1}	0.8380×10^{-4}
$\delta F_A(Q_{15}^2)$	-0.5317×10^{-3}	0.1134×10^{-2}	0.1126×10^{-2}	0.1033×10^{-1}	0.2115×10^{-1}	0.1714×10^{-2}
$\delta F_A(Q_{16}^2)$	-0.3779×10^{-2}	-0.2371×10^{-2}	-0.2401×10^{-2}	0.3795×10^{-1}	0.2977×10^{-1}	-0.4476×10^{-2}

Table E.7: *Systematic error contributions to CCQE parameters from detector response simulation parameter variations. The fit parameter variations δ are calculated as the "unisim" best-fit parameters minus the central value Monte Carlo values. This table is continued in E.8 and E.9.*

	cher	*ext*	*pmt*	*ref*	*scat*	*tau4*	*uvext*	*uvf2*
E_B	0.6447×10^{-4}	-0.8860×10^{-2}	0.6568×10^{-2}	-0.1275×10^{-2}	0.6101×10^{-3}	-0.2499×10^{-3}	-0.6121×10^{-3}	-0.3725×10^{-2}
p_F	0.1511×10^{-1}	0.1072×10^{-2}	0.1084×10^{-3}	0.2268×10^{-2}	0.2179×10^{-1}	0.3487×10^{-4}	0.0000	0.1789×10^{-1}
$\delta F_A(Q^2_1)$	-0.6006×10^{-1}	0.1314	0.4720×10^{-1}	0.5820×10^{-1}	-0.8447×10^{-1}	0.3520×10^{-1}	-0.4430×10^{-2}	-0.3875×10^{-1}
$\delta F_A(Q^2_2)$	-0.5100×10^{-2}	0.7693×10^{-1}	0.7309×10^{-1}	0.2135×10^{-1}	-0.1073	0.1244×10^{-1}	-0.6938×10^{-2}	0.3487×10^{-1}
$\delta F_A(Q^2_3)$	0.6623×10^{-2}	0.8298×10^{-1}	0.6662×10^{-1}	0.1386×10^{-1}	-0.7742×10^{-1}	-0.3433×10^{-2}	-0.1273×10^{-1}	0.5756×10^{-1}
$\delta F_A(Q^2_4)$	0.7304×10^{-2}	0.8121×10^{-1}	0.4801×10^{-1}	0.1446×10^{-1}	-0.2221×10^{-1}	0.2765×10^{-1}	-0.1744×10^{-1}	0.5139×10^{-1}
$\delta F_A(Q^2_5)$	0.2164×10^{-1}	0.4414×10^{-1}	0.2130×10^{-1}	0.2000×10^{-1}	-0.3639×10^{-1}	0.5184×10^{-2}	-0.1956×10^{-1}	0.4251×10^{-1}
$\delta F_A(Q^2_6)$	-0.2069×10^{-1}	0.4806×10^{-1}	0.3333×10^{-1}	0.3317×10^{-1}	-0.7473×10^{-2}	0.1691×10^{-1}	-0.1818×10^{-1}	0.5195×10^{-1}
$\delta F_A(Q^2_7)$	0.1676×10^{-1}	0.4823×10^{-1}	0.2791×10^{-1}	0.1715×10^{-1}	0.1570×10^{-1}	0.2727×10^{-1}	-0.1681×10^{-1}	0.4980×10^{-1}
$\delta F_A(Q^2_8)$	0.4611×10^{-1}	0.4687×10^{-1}	-0.1424×10^{-2}	0.3742×10^{-1}	0.8871×10^{-1}	0.9089×10^{-1}	-0.2459×10^{-1}	0.6357×10^{-1}
$\delta F_A(Q^2_9)$	0.2198×10^{-1}	0.1427×10^{-1}	0.2990×10^{-1}	0.3698×10^{-1}	0.1008	0.7466×10^{-1}	-0.2005×10^{-1}	0.4155×10^{-1}
$\delta F_A(Q^2_{10})$	0.1577×10^{-1}	0.1200×10^{-1}	0.2030×10^{-1}	0.2113×10^{-1}	0.8313×10^{-1}	0.1036	-0.2015×10^{-1}	0.4855×10^{-1}
$\delta F_A(Q^2_{11})$	0.4212×10^{-1}	0.2086×10^{-1}	-0.4715×10^{-2}	0.3356×10^{-1}	0.3553×10^{-1}	0.4564×10^{-1}	-0.2619×10^{-1}	0.1833×10^{-1}
$\delta F_A(Q^2_{12})$	0.3855×10^{-1}	0.2959×10^{-1}	0.2361×10^{-1}	0.3581×10^{-1}	0.3580×10^{-1}	0.3684×10^{-1}	-0.2485×10^{-1}	0.7200×10^{-2}
$\delta F_A(Q^2_{13})$	0.6159×10^{-1}	0.2100×10^{-1}	0.9734×10^{-2}	0.2911×10^{-1}	0.5096×10^{-1}	0.5849×10^{-1}	-0.1571×10^{-1}	0.2337×10^{-1}
$\delta F_A(Q^2_{14})$	0.5584×10^{-1}	0.8147×10^{-2}	0.2053×10^{-1}	0.4428×10^{-1}	0.1367	0.1452	-0.2133×10^{-1}	0.4342×10^{-1}
$\delta F_A(Q^2_{15})$	0.7066×10^{-1}	0.2708×10^{-1}	0.1627×10^{-1}	0.4650×10^{-1}	0.1013	0.8248×10^{-1}	-0.1740×10^{-1}	0.5318×10^{-1}
$\delta F_A(Q^2_{16})$	0.8264×10^{-1}	0.3647×10^{-1}	0.1324×10^{-2}	0.6798×10^{-1}	0.1932	0.1867	-0.2031×10^{-1}	0.3427×10^{-2}

Table E.8: *Systematic error contributions to CCQE parameters from detector response simulation parameter variations. The fit parameter variations δ are calculated as the "unisim" best-fit parameters minus the central value Monte Carlo values.*

	uvf3	*uvf4*	*sci4*	*flu1*	*flu2*	*flu3*	*flu4*
E_B	-0.3631×10^{-4}	0.0000	0.8825×10^{-2}	0.5908×10^{-2}	0.4375×10^{-3}	0.1920×10^{-4}	0.4487×10^{-2}
p_F	-0.3725×10^{-6}	0.1175	0.1138×10^{-1}	0.2776×10^{-1}	0.6309×10^{-3}	-0.7173×10^{-4}	0.8387×10^{-2}
$\delta F_A(Q_1^2)$	0.1050	-0.5564	-0.3539×10^{-1}	-0.1423	0.3703×10^{-1}	0.3402×10^{-3}	0.2137×10^{-1}
$\delta F_A(Q_2^2)$	0.9506×10^{-1}	-0.3982	-0.7262×10^{-2}	-0.6254×10^{-1}	0.2266×10^{-1}	0.5748×10^{-1}	0.4274×10^{-1}
$\delta F_A(Q_3^2)$	0.7244×10^{-1}	-0.3330	-0.4725×10^{-3}	-0.4241×10^{-1}	0.4765×10^{-1}	0.3856×10^{-1}	0.6237×10^{-1}
$\delta F_A(Q_4^2)$	0.5735×10^{-1}	-0.2300	0.1415×10^{-1}	-0.1345×10^{-1}	0.3184×10^{-1}	0.4305×10^{-1}	0.2580×10^{-1}
$\delta F_A(Q_5^2)$	0.3713×10^{-1}	-0.1289	-0.1186×10^{-1}	-0.2107×10^{-1}	0.3148×10^{-1}	0.3010×10^{-1}	0.2680×10^{-1}
$\delta F_A(Q_6^2)$	0.2564×10^{-1}	-0.1197	0.8955×10^{-2}	-0.1629×10^{-1}	0.3101×10^{-1}	0.4726×10^{-1}	0.1922×10^{-1}
$\delta F_A(Q_7^2)$	0.2949×10^{-1}	-0.9538×10^{-1}	0.2504×10^{-1}	0.1284×10^{-1}	0.1805×10^{-1}	0.4130×10^{-1}	0.9477×10^{-2}
$\delta F_A(Q_8^2)$	0.1301×10^{-1}	-0.7671×10^{-1}	-0.2436×10^{-1}	-0.2708×10^{-1}	0.1821×10^{-1}	0.3407×10^{-1}	-0.4557×10^{-2}
$\delta F_A(Q_9^2)$	0.9063×10^{-2}	-0.3412×10^{-1}	0.1065×10^{-1}	0.2888×10^{-1}	0.3433×10^{-1}	0.4735×10^{-1}	-0.1317×10^{-1}
$\delta F_A(Q_{10}^2)$	0.1322×10^{-1}	-0.1440×10^{-1}	0.3118×10^{-1}	0.5626×10^{-2}	0.3894×10^{-1}	0.3790×10^{-1}	-0.2695×10^{-1}
$\delta F_A(Q_{11}^2)$	0.1831×10^{-1}	0.2816×10^{-1}	0.1124×10^{-1}	-0.8379×10^{-2}	0.1507×10^{-1}	0.5341×10^{-1}	-0.1620×10^{-1}
$\delta F_A(Q_{12}^2)$	-0.2105×10^{-2}	0.5452×10^{-2}	-0.1309×10^{-1}	0.1943×10^{-1}	0.1640×10^{-1}	0.7060×10^{-2}	0.2667×10^{-2}
$\delta F_A(Q_{13}^2)$	-0.2325×10^{-1}	0.3595×10^{-1}	-0.3780×10^{-1}	0.1735×10^{-1}	0.2587×10^{-1}	0.3601×10^{-1}	-0.1598×10^{-1}
$\delta F_A(Q_{14}^2)$	0.7284×10^{-2}	0.5754×10^{-1}	0.1485×10^{-1}	0.1463×10^{-1}	0.3748×10^{-1}	0.5425×10^{-1}	0.3283×10^{-1}
$\delta F_A(Q_{15}^2)$	-0.2177×10^{-1}	0.3398×10^{-1}	-0.2176×10^{-2}	0.1133×10^{-1}	0.3836×10^{-1}	0.2408×10^{-1}	-0.8895×10^{-2}
$\delta F_A(Q_{16}^2)$	-0.4958×10^{-2}	0.6729×10^{-1}	0.3589×10^{-1}	0.4751×10^{-1}	0.5430×10^{-1}	0.5052×10^{-1}	-0.1859×10^{-1}

Table E.9: *Systematic error contributions to CCQE parameters from detector response simulation parameter variations. The fit parameter variations δ are calculated as the "unisim" best-fit parameters minus the central value Monte Carlo values.*

	sci2	*sci3*	*birks*	*tsmear*	*scatba*	*tau2*	*tau3*
E_B	0.1404×10^{-5}	-0.9016×10^{-2}	0.5388×10^{-2}	0.0000	0.1623×10^{-4}	0.0000	0.4755×10^{-2}
p_F	0.2295×10^{-5}	0.8872×10^{-1}	0.9855×10^{-2}	0.0000	0.2846×10^{-5}	0.0000	0.1682×10^{-1}
$\delta F_A(Q^2_1)$	-0.3499	-0.3680	0.4979×10^{-2}	-0.1863×10^{-2}	0.8195×10^{-1}	-0.2028×10^{-2}	-0.6343×10^{-1}
$\delta F_A(Q^2_2)$	-0.1159	-0.2673	0.2056×10^{-2}	0.3519×10^{-2}	0.2578×10^{-1}	0.1878×10^{-2}	-0.4546×10^{-1}
$\delta F_A(Q^2_3)$	-0.3087×10^{-1}	-0.1595	0.4842×10^{-2}	0.2846×10^{-2}	0.2403×10^{-1}	0.1410×10^{-2}	-0.6174×10^{-2}
$\delta F_A(Q^2_4)$	0.2510×10^{-1}	-0.1156	0.7612×10^{-2}	0.1158×10^{-2}	0.3521×10^{-1}	-0.1526×10^{-2}	0.7857×10^{-2}
$\delta F_A(Q^2_5)$	0.4020×10^{-1}	-0.7599×10^{-1}	0.8364×10^{-2}	0.2822×10^{-2}	0.1479×10^{-1}	-0.1059×10^{-2}	0.1721×10^{-1}
$\delta F_A(Q^2_6)$	0.6823×10^{-1}	-0.5832×10^{-1}	0.1281×10^{-1}	0.1183×10^{-2}	0.2935×10^{-1}	0.1164×10^{-2}	0.1762×10^{-1}
$\delta F_A(Q^2_7)$	0.6660×10^{-1}	-0.4293×10^{-1}	0.1315×10^{-1}	0.4480×10^{-2}	0.2372×10^{-1}	0.8217×10^{-3}	-0.6916×10^{-2}
$\delta F_A(Q^2_8)$	0.5803×10^{-1}	-0.3133×10^{-1}	0.8281×10^{-2}	0.4286×10^{-4}	0.2001×10^{-1}	-0.2433×10^{-2}	0.3419×10^{-1}
$\delta F_A(Q^2_9)$	0.7968×10^{-1}	-0.1534×10^{-1}	0.4197×10^{-2}	0.1684×10^{-2}	0.1726×10^{-1}	0.1829×10^{-2}	-0.2657×10^{-2}
$\delta F_A(Q^2_{10})$	0.8756×10^{-1}	-0.1446×10^{-1}	0.9623×10^{-2}	0.2505×10^{-2}	0.3450×10^{-1}	-0.5286×10^{-3}	0.3261×10^{-2}
$\delta F_A(Q^2_{11})$	0.8434×10^{-1}	0.6909×10^{-2}	0.4959×10^{-2}	0.1146×10^{-2}	0.2088×10^{-1}	-0.2229×10^{-2}	0.1688×10^{-1}
$\delta F_A(Q^2_{12})$	0.8475×10^{-1}	-0.3276×10^{-2}	0.4669×10^{-2}	-0.7886×10^{-3}	0.1811×10^{-1}	-0.1753×10^{-2}	0.1689×10^{-1}
$\delta F_A(Q^2_{13})$	0.8963×10^{-1}	-0.1641×10^{-1}	0.1145×10^{-1}	0.5352×10^{-2}	0.2685×10^{-1}	-0.5128×10^{-2}	0.1508×10^{-1}
$\delta F_A(Q^2_{14})$	0.1152	0.6007×10^{-2}	0.9260×10^{-2}	0.1592×10^{-2}	0.2173×10^{-1}	0.2873×10^{-2}	0.3602×10^{-1}
$\delta F_A(Q^2_{15})$	0.8982×10^{-1}	0.3261×10^{-1}	0.5948×10^{-2}	0.3061×10^{-2}	0.2015×10^{-1}	-0.5295×10^{-3}	0.4409×10^{-1}
$\delta F_A(Q^2_{16})$	0.1222	0.4995×10^{-1}	0.6601×10^{-2}	-0.4829×10^{-3}	0.9522×10^{-2}	-0.7612×10^{-4}	0.3290×10^{-1}

Appendix F

Chapter 7 Oscillation Sensitivity Calculation Details

Table F.1: *Fractional normalization uncertainty for each π^+ simulation parameter, for ν_μ, ν_e, and combined fits. Parameter correlations are not included.*

source	ν_μ	ν_e	*combined*
$\pi^+ c_1$	0.1661	0.1348	0.1658
$\pi^+ c_2$	0.0637	0.0543	0.0636
$\pi^+ c_3$	-0.0705	-0.0653	-0.0704
$\pi^+ c_4$	-0.1029	-0.1058	-0.1029
$\pi^+ c_5$	0.0525	0.0493	0.0524
$\pi^+ c_6$	-0.0534	-0.0427	-0.0533
$\pi^+ c_7$	0.0308	0.0238	0.0308
$\pi^+ c_8$	-0.0145	-0.0131	-0.0145

Table F.2: *Fractional normalization uncertainty for each K^+ simulation parameter, for ν_μ, ν_e, and combined fits. Parameter correlations are not included.*

source	ν_μ	ν_e	*combined*
$K^+ c_1$	0.0023	0.0552	0.0027
$K^+ c_2$	0.0007	0.0227	0.0009
$K^+ c_3$	-0.0008	-0.0270	-0.0010
$K^+ c_4$	-0.0011	-0.0438	-0.0015
$K^+ c_5$	0.0006	0.0204	0.0008
$K^+ c_6$	-0.0009	-0.0213	-0.0011
$K^+ c_7$	0.0006	0.0107	0.0007
$K^+ c_8$	-0.0006	-0.0076	-0.0007
$K^+ c_9$	0.0000	0.0000	0.0000

Table F.3: *Fractional normalization uncertainty for each neutrino interaction cross section simulation parameter, for ν_μ, ν_e, and combined fits. Parameter correlations are not included.*

source	ν_μ	ν_e	*combined*
$\nu\ \sigma\ +m_A^{QE}$	0.0462	0.0415	0.0462
$\nu\ \sigma\ +p_F$	-0.1404	-0.1707	-0.1407
$\nu\ \sigma\ +E_B$	-0.2145	-0.2000	-0.2144
$\nu\ \sigma\ +\Delta s$	0.0000	-0.0228	-0.0002
$\nu\ \sigma\ +m_A^{1\pi}$	0.0013	0.0084	0.0014
$\nu\ \sigma\ +m_A^{N\pi}$	0.0000	-0.0239	-0.0002
$\nu\ \sigma\ +m_A^{coh}$	0.0057	-0.0005	0.0058
$\nu\ \sigma\ +\sigma_{DIS}$	0.0000	-0.0217	-0.0002
$\nu\ \sigma\ +\Delta \rightarrow \gamma\gamma$	0.0000	0.0004	0.0000

Table F.4: *Fractional normalization uncertainty summary, for ν_μ, ν_e, and combined fits.*

source	ν_μ	ν_e	*combined*
uncorrelated total error	0.3491	0.3483	0.3489
correlated total error	0.1088	0.1037	0.1084
total events	91611	799	92410

Table F.5: *Correlation matrices for (i) the Sanford-Wang π^+ parameters, (ii) the Sanford-Wang K^+ parameters, and (iii) the neutrino interaction cross section parameters used in the oscillation fits.*

	c_1	c_2	c_3	c_4	c_5	c_6	c_7	c_8
c_1	1.0000000000	0.9923313856	0.9936071038	0.9918437600	0.9924814105	0.9919452071	0.9922234416	0.9916135073
c_2	0.9923313856	1.0000000000	0.9970705509	0.9953101873	0.9958553910	0.9953696728	0.9959815741	0.9942911863
c_3	0.9936071038	0.9970705509	1.0000000000	0.9962370992	0.9970048666	0.9958888292	0.9967896342	0.9952568412
c_4	0.9918437600	0.9953101873	0.9962370992	1.0000000000	0.9951412082	0.9941892028	0.9951506853	0.9933677316
c_5	0.9924814105	0.9958553910	0.9970048666	0.9951412082	1.0000000000	0.9951121211	0.9960127473	0.9940157533
c_6	0.9919452071	0.9953696728	0.9958888292	0.9941892028	0.9951121211	1.0000000000	0.9949533939	0.9931093454
c_7	0.9922234416	0.9959815741	0.9967896342	0.9951506853	0.9960127473	0.9949533939	1.0000000000	0.9940701127
c_8	0.9916135073	0.9942911863	0.9952568412	0.9933677316	0.9940157533	0.9931093454	0.9940701127	1.0000000000

	c_1	c_2	c_3	c_4	c_5	c_6	c_7	c_8	c_9
c_1	1.0000000000	-0.7999950647	0.5620495081	-0.5543355942	0.4768086672	-0.3727486730	-0.4333691001	0.3181966543	-0.0020462861
c_2	-0.7999950647	1.0000000000	-0.3383451700	0.4407133460	-0.3703078628	0.2895865142	-0.0402938798	-0.5387134552	-0.0057730838
c_3	0.5620495081	-0.3383451700	1.0000000000	-0.9506055713	0.8660150766	-0.1357219219	-0.3014900386	0.1074236929	-0.0001874897
c_4	-0.5543355942	0.4407133460	-0.9506055713	1.0000000000	-0.8654692173	-0.0339770876	0.1274360120	-0.1985262632	0.0000151858
c_5	0.4768086672	-0.3703078628	0.8660150766	-0.8654692173	1.0000000000	0.0837469921	-0.1407952011	0.1180829257	-0.0013513683
c_6	-0.3727486730	0.2895865142	-0.1357219219	-0.0339770876	0.0837469921	1.0000000000	0.5813887715	0.0428055227	-0.0085262023
c_7	-0.4333691001	-0.0402938798	-0.3014900386	0.1274360120	-0.1407952011	0.5813887715	1.0000000000	0.4656391442	0.0083562285
c_8	0.3181966543	-0.5387134552	0.1074236929	-0.1985262632	0.1180829257	0.0428055227	0.4656391442	1.0000000000	0.0094732828
c_9	-0.0020462861	-0.0057730838	-0.0001874897	0.0000151858	-0.0013513683	-0.0085262023	0.0083562285	0.0094732828	1.0000000000

	m_A^{QE}	p_F	E_B	Δ_s	$m_A^{1\pi}$	$m_A^{N\pi}$	m_A^{coh}	σ_{DIS}	$\Delta \to \gamma\gamma$
m_A^{QE}	1.000	-0.205	0.430	0.000	0.000	0.000	0.000	0.000	0.000
p_F	-0.205	1.000	-0.924	0.000	0.000	0.000	0.000	0.000	0.000
E_B	0.430	-0.924	1.000	0.000	0.000	0.000	0.000	0.000	0.000
Δs	0.000	0.000	0.000	1.000	0.000	0.000	0.000	0.000	0.000
$m_A^{1\pi}$	0.000	0.000	0.000	0.000	1.000	0.000	0.000	0.000	0.000
$m_A^{N\pi}$	0.000	0.000	0.000	0.000	0.000	1.000	0.000	0.000	0.000
m_A^{coh}	0.000	0.000	0.000	0.000	0.000	0.000	1.000	0.000	0.000
σ_{DIS}	0.000	0.000	0.000	0.000	0.000	0.000	0.000	1.000	0.000
$\Delta \to \gamma\gamma$	0.000	0.000	0.000	0.000	0.000	0.000	0.000	0.000	1.000